The Thesis Committee for Erick M. Wright
Certifies that this is the approved version of the following thesis:

A Comprehensive Study of Nano-Scale Grain Boundary Channels in Fracture Cements Using Scanning Electron Microscopy, Electron Backscatter Diffraction, and Transmission Electron Microscopy

APPROVED BY
SUPERVISING COMMITTEE:

Supervisor:

Peter Eichhubl

William Fisher

Whitney Behr

A Comprehensive Study of Nano-Scale Grain Boundary Channels in Fracture Cements Using Scanning Electron Microscopy, Electron Backscatter Diffraction, and Transmission Electron Microscopy

by

Erick M. Wright, B.S.

Thesis

Presented to the Faculty of the Graduate School of

The University of Texas at Austin

in Partial Fulfillment

of the Requirements

for the Degree of

Master of Science in Geological Sciences

The University of Texas at Austin

May 2017

Dedication

In memory of Declan, Daniel, Robbie, and Andi.

Acknowledgements

I would like to thank my advisor Dr. Peter Eichhubl for his guidance, intellectual support, and input on this project and throughout my time as a graduate student at UT Austin. I would also like to thank the members of my thesis committee for reviewing this work. I thank Christopher J. Landry for the insightful input he provided. Our many discussions early in this project about NGBCs, ion milling sample preparation, and SEM imaging techniques greatly improved this work. I would like to express my appreciation for the various sources of funding I received during my graduate career. I thank the BP Fellowship Fund and The Elizabeth M. Teagle Scholarship Fund in Petroleum Geology Fund, which were provided by the Jackson School of Geosciences. I also thank the Fracture Research and Application Consortium (FRAC) for providing funds for initial analytical fees. I thank Statoil for providing further funding. This work was also partially supported by AAPG Grants-in-Aid and GSA Grants-in-Aid.

I thank members of FRAC for providing sample materials for this project. I also would like to thank Patrick Smith for his time and patience in training and assisting me with ion milling sample preparation and discussions about SEM and TEM techniques. I thank Cerium Laboratories for providing high quality TEM sample preparation and Dr. Shouliang Zhang and Dr. Damon Smith for assistance with TEM analysis. I thank Dr. Richard Piner for his assistance with EBSD analysis.

Most importantly, this work would not have been completed without encouragement and love from my girlfriend, Anna. She also put forth a great effort in proof-reading and editing this work. I am also thankful for the support of my friends and family.

Abstract

A Comprehensive Study of Nano-Scale Grain Boundary Channels in Fracture Cements Using Scanning Electron Microscopy, Electron Backscatter Diffraction, and Transmission Electron Microscopy

Erick M. Wright, M.S. Geo. Sci.

The University of Texas at Austin, 2017

Supervisor: Peter Eichhubl

Natural fractures in shale reservoirs are frequently filled with mineral cement that lack any residual fracture porosity visible under the petrographic microscope and are generally interpreted to be impermeable to fluid flow. Scanning electron microscopy of calcite, dolomite, quartz, and barite fracture cements from a variety of shale and low-permeability sandstone formations, prepared using broad ion beam milling, provides evidence of open to partially healed elongate pores that are on the order of hundreds of nanometers in aperture. In calcite, dolomite, quartz, and barite fracture cements, these pores have apertures of about 10-400 nm. In quartz fracture cements that have experienced low grade metamorphic temperatures in excess of 250^{O}C, they are up to 600 nm. These pores have been previously overlooked because traditional thin sectioning and polishing destroys sub-micron details of the fracture cement pore structure. Ion milling preserves these details. Electron backscatter diffraction shows that these pores occur along most grain boundaries within the blocky or columnar fracture cement. Mineral cement crystal faces are rarely

faceted on the nano-to-micrometer scale, but contain varying degrees of roughness with distinct morphologies. Pores tend to increase in aperture with increasing maximum formation temperature, indicating dissolution-precipitation kinetics strongly influences grain boundary structure. Stress relaxation from formation exhumation may also favor wider channel apertures, evidenced by a trend of wider apertures with increased distance of exhumation. HRTEM analysis shows different crystallographic domains with possible amorphous regions bridging across grain boundary channels, demonstrating that these channels are complex structures, contrasting the conventional view of diagenetic cement grain boundaries as simple crystallographic dislocations or discontinuities. I propose a model of dissolution-precipitation along grain boundaries that preserves NGBC ubiquitously in carbonate and quartz fracture cements that have experienced diagenetic and low-grade metamorphic conditions. While partially healed, these pores are frequently well connected and have strong implications for understanding flow through matrix cements of low permeability reservoirs. They may act as conduits for fluid flow along and across fully cemented natural fractures. When their effects are considered, they may universally increase estimates of formation permeability of low permeability formations containing cemented fractures.

Table of Contents

List of Tables

List of Figures

Chapter 1: Introduction

Barren and partially cemented opening-mode fractures are known to locally increase permeability, creating preferred pathways for fluid flow (Philip et al., 2002). In formations of otherwise low-permeability, they provide potential pathways for migration and production of oil and gas, as well as potential leakage pathways for hydrocarbons and injected waste fluids across top seals (Gale and Holder, 2010; Shukla et al., 2010; Walton and McLennan, 2013). Flow through these open and partially cemented fractures has been a topic of interest for decades (Cacas et al., 1990; Brown, 1995; Zimmerman and Bodvarsson, 1996; Oron and Berkowitz, 1998; Eker and Akin, 2006; Tokan-Lawal et al., 2017), but fractures in hydrocarbon reservoirs are commonly observed to be completely filled with mineral cements (Engelder et al., 2009; Gale et al., 2014) with little attention given to their fluid flow properties.

A lack of discernable pore space at the scale of conventional petrographic microscopy and scanning electron microscopy (SEM) has led to the understanding that diagenetic cements filling fractures completely occlude fluid flow (Philip et al., 2002; Gale et al., 2007; Loucks et al., 2009; Olson et al., 2009). However, many studies of low permeability metamorphic rocks that were also once thought to be impermeable have shown that open and potentially conductive nanometer-scale voids exist along grain and phase boundaries (Desbois et al., 2012; Kruhl et al., 2013; Bukovská et al., 2015).

In the case of fracture cements, previous observations using high resolution SEM and ion milling sample preparation revealed the presence of partially healed elongate pores along grain boundaries of calcite within a fully cemented fracture in the Eagle Ford Shale (Landry et al., 2016). Following similar observations in metamorphic rocks and synthetic aggregates made by Kruhl et al. (2013), Liteanu et al., (2012), Olgaard and Fitz Gerald

(1993), and van Noort et al. (2008), these pores were designated as nano-scale grain boundary channels (NGBCs). They were interpreted to be representative of subsurface reservoir conditions due to the presence of cement bridges that partially heal and fill the pores. These pores are consistently about 100 nm wide with various degrees of nanometer-scale undulation and non-faceted crystal shapes (Figure 1.1). According to Landry et al. (2016), when the occurrences of NGBCs are considered and upscaled to the reservoir scale, they are estimated to have the capability to increase the overall formation permeability by an order of magnitude. To my knowledge, the previous study of calcite fracture cement from the Eagle Ford Shale is the first study to identify nanometer-scale pore structures along grain boundaries of natural, completely cemented fractures. Because this study was based on a single suite of samples from a single core in the Eagle Ford Formation, it left unresolved how common these features are within fracture cements. This study also did not address mechanisms of formation of NGBCs. This thesis is a comprehensive study of NGBCs hosted in fully cemented opening mode fractures sampled from many formations.

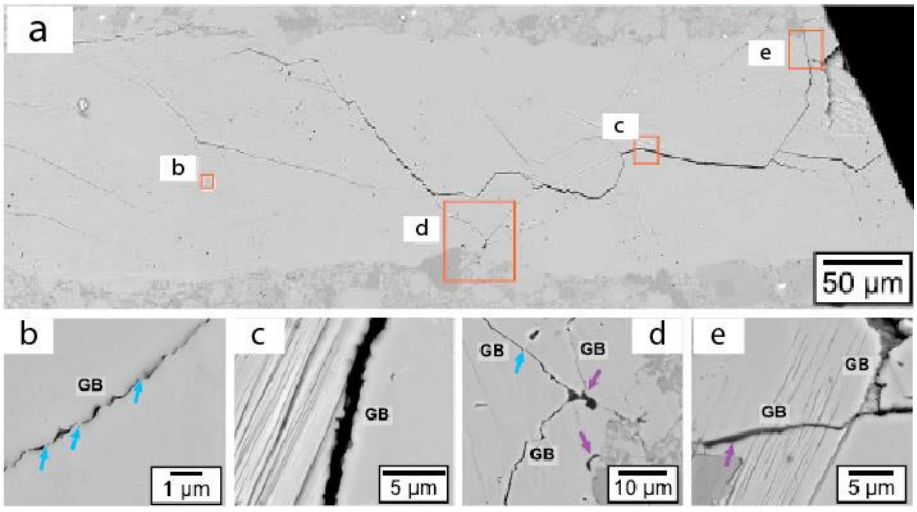

Figure 1.1: Backscattered electron micrographs showing examples of NGBCs from the Eagle Ford Formation. Sample was prepared using cross sectional broad beam argon ion milling. (a) Overview of calcite cemented fracture. Boxes show location of (b-e). (b-e) Detail of (a) showing examples of open grain boundaries. Grain edges tend to be wavy and non-mating. Blue arrows indicate bridging cement, and purple arrows indicate solid hydrocarbon fills. Modified from (Landry et al., 2016).

The structure of grain boundaries in sedimentary rocks has been of interest to geologists since pressure solution was first described by Weyl (1959). Since then much work has been done to model and experimentally reproduce natural grain boundary structures as reviewed further in chapter 2. However, those studies are mainly focused on grain boundaries under stress. Opening mode fractures precipitate cements in initially stress free environments and when pore fluid pressures exceed the lithostatic pressure.

I employed broad ion beam milling and several electron microscopy techniques to characterize grain boundary pore structures of fracture cements in several low permeability formations with various mineral cement compositions. In this thesis, I tested several hypotheses. First, since prior observations of these channels have only been documented in calcite cemented fractures of the Eagle Ford Shale, I tested whether these features are common to all fracture cements, or if they are mineral or formation specific. Next, I

investigated whether the occurrence of NGBCs is temperature dependent. Because porosity in bulk rocks and fractures tends to decrease due to an increase in cementation with increasing maximum formation temperature, I sampled rocks ranging in temperatures from 90^{O}C to in excess of 250 ^{O}C to test whether increasing formation temperature creates narrower NGBC apertures (Walderhaug et al., 2009).

Because fracturing along grain boundaries has been documented to occur during formation exhumation in low permeability rocks, I also tested whether greater distances of formation exhumation favor wider NGBCs (Vollbrecht et al., 1991; Anders et al., 2014). I used electron backscattered diffraction (EBSD) to distinguish NGBCs from microfractures that may have occurred during exhumation or core retrieval. EBSD also allowed me to test whether crystal orientation effects the width of NGBCs. Crystallographic orientation has been shown to influence pressure solution rate and controls faceting during recrystallization of quartz at high temperatures (Becker, 1995; Kruhl, 2001).

Since NGBCs were first documented by Landry et al., (2016) to contain various bridging cement and grain boundary morphologies with various degrees of undulation and non-faceted growth, I investigated if these textures follow any temperature regime. I compared these textural observations with what has been observed experimentally to interpret the processes that may control the occurrence of these textures. I performed transmission electron microscopy (TEM) on calcite-calcite grain boundaries to observe the atomic structure along the grain boundaries and within bridging cements to test whether these grain boundaries are simple crystallographic discontinuities or if they are more complex structures.

OUTLINE OF THESIS

Chapter 2 of this thesis gives an overview of previously published literature related to this thesis with a focus on the current understanding of voids in grain boundaries of low permeable materials and pressure solution. Chapter 3 outlines the details of the methods I employed and procedures I followed to carry out this study. Chapter 4 is a stand-alone journal style article focusing on the results, discussion, and conclusions of this thesis to be submitted to the Journal of Geophysical Research.

Chapter 2: Background

This chapter reviews the current understanding of topics relevant to this thesis. Attention is given to the structure of grain boundaries and pressure solution in rocks.

FRACTURE OPENING AND SEALING

Mode 1, or opening mode fractures, open in the direction of the least principal stress σ_3, with the plane of the fracture parallel to the greatest principle stress σ_1 (Zoback, 2007). The opening of mode 1 fractures occurs when an effective tensile normal stress acts perpendicular to the fracture (Twiss and Moores, 1992). Effective tensile σ_3 stress conditions occur as a result of bending during folding or when the pore pressure exceeds the least principal stress (Secor, 1965; Pollard and Aydin, 1988).

Open fractures in the presence of reactive fluids tend to fill with mineral cements which can partly or completely fill the open pore spaces (Batzle and Simmons, 1977; Eichhubl and Boles, 1998; Milodowski et al., 1998; Hood et al., 2003; Lander and Laubach, 2015). In some cases, it has been suggested that mineral cement precipitation drives fracture opening (Wiltschko and Morse, 2001). The degree to which a fracture is filled with mineral cement depends on whether the rate of mineral growth can keep up with the rate of fracture growth (Laubach, 2003, Olson et al., 2009).

Factors that are important to mineral cement precipitation kinetics are temperature, pressure, degree of supersaturation of dissolved species in solution, and detrital mineral composition (Walderhaug, 1996). While precipitation rates follow a positive correlation with temperature, it has been argued that the availability of broken, non-euhedral surfaces for new cement growth is as important as temperature is to growth rates in quartz and dolomite cements (Walderhaug, 2000; Lander et al., 2008; Gale et al., 2010) (Figure 2.1). It is generally believed that the permeability and pore space in fully cemented sedimentary rock are non-existent

(Philip et al., 2002; Laubach and Ward, 2006; Olson et al., 2009; Gale et al., 2010; Gasparrini et al., 2014). However, in chapter 4 I show that previously overlooked nanometer-scale pore space is commonly preserved along grain boundaries even in fractures that are otherwise completely cemented and that this nanometer-scale pore space is ubiquitous in all formations studied.

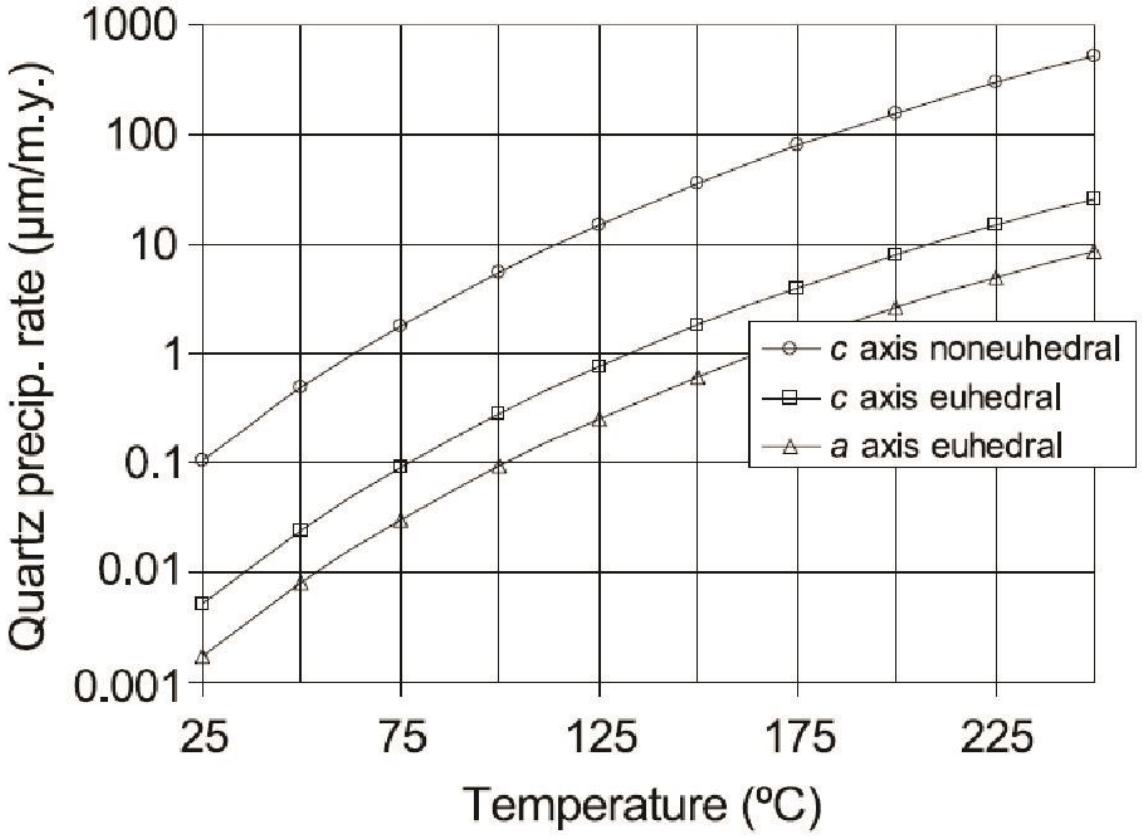

Figure 2.1: Plot of the rate of quartz precipitation rates as a function of temperature for quartz cementation with a fracture growing: parallel to c-axis growing on non-euhedral surfaces (fastest), parallel to c-axis on euhedral surfaces, and parallel to the a-axis on euhedral surfaces (slowest). Modified from (Olson et al., 2009).

GRAIN BOUNDARIES

Grain Boundary Description

A grain boundary is a region that separates two crystals of the same composition and structure with opposing lattice orientation directions described geometrically using five independent variables, or degrees of freedom (Sutton and Balluffi, 1995). Three of these describe the three-dimensional rotation that would bring the two crystals together—two for the rotation axis [*uvw*], which is defined by two direction cosines, and one for the angle θ quantifying the degree of rotation around this axis. Two additional variables describe the grain boundary plane, defined by the direction cosines of its normal *n*. In natural samples, the plane of the grain boundary is difficult to determine in three dimensions. Therefore, grain boundaries are generally described by a misorientation angle, which is the smallest possible rotation that would bring the lattices into alignment. Grain boundaries are either pure twist, containing the axis of rotation perpendicular to the grain boundary plane, pure tilt, containing the axis of rotation parallel to the grain boundary plane, or a combination of both. They are further characterized as either low-angle grain boundaries (~<15º) or high angle grain boundaries (>15º) (Priester, 2013). This characterization has implications for grain boundary energy, as described later in this section (Read and Shockley, 1950; Wolf, 1990).

Grain Boundaries in Low Permeability Crystalline Materials

Generally, grain boundaries in crystalline metals and rocks are regarded as being stable, impermeable, compact features, even at high angles of misorientation (Wolf and Merkle, 1992). In metals, grain boundary voids are generally associated with applied tensile stress or the presence of particles and impurities leading to material failure (Hull and Rimmer, 1959; Cocks and Ashby, 1982). Several mechanisms of cavity nucleation

have been proposed but have not been experimentally verified (Riedel, 1987). The possible initiation mechanisms include the following: cracking or vacancies due to pileup of dislocations, presence of a particle within the boundary under tensile or shear stress causing a weak interface, grain boundary sliding at steps or triple junctions, or a combination of dislocation pile up and weak particle interface interaction (Sutton and Balluffi, 1995) (Figure 2.2).

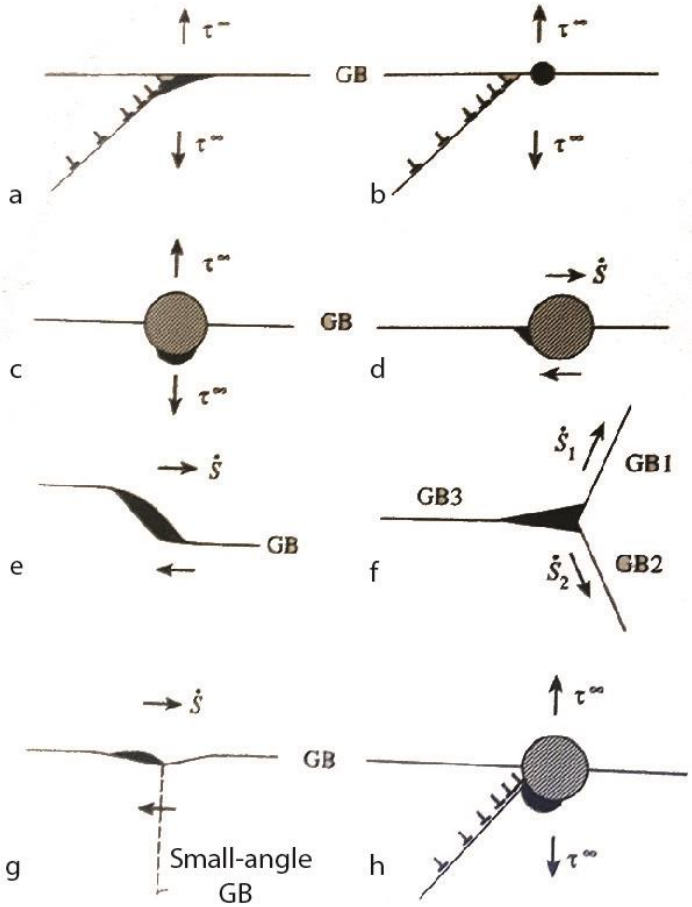

Figure 2.2: Models for void nucleation as summarized by Sutton and Balluffi (1995). Nucleation of voids along grain boundaries in metals can be caused by the following: (a) cracking at high stress caused by dislocation pile-up, (b) vacancy aggregation caused by dislocation pile-up, (c) weak particle/matrix interface under tensile stress, (d) sliding along a grain boundary containing a weak particle/matrix interface, (e) high tensile stress produced at step by sliding, (f) high tensile stress produced at a triple junction by sliding, (g) high tensile stress produced by sliding at a depression at an intersection with low angle grain boundary, and (h) combination of dislocation pile-up and weak particle matrix interface.

In metamorphic rocks, pores along grain boundaries are generally associated with reworking of fluid films and fluid inclusions during grain boundary migration associated with dynamic recrystallization. For instance, Hay and Evans (1988) used TEM imaging to demonstrate that pores along metamorphosed calcite grain boundaries in compaction experiments are not stable, and grain boundaries are not wetted by a fluid phase, so that mass transport must then occur along fractures, joints, and migrating grain boundaries. Mancktelow et al. (1998) and Mancktelow and Pennacchioni (2004) reported isolated nanometer-scale pores and millimeter-scale vug-like pores along grain boundaries in quartz-rich mylonites using conventional SEM imaging. They interpreted them to have formed as a result of recrystallization and reworking of fluid inclusions during metamorphism.

Grain boundary voids caused by secondary processes in igneous and metamorphic rocks have been reported. Vollbrecht et al. (1991) observed voids along grain boundaries in granitic igneous rocks and interpreted them to have been caused by fracturing during exhumation. Kruhl et al. (2013) observed open voids along grain boundaries of several grades of quartz-rich metamorphic rocks and attributed them to anisotropic contractional cooling during exhumation and retrograde metamorphism. The presence of voids along grain boundaries in lower temperature materials, such as sedimentary rocks, is mainly thought to be related to dissolution-precipitation reactions initiated by stress, as in grain boundaries undergoing pressure solution, which I describe in detail later in this chapter. This thesis investigates their presence in diagenetic cements hosted in initially stress free opening mode fractures.

Influence of Interfacial Energy on the Structure of Grain Boundaries

A system composed of two components forming interfaces, or grain boundaries, has an excess of free energy that is a function of the Gibbs free energy of the entire system, the Helmholtz free energy of the system, and the grand potential of the system (Gibbs, 1878; Cahn and Hilliard, 1958). At the atomic scale, the energy of a low angle crystalline grain boundary is a function of the density of dislocations along the boundary. An increase in misorientation between the grains creates more dislocations per area, thus linking the misorientation angle to the energy (Read and Shockley, 1950). This holds true for low angle grain boundaries, but above 15º, dislocations start to overlap and this no longer holds true. Grain boundary energy becomes nearly uniform for high angle grain boundaries, except at special values of misorientation where energy drops to very low values. The orientation of the grain boundary plane has a greater impact on the grain boundary energy than the misorientation (Wolf, 1990) (Figure 2.3).

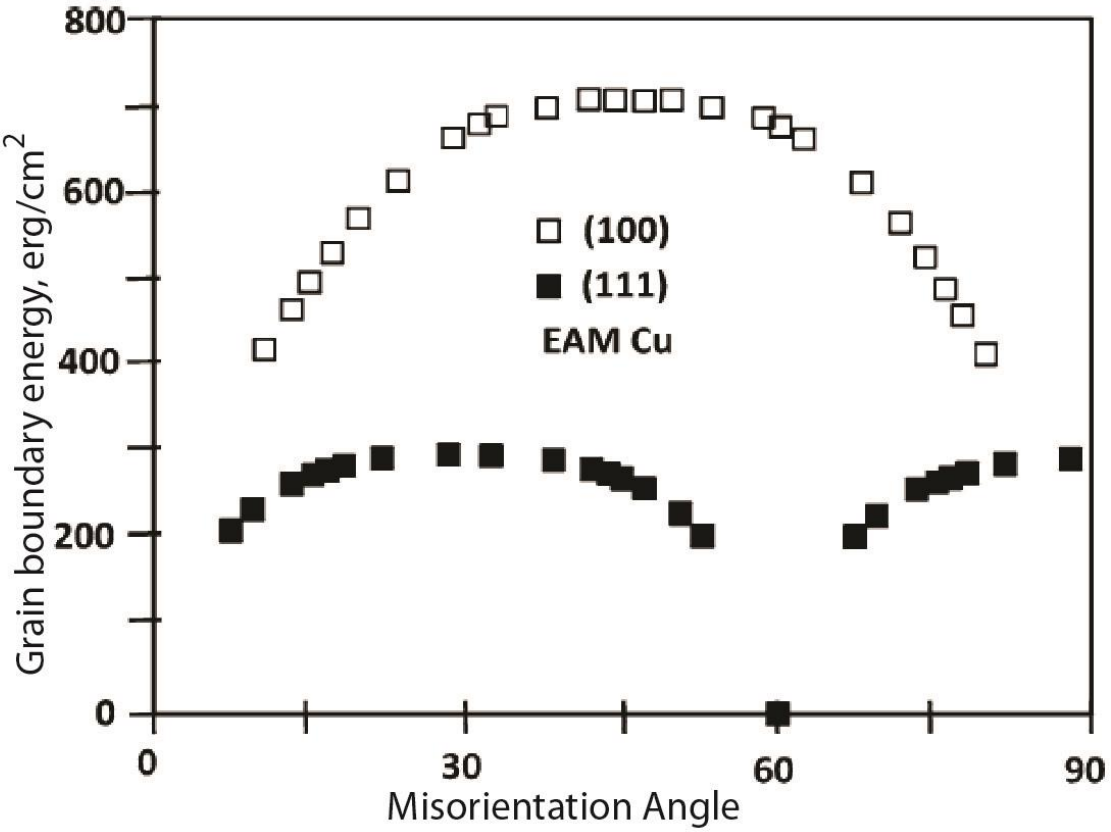

Figure 2.3: Correlation between grain boundary energy and misorientation angle for twist grain boundary planes oriented at (100) (open squares) and (111) (closed squares) for copper using an embedded atom model potential. The difference in the orientation of the grain boundary plane has a much greater influence on the energy of the boundary than the misorientation between them at high angle boundaries. Modified from (Rohrer, 2011).

While these boundaries are stable and generally impermeable structures, they can undergo changes in their structure to reduce the interfacial free energy of the system. A reduction in the energy per unit area of the system drives the process of grain growth and coarsening in ceramics and metals (Gibbs, 1878; Mullins, 1956; Kang, 2004). Grains grow larger during sintering, annealing, and deformation at the expense of other grains, causing grain boundary mobility to minimize interfacial free energy (Yan et al., 1976; Voorhees, 1985; Larala et al., 1989; Rollett et al., 2004; Gottstein and Shvindlerman, 2010). Grain boundary complexions, which is the term used for an interfacial material that is in thermodynamic equilibrium with the neighboring phases, have a stable thickness on the order of atomic layers to a nanometer and may cause abrupt changes to the chemical or physical structure of a grain boundary at critical values of temperature and pressure (Cantwell et al., 2014).

Similar to ceramics and metals, interfaces in metamorphic rocks undergo similar changes to drive toward the lowest energy state. The highest rates of grain boundary migration due to recrystallization and grain growth occur at high angle grain boundaries at high temperatures in the presence of water (Schmid et al., 1980; Urai et al., 1986; Schmid et al., 1987). The results of grain boundary migration are sutured grain boundaries, kink-band boundaries, and deformation twin boundaries (Stünitz and Gerald, 1993; Vernon, 2004). While many quartz grain boundaries formed by grain boundary migration appear to be rounded, there is evidence that the equilibrium shapes are compact, straight segments with steps (Kruhl, 2001; Kruhl and Peternell, 2002). Mainly, pores thought to exist along these grain boundaries are isolated pores created by fluid films reworked subsequently to grain boundary motion, as mentioned earlier (Urai, 1983; Mancktelow et al., 1998; Mancktelow and Pennacchioni, 2004).

PRESSURE SOLUTION

Unlike mechanisms such as grain boundary migration that occur under metamorphic conditions, deformation by pressure solution is important at both diagenetic and metamorphic conditions (Wassmann and Stöckhert, 2013). Pressure solution was first observed and described by Weyl (1959) and has been widely studied since. It is defined as a three-step process that includes the dissolution of soluble minerals occurring at stressed grain contacts, diffusion and transport of dissolved material away from the grain contact area, and precipitation of the dissolved species onto a substrate within the pore fluid (Gratier et al., 2013) (Figure 2.4).

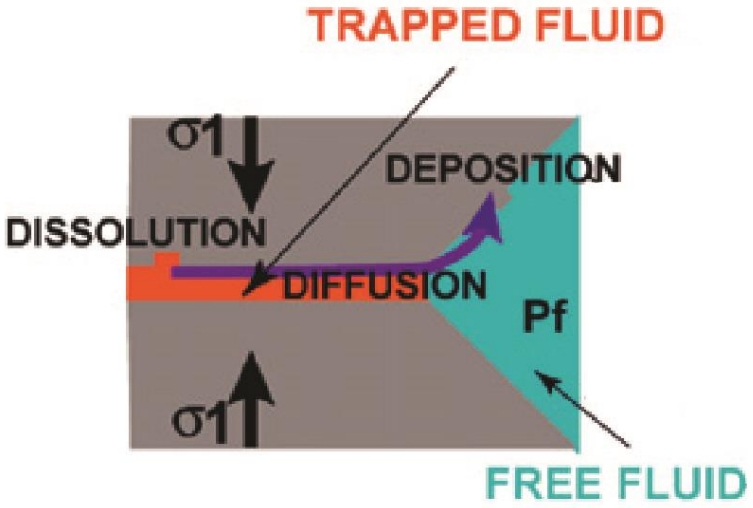

Figure 2.4: Schematic of the pressure solution process at the grain scale. Pressure (σ_1) acts on two grains (grey) containing a pore fluid between them (orange). Diffusion from the grain occurs via the pore fluid into the free pore fluid (blue). Deposition occurs on the grain faces in the free pore fluid. From Gratier et al., 2013.

Theoretical Studies

The theoretical framework for pressure solution was laid out with the recognition of interactions between mechanical and chemical processes by Sorby (1864). Gibbs (1878) subsequently proposed that differences in chemical potential can be caused by pressure and

interfacial tension. These ideas were later formulated into the three-step process of pressure solution by Weyl (1959), who also theorized that a thin fluid film exists at the grain contacts. The structure and properties of this thin fluid film is a topic of debate to this day.

Dissolution at the grain contact is activated by a normal stress along the loaded grain contacts (Paterson, 1973). This process occurs in a dynamic equilibrium condition occurring microscopically at the grain contact (Lehner and Bataille, 1984; Spiers and Schutjens, 1990). The transport mechanism is driven by a stress-induced difference in chemical potential between the stressed contact and deposition site (Weyl, 1959; Rutter and Elliott, 1976; Dewers and Ortoleva, 1990; Renard et al., 1999).

Rate laws for pressure solution have been proposed based on thermodynamic and kinetic laws. Depending on the rate limiting step, there can be many rate laws (Raj, 1982). While normal stress is thought to be the greatest driving force for pressure solution, rates are also affected by interfacial forces, strain energy, grain size, and crystallographic orientation (Rutter and Elliott, 1976; Raj and Chyung, 1981; Tada and Siever, 1986; Becker, 1995; Heidug, 1995; Alcantar et al., 2003; Greene et al., 2009).

Experimental Studies

Compaction experiments as early as the mid-1970s on salt (Rutter and Elliott, 1976) and quartz (De Boer et al., 1977; Robin, 1978) simulated pressure solution in compaction experiments. Since then, more advanced experiments have been performed on several different minerals, leading to the understanding of several aspects of the pressure solution processes, as highlighted below. Direct observations of the structure of the interface during these experiments are limited by resolution capabilities (Hickman and Evans, 1991; Gratier, 1993). Understanding of compaction experiments while measuring some other parameter at the grain boundary or mineral-fluid interface such as strain, transport

properties, impedance, or surface forces are complicated not only by the nanometer-scale resolution required for observation, but also by the coupling of pressure solution processes with plastic deformation and electrochemical interactions (Gratier et al., 2013).

From compaction experiments, it was observed that pressure solution is not a steady state process, but follows a power-law time dependence, and strain rate is controlled by grain boundary geometry and stress (Dysthe et al., 2002; Gratier et al., 2009; Croizé et al., 2010). Observation of a dynamic grain interface with channels and islands was observed using confocal microscopy (Karce et al., 2008). Hickman & Evans (1991; 1995) documented the retarding effects of grain boundary healing through compaction experiments using halite pressed against a glass lens.

In situ measurements of the transport properties of the grain boundary during pressure solution experiments showed that transport is dependent of the grain boundary structure (de Meer et al., 2002; Alcantar et al., 2003; Van Noort et al., 2011). Experiments also led to the understanding that fracturing increases the rate of pressure solution (Gratier et al., 1999; Zubtsov et al., 2004). Later, experiments conducted with a surface forces apparatus led to the understanding that electrochemical reactions driving dissolution between quartz and clay minerals also increase the rate of pressure solution (Anzalone et al., 2006; Greene et al., 2009; Kristiansen et al., 2011). The role of pressure on surface dissolution may be limited to maintaining close contact between quartz and clay mineral rather than driving dissolution as in conventional pressure solution (J. Boles, oral communication). Several of the studies mentioned above have been fundamental to the current understanding of pressure solution processes in both diagenetic and metamorphic rocks, but it is unclear if they relate to the processes governing the structure of grain boundaries of fracture cements filling opening-mode fractures where grain surfaces, at least

at the time of fracture opening, are free from compressive stresses acting upon the fracture surfaces.

Pressure Solution Grain Boundary Models

The parameters important to the transport process are the transport length, the diffusion coefficient of the material in the grain boundary region, and the fluid film, or grain boundary, thickness (Dysthe, 2014). Because the structure of the grain boundary determines the rate at which material is transported, there have been several models that predict the structure of the stressed, fluid-filled grain boundary.

Generally, there are four models that have been proposed and debated based on interpretations of theoretical and experimental studies (Figure 2.5). The first two models described here consider a static grain boundary, whereas the latter two assume a dynamic grain boundary structure. The thin fluid film model assumes that each grain boundary is continuously flat and contains a thin fluid film on the order of 1-100 nm (Weyl, 1959; Hickman and Evans, 1995). This film is assumed to be structured and able to transmit stress, allowing diffusive transport during deformation. The static island-channel model proposes that grain boundaries are in contact, containing contacting "islands" and open "channels" (den Brok, 1998). Microcracking causes the channels to form where pore fluids interact with the grain surfaces, allowing transport of diffused "island" material. Therefore, according to this model, the rate at which microcracking can occur governs the rate at which pressure solution occurs.

The dynamic rough model assumes a rough grain boundary with contact regions that continuously dissolve and form new contact regions (Lehner, 1995). These contact areas do not inhibit transport. Therefore, the limiting transport length is the radius of the grain boundary. The dynamic island-channel model (Spiers and Schutjens, 1999; Dysthe

et al., 2003; van Noort et al., 2008) is similar to the static island-channel model. However, the dynamic model results in an increase in the island size due to strain hardening. Depending on the structure of the interface, keeping all other parameters equal, strain rates are estimated to be up to seven orders of magnitude different for different grain interface models (Dysthe, 2014).

These grain boundary models are representative of grains undergoing active pressure solution under an imposed normal stress, whereas this thesis is concerned with mostly monomineralic cement grains filling opening mode fractures that are free from normal stresses acting on the fracture surfaces, apart from the fluid pressure acting within the fracture. Therefore, these models are not likely to accurately describe the structure of NGBCs.

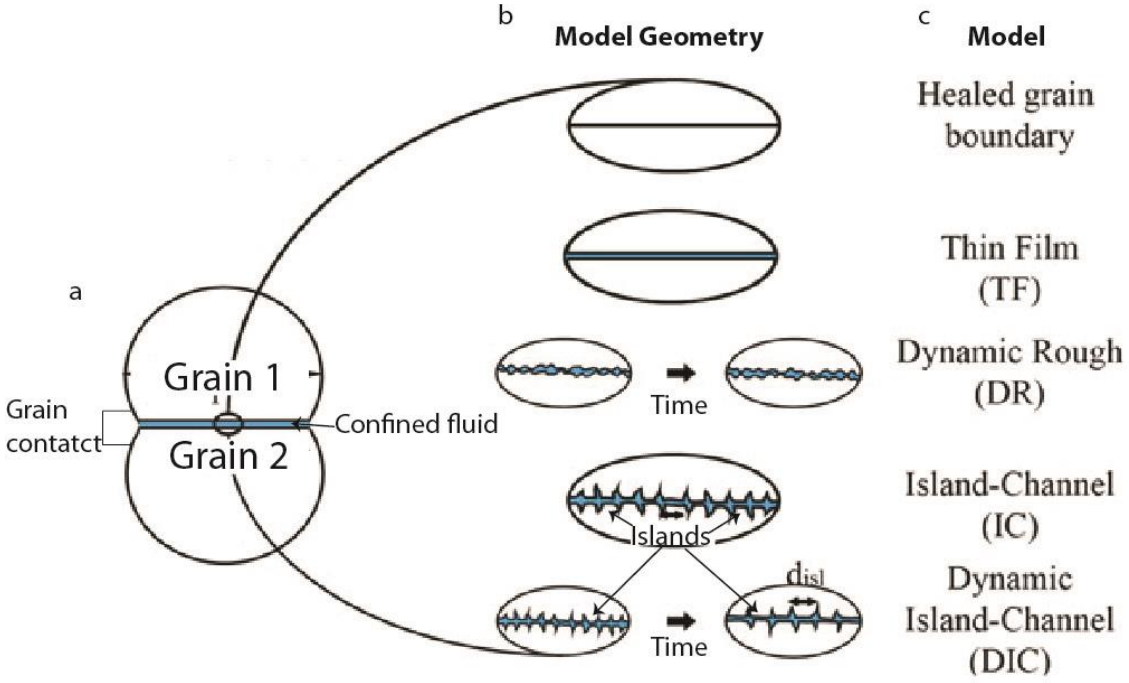

Figure 2.5: Grain boundary models as summarized by Dysthe (2014). (a) Two grains in contact containing a pore fluid between them. Circle indicates location of (b). (b) Geometry of models presented with model names in (c).

Crystal Growth Within Fractures and Pores

A crystal growing in confinement, such as a pore or fracture, is able to exert a force on its surroundings, as long as a supersaturated thin fluid film exists to provide deposition of material needed for growth (Renard and Ortoleva, 1997). The force exerted is a function of the supersaturation, crystal-fluid interfacial energy, and local curvature (Steiger, 2005). When a crystal grows in confinement, the required space for growth is accommodated by either dissolution or fracturing, depending on the properties of the host rock and kinetics of mineral growth (Fletcher and Merino, 2001). Crystals growing from solution under a normal stress have been observed to coarsen initially and are thought to eventually smooth out (Angheluta et al., 2009; Jettestuen et al., 2009; Røyne and Dysthe, 2012).

Chapter 3: Methods

This chapter details and justifies the methods employed and the workflow followed for this thesis.

SAMPLE SELECTION CRITERIA

Fractures used for this study were selected from both core and outcrops from several formations, spanning a range of burial histories, host rock compositions, and mineral cement composition. Although some came from outcrops, preference was given to core to rule out effects of exhumation and outcrop contamination. Suitable samples are those that contain the following criteria: 1) fully cemented fractures containing mostly a single, coarse grained mineral cement; 2) at least hundreds of microns in aperture; 3) are competent enough to withstand cutting and shaping prior to ion milling; 4) have minimal fracture porosity when viewed in thin section and hand sample; and 5) are contained within a low permeable host rock. Data for maximum burial temperatures and distance of exhumation were derived from previously published literature. Details of all samples are contained in Table 3.1.

Sample Number	Fm.	Cement	Locality	Sampled Depth (ft)[m]	Max Depth (m)	Exhumation (m)	Max Temp (°C)
BRTC1-12083	Barnett	Barite	West Texas Delaware Basin, Pecos County	12083 [3683]	3683[A]	0	105-110
BRTC1-12421	Barnett	Calcite+ Barite	West Texas Delaware Basin, Pecos County	12421 [3786]	3786[A]	0	105-110
06212-2	Campito	Quartz+ Calcite	White Inyo Mountains	Outcrop	10000[B]	10000	250
12-RF-2	Cardium	Calcite	Ram Falls, Alberta, Canada	Outcrop	5000[C]	5000	100-120
12-BR-3	Cardium	Quartz	Bow River, Alberta, Canada	Outcrop	5000[C]	5000	100-120
HF-18000	Haynesville	Calcite	Louisiana East flank of Sabine uplift	18000 [5000]	5486[D]	0	150-170
M-3658.5B	Marcellus	Calcite+ Quartz	Appalachian Plateau	6358.5 [1938]	4938[E]	3000	150-160
A1-4982.2	Monterey	Dolomite	A1 Well, Platform Irene, Offshore Santa Maria Basin, California	4982.2 [1519]	2319[F]	1500	110
2/26/95-2	Monterey	Dolomite	Jalama Beach, Santa Maria Basin, California	Outcrop	750[G]	750	80
NAM-2744.5	New Albany	Calcite	Pike County, Indiana	2774.5 [846]	2169[H]	1323	90-100
NAM-2784	New Albany	Calcite	Pike County, Indiana	2784 [849]	2172[H]	1323	90-100
NAC-3590	New Albany	Calcite	West Kentucky, Rough Creek Fault	3590 [1094]	2417[H]	1323	90-100
12-GC-9	Nikanassin	Calcite	Grand Cache, Alberta, Canada	Outcrop	7000[I]	7000	170-200
12-GC-12	Nikanassin	Calcite+ Quartz	Grand Cache, Alberta, Canada	Outcrop	7000[I]	7000	170-200
SFOT-1-10106.8	Travis Peak	Quartz	SW flank Sabine Arch Nacogdoches County, TX	10106.8 [3081]	3481[J]	400	140-170

Table 3.1: Samples used in this thesis. Sources: A: Luo et al., 1994; B: Doungkaew, 2017; C: Hardebol et al., 2009; D: Nunn, 2012; E: Evans, 1995; F: Eichhubl and Boles, 1998; G: Keller and Isaacs, 1985; McCrory, 1995; H: Strąpoć et al., 2010; I: Kalkreuth and McMechan, 1996; J: Dutton and Diggs, 1990.

TECHNIQUES FOR DOCUMENTING NANOMETER-SCALE PORES IN ROCKS

Imaging nanometer sized pores using traditional thin section and SEM techniques is difficult because the polishing process causes plucking of grains due to differential hardness in samples. Epoxy, which is traditionally used for thin section impregnation, further obscures nanometer scale structures. Focused ion beam (FIB) milling has been used to image low permeability rocks, such as shales and metamorphic rocks, by employing either slice and image techniques coupled to the SEM or as preparation for transmission electron microscopy (Wirth, 2009; Curtis et al., 2010; Bernard et al., 2012; Curtis et al., 2012; Kruhl et al., 2013; Bukovská et al., 2015). FIB slice and image, as well as TEM imaging, are limited to very small sample sizes, and the gallium ion gun used for FIB milling is highly destructive and can cause many artifacts to the sample.

Broad beam argon ion milling produces a polished area of up to several mm^2, while FIB milling can produce a sample of only about 100 μm^2 and was initially applied to geologic studies by Loucks et al (2009). This technique has been employed extensively to image and characterize pores in mudrocks, rocksalt, dolomites, and tight-gas sandstones (Wang and Reed, 2009; Desbois et al., 2011; Desbois et al., 2012; Loucks et al., 2012; Olanipekun and Azmy, 2016). To my knowledge, Landry et al. (2016) were the first to employ this technique on fracture filling diagenetic cement.

LABORATORY WORKFLOW

Several imaging techniques were utilized for this study. A strict workflow was followed to carry out all desired imaging and analysis on a single sample. A summary of the techniques used are provided in table 3.2. The details of these techniques are explained further in the following sections.

First, samples were screened for suitability using previously prepared thin sections, when possible. Selected samples were then cut and ion milled. Next, electron backscatter

diffraction (EBSD) data was collected under low vacuum mode with no conductive coating. The iridium coating used for scanning electron microscopy (SEM) imaging interferes with the EBSD diffraction patterns, so EBSD data must be collected first. Next, samples are iridium coated and imaged using SEM. Samples were then prepared for transmission electron microscopy (TEM) using focused ion beam SEM (FIB/SEM) coupled with *in situ* lift out, conducted commercially by Cerium Laboratories, Austin, TX. TEM imaging is performed last because of the destructive nature of TEM sample preparation.

Technique	Instrument	Machine Settings	Data Obtained
Ion Milling Preparation	Leica TIC 020	8 kV for 10 hours	Sample Preparation
EBSD	Oxford Instruments Nordlys EBSD/Phillips XL30/ FEI Quanta FEG 600	30 kV, 2-10 µm step size	Grain orientation, grain boundaries
Inlens SE	Zeiss Sigma FE-SEM	7-10 kV, 7-10 µm aperture	SEM mosaic, high resolution SEM
SE2	Zeiss Sigma FE-SEM	7-15 kV, 10-30 µm aperture	Sample topography
BSE	Zeiss Sigma FE-SEM	15-30 kV, 60-120 µm aperture	Atomic weight contrast
EDS	Zeiss Sigma FE-SEM	15-30 kV, 60-120 µm aperture	Chemical composition
FIB/SEM	Commercial Preparation on FEI Strata 400S	5-30 kV	Sample x-section, TEM sample preparation
TEM	JEOL 2010F	200 kV	Nanometer scale orientation, chemistry

Table 3.2: Summary of imaging techniques, instruments, parameters, and the purpose of each technique used in this thesis.

SAMPLE PREPARATION

Grain boundary channels are below the resolution of transmitted light petrographic analysis and cannot be imaged with SEM on conventional polished thin sections because mechanical polishing destroys nanometer scale features. I employed broad beam argon ion milling, which ensures an even polish with little preparation artifacts, while eliminating the damage caused by traditional mechanical polishing. When combined with Field Emission-SEM, I could resolve features as small as one nanometer. Cross sectional ion milling places a shield over the sample and concentrates the ions, producing a polished area that is about 2 mm^2 in area with little damage and minimal artifacts. However, streaking across the surface does occur due to differences in material properties (e.g. fracture walls, edge of sample) (Figure 3.1).

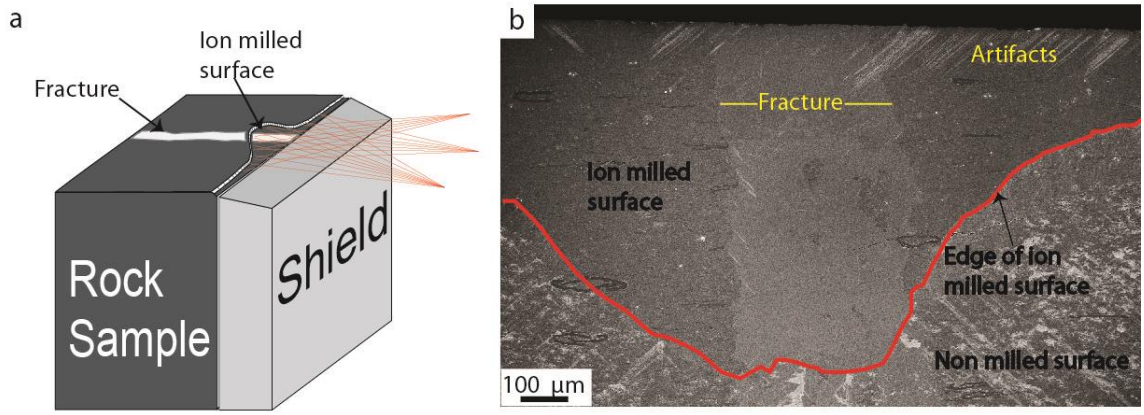

Figure 3.1: (a) Schematic representation of the ion milling process. (b) Inlens SEM micrograph of a representative ion milled surface of a calcite cemented fracture in New Albany Shale, sample NAM-2784. The ion milled area is outlined in red. The aperture of the fracture is outlined in yellow. White linear streaks along the edge of the sample are artifacts from the milling process.

Sample Shaping and Mounting for Ion Milling

First, a selected sample was cut from core or large outcrop sample with a large slab saw or trim saw. Samples must be cut further with a slow speed saw to about 1-3 cm in width and about 1 cm in thickness to fit into the ion miller. The edges that fit between the mask and mount must be parallel to ensure that the sample sits evenly in the chamber. After cutting, the sample must contain the intact fracture, a sharp edge free of plucked or chipped grain, and two parallel sides perpendicular to the edge of the surface that is to be milled.

After a sample is cut small enough to fit into the ion mill chamber, it is mounted to a glass slide, which is attached to the sample holder. The sample is attached to the slide with a small amount of carbon paint and centered using a jig as a guide. The jig is then removed from the slide, and the holder is placed into the ion miller (Figure 3.2).

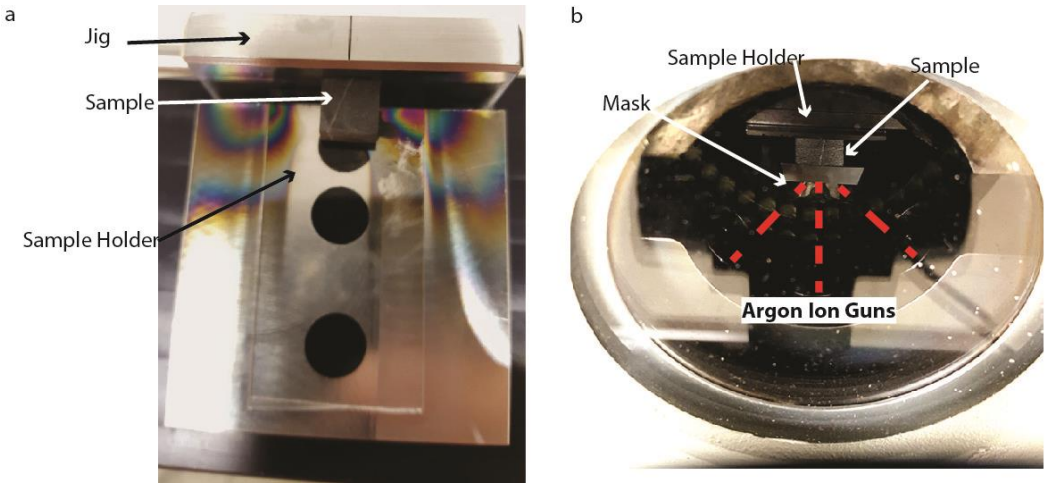

Figure 3.2: (a) Example of a sample mounted to the ion milling sample holder attached to the jig prior to insertion into the ion miller. The milling surface on the sample is abutted against the jig. (b) Sample after being loaded into the ion mill chamber. The orientation of the sample is perpendicular to the orientation of the sample in (a). Argon ions are sent in the plane of the image toward the sample. The milling surface is in the plane of the image.

Ion Milling

Ion milling was performed on a Leica TIC02 Ion Miller. After the sample is inserted into the chamber and under high vacuum, the rest of the process is automated. All samples were milled using 8 KeV and 2.8 mA running for 10 hours.

Mounting Prior to Imaging

After ion milling and prior to SEM imaging, samples were mounted on a stub designed to hold samples for SEM imaging. A piece of two-sided conductive carbon tape is used to hold the sample on the stub. A layer of iridium is placed on top of the sample to reduce the effects of charging during interaction with the electron beam. Samples were coated with between 4-6 nm of iridium using a Leica ACE 600 High Vacuum Coater. To further reduce charging effects, carbon paint is applied to the sides of the sample.

IMAGE COLLECTION

Instrumentation

A Zeiss Sigma Field Emission Scanning Electron Microscope within the Bureau of Economic Geology was used for high resolution secondary electron (SE2), inlens secondary electron (inlens SE), backscattered electron (BSE), variable pressure secondary electron (VPSE), and EDS imaging. An FEI XL30 Environmental Scanning Electron Microscope (ESEM) within the Department of Geological Sciences at UT Austin and a FEI Quanta FEG 600 within The Texas Materials Institute at UT Austin were used for electron backscattered diffraction (EBSD) imaging, a dual beam FEI Strata 400S at Cerium Laboratories was used for preparing Transmission Electron Microscopy (TEM) samples, and a JEOL 2010F Transmission Electron Microscope within The Texas Materials Institute at UT Austin was used for high resolution transmission electron microscopy (HRTEM) and scanning transmission electron microscopy (STEM) imaging.

IMAGING TECHNIQUES

Electron Backscatter Diffraction

Electron backscatter diffraction (EBSD) is used to obtain crystallographic orientations of samples. When collecting EBSD data, the sample is tilted at 70 degrees and a high accelerating voltage and high beam current are used to diffract backscattered electrons toward the detector. The EBSD detector is a combination of a phosphor screen and a digital camera. The phosphorescent screen detects a characteristic pattern of electrons created by the crystal structure and orientation that is read by the camera. I scanned samples using EBSD to map the orientations of grains in cements, to locate grain boundaries, to differentiate grain boundaries from microfractures, and to obtain misorientation angles between grains. EBSD data was collected under low vacuum mode using a step size of 5-10 μm and accelerating voltage of 30 kV.

Inlens Secondary Electron

The inlens secondary electron detector was employed for imaging mosaics in SEM for comparison with EBSD grain maps and to obtain high resolution SEM images. Mosaics were obtained with pixel resolutions of 75 nm. High resolution images were obtained with pixel resolutions of up to 1 nm.

The inlens detector is positioned directly above the sample, inside the SEM pole piece, and has a very small interaction volume, and for those reasons provides the best spatial resolution with both the least beam interaction and damage incurred by the sample. The inlens detector also shows an edge charging effect, especially at lower magnifications. This effect can be utilized to highlight edges and interfaces between a solid and empty space, which in this case highlights fractures and grain boundaries. Typical beam conditions used for inlens SE were 5-10 kV with a 7-10 μm aperture.

Transmission Electron Microscopy

The Transmission Electron Microscope uses a high accelerating voltage on thin samples to obtain sub-nanometer scale resolution images. I used TEM primarily to analyze the atomic structure close to and within NGBCs and obtain chemical composition information at the nanometer scale. The sub-nanometer resolution obtained using TEM is achieved by the high accelerating voltage transmitted through the sample. This is not possible with EBSD or EDS on SEM systems.

Everhart Thornley, Backscattered Electron, and Energy-dispersive X-ray Spectroscopy

I used the Everhart Thornley, backscattered electron, and energy-dispersive X-ray spectroscopy detectors less commonly than the previously described imaging techniques. The SE2 detector, commonly known as the Everhart Thornley, or E-T detector, detects both secondary electrons and backscattered electrons. It is the most commonly used, most basic detector of most SEM systems. Because of the position and gain applied to the detector, it is very efficient at collecting secondary electrons and less efficient at collecting backscattered electrons, making the SE2 image a mostly topographic signal with a very small contribution relying on the atomic mass of the material. SE2 mode relies on a deeper interaction volume than the inlens secondary electron detector, which slightly compromises spatial resolution. For most purposes in this study, because of the ability for the inlens secondary electron detector to work with lower accelerating voltage and greater spatial resolution, it was generally favored over SE2 mode.

I used the backscattered electron (BSE) detector mostly for low magnification imaging. The BSE detector requires a high interaction volume and high beam energy because backscattered electrons are high energy electrons. Therefore, they require high energy to scatter from the sample to the detector. Typical beam settings under BSE mode

are 15-25 kV and aperture of 60-120 μm. Because of the higher current, resolution is compromised when compared to that of the secondary electron detectors. The advantage of BSE over SE detectors is that it can give chemical compositional information; materials composed of atoms of higher atomic number will appear brighter than those of lower atomic number.

Energy-dispersive X-ray spectroscopy (EDS) provides semi-quantitative chemical compositional information. To do so requires a higher accelerating voltage and higher beam current, which can cause sample damage and a reduction in spatial resolution. EDS was used sparsely in this study to identify mineral cement compositions and secondary infill, such as hydrocarbon and clay minerals.

POST-ACQUISITION

Samples were characterized based on the range and sample mean of measured apertures and the relative abundance of morphologies observed that are created by various textures of bridging cements and grain boundaries. Below I outline the procedure I followed in order to map grain boundaries, measure the aperture of NGBCs, characterize samples, and calculate relative abundances of observed morphologies.

EBSD Grain Map Processing

Following acquisition, EBSD data was processed using Oxford's EBSD Channel 5 data processing software. The software removes pixilation and anomalous incorrect data points, fills small areas of zero solution using iteration of neighboring data points, and composes the data points into grain maps. Inverse pole figures were composed to display orientations with respect to the c-axis of calcite and quartz grains. Channel 5 software also calculates relative misorientation angles between neighboring grains.

Measuring NGBC Apertures

Following SEM image acquisition, I optimized contrast and brightness of micrographs using Adobe Photoshop. I compared EBSD grain maps with secondary electron mosaics to identify locations of grain boundaries (Figure 3.2). Elongate pores imaged with inlens SE were determined to be either NGBCs or fractures based on their relationship with EBSD inverse pole figures. Pores located along areas of crystallographic misorientation are considered NGBCs; pores located within domains of the same orientation are considered microfractures.

I adopted the method of Landry et al. (2016) when determining if the grain boundary aperture was likely to be representative of the aperture at subsurface conditions, free of dilation induced during core retrieval and/or sample handling (Figure 3.3). Only open NGBCs that contain bridging cement that traversed the width of the NGBC were accepted as naturally occurring and representing *in situ* apertures. Wavy, non-mating edges are also likely to have formed in the subsurface, but only those contacting neighboring grains or containing bridging cement traversing the entire width of the channel can be assumed to represent apertures free of dilation during core retrieval and/or handling. Landry et al. (2016) applied criteria to describe grain boundaries as conductive or non-conductive based on the amount of bridging cement present. I only applied criteria to differentiate between microfractures, possibly dilated grain boundaries, and grain boundaries representative of initial apertures prior to core or outcrop retrieval (Figure 3.4).

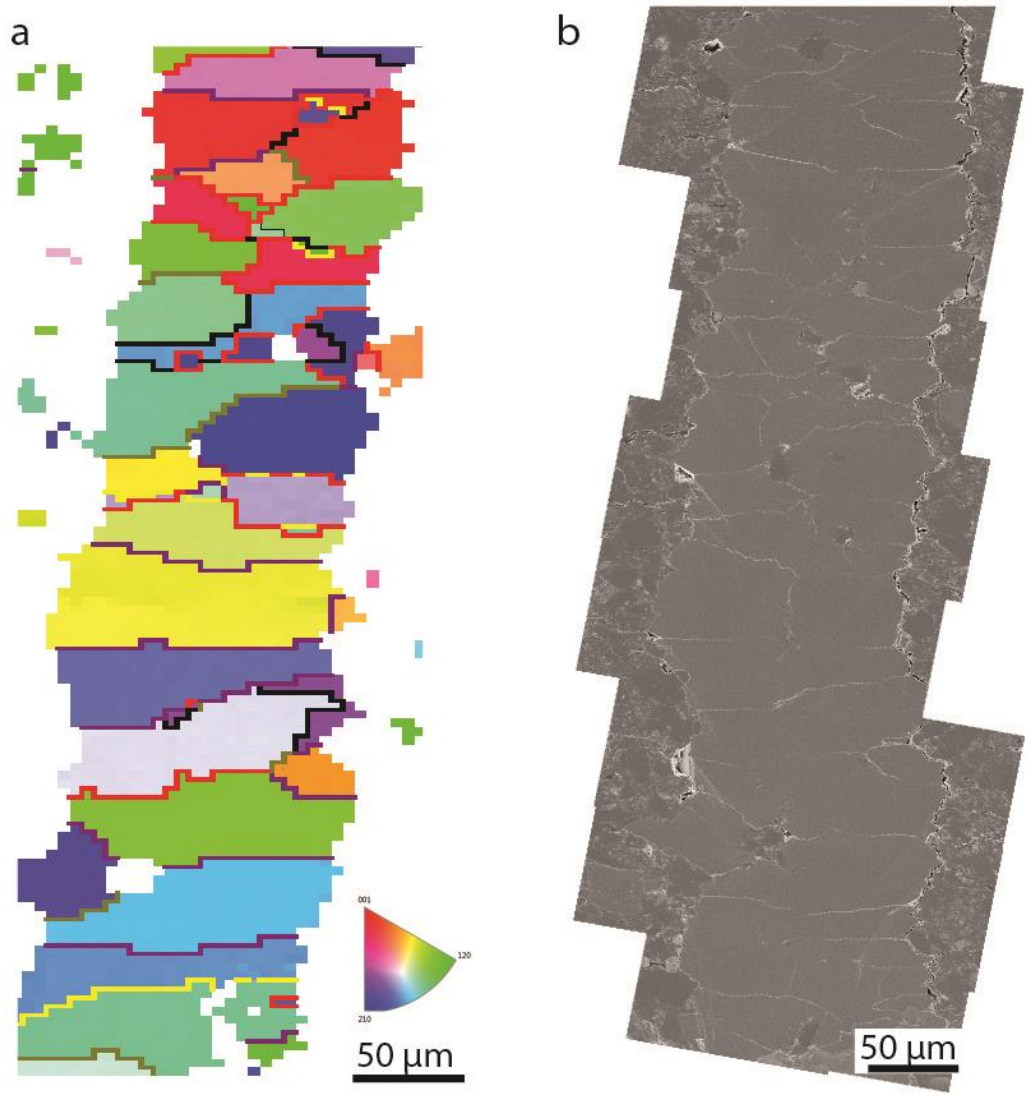

Figure 3.3: (a) EBSD inverse pole figure and (b) inlens secondary electron mosaic of same area from a calcite cemented fracture. (a) Colors represent different crystallographic orientations. The interface where two colors meet are grain boundaries. (b) Bright linear features within the fracture are locations of grain boundaries and intergranular fractures, which I differentiated by comparing the image to the EBSD inverse pole figure.

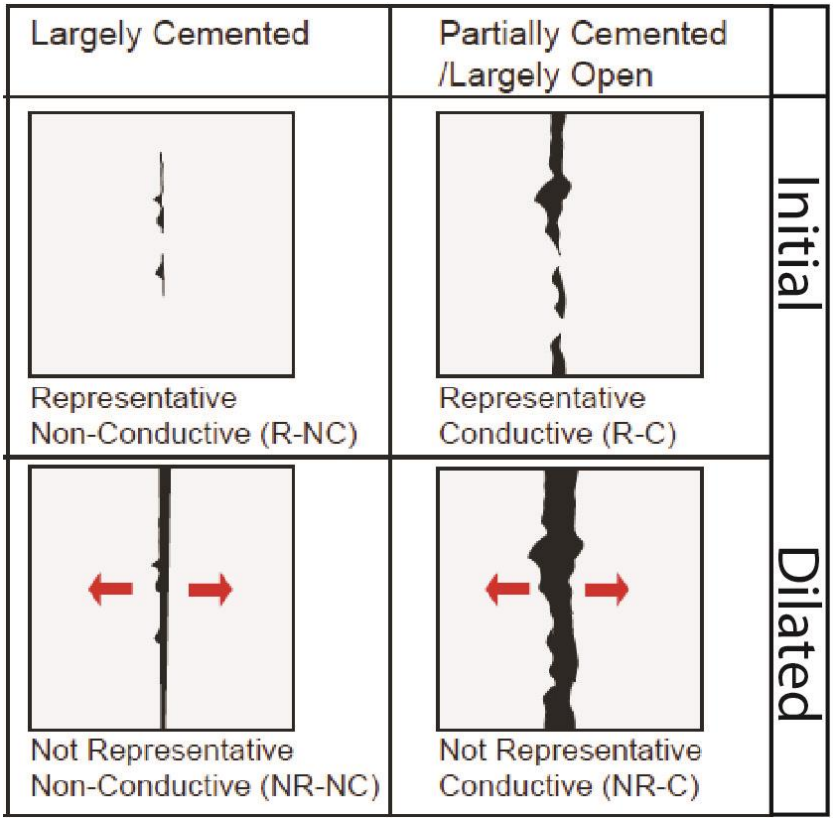

Figure 3.4: Schematic representation of criteria used to characterize NGBCs by Landry et al. (2016) and adopted for this thesis. NGBCs that can be described as representative of initial grain boundary apertures are those that contain bringing cement that traverses and partially fills the NGBC (R-NC, R-C). The degree to which they are filled indicates whether they may be conductive or not. If they do not fit the criteria as representative, they may be dilated during core retrieval and handling (NR-NC, NR-C). Red arrows indicate the direction of possible dilation.

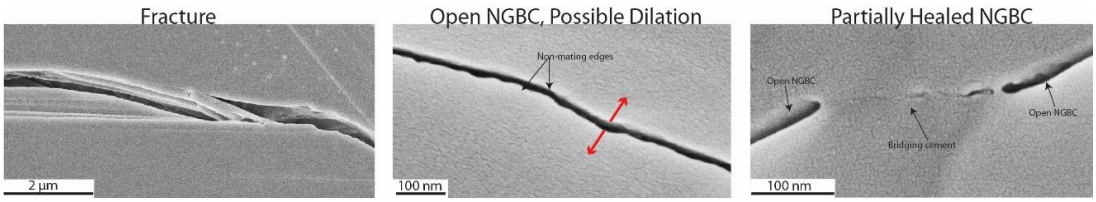

Figure 3.5: Examples of inlens SEM micrographs from this thesis applying the adopted criteria from Landry et al. (2016) (Figure 3.4).

Measuring a Single NGBC Mean Aperture

Using the high magnification inlens SE micrographs, I measured the width of open NGBCs with a calibrated ruler in Adobe Photoshop. Several measurements were taken over a representative area normal to the NGBC walls in each image. I avoided areas that are narrow because of curvature adjacent to bridging cements or widened by pitting and triple junctions. A mean aperture was calculated for each grain boundary (Table 3.3). An overall sample mean was calculated for entire samples using mean apertures of all representative grain boundaries measured within a sample (Table 3.4).

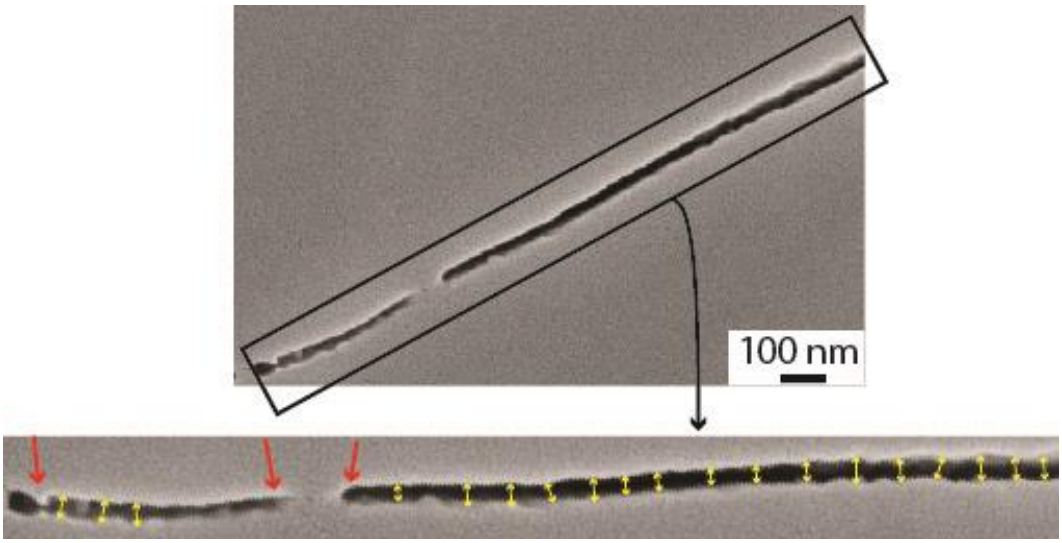

Figure 3.6: Example of method for measuring a portion of a single NGBC from a calcite cemented fracture in the New Albany Shale, sample 2774.5. Yellow lines represent measured sites. Red lines indicate areas that are narrow compared to the overall grain boundary due to curvature near bridging cements.

Measurement Number	Length (nm)
1	23.16
2	25.13
3	22.14
4	27.66
5	27.95
6	29.66
7	26.53
8	25.52
9	30.59
10	27.08
11	28.68
12	29.20
13	31.00
14	28.02
15	25.89
16	17.78
17	18.57
18	15.06
19	20.31
NGBC Mean Aperture	**25.26**

Table 3.3: Examples of measurements from a single NGBC from example shown in Figure 3.5.

Grain Boundary Number	Mean Aperture
1	11.92
2	14.95
3	14.98
4	16.84
5	18.24
6	18.97
7	19.78
8	22.92
9	23.24
10	25.09
11	26.21
12	28.49
13	29.32
14	48.12
15	58.51
16	25.26
Overall Sample Mean	**25.18**

Table 3.4: Example of all measured grain boundary mean apertures with the overall sample mean from a calcite cemented fracture from the New Albany Shale, sample NAM-2774.5.

Characterizing Samples by Occurrences of NGBC Textures

After establishing six distinct morphologies, which are discussed further in chapter 4, I ranked how commonly observed these morphologies are in each sample. To do so, I examined each SEM image closely and assigned each to one or more textural characterizations. I divided the number of observed occurrences by the total number of all observations within one sample, creating a percentage of NGBC texture for each sample. Based on the percent of a texture observed in a sample, I ranked them as being dominant (> 45%), abundant (30%-45%), common (15%-29%), rare (<15%), or not observed.

TEM Processing

TEM micrographs were processed using Gatan's Digital Micrograph software. Interpretations and comparisons of lattice fringe patterns were conducted using Adobe Photoshop and Adobe Illustrator.

Chapter 4: Nano-scale Grain Boundary Channels in Fracture Cements of Unconventional Reservoirs

Introduction

Flow through open and partially cemented fractures has been a topic of interest for decades (Cacas et al., 1990; Brown, 1995; Zimmerman and Bodvarsson, 1996; Oron and Berkowitz, 1998; Eker and Akin, 2006; Tokan-Lawal et al., 2017). Because of their ability to enhance local permeability in otherwise low permeability formations, they are of great significance to oil and gas recovery and cap seal for CO_2 sequestration (Gale and Holder, 2010; Shukla et al., 2010; Walton and McLennan, 2013). However, fractures are commonly observed to be completely filled with mineral cements (Engelder et al., 2009; Gale et al., 2014). Much less attention has been given to understand flow through these fully cemented fractures. A lack of discernable pore space at the scale of conventional petrographic and SEM microscopy has led to the commonly accepted notion that diagenetic cements filling fractures completely occlude fluid flow (Philip et al., 2002; Gale et al., 2007; Loucks et al., 2009). However, Landry et al. (2016) showed that partially healed elongate pores on the order of 100 nm are preserved along grain boundaries of calcite fracture cements in the Eagle Ford Shale. These authors interpreted these pores to exist *in situ* based on the presence of non-faceted calcite grain boundaries and bridging cement partially filling grain boundaries. They also estimated that, when up scaled to the reservoir scale, nano-scale grain boundary channels can increase the overall formation permeability by at least an order of magnitude. Following similar observations in metamorphic rocks and synthetic aggregates made my Kruhl et al. (2013), Liteanu et al., (2012), Olgaard et al. (1993), and van Noort et al. (2008), they designated these pores as nano-scale grain boundary channels (NGBCs). While the existence of similar nano-scale pore structures along grain boundaries has been observed by the above-mentioned authors and others (Mancktelow and

Pennacchioni, 2004; Desbois et al., 2012), it is currently unknown if nanoscale grain boundary channels are inherent features at grain boundaries of diagenetic cements and what processes control their aperture and morphology. Models predicting the geometric structure and thickness of grain boundaries undergoing pressure solution predict grain boundary thicknesses containing fluid films ranging from 2 nm to several micrometers and grain faces with rough surfaces creating channel, island, and ridge microstructures (Weyl 1959; Lehner, 1995; den Brok, 1998; Spiers and Schutjens, 1999; Dysthe, 2002; Koehn et al., 2006). These models exist in an attempt to understand the transport properties and strain rates of compacting grains and assume a solid stress exists at the grain boundary, driving dissolution-precipitation reactions. It is unknown whether these models are applicable to grain boundaries of fracture cements grown within initially stress-free opening mode fractures because of the uncertain stress magnitude at the cement grain boundaries.

Here, I provide a comprehensive study of fracture cements in a wide range of diagenetic conditions and up to low-grade metamorphic conditions to show that these features are ubiquitous along grain boundaries, characterized by a complex, permeable structure. I test whether mineral cement composition or temperature and exhumation history affect the size and morphology of pores along grain boundaries. To do so, I employed high resolution field emission scanning electron microscopy (FE-SEM), electron backscattered diffraction (EBSD), and transmission electron microscopy (TEM) on broad-ion-beam prepared samples containing fractures fully cemented with various compositions from several formations that have experienced a range of burial histories. I compare my observations to previous observations of grain boundary structure, experimental observations, and theoretical results. I contest that this study of the grain boundary structure of diagenetic cements filling fractures may also have implications that lead to a better

understanding of flow through matrix cements of low permeability rocks exposed to diagenetic conditions.

Samples

Fully-cemented natural macrofractures were sampled from core and outcrop of nine formations of low matrix porosity and permeability. Low permeability formations were selected because of the potential for nano-scale pore structures in fracture cement to increase the overall formation permeability. Sampled formations hosting these sampled fractures include the Devonian New Albany and Marcellus Shales, the Mississippian Barnett Shale, the Cretaceous Cardium, Nikanassin, and Travis Peak Sandstones, the Jurassic Haynesville Shale, the Miocene Monterey Formation, and low-grade metamorphic sandstone of the Pre-Cambrian Campito Formation (Table 1). With the exception of the New Albany Shale and Cardium Sandstone, all formations were sampled at a single location. This suite of samples provides a range in host rock and cement compositions, tectonic regime, and maximum burial temperature ranging from 90˚C to in excess of 250˚C. Fractures range in aperture from 0.1-1.0 mm and completely cemented with coarse grained, euhedral, diagenetic cement including calcite, dolomite, quartz, calcite+quartz, barite, and barite+calcite+quartz.

Methods

A first determination of cement mineral composition and texture was obtained using transmitted light petrography on polished petrographic thin sections (Figure 4.1a). Selected samples were prepared with argon ion beam milling on Leica's EM TIC020 and EM TIC 3X Three-Beam Ar-Ion Millers using a beam voltage of 5-8 kV at 2.2-2.8 mA for 6-10 hours (Figure 4.1b). Mineral phases, locations of grain boundaries, and

Sample Number	Fm.	Cement	Locality	Sampled Depth (ft)[m]	Max Depth (m)	Exhumation (m)	Max Temp (°C)
BRTC1-12083	Barnett	Barite	West Texas Delaware Basin, Pecos County	12083 [3683]	3683[A]	0	105-110
BRTC1-12421	Barnett	Calcite+ Barite	West Texas Delaware Basin, Pecos County	12421 [3786]	3786[A]	0	105-110
06212-2	Campito	Quartz+ Calcite	White Inyo Mountains	Outcrop	10000[B]	10000	250
12-RF-2	Cardium	Calcite	Ram Falls, Alberta, Canada	Outcrop	5000[C]	5000	100-120
12-BR-3	Cardium	Quartz	Bow River, Alberta, Canada	Outcrop	5000[C]	5000	100-120
HF-18000	Haynesville	Calcite	Louisiana East flank of Sabine uplift	18000 [5000]	5486[D]	0	150-170
M-3658.5B	Marcellus	Calcite+ Quartz	Appalachian Plateau	6358.5 [1938]	4938[E]	3000	150-160
A1-4982.2	Monterey	Dolomite	A1 Well, Platform Irene, Offshore Santa Maria Basin, California	4982.2 [1519]	2319[F]	1500	110
2/26/95-2	Monterey	Dolomite	Jalama Beach, Santa Maria Basin, California	Outcrop	750[G]	750	80
NAM-2744.5	New Albany	Calcite	Pike County, Indiana	2774.5 [846]	2169[H]	1323	90-100
NAM-2784	New Albany	Calcite	Pike County, Indiana	2784 [849]	2172[H]	1323	90-100
NAC-3590	New Albany	Calcite	West Kentucky, Rough Creek Fault	3590 [1094]	2417[H]	1323	90-100
12-GC-9	Nikanassin	Calcite	Grand Cache, Alberta, Canada	Outcrop	7000[I]	7000	170-200
12-GC-12	Nikanassin	Calcite+ Quartz	Grand Cache, Alberta, Canada	Outcrop	7000[I]	7000	170-200
SFOT-1-10106.8	Travis Peak	Quartz	SW flank Sabine Arch Nacogdoches County, TX	10106.8 [3081]	3481[J]	400	140-170

Table 4.1: Samples used in study. Sources: A: Luo et al., 1994; B: Doungkaew, 2017; C: Hardebol et al., 2009; D: Nunn, 2012; E: Evans, 1995; F: Eichhubl and Boles, 1998; G: Keller and Isaacs, 1985; McCrory, 1995; H: Strąpoć et al., 2010; I: Kalkreuth and McMechan, 1996; J: Dutton and Diggs, 1990.

crystallographic orientation of cement crystals were obtained from electron backscattered diffraction (EBSD) (Figure 4.1c). EBSD was conducted using an Oxford Instruments Nordlys Detector on a Phillips XL30 at the Jackson School of Geosciences and an FEI Quanta FEG 600 at The Materials Institute's Characterization Laboratory at The University of Texas at Austin under low vacuum mode using an accelerating voltage of 30 kV.

Ion-milled samples were coated with 4-6 nm of iridium using a Leica EM ACE600 Sample Coater. Secondary and backscattered electron images were created with dimensions of 1024 x 768 pixels using a Zeiss Sigma FE-SEM with a beam accelerating voltage between 5-15 kV. Inlens secondary electron montages were created with a pixel resolution of 75 nm (Figure 4.1d). High magnification images were collected with pixel resolutions of up to 1 nm (Figures 4.2 b-f). Preparation for transmission electron microscopy was conducted with focused ion beam SEM (FIB-SEM) coupled with *in situ* lift out on a dual beam FEI Strata 400S at Cerium Laboratories, Austin, Texas. High resolution transmission electron microscopy (HRTEM) imaging was conducted on a JEOL 2010F at the Materials Institute at the University of Texas at Austin using an accelerating voltage of 200 kV (Figure 4.2a).

Apertures of NGBC's were measured on inlens secondary electron images perpendicular to the trace of the pore using a calibrated ruler in Adobe Photoshop (Figure 4.3a). The average aperture for a single grain boundary was calculated based on 3 to 19 measurements. A sample mean was calculated based on 1 to 38 single grain boundary mean apertures (Figures 4.3b, 4.3c).

Because core retrieval and handling can cause microfracturing and dilation of preexisting microfractures and grain boundaries (Landry et al., 2016), I only measured apertures of partially open grain boundaries containing intact cement bridges that

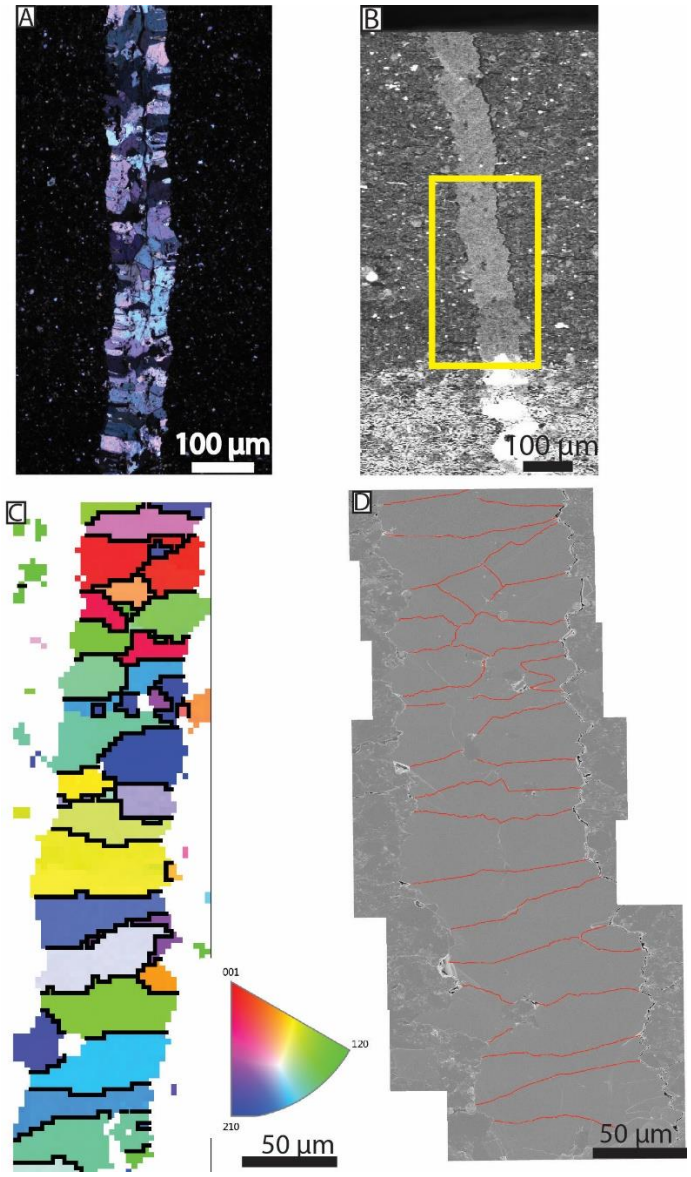

Figure 4.1: (a) Polarized transmitted light thin section micrograph of calcite cemented fracture, New Albany Formation at 2744.5 feet, sample NAM-2744.5. No microscale porosity is visible under the microscope; (b) Back Scattered Electron micrograph of ion milled surface with calcite cemented fracture trending up and down. Yellow box is location of (c) and (d).; (c) Electron backscattered diffraction inverse pole figure. Colors represent crystallographic orientation of grains. (d) Inlens secondary electron montage of (c). Red lines map the location of elongate pores which follow the location of grain boundaries as mapped by EBSD in (c).

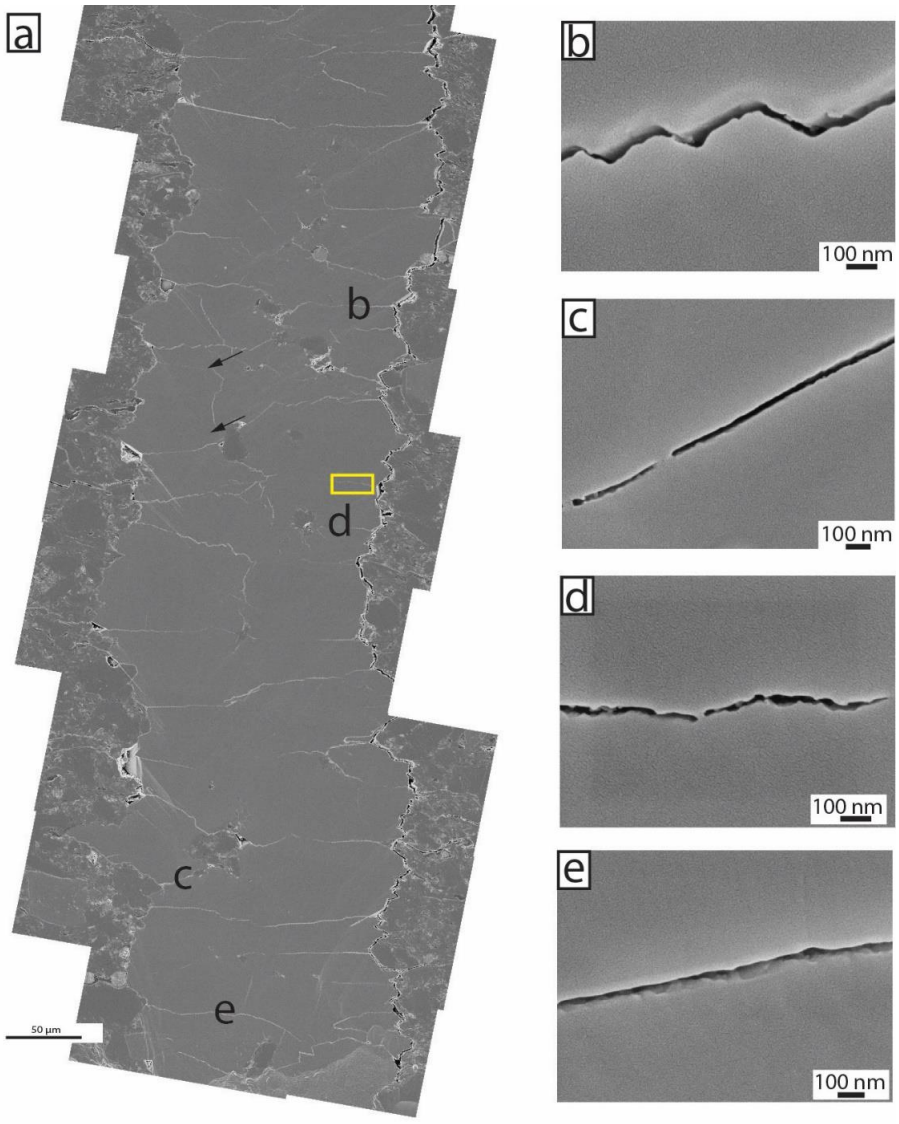

Figure 4.2: (a) Inlens secondary electron montage from sample NAM-2744.5 with locations of (b-e). Yellow box represents location of TEM sample (Figure 4.13). Arrows indicate locations of intergranular microfractures. (b-e) Detailed inlens secondary electron micrographs of (a). The range of apertures and NGBC morphologies throughout samples can be variable.

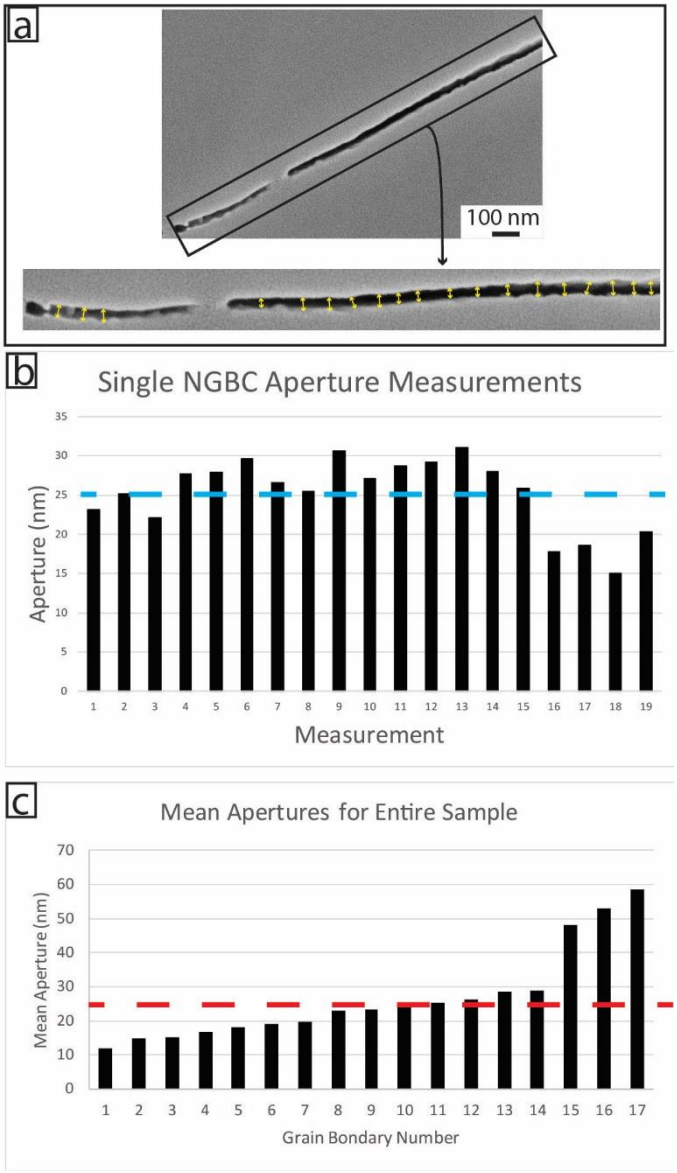

Figure 4.3: Representative example of the method used for measuring and characterizing sample aperture for a single NBGC. (a): Channels are measured at 100-200 nm intervals along the trace of, and orthogonal to, the grain boundary. (b): Measured apertures (black) throughout the channel are averaged to acquire the mean aperture for a single NGBC. Mean NGBC aperture is represented by the blue dashed line in (b). (c): NGBC mean apertures from entire sample shown in Figures 4.1 and 4.2. Blue dashed line represents the overall sample mean aperture.

completely traverse the grain boundary, thus ascertaining that the apertures are representative of *in situ* conditions. The exception are grain boundaries in barite that are generally unbridged. In this case, my measurements are maximum estimates of *in situ* apertures.

Samples are characterized by the range of single grain boundary mean apertures, sample mean aperture, dominant grain boundary bridging cement morphology, and the amount of bridging cement. I define a mean aperture as the mean of measurements taken along a single grain boundary that is interpreted to represent subsurface conditions. Therefore, the range of mean apertures in a sample is the range of the narrowest to the widest measured mean aperture in a sample. The relative abundance of textures was determined by dividing the number of times a texture is observed by the total number of grain boundary texture observations within a single sample.

Results

General Characteristics of NGBCs

Comparisons between secondary electron micrographs and EBSD grain maps show that NGBCs in fracture cements occur preferentially along grain boundaries (Figures 4.1 c, d). Open channels occur both with and without bridging cement (Figure 4.2). Intragranular microfractures are differentiated from grain boundaries by a lack of orientation contrast across them and are observed cutting across cement grains (Figure 4.2 a). Walls of NGBCs tend to be parallel, but aperture profiles tend to have nanometer scale variability due to wavy or rough surfaces. Measurements of SEM images show that all formations and cement compositions sampled contain nano-scale grain boundary channels with overall sample mean apertures and ranges of mean apertures on the order of several hundred nanometers (Figure 4.4).

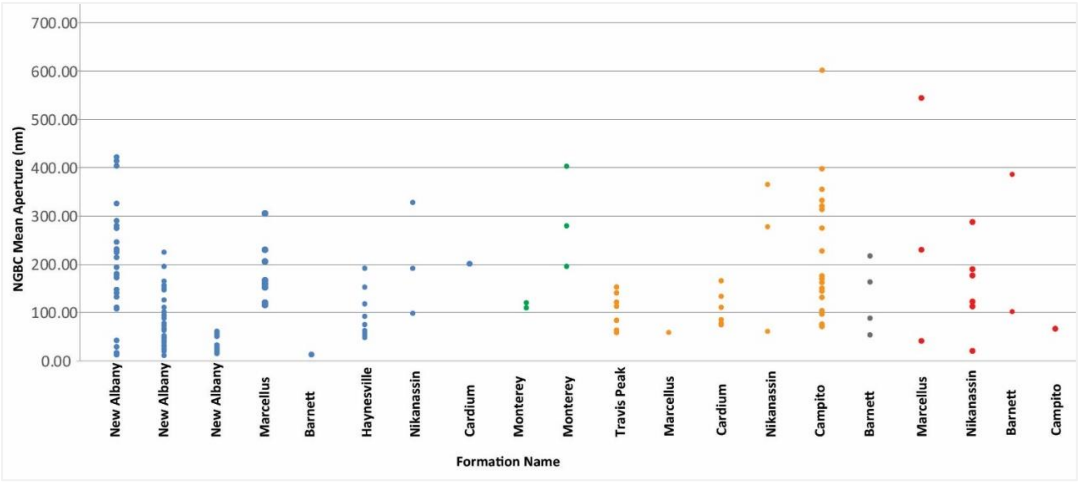

Figure 4.4: Mean apertures of all channels. Colors represent mineral composition. Blue: calcite, green: dolomite, orange: quartz, gray: barite, red: phase boundaries. Mean aperture ranges vary between samples, but ranges are comparable throughout all sampled minerals, except phase boundaries.

As outlined below, I observed NGBCs with varying textures and mean apertures. Overall sample mean apertures, and ranges of mean apertures throughout samples also vary. Textures observed along edges of grain boundaries of quartz, carbonate, and barite fracture cements were grouped into three types: (1) cuspate-lobate texture that creates a non-mating contact with neighboring grains (Figure 4.5 a); (2) faceted crystal face that, when in contact with the neighboring cement grain, creates a flat, mating grain boundary contact with a high aspect ratio of grain-grain contact relative to the width of the grain boundary channel (Figures 4.5 c, d); and (3) negative crystal shapes at grain edges (Figures 4.5 e, f). Bridging cement that partially fills NGBCs follows three common and distinct morphologies characterized by the following: (1) cement bridges that do not completely traverse the NGBC (Figures 4.6 a, b); (2) bridging cement with flat, planar edges leading to rectangular shaped pores (Figures 4.6 c, d); (3) bridging cement with curved edges creating meniscus-shaped pores (Figures 4.6 e, f).

The occurrence of these textures is variable among samples (Table 2.2). A single grain boundary may contain several of these textures. For instance, negative crystals, faceted crystal faces, and meniscus shaped bridges are all observed along grain boundaries in Marcellus fracture cement.

Characterization of NGBCs in Carbonate Cements

Observed single grain boundary mean apertures of calcite-calcite grain boundaries range from 10 nm to 435 nm (Figure 4.4). Overall, cuspate-lobate textures are the most commonly observed grain boundary textures in calcite, while negative crystal shapes are least common.

The calcite-calcite grain boundaries in the Marcellus sample contain NGBCs with mean apertures ranging between 100 to 270 nm (Figure 4.4). NGBCs contain less bridging

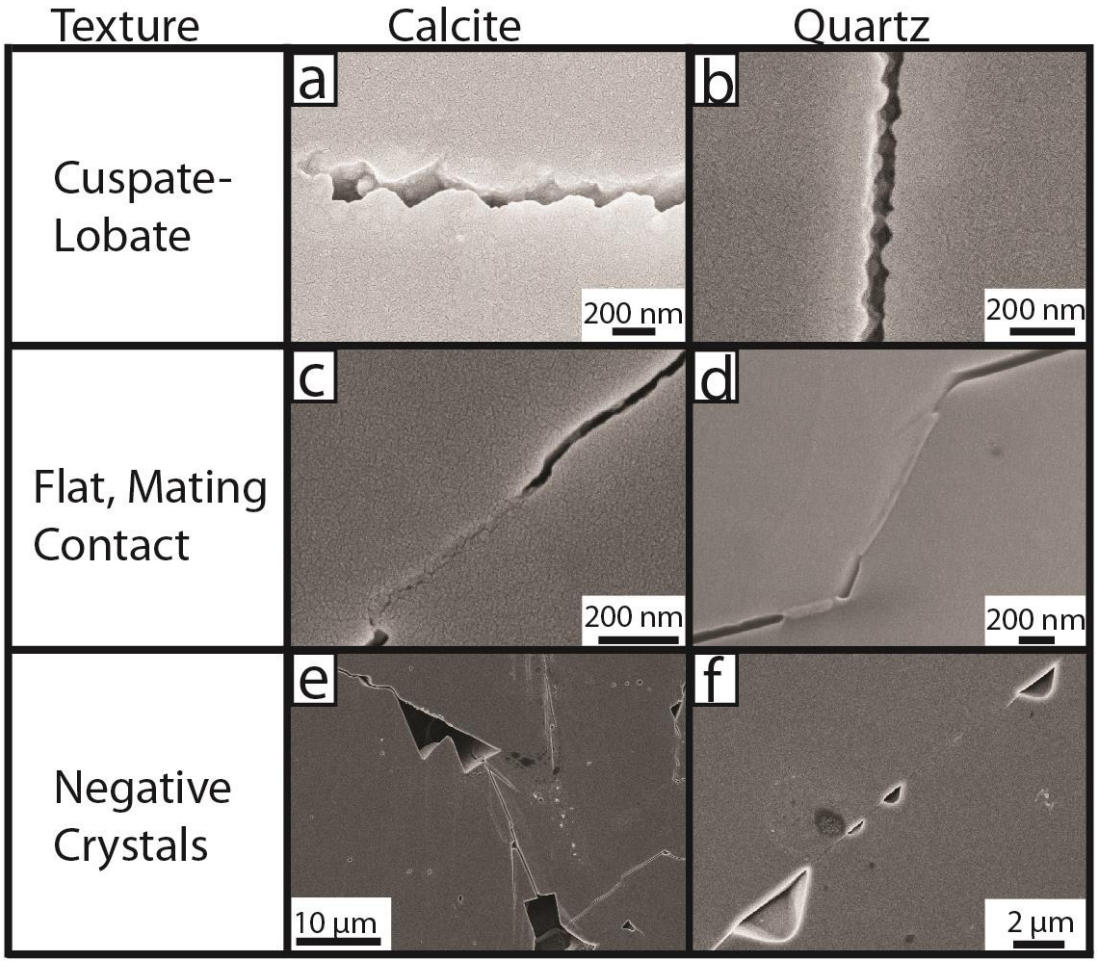

Figure 4.5: Commonly observed NGBC textures along grain boundaries in calcite (middle column) and quartz (right column). (a, b) Cuspate-lobate textures in calcite, New Albany Formation, sample NAC-3590 (a) and in quartz from the Travis Peak Formation, sample SFOT-1-10106.8 (b) form along crystal faces and create undulating textures. ;(c, d) Flat, mating contacts in calcite from the New Albany Formation, sample NAM2744.5 (c) and the Travis Peak Formation, sample SFOT-1-10106.8, form faceted crystal faces at grain boundaries, and when in contact with a neighboring faceted crystal, create bridging cement with high aspect ratios relative to the width of the grain boundary channel. (e, f) Negative crystal shaped pores in calcite (e) and quartz (f) from the Marcellus Formation, sample M-3658.5B, forming along mostly faceted crystal faces. Negative crystals are also observed along non-faceted surfaces.

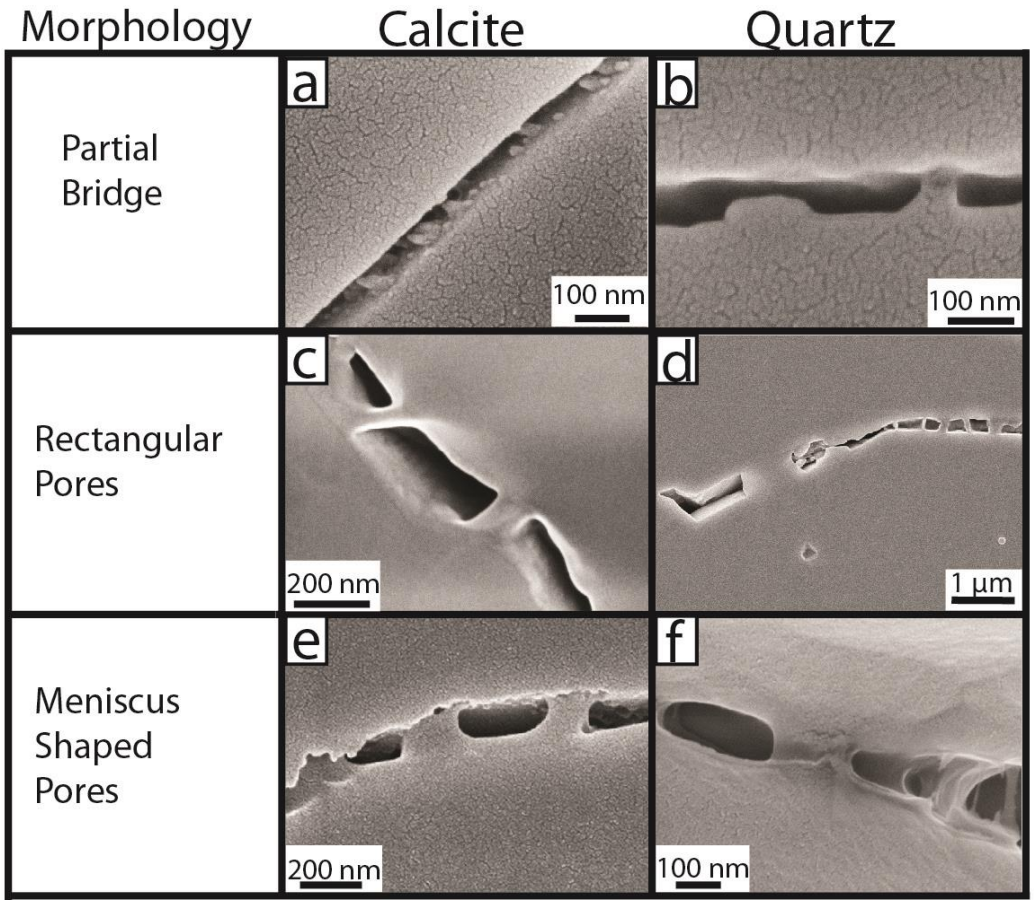

Figure 4.6: Examples of commonly observed bridging cement textures forming grain boundaries in calcite (middle column) and quartz (right column). (a, b) Partial bridges that do not traverse the entire channel in calcite from the New Albany Formation, sample NAM-2784 (a) and in quartz form the Travis Peak Formation, sample SFOT-1-10106.8 (b). Fully developed bridge adjacent to a partial bridge illustrating the growth development of a bridge and that the partial bridge does not represent a broken fully formed bridge. (c, d) Fully formed cement bridges with a low aspect ratio compared to the width of the grain boundary channel, creating pores along the NGBC that are rectangular or box shaped, in calcite from the Nikanassin Formation, sample 12-GC-9 (c) and in quartz from the Travis Peak Formation, sample SFOT-1-10106.8. (e, f) Fully formed cement bridges with curved edges and a low aspect ratio compared to the width of the grain boundary channel, creating pores along the NGBC that are meniscus shaped in calcite from The New Albany Formation, sample NAM-2784 (e) and in quartz from the Cardium Formation, sample 12-BR-3(f).

Formation	Mineral	Partial Bridge	Rectangular Pores	Meniscus Pores	Cuspate-Lobate	Mating Edges	Negative Crystal	Max Temp
New Albany	Calcite	●	●	●●	●●●	●●●	●	95
New Albany	Calcite	●●	●	●	●●	●●	●	95
New Albany	Calcite		●●	●	●●●●	●	●	105
New Albany	Calcite		●	●	●●●●	●	●	105
Barnett	Calcite					●●●●		110
Cardium	Calcite				●●●●	●●		110
Cardium	Quartz		●●	●●●	●	●		110
Monterey	Dolomite		●●●	●●	●●●			110
Travis Peak	Quartz	●	●	●●	●●●	●●	●●	155
Marcellus	Calcite			●●●	●●●		●●	155
Marcellus	Quartz		●●	●●		●●	●●	155
Haynesville	Calcite	●	●●●	●●●	●●	●●		160
Nikanassin	Calcite		●●	●●●		●●●		185
Nikanassin	Quartz			●●	●●●	●●	●●	185
Campito	Quartz	●	●	●	●●●		●●●	250

● Rare ●● Common ●●● Abundant ●●●● Dominant

Table 4.2: Occurrences of grain boundary and bridging cement textures ranked relative to all other textures within the same sample. Textures are determined to be either dominant, abundant, common, or rare. No dots indicate that the texture is not observed in that sample. Blue: calcite, orange: quartz, green: dolomite. Samples arranged with increasing temperature demonstrating no trend of NGBC texture with increasing temperature.

cements than in calcite-calcite grain boundaries of other formations (Figure 4.7 d). Negative crystal structures are abundant along grain boundaries (Figure 4.5 e, Table 4.2). Of the three fractures sampled from the New Albany Shale, each fracture contains a different range of NGBC apertures and morphologies. NGBCs have a range of 19 to 435 nm in the sample from Western Kentucky from 3590 feet (Figure 4.4), and grain edges are dominated by cuspate-lobate edges. Bridging cements creating meniscus and rectangular shaped pores are common (Table 4.2). The two samples from Pike County, sampled from 2784 and 2744.5 feet, have apertures with widths that range from 21 to 256 nm and 11 to 59 nm respectively (Figure 4.4). The Pike County samples do not seem to have a dominant grain boundary texture, but rarely contain negative crystal structures. Within the sample from 2784 feet, NGBCs sometimes occur as saw tooth patterns, oriented sub-parallel to bedding (Figures 4.8 c, d).

Calcite fracture cement in the sample from the Barnett Shale is coarse grained, containing only one grain boundary in the prepared section of the sample. This grain boundary has a mean aperture of 18 nm and is dominated by a flat, mating texture (Figure 4.7 b).

The Haynesville Shale has a geologic history similar to that of the Barnett. Mean apertures in the Haynesville Shale range between 37 to193 nm (Figure 4.4). No dominant grain boundary texture or bridging cement morphology is observed (Figure 4.7 e, Table 4.2). Solid hydrocarbons are commonly found filling NGBCs (Figure 4.8 b).

The outcrop sample from the Nikanassin Sandstone displays a wide range of mean apertures varying from being completely cemented along large portions of grain boundaries to being open as much as 350 nm (Figure 4.4). In the outcrop sample from the Cardium, coarse grained cement creates a single grain boundary that varies from being largely cemented to open as much as 27 nm. Calcite fracture cement in the Cardium sample

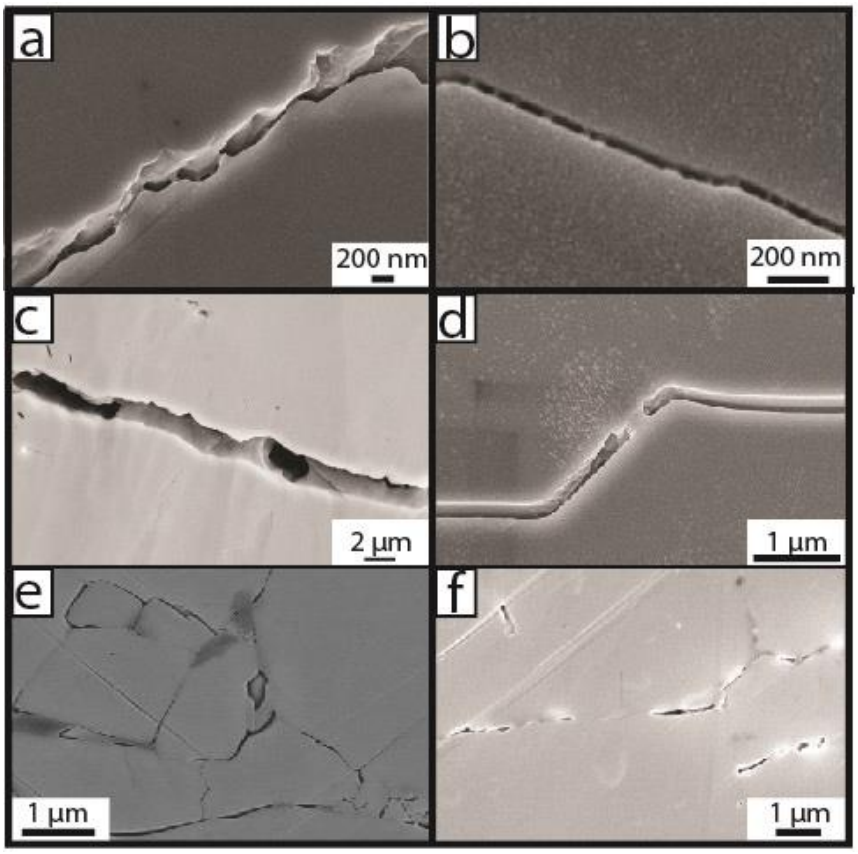

Figure 4.7: SEM micrographs of NGBCs in calcite. (a) Inlens secondary electron micrograph of cuspate-lobate and meniscus shaped sample NAC-3590. (b) Inlens secondary electron micrograph of a narrow NGBC with faceted edges, subtle meniscus bridges, and flat, mating contact from the Barnett Formation, sample BRTC1-12421. (c) Secondary electron micrograph of a wide NGBC with rough edges and high aspect ratio bridging cement creating meniscus shaped pores from the Cardium Formation, sample 12-RF-2. (d) Secondary electron micrograph of a mostly faceted calcite with subtle roughness and slightly meniscus shaped, low aspect ratio bridging cement in the Marcellus Formation, sample M-3658.5B. (e) Secondary electron and backscattered electron mixed signal SEM micrograph. Mostly faceted, fine grained calcite from the Haynesville Formation, sample HF-18000, forms some high-aspect-ratio bridging cement and some low-aspect-ratio bridging cement. Hydrocarbon partially fills some of these NGBCs. (f) Inlens secondary electron micrograph of NGBCs with a high degree of in cement infill along faceted calcite in sample 12-GC-9, Nikanassin Formation.

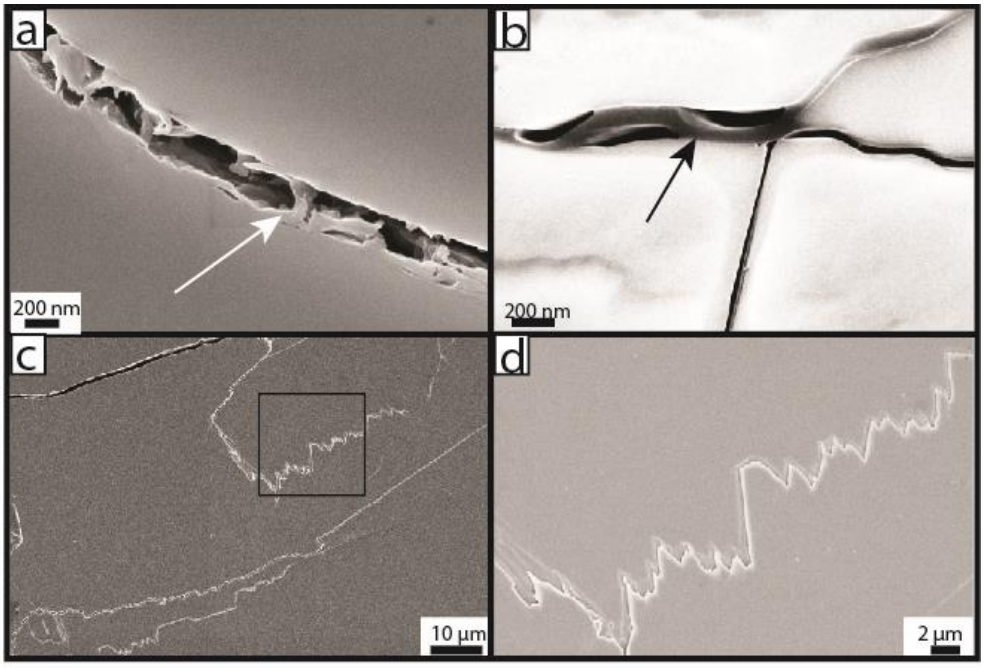

Figure 4.8: Secondary features observed within or along NGBCs in quartz and calcite. (a): Inlens secondary electron micrograph of chlorite filling an NGBC between two quartz grains in the Campito Formation, sample 06212-2. (b) Backscattered electron micrograph of hydrocarbon (black arrow) filling NGBCs between calcite grains in the Haynesville Formation, sample HF-18000. (c) Saw tooth patterns forming NGBCs in the New Albany Formation, NAM-2784. (d) Detail of (c). Saw tooth patterns.

is dominated by a cuspate-lobate texture with portions of flat-mating edges (Figure 4.7 c, Table 4.2), while the Nikanassin Sandstone is dominated by flat, mating grain edges with bridging cement, creating both rectangular and meniscus pores and a high degree of cement infilling grain boundaries (Figure 4.7 f, Table 4.2).

Dolomite sampled from the Monterey Formation from the A1 core (Figure 4.9 a) and Jalama Beach, California (Figure 4.9 b) are similar to those seen in calcite fracture cements, with a wide range of apertures (Figure 4.4). Observed grain boundary channels in dolomite are 50 to 400 nm and contain abundant rectangular shaped pores with cuspate-lobate crystal edges (Table 4.2).

Characterization of NGBCs in Quartz Fracture Cements

Channel apertures at quartz-quartz grain boundaries range from 63 to 600 nm (Figure 4.4). While cuspate-lobate textures are common or abundant in quartz as well as carbonates, flat-mating edges with negative crystals are more common in quartz than in carbonate fracture cement (Table 4.2). Cement bridging at quartz-quartz grain boundaries is generally less abundant than in carbonate cements, leaving more of the grain boundary channel pore space open (Figure 4.10).

The lower temperature samples from the Travis Peak, Cardium, and Marcellus Formations display mean apertures that are consistently between 60 to165 nm (Figure 4.4). Grain edges of the Travis Peak (Figures 4.6 b, d; 4.10 b) are abundantly cuspate-lobate, while flat, mating edges and negative crystals are also common. Bridges create both rectangular and meniscus shaped pores (Table 4.2). The Cardium samples contain both flat, mating and cuspate-lobate edges, void of any negative crystal shapes. Meniscus pores are more abundantly observed than rectangular pores (Figure 4.10 a). Grain edges in the Marcellus are flat with negative crystal structures along boundaries (Figure 4.7 f).

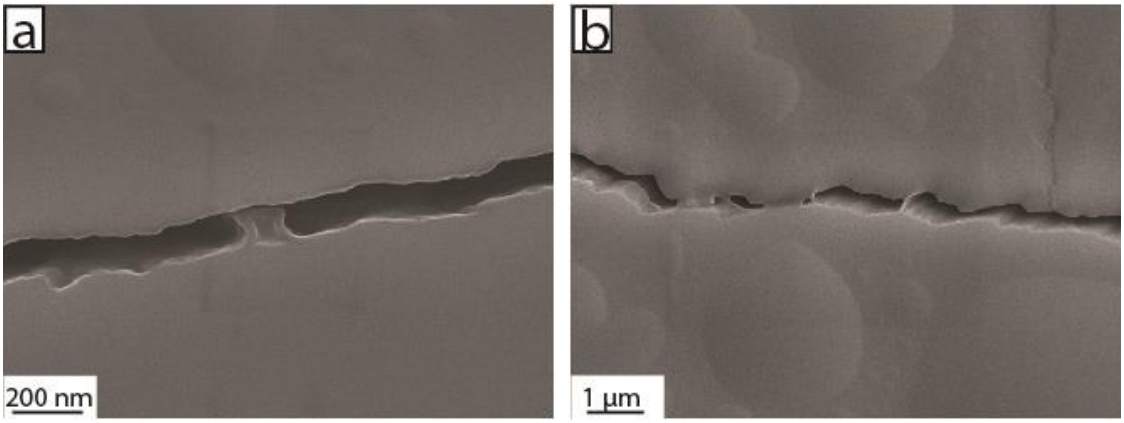

Figure 4.9: Secondary electron micrographs of NGBCs formed in dolomite. Cuspate-lobate crystal edges and meniscus shaped bridges dominate dolomite from the Monterey Formation, outcrop at Jalama Beach sample 2/26/95-2 (a) and core sample A1-4982.2 (b). Sample surface texture is artifact of SEM sample preparation.

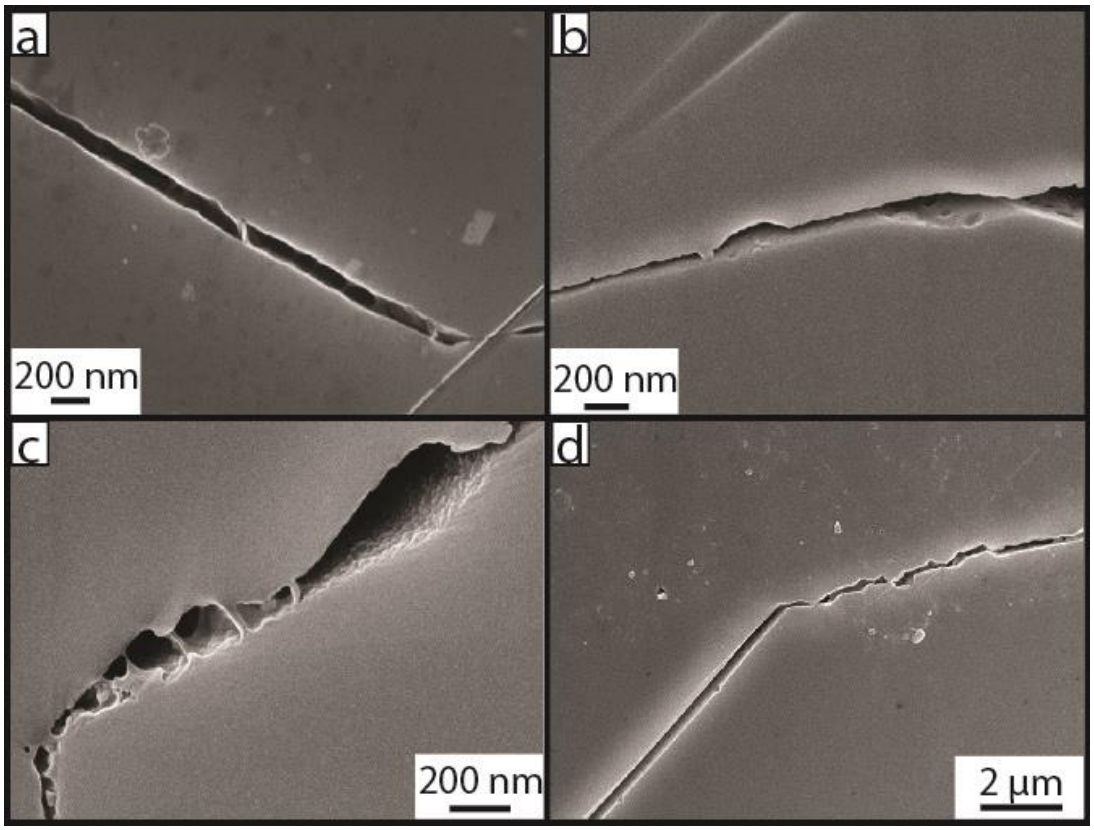

Figure 4.10: Inlens secondary electron SEM micrographs of NGBCs in quartz. (a) Faceted quartz with a narrow, wispy curved bridge and subtle meniscus shaped bridges from the Cardium Formation, sample 12-BR-3. (b) Cuspate-lobate (top grain) approaching a mostly faceted quartz grain in the Travis Peak Formation, sample SFOT-1-1016.8. Pitting and negative crystal shapes occur on both grain edges with a rectangular ridge between the grains. (c) Pitting and roughness along quartz cement grains with narrow, slightly meniscus shaped bridges from the Campito Formation, sample 06212-2. (d) Cuspate-lobate textures along quartz grains transitions to faceted faces along the same NGBC from the Nikanassin Formation, sample 12-GC-12.

The ranges of apertures of NGBCs in quartz-quartz grain boundaries in the higher temperature Nikanassin and Campito Formations are greater, spanning aperture values from 67 to 355 nm in the Nikanassin and 72 to 600 nm in the Campito Formation (Figure 4.4). Both high temperature samples contain cuspate-lobate textures, negative crystal structures, and flat, mating textures (Figures 4.12 c, d; Table 4.2). Several quartz-quartz grain boundaries in the Campito sample are partially filled with chlorite (Figure 4.8 a).

Characterization of NGBCs in Barite Fracture Cement

A horizontal bedding-parallel fracture filled with fibrous barite cement was sampled from the Barnett Shale in the Delaware Basin. NGBCs in this fibrous cement extend across the entire aperture of the fracture with mean apertures ranging from 45 to 220 nm (Figure 4.4). Grain boundary channels in barite were not observed to contain bridging cement, but the edges of grain boundaries have a subtle cuspate-lobate texture (Figure 4.11 a, b). Without the presence of bridging cement, I cannot ascertain if measured apertures of NGBCs in Barite are representative of *in situ* apertures. Observed apertures may have been expanded with stress release during core extraction, and the values plotted in Figure 4.4 are maximum estimates of *in situ* values.

Characterization of NGBCs at Phase Boundaries in Fracture Cements

Phase boundaries occurring between different mineral phases, including calcite-quartz (Figure 4.12 a) and calcite-barite (Figure 4.12 b), sometimes occur as open channels with mean apertures that are up to 540 nm; at other times, grains are in contact along large portions of the boundary without open channels. Where channels exist, they rarely contain bridging cement. Neighboring grain edges rarely display similar geometric characteristics to each other. For example, grain edges of calcite in close contact with barite show roughness (Figure 4.12 b), while the neighboring barite grain edge is flat.

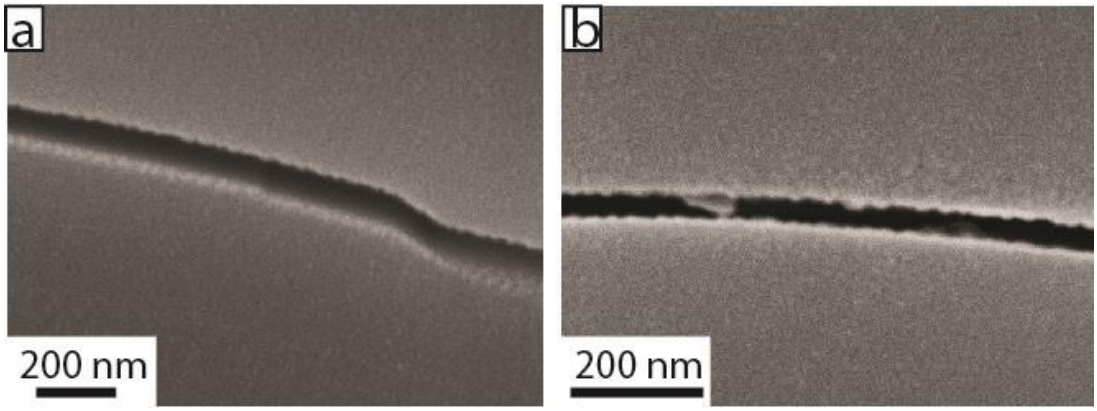

Figure 4.11: Inlens secondary electron micrographs of NGBCs in barite, Barnett Formation sample RTC1-12083. Subtle cuspate-lobate crystal edges occur throughout the sample, but no bridges traverse the NGBC.

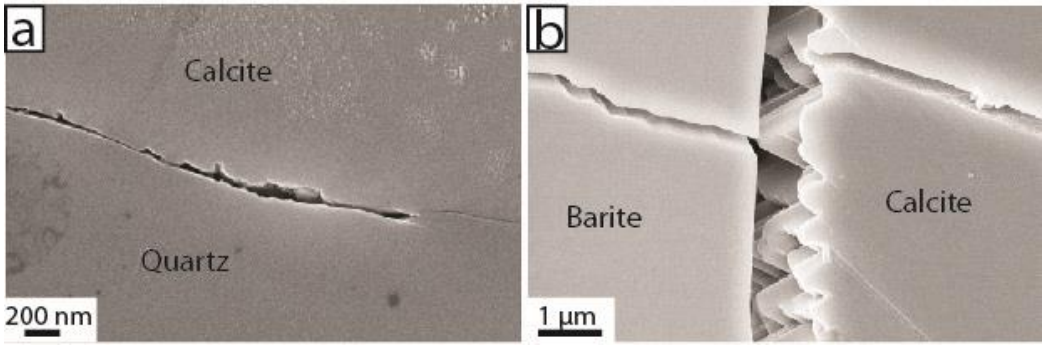

Figure 4.12: Inlens secondary electron micrographs of NGBCs at phase boundaries. (a) Boundary between a calcite (top of image) and a quartz grain (bottom) from the Campito Formation, sample 06212-2. The quartz is mostly faceted while the calcite shows a rough, cuspate-lobate texture. Bridging cement at phase boundaries occurs as high aspect ratio cement. (b) NGBC between calcite (right) and quartz (left) Barnett Formation, sample BRTC1-12421. Barite has a planar crystal face, while calcite is rough, indicating that the barite facet controls the position of the phase boundary.

HRTEM in Calcite Cements

HRTEM imaging was conducted on calcite-calcite grain boundaries from the New Albany Shale (Figure 4.13) and the Barnett Shale. Contrasting lattice patterns between neighboring grains confirms that sampled regions are grain boundaries, further validating EBSD results (Figures 4.13a, 4.14a). Portions of grain boundaries contain no voids, while other portions do (Figure 4.14a). At the scale of SEM imaging, voids are observed to be completely void of calcite, or any other phase of cement. However, in bright field TEM images, a network of thin bridging cement is seen (Figure 4.13 b). These films contain several 1 to 5 nm lattice domains that differ from that of the neighboring grains. Each domain seems to have a unique orientation, different from the surrounding lattice domains contained within the bridge. Bridges also contain domains that lack clear lattice orientations and that I interpret as amorphous material (Figures 4.13 b, c).

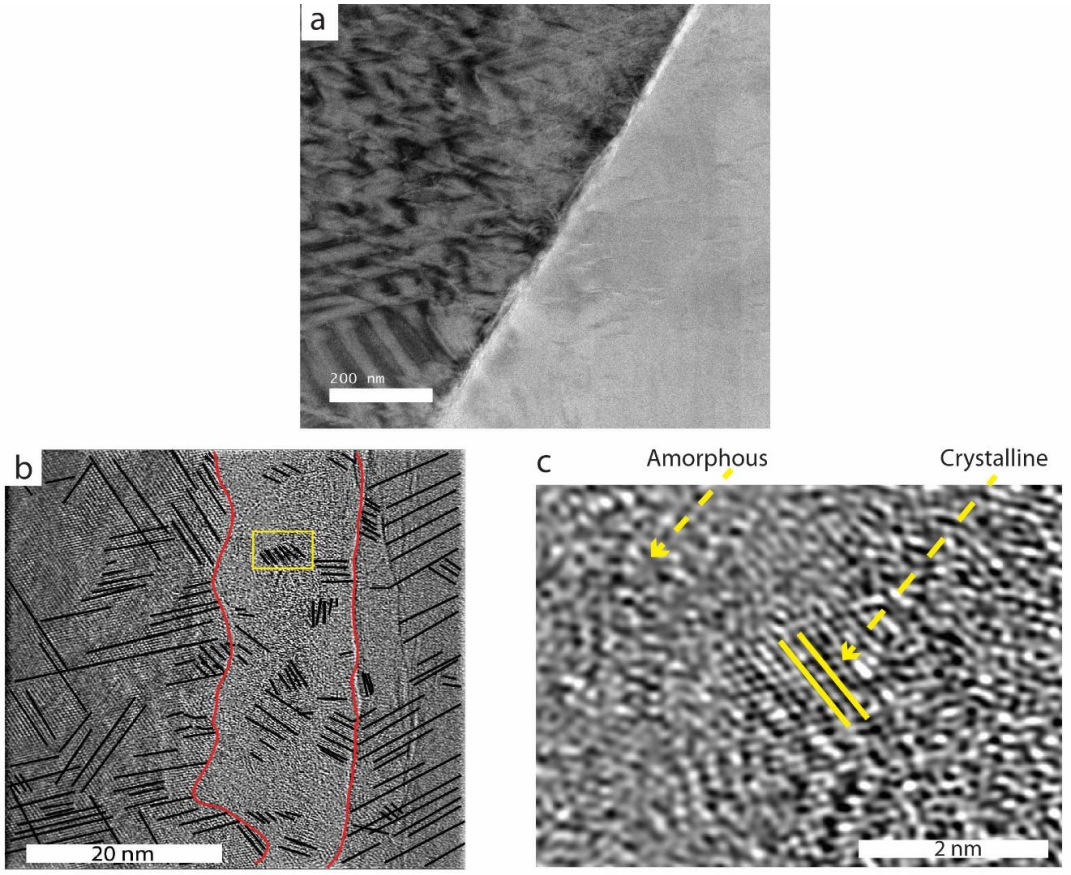

Figure 4.13: Bright field TEM micrographs of grain boundary formed between two calcite crystals from the New Albany Formation, sample NAM-2744.5. Location of grain boundary shown in Figure 4.2. (a) Low magnification image showing lattice orientation contrast at the grain boundary of the two neighboring grains. (b) Processed and interpreted HRTEM micrograph. Two neighboring grains are contrasted by the grain boundary region, which contains several different lattice orientations and possibly amorphous regions. Red lines outline domains of contrasting lattice orientations. The domain bounded by the two red lines is the grain boundary region, containing what we interpret to be possibly amorphous material containing several 1-5 nm crystalline domains. Yellow box is location of c. (c) ~1-2 nm crystalline domain within the grain boundary, surrounded by possibly amorphous material.

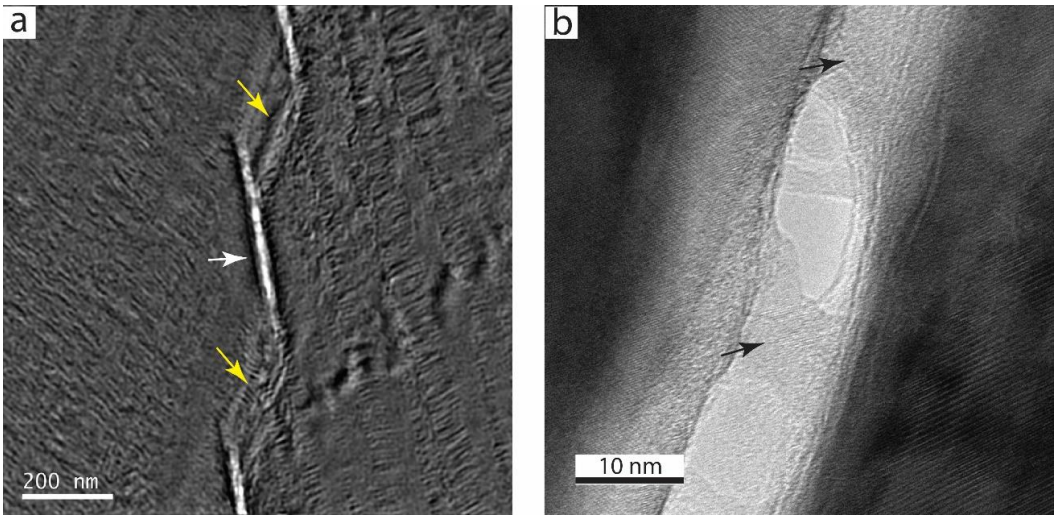

Figure 4.14: Bright field TEM micrographs of a grain boundary formed between two calcite crystals in the Barnett Formation, sample BRTC1-12421. (a) Processed low magnification image showing contrast at the grain boundary with open voids (white arrows) and regions of completely contacting grain boundaries (yellow arrows). (b) HRTEM micrograph of grain boundary region containing voids (bright oval regions) and thin bridging cement films (arrows).

Discussion

Processes of NGBC Formation

I have shown that NGBCs are common features of fracture cements of varying mineralogical composition occurring in a wide range of diagenetic burial conditions. I have also shown that NGBCs occur with various textures and mean apertures, both of which are not controlled by mineralogical composition (Figures 4.4-4.6).

Greater maximum burial temperature appears to favor wider grain boundary channels (Figure 4.15). The overall sample mean aperture and the range of grain boundary mean apertures increase with an increase in maximum formation temperature (Figure 4.15) and with increasing distance of formation exhumation (Figure 4.16). Although fracturing has long been known to be associated with exhumation (Vollbrecht et al., 1991; Anders et al., 2014), my observation of NGBCs in fracture cements sampled from formations that have experienced little or no exhumation, such as the Barnett and Haynesville Formations, discounts release of confinement as the primary mechanism for NGBC creation or preservation. However, while I can discount exhumation as the sole cause for the formation of NGBCs, I cannot discount the effect of exhumation on NGBC growth in those samples that have undergone natural exhumation. Stress release during core retrieval for cored samples has been discounted for NGBC growth by Landry et al. (2016) based on the irregular non-mating surfaces of NGBCs compared to mating fracture-like surfaces of microfractures contained in the same samples.

The trend of increasing aperture range and mean aperture with increasing temperature suggests that the pore structure of NGBCs are controlled by dissolution-precipitation kinetics. While higher temperatures generally favor porosity reduction by solution-precipitation reactions in sedimentary sequences under diagenetic conditions

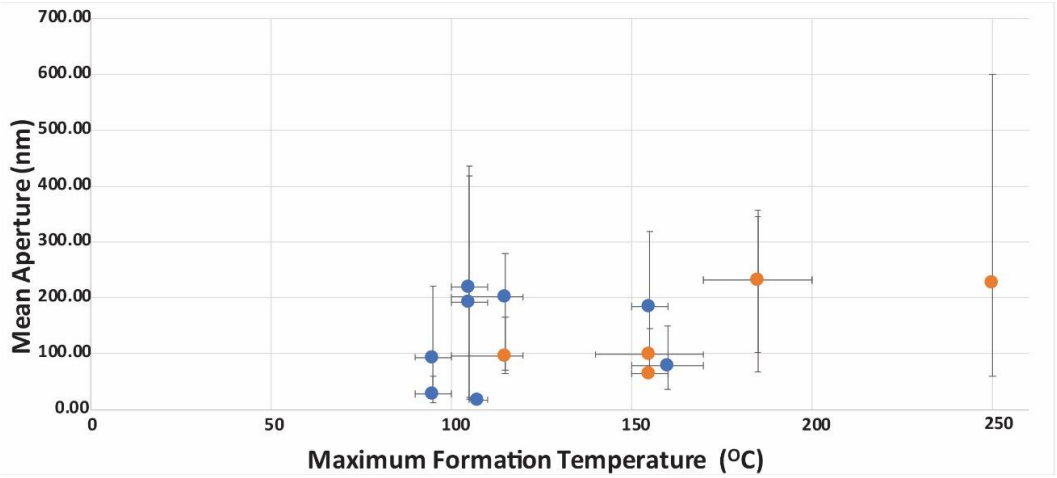

Figure 4.15: Mean aperture as a function of maximum formation temperature. Dots (calcite in blue, quartz in orange) represent the overall sample mean. Bars on the x-axis represent the range of previously reported temperatures (Table 1); bars on the y-axis represent the range of mean single NGBC mean apertures for a sample. Mean and range of aperture tend to increase with increased maximum formation temperature.

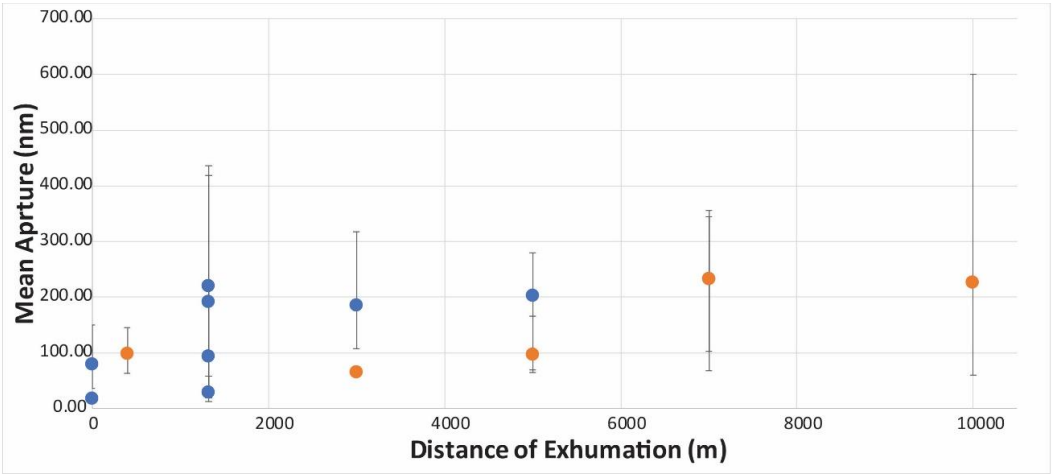

Figure 4.16: Mean aperture plotted as a function of approximate distance of formation exhumation. Dots (blue: calcite, orange: quartz) represent overall sample mean. Bars on the y-axis represent the range of mean single NGBC mean aperture values for a sample. Mean and range of aperture tends to increase with increased distance of formation exhumation.

(Lander et al., 2008), the nano-scale environment of NGBCs, in contrast to macro-pores, may favor dissolution and thus wider NGBCs at higher temperatures.

Although observed NGBC textures are not specific to any temperature regime (Table 4.2), I interpret these textures to form at different stages of fracture cementation. Flat, mating bridging cements, which I interpret as faceted grain boundaries, are expected to form when carbonate and silicate minerals grow from solution in a stress-free environment and are analogous to necks formed during grain boundary healing (Hickman and Evans, 1995). Grain boundary healing is thought to retard pressure solution processes. In the absence of stress, fluid will be expelled to triple grain junctions and fully seal remaining pore space unless a yield stress is overcome to drive dissolution and initiate pressure solution (Revil, 2001; Schenk and Urai, 2004; Revil et al., 2006; van Noort et al., 2008). This healed grain boundary structure, void of pore space, would be expected in NGBCs of opening mode fractures that provide for an initially stress-free environment for cement growth when the fracture is either barren or lined with mineral cement. However, contacting cement grain boundaries may allow transmission of solid stresses, especially following complete fracture cementation, whereas open NGBCs are free of stress.

I propose that initial precipitation in a stress free environment is followed by crystal growth that is affected by force of crystallization imposed by neighboring crystals. This shift from stress-free, smooth crystal growth occurs after complete cementation due to crystal convergence. If force of crystallization overcomes a yield stress, the system may shift from precipitation and crystal growth to a process involving precipitation within open grain boundary channels and dissolution at healed grain boundaries in contact with each other. Force of crystallization is known to have the ability to induce local dissolution, drive replacement reactions, and facilitate fracture opening under high degrees of supersaturation and may be sufficient to induce nanometer scale dissolution-precipitation processes

observed here (Dewers and Ortoleva, 1990; Fletcher and Merino, 2001; Røyne et al., 2011; Cobbold et al., 2013). I interpret the product of partial dissolution of faceted, fully healed grain boundaries to be bridges with a low width to height aspect ratio relative to the length of the NGBC, creating either rectangular or meniscus shaped pores.

TEM results showing a seemingly disordered pattern of lattice domains coupled with amorphous regions indicate that bridging cements partially filling NGBCs are more complex than a simple crystallographic discontinuity. Although TEM sample preparation using focused ion beam can cause ordered crystals to become amorphous under beam interaction, the amorphous material shown here is contained only in the bridging cement and not in the neighboring crystals. If the amorphous structure is a feature induced by FIB interaction, I would observe them not only in the bridging cement, but also in one or both neighboring grains. Although amorphous calcium carbonate (ACC) is unstable under ambient conditions and thus not known to occur in geological systems, it can be stabilized under laboratory conditions by controlling several variables such as particle size, saturation, and confinement (Nudelman et al., 2010; Stephens et al., 2010). The nanometer sized particles surrounding amorphous material may indicate a growth process similar to particle attachment and non-classical nucleation in calcite and other minerals in biological systems (Banfield, 2000; De Yoreo et al., 2015). This indicates a process of cement precipitation occurring within NGBCs that is different from the euhedral crustal growth into free fluid-filled fracture space. I speculate that this amorphous crystal growth is limited to the confined conditions of the NGBCs.

I interpret faceted, healed boundaries to be grain boundaries at or near equilibrium, while cuspate-lobate textures and partial bridges are intermediate, non-equilibrium textures that occur between open stress-free NGBCs and mating, faceted, healed NGBCs. Negative crystal shapes along faceted grain boundaries are interpreted to result from trapping of

confined fluids during convergence of cement grains, forming fluid inclusion-like structures during healing of grain boundaries, similar to observations reported by Desbois et al. (2012) in grain boundaries of rock salt using BIB-SEM. I interpret cuspate-lobate textures to be the product of crystals growing under the presence of stress in response to the confinement created by neighboring grains, similar to what has been observed in experiments (Bisschop and Dysthe, 2006; Angheluta et al., 2009; Jettestuen et al., 2009; Røyne and Dysthe, 2012). These studies concluded that crystals growing under stress produce growth rims and nanometer to micrometer scale roughness which coarsen with time. Furthermore, Jettestuen et al., (2009) observed an undulation in steps arguing for a coupled dissolution-precipitation process. I interpret partially bridged cement that does not traverse NGBCs to either reflect incipient bridging cement growth or the partial dissolution of a formerly intact cement bridge.

I envision a process of NGBC formation akin to the island-channel model of pressure solution (Spiers and Schutjens, 1999; Dysthe et al., 2003; van Noort et al., 2008). The dynamic island-channel model of pressure solution assumes a non-equilibrium system of contacting asperities referred to as islands, and fluid filled channels at grain contacts that are constantly changing at the nanometer scale, but overall preserve the structure at the millimeter scale (Elliott, 1973; Raj, 1982; Lehner, 1995; Ghoussoub and Leroy, 2001; van Noort et al., 2008). The rate of pressure solution has been shown to be temperature dependent (Renard et al., 1997). I adapt this model to NGBCs by assuming that the stress needed for pressure solution is provided by the force of crystallization as the fracture becomes increasingly cemented. The temperature dependence inferred here for NGBC aperture suggests a thermally activated process of deformation similar to that of the temperature dependence observed for pressure solution. In addition, the observed width of channels are on the same order as observed in pressure solution studies (Spiers et al., 2003;

de Meer et al., 2005). Structures similar to NGBCs described here have been observed in metamorphic rocks and rock salt and compared to the island-channel model (Desbois et al., 2012; Bukovská et al., 2015).

My model differs from pressure solution-based models in that the source of stress between grains is provided internally by force of crystallization and does not rely on burial or tectonics. After complete fracture cementation, fluids are confined due to a self-confinement as a result of crystal growth. Sites under stress due to crystallization force applied by the convergence of faceted faces and asperities at cement bridges undergo dissolution. Sites not under stress are located at open NGBCs, where precipitation may occur. This may drive a pressure solution-like reaction; however, grain boundaries remain macroscopically stable with no overall displacement through a dynamic process of precipitation and dissolution at the nanometer scale.

I hypothesize that this structure is inherent to carbonate and silicate fracture cements, preserving pore space along grain boundaries under typical diagenetic conditions. This structure can transition from mostly open, incompletely cemented pore space to healed, mating grain boundaries with negative crystal structures. At an intermediate stage, crystal faces roughen with varying degrees of porosity and with irregular, non-euhedral cement bridge geometry.

Phase boundaries, which separate mineral grains of different compositions, tend to have a wider range and mean aperture than grain boundaries between minerals of the same composition; cement bridges are less common at phase boundaries (Figures 4.4, 4.12). Phase boundaries are known to be the sites of enhanced dissolution and replacement reactions (Greene et al., 2009; Kristiansen et al., 2011; Wassmann and Stöckhert, 2013). It is known that monomineralic rocks are more prone to neck growth and/or grain boundary healing than heterogeneous rocks (Hickman and Evans, 1991; Hickman and Evans, 1995;

Zubtsov et al., 2004; van Noort et al., 2007). Replacement reactions drive dissolution in the older mineral, creating pore space and allowing precipitation of the new mineral (Fletcher and Merino, 2001; Putnis, 2002; Putnis and Putnis, 2007; Putnis and John, 2010). A similar process may be inferred for the barite-calcite phase boundary in Figure 4.12b, where a rough multifaceted calcite crystal is in contact with a single planar facet of barite, suggesting that the crystallographic orientation of the calcite prevents formation of mating phase boundaries.

Phase boundaries are also preferred sites for precipitation-dissolution reactions because of the tendency for electrochemical interactions between phyllosilicates and quartz to drive dissolution of quartz (Alcantar et al., 2003; Israelachvili et al., 2013). Quartz grain boundaries partially filled with chlorite in the Campito sample (Figure 4.8) may reflect such conditions. These reactions would not apply to NGBCs that separate grains of the same composition.

Implications for Fracture Flow in Formations of Low Matrix Permeability

The features described here are similar to earlier observations of NGBCs in calcite fracture cement in the Eagle Ford Formation (Landry et al., 2016). In that earlier study, flow estimates of grain boundary channel networks were up scaled, and if added to previous permeability estimates, can potentially increase overall formation permeability at least an order of magnitude. This study demonstrates that elongate pores within nano-scale grain boundary channels are common in all sampled low permeability formations containing quartz, calcite, barite and dolomite fracture cement. These features may universally increase estimates of formation permeability in low permeability reservoirs containing cemented natural fractures.

Conclusions

The abundance of NGBCs, with consistently similar apertures and textures, indicates that these features are innate to grain boundaries of diagenetic cements filling fully cemented fractures. Higher temperatures seem to favor wider NGBC apertures. NGBSs are not purely a product of dilation during exhumation or core retrieval. TEM imaging has offered insight further into the fact that these grain boundary regions are complex domains, far more complex than the traditional model of fully healed grain boundaries void of porosity. I propose that nanometer scale dissolution-precipitation reactions allow grain boundary pores to be preserved, maintaining a macroscopically stable structure. Pores are manifested differently in monomineralic grain boundaries compared to interphase boundaries, where replacement reactions and/or differences in surface potentials likely drive one mineral to preferentially dissolve over the other. Because of their ubiquity, NGBCs can significantly contribute to permeability of otherwise tightly cemented fractures.

Appendix A: NGBC Aperture Data and Images

SAMPLE: NAM-2774.5, NEW ALBANY FORMATION

Mineral Cement	Rock Type	Sampled Depth (ft)	Sampled Depth (m)	Max Depth (m)	Exhumed (m)	Max T (^{o}C)	Range (nm)	Sample Mean (nm)
Calcite	Shale	2774.5	845	2168	1323	90-100	12-59	28.27

Table A1: Summary of sample NAM-2774.5

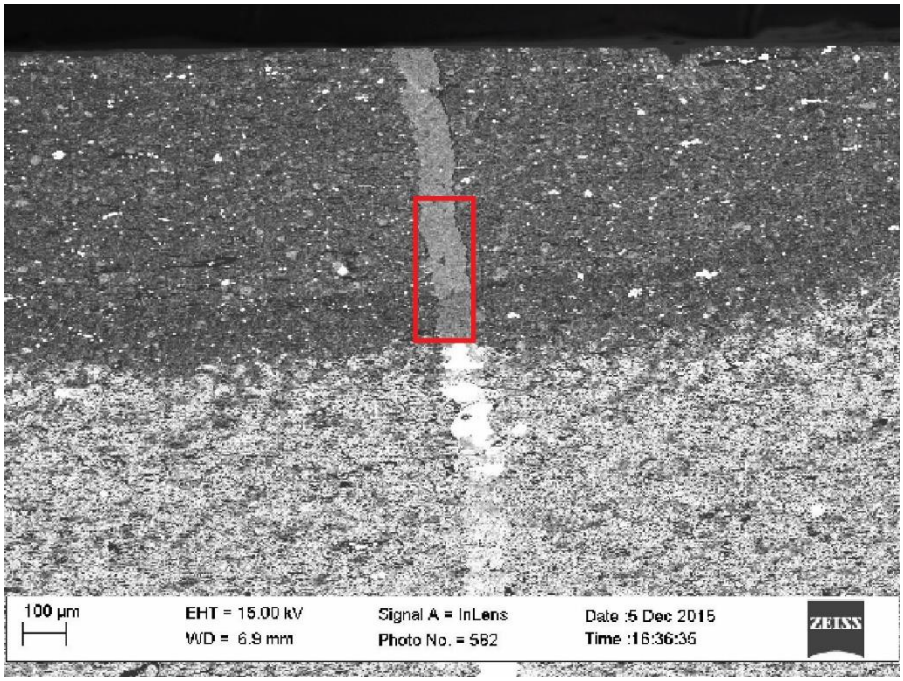

Figure A.1: Inlens SE micrograph of sample NAM-2774.5. Box indicates area used for EBSD analysis and NGBC aperture measurements

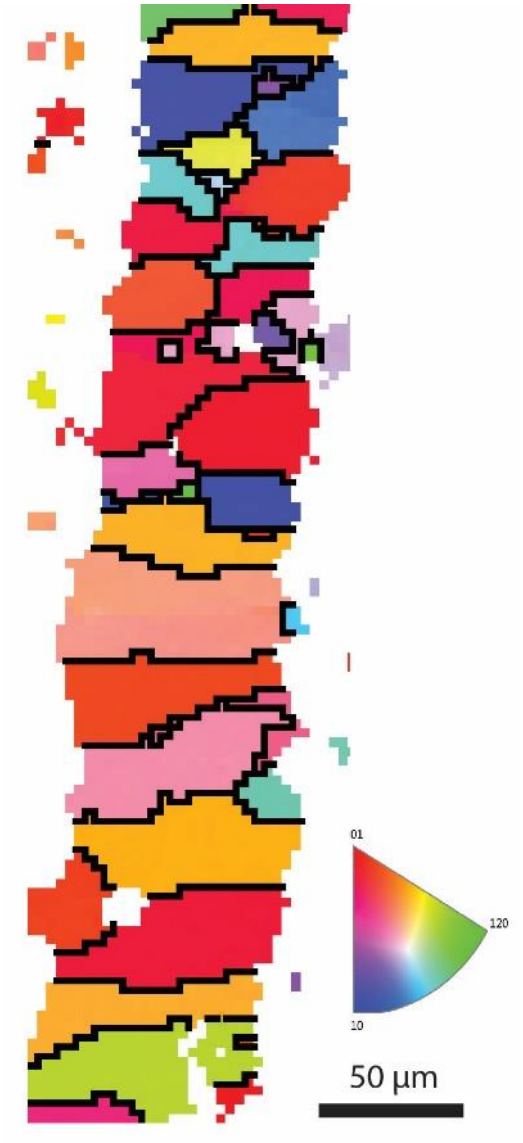

Figure A.2: EBSD inverse pole figure from sample NAM-2774.5.

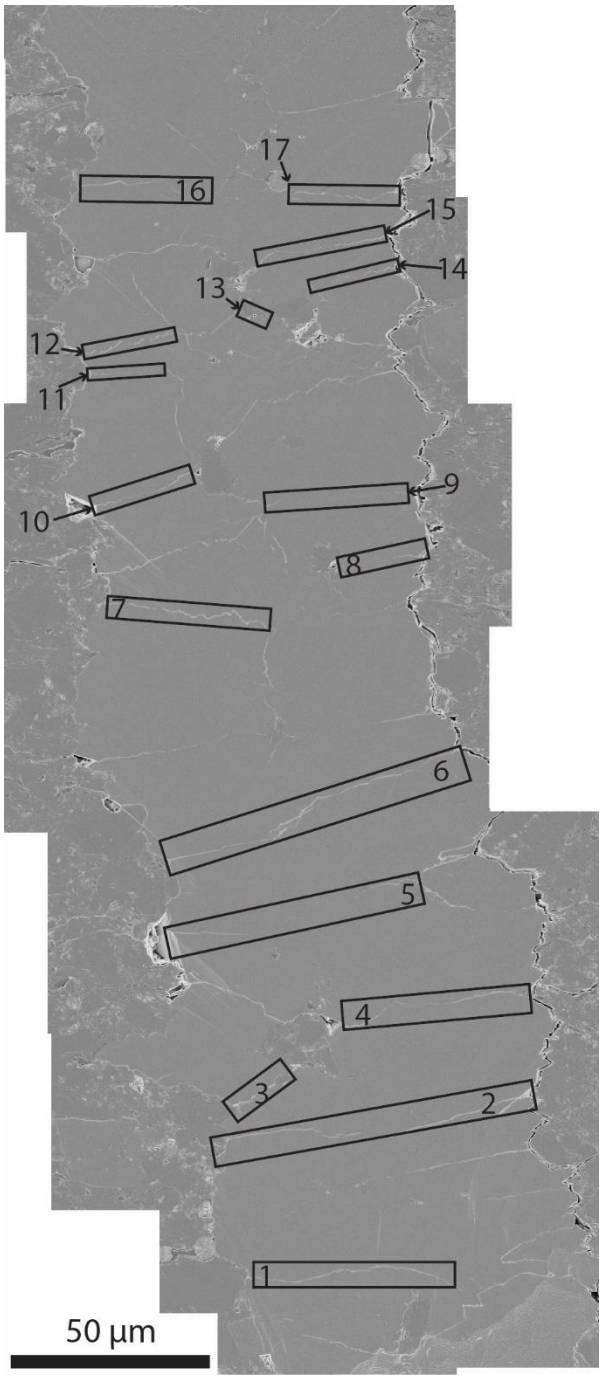

Figure A.3: Inlens SE mosaic of sample NAM-2774.5. Boxes indicate location of grain boundaries used for NGBC aperture measurements.

Grain Boundary	Aperture (nm)
1	52.97
2	58.51
3	25.26
4	22.92
5	16.84
6	28.49
7	51.08
8	23.24
9	19.78
10	14.98
11	11.92
12	48.12
13	25.09
14	18.97
15	28.91
16	14.95
17	26.21
Sample Mean	28.72

Table A.2: NGBC mean apertures and sample mean from sample NAM-2774.5.

Grain Boundary 1

Image	Measurement Number	Aperture (nm)
A	1	53.49
A	2	48.05
A	3	57.31
A	4	53.01
Mean Aperture		52.97

Table A.3: NGBC measurements and mean aperture from grain boundary 1 in sample NAM-2774.5.

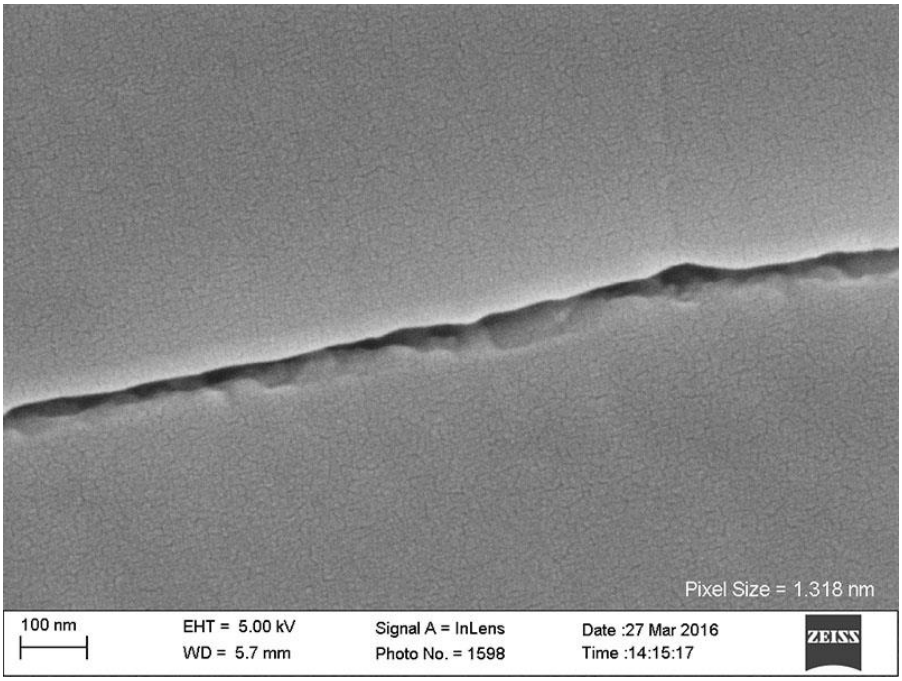

Figure A.4: Inlens SE micrograph from sample NAM-2774.5. Grain boundary 1, image A.

Grain Boundary 2

Image	Measurement Number	Aperture (nm)
A	1	59.88
A	2	65.06
A	3	66.22
A	4	72.09
A	5	41.86
A	6	49.45
A	7	54.97
Mean Aperture		58.51

Table A.4: NGBC measurements and mean aperture from grain boundary 2 in sample NAM-2774.5.

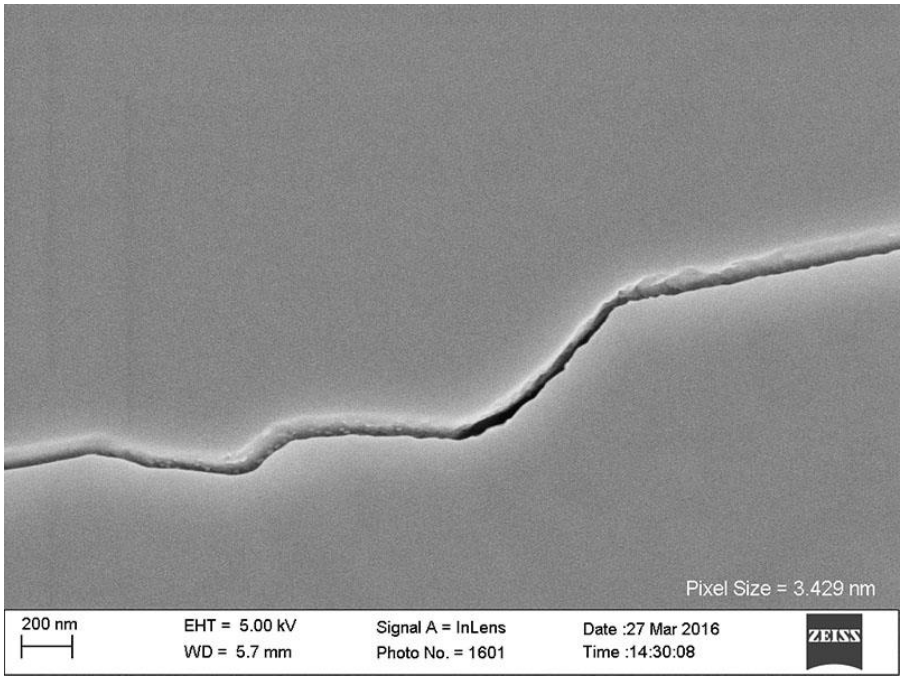

Figure A.5: Inlens SE micrograph from sample NAM-2774.5. Grain boundary 2, image A.

Grain Boundary 3

Image	Measurement Number	Aperture (nm)
A	1	23.16
A	2	25.13
A	3	22.14
A	4	27.66
A	5	27.95
A	6	29.66
A	7	26.53
A	8	25.52
A	9	30.59
A	10	27.08
A	11	28.68
A	12	29.20
A	13	31.00
A	14	28.02
A	15	25.89
A	16	17.78
A	17	18.57
A	18	15.06
A	19	20.31
Mean Aperture		25.26

Table A.5: NGBC measurements and mean aperture from grain boundary 3 in sample NAM-2774.5.

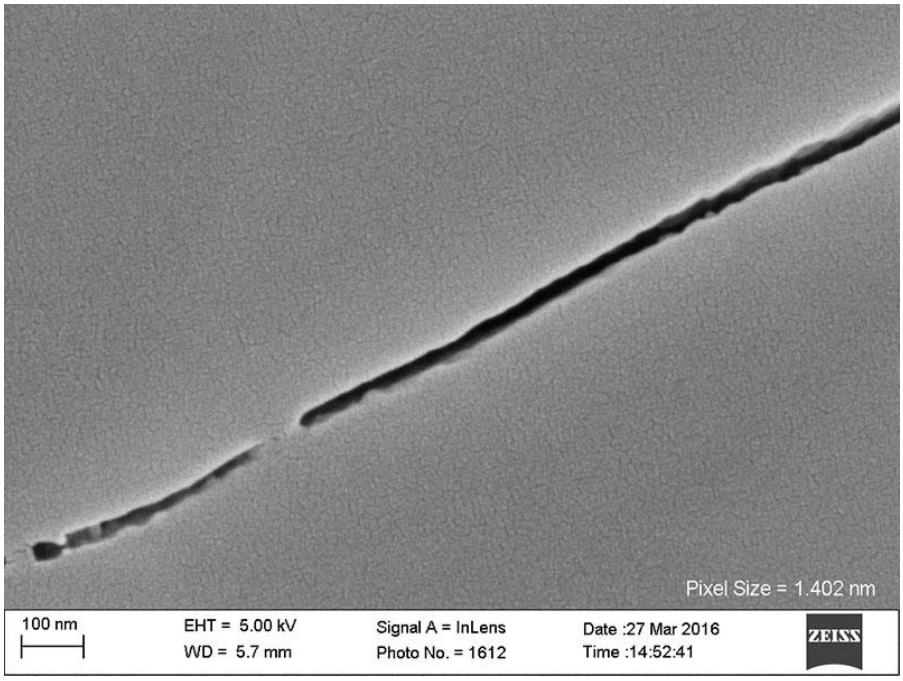

Figure A.6: Inlens SE micrograph from sample NAM-2774.5. Grain boundary 3, image A.

Grain Boundary 4

Image	Measurement Number	Aperture (nm)
A	1	25.31
A	2	24.57
A	3	26.95
A	4	31.62
B	1	15.78
B	2	14.57
B	3	14.57
C	1	28.53
C	2	22.02
D	1	22.00
D	2	21.07
D	3	22.85
D	4	25.55
D	5	25.51
Mean Aperture		22.92

Table A.6: NGBC measurements and mean aperture from grain boundary 4 in sample NAM-2774.5.

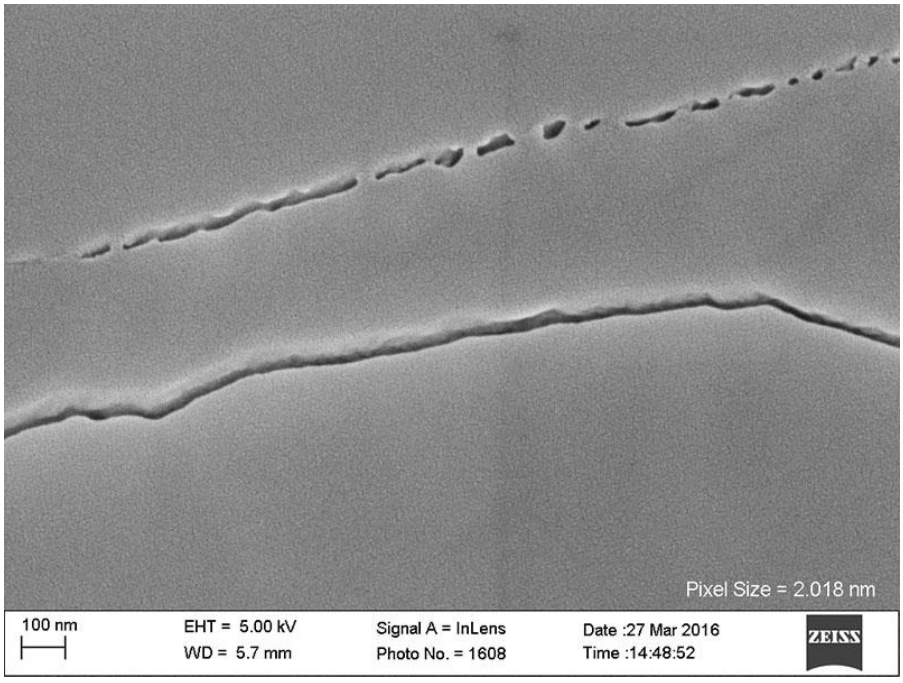

Figure A.7: Inlens SE micrograph from sample NAM-2774.5. Grain boundary 4, image

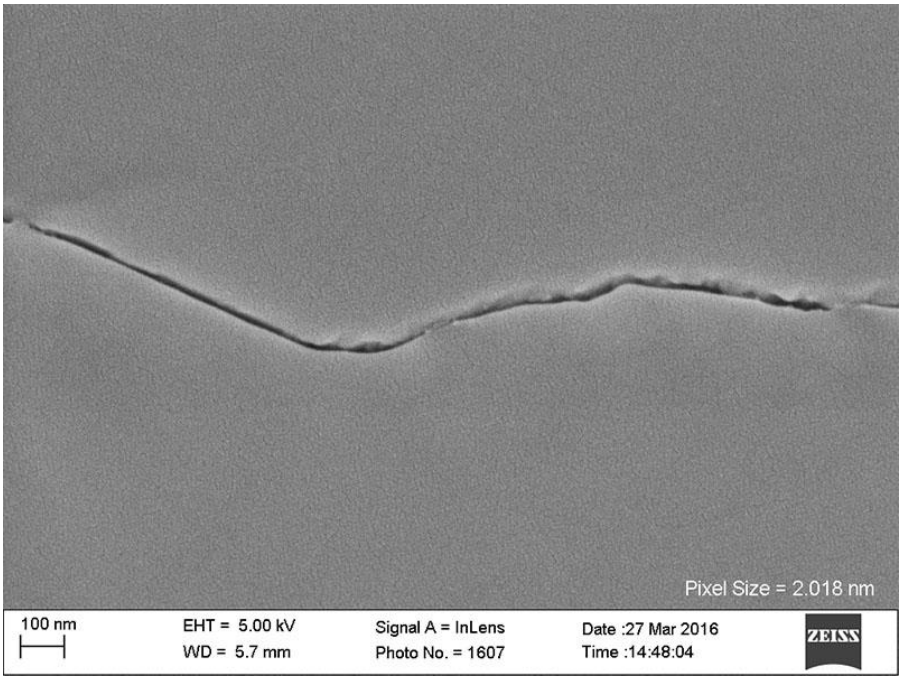

Figure A.8: Inlens SE micrograph from sample NAM-2774.5. Grain boundary 4, image B

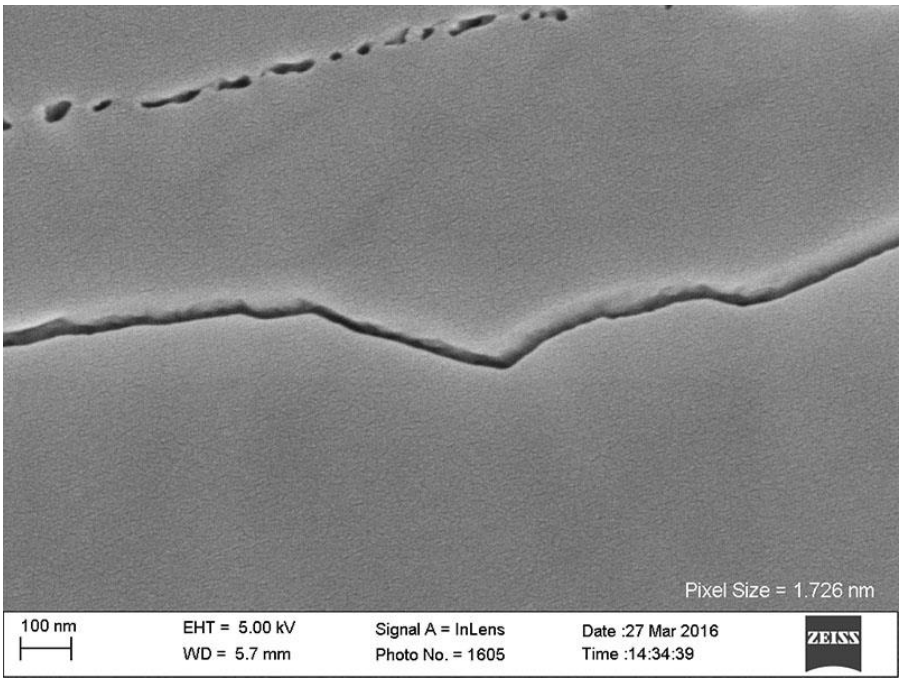

Figure A.9: Inlens SE micrograph from sample NAM-2774.5. Grain boundary 4, image C.

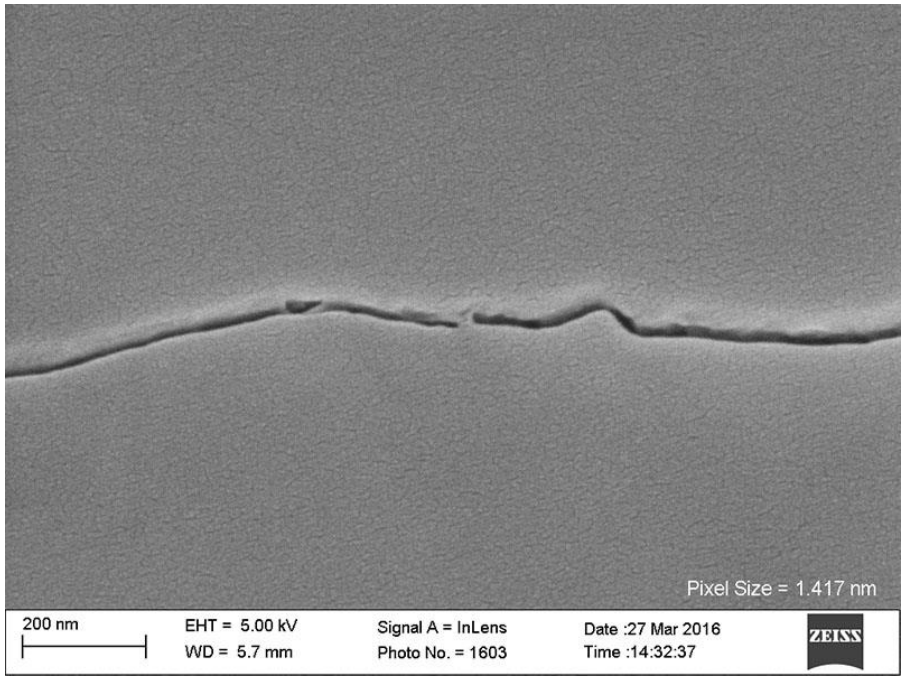

Figure A.10: Inlens SE micrograph from sample NAM-2774.5. Grain boundary 4, image D.

Grain Boundary 5

Image	Measurement Number	Aperture (nm)
A	1	20.07
A	2	21.22
A	3	14.90
B	1	13.30
B	2	16.41
B	3	15.16
Mean Aperture		16.84

Table A.7: NGBC measurements and mean aperture from grain boundary 5 in sample NAM-2774.5.

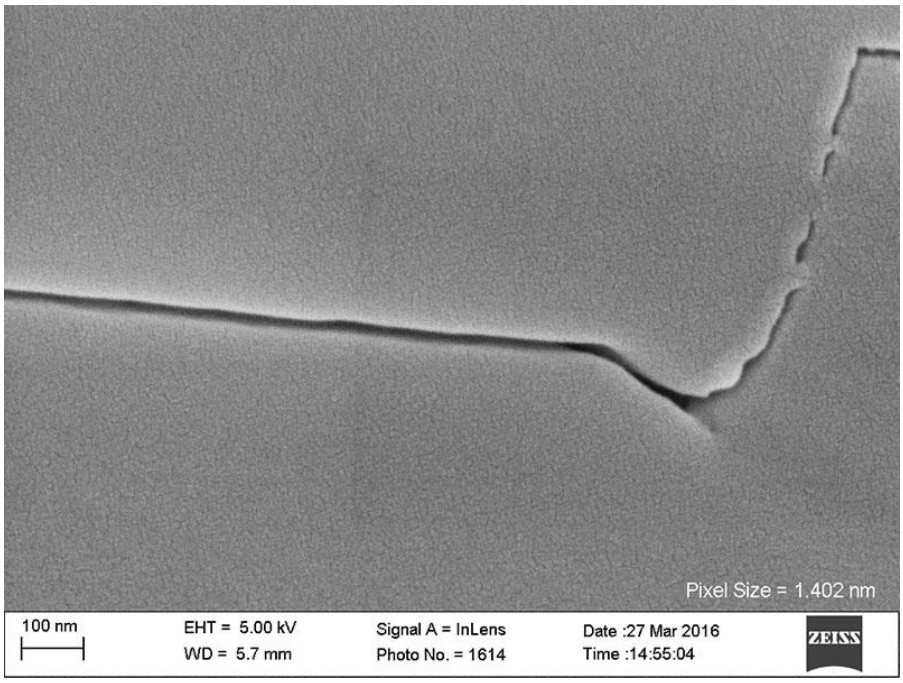

Figure A.11: Inlens SE micrograph from sample NAM-2774.5. Grain boundary 5, image A.

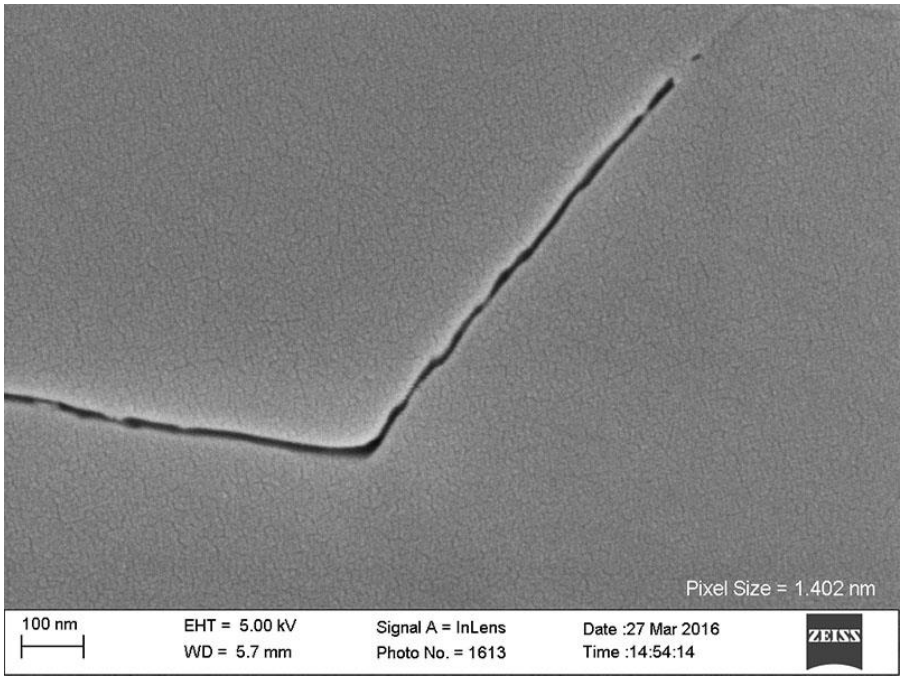

Figure A.12: Inlens SE micrograph from sample NAM-2774.5. Grain boundary 5, image B.

Grain Boundary 6

Image	Measurement Number	Aperture (nm)
A	1	35.28
A	2	30.00
B	1	29.31
B	2	25.91
B	3	21.95
Mean Aperture		28.49

Table A.8: NGBC measurements and mean aperture from grain boundary 6 in sample NAM-2774.5.

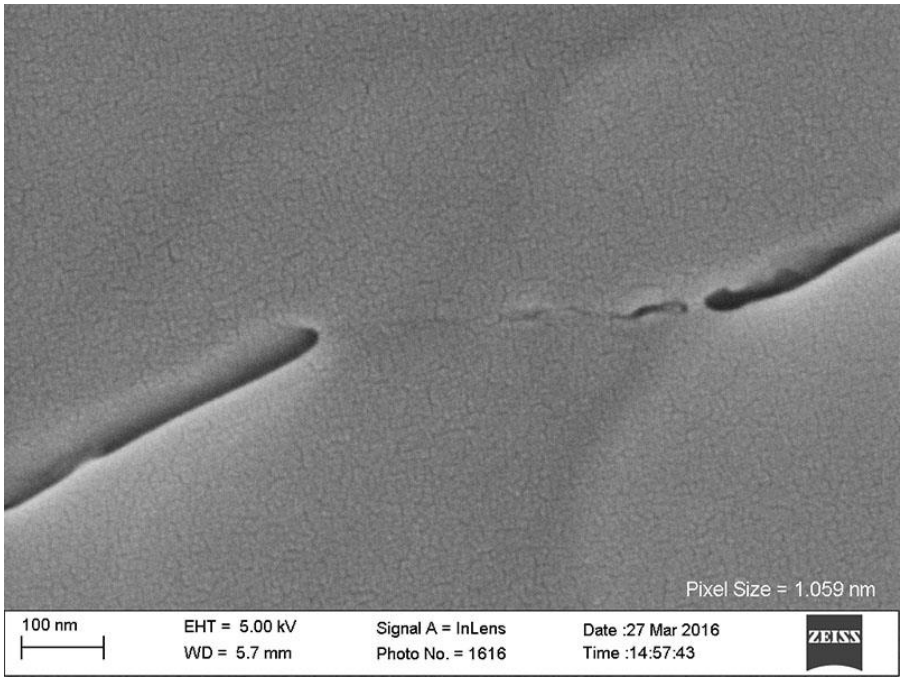

Figure A.13: Inlens SE micrograph from sample NAM-2774.5. Grain boundary 6, image A.

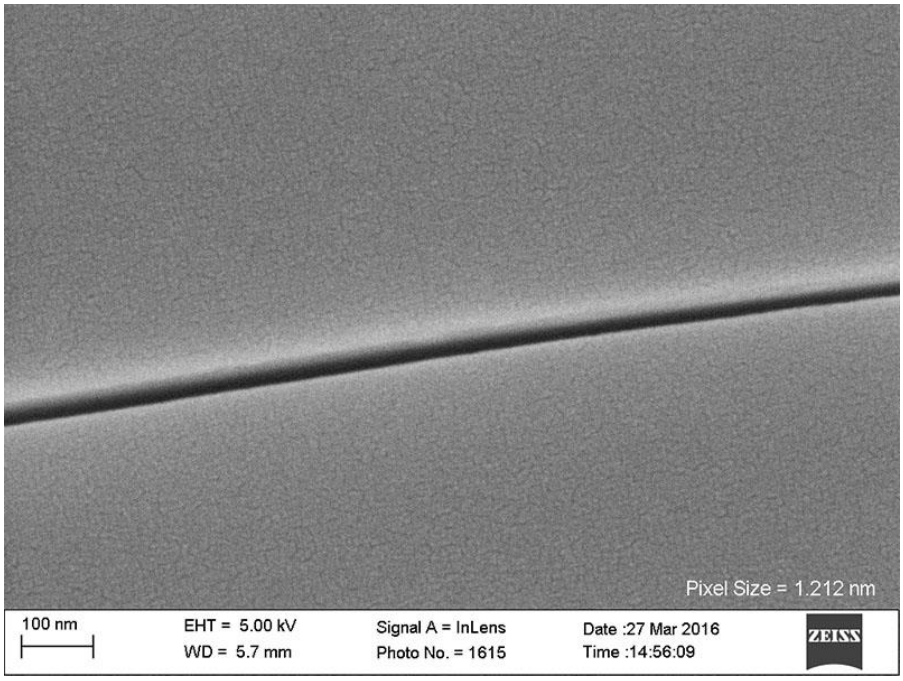

Figure A.14: Inlens SE micrograph from sample NAM-2774.5. Grain boundary 6, image B.

Grain Boundary 7

Image	Measurement Number	Aperture (nm)
A	1	57.00
A	2	47.20
A	3	55.88
A	4	53.64
A	5	41.67
Mean Aperture		51.08

Table A.9: NGBC measurements and mean aperture from grain boundary 7 in sample NAM-2774.5.

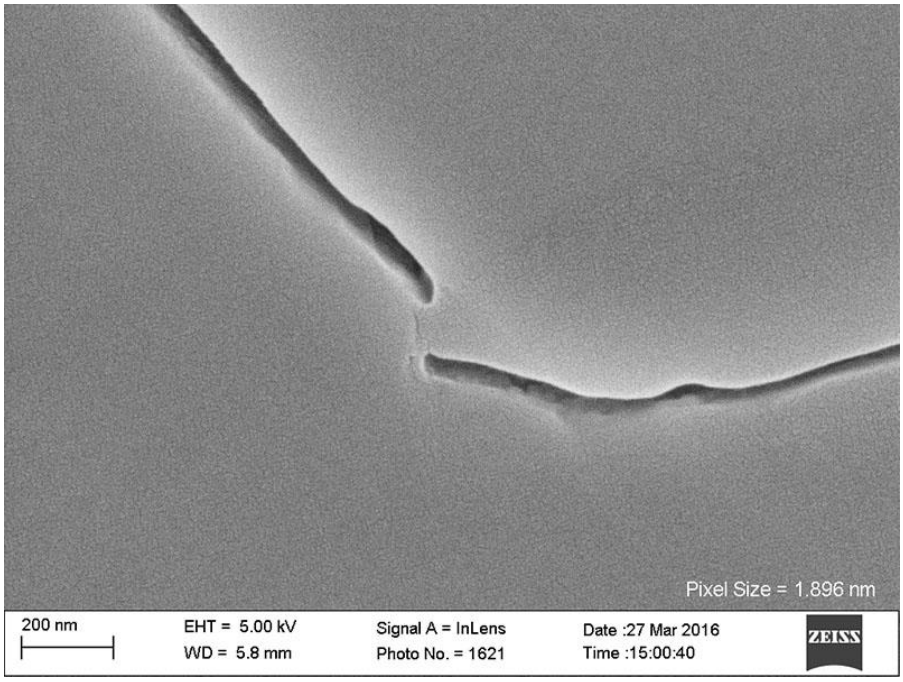

Figure A.15: Inlens SE micrograph from sample NAM-2774.5. Grain boundary 7, image A.

Grain Boundary 8

Image	Measurement Number	Aperture (nm)
A	1	24.18
A	2	24.18
A	3	24.05
A	4	20.55
Mean Aperture		23.24

Table A.10: NGBC measurements and mean aperture from grain boundary 8 in sample NAM-2774.5.

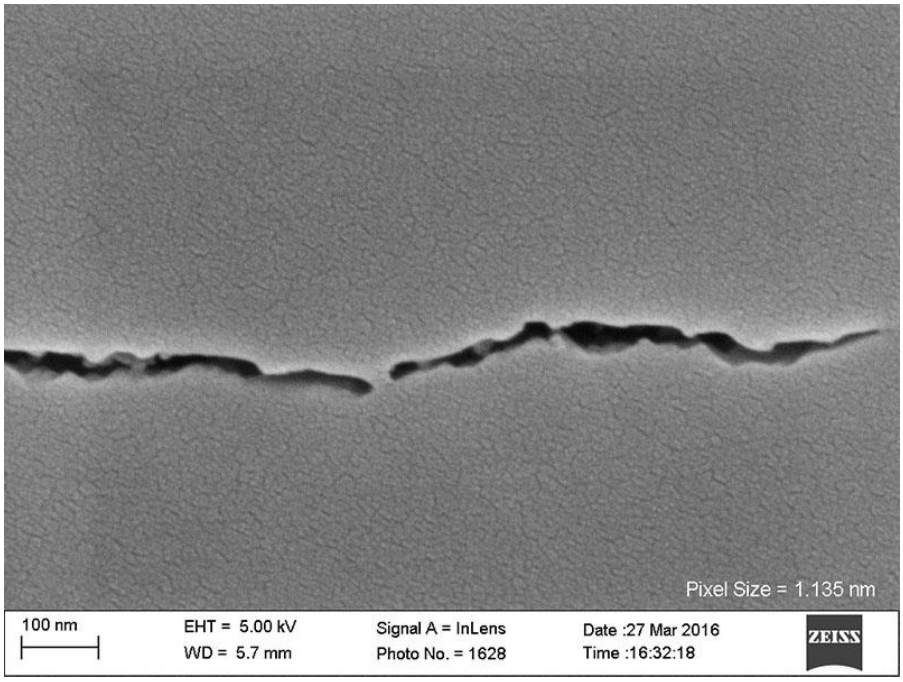

Figure A.16: Inlens SE micrograph from sample NAM-2774.5. Grain boundary 8, image A.

Grain Boundary 9

Image	Measurement Number	Aperture (nm)
A	1	22.06
A	2	17.49
Mean Aperture		19.78

Table A.11: NGBC measurements and mean aperture from grain boundary 9 in sample NAM-2774.5.

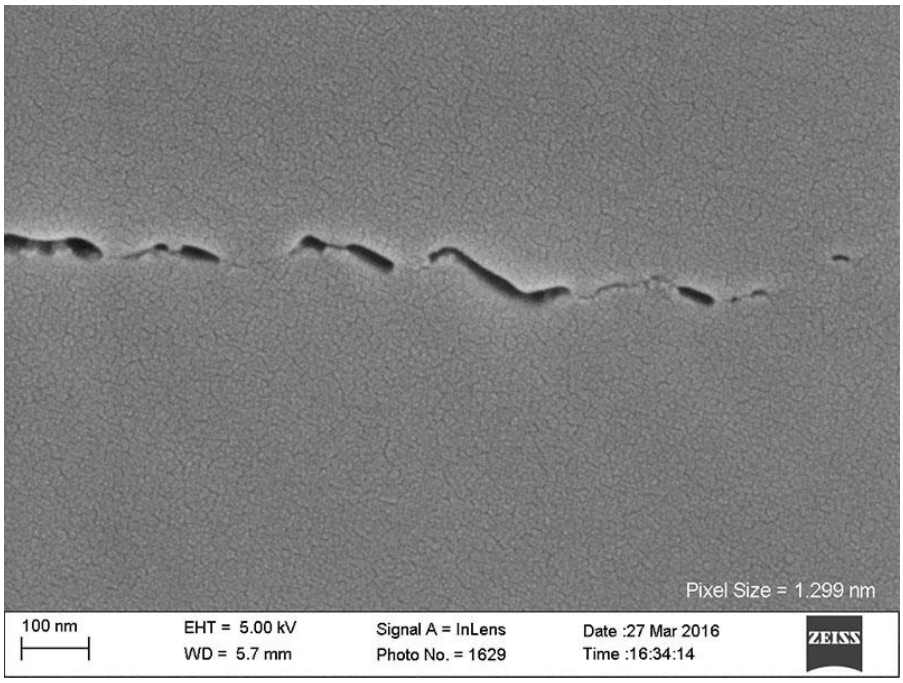

Figure A.17: Inlens SE micrograph from sample NAM-2774.5. Grain boundary 9, image A.

Grain Boundary 10

Image	Measurement Number	Aperture (nm)
A	1	12.86
A	2	15.43
A	3	15.64
B	1	16.06
B	2	13.67
B	3	16.24
Mean Aperture		14.98

Table A.12: NGBC measurements and mean aperture from grain boundary 10 in sample NAM-2774.5.

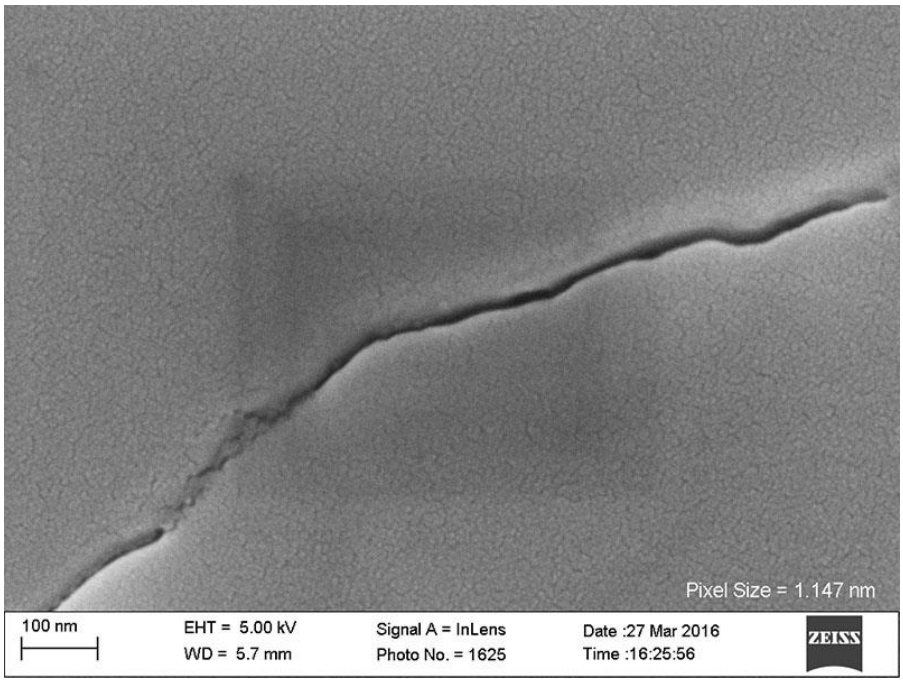

Figure A.18: Inlens SE micrograph from sample NAM-2774.5. Grain boundary 10, image A.

Grain Boundary 11

Image	Measurement Number	Aperture (nm)
A	1	9.03
A	2	8.08
A	3	7.51
B	1	15.66
B	2	15.01
B	3	16.22
Mean Aperture		11.92

Table A.13: NGBC measurements and mean aperture from grain boundary 11 in sample NAM-2774.5.

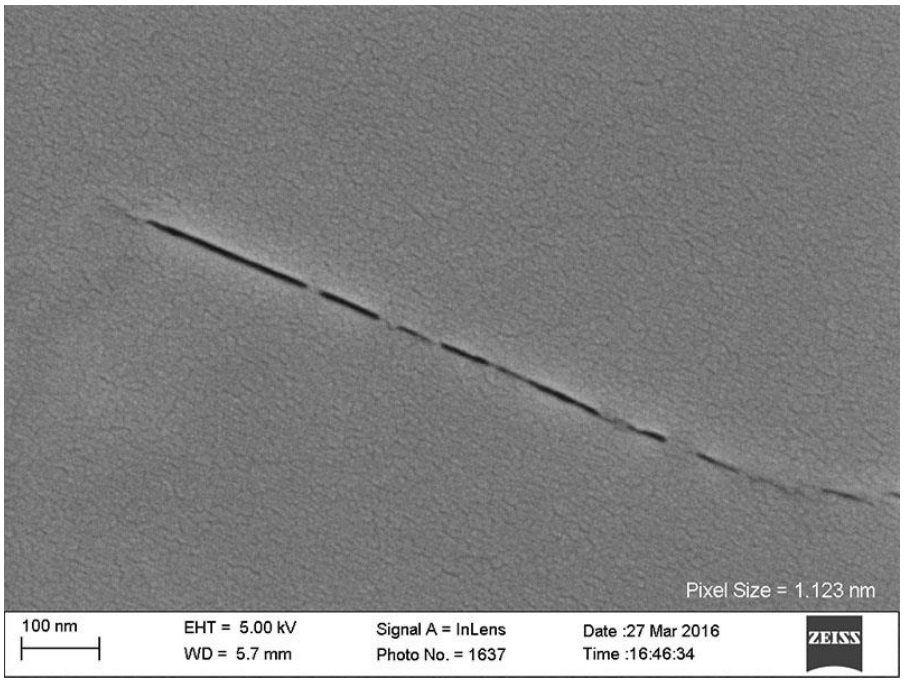

Figure A.19: Inlens SE micrograph from sample NAM-2774.5. Grain boundary 11, image A.

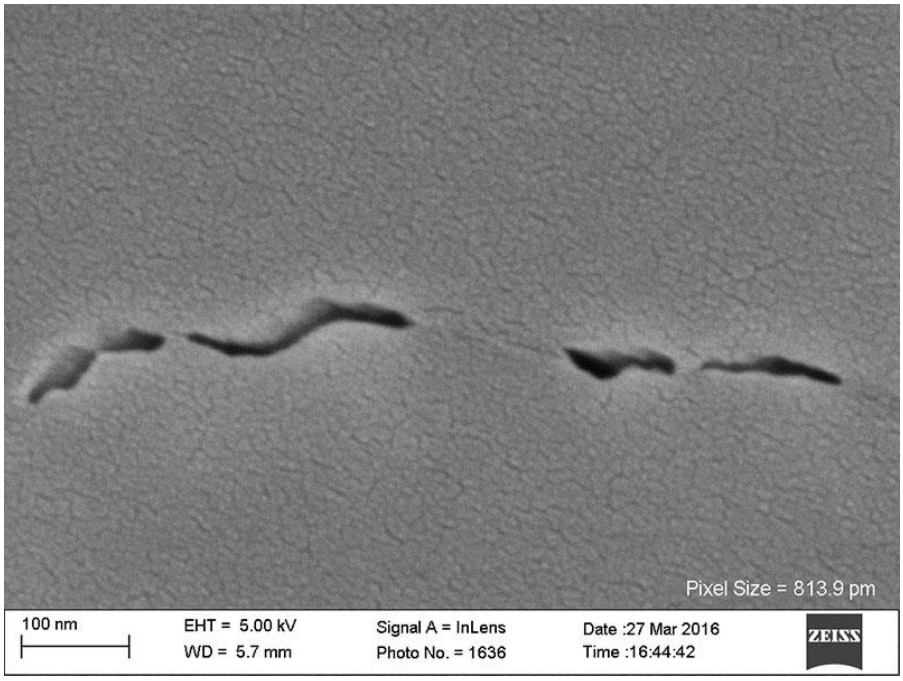

Figure A.20: Inlens SE micrograph from sample NAM-2774.5. Grain boundary 11, image B.

Grain Boundary 12

Image	Measurement Number	Aperture (nm)
A	1	39.60
A	2	51.05
A	3	46.95
A	4	53.73
A	5	49.25
Mean Aperture		48.12

Table A.14: NGBC measurements and mean aperture from grain boundary 12 in sample NAM-2774.5.

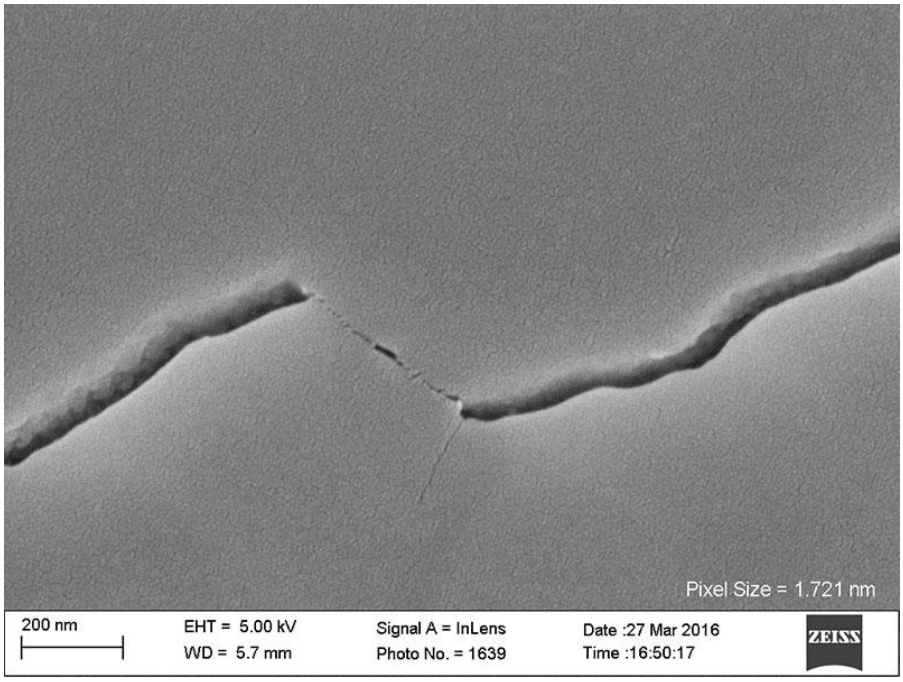

Figure A.21: Inlens SE micrograph from sample NAM-2774.5. Grain boundary 12, image A.

Grain Boundary 13

Image	Measurement Number	Aperture (nm)
A	1	29.48
A	2	22.21
A	3	31.28
A	4	20.38
A	5	22.12
Mean Aperture		25.09

Table A.15: NGBC measurements and mean aperture from grain boundary 13 in sample NAM-2774.5.

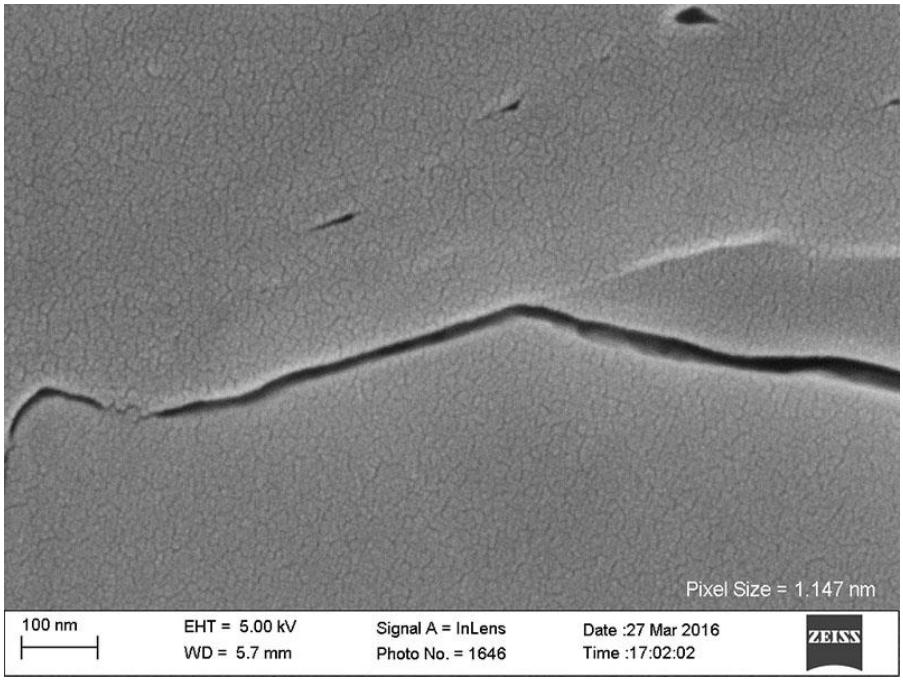

Figure A.22: Inlens SE micrograph from sample NAM-2774.5. Grain boundary 13, image A.

Grain Boundary 14

Image	Measurement Number	Aperture (nm)
A	1	21.54
A	2	15.01
A	3	17.78
A	4	22.18
A	5	18.36
Mean Aperture		18.97

Table A.16: NGBC measurements and mean aperture from grain boundary 14 in sample NAM-2774.5.

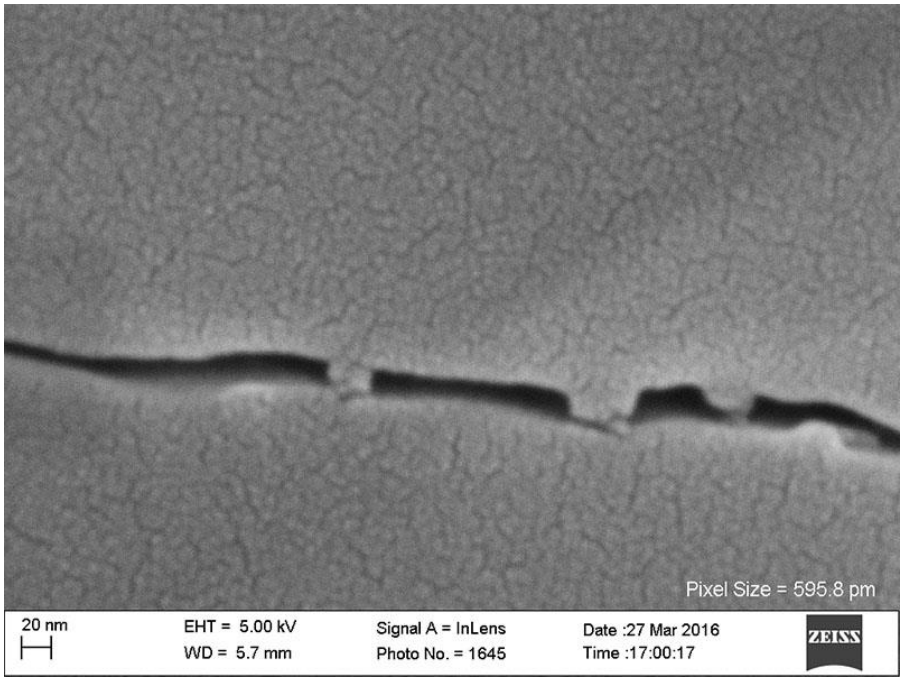

Figure A.23: Inlens SE micrograph from sample NAM-2774.5. Grain boundary 14, image A.

Grain Boundary 15

Image	Measurement Number	Aperture (nm)
A	1	33.24
A	2	25.34
A	3	28.00
A	4	31.14
A	5	25.78
A	6	32.71
A	7	26.12
Mean Aperture		28.91

Table A.17: NGBC measurements and mean aperture from grain boundary 15 in sample NAM-2774.5.

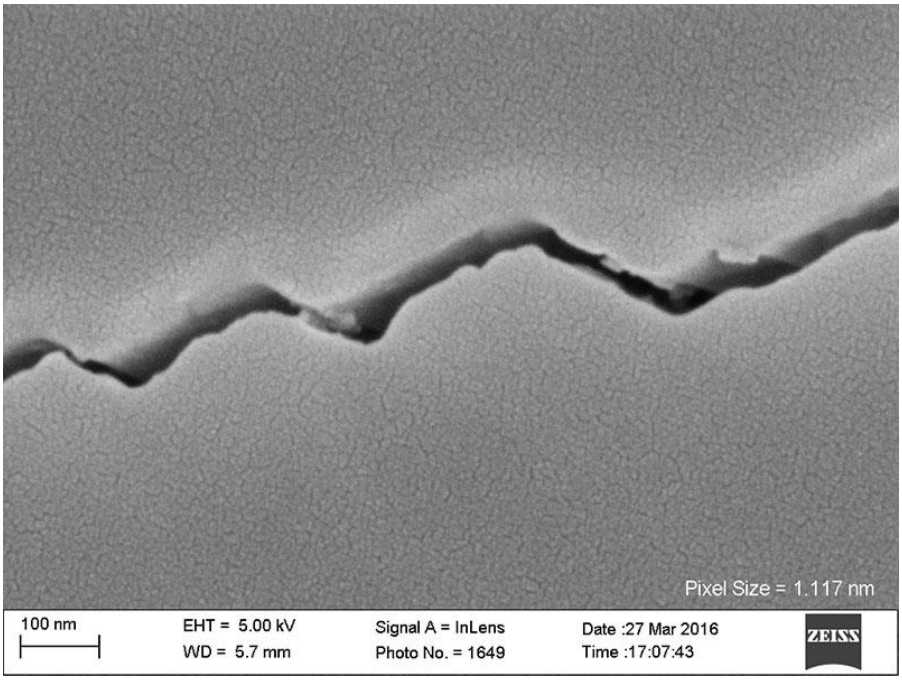

Figure A.24: Inlens SE micrograph from sample NAM-2774.5. Grain boundary 15, image A.

Grain Boundary 16

Image	Measurement Number	Aperture (nm)
A	1	15.78
A	2	14.60
A	3	13.42
A	4	16.01
Mean Aperture		14.95

Table A.18: NGBC measurements and mean aperture from grain boundary 16 in sample NAM-2774.5.

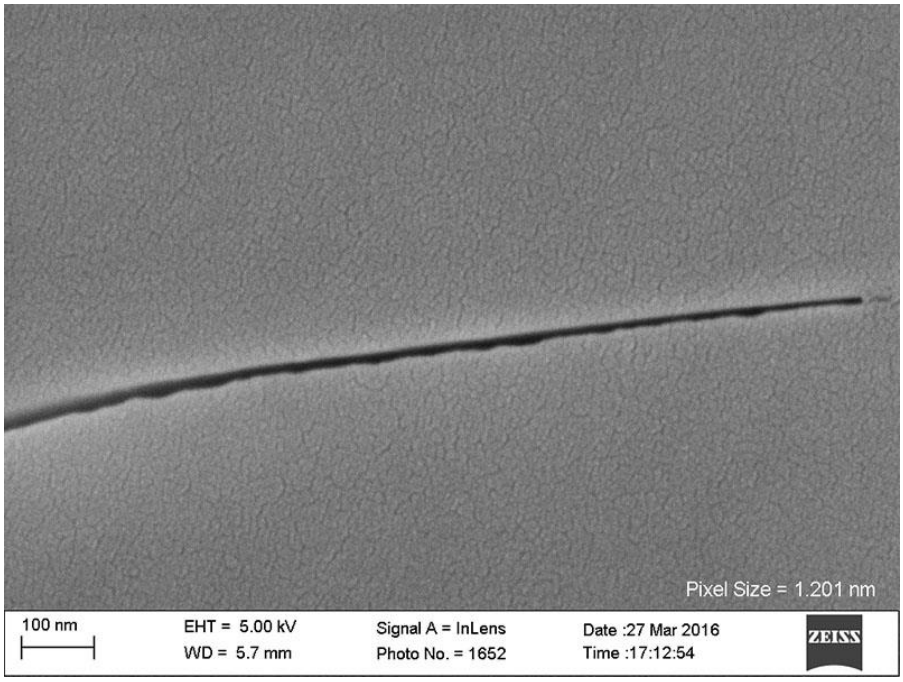

Figure A.25: Inlens SE micrograph from sample NAM-2774.5. Grain boundary 16, image A.

Grain Boundary 17

Image	Measurement Number	Aperture (nm)
A	1	15.78
A	2	18.77
A	3	18.92
B	1	33.18
B	2	21.79
B	3	45.15
B	4	29.87
Mean Aperture		26.21

Table A.19: NGBC measurements and mean aperture from grain boundary 17 in sample NAM-2774.5.

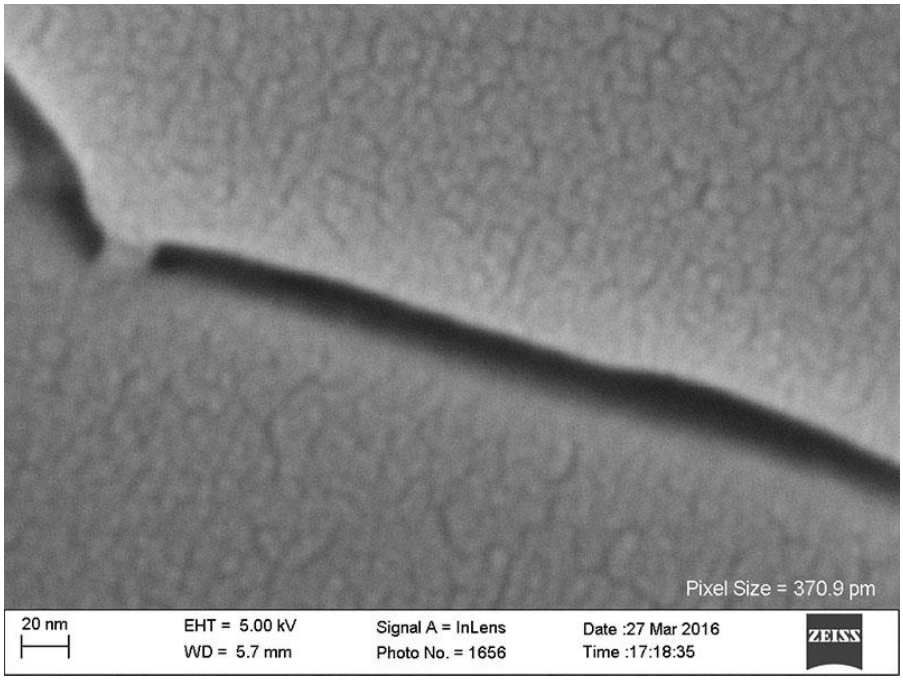

Figure A.26: Inlens SE micrograph from sample NAM-2774.5. Grain boundary 17, image A.

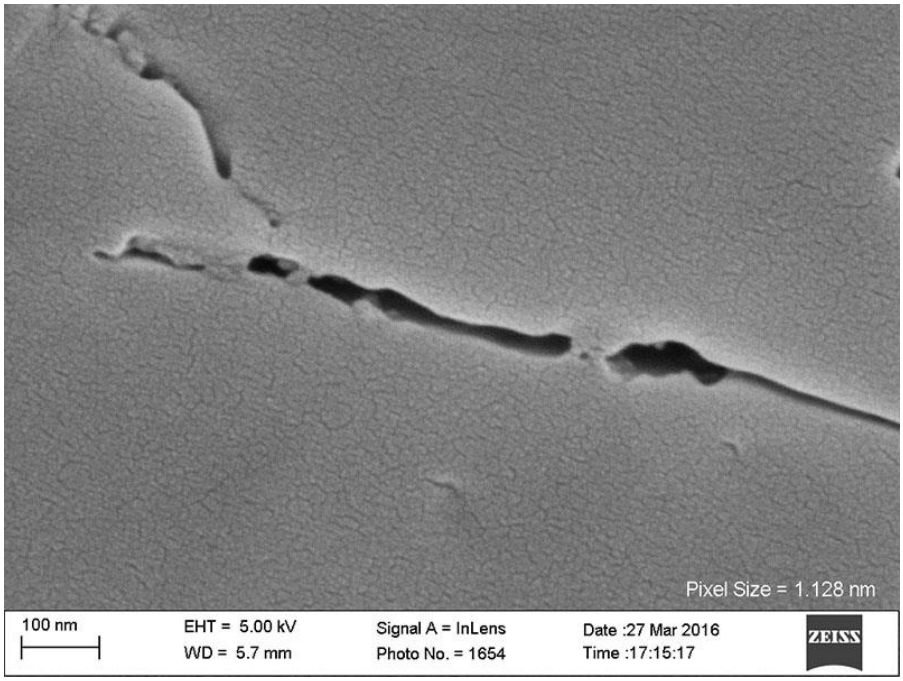

Figure A.27: Inlens SE micrograph from sample NAM-2774.5. Grain boundary 17, image B.

SAMPLE: NAM-2784, NEW ALBANY FORMATION

Mineral Cement	Rock Type	Sampled Depth (ft)	Sampled Depth (m)	Max burial depth (m)	Exhumed (m)	Max T (^{O}C)	Range (nm)	Sample Mean (nm)
Calcite	Shale	2784	848.5	2170	1323	90-100	21-256	93.23

Table A20: Summary of sample NAM-2784.

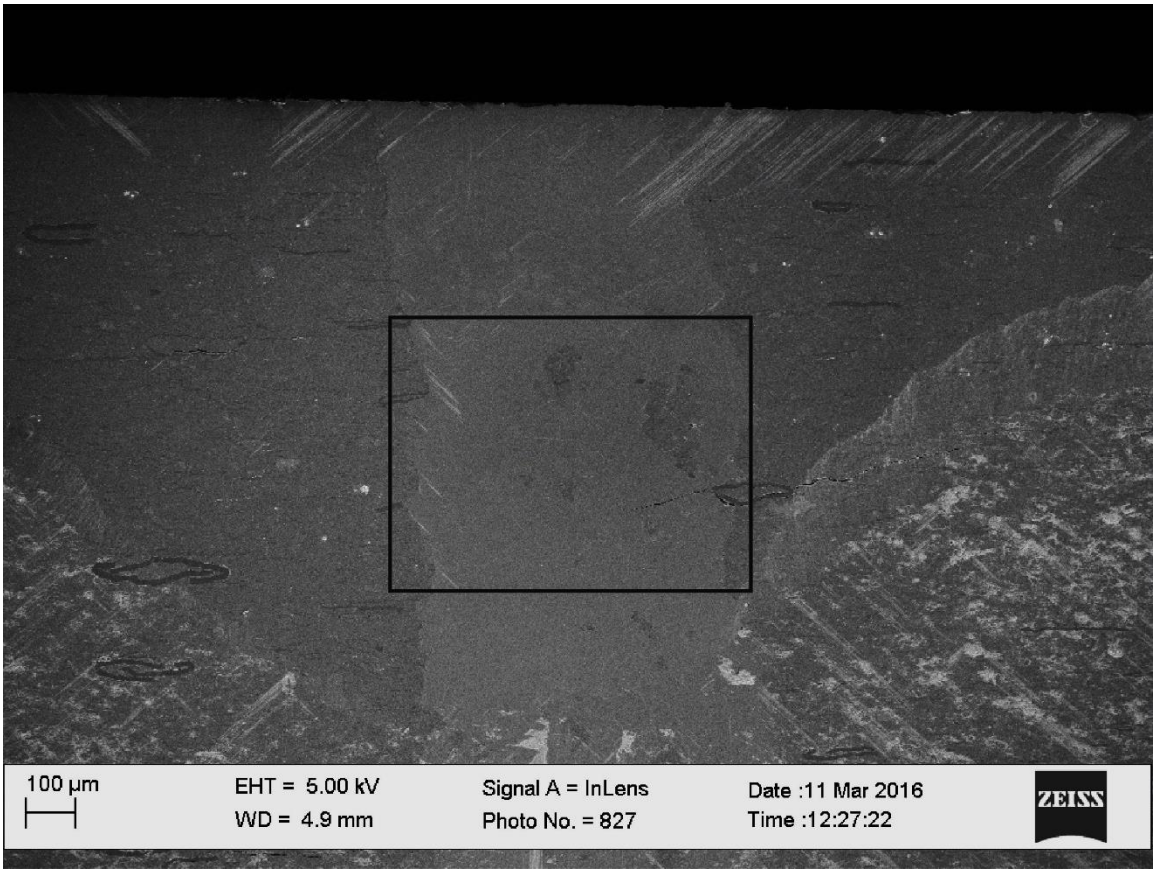

Figure A.28: Inlens SE micrograph of sample NAM-2784. Box indicates area imaged for EBSD analysis and NGBC aperture measurements.

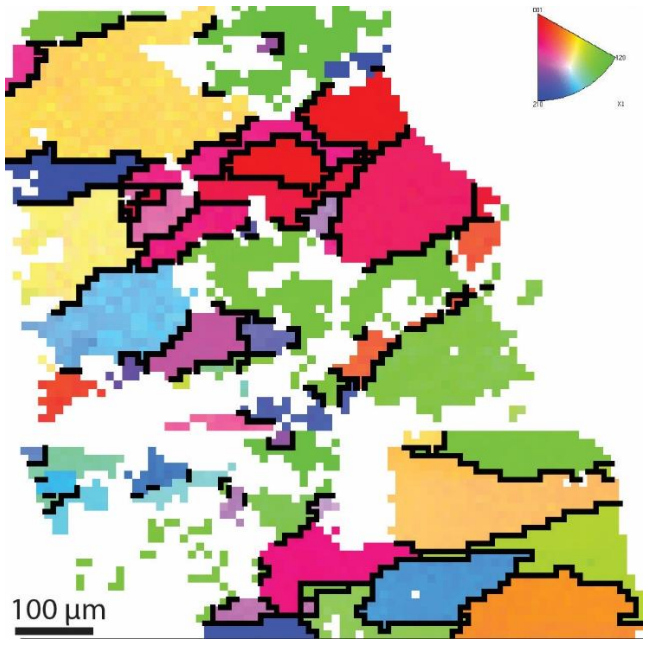

Figure A.29: EBSD inverse pole figure from sample NAM-2784.

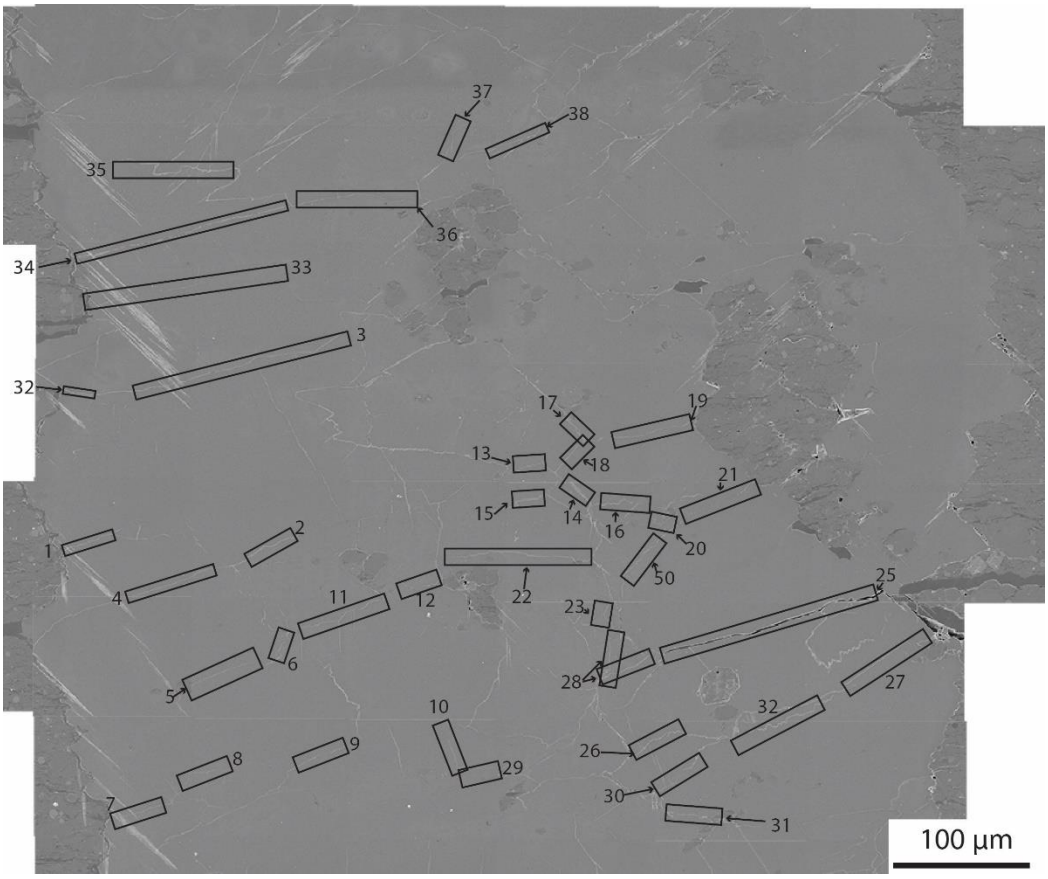

Figure A.30: Inlens SE mosaic of sample NAM-2774.5. Boxes indicate locations of grain boundaries used for NGBC aperture measurements.

Grain Boundary	Mean Aperture (nm)
1	105.60
2	78.38
3	112.18
4	65.76
5	53.45
6	41.45
7	34.65
8	61.81
9	61.03
10	44.24
11	62.49
12	60.92
13	65.30
14	179.40
15	66.27
16	60.81
17	130.48
18	181.03
19	34.16
20	50.48
21	89.24
22	112.45
23	66.01
24	43.74
25	81.00
26	147.54
27	120.67
28	81.03
29	30.03
30	190.17
31	223.67
32	170.17
33	35.59
34	174.18
35	256.55
36	94.31
37	55.43
38	21.17
Sample Mean	93.23

Table A.21: NGBC mean apertures and sample mean from sample NAM-2784.

Grain Boundary 1

mage	Measurement Number	Length (nm)
A	1	88.99
A	2	123.37
A	3	114.98
A	4	121.94
A	5	86.48
B	1	116.02
B	2	116.02
B	3	54.90
B	4	109.49
B	5	123.82
Mean Aperture		105.60

Table A.22: NGBC measurements and mean aperture from grain boundary 1 in sample NAM-2784.

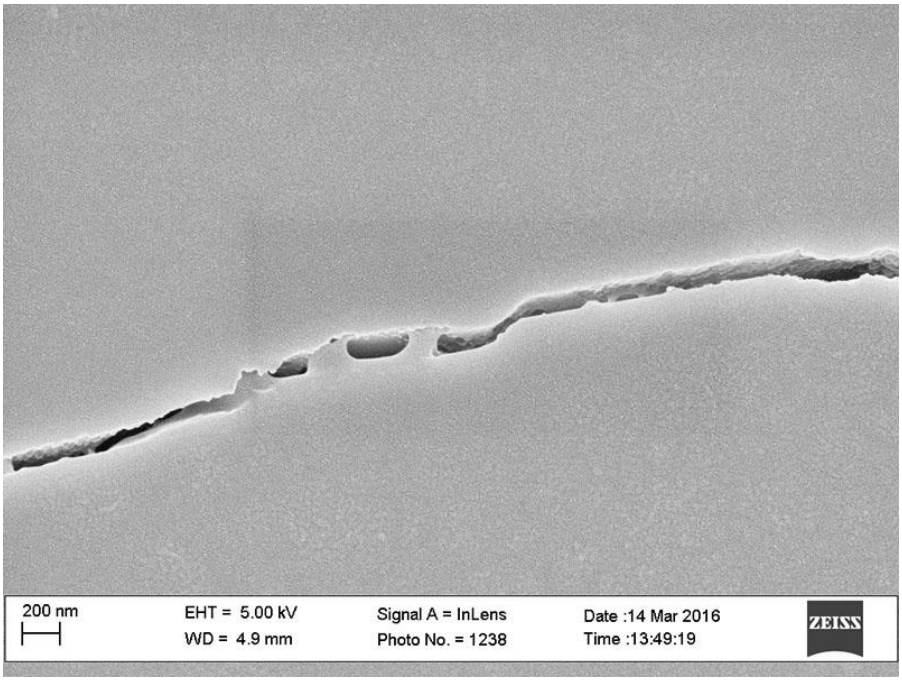

Figure A.31: Inlens SE micrograph from sample NAM-2784. Grain boundary 1, image A.

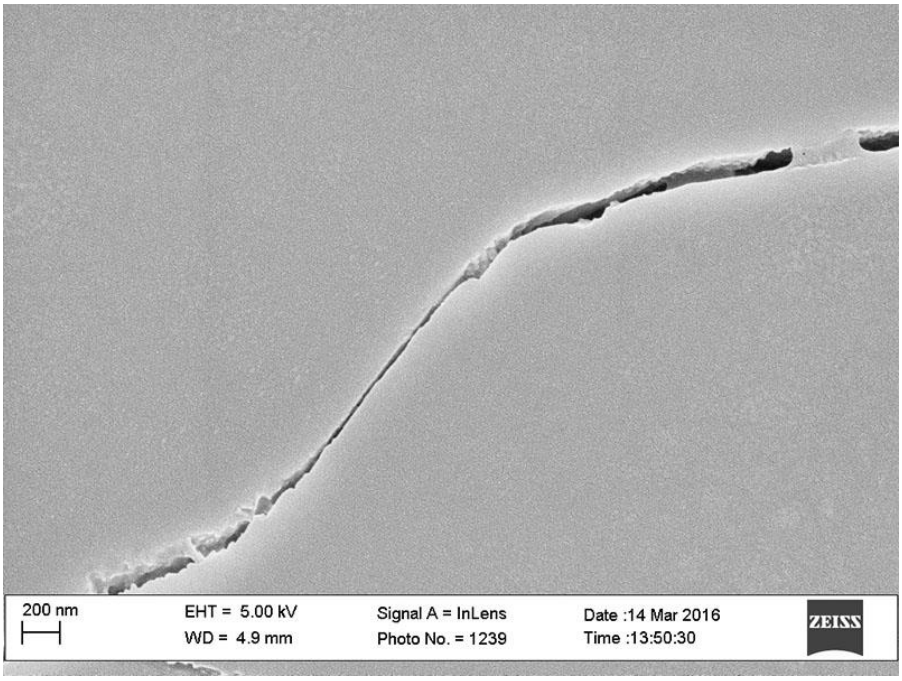

Figure A.32: Inlens SE micrograph from sample NAM-2784. Grain boundary 1, image B.

Grain boundary 2

A	1	80.95
A	2	80.95
A	3	99.97
A	4	85.87
A	5	65.27
A	6	57.24
Mean Aperture		78.38

Table A.23: NGBC measurements and mean aperture from grain boundary 2 in sample NAM-2784.

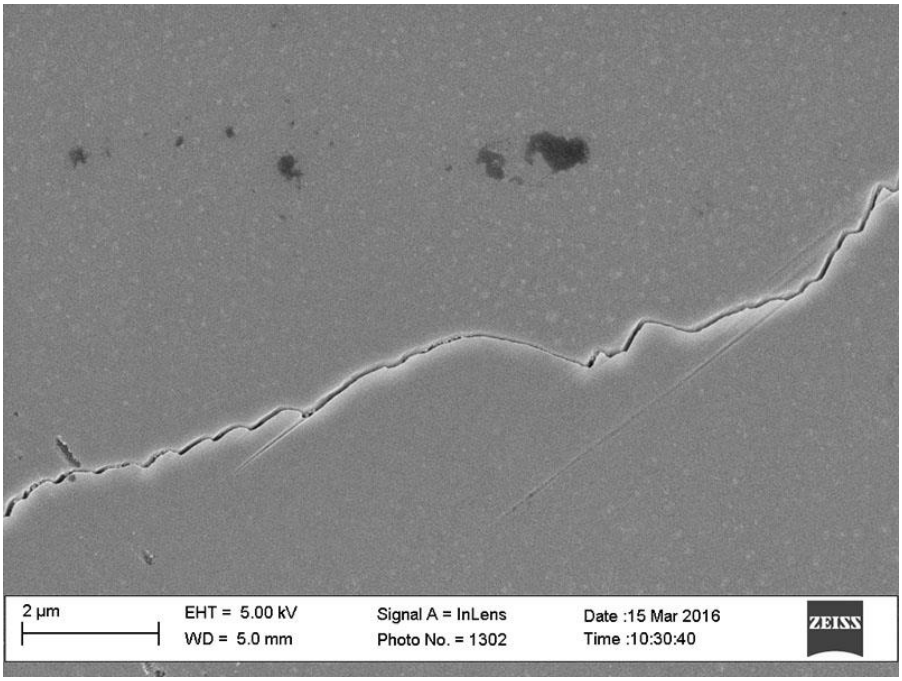

Figure A.33: Inlens SE micrograph from sample NAM-2784. Grain boundary 2, image A.

Grain boundary 3

Image	Measurement Number	Length (nm)
A	1	113.67
A	2	118.24
A	3	120.76
A	4	120.76
A	5	101.16
A	6	98.47
Mean Aperture		112.18

Table A.24: NGBC measurements and mean aperture from grain boundary 3 in sample NAM-2784.

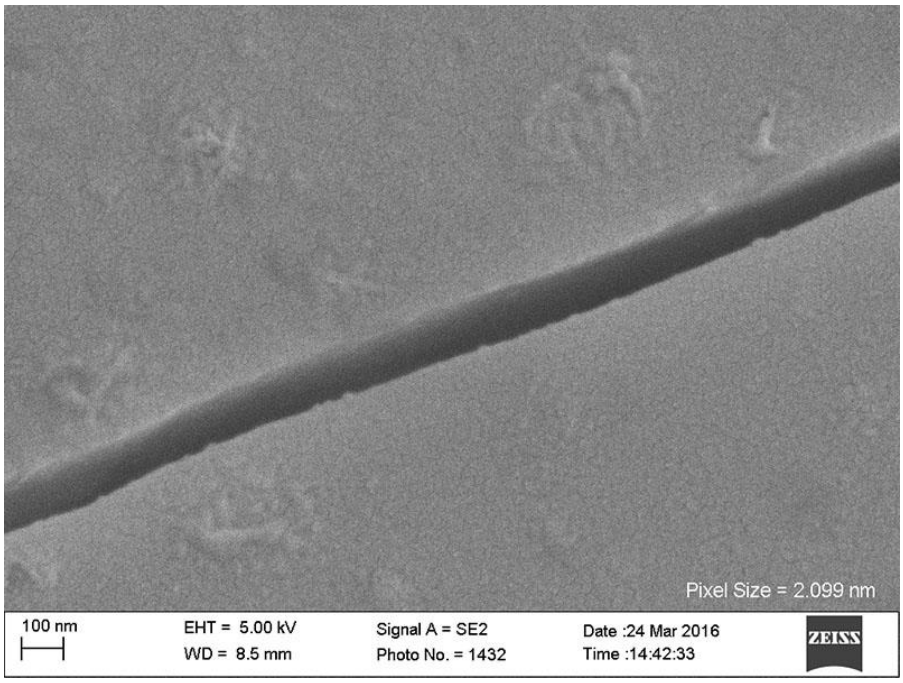

Figure A.34: Inlens SE micrograph from sample NAM-2784. Grain boundary 3, image A.

Grain boundary 4

Image	Measurement Number	Length (nm)
A	1	55.79
A	2	60.29
A	3	81.23
A	4	67.13
A	5	46.01
B	1	71.50
B	2	65.06
B	3	70.30
B	4	74.50
Mean Aperture		65.76

Table A.25: NGBC measurements and mean aperture from grain boundary 4 in sample NAM-2784.

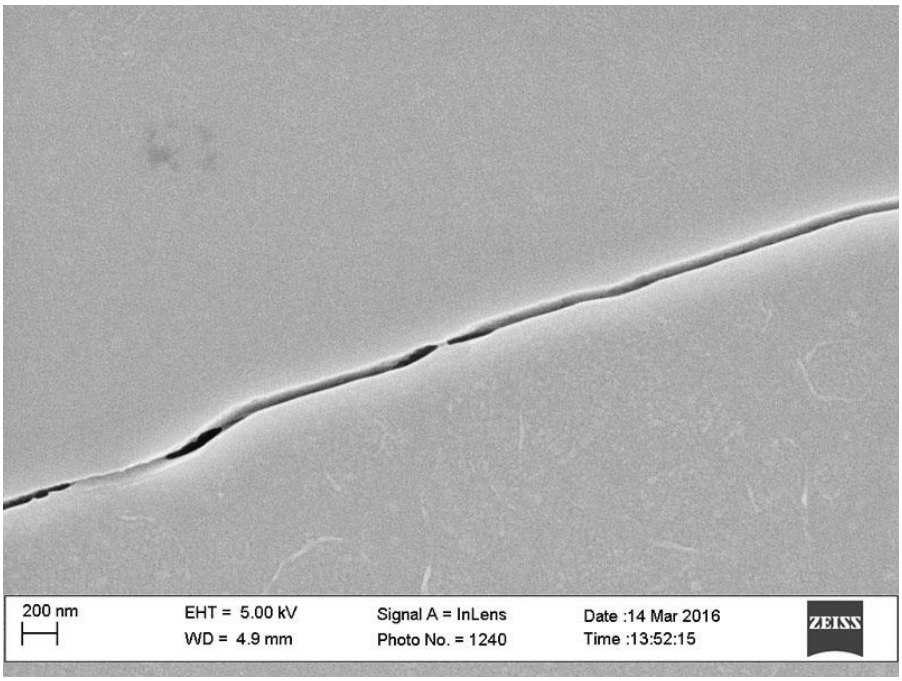

Figure A.35: Inlens SE micrograph from sample NAM-2784. Grain boundary 4, image A.

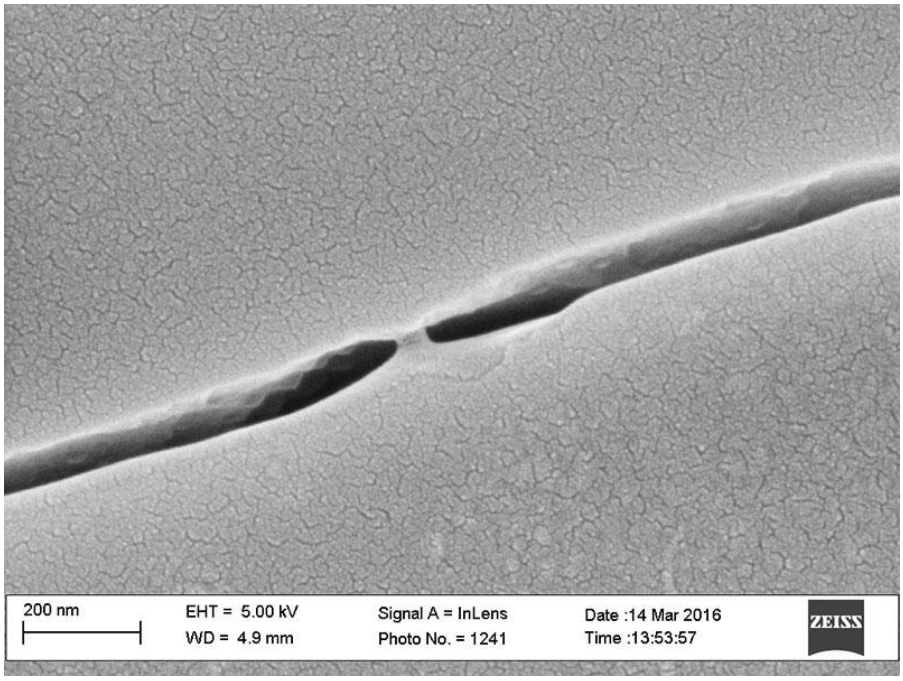

Figure A.36: Inlens SE micrograph from sample NAM-2784. Grain boundary 4, image B.

Grain boundary 5

Image	Measurement Number	Length (nm)
A	1	73.84
A	2	71.71
A	3	62.95
A	4	52.89
B	1	61.48
B	2	50.24
B	3	55.61
C	1	45.12
C	2	41.22
C	3	36.50
C	4	31.90
D	1	61.82
D	2	50.62
D	3	50.62
D	4	55.19
Mean Aperture		53.45

Table A.26: NGBC measurements and mean aperture from grain boundary 5 in sample NAM-2784.

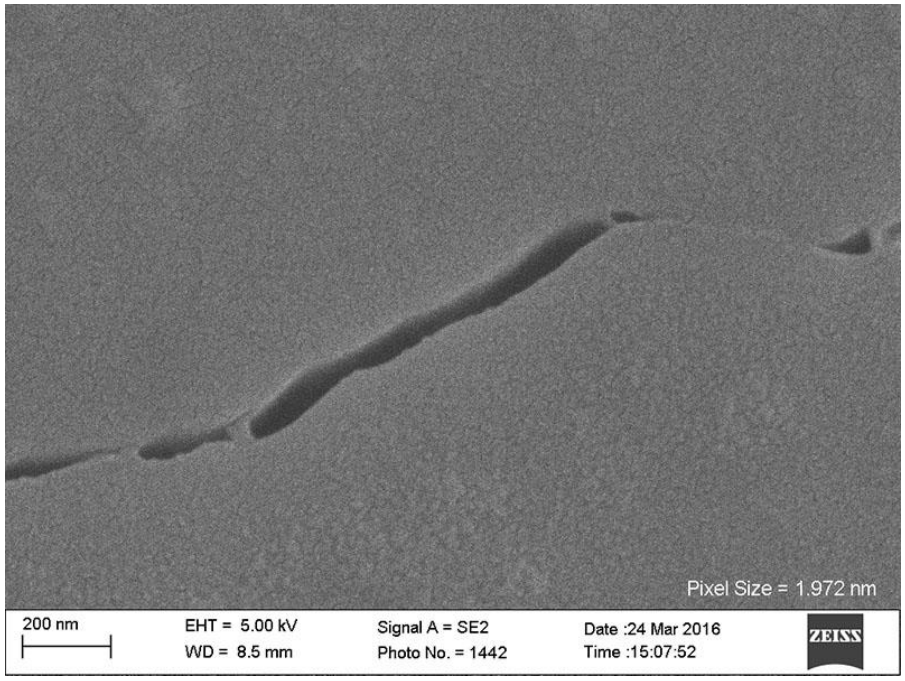

Figure A.37: Inlens SE micrograph from sample NAM-2784. Grain boundary 5, image A.

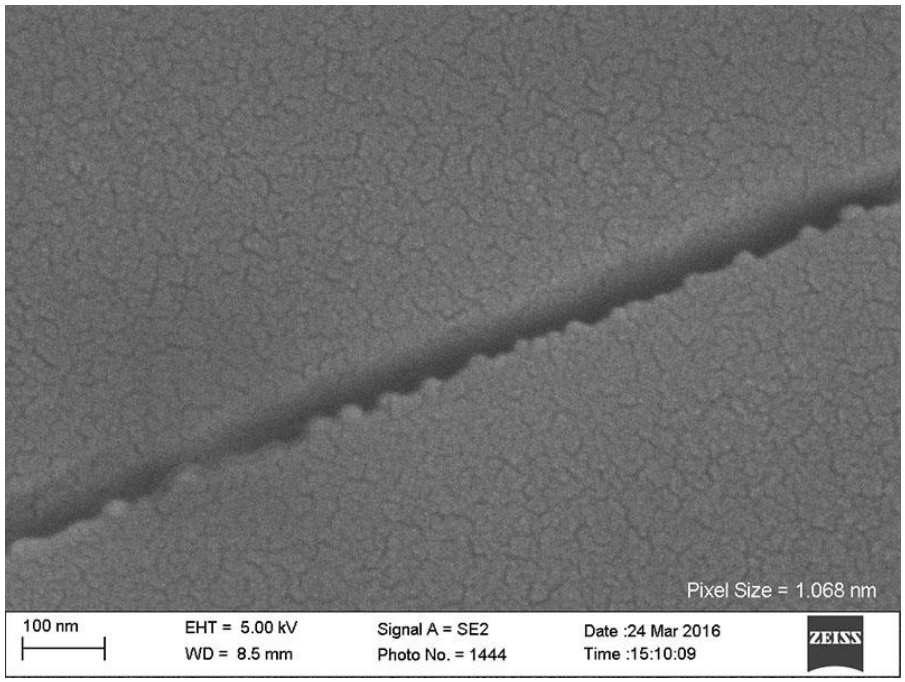

Figure A.38: Inlens SE micrograph from sample NAM-2784. Grain boundary 5, image B

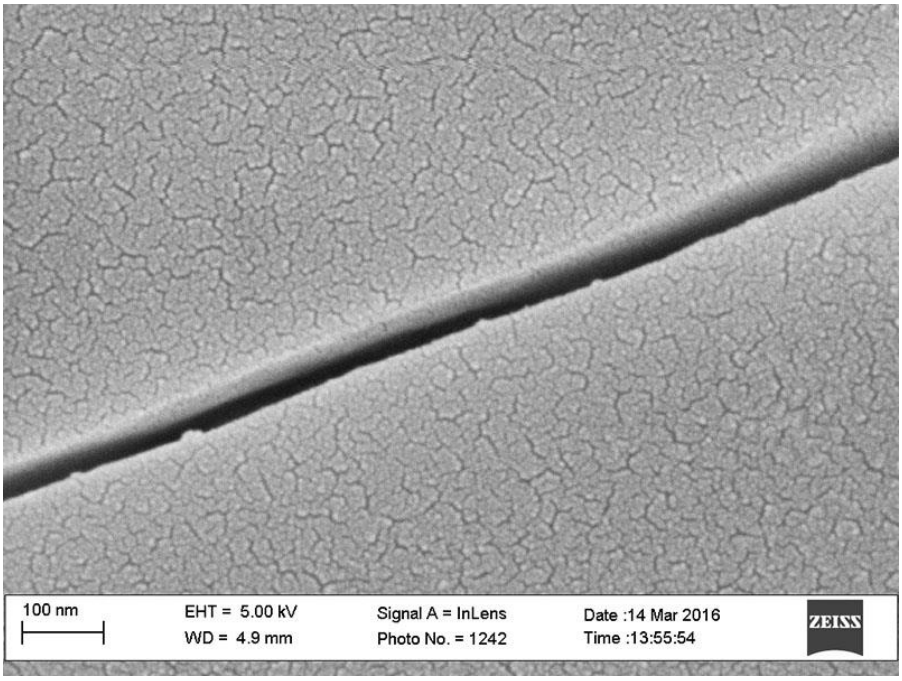

Figure A.39: Inlens SE micrograph from sample NAM-2784. Grain boundary 5, image C

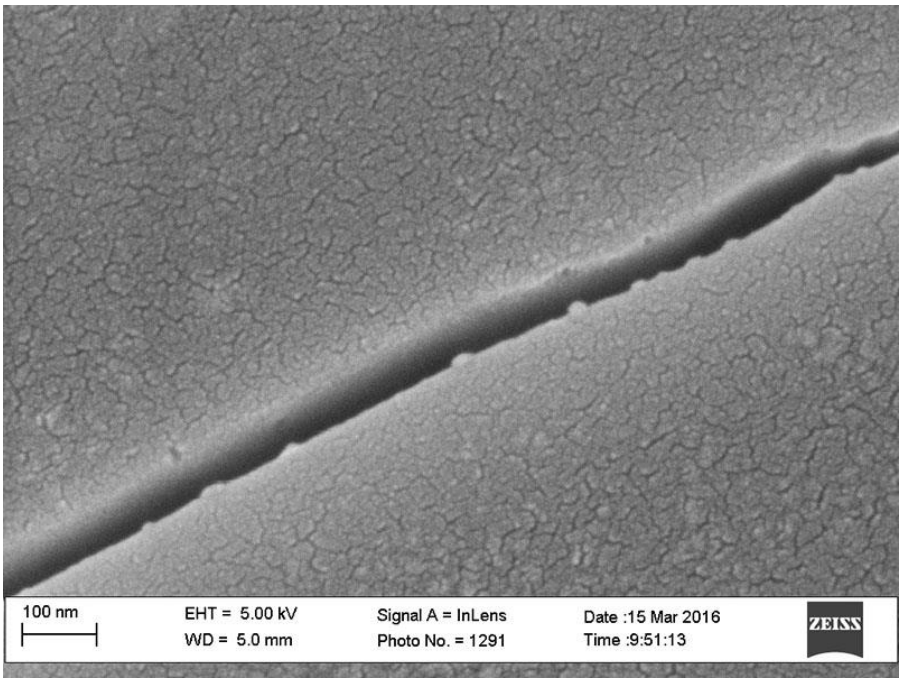

Figure A.4: Inlens SE micrograph from sample NAM-2784. Grain boundary 5, image D

Grain boundary 6

Image	Measurement Number	Length (nm)
A	1	31.72
A	2	41.75
A	3	50.86
Mean Aperture		41.45

Table A.27: NGBC measurements and mean aperture from grain boundary 6 in sample NAM-2784.

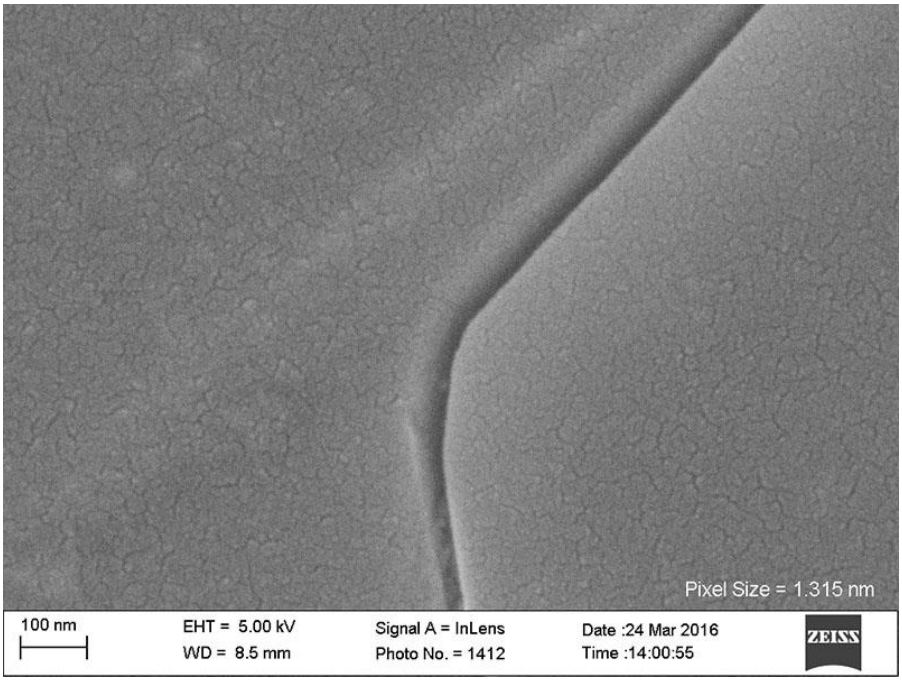

Figure A.40: Inlens SE micrograph from sample NAM-2784. Grain boundary 6, image A

Grain boundary 7

Image	Measurement Number	Length (nm)
A	1	34.65
Mean Aperture		34.65

Table A.28: NGBC measurements and mean aperture from grain boundary 7 in sample NAM-2784.

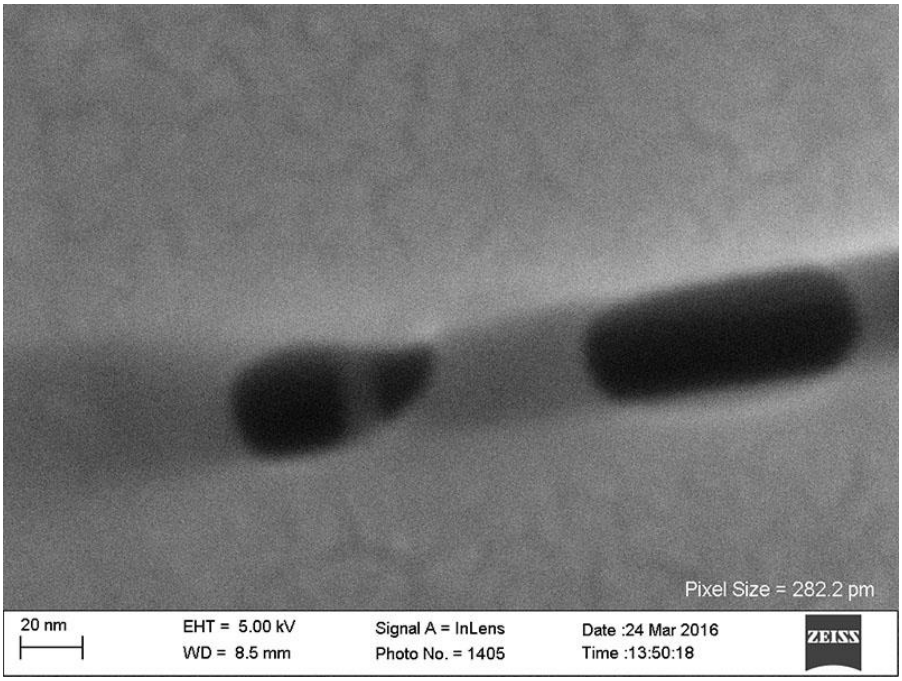

Figure A.41: Inlens SE micrograph from sample NAM-2784. Grain boundary 7, image A.

Grain boundary 8

Image	Measurement Number	Length (nm)
A	1	43.75
A	2	60.28
A	3	71.17
A	4	75.47
A	5	48.24
A	6	71.97
Mean Aperture		61.81

Table A.29: NGBC measurements and mean aperture from grain boundary 8 in sample NAM-2784.

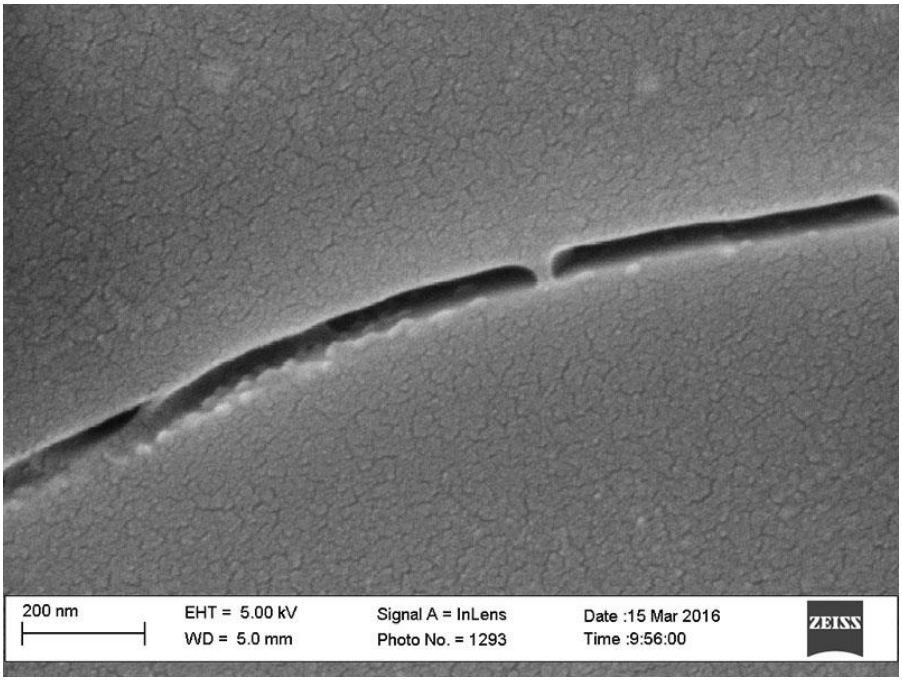

Figure A.42: Inlens SE micrograph from sample NAM-2784. Grain boundary 8, image A.

Grain boundary 9

Image	Measurement Number	Length (nm)
A	1	83.61
A	2	77.86
A	3	60.98
A	4	45.22
B	1	50.90
B	2	61.02
B	3	47.59
Mean Aperture		61.03

Table A.30: NGBC measurements and mean aperture from grain boundary 9 in sample NAM-2784.

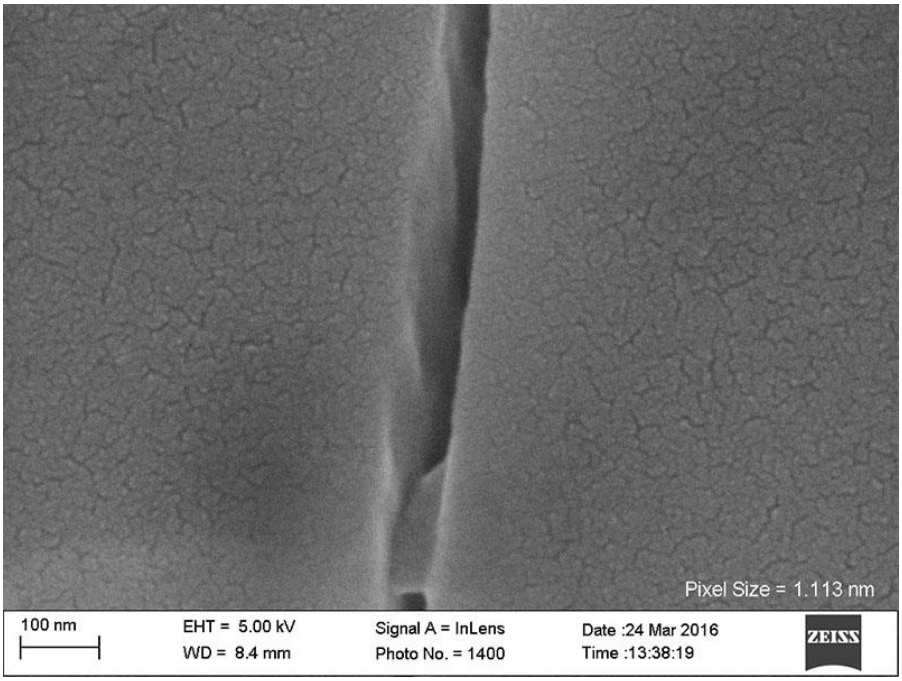

Figure A.43: Inlens SE micrograph from sample NAM-2784. Grain boundary 9, image A.

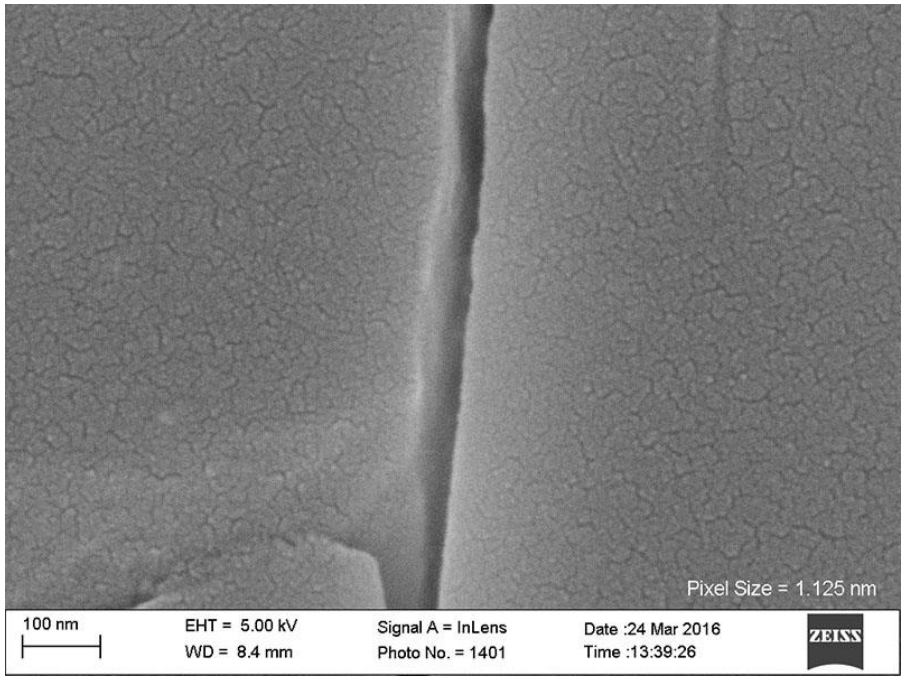

Figure A.44: Inlens SE micrograph from sample NAM-2784. Grain boundary 9, image B.

Grain boundary 10

Image	Measurement Number	Length (nm)
A	1	46.63
A	2	29.98
A	3	32.72
B	1	42.43
B	2	60.45
B	3	53.22
Mean Aperture		44.24

Table A.31: NGBC measurements and mean aperture from grain boundary 10 in sample NAM-2784.

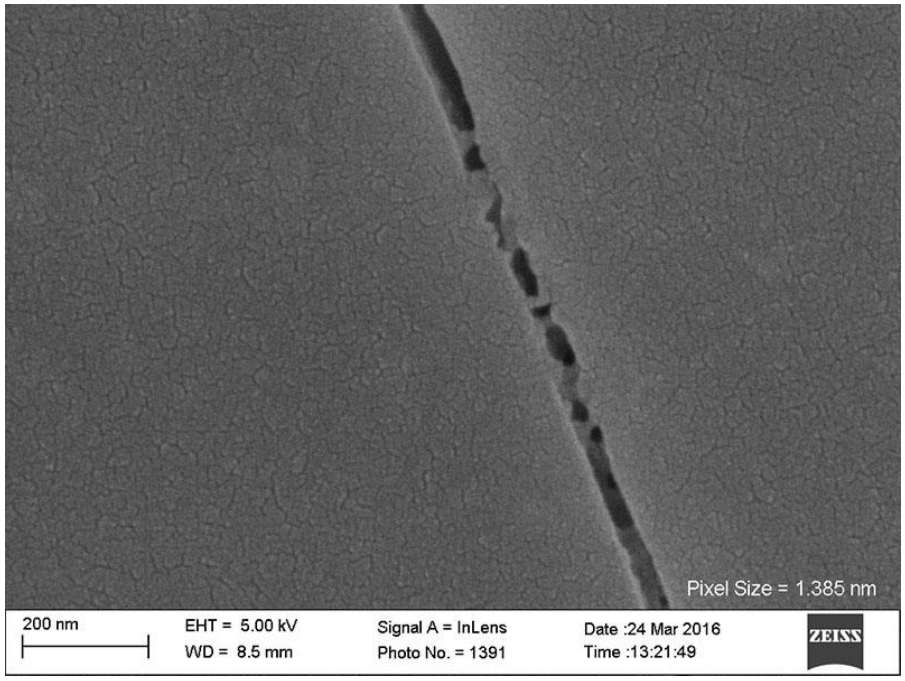

Figure A.45: Inlens SE micrograph from sample NAM-2784. Grain boundary 10, image A.

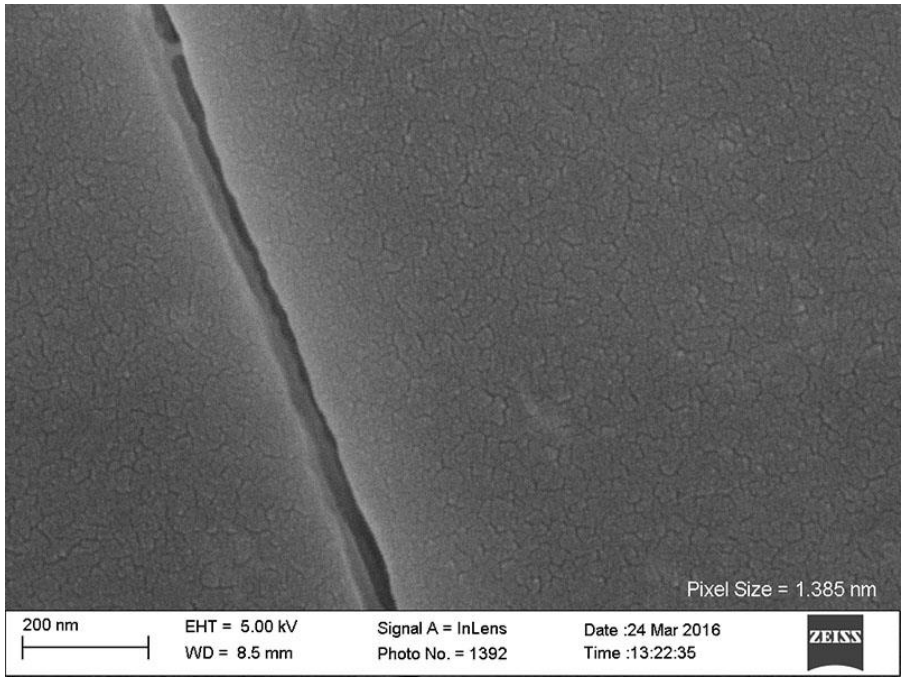

Figure A.46: Inlens SE micrograph from sample NAM-2784. Grain boundary 10, image B.

Grain boundary 11

Image	Measurement Number	Length (nm)
A	1	41.65
A	2	37.74
A	3	44.04
A	4	40.71
B	1	59.98
B	2	53.46
B	3	126.36
B	4	37.80
B	5	56.60
B	6	69.14
B	7	119.96
Mean Aperture		62.49

Table A.32: NGBC measurements and mean aperture from grain boundary 11 in sample NAM-2784.

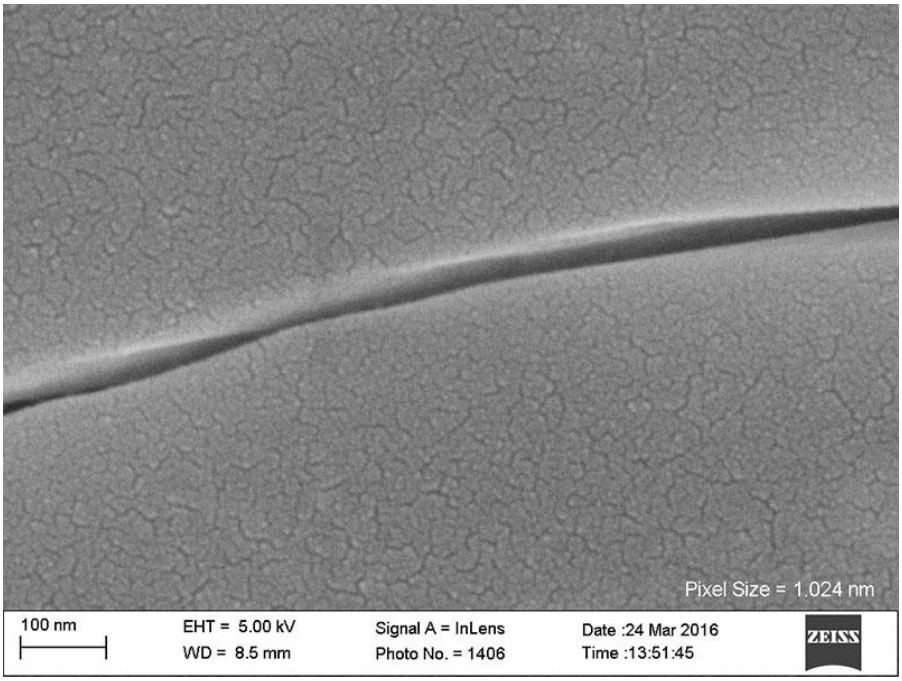

Figure A.47: Inlens SE micrograph from sample NAM-2784. Grain boundary 11, image A.

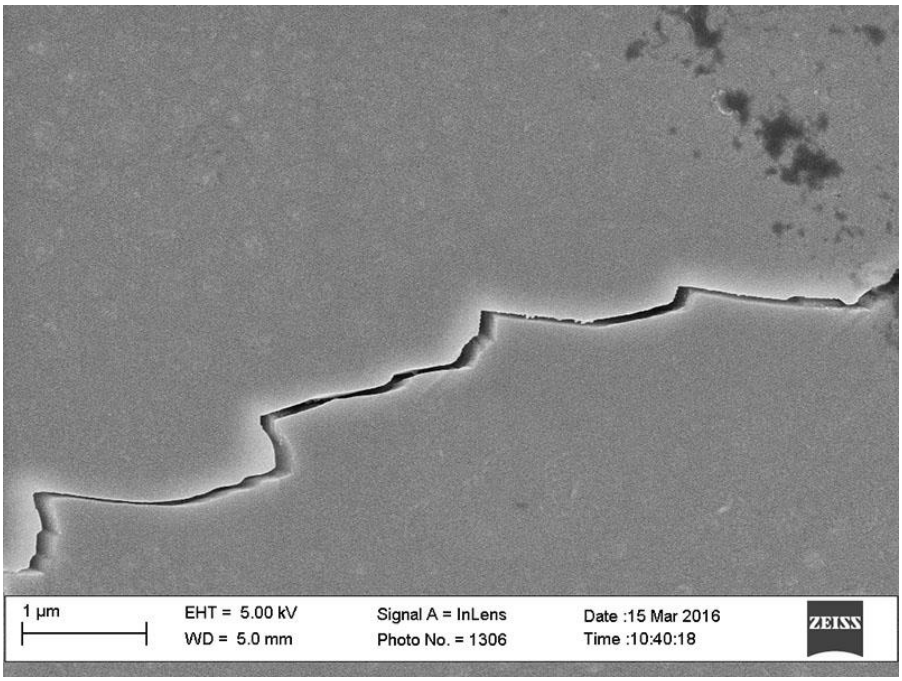

Figure A.48: Inlens SE micrograph from sample NAM-2784. Grain boundary 11, image A.

Grain boundary 12

Image	Measurement Number	Length (nm)
A	1	63.27
A	2	49.21
A	3	53.54
A	4	60.06
A	5	78.60
A	6	63.27
A	7	74.73
B	1	56.28
B	2	54.19
B	3	56.01
Mean Aperture		**60.92**

Table A.33: NGBC measurements and mean aperture from grain boundary 12 in sample NAM-2784.

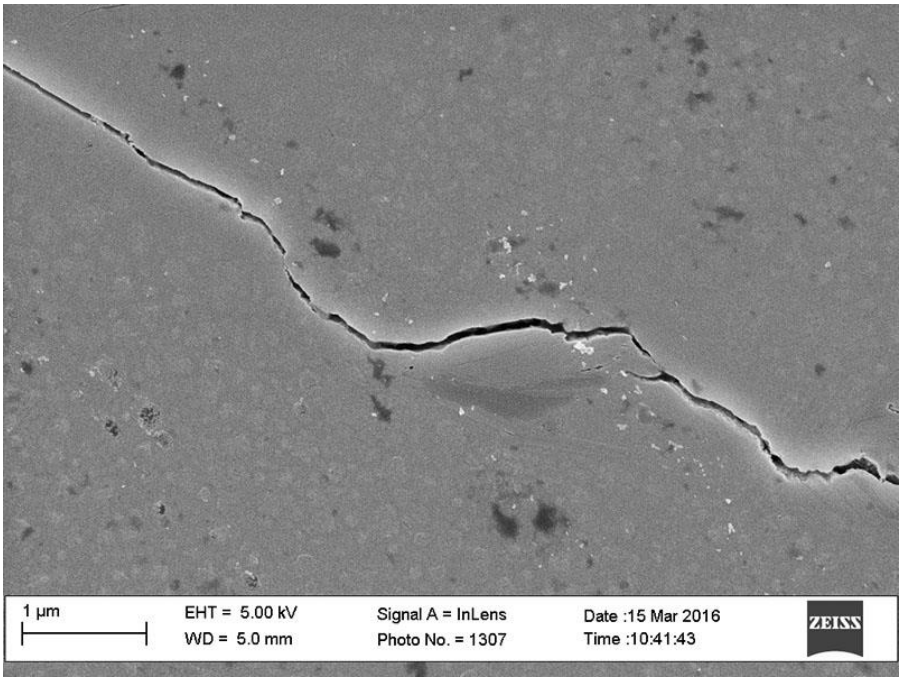

Figure A.49: Inlens SE micrograph from sample NAM-2784. Grain boundary 12, image A

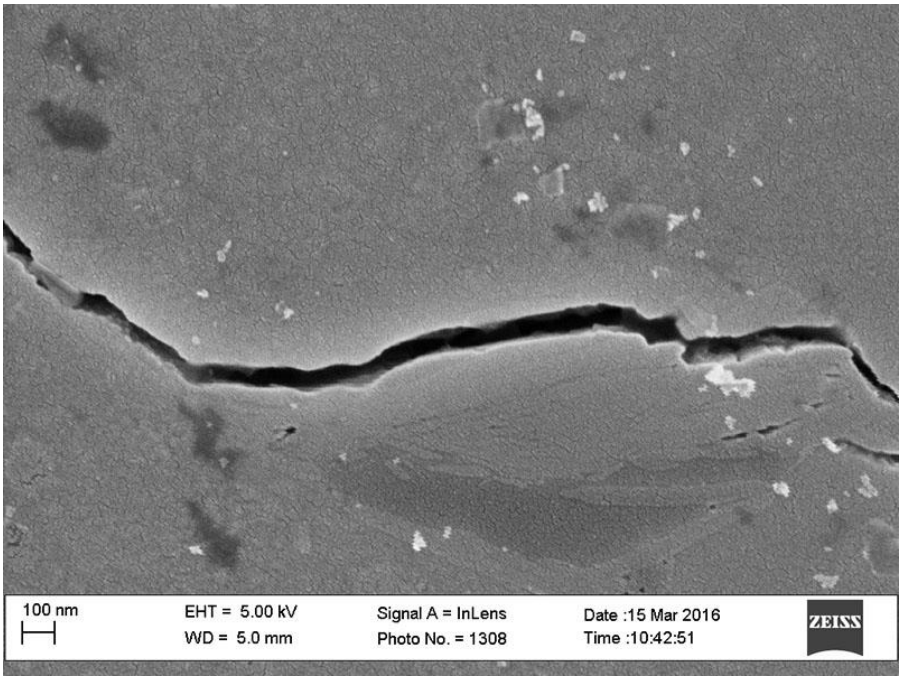

Figure A.50: Inlens SE micrograph from sample NAM-2784. Grain boundary 13, image B.

Grain boundary 13

Image	Measurement Number	Length (nm)
A	1	47.46
A	2	73.08
A	3	66.50
A	4	77.34
A	5	62.09
Mean Aperture		65.30

Table A.34: NGBC measurements and mean aperture from grain boundary 13 in sample NAM-2784.

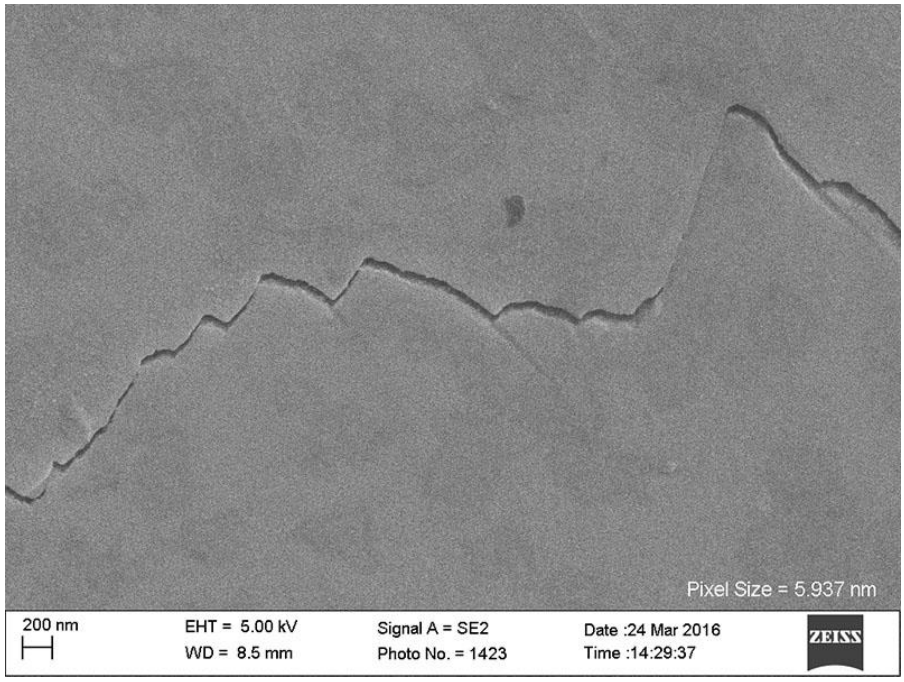

Figure A.51: Inlens SE micrograph from sample NAM-2784. Grain boundary 13, image A.

Grain boundary 14

Image	Measurement Number	Length (nm)
A	1	193.46
A	2	151.26
A	3	193.46
Mean Aperture		179.40

Table A.35: NGBC measurements and mean aperture from grain boundary 14 in sample NAM-2784.

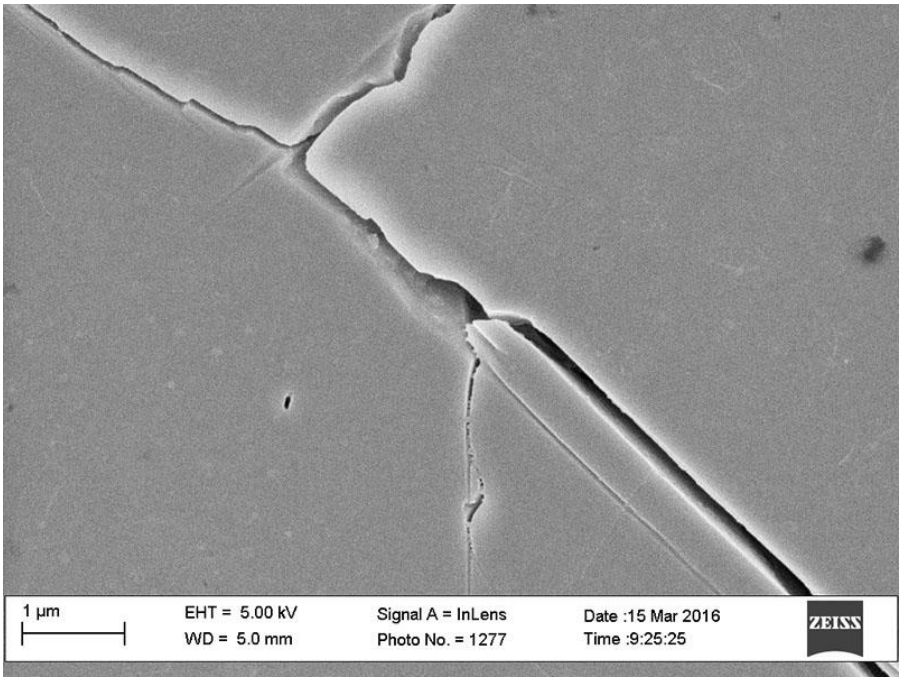

Figure A.52: Inlens SE micrograph from sample NAM-2784. Grain boundary 14, image A

Grain boundary 15

Image	Measurement Number	Length (nm)
A	1	96.81
A	2	74.25
A	3	52.50
A	4	61.22
A	5	52.50
A	6	59.40
A	7	67.23
Mean Aperture		66.27

Table A.36: NGBC measurements and mean aperture from grain boundary 15 in sample NAM-2784.

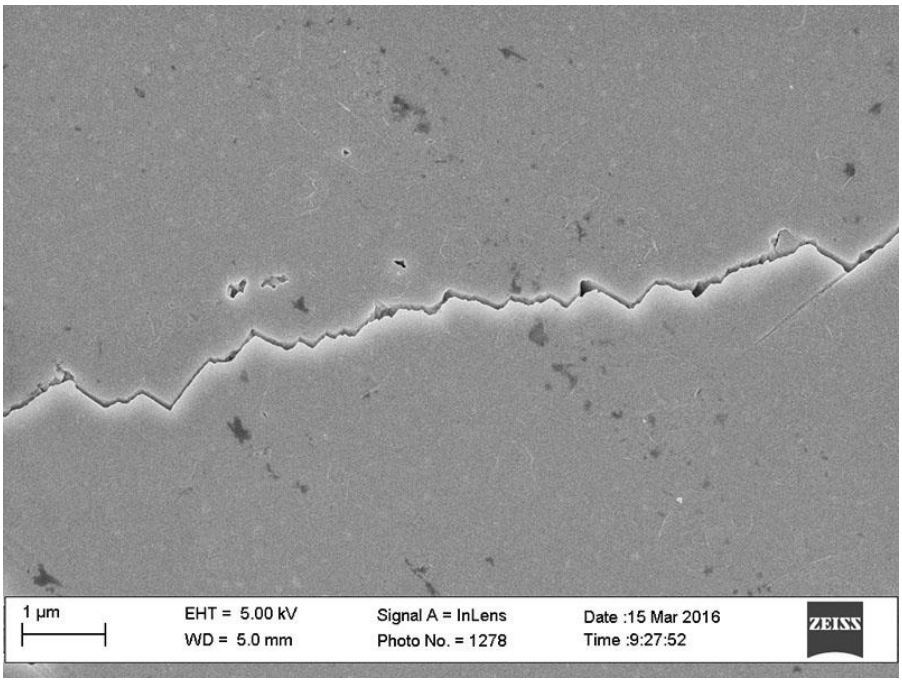

Figure A.53: Inlens SE micrograph from sample NAM-2784. Grain boundary 15, image A.

Grain boundary 16

Image	Measurement Number	Length (nm)
A	1	61.96
A	2	57.63
A	3	61.58
A	4	68.65
A	5	58.36
A	6	57.09
A	7	59.62
A	8	61.58
Mean Aperture		60.81

Table A.37: NGBC measurements and mean aperture from grain boundary 16 in sample NAM-2784.

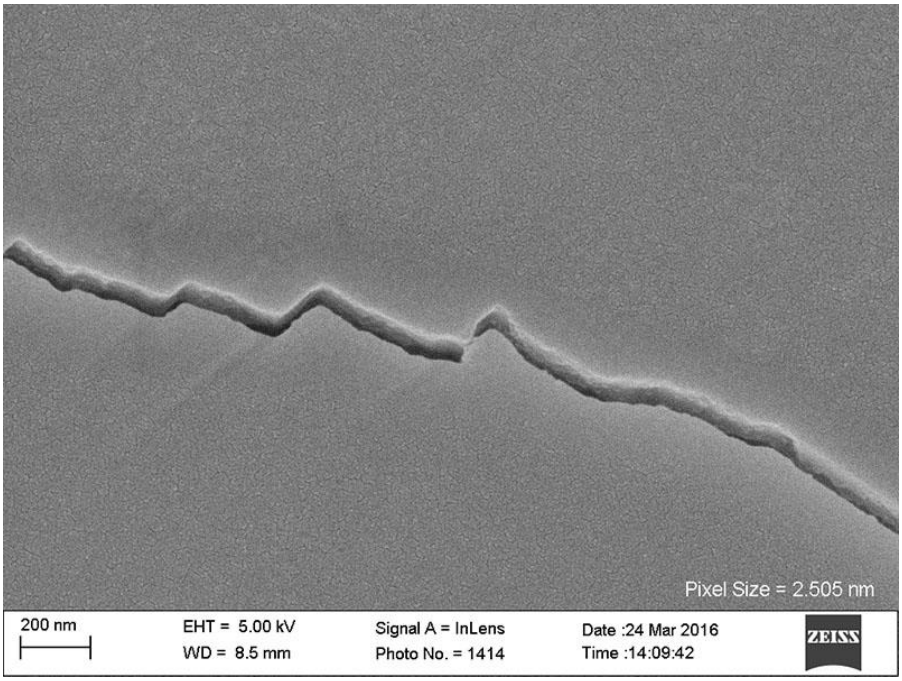

Figure A.54: Inlens SE micrograph from sample NAM-2784. Grain boundary 16, image A.

Grain boundary 17

Image	Measurement Number	Length (nm)
A	1	129.09
A	2	131.86
Mean Aperture		130.48

Table A.38: NGBC measurements and mean aperture from grain boundary 17 in sample NAM-2784.

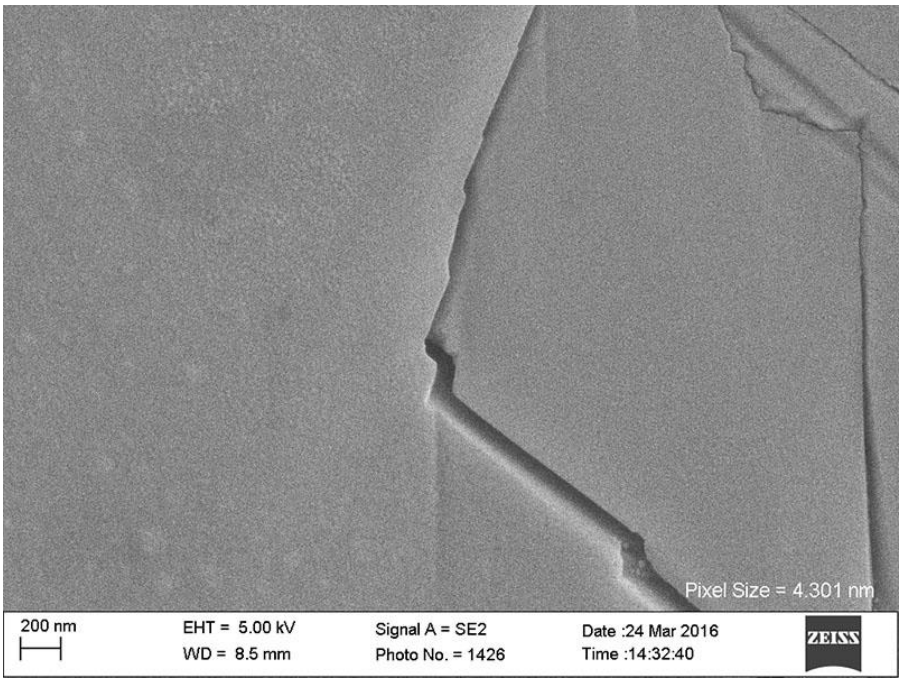

Figure A.55: Inlens SE micrograph from sample NAM-2784. Grain boundary17, image A.

Grain boundary 18

Image	Measurement Number	Length (nm)
A	1	220.92
A	2	213.66
A	3	177.41
A	4	138.71
A	5	154.45
Mean Aperture		181.03

Table A.39: NGBC measurements and mean aperture from grain boundary 18 in sample NAM-2784.

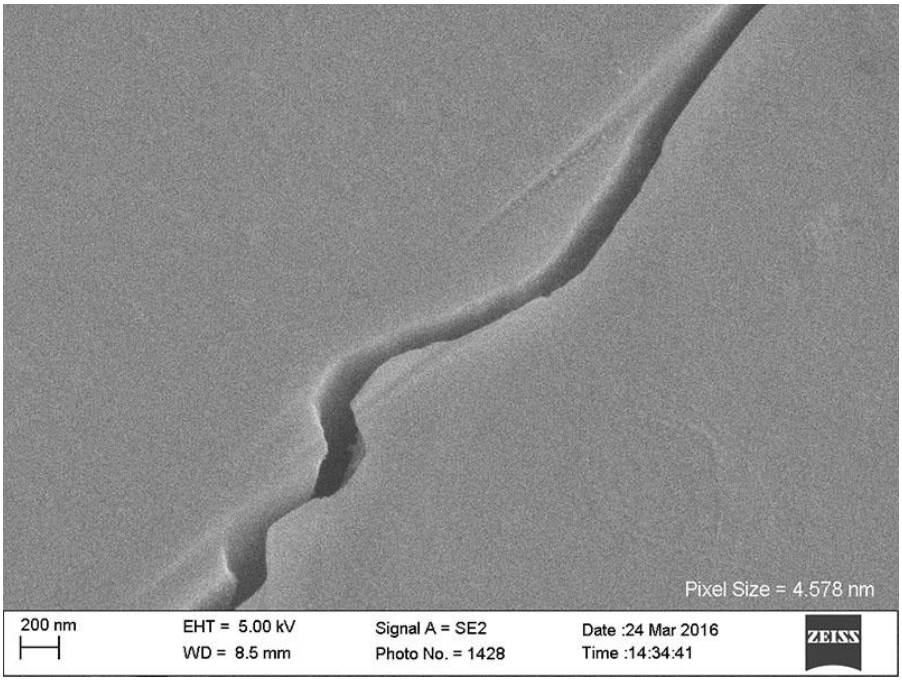

Figure A.56: Inlens SE micrograph from sample NAM-2784. Grain boundary 18, image A

Grain boundary 19

Image	Measurement Number	Length (nm)
A	1	41.79
A	2	30.14
A	3	24.37
A	4	41.37
B	1	42.98
B	2	24.34
Mean Aperture		34.16

Table A.40: NGBC measurements and mean aperture from grain boundary 19 in sample NAM-2784.

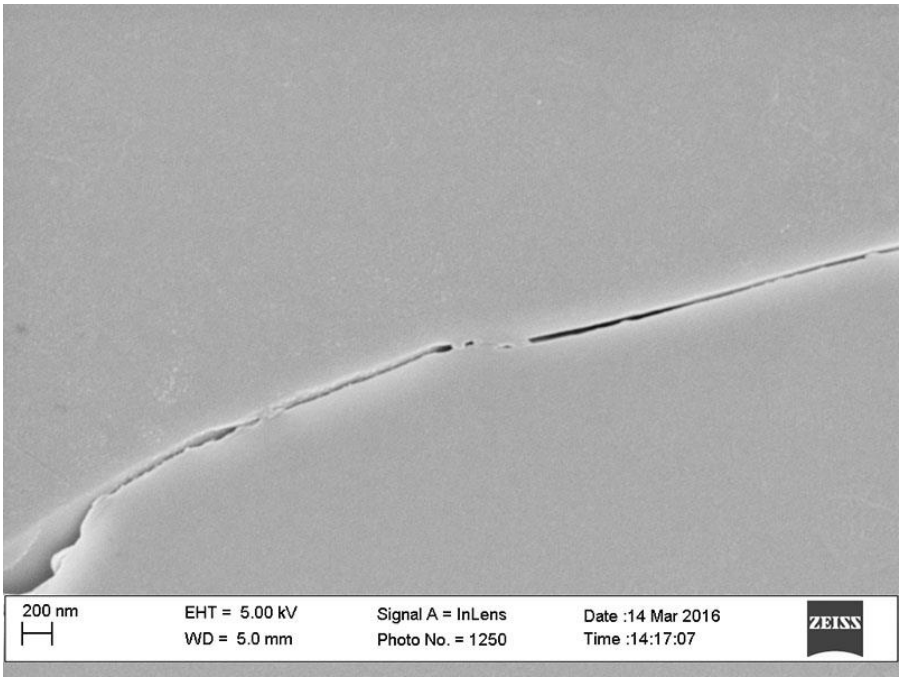

Figure A.57: Inlens SE micrograph from sample NAM-2784. Grain boundary 19, image A.

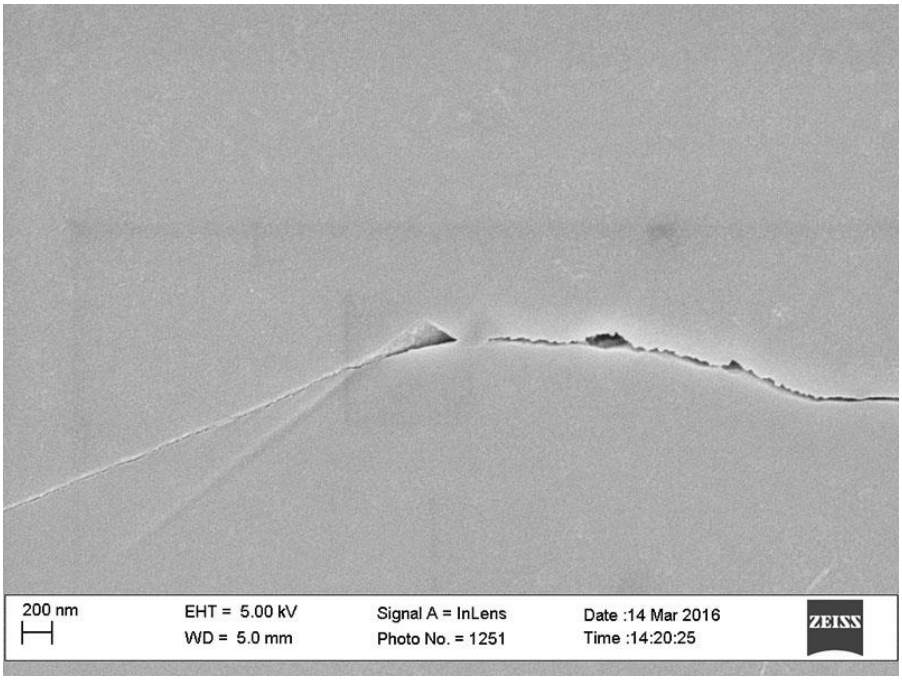

Figure A.58: Inlens SE micrograph from sample NAM-2784. Grain boundary 19, image B.

Grain boundary 20

Image	Measurement Number	Length (nm)
A	1	52.37
A	2	47.10
A	3	51.97
Mean Aperture		50.48

Table A.41: NGBC measurements and mean aperture from grain boundary 20 in sample NAM-2784.

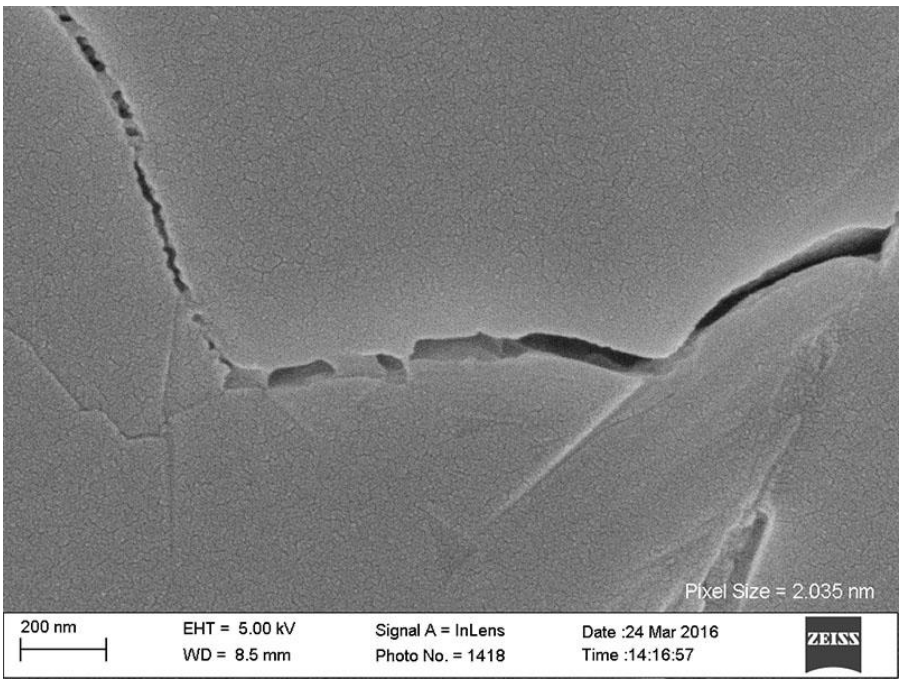

Figure A.59: Inlens SE micrograph from sample NAM-2784. Grain boundary 20, image B.

Grain boundary 21

Image	Measurement Number	Length (nm)
A	1	103.62
A	2	98.65
A	3	98.61
A	4	106.45
A	5	109.36
B	1	106.59
B	2	89.19
B	3	91.13
B	4	90.09
C	1	73.10
C	2	60.25
C	3	82.80
C	4	78.42
C	5	74.13
C	6	80.95
C	7	90.92
C	8	82.80
Mean Aperture		89.24

Table A.42: NGBC measurements and mean aperture from grain boundary 21 in sample NAM-2784.

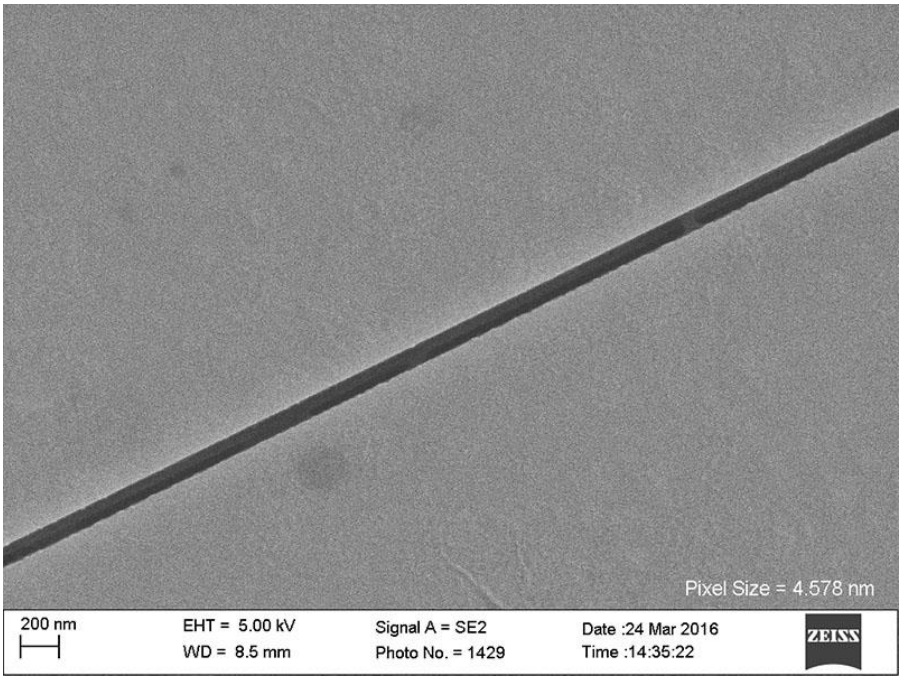

Figure A.60: Inlens SE micrograph from sample NAM-2784. Grain boundary 21, image A.

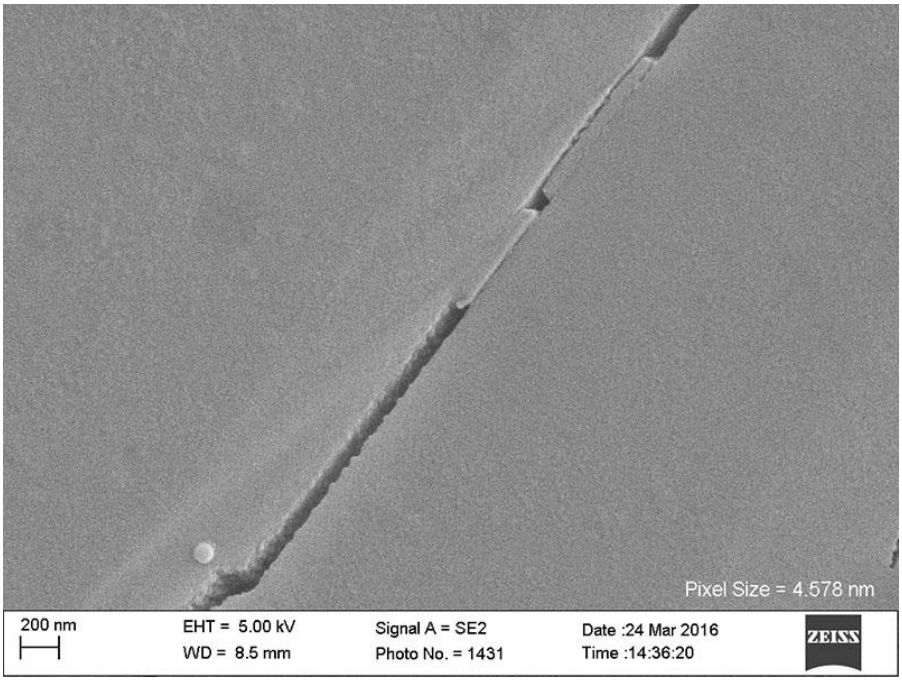

Figure A.61: Inlens SE micrograph from sample NAM-2784. Grain boundary 21, image B.

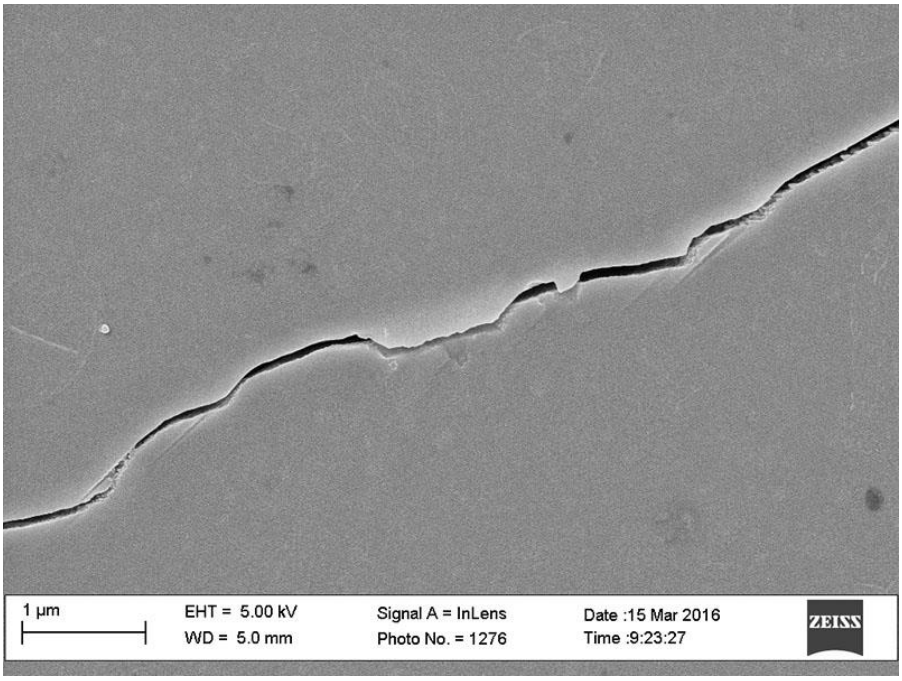

Figure A.62: Inlens SE micrograph from sample NAM-2784. Grain boundary 21, image C.

Grain boundary 22

Image	Measurement Number	Length (nm)
A	1	110.01
A	2	131.76
B	1	136.67
B	2	154.94
B	3	155.79
B	4	150.38
B	5	139.91
C	1	138.80
C	2	93.01
C	3	124.44
C	4	128.19
C	5	122.13
D	1	65.38
D	2	70.19
D	3	57.79
D	4	65.56
D	5	66.70
Mean Aperture		112.45

Table A.43: NGBC measurements and mean aperture from grain boundary 22 in sample NAM-2784.

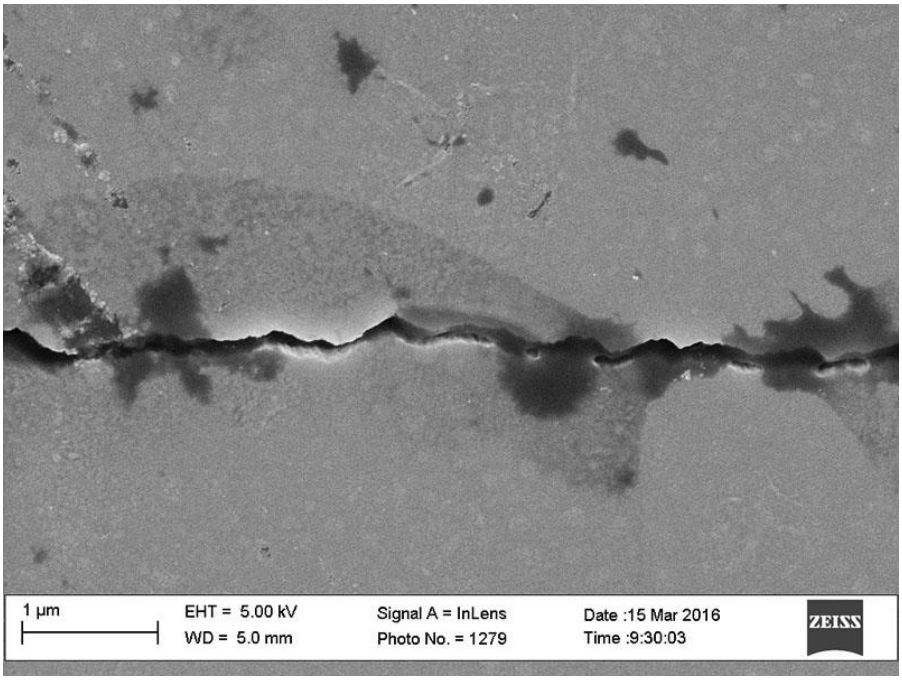

Figure A.63: Inlens SE micrograph from sample NAM-2784. Grain boundary 22, image A.

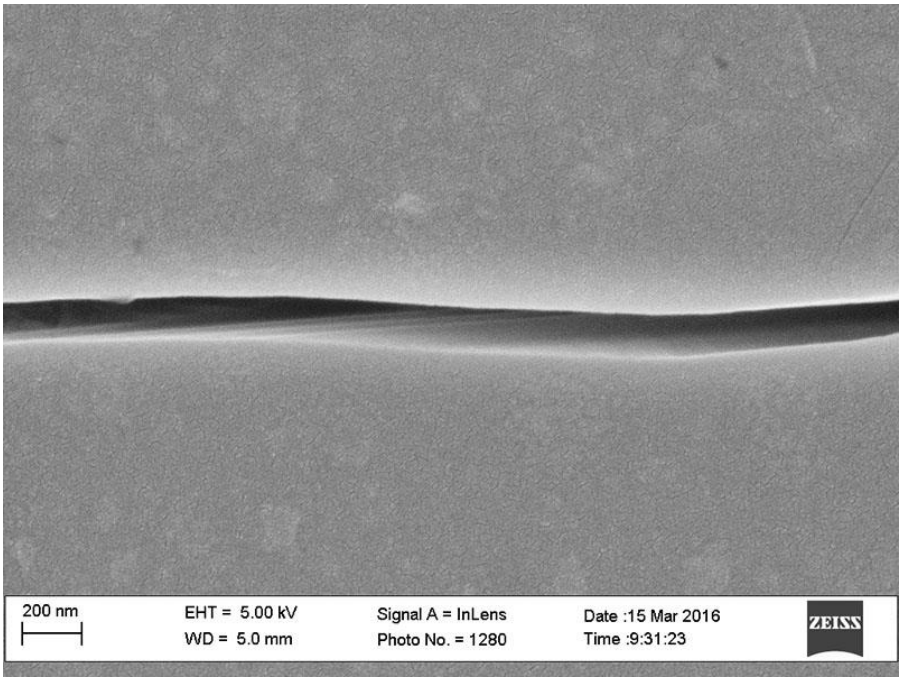

Figure A.64: Inlens SE micrograph from sample NAM-2784. Grain boundary 22, image B.

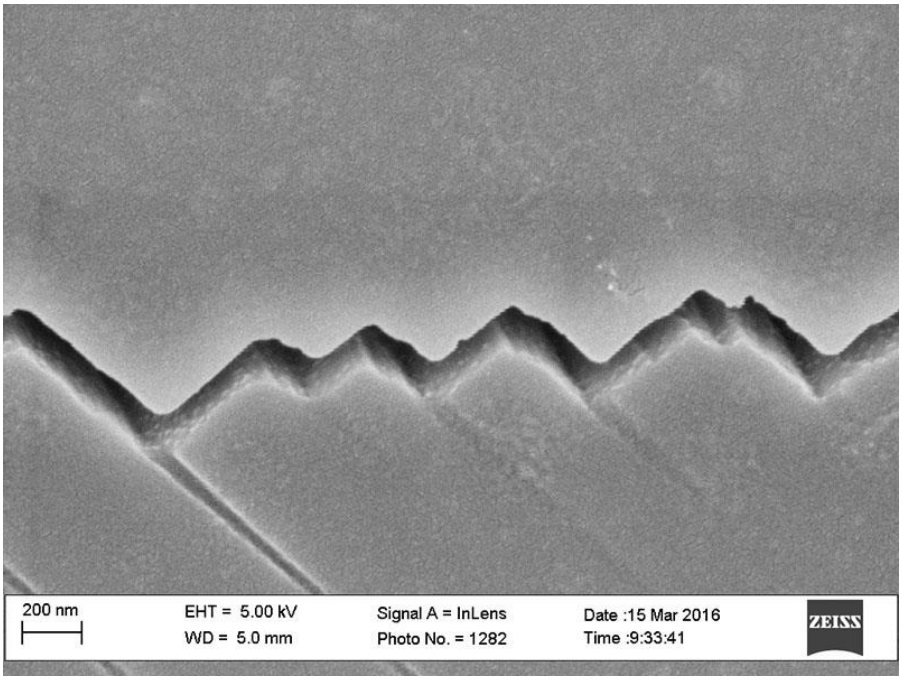

Figure A.65: Inlens SE micrograph from sample NAM-2784. Grain boundary 22, image C.

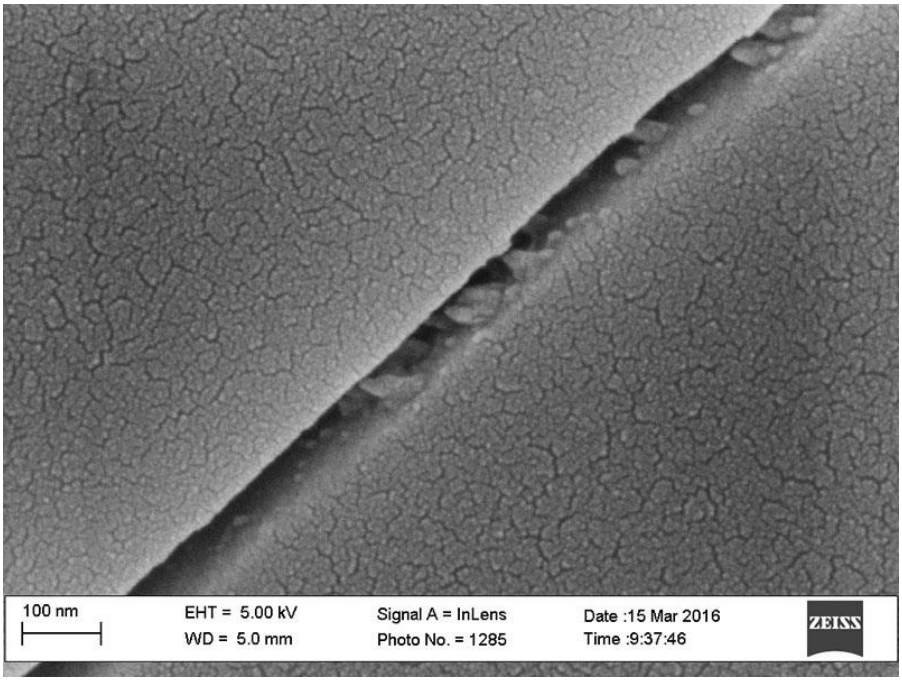

Figure A.66: Inlens SE micrograph from sample NAM-2784. Grain boundary 22, image D.

Grain boundary 23

Image	Measurement Number	Length (nm)
A	1	68.64
A	2	63.39
Mean Aperture		66.01

Table A.44: NGBC measurements and mean aperture from grain boundary 23 in sample NAM-2784.

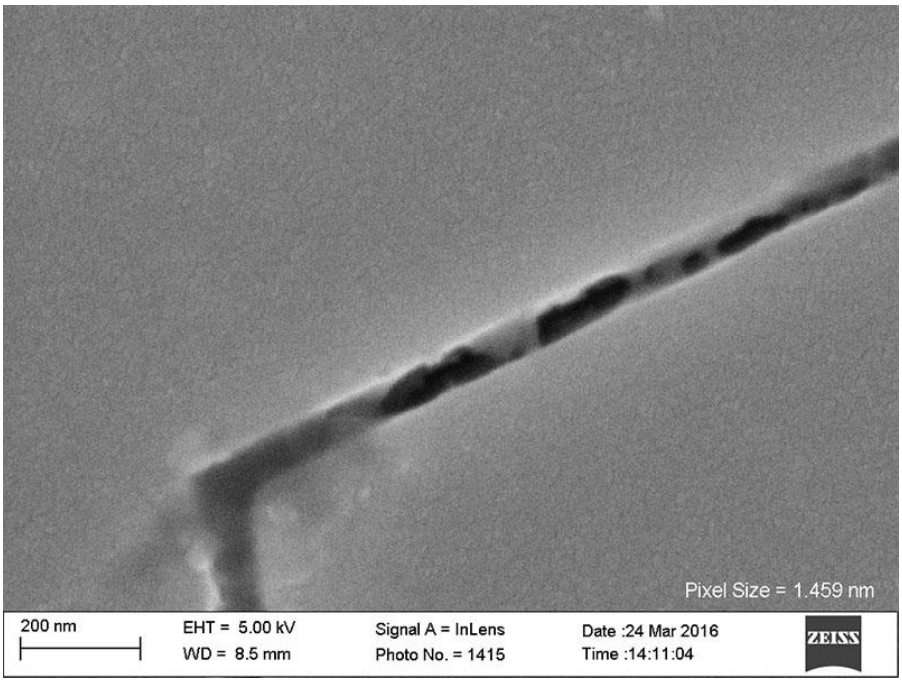

Figure A.67: Inlens SE micrograph from sample NAM-2784. Grain boundary 23, image A.

Grain boundary 24

Image	Measurement Number	Length (nm)
A	1	44.76
A	2	43.88
A	3	47.51
A	4	46.10
A	5	44.30
A	6	35.89
Mean Aperture		43.74

Table A.45: NGBC measurements and mean aperture from grain boundary 24 in sample NAM-2784.

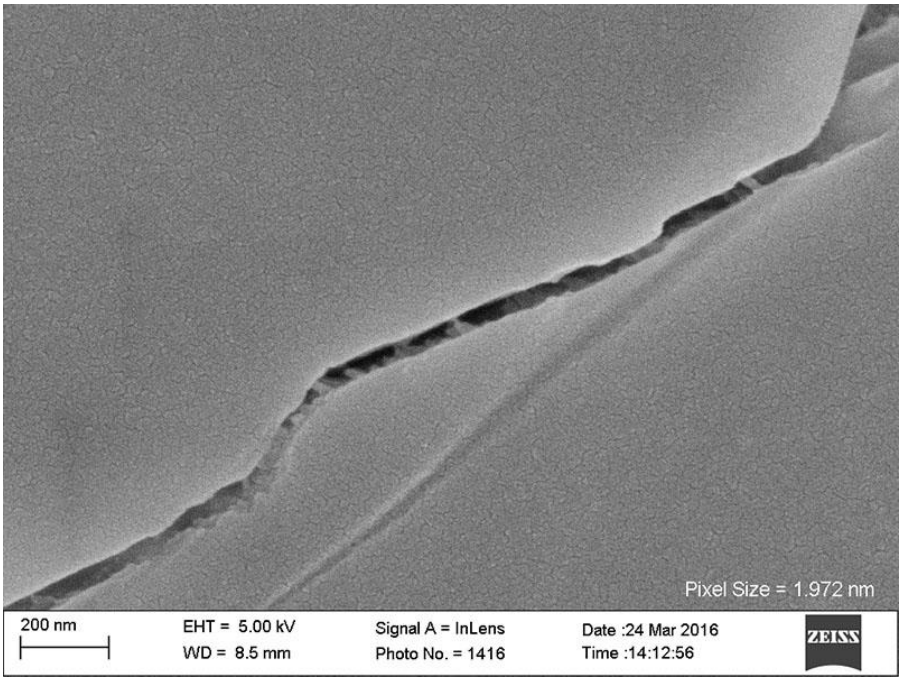

Figure A.68: Inlens SE micrograph from sample NAM-2784. Grain boundary 24, image A.

Grain boundary 25

Image	Measurement Number	Length (nm)
A	1	80.76
A	2	69.86
A	3	89.96
A	4	89.96
A	5	74.48
Mean Aperture		81.00

Table A.46: NGBC measurements and mean aperture from grain boundary 25 in sample NAM-2784.

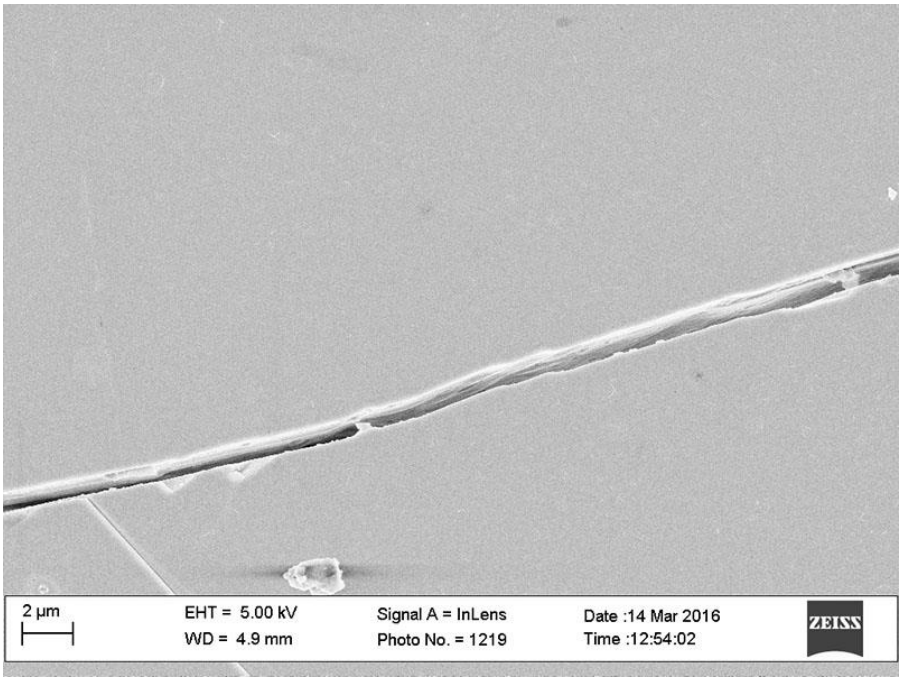

Figure A.69: Inlens SE micrograph from sample NAM-2784. Grain boundary 25, image A.

Grain boundary 26

Image	Measurement Number	Length (nm)
A	1	126.65
A	2	168.42
Mean Aperture		147.54

Table A.47: NGBC measurements and mean aperture from grain boundary 26 in sample NAM-2784.

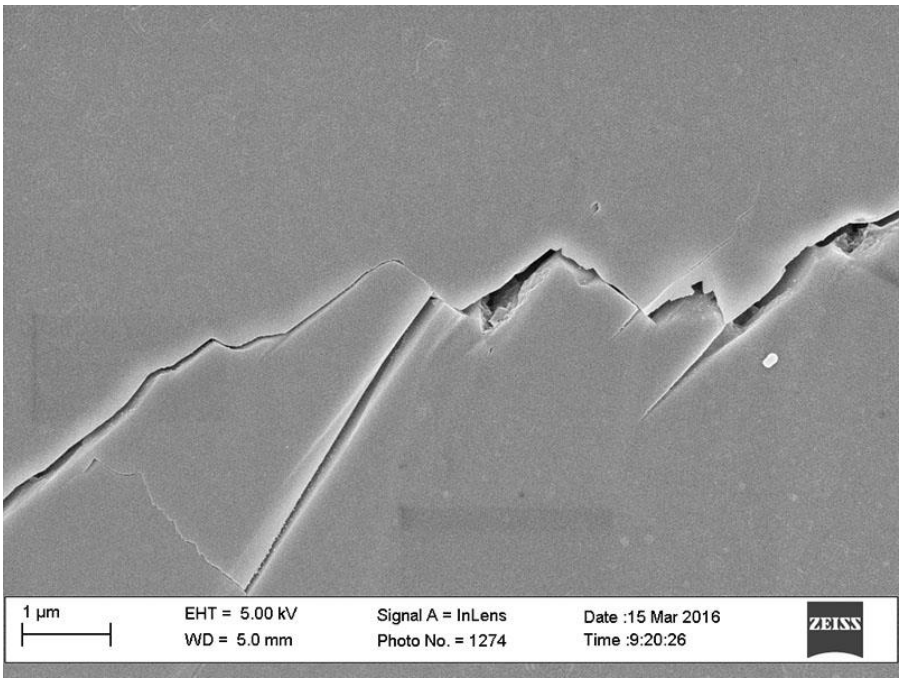

Figure A.70: Inlens SE micrograph from sample NAM-2784. Grain boundary 26, image A.

Grain boundary 27

Image	Measurement Number	Length (nm)
A	1	79.77
A	2	59.00
A	3	69.64
A	4	76.54
B	1	142.21
B	2	142.21
B	3	151.24
B	4	153.98
B	5	142.21
B	6	142.21
B	7	142.21
B	8	118.10
C	1	131.14
C	2	135.70
C	3	123.94
Mean Aperture		120.67

Table A.48: NGBC measurements and mean aperture from grain boundary 27 in sample NAM-2784.

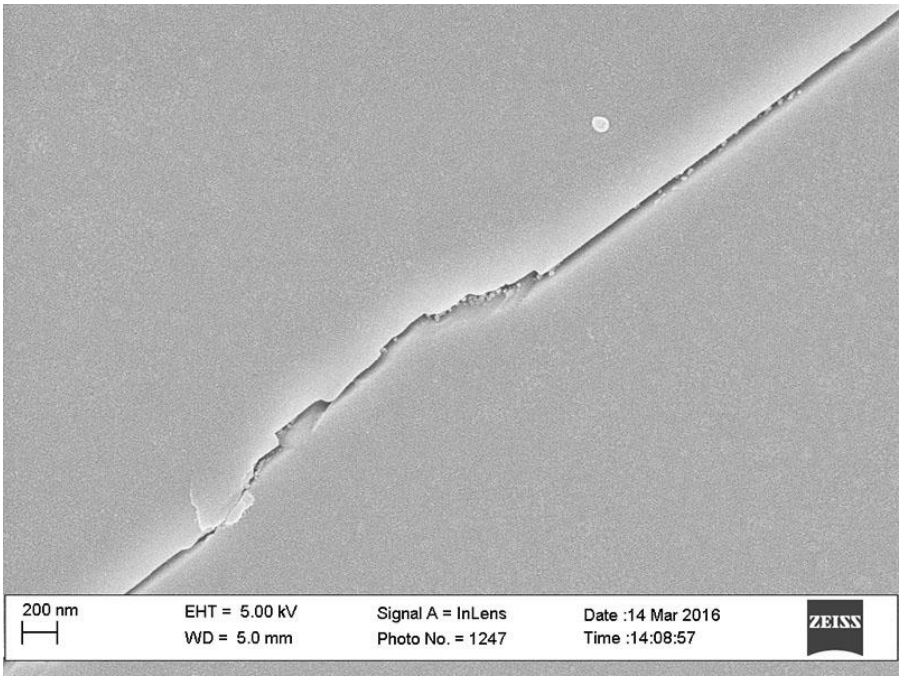

Figure A.71: Inlens SE micrograph from sample NAM-2784. Grain boundary 27, image A.

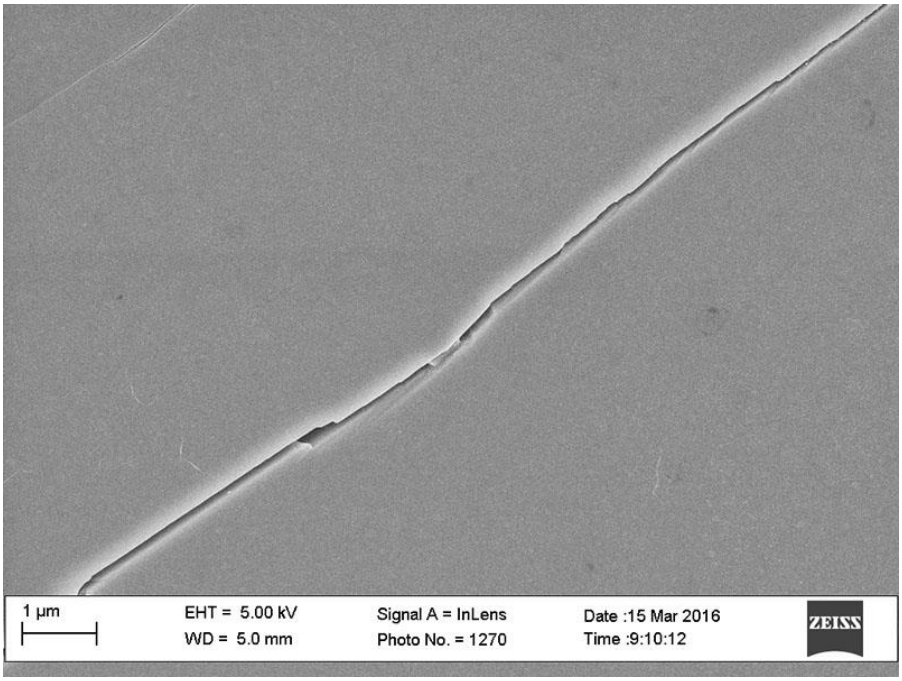

Figure A.72: Inlens SE micrograph from sample NAM-2784. Grain boundary 27, image B.

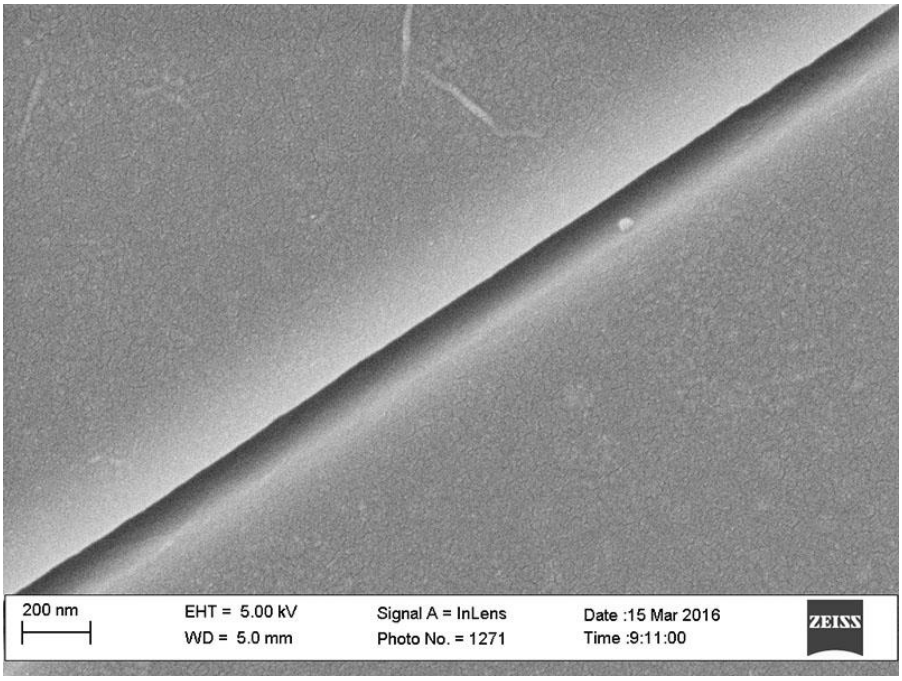

Figure A.73: Inlens SE micrograph from sample NAM-2784. Grain boundary 27, image C.

Grain boundary 28

Image	Measurement Number	Length (nm)
A	1	72.62
A	2	83.39
A	3	82.08
B	1	57.00
B	2	59.71
B	3	70.95
B	4	66.03
C	1	82.44
C	2	94.41
C	3	85.56
C	4	83.58
C	5	98.35
C	6	81.96
D	1	113.20
D	2	84.11
Mean Aperture		81.03

Table A.49: NGBC measurements and mean aperture from grain boundary 28 in sample NAM-2784.

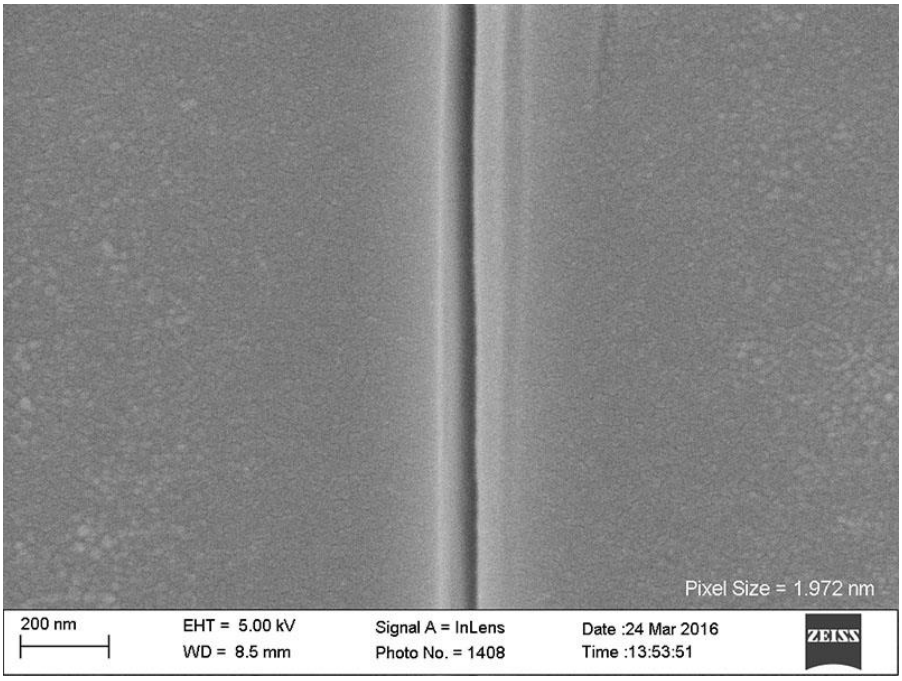

Figure A.74: Inlens SE micrograph from sample NAM-2784. Grain boundary 28, image A.

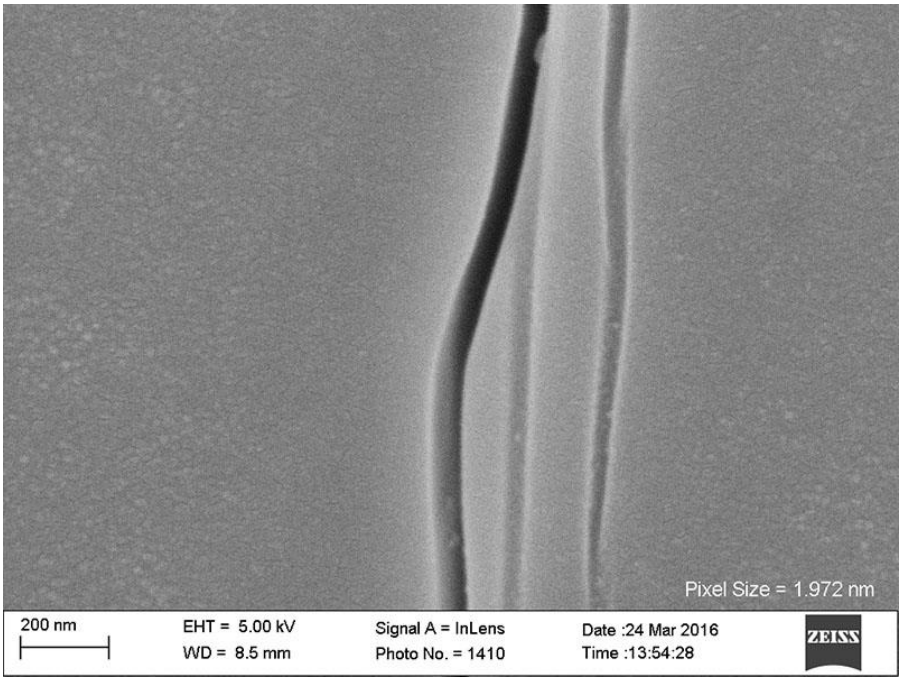

Figure A.75: Inlens SE micrograph from sample NAM-2784. Grain boundary 28, image B.

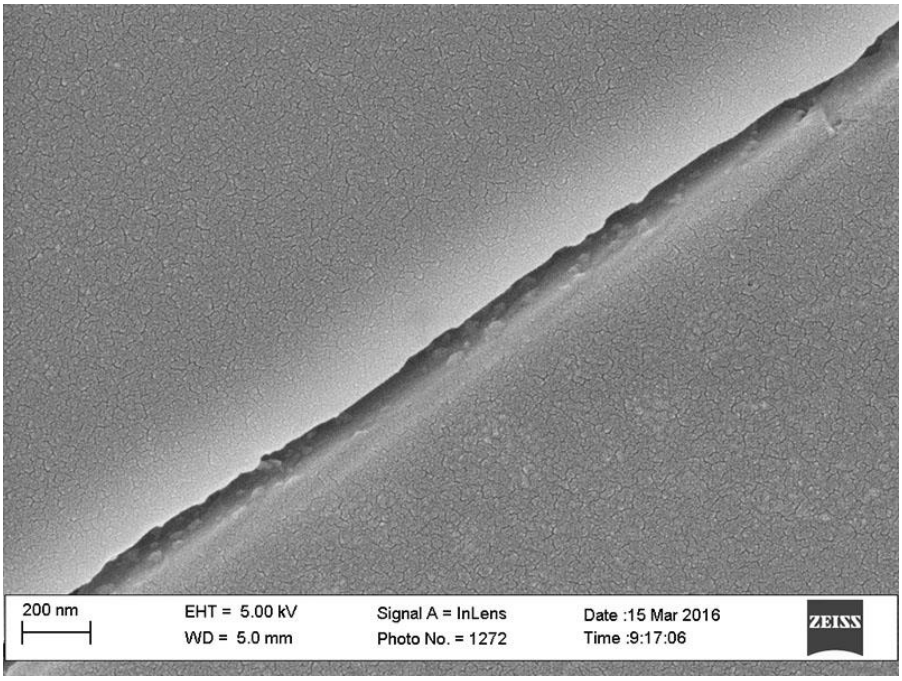

Figure A.76: Inlens SE micrograph from sample NAM-2784. Grain boundary 28, image C.

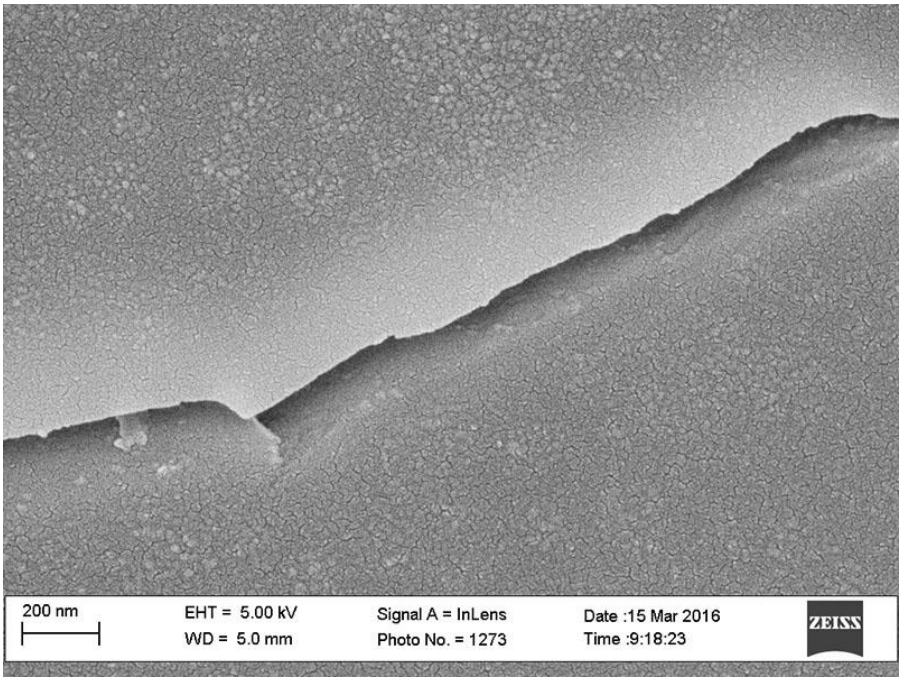

Figure A.77: Inlens SE micrograph from sample NAM-2784. Grain boundary 28, image D.

Grain boundary 29

Image	Measurement Number	Length (nm)
A	1	30.03
Mean Aperture		30.03

Table A.50: NGBC measurements and mean aperture from grain boundary 29 in sample NAM-2784.

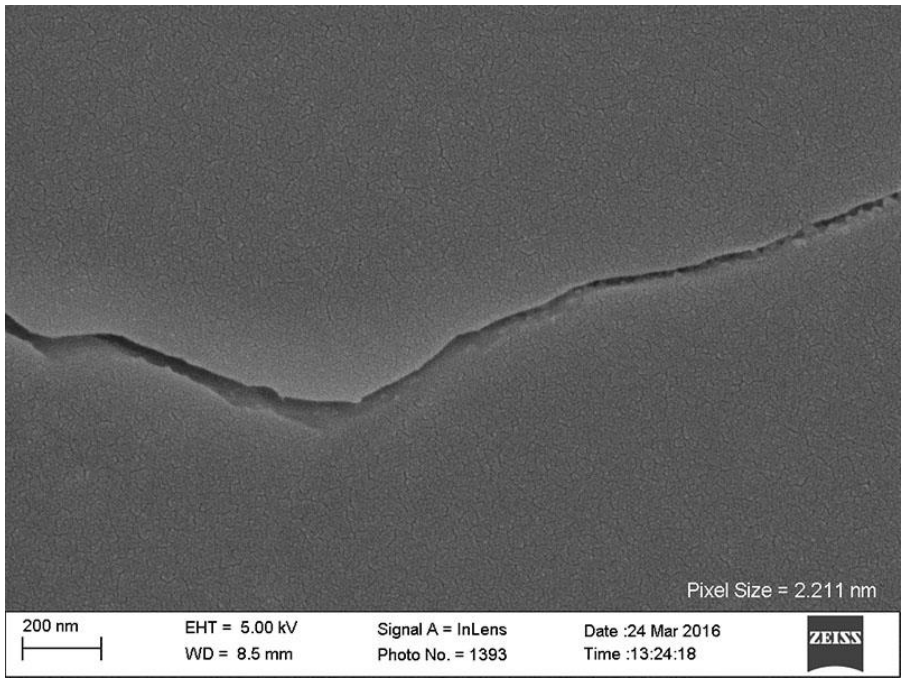

Figure A.78: Inlens SE micrograph from sample NAM-2784. Grain boundary 29, image A.

Grain boundary 30

Image	Measurement Number	Length (nm)
A	1	200.25
A	2	137.61
A	3	212.73
A	4	210.09
Mean Aperture		190.17

Table A.51: NGBC measurements and mean aperture from grain boundary 30 in sample NAM-2784.

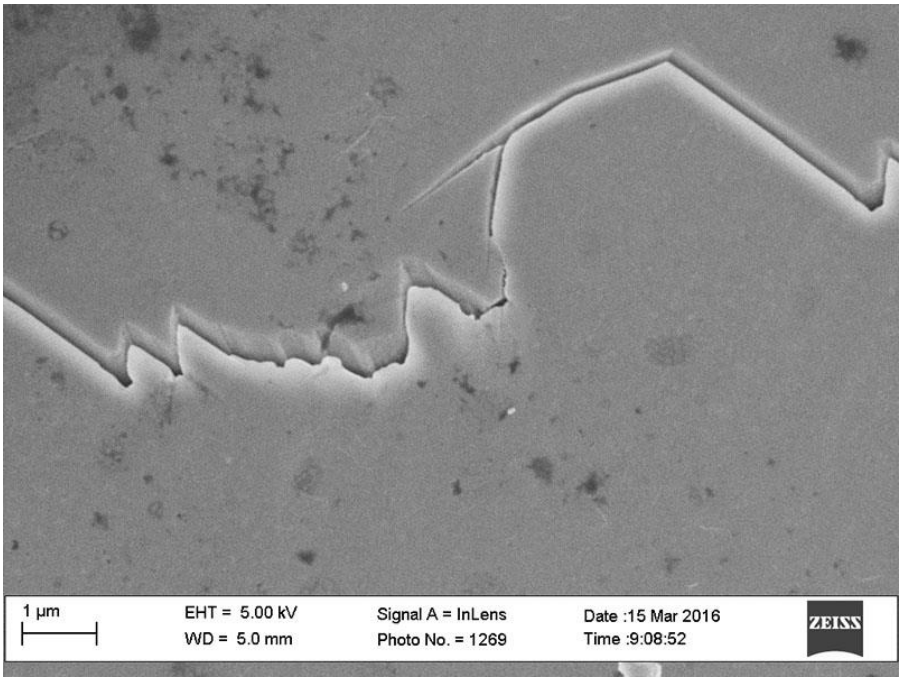

Figure A.79: Inlens SE micrograph from sample NAM-2784. Grain boundary 30, image A.

Grain boundary 31

Image	Measurement Number	Length (nm)
A	1	215.60
A	2	231.74
Mean Aperture		223.67

Table A.52: NGBC measurements and mean aperture from grain boundary 31 in sample NAM-2784.

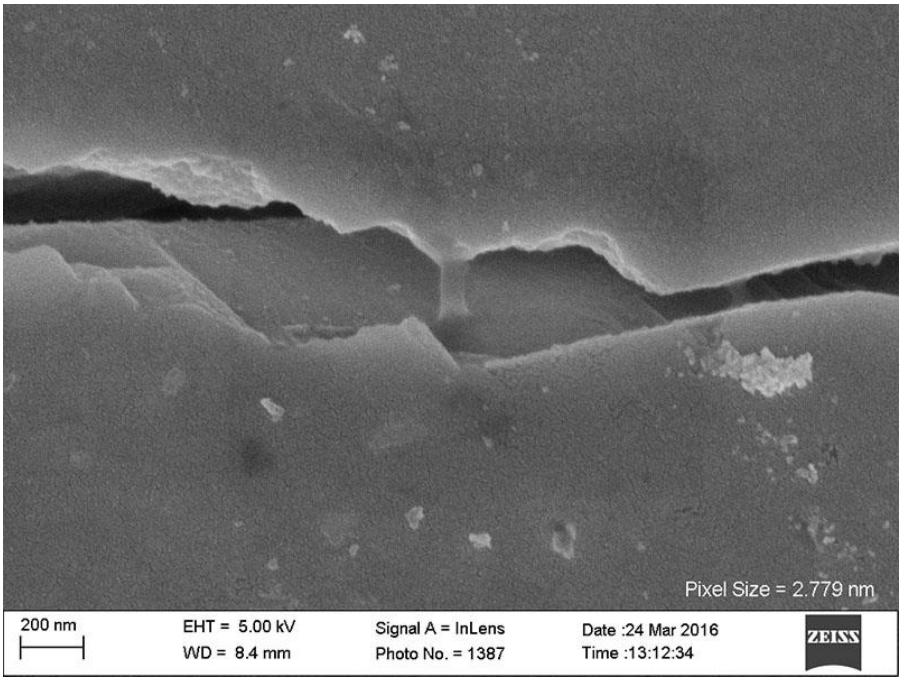

Figure A.80: Inlens SE micrograph from sample NAM-2784. Grain boundary 31, image A.

Grain boundary 32

Image	Measurement Number	Length (nm)
A	1	163.61
A	2	183.96
A	3	238.37
A	4	94.75
Mean Aperture		170.17

Table A.53 NGBC measurements and mean aperture from grain boundary 32 in sample NAM-2784.

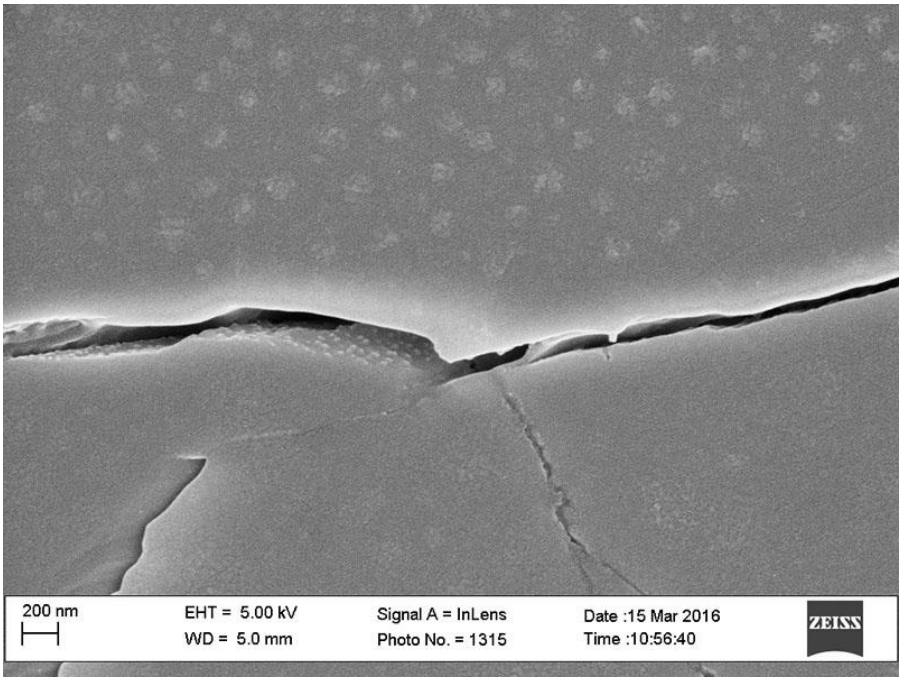

Figure A.81: Inlens SE micrograph from sample NAM-2784. Grain boundary 32, image A.

Grain boundary 33

Image	Measurement Number	Length (nm)
A	1	29.98
A	2	33.94
A	3	41.39
A	4	44.97
A	5	48.86
A	6	30.93
B	1	33.74
B	2	34.55
B	3	31.85
B	4	25.68
Mean Aperture		35.59

Table A.54: NGBC measurements and mean aperture from grain boundary 33 in sample NAM-2784.

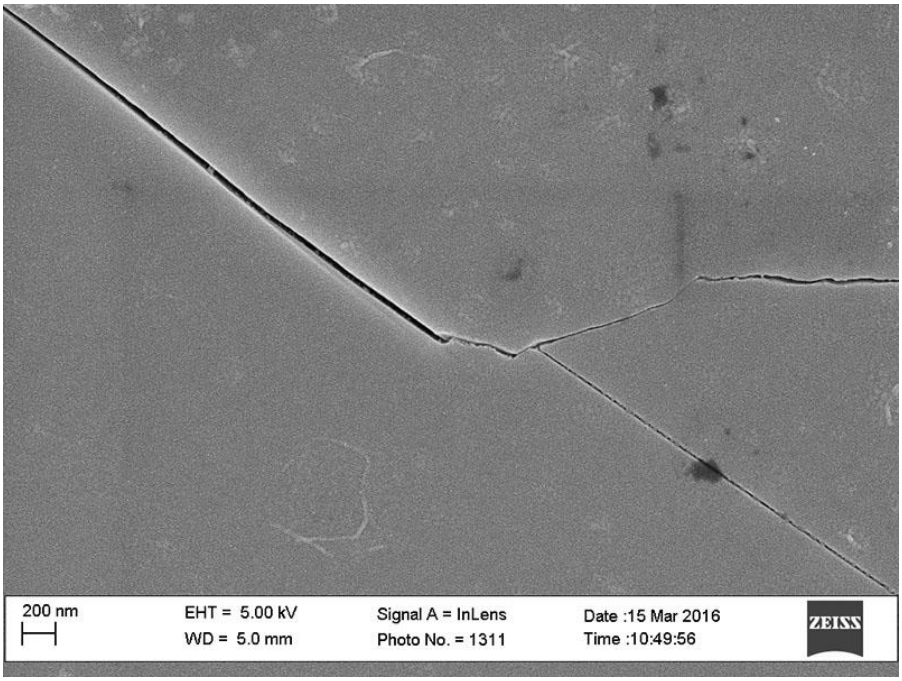

Figure A.82: Inlens SE micrograph from sample NAM-2784. Grain boundary 33, image A.

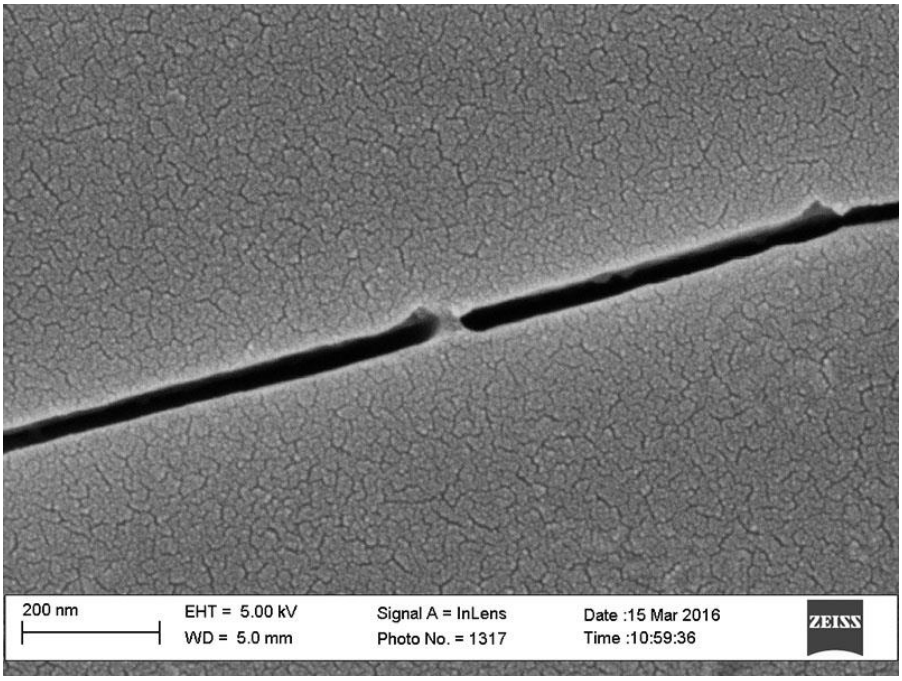

Figure A.83: Inlens SE micrograph from sample NAM-2784. Grain boundary 33, image B.

Grain boundary 34

Image	Measurement Number	Length (nm)
A	1	248.82
A	2	240.51
A	3	236.33
A	4	220.15
B	1	106.63
B	2	118.43
B	3	118.43
B	4	162.96
B	5	138.76
B	6	150.80
Mean Aperture		174.18

Table A.55: NGBC measurements and mean aperture from grain boundary 34 in sample NAM-2784.

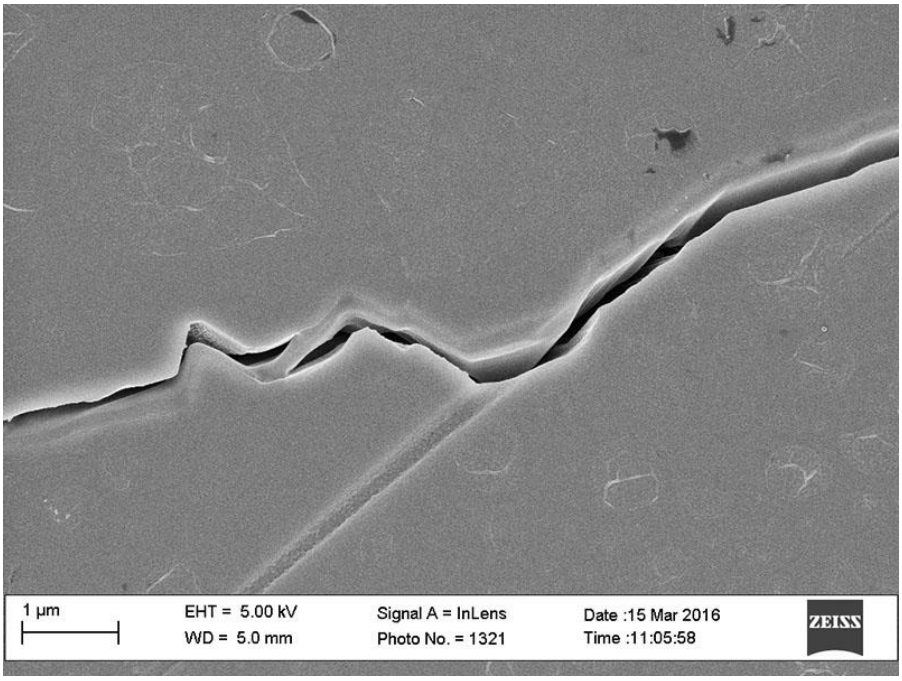

Figure A.84: Inlens SE micrograph from sample NAM-2784. Grain boundary 34, image A.

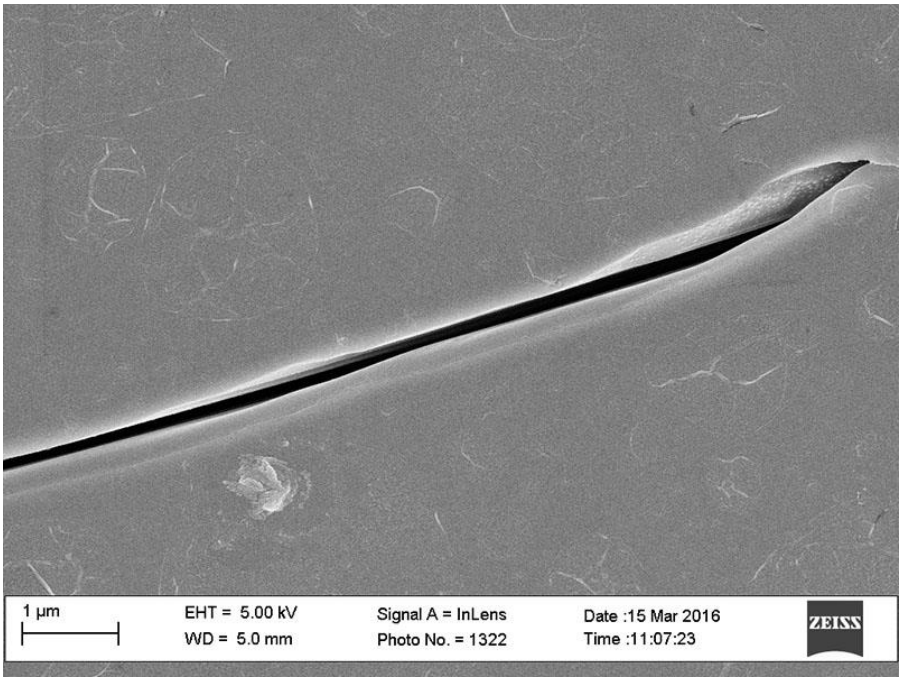

Figure A.85: Inlens SE micrograph from sample NAM-2784. Grain boundary 34, image B.

Grain boundary 35

Image	Measurement Number	Length (nm)
A	1	259.48
A	2	253.30
A	3	256.87
Mean Aperture		256.55

Table A.56: NGBC measurements and mean aperture from grain boundary 35 in sample NAM-2784.

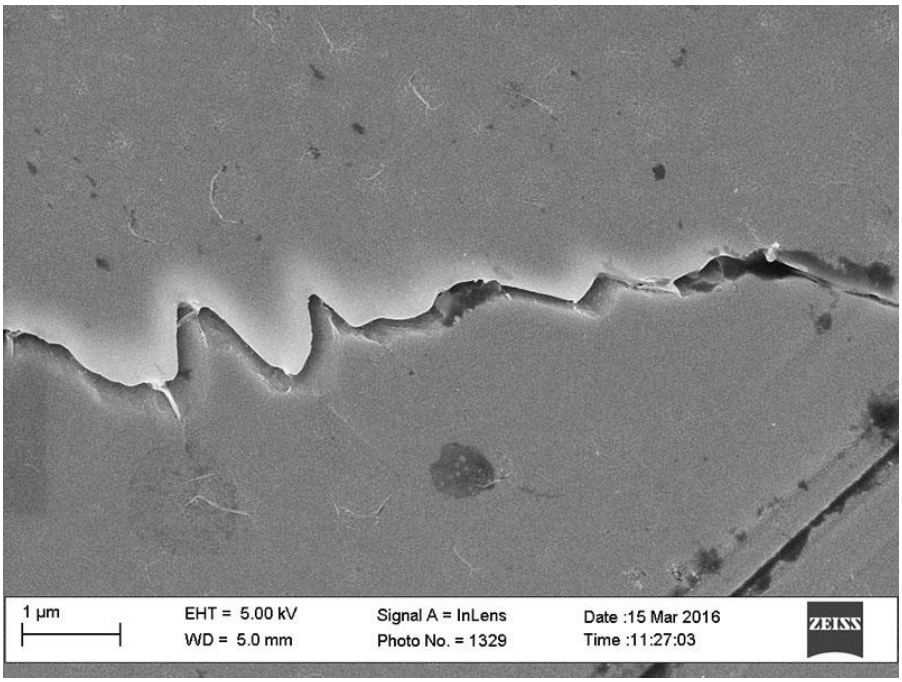

Figure A.86: Inlens SE micrograph from sample NAM-2784. Grain boundary 35, image A.

Grain boundary 36

Image	Measurement Number	Length (nm)
A	1	94.88
A	2	95.91
A	3	91.29
A	4	97.34
A	5	93.21
A	6	93.21
Mean Aperture		94.31

Table A.57: NGBC measurements and mean aperture from grain boundary 36 in sample NAM-2784.

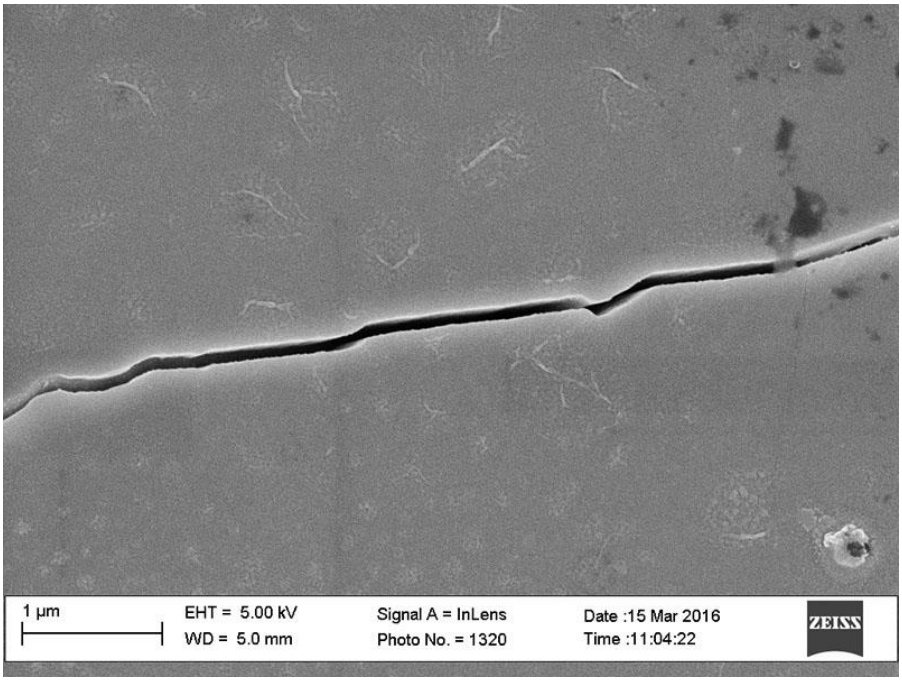

Figure A.87: Inlens SE micrograph from sample NAM-2784. Grain boundary 36, image A.

Grain boundary 37

Image	Measurement Number	Length (nm)
A	1	76.60
A	2	56.13
A	3	52.26
A	4	36.72
Mean Aperture		55.43

Table A.58: NGBC measurements and mean aperture from grain boundary 37 in sample NAM-2784.

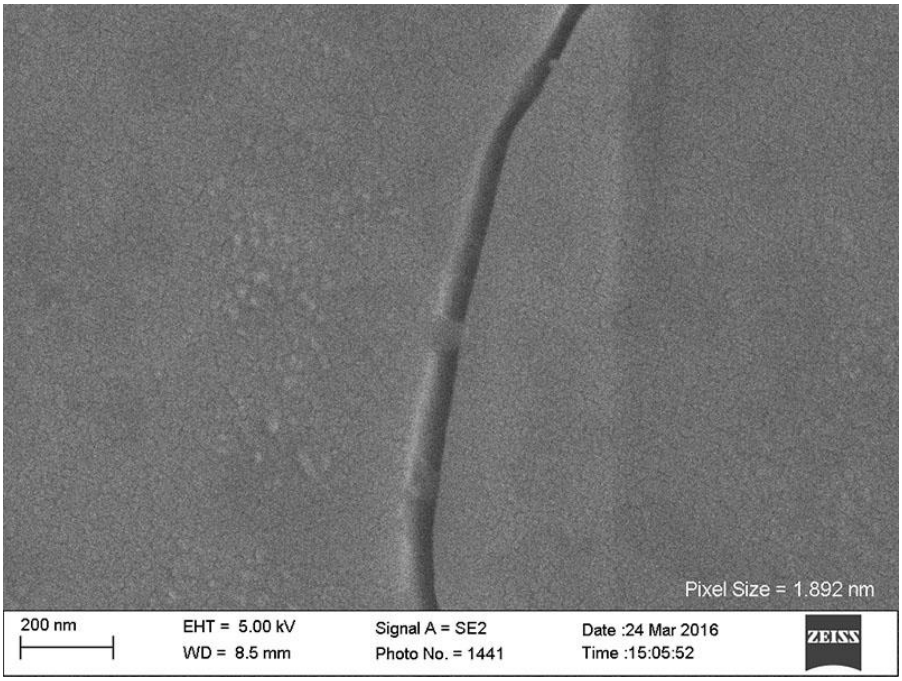

Figure A.88: Inlens SE micrograph from sample NAM-2784. Grain boundary 37, image A.

Grain boundary 38

Image	Measurement Number	Length (nm)
A	1	19.32
A	2	19.32
A	3	24.88
Mean Aperture		21.17

Table A.59: NGBC measurements and mean aperture from grain boundary 38 in sample NAM-2784.

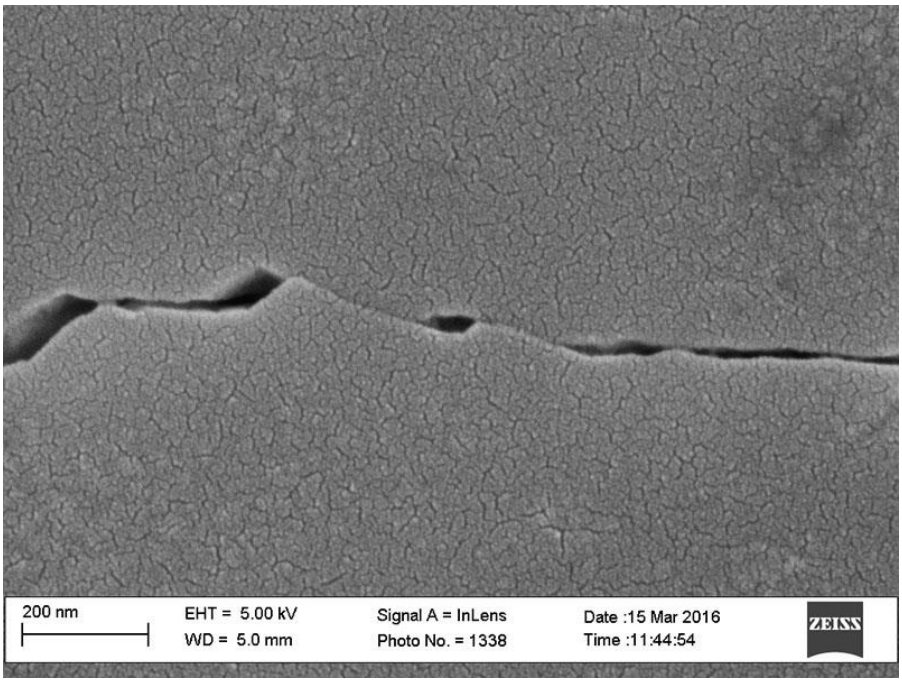

Figure A.89: Inlens SE micrograph from sample NAM-2784. Grain boundary 38, image A

SAMPLE NAC-3590-1, NEW ALBANY FORMATION

Mineral Cement	Rock Type	Sampled Depth (ft)	Sampled Depth (m)	Max burial depth (m)	Exhumed (m)	Max T (°C)	Range (nm)	Sample Mean (nm)
Calcite	Shale	3590	1094.232	2417.232	1323	100-110	18-418	191.76

Table A.60: Summary of sample NAC-3590-1

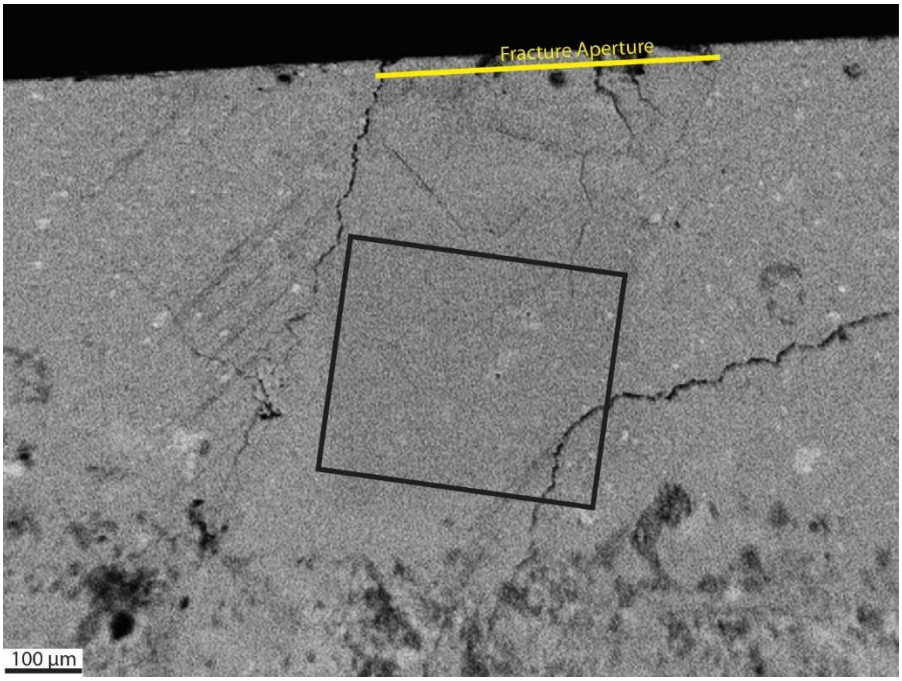

Figure A.90: BSE micrograph of sample NAC-3590-1. Box indicates area used for EBSD analysis and NGBC aperture measurements.

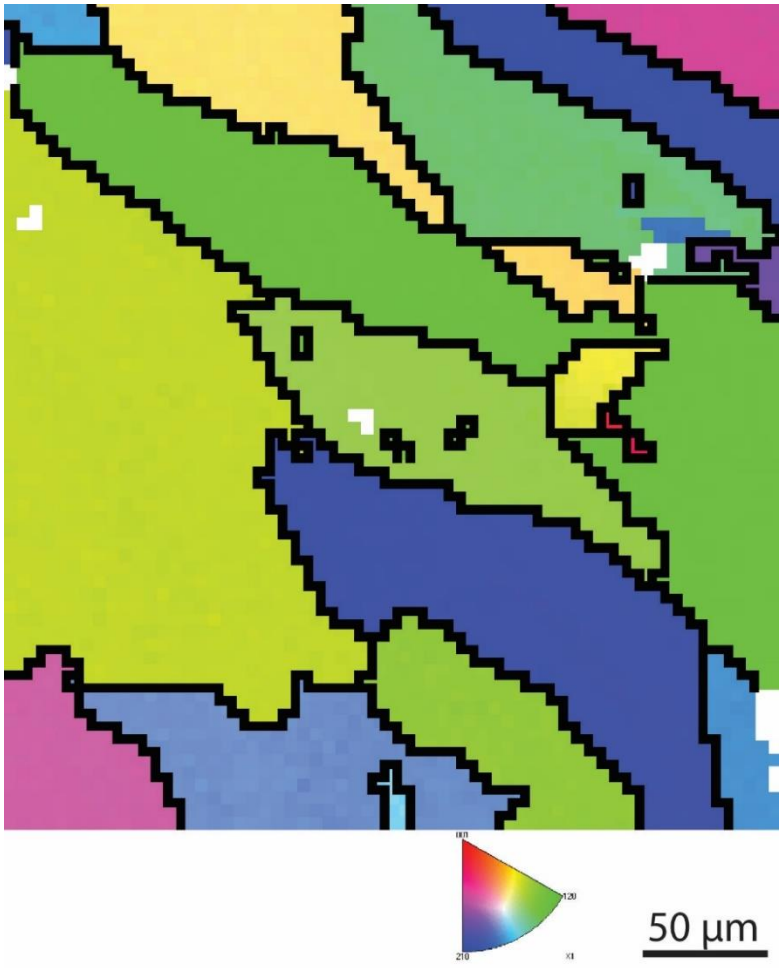

Figure A.91: EBSD inverse pole figure from sample NAC-3590-1.

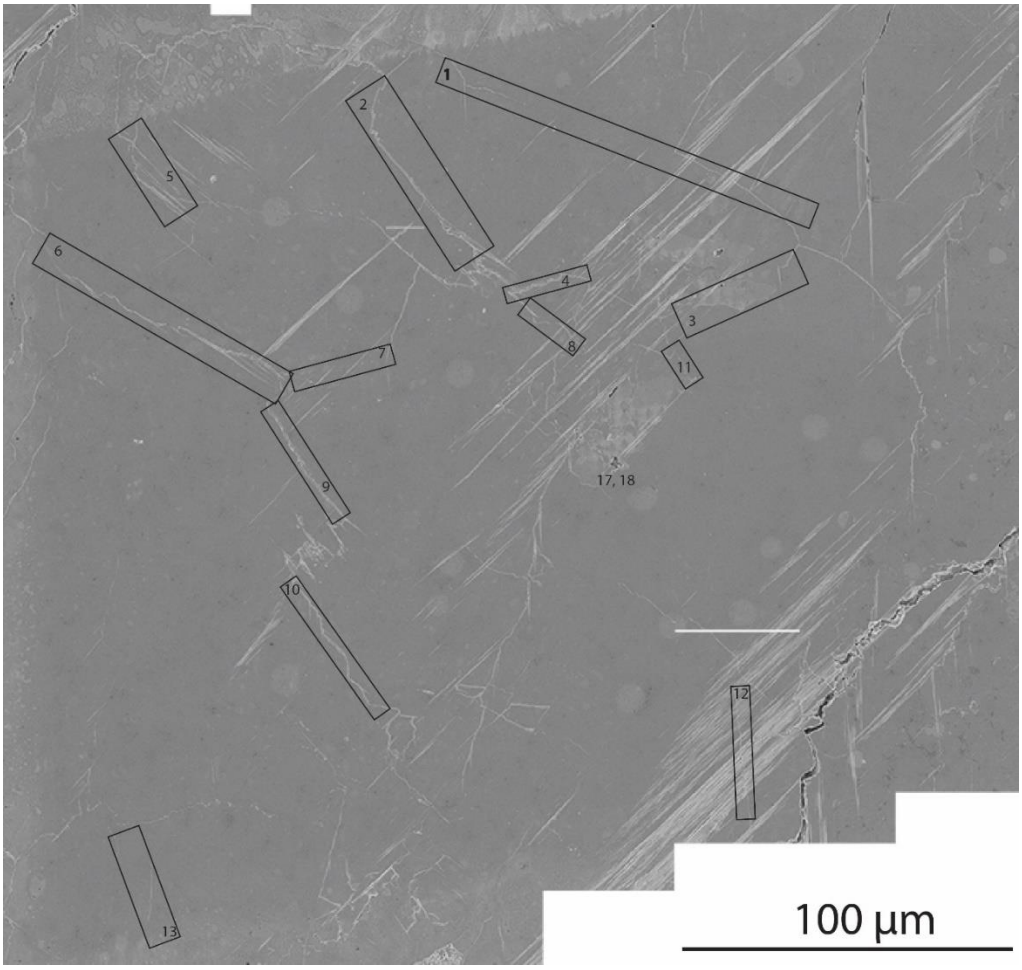

Figure A.92: Inlens SE mosaic of sample NAC-3590-1. Boxes indicate location of grain boundaries used for NGBC aperture measurements.

Grain Boundary	Mean Aperture (nm)
1	141.26
2	291.49
3	118.75
4	182.12
5	115.66
6	238.49
7	240.97
8	203.82
9	418.27
10	339.09
11	35.26
12	149.04
13	18.62
Sample Mean	191.76

Table A.61: NGBC mean apertures and sample mean from sample NAC-3590-1.

Grain Boundary 1

Image	Measurement Number	Length (nm)
A	1	148.92
A	2	142.29
A	3	143.82
A	4	113.14
A	5	142.37
A	6	157.04
Mean Aperture		141.26

Table A.62: NGBC measurements and mean aperture from grain boundary 1 in sample NAC-3590-1.

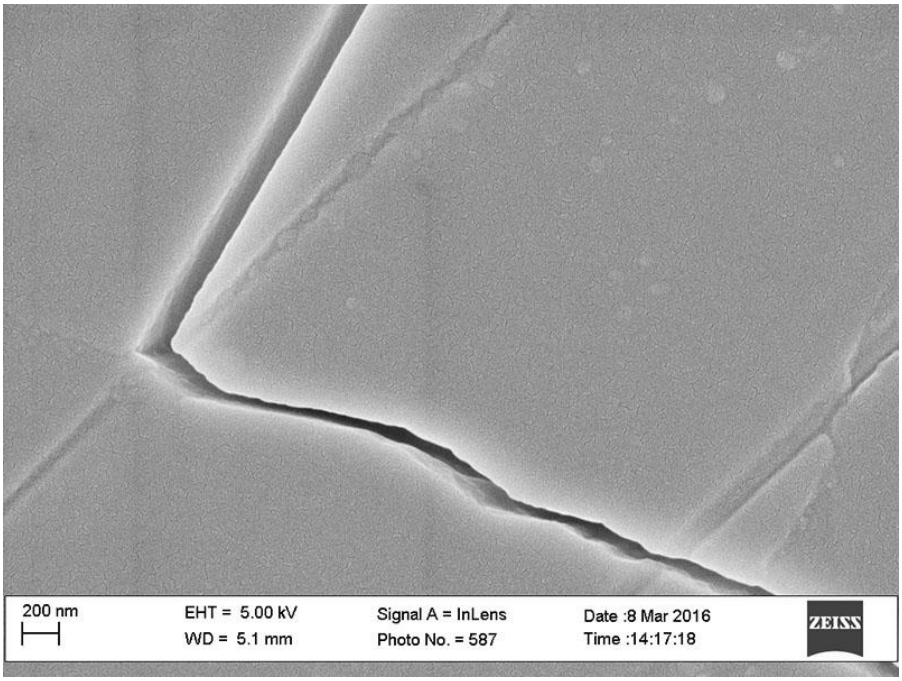

Figure A.93: Inlens SE micrograph from sample NAC-3590-1. Grain boundary 1, image A.

Grain Boundary 2

Image	Measurement Number	Length (nm)
A	1	260.30
A	2	237.35
A	3	198.96
A	1	192.15
A	2	261.75
A	3	203.69
B	1	221.07
B	2	234.34
B	3	253.47
B	4	357.70
B	5	635.09
B	6	293.62
B	7	246.33
B	8	363.41
B	9	377.85
B	10	326.81
Mean Aperture		291.49

Table A.63: NGBC measurements and mean aperture from grain boundary in sample NAC-3590-1.

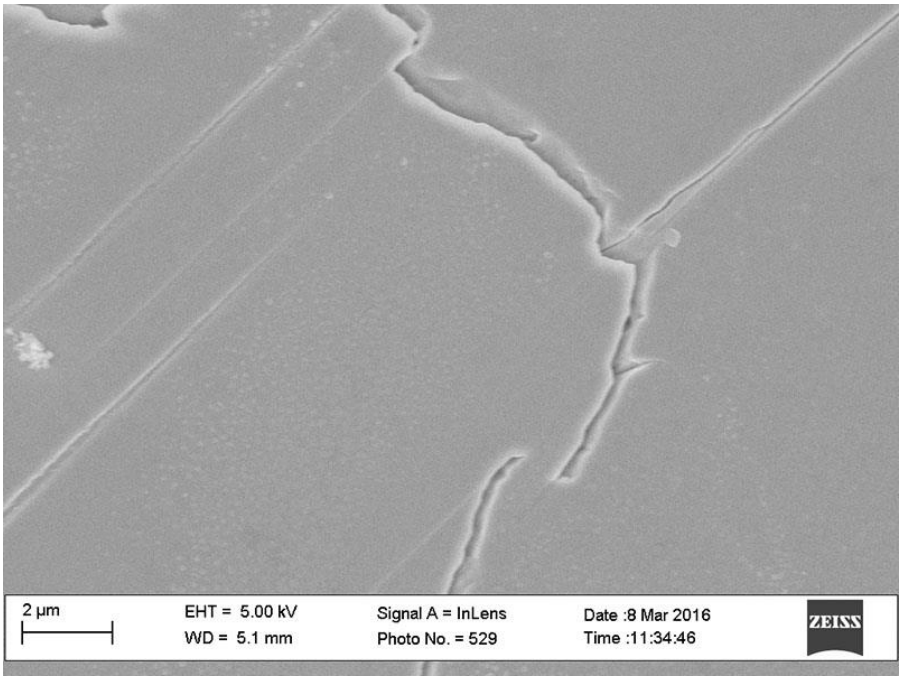

Figure A.94: Inlens SE micrograph from sample NAC-3590-1. Grain boundary2, image A.

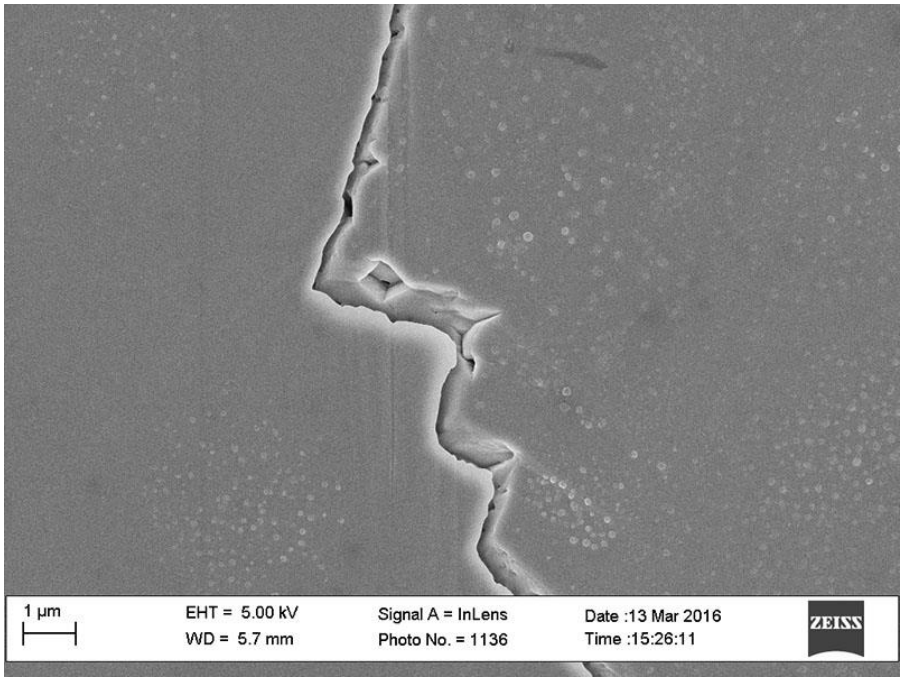

Figure A.95: Inlens SE micrograph from sample NAC-3590-1. Grain boundary 2, image A.

Grain Boundary 3

Image	Measurement Number	Length (nm)
A	1	123.27
A	2	135.19
A	3	123.27
A	4	103.34
A	5	121.59
A	6	101.33
A	7	123.27
Mean Aperture		118.75

Table A.64: NGBC measurements and mean aperture from grain boundary 3 in sample NAC-3590-1.

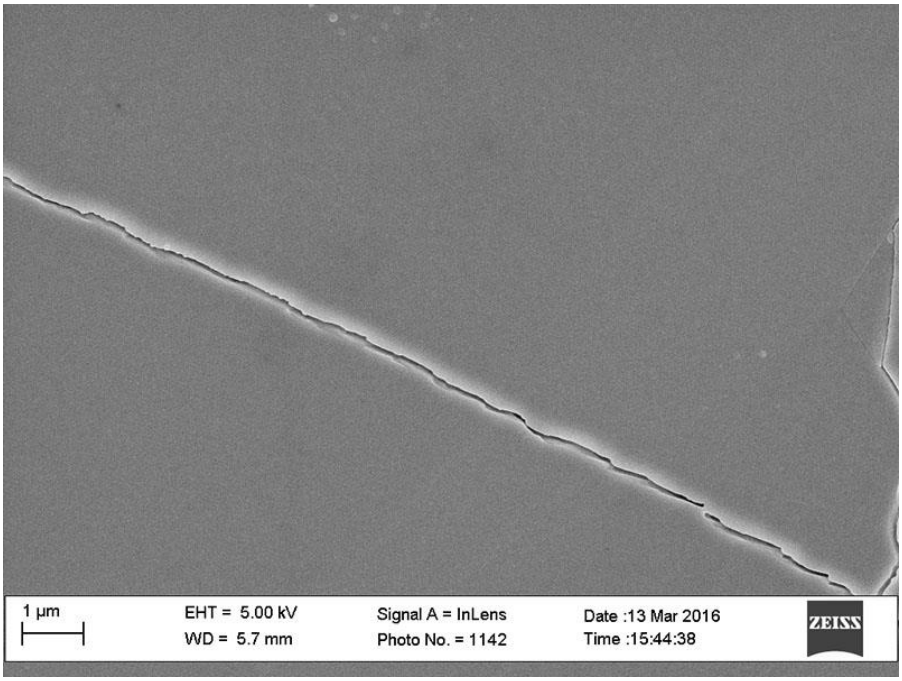

Figure A.96: Inlens SE micrograph from sample NAC-3590-1. Grain boundary 3, image A.

Grain Boundary 4

Image	Measurement Number	Length (nm)
A	1	147.24
A	2	167.87
A	3	125.13
A	4	143.09
A	5	164.98
A	6	112.99
B	1	217.57
B	2	318.94
B	3	231.96
B	4	214.90
B	5	158.65
Mean Aperture		182.12

Table A.65: NGBC measurements and mean aperture from grain boundary 4 in sample NAC-3590-1.

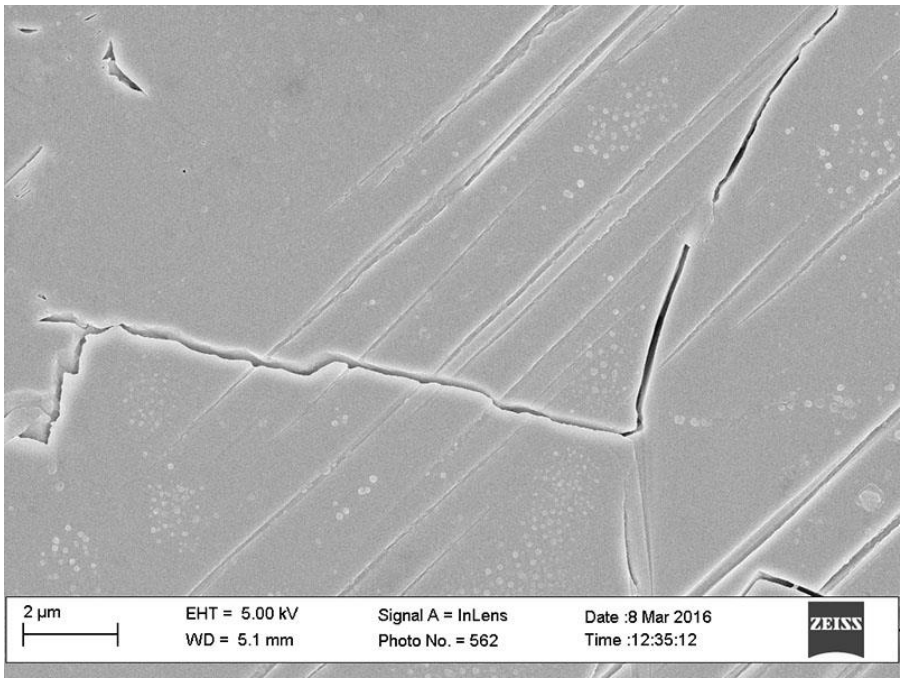

Figure A.97: Inlens SE micrograph from sample NAC-3590-1. Grain boundary 4, image A.

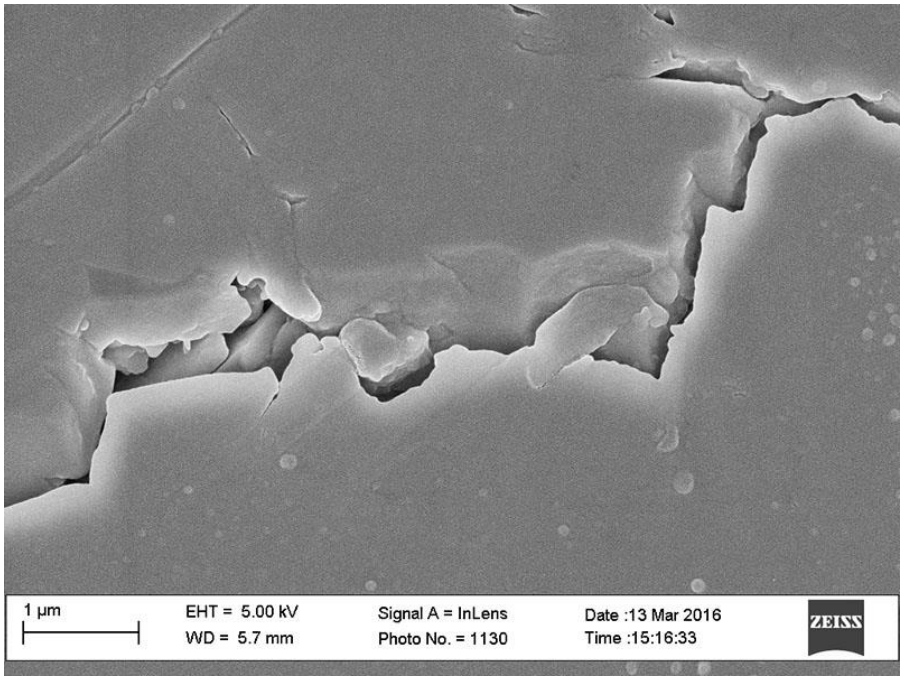

Figure A.98: Inlens SE micrograph from sample NAC-3590-1. Grain boundary 4, image B.

Grain Boundary 5

Image	Measurement Number	Length (nm)
A	1	105.30
A	2	73.00
A	3	166.50
A	4	115.49
A	5	117.99
	Mean Aperture	115.66

Table A.66: NGBC measurements and mean aperture from grain boundary 5 in sample NAC-3590-1.

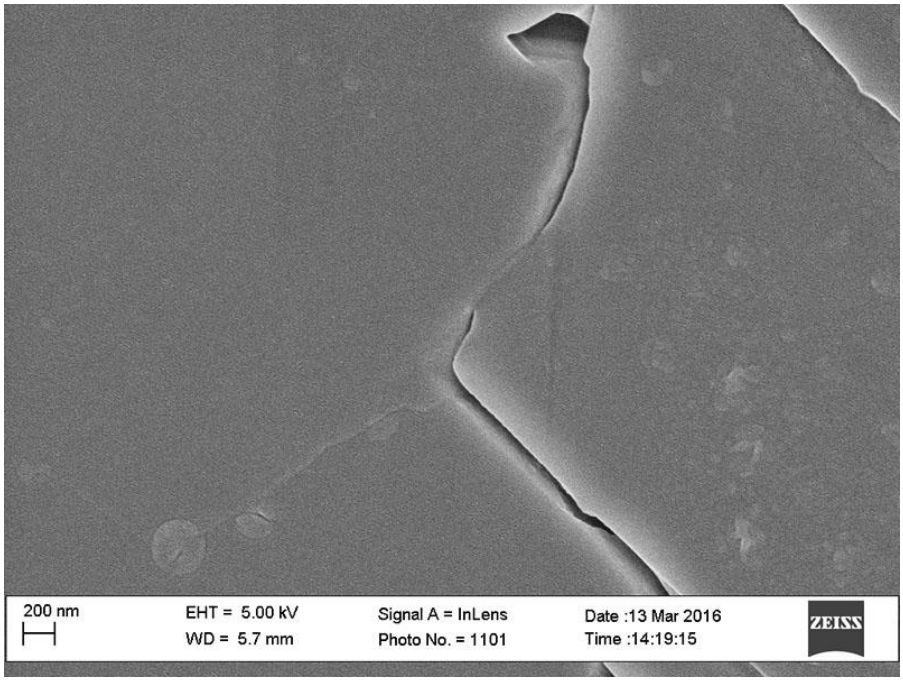

Figure A.99: Inlens SE micrograph from sample NAC-3590-1. Grain boundary 5, image

Grain Boundary 6

Image	Measurement Number	Length (nm)
A	1	662.02
A	2	487.21
B	3	234.17
B	1	165.58
B	2	230.43
B	3	205.91
C	1	360.26
C	2	227.80
C	3	259.74
C	4	351.39
D	5	208.72
D	6	219.22
D	7	219.22
D	8	204.26
D	9	223.59
E	1	131.44
E	2	167.05
E	3	185.14
E	4	199.85
E	4	146.96
F	1	427.89
F	2	551.83
F	3	538.21
F	4	662.77
G	1	441.46
G	2	111.04
G	3	117.94
G	4	77.56
G	5	105.84
G	6	130.07
G	7	101.12
G	8	202.24
G	9	187.58
G	10	251.46
G	11	111.04
H	1	115.40
H	2	112.00
H	3	131.88
H	4	112.10
I	5	180.30

Table A.67: NGBC measurements and mean aperture from grain boundary 6 in sample NAC-3590-1.

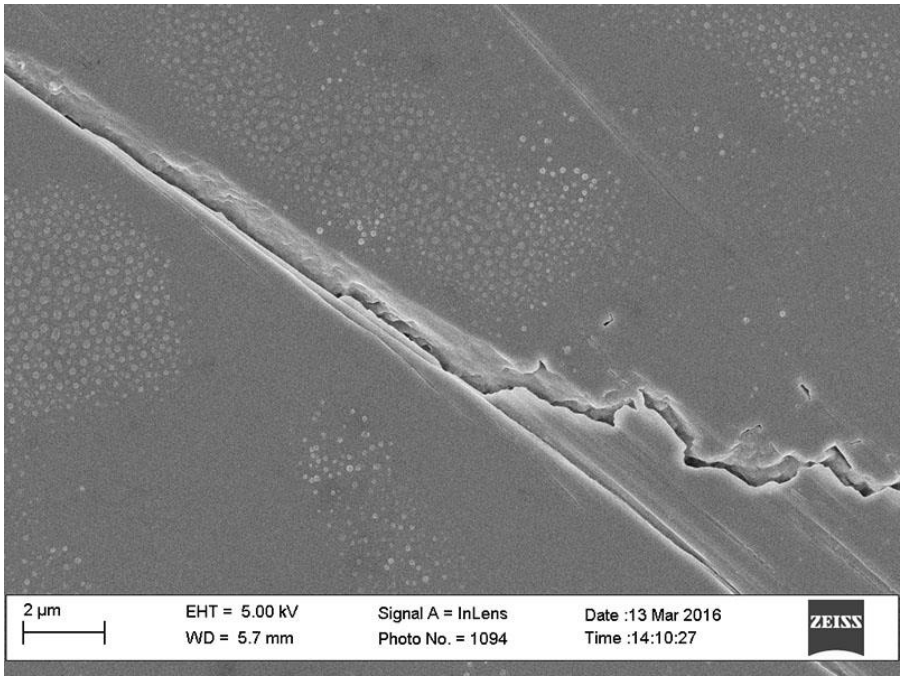

Figure A.100: Inlens SE micrograph from sample NAC-3590-1. Grain boundary 6, image A.

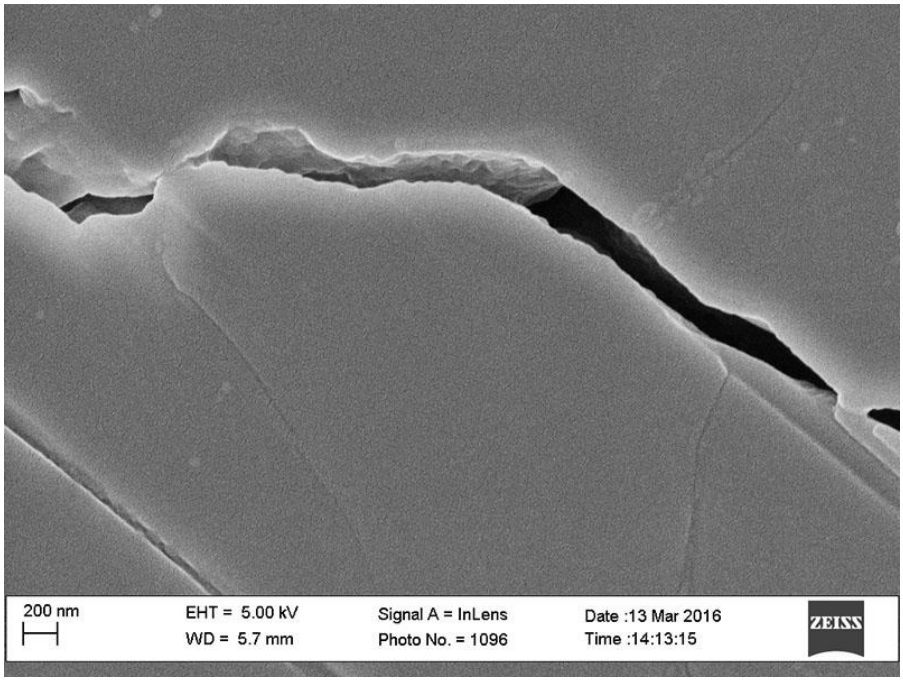

Figure A.101: Inlens SE micrograph from sample NAC-3590-1. Grain boundary 6, image B.

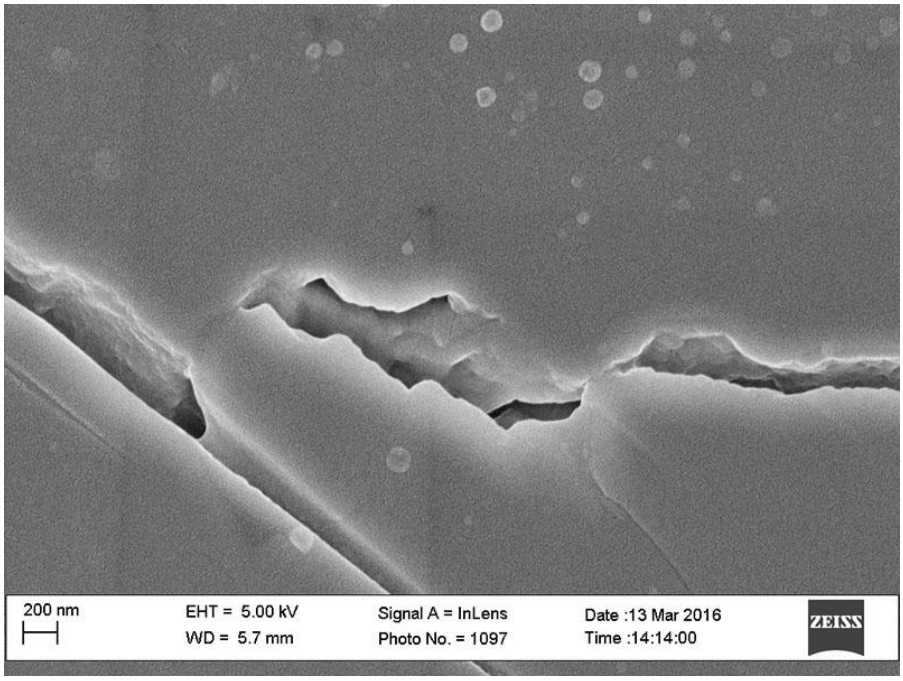

Figure A.102: Inlens SE micrograph from sample NAC-3590-1. Grain boundary 6, image C.

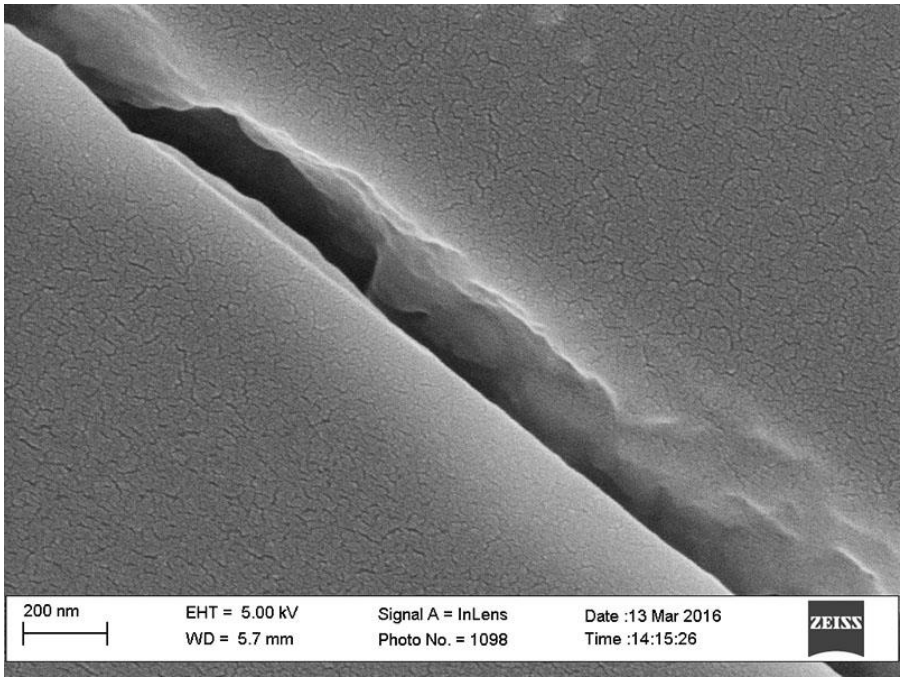

Figure A.103: Inlens SE micrograph from sample NAC-3590-1. Grain boundary6, image D.

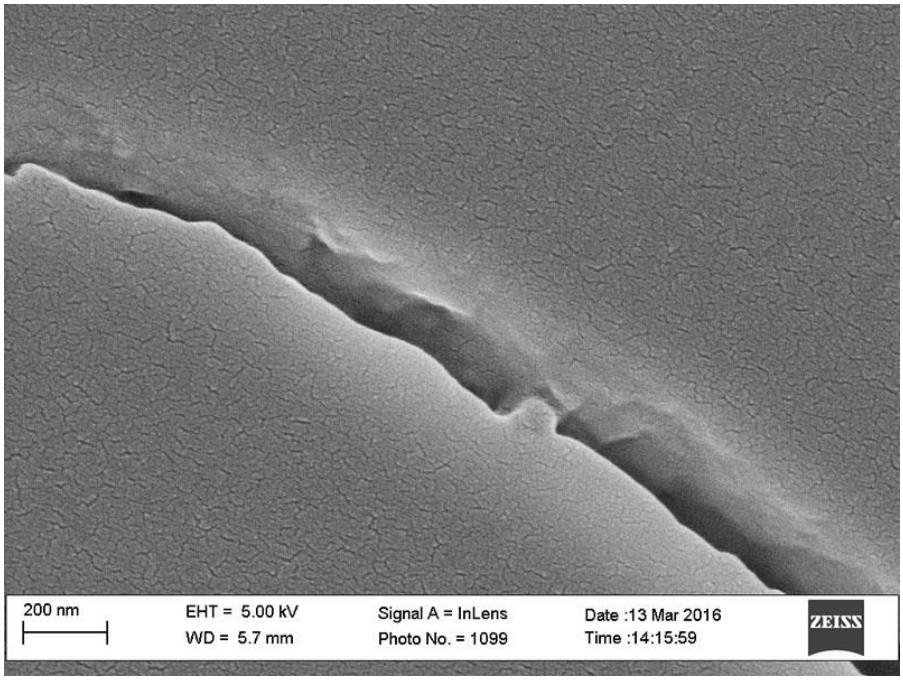

Figure A.104: Inlens SE micrograph from sample NAC-3590-1. Grain boundary 6, image E.

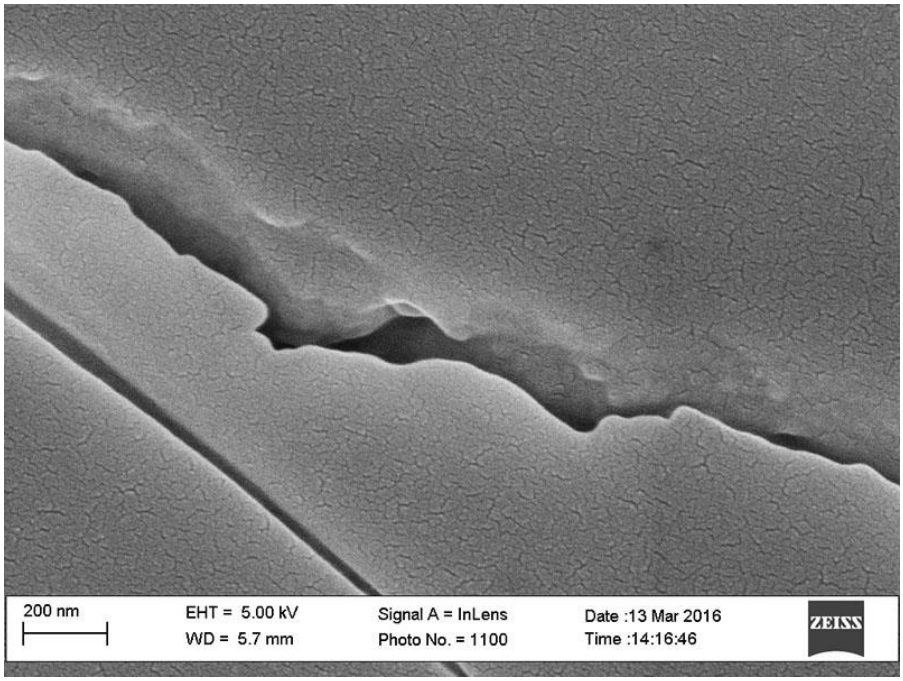

Figure A.105: Inlens SE micrograph from sample NAC-3590-1. Grain boundary 6, image F.

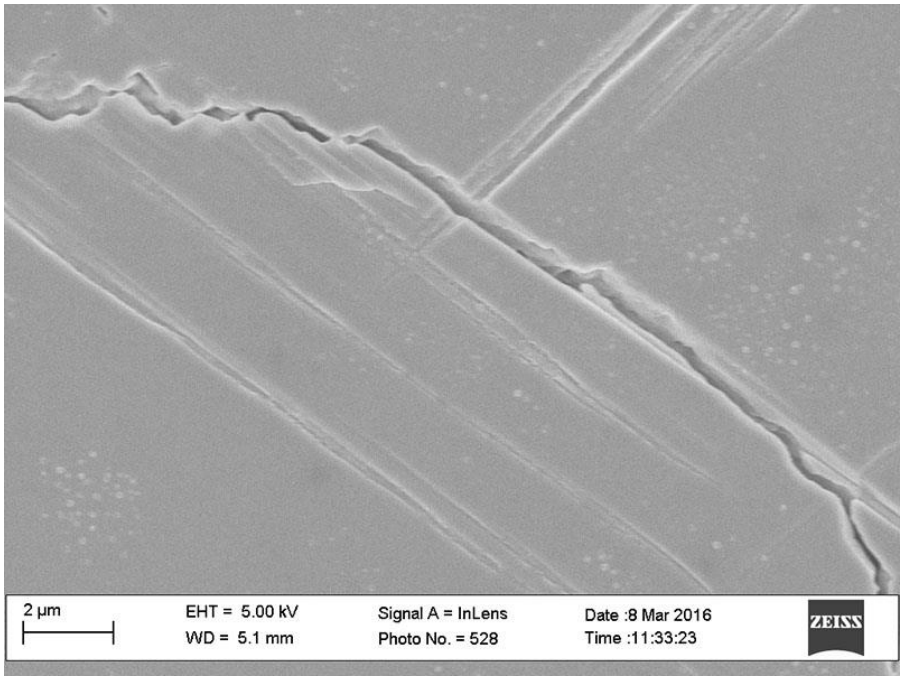

Figure A.106: Inlens SE micrograph from sample NAC-3590-1. Grain boundary 6, image G.

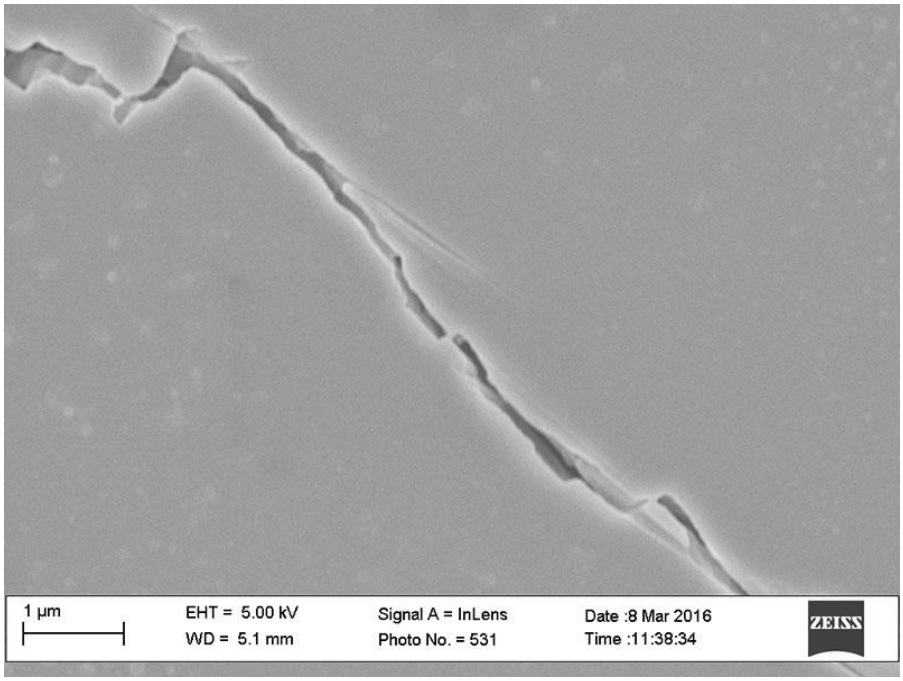

Figure A.107: Inlens SE micrograph from sample NAC-3590-1. Grain boundary 6, image H.

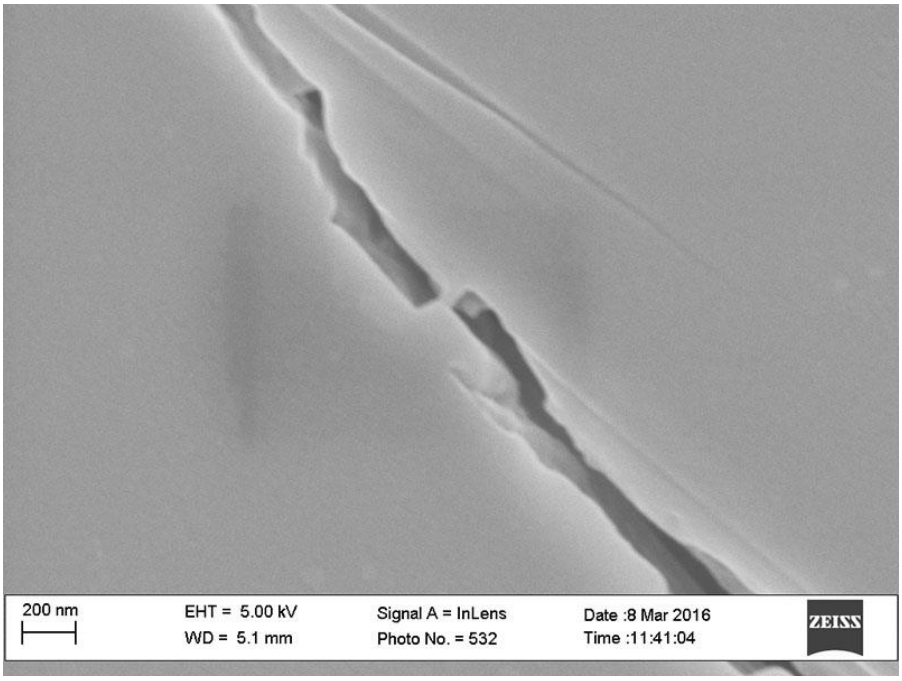

Figure A.108: Inlens SE micrograph from sample NAC-3590-1. Grain boundary 6, image I.

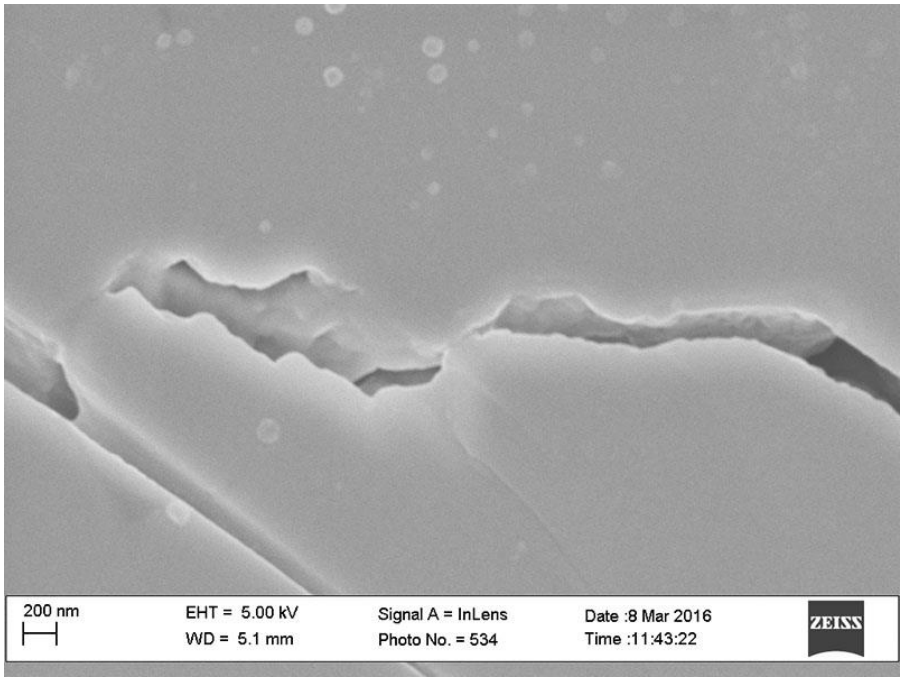

Figure A.109: Inlens SE micrograph from sample NAC-3590-1. Grain boundary 6, image J.

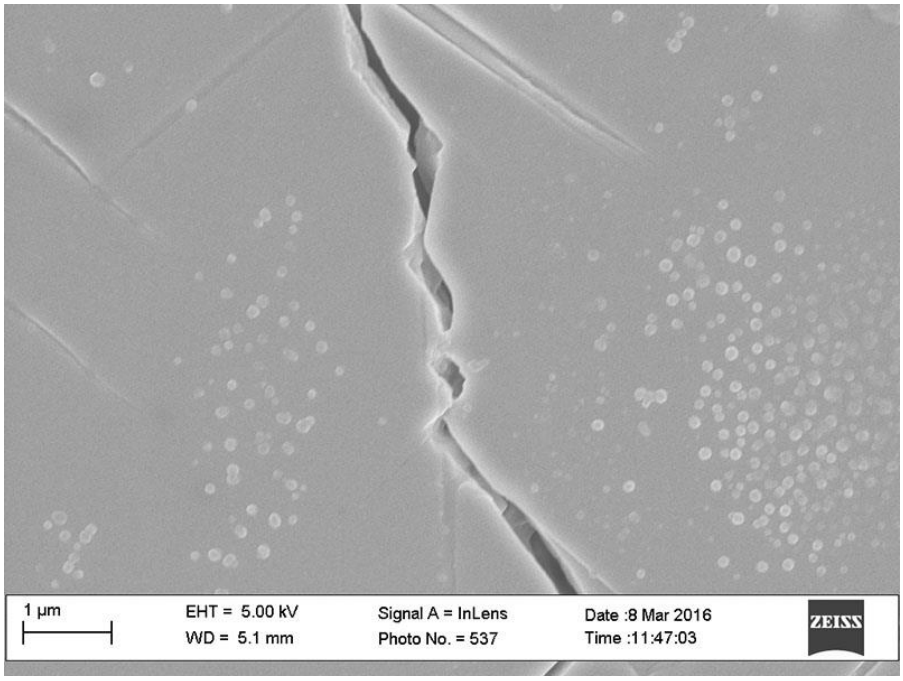

Figure A.110: Inlens SE micrograph from sample NAC-3590-1. Grain boundary 6, image K.

Grain Boundary 7

Image	Measurement Number	Length (nm)
A	1	262.05
A	2	270.02
A	3	231.51
A	4	200.99
A	5	240.28
	Mean Aperture	240.97

Table A.68: NGBC measurements and mean aperture from grain boundary 7 in sample NAC-3590-1.

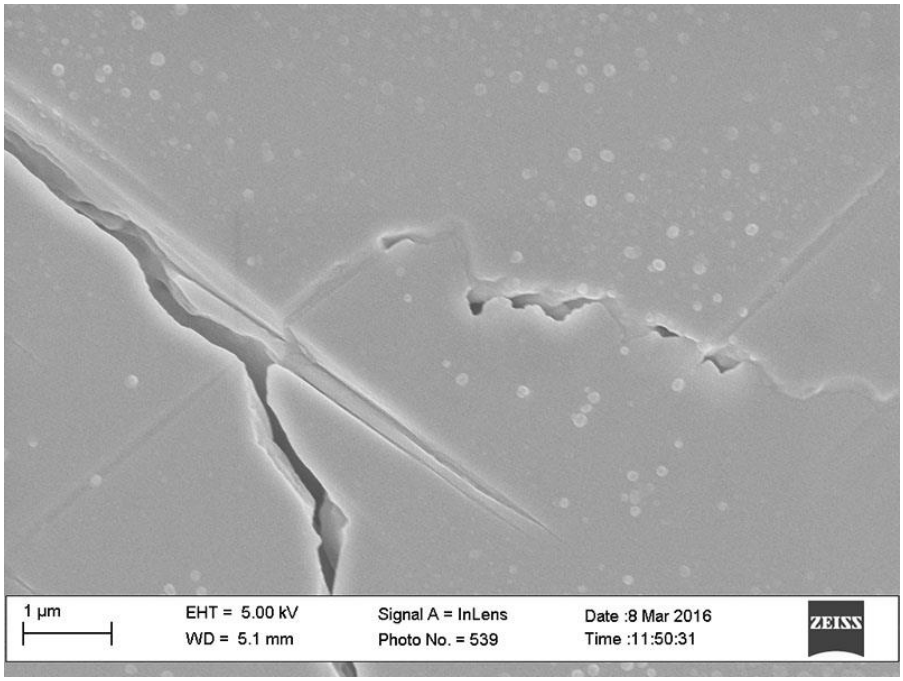

Figure A.111: Inlens SE micrograph from sample NAC-3590-1. Grain boundary 7, image A.

Grain Boundary 8

Image	Measurement Number	Length (nm)
A	1	188.21
A	2	204.54
A	3	192.34
A	4	216.79
A	5	197.20
A	6	223.86
	Mean Aperture	203.82

Table A.69: NGBC measurements and mean aperture from grain boundary 8 in sample NAC-3590-1.

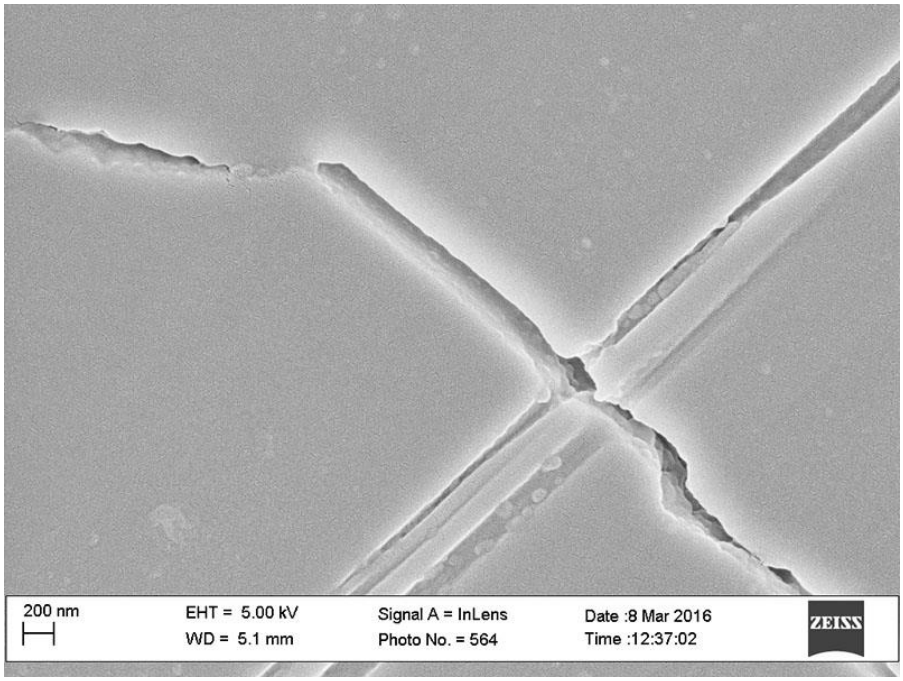

Figure A.112: Inlens SE micrograph from sample NAC-3590-1. Grain boundary 8, image A.

Grain Boundary 9

Image	Measurement Number	Length (nm)
A	1	319.47
A	2	322.35
A	3	512.62
A	4	447.18
A	5	387.42
B	1	480.53
B	2	442.51
B	3	464.90
B	4	387.42
	Mean Aperture	418.27

Table A.70: NGBC measurements and mean aperture from grain boundary 9 in sample NAC-3590-1.

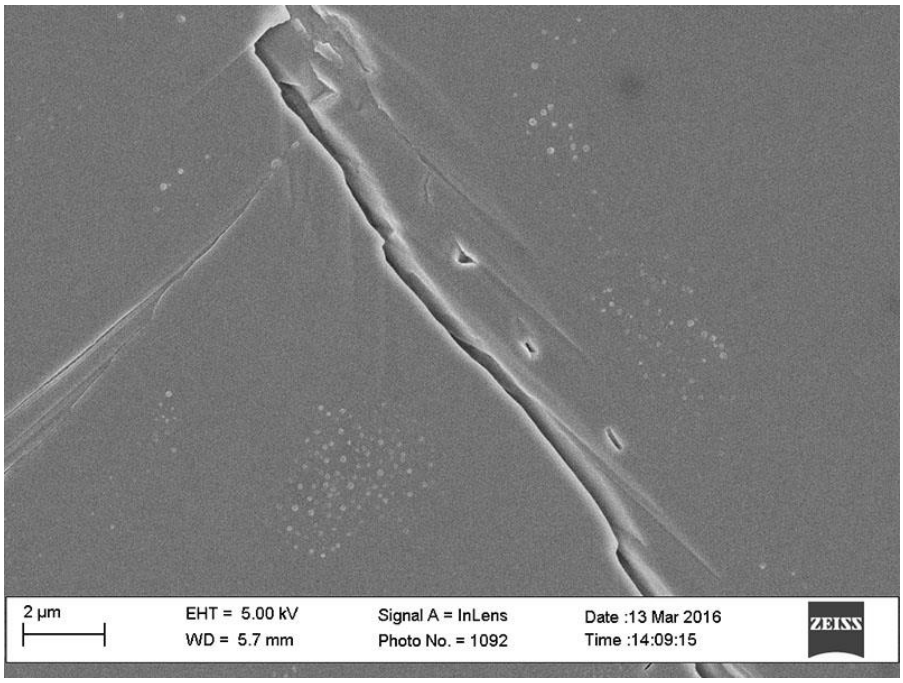

Figure A.113: Inlens SE micrograph from sample NAC-3590-1. Grain boundary 9, image A.

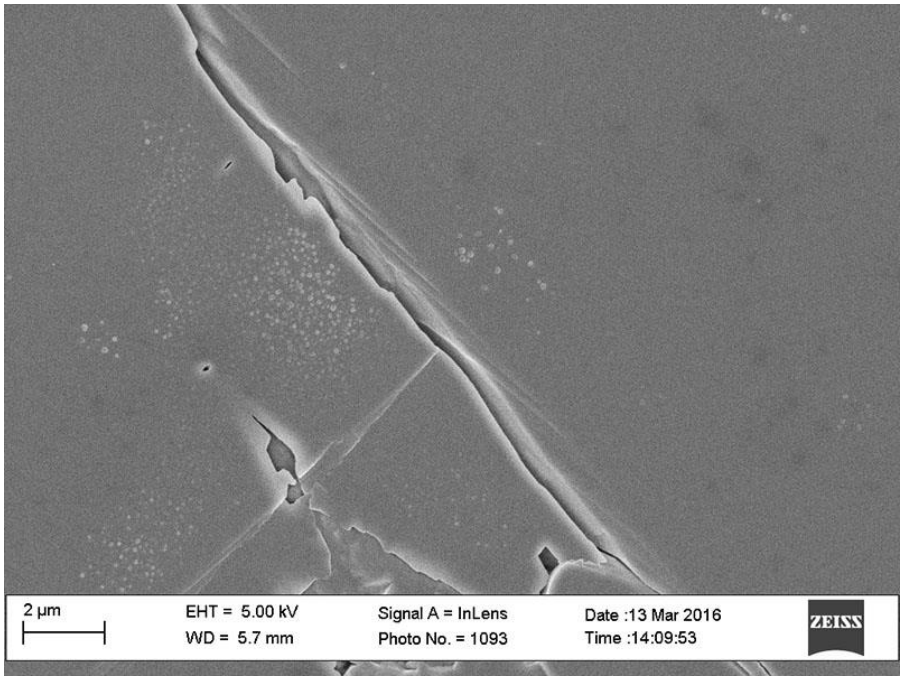

Figure A.114: Inlens SE micrograph from sample NAC-3590-1. Grain boundary 9, image B.

Grain Boundary 10

Image	Measurement Number	Length (nm)
A	1	370.93
A	2	326.84
A	3	473.22
A	4	364.12
A	5	435.43
A	6	451.21
A	7	519.05
B	1	320.11
B	2	322.67
B	3	360.86
C	4	248.60
D	1	449.06
D	2	249.15
D	3	375.67
D	4	441.21
E	1	189.29
E	2	243.68
E	3	267.69
E	4	264.26
F	1	309.38
F	2	267.69
G	1	271.76
G	2	277.24
	Mean Aperture	339.09

Table A.71: NGBC measurements and mean aperture from grain boundary 10 in sample NAC-3590-1.

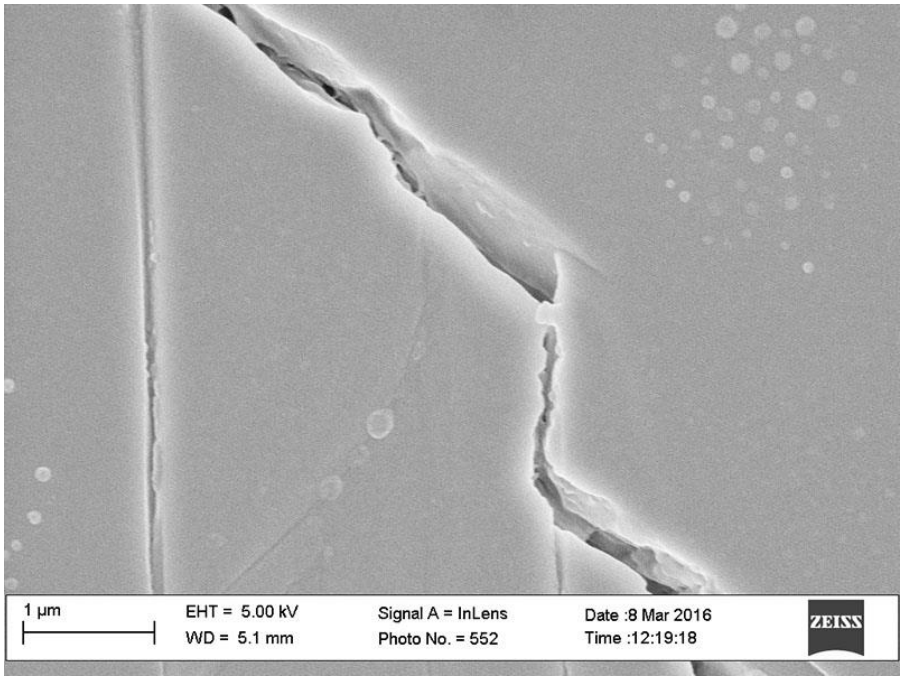

Figure A.115: Inlens SE micrograph from sample NAC-3590-1. Grain boundary 10, image A.

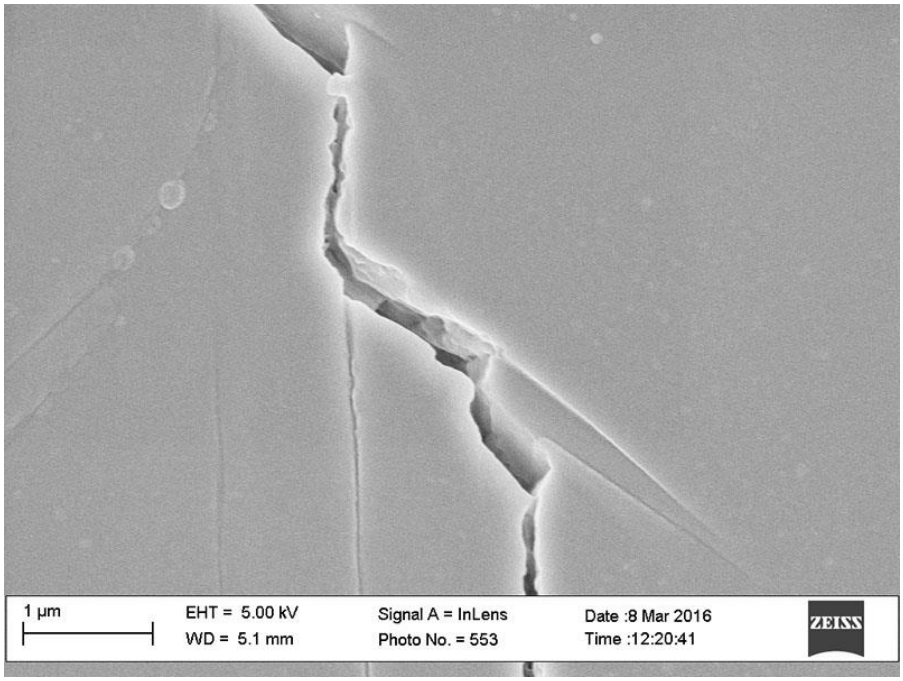

Figure A.116: Inlens SE micrograph from sample NAC-3590-1. Grain boundary 10, image B.

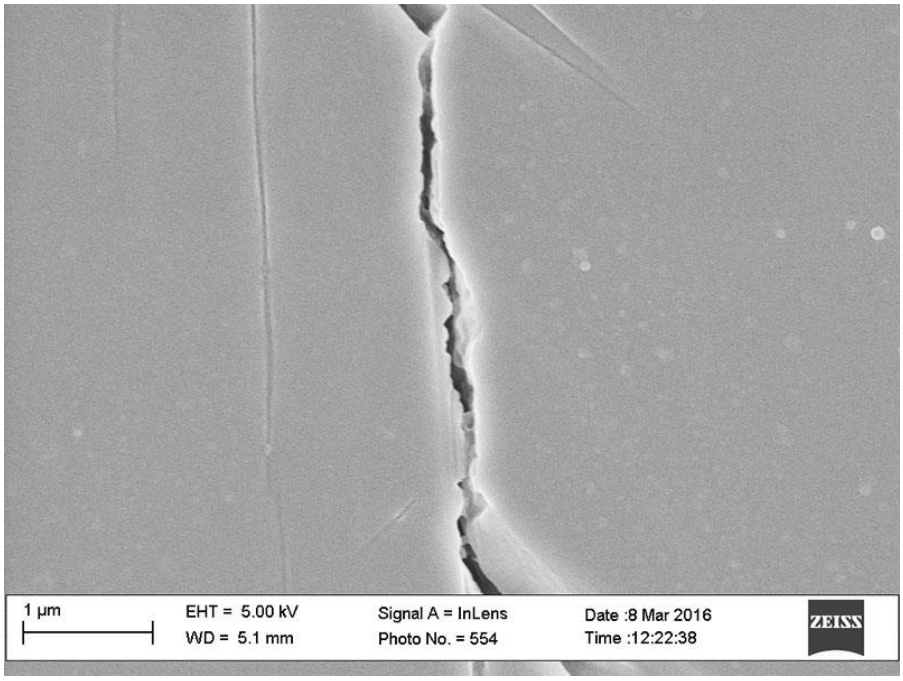

Figure A.117: Inlens SE micrograph from sample NAC-3590-1. Grain boundary 10, image C.

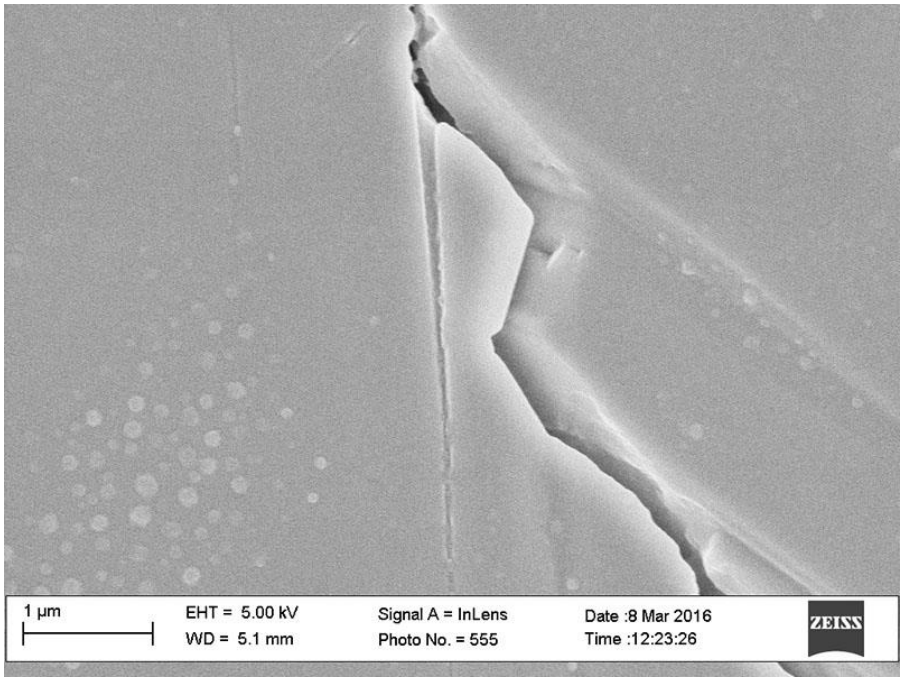

Figure A.118: Inlens SE micrograph from sample NAC-3590-1. Grain boundary 10, image D.

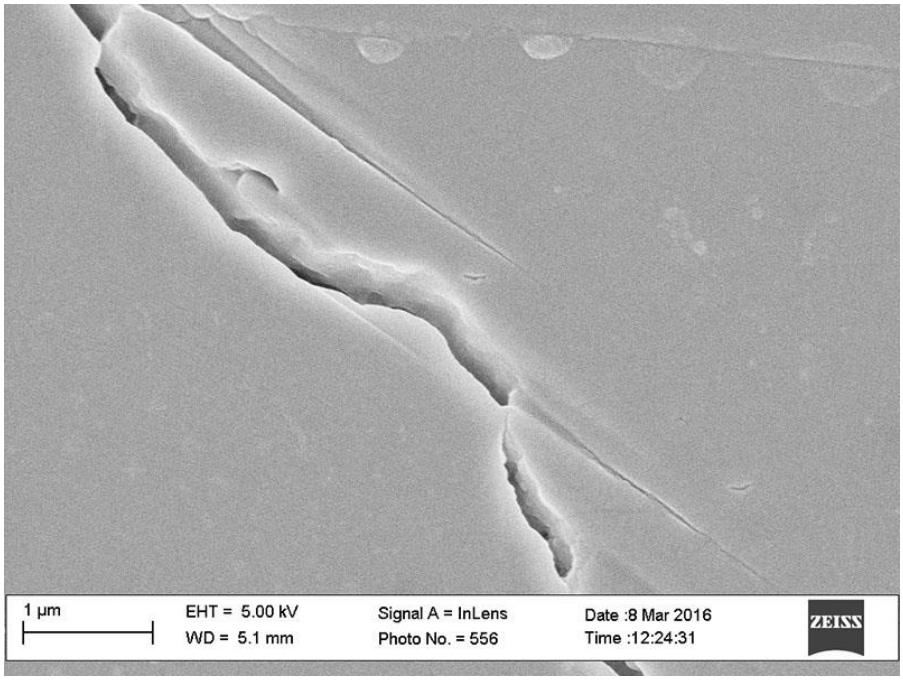

Figure A.119: Inlens SE micrograph from sample NAC-3590-1. Grain boundary 10, image E.

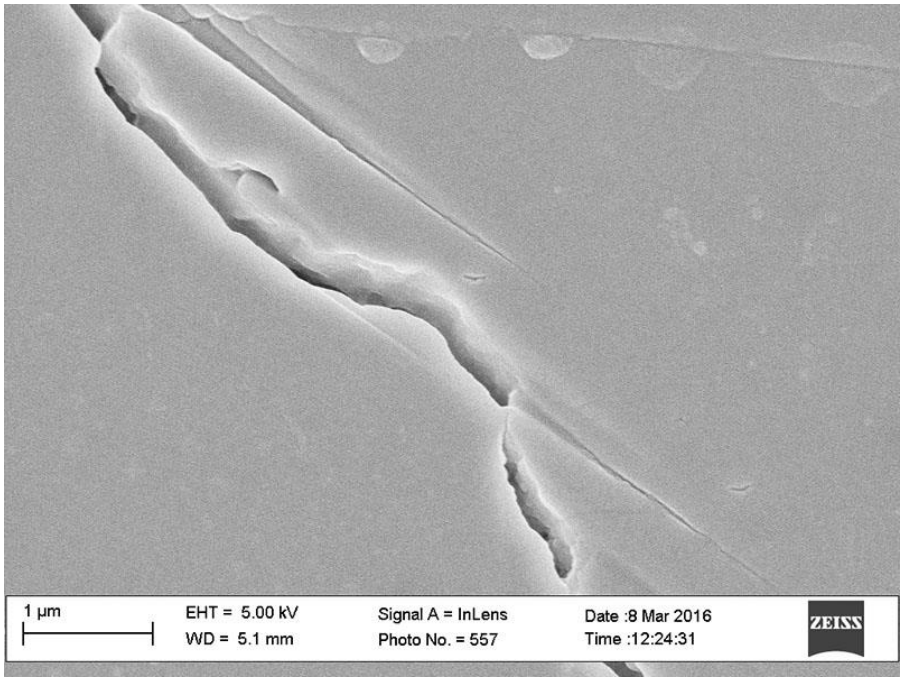

Figure A.120: Inlens SE micrograph from sample NAC-3590-1. Grain boundary 10, image F.

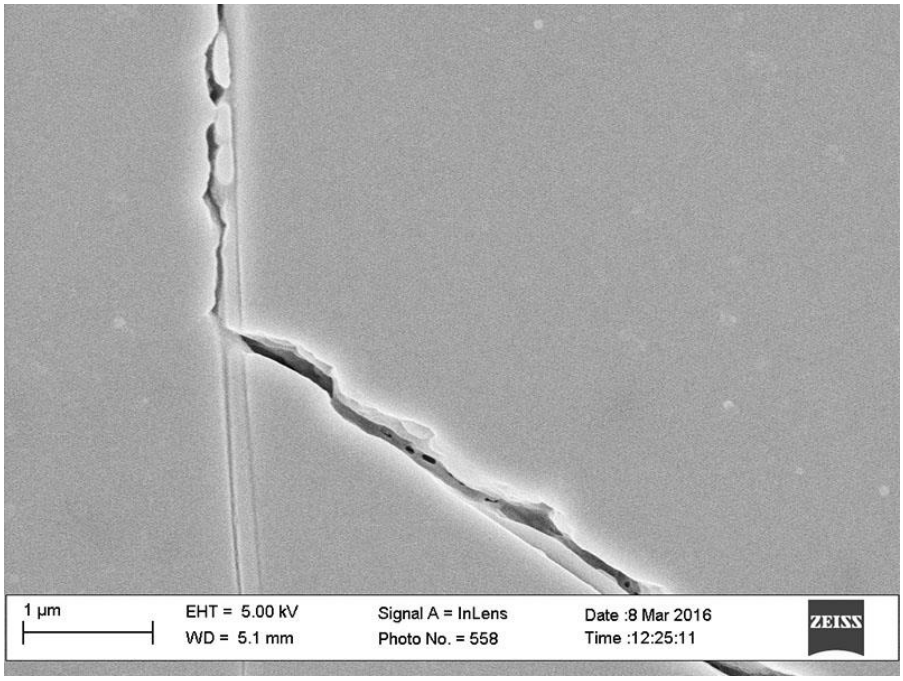

Figure A.121: Inlens SE micrograph from sample NAC-3590-1. Grain boundary 10, image G.

Grain Boundary 11

Image	Measurement Number	Length (nm)
A	1	33.41
A	2	34.29
A	3	38.09
	Mean Aperture	35.26

Table A.72: NGBC measurements and mean aperture from grain boundary 11 in sample NAC-3590-1.

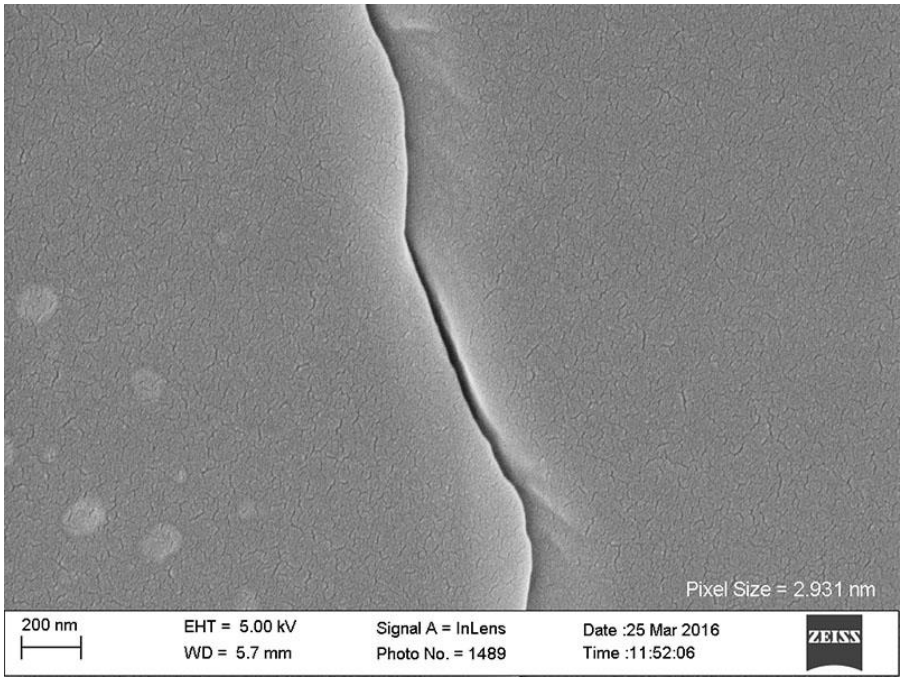

Figure A.122: Inlens SE micrograph from sample NAC-3590-1. Grain boundary 11, image A.

Grain Boundary 12

Image	Measurement Number	Length (nm)
A	1	144.80
A	2	159.28
A	3	145.52
A	4	101.36
A	5	130.32
A	6	173.76
A	7	188.24
	Mean Aperture	149.04

Table A.73: NGBC measurements and mean aperture from grain boundary 12 in sample NAC-3590-1.

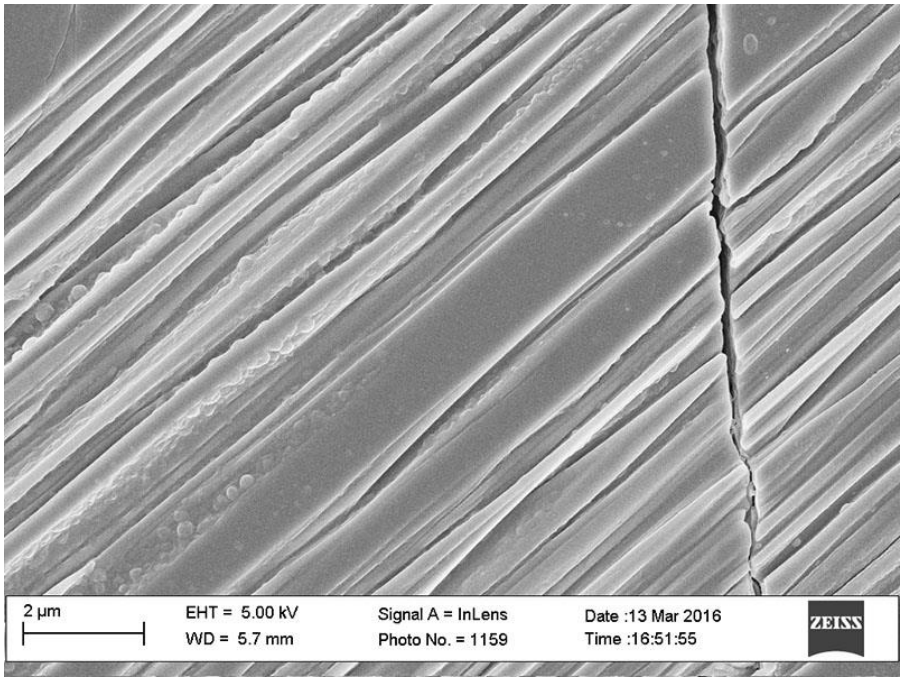

Figure A.123: Inlens SE micrograph from sample NAC-3590-1. Grain boundary 12, image A.

Grain Boundary 13

Image	Measurement Number	Length (nm)
A	1	16.92
A	2	15.40
A	3	15.25
B	1	25.75
B	2	19.19
B	3	19.19
	Mean Aperture	18.62

Table A.74: NGBC measurements and mean aperture from grain boundary 13 in sample NAC-3590-1.

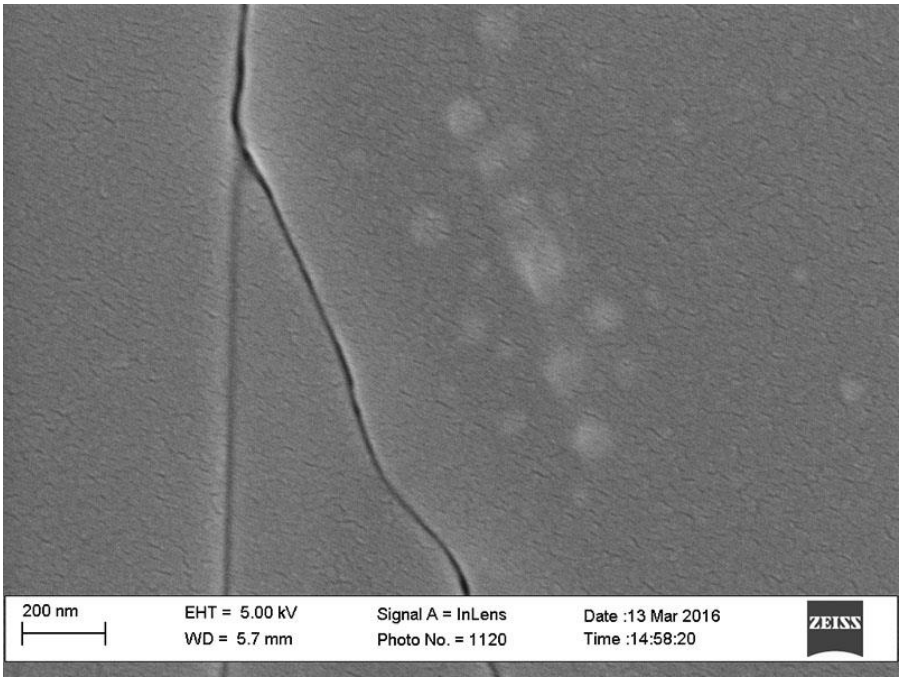

Figure A.124: Inlens SE micrograph from sample NAC-3590-1. Grain boundary 13, image A.

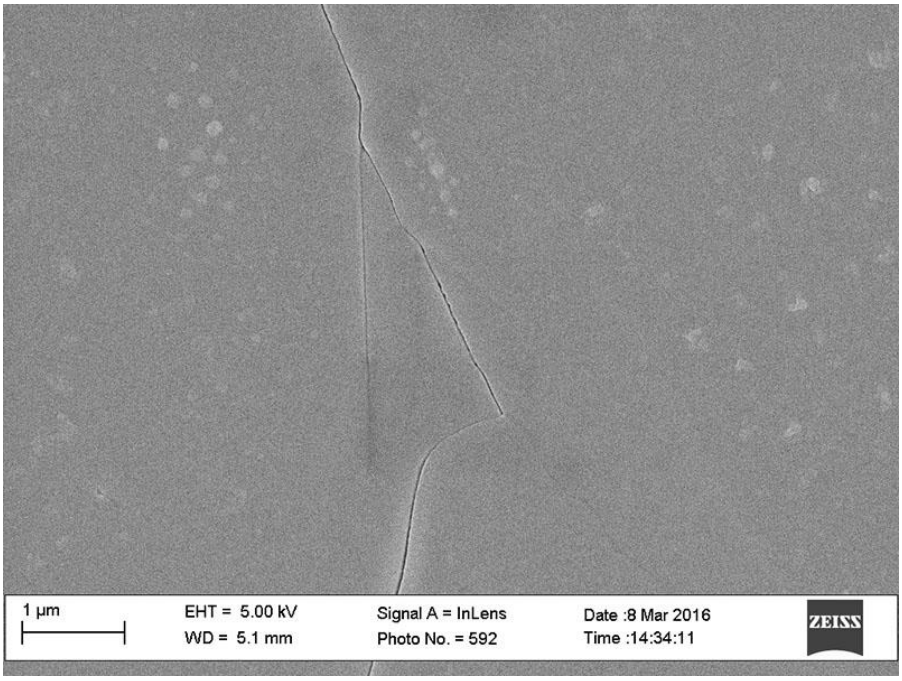

Figure A.125: Inlens SE micrograph from sample NAC-3590-1. Grain boundary 13, image B.

SAMPLE: NAC-3590-2, NEW ALBANY FORMATION

Mineral Cement	Rock Type	Sampled Depth (ft)	Sampled Depth (m)	Max burial depth (m)	Exhumed (m)	Max T (^{o}C)	Range (nm)	Sample Mean (nm)
Calcite	Shale	3590	1094.232	2417.232	1323	100-110	22-436	217.22

Table 75: Summary of sample NAC-3590-2

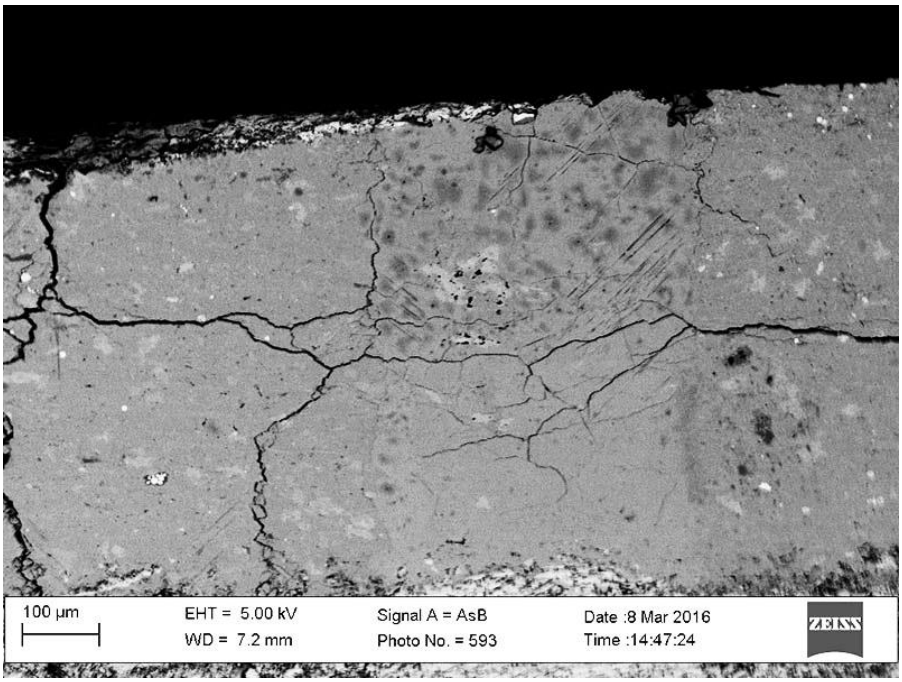

Figure A.126: BSE micrograph of sample NAC-3590-2. Box indicates area used for EBSD and NGBC aperture measurements.

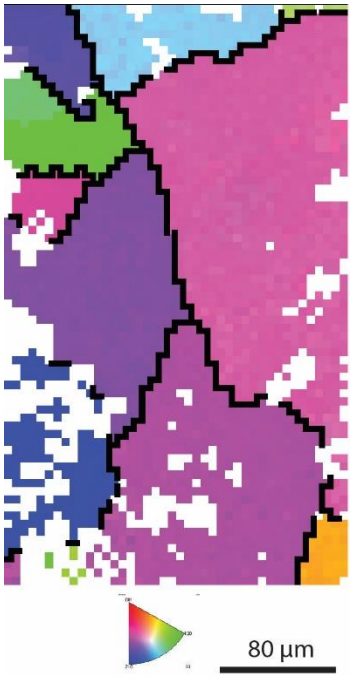

Figure A.127: EBSD inverse pole figure from sample NAC-3590-2.

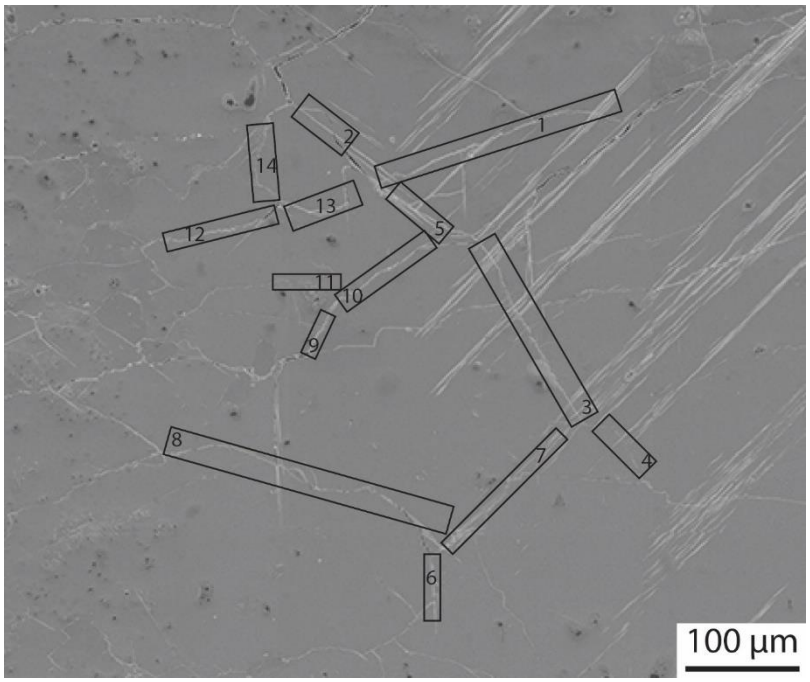

Figure A.128: Inlens SE mosaic of sample NAC-3590-2. Boxes indicate locations of grain boundaries used for NGBC aperture measurements.

Grain Boundary	Length (nm)
1	257.10
2	242.48
3	23.29
4	157.29
5	187.20
6	190.11
7	48.99
8	234.85
9	436.47
10	428.20
11	22.68
12	301.70
13	224.24
14	286.40
Sample Mean	217.22

Table A1: NGBC mean apertures and sample mean from sample NAC-3590-2.

Grain Boundary 1

Image	Measurement Number	Length (nm)
A	1	238.80
A	2	220.16
A	3	241.77
A	4	288.79
A	5	231.83
A	6	296.58
A	7	281.79
	Mean Aperture	257.10

Table A.76: NGBC measurements and mean aperture from grain boundary 1 in sample NAC-3590-2.

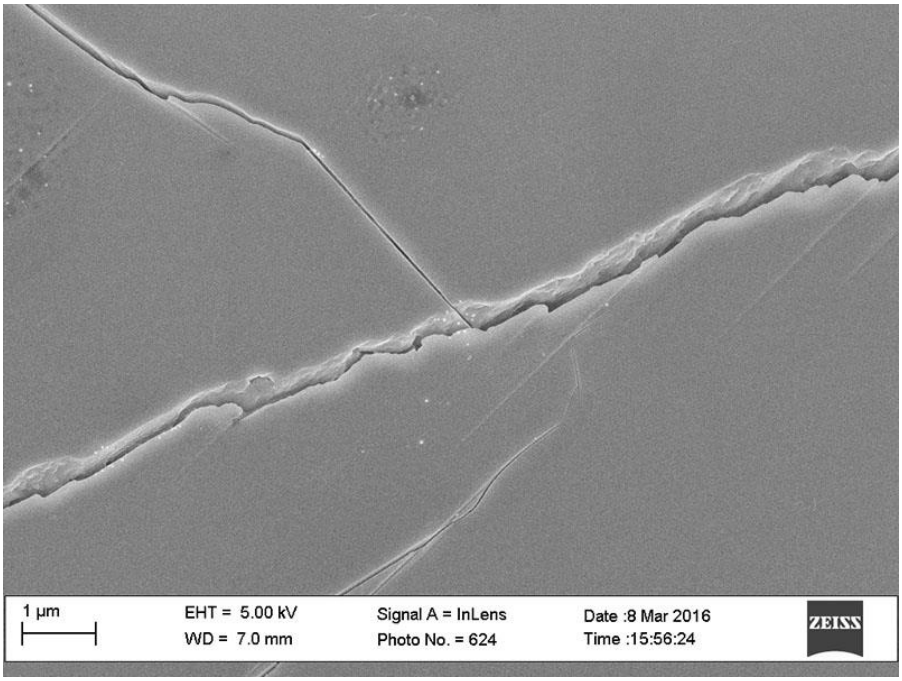

Figure A.129: Inlens SE micrograph from sample NAC-3590-2. Grain boundary 1, image A.

Grain Boundary 2

Image	Measurement Number	Length (nm)
A	1	145.58
A	2	143.14
A	3	124.52
B	1	327.52
B	2	364.24
B	3	349.88
	Mean Aperture	242.48

Table A.77: NGBC measurements and mean aperture from grain boundary 2 in sample NAC-3590-2.

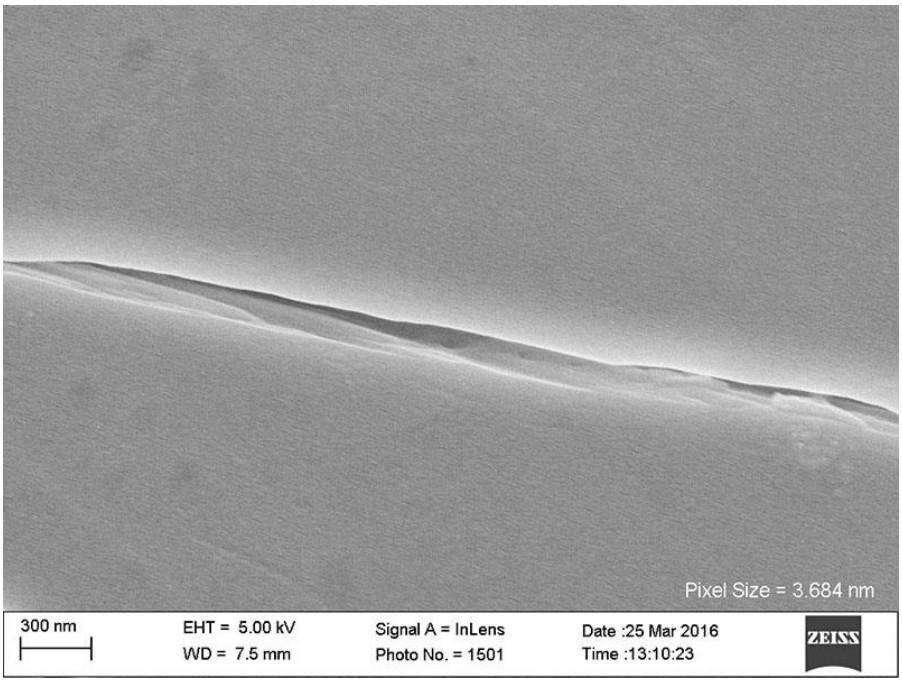

Figure A.130: Inlens SE micrograph from sample NAC-3590-2. Grain boundary 2, image A.

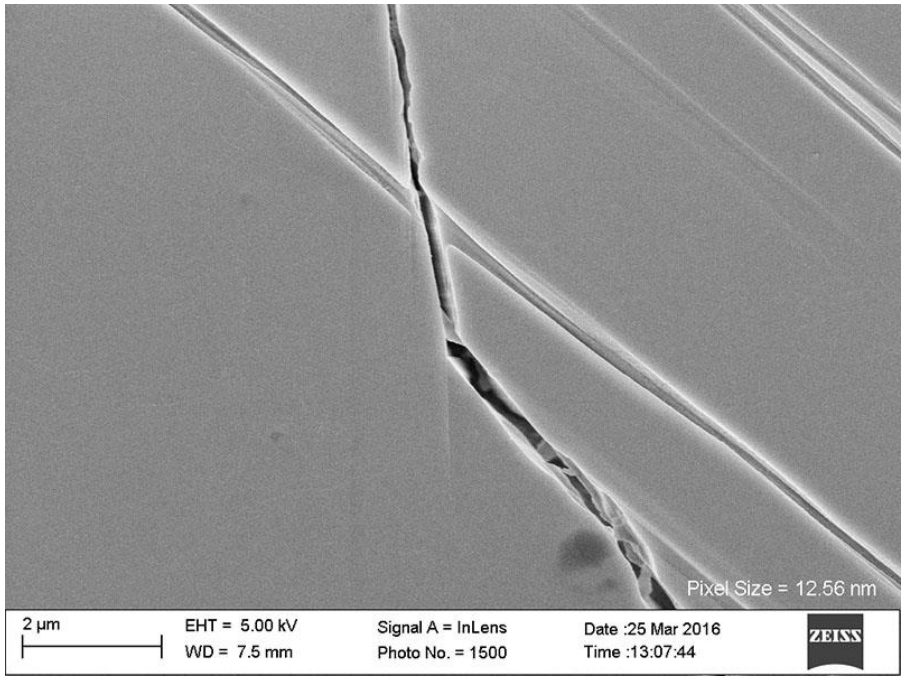

Figure A.131: Inlens SE micrograph from sample NAC-3590-2. Grain boundary 2, image B.

Grain Boundary 3

Image	Measurement Number	Length (nm)
A	1	155.76
A	2	164.19
A	3	116.10
B	1	209.16
B	2	157.84
B	3	174.30
B	4	122.01
C	1	158.95
C	2	158.95
C	3	159.61
C	4	174.00
C	5	173.40
C	6	158.95
C	7	158.95
C	8	130.05
C	9	144.50
	Mean Aperture	157.29

Table A.78: NGBC measurements and mean aperture from grain boundary 3 in sample NAC-3590-2.

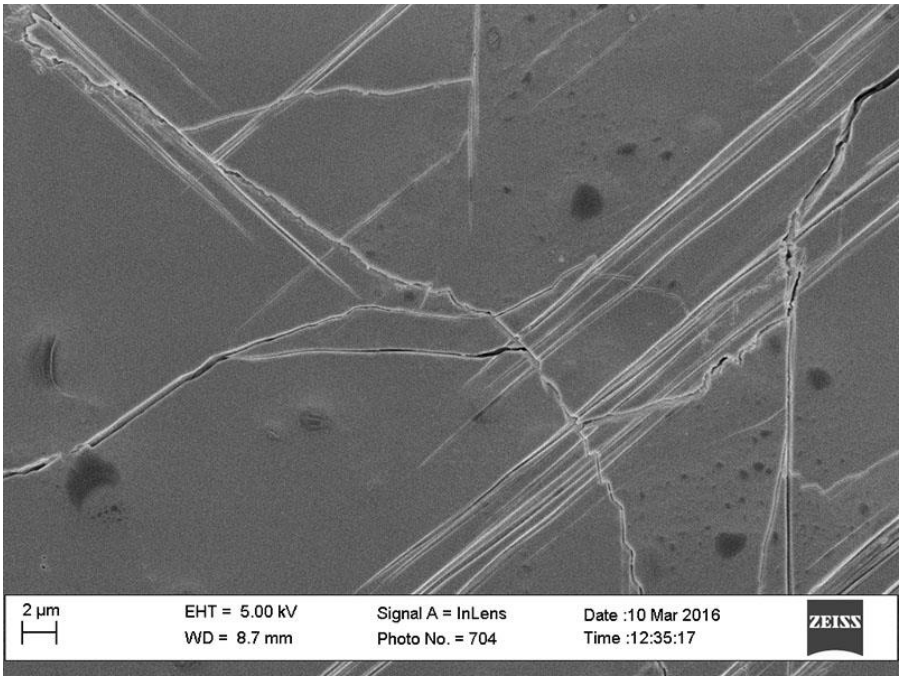

Figure A.132: Inlens SE micrograph from sample NAC-3590-2. Grain boundary 3, image A.

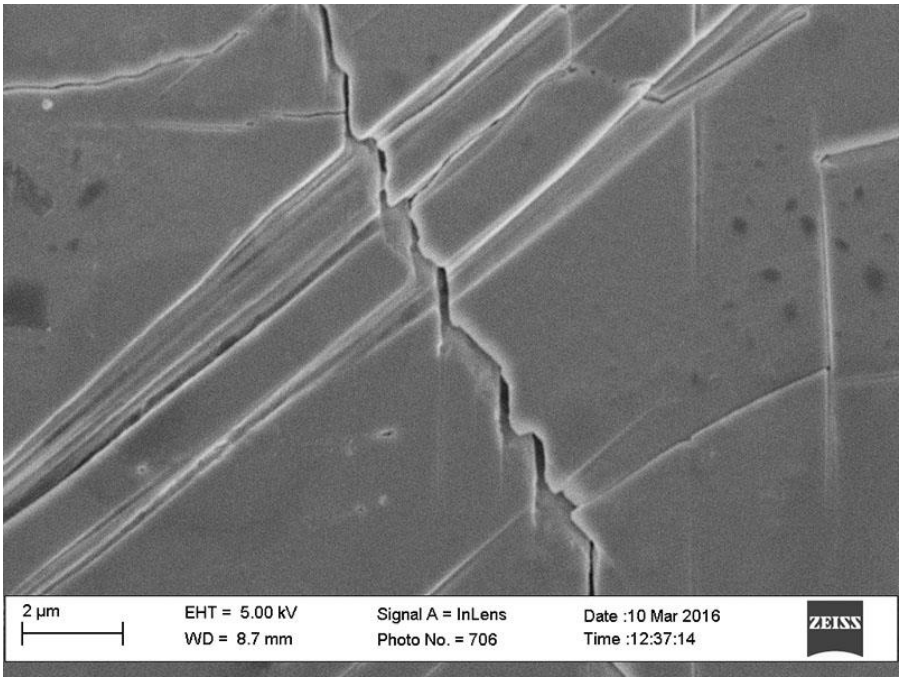

Figure A.133: Inlens SE micrograph from sample NAC-3590-2. Grain boundary 3, image B.

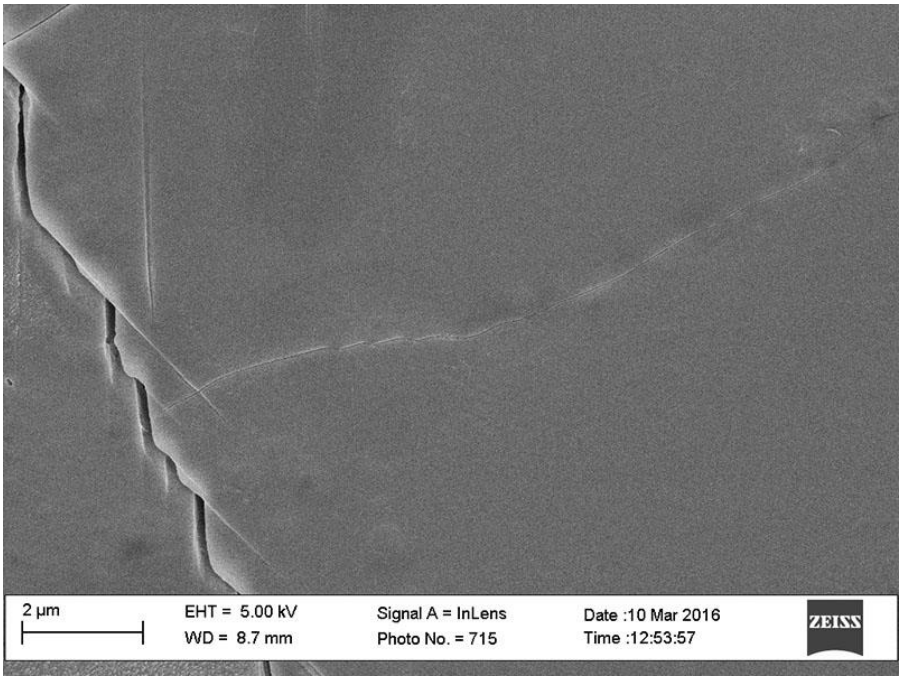

Figure A.134: Inlens SE micrograph from sample NAC-3590-2. Grain boundary 3, image C.

Grain Boundary 4

Image	Measurement Number	Length (nm)
A	1	25.01
A	2	24.01
A	3	21.46
A	4	29.12
A	5	26.78
A	6	22.03
A	7	18.10
A	8	16.58
A	9	20.84
B	1	20.08
B	2	18.93
B	3	20.84
B	4	15.72
B	5	17.31
B	6	22.41
B	7	31.45
B	8	21.99
B	9	33.77
C	1	21.46
C	2	22.92
C	3	20.23
C	4	26.57
C	5	23.22
C	6	24.13
C	7	37.31
	Mean Aperture	23.29

Table A.79: NGBC measurements and mean aperture from grain boundary 4 in sample NAC-3590-2.

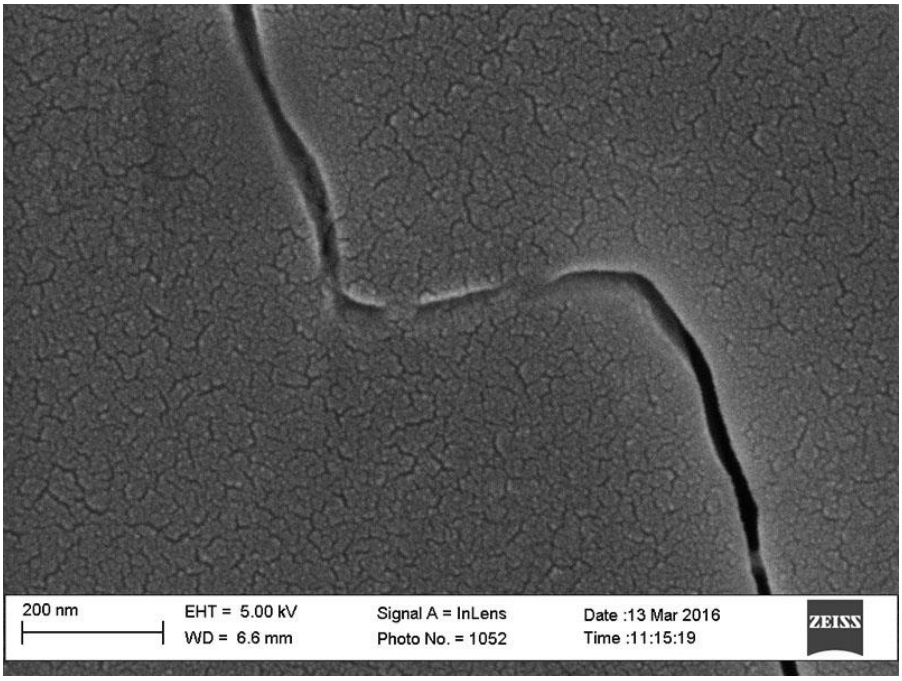

Figure A.135: Inlens SE micrograph from sample NAC-3590-2. Grain boundary 4, image A.

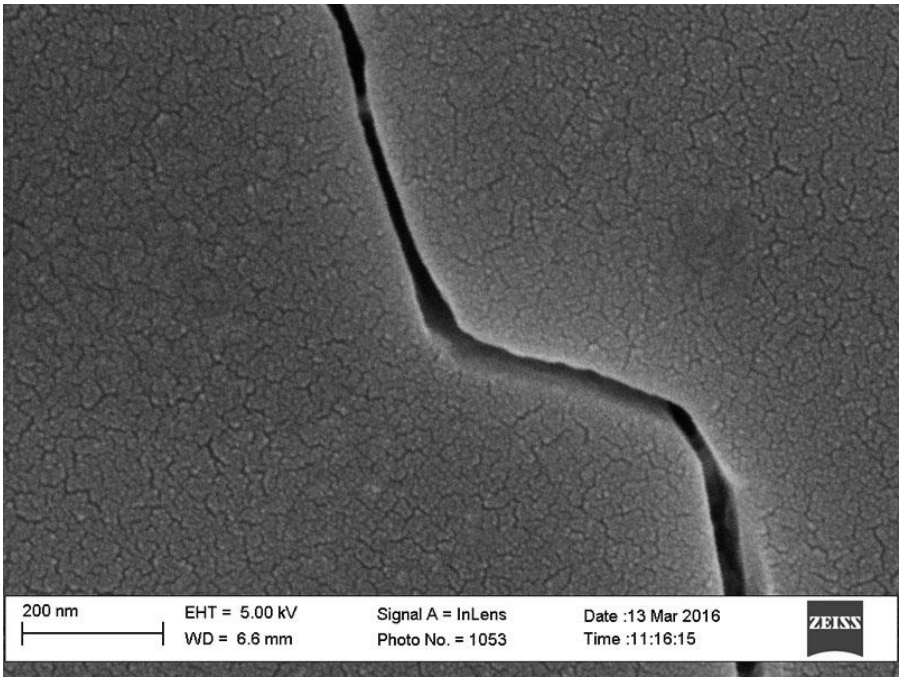

Figure A.136: Inlens SE micrograph from sample NAC-3590-2. Grain boundary 4, image B.

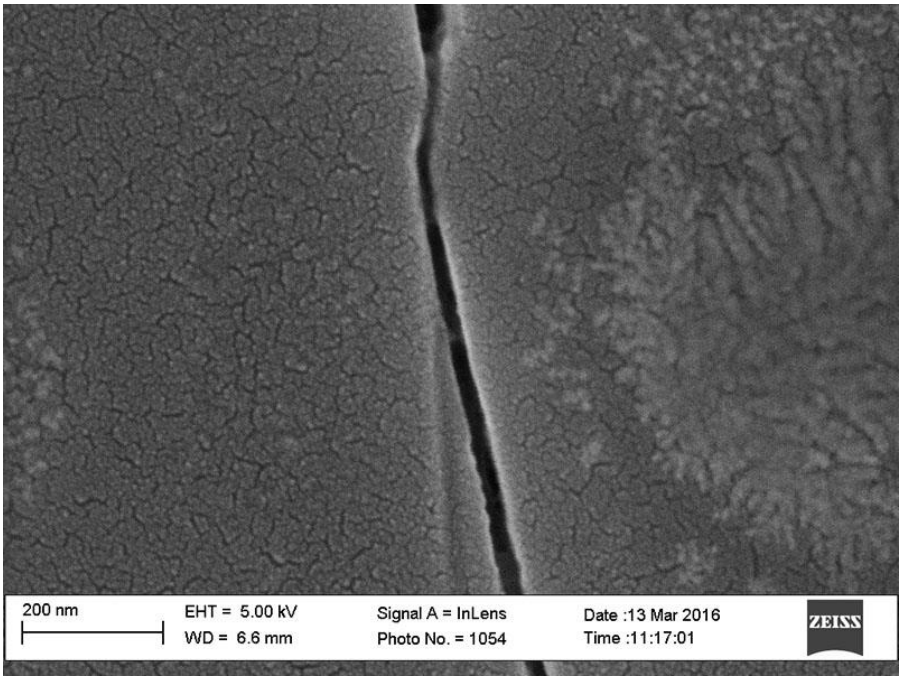

Figure A.137: Inlens SE micrograph from sample NAC-3590-2. Grain boundary 4, image C.

Grain Boundary 5

Image	Measurement Number	Length (nm)
A	1	187.20
	Mean Aperture	187.20

Table A.80: NGBC measurements and mean aperture from grain boundary 5 in sample NAC-3590-2.

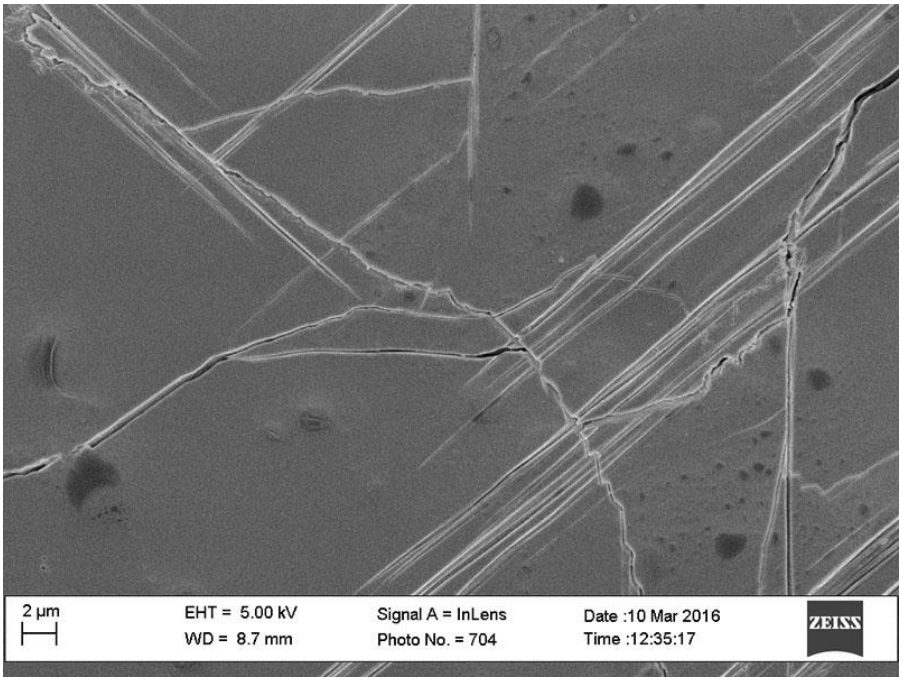

Figure A.138: Inlens SE micrograph from sample NAC-3590-2. Grain boundary 5, image A.

Grain Boundary 6

Image	Measurement Number	Length (nm)
A	1	198.54
A	2	193.42
A	3	178.37
	4	190.11

Table A.81: NGBC measurements and mean aperture from grain boundary 6 in sample NAC-3590-2.

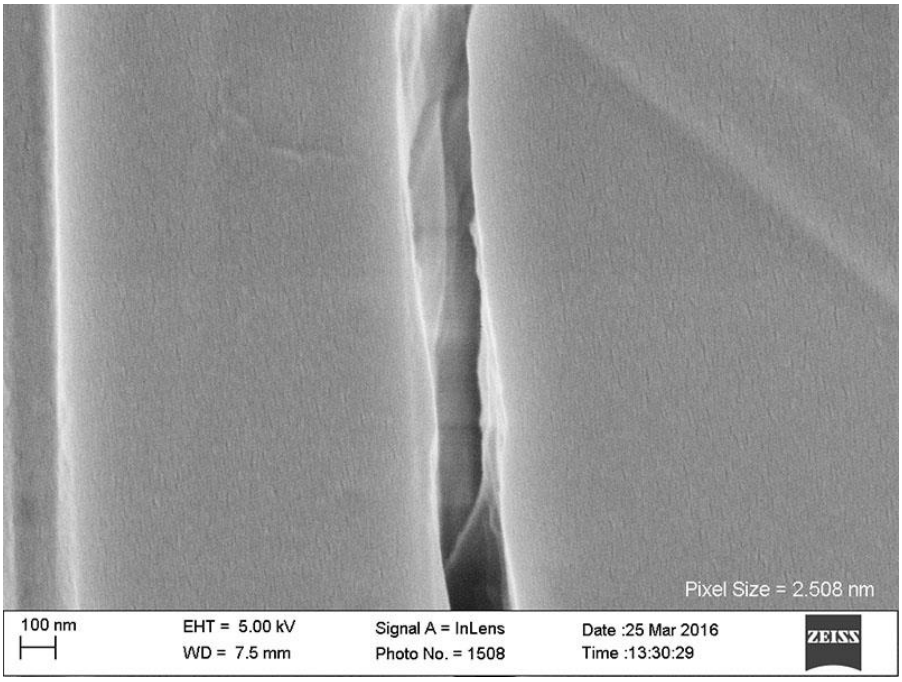

Figure A.139: Inlens SE micrograph from sample NAC-3590-2. Grain boundary 6, image A.

Grain Boundary 7

Image	Measurement Number	Length (nm)
A	1	36.12
A	2	31.20
A	3	61.56
A	4	62.34
A	5	53.72
	Mean Aperture	48.99

Table A.82: NGBC measurements and mean aperture from grain boundary 7 in sample NAC-3590-2.

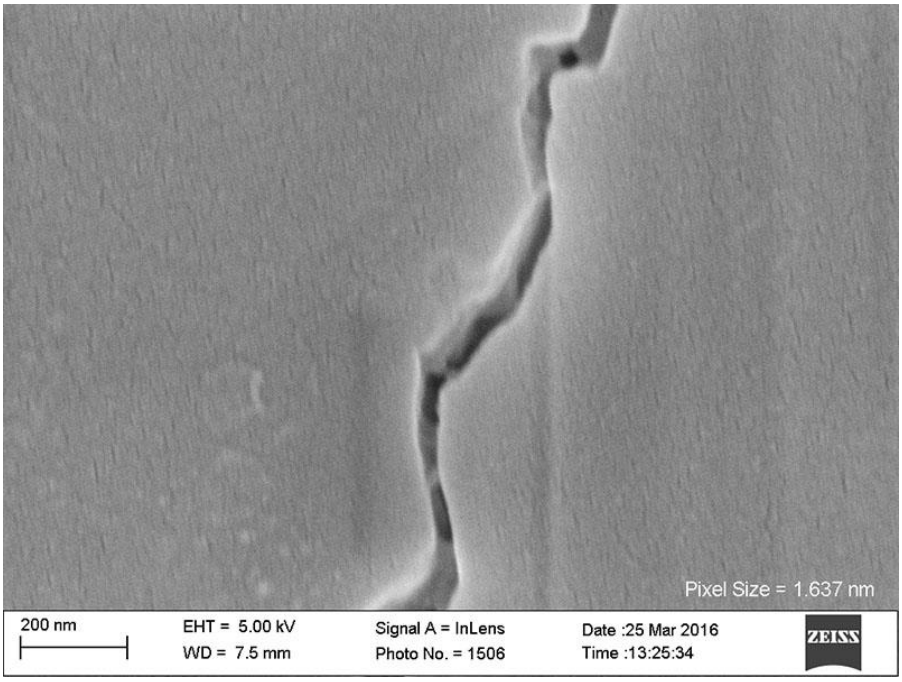

Figure A.140: Inlens SE micrograph from sample NAC-3590-2. Grain boundary 7, image A.

Grain Boundary 8

Image	Measurement Number	Length (nm)
A	1	271.27
A	2	238.21
A	3	230.43
A	4	234.55
A	5	298.97
A	6	146.28
A	7	150.78
B	1	152.25
B	2	157.61
B	3	176.40
B	4	160.64
B	5	167.63
B	6	155.32
C	1	284.10
C	2	260.10
C	3	281.63
C	4	260.10
C	5	273.22
C	6	300.85
C	7	321.11
C	8	314.50
C	9	273.22
C	10	217.08
D	1	250.15
D	2	268.77
D	3	279.67
D	4	265.32
D	5	218.75
D	6	286.18
D	7	218.75
D	8	197.76
D	9	171.60
D	10	278.85
D	11	214.50
D	12	259.18
D	13	218.75
	Mean Aperture	234.85

Table A.83: NGBC measurements and mean aperture from grain boundary 8 in sample NAC-3590-2.

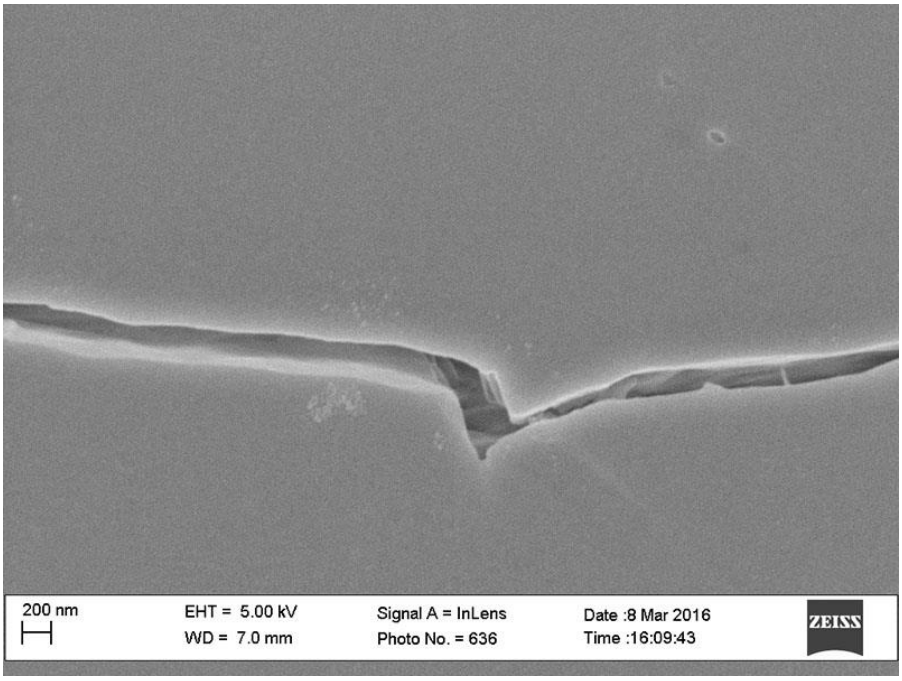

Figure A.141: Inlens SE micrograph from sample NAC-3590-2. Grain boundary 8, image A.

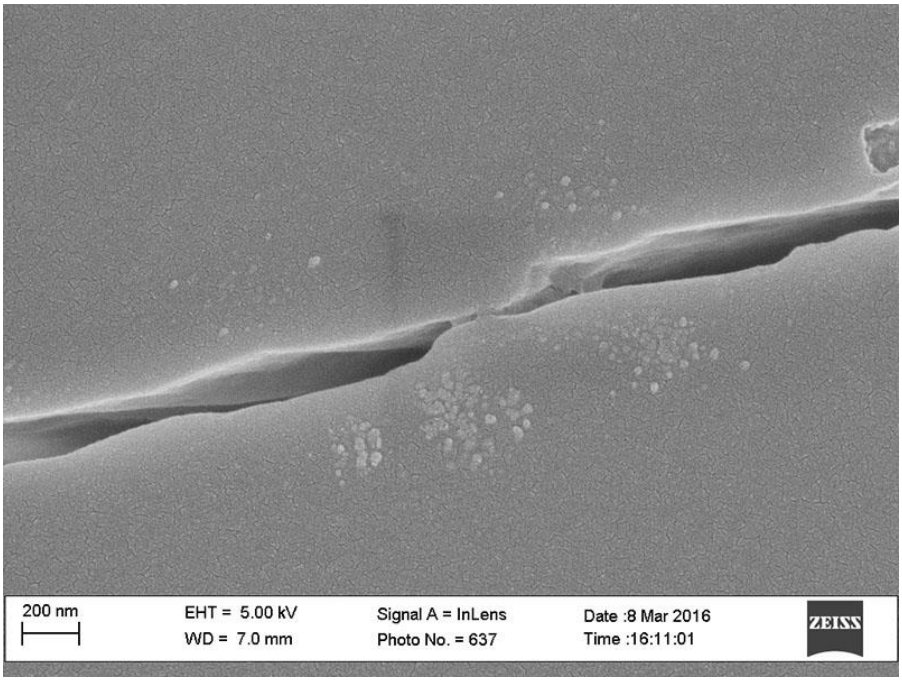

Figure A.142: Inlens SE micrograph from sample NAC-3590-2. Grain boundary 8, image B.

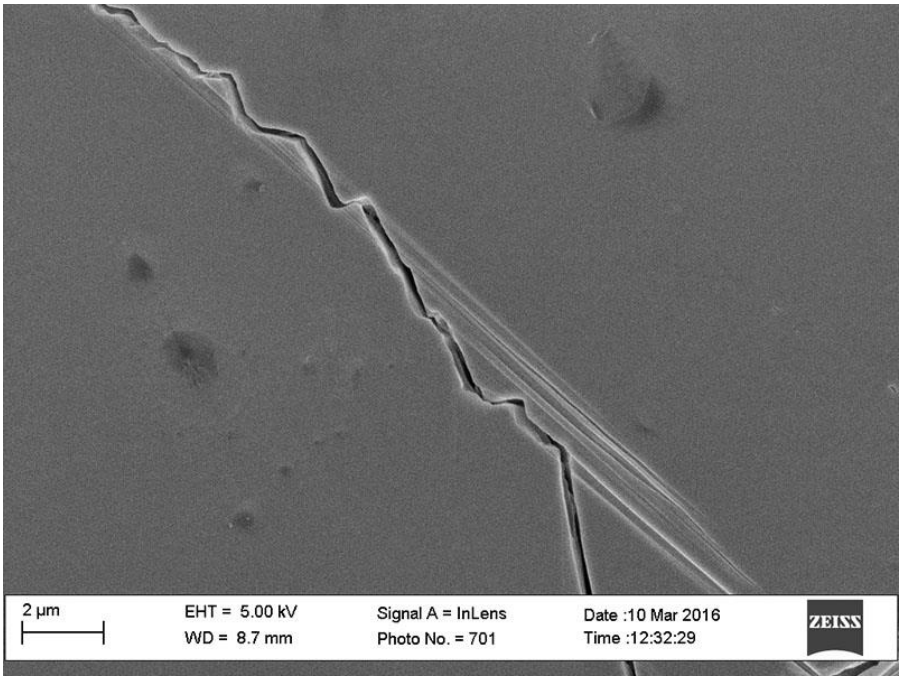

Figure A.143: Inlens SE micrograph from sample NAC-3590-2. Grain boundary 8, image C.

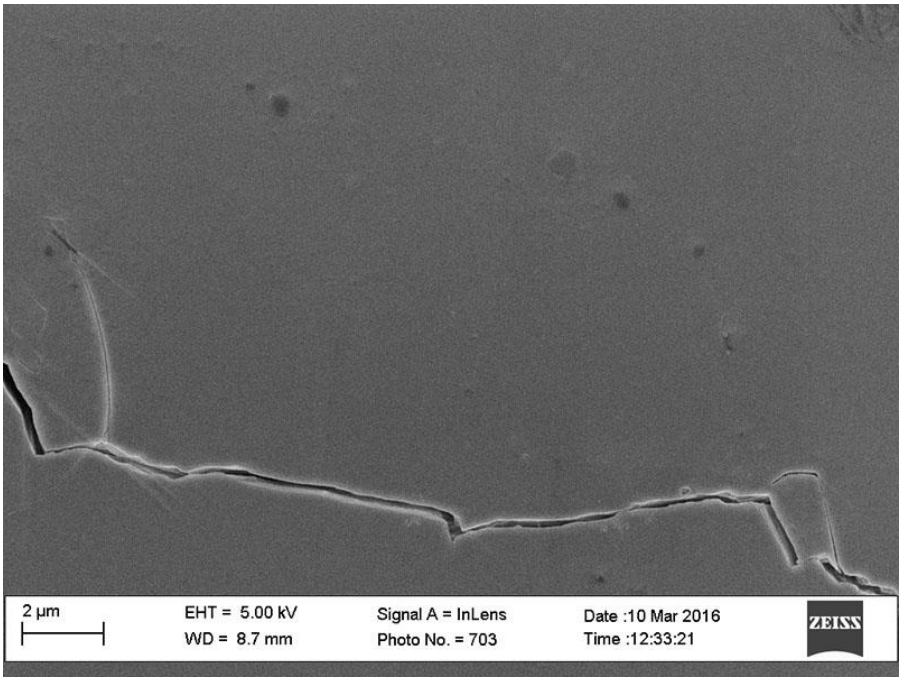

Figure A.144: Inlens SE micrograph from sample NAC-3590-2. Grain boundary 8, image D.

Grain Boundary 9

Image	Measurement Number	Length (nm)
A	1	408.41
A	2	385.55
A	3	408.41
A	4	476.41
A	5	503.57
	Mean Aperture	436.47

Table A.84: NGBC measurements and mean aperture from grain boundary 9 in sample NAC-3590-2.

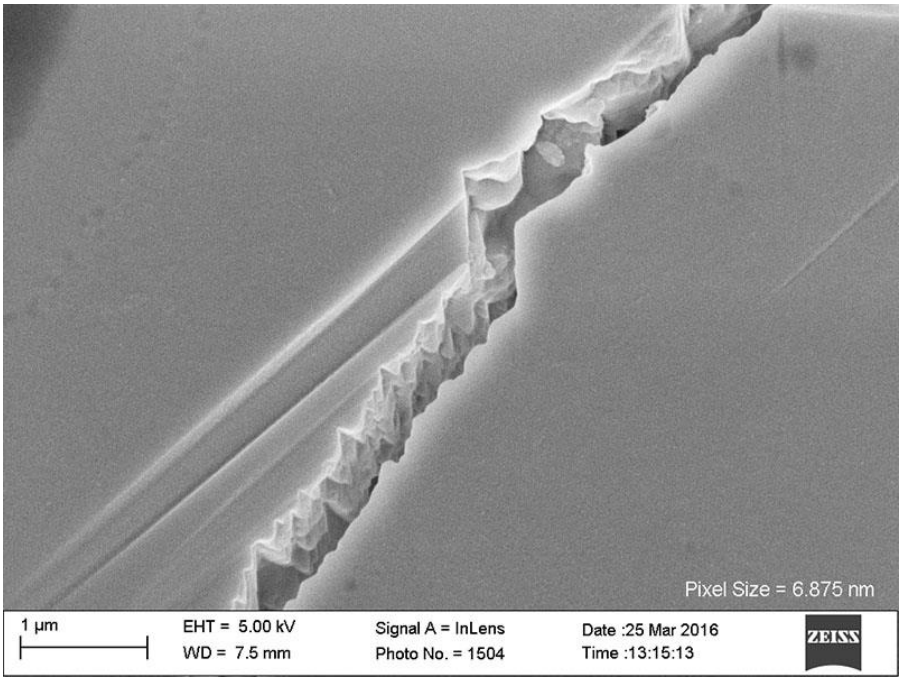

Figure A.145: Inlens SE micrograph from sample NAC-3590-2. Grain boundary 9, image A.

Grain Boundary 10

Image	Measurement Number	Length (nm)
A	1	444.38
A	2	415.70
A	3	428.79
A	4	395.24
B	1	402.82
B	2	430.94
B	3	438.49
B	4	469.22
	Mean Aperture	428.20

Table A.85: NGBC measurements and mean aperture from grain boundary 10 in sample NAC-3590-2.

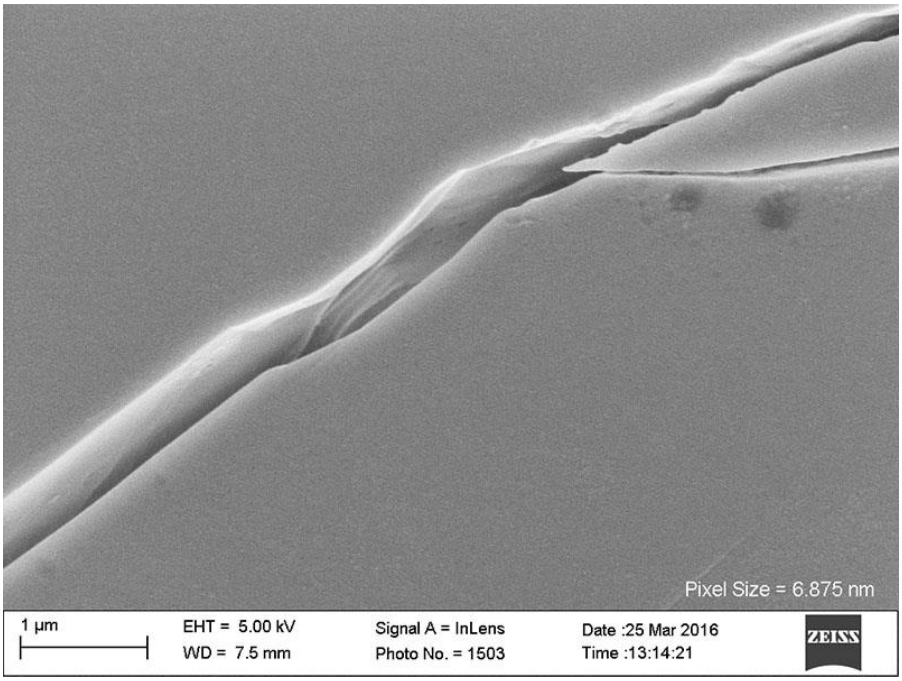

Figure A.146: Inlens SE micrograph from sample NAC-3590-2. Grain boundary 10, image A.

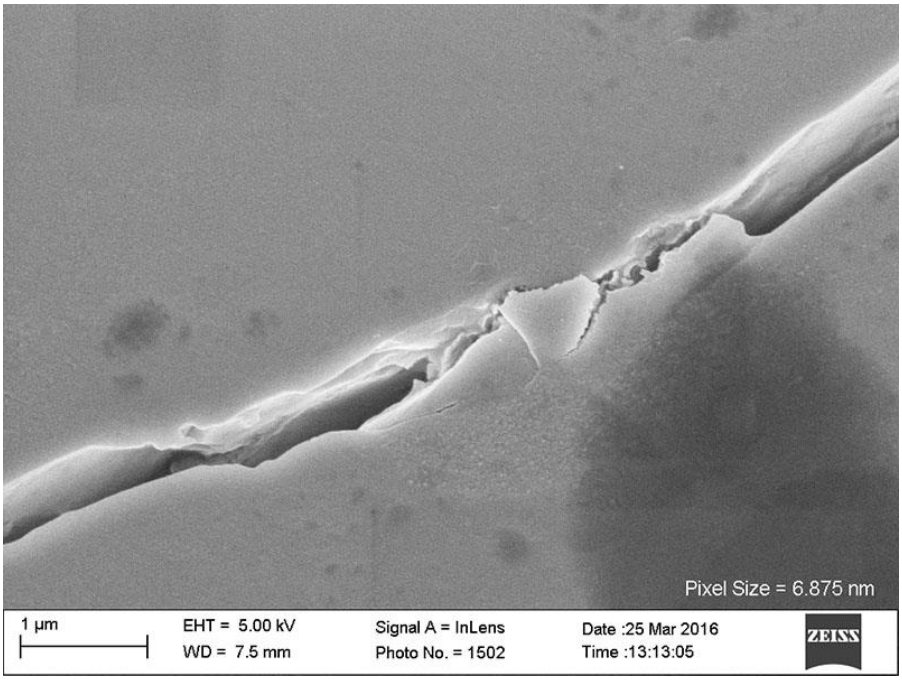

Figure A.147: Inlens SE micrograph from sample NAC-3590-2. Grain boundary 10, image B.

Grain Boundary 11

Image	Measurement Number	Length (nm)
A	1	17.56
A	2	15.83
A	3	13.17
A	4	11.45
A	5	13.17
B	1	22.38
B	2	24.28
B	3	22.38
B	4	26.70
B	5	32.91
B	6	30.47
B	7	31.04
B	8	33.54
	Mean Aperture	22.68

Table A.86: NGBC measurements and mean aperture from grain boundary 11 in sample NAC-3590-2.

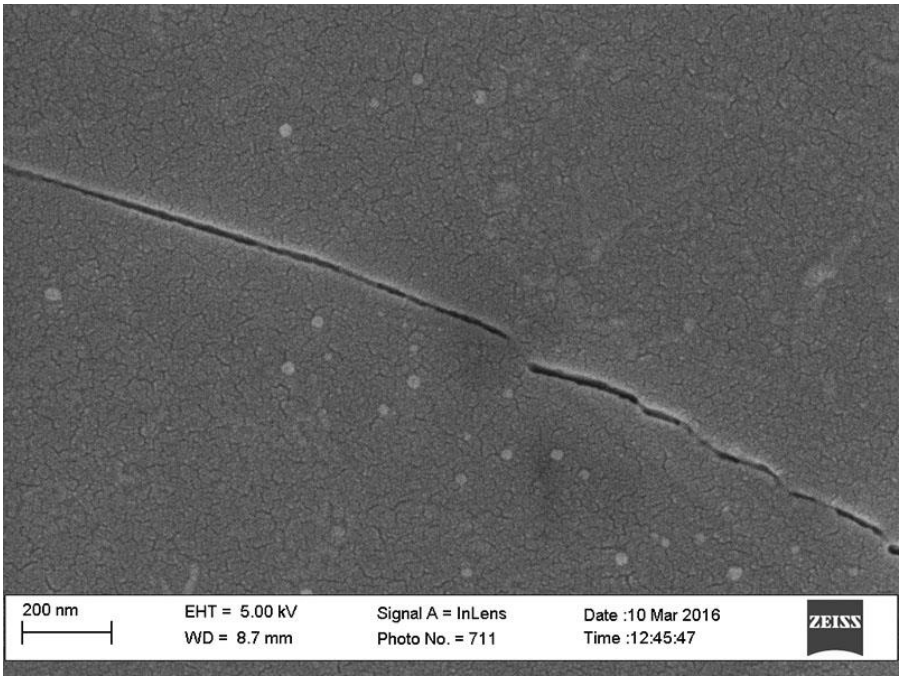

Figure A.148: Inlens SE micrograph from sample NAC-3590-2. Grain boundary 11, image A.

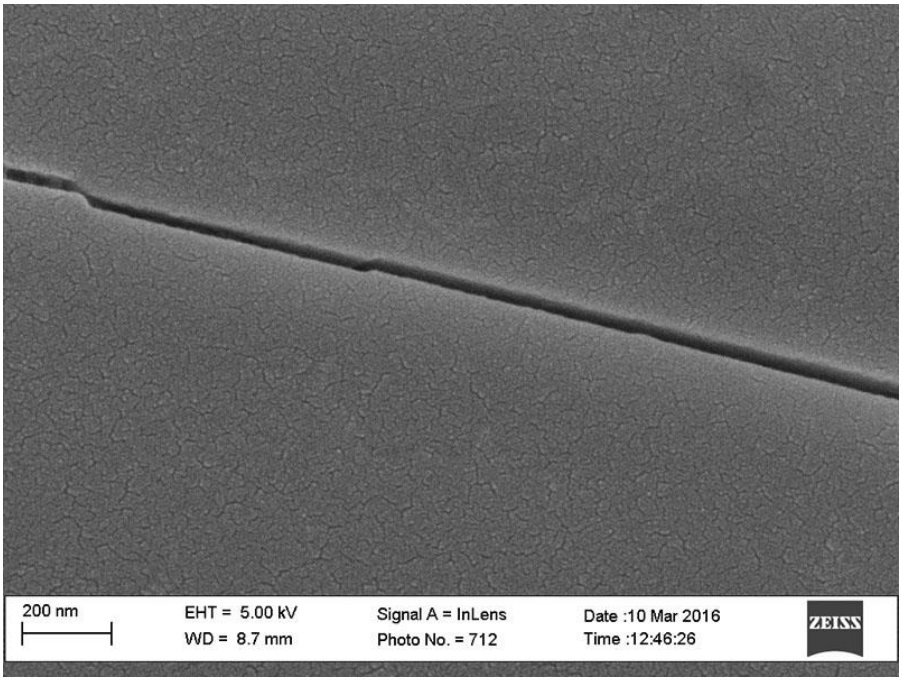

Figure A.149: Inlens SE micrograph from sample NAC-3590-2. Grain boundary 11, image A.

Grain Boundary 12

Image	Measurement Number	Length (nm)
A	1	225.12
A	2	193.02
A	3	244.76
A	4	151.54
A	5	163.09
A	6	171.45
B	1	270.46
B	2	382.73
B	3	350.28
B	4	360.30
B	5	372.51
C	1	381.27
C	2	372.42
C	2	383.66
C	2	388.48
C	2	383.96
C	2	333.93
	Mean Aperture	301.70

Table A.87: NGBC measurements and mean aperture from grain boundary 12 in sample NAC-3590-2.

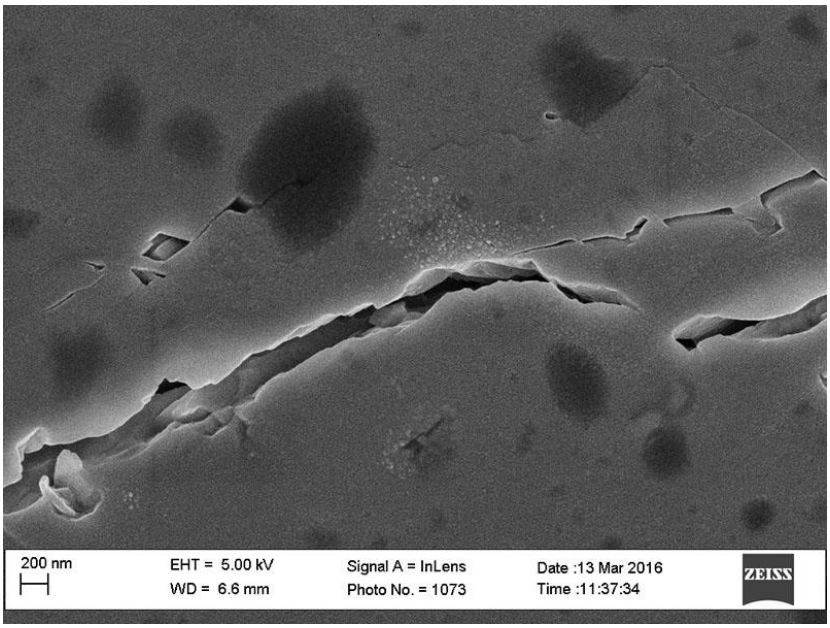

Figure A.150: Inlens SE micrograph from sample NAC-3590-2. Grain boundary 12, image A.

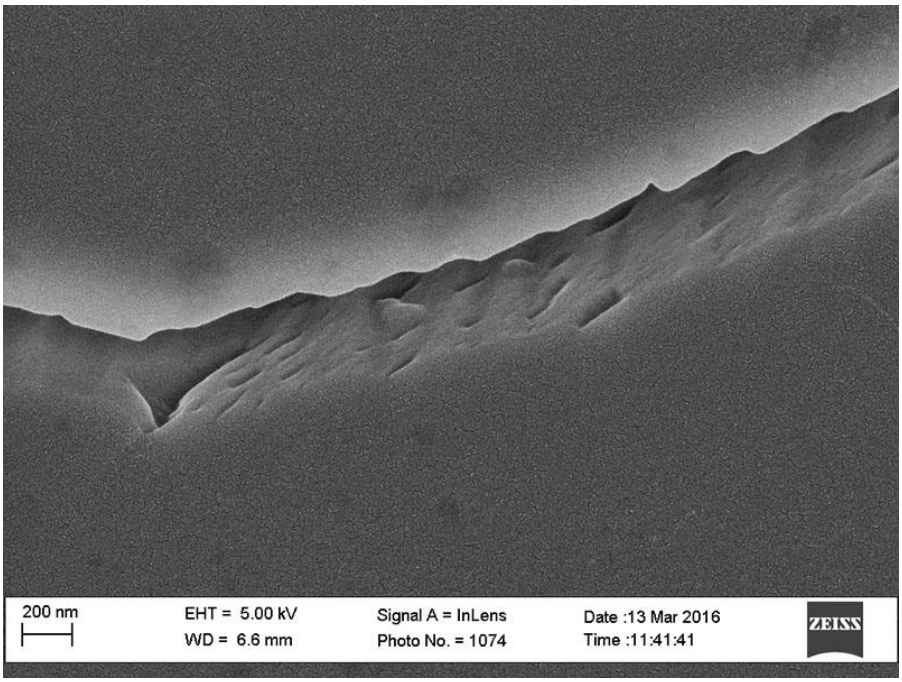

Figure A.151: Inlens SE micrograph from sample NAC-3590-2. Grain boundary 12, image B.

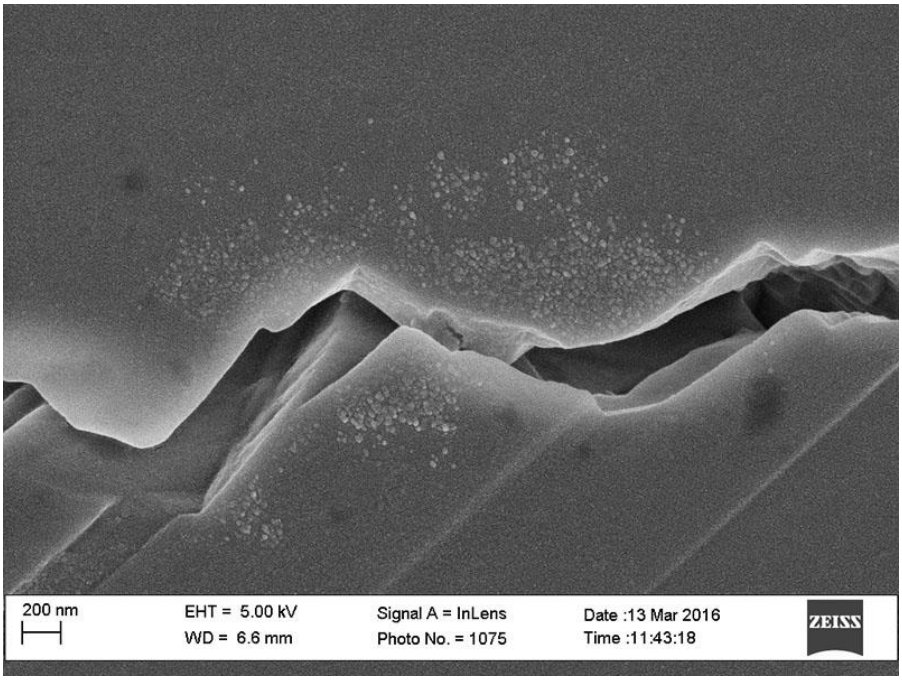

Figure A.152: Inlens SE micrograph from sample NAC-3590-2. Grain boundary 12, image A.

Grain Boundary 13

Image	Measurement Number	Length (nm)
A	1	253.66
A	2	207.59
A	3	215.26
A	4	215.26
A	5	215.26
A	6	223.34
A	7	239.29
	Mean Aperture	224.24

Table A.88: NGBC measurements and mean aperture from grain boundary 13 in sample NAC-3590-2.

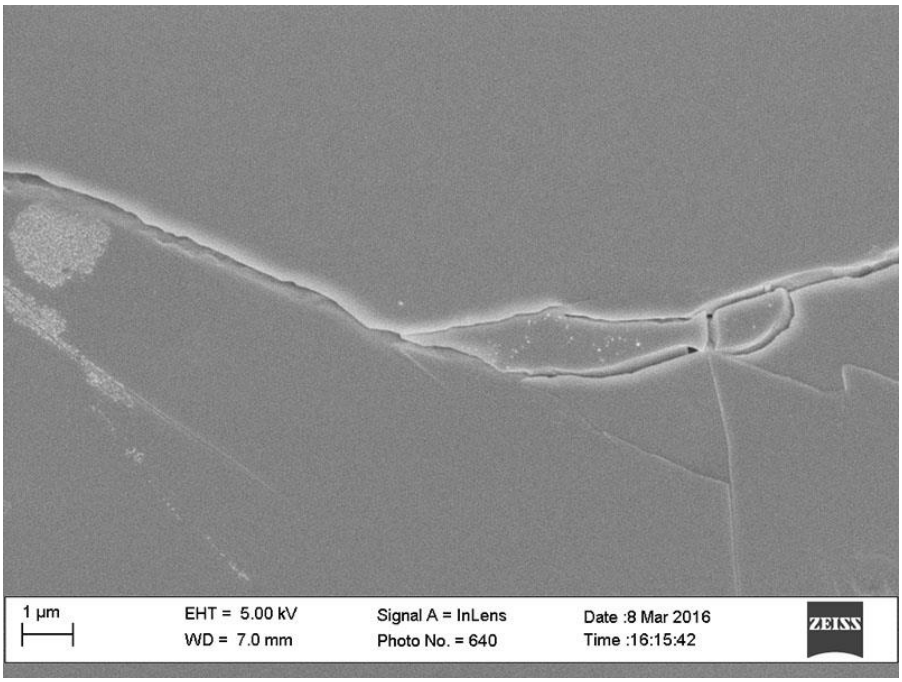

Figure A.153: Inlens SE micrograph from sample NAC-3590-2. Grain boundary 13, image A.

Grain Boundary 14

Image	Measurement Number	Length (nm)
A	1	412.68
A	2	315.85
A	3	275.42
A	4	141.67
	Mean Aperture	286.40

Table A.89: NGBC measurements and mean aperture from grain boundary 14 in sample NAC-3590-2.

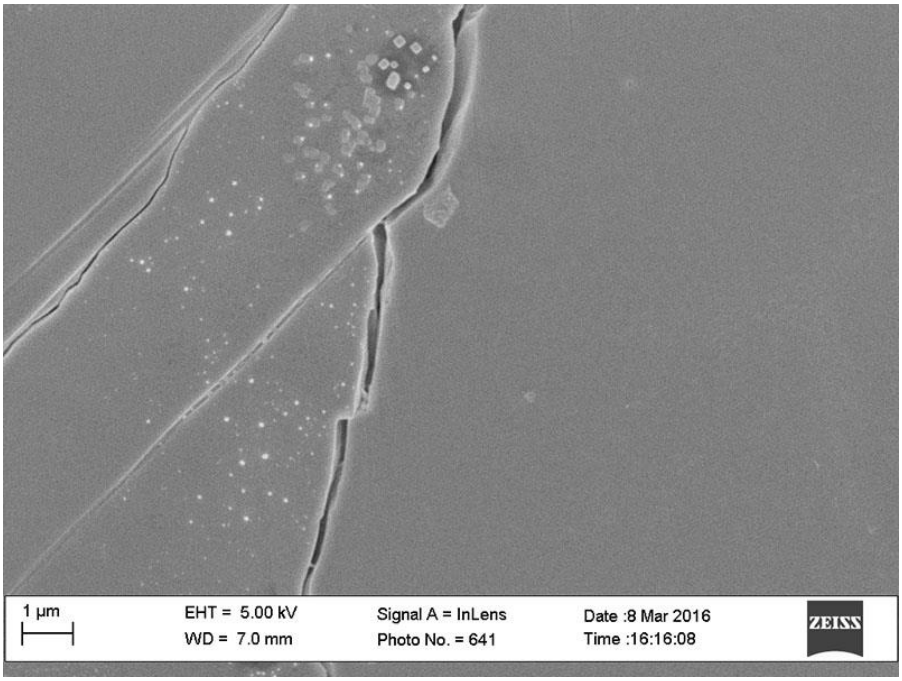

Figure A.154: Inlens SE micrograph from sample NAC-3590-2. Grain boundary 14, image A.

SAMPLE M-3658.5B, MARCELLUS FORMATION

Mineral Cement	Rock Type	Sampled Depth (ft)	Sampled Depth (m)	Max burial depth (m)	Exhumed (m)	Max T (°C)	Range (nm)	Sample Mean (nm)
Calcite	Shale	6358.5	1938.1	4938	3000	150-160	108-318	164.69
Calcite-Quartz	Shale	6358.5	1938.1	4938	3000	150-160	40-540	269.51
Quartz	Shale	6358.5	1938.1	4938	3000	150-160	65	64.27

Table A.90: Summary of sample M-3658.5B

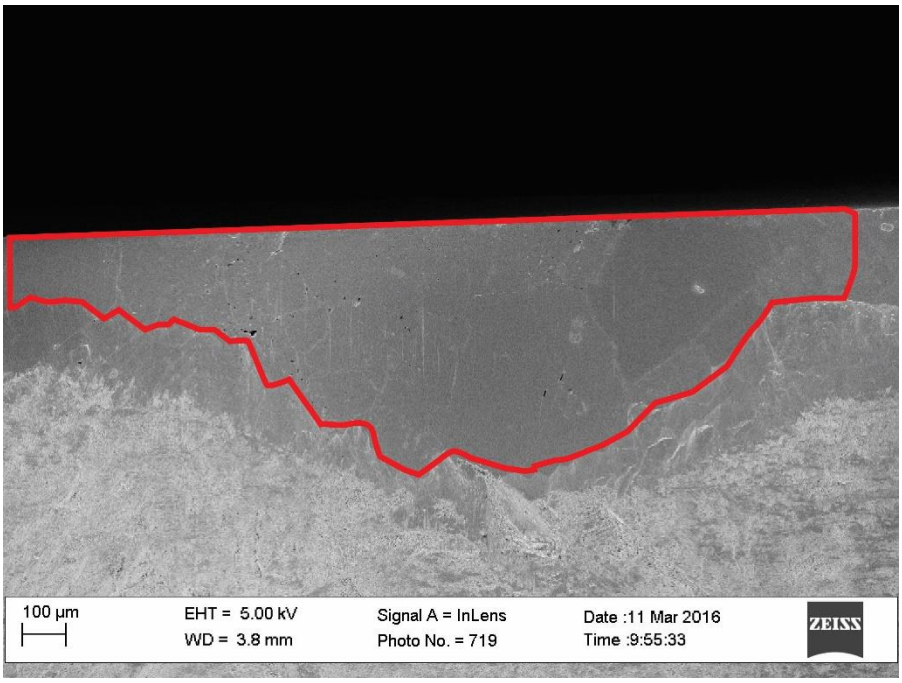

Figure A.155: Inlens SE micrograph of sample M3658.5B. Red outline indicates area used for EBSD analysis and NGBC aperture measurements.

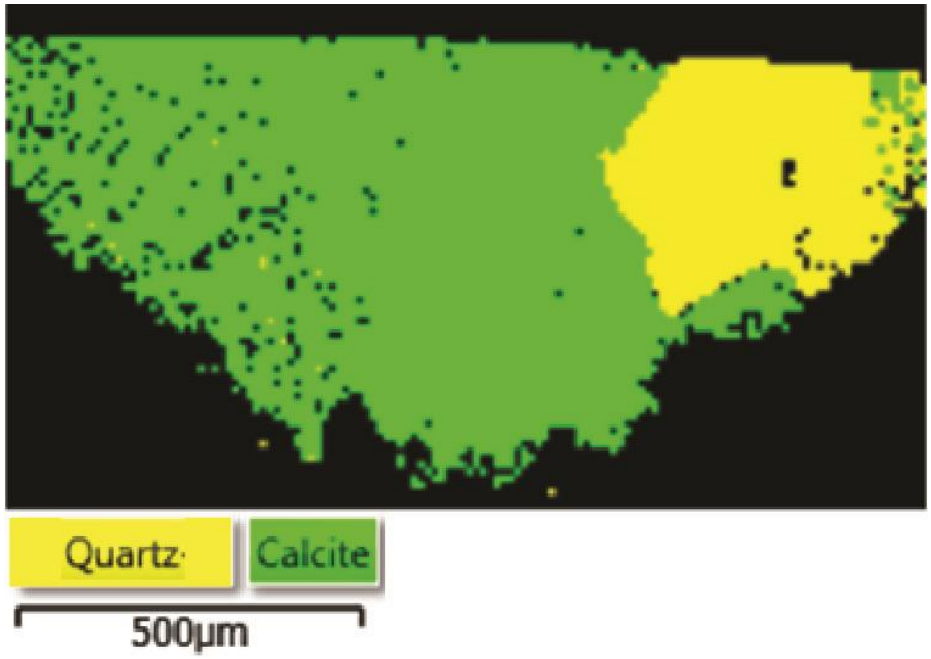

Figure A.156: EBSD phase map from sample M-3658.5B.

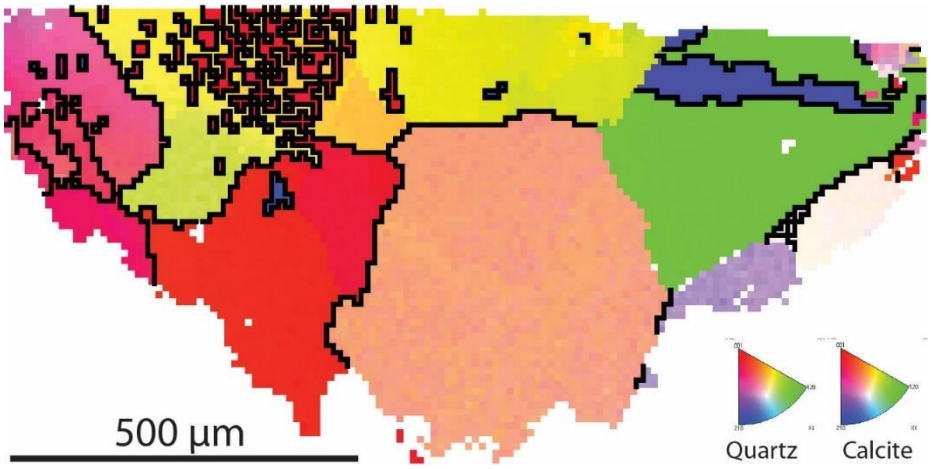

Figure A.157: EBSD inverse pole figure from sample M-3658.5B.

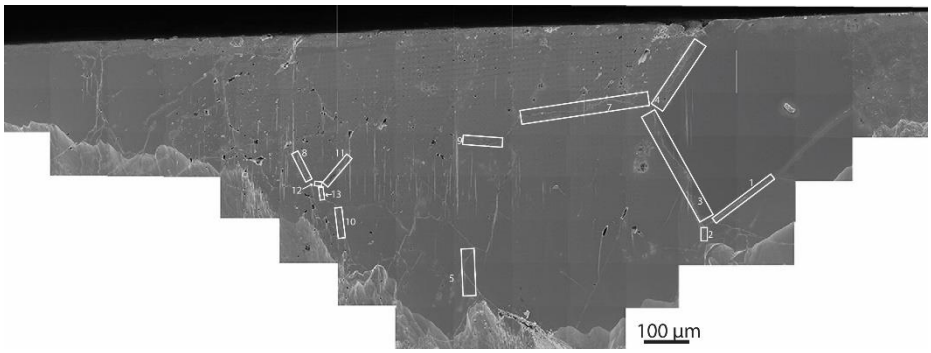

Figure A.158: Inlens SE mosaic of sample M-3658.5B. Boxes indicate location of grain boundaries used for NGBC aperture measurements.

Grain Boundary	Mean Aperture (nm)
1	64.27
Sample Mean	64.27

Table A.91: NGBC mean apertures and sample mean within quartz grain boundaries from sample M-3658.5B.

Grain Boundary	Mean Aperture (nm)
2	228.28
3	40.87
4	539.38
Sample Mean	269.51

Table A.92: NGBC mean apertures and sample mean within calcite-quartz phase boundaries from sample M-3658.5B.

Grain Boundary	Mean Aperture (nm)
5	205.53
6	270.48
7	152.09
8	139.10
9	185.04
10	108.09
11	112.00
12	145.15
Sample Mean	164.04

Table A.93: NGBC mean apertures and sample mean within calcite grain boundaries from sample M-3658.5B.

Grain Boundary 1 (Quartz)

Image	Measurement Number	Length (nm)
A	1	58.43
A	2	58.63
A	3	64.45
A	4	75.58
	Mean Aperture	64.27

Table A.94: Quartz NGBC measurements and mean aperture from grain boundary 1 in sample M-3658.5B.

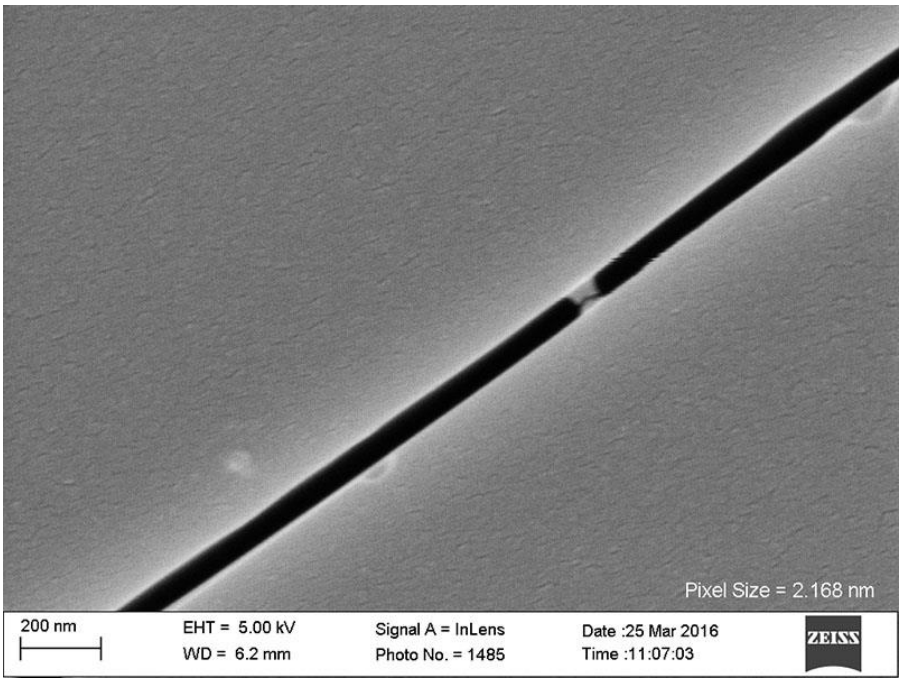

Figure A.159: Inlens SE micrograph from sample M-3658.5B. Grain boundary 1, image A.

Grain Boundary 2 (Quartz-Calcite)

Image	Measurement Number	Aperture (nm)
A	1	46.60
A	2	43.93
A	3	37.41
A	4	46.60
A	5	37.41
A	6	46.60
A	7	37.41
A	8	31.06
	Mean Aperture	40.87

Table A.95: NGBC measurements and mean aperture from grain boundary 2 in sample M-3658.5B.

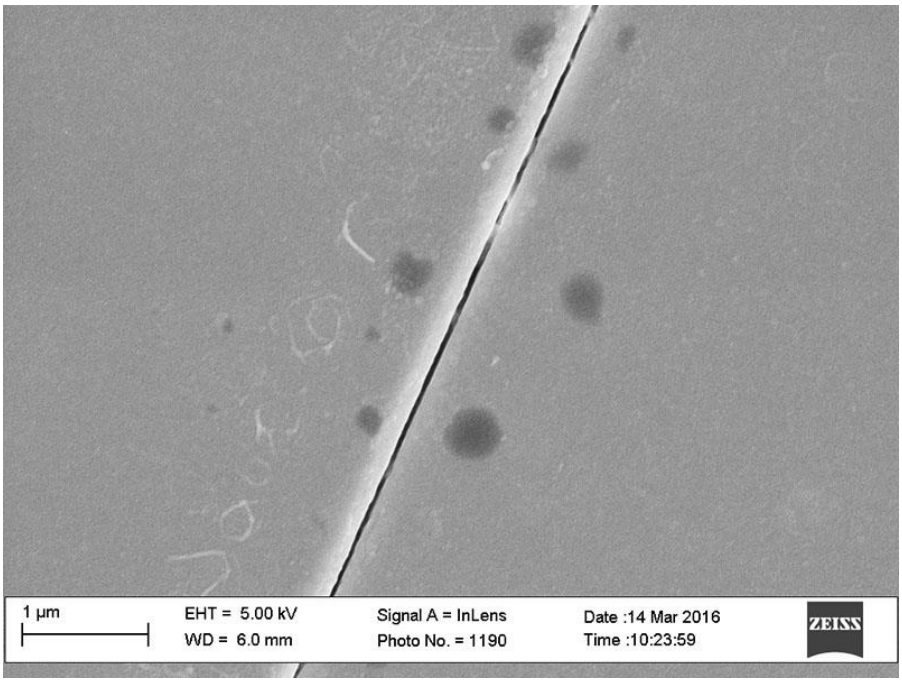

Figure A.160: Inlens SE micrograph from sample M-3658.5B. Grain boundary 2, image A.

Grain Boundary 3 (Quartz-Calcite)

Image	Measurement Number	Aperture (nm)
A	1	589.54
A	2	643.74
A	3	642.11
A	4	611.26
A	5	582.22
B	1	615.46
B	2	543.83
B	3	560.39
B	4	530.90
B	5	566.47
C	1	490.22
C	2	471.20
C	3	471.20
C	4	470.54
C	5	459.62
C	6	491.97
D	1	494.19
D	2	474.00
	Mean Aperture	539.38

Table A.96: NGBC measurements and mean aperture from grain boundary 3 in sample M-3658.5B.

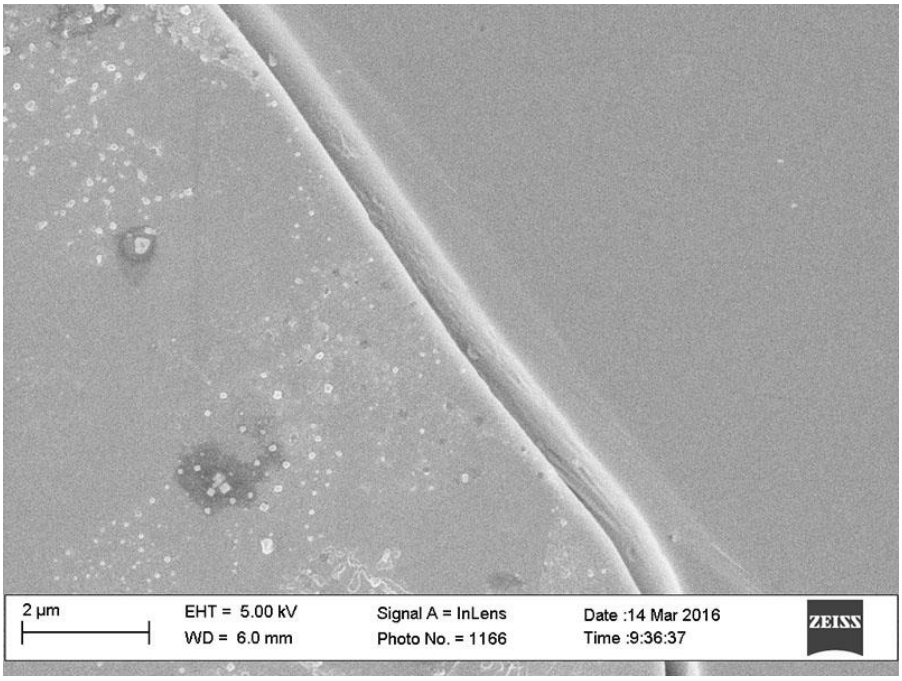

Figure A.161: Inlens SE micrograph from sample M-3658.5B. Grain boundary 3, image A.

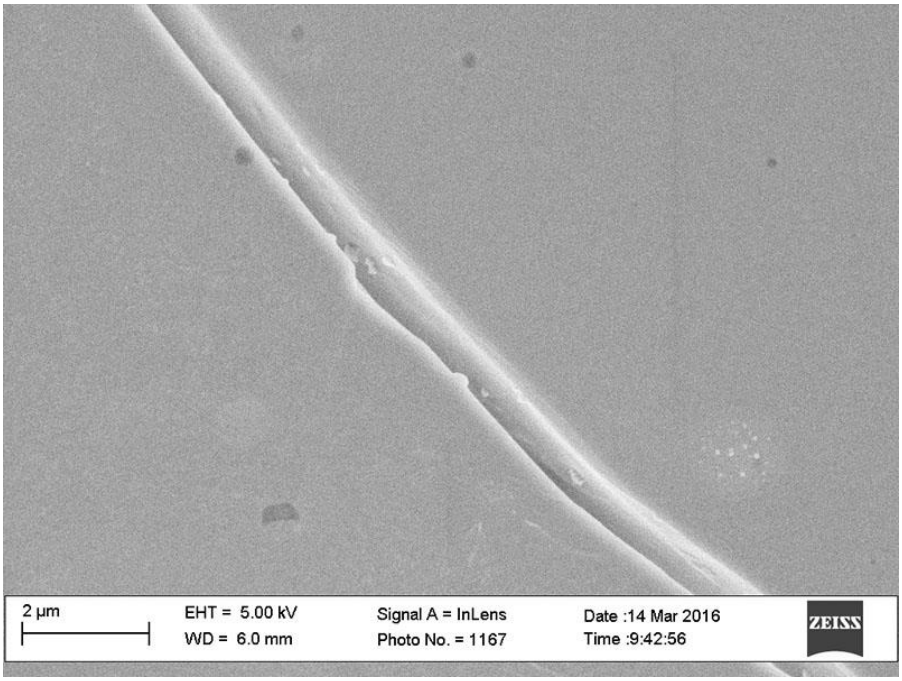

Figure A.162: Inlens SE micrograph from sample M-3658.5B. Grain boundary 3, image B.

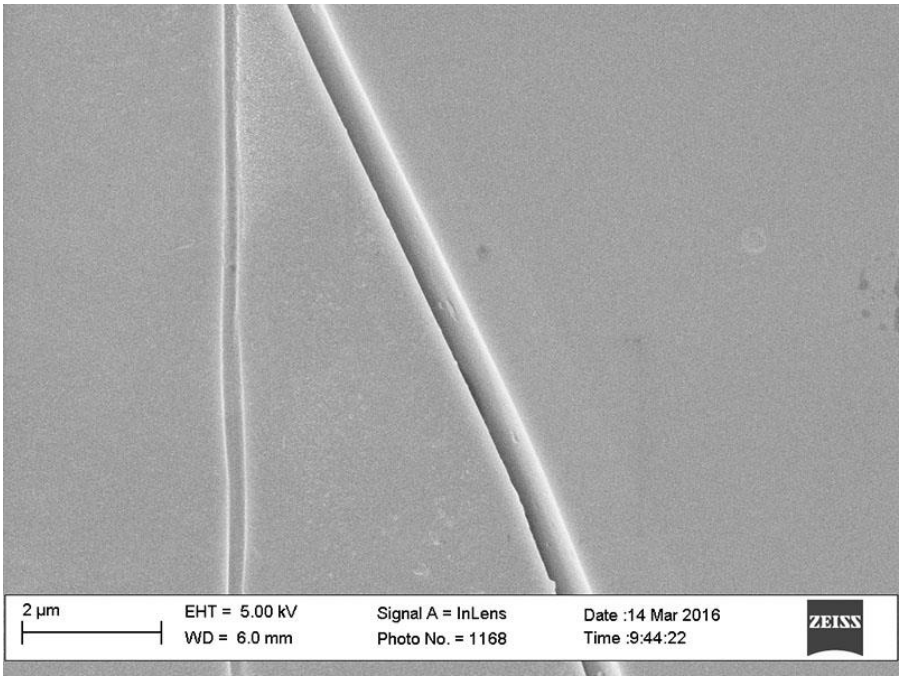

Figure A.163: Inlens SE micrograph from sample M-3658.5B. Grain boundary 3, image C.

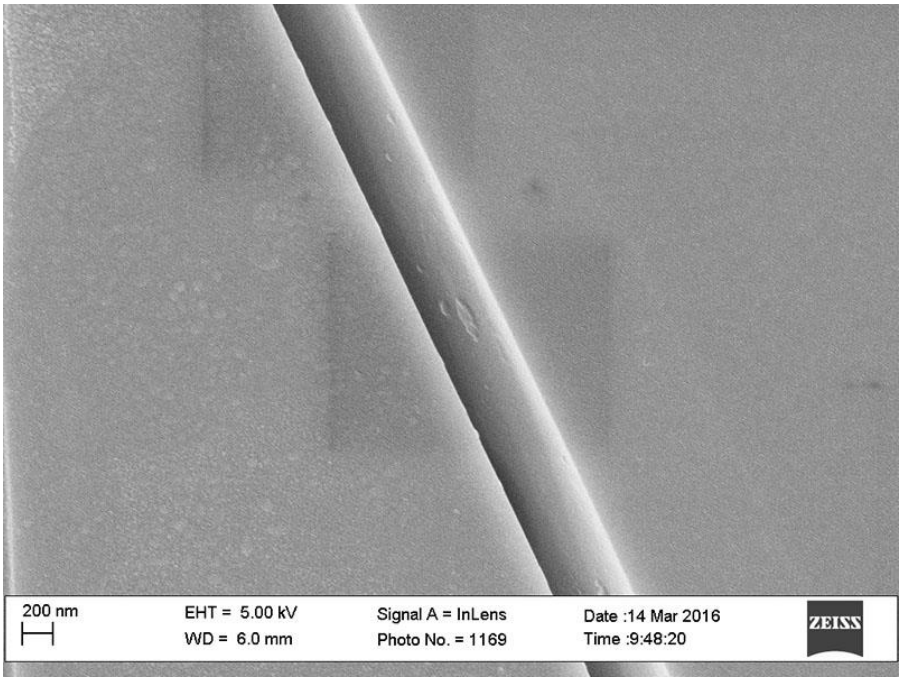

Figure A.164: Inlens SE micrograph from sample M-3658.5B. Grain boundary 3, image D.

Grain Boundary 4 (Quartz-Calcite)

Image	Measurement Number	Length (nm)
A	1	299.81
A	2	295.06
A	3	324.13
A	4	356.88
A	5	320.79
A	6	266.21
A	7	206.59
A	8	351.28
A	9	354.17
A	10	334.10
B	1	252.91
B	2	215.44
B	3	209.85
B	4	185.82
C	1	255.80
C	2	269.17
C	3	324.83
C	4	374.22
C	5	234.32
C	6	282.71
D	1	337.41
D	2	301.44
D	3	209.92
D	4	239.68
D	5	217.14
E	1	83.86
E	2	107.37
E	3	99.86
E	4	84.88
E	5	114.89
F	1	142.34
F	2	139.33
F	3	127.74
F	4	146.00
F	5	90.02
G	1	168.14
G	2	176.58
G	3	201.60
G	4	200.71
	Mean Aperture	228.28

Table A.97: NGBC measurements and mean aperture from grain boundary 4 in sample M-3658.5B.

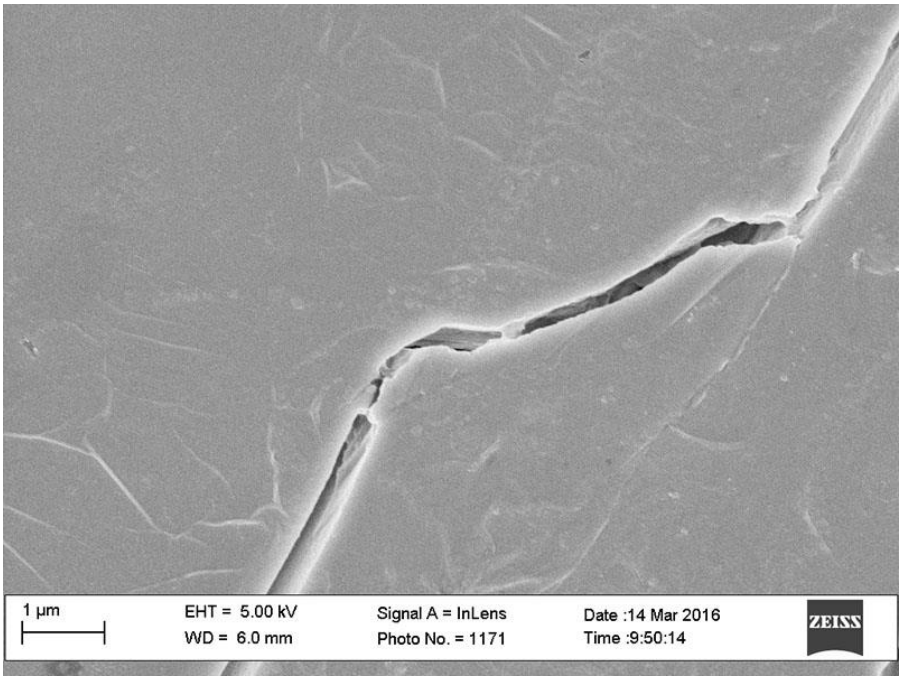

Figure A.165: Inlens SE micrograph from sample M-3658.5B. Grain boundary 4, image A.

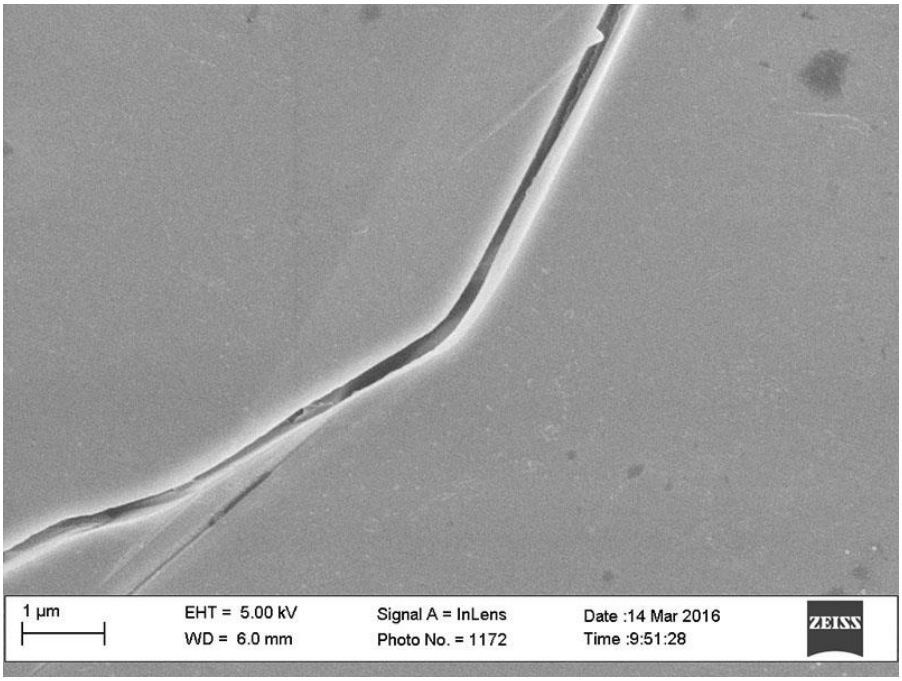

Figure A.166: Inlens SE micrograph from sample M-3658.5B. Grain boundary 4, image B.

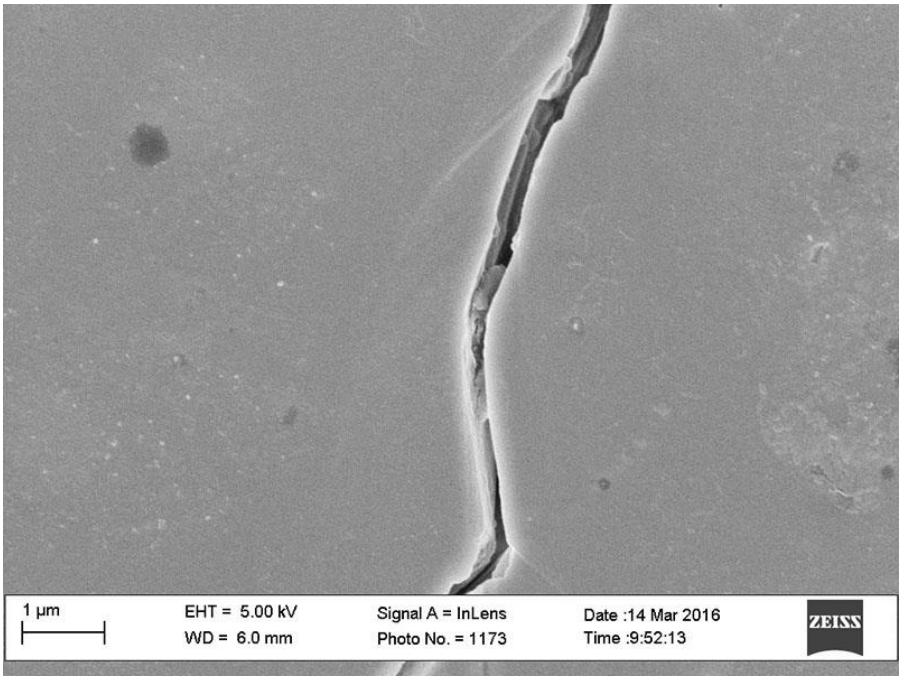

Figure A.167: Inlens SE micrograph from sample M-3658.5B. Grain boundary 4, image C.

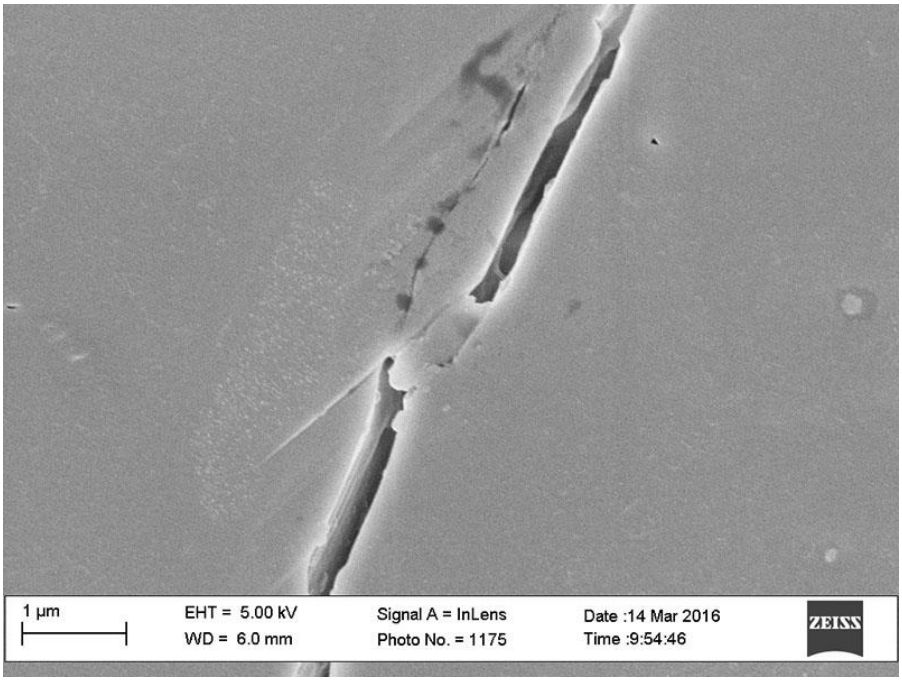

Figure A.168: Inlens SE micrograph from sample M-3658.5B. Grain boundary 4, image D.

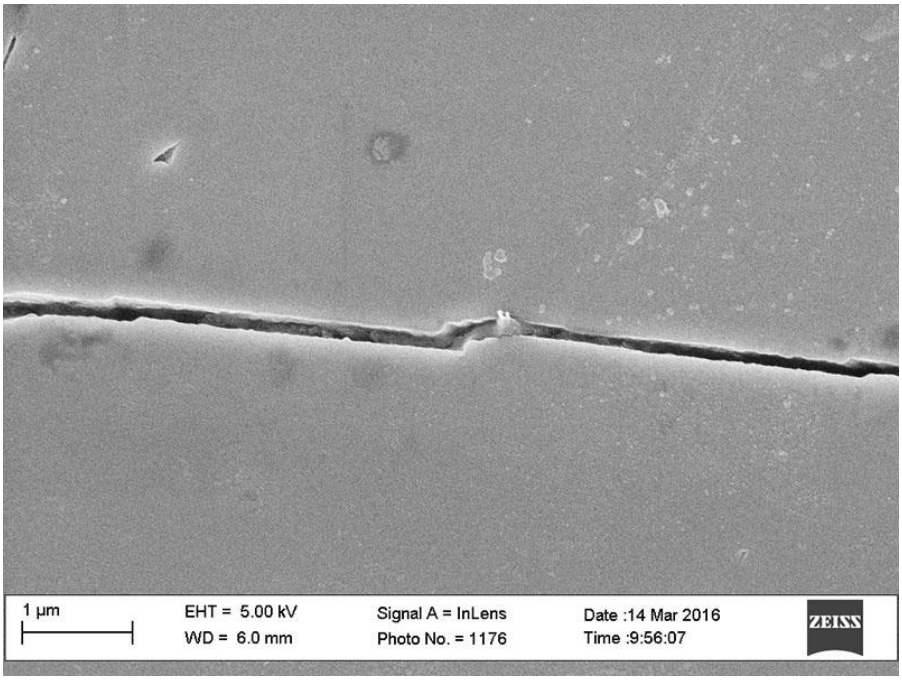

Figure A.169: Inlens SE micrograph from sample M-3658.5B. Grain boundary 4, image E.

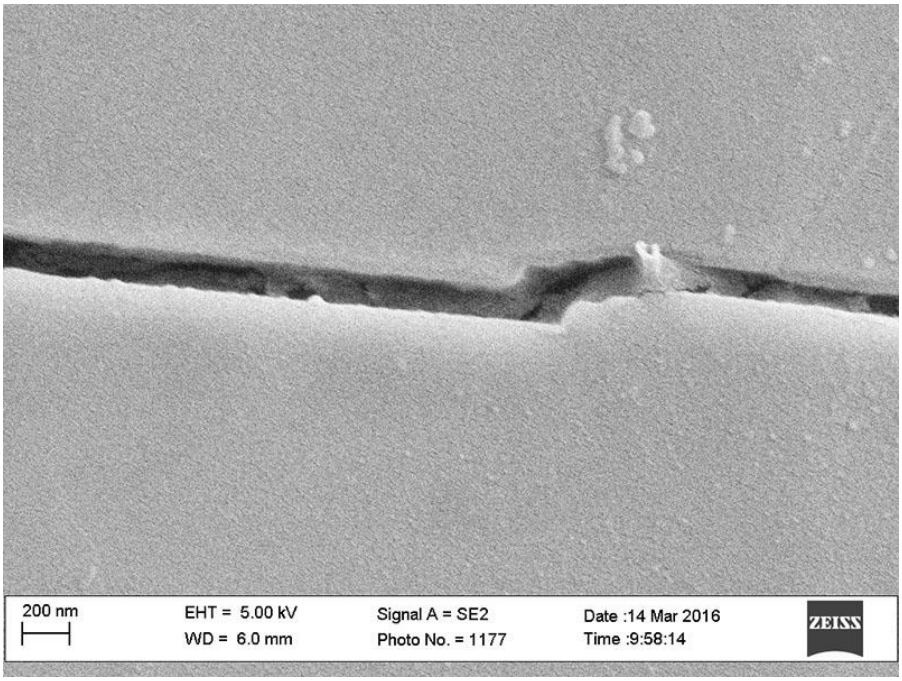

Figure A.170: Inlens SE micrograph from sample M-3658.5B. Grain boundary 4, image F.

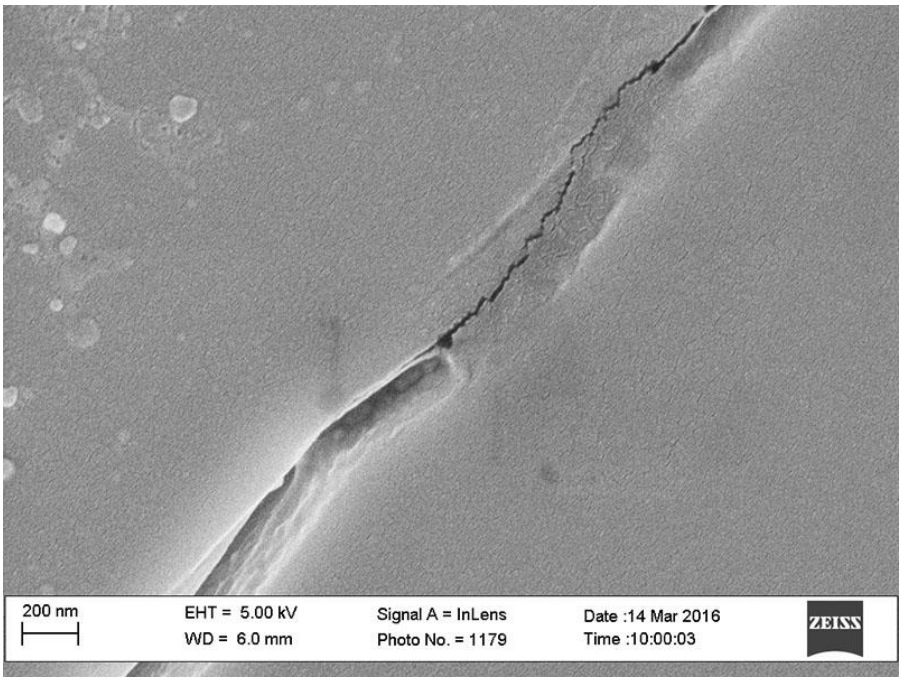

Figure A.171: Inlens SE micrograph from sample M-3658.5B. Grain boundary 4, image G.

Grain Boundary 5 (Calcite-Calcite)

Image	Measurement Number	Length (nm)
A	1	245.83
A	2	284.59
A	3	223.25
A	4	213.26
B	1	403.30
B	2	413.99
B	3	423.12
B	4	401.95
B	5	297.36
B	6	397.85
C	1	396.23
C	2	403.41
C	3	365.11
C	4	396.23
C	5	276.74
C	6	284.41
C	7	270.17
D	1	168.93
D	2	338.06
D	3	173.20
D	1	213.53
D	2	196.49
D	3	206.57
	Mean Aperture	205.53

Table A.98: NGBC measurements and mean aperture from grain boundary 5 in sample M-3658.5B.

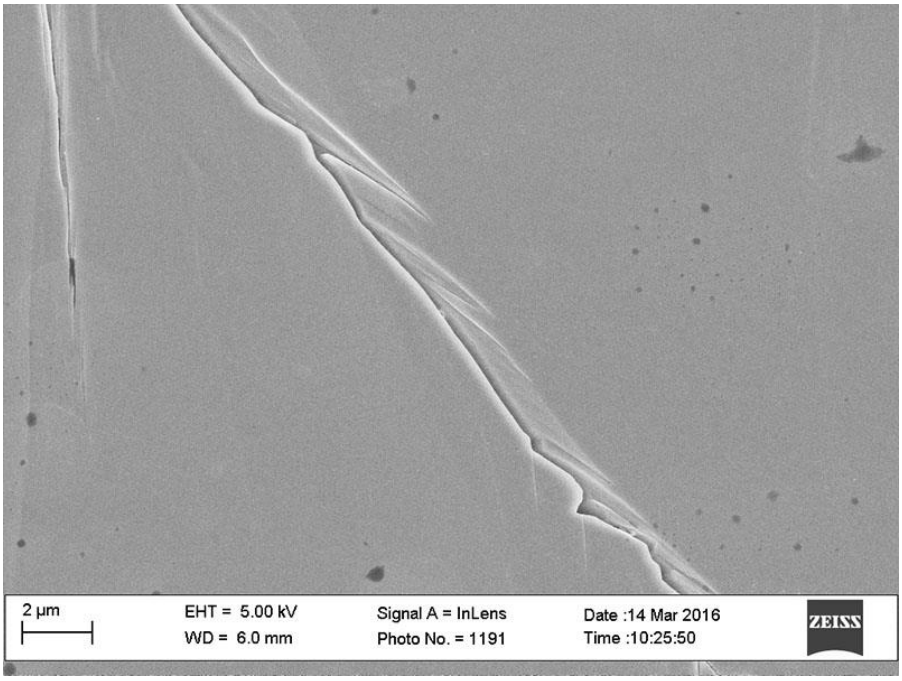

Figure A.172: Inlens SE micrograph from sample M-3658.5B. Grain boundary 5, image A.

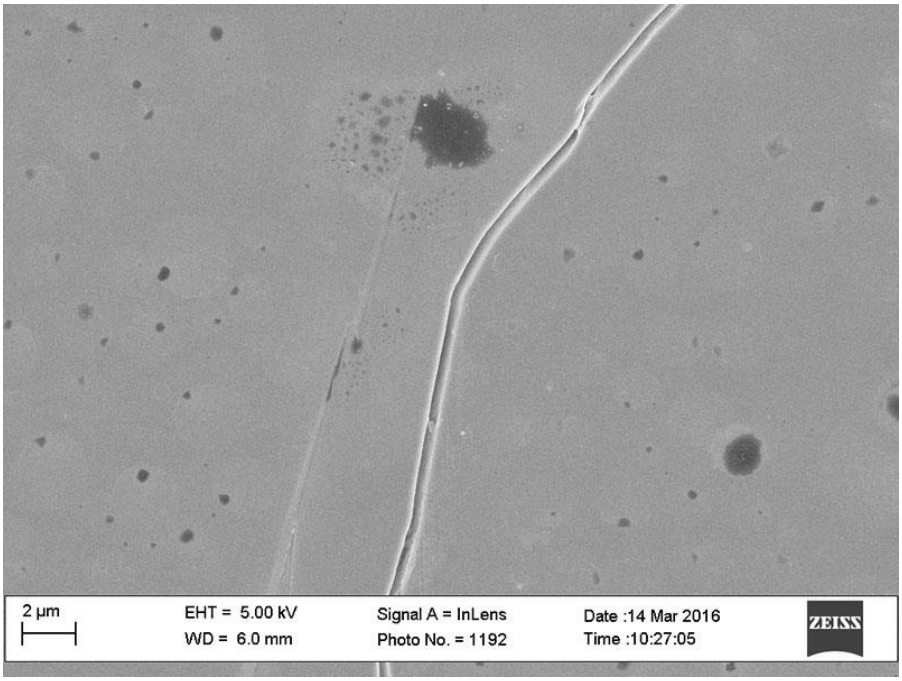

Figure A.173: Inlens SE micrograph from sample M-3658.5B. Grain boundary 5, image B.

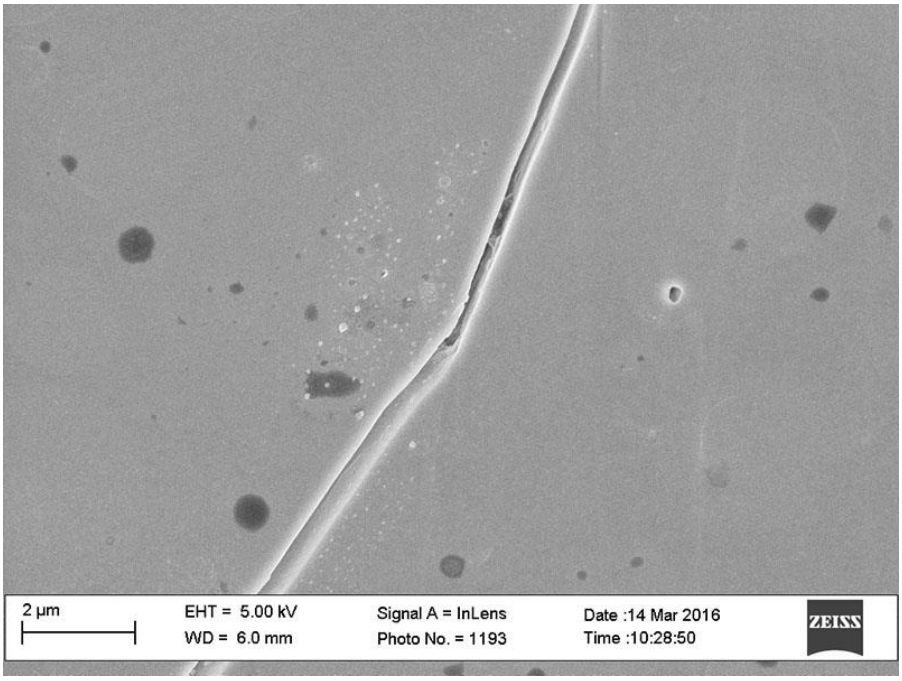

Figure A.174: Inlens SE micrograph from sample M-3658.5B. Grain boundary 5, image C.

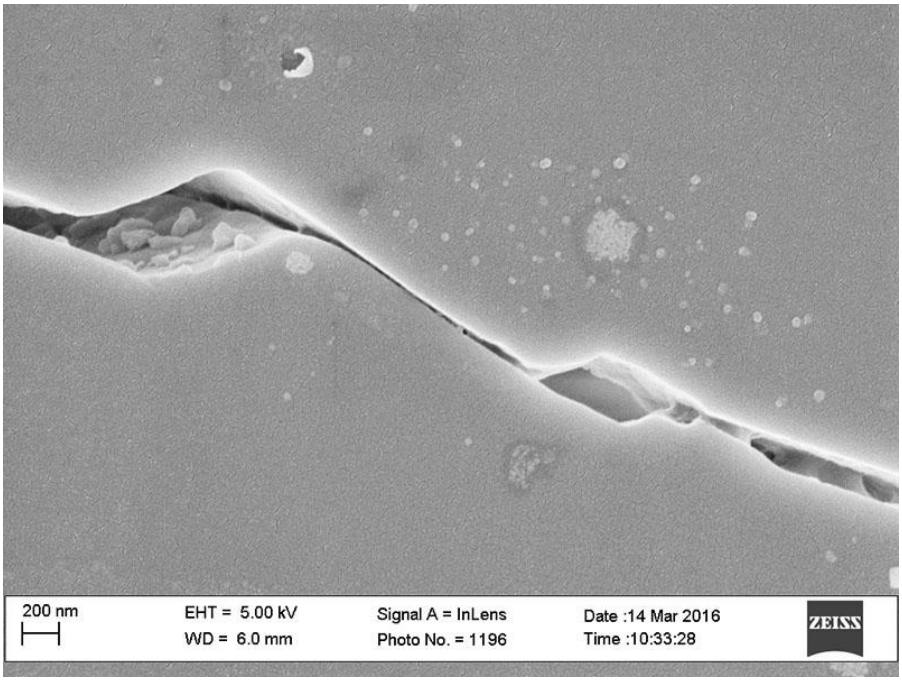

Figure A.175: Inlens SE micrograph from sample M-3658.5B. Grain boundary 5, image D.

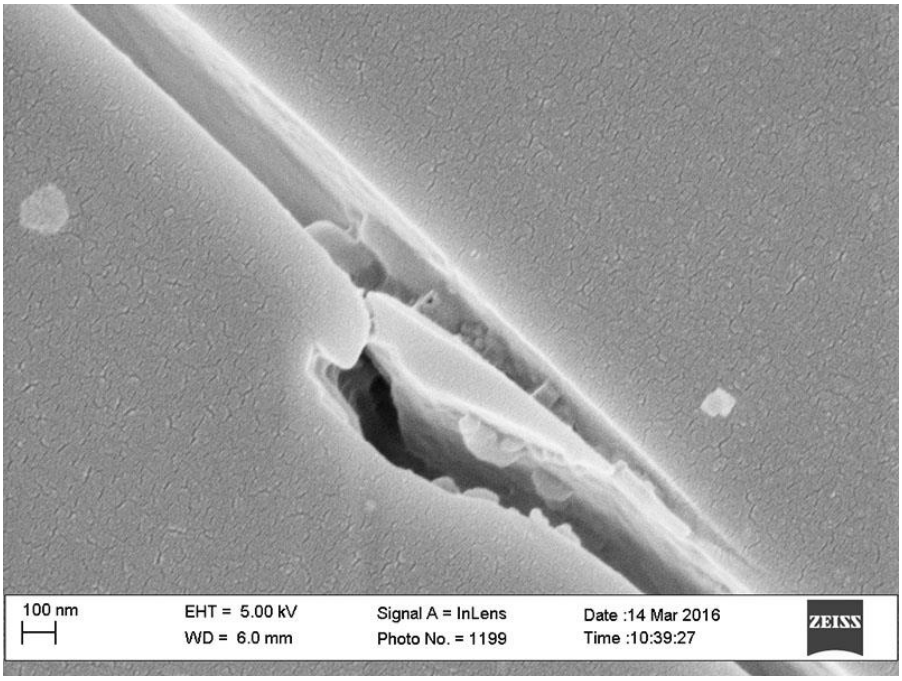

Figure A.176: Inlens SE micrograph from sample M-3658.5B. Grain boundary 5, image E.

Grain Boundary 6 (Calcite-Calcite)

Image	Measurement Number	Length (nm)
A	1	291.08
A	2	302.72
A	3	304.31
B	1	287.12
B	2	302.64
B	3	296.43
B	4	271.74
B	5	272.04
C	1	322.91
C	2	321.23
C	3	317.53
C	4	311.43
C	5	327.44
D	1	302.18
D	2	295.94
D	3	302.18
D	4	272.23
E	1	138.92
E	2	111.35
E	3	98.23
E	4	180.73
E	5	320.19
	Mean Aperture	270.48

Table A.99: NGBC measurements and mean aperture from grain boundary 6 in sample M-3658.5B.

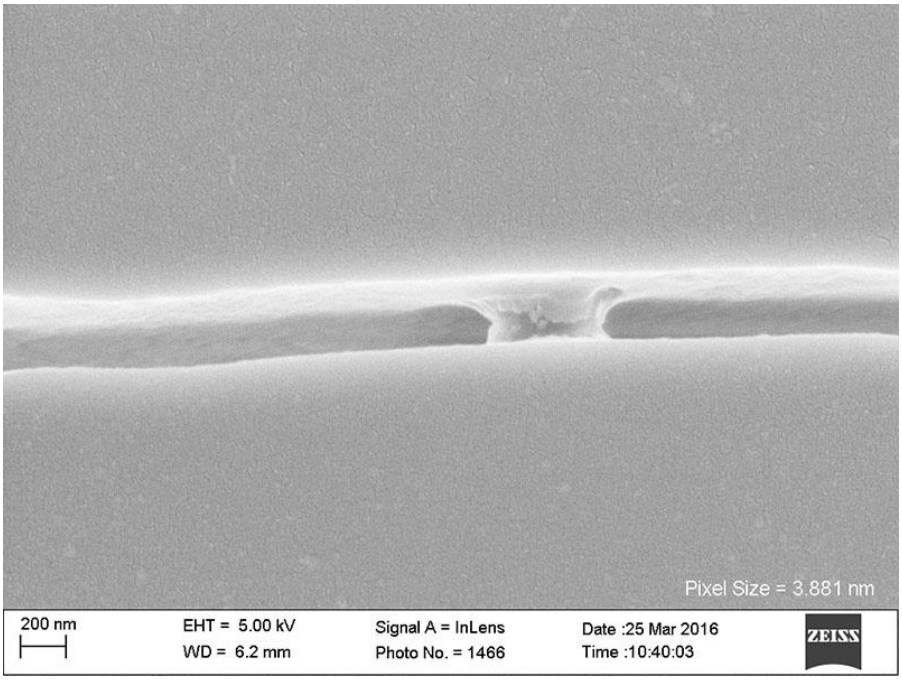

Figure A.177: Inlens SE micrograph from sample M-3658.5B. Grain boundary 6, image A.

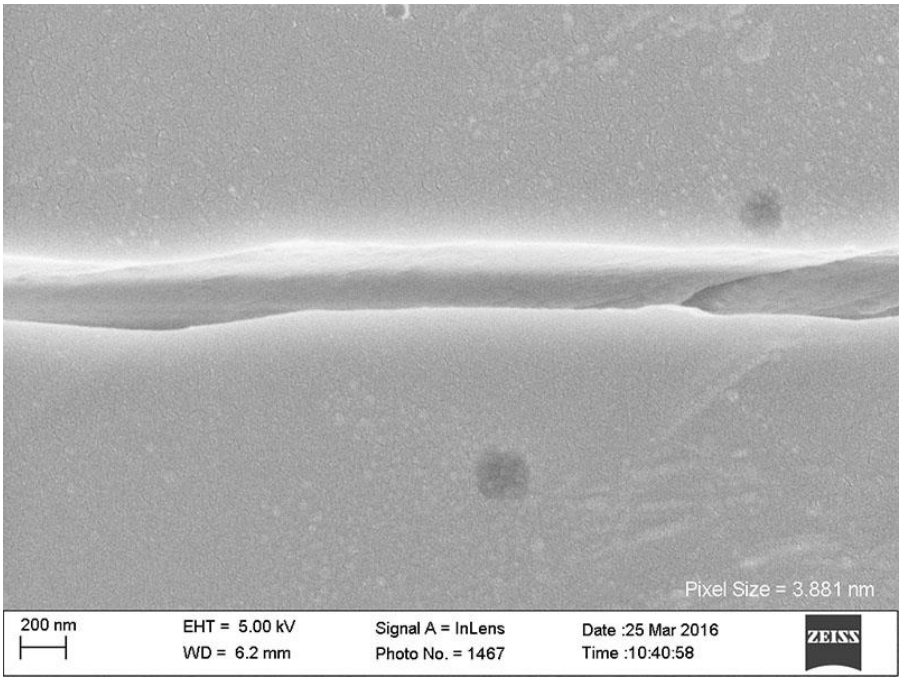

Figure A.178: Inlens SE micrograph from sample M-3658.5B. Grain boundary 6, image B.

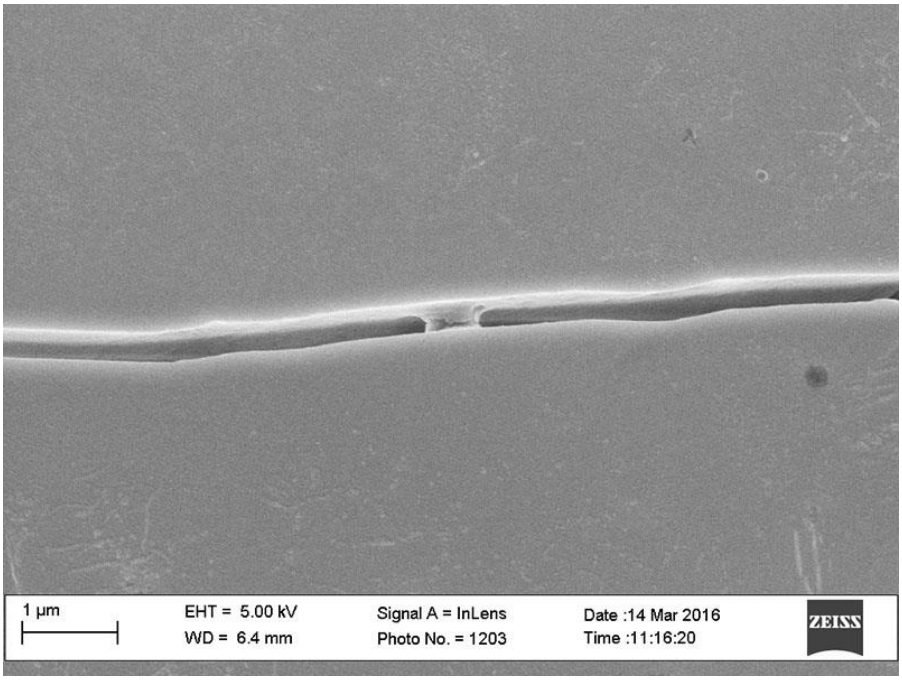

Figure A.179: Inlens SE micrograph from sample M-3658.5B. Grain boundary 6, image C.

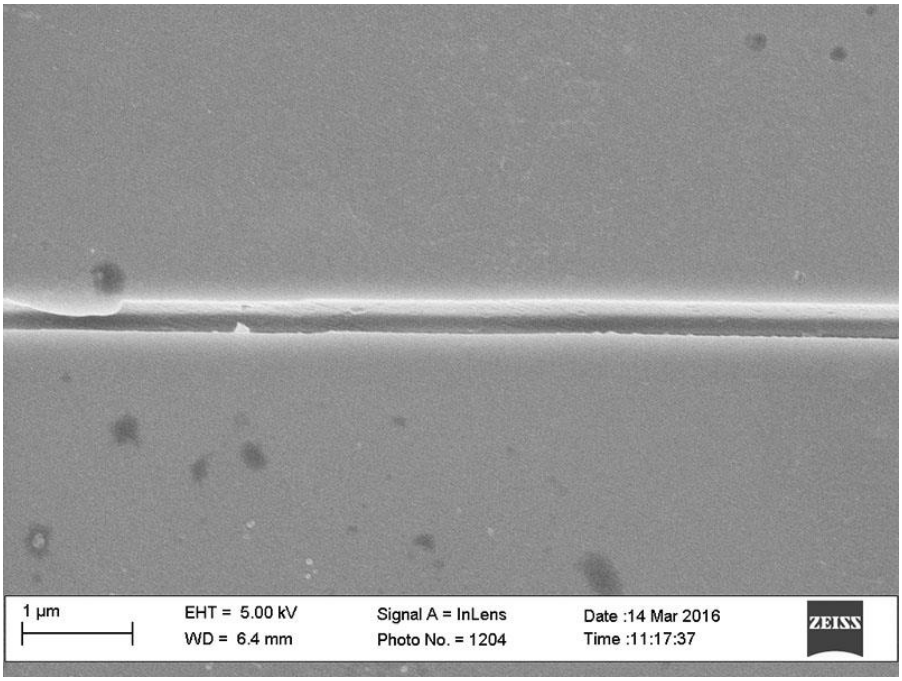

Figure A.180: Inlens SE micrograph from sample M-3658.5B. Grain boundary 6, image D.

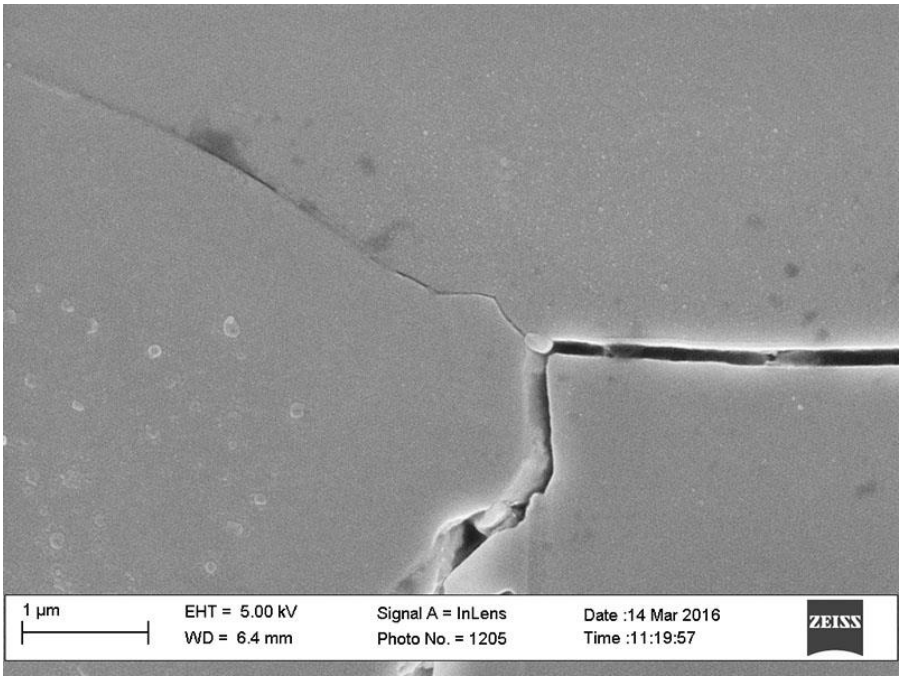

Figure A.181: Inlens SE micrograph from sample M-3658.5B. Grain boundary 6, image E.

Grain Boundary 7(Calcite-Calcite)

Image	Measurement Number	Length (nm)
A	1	125.04
A	2	154.89
A	3	168.13
A	4	131.43
B	1	141.48
B	2	139.75
B	3	172.54
B	4	183.42
	Mean Aperture	152.09

Table A.100: NGBC measurements and mean aperture from grain boundary 7 in sample M-3658.5B.

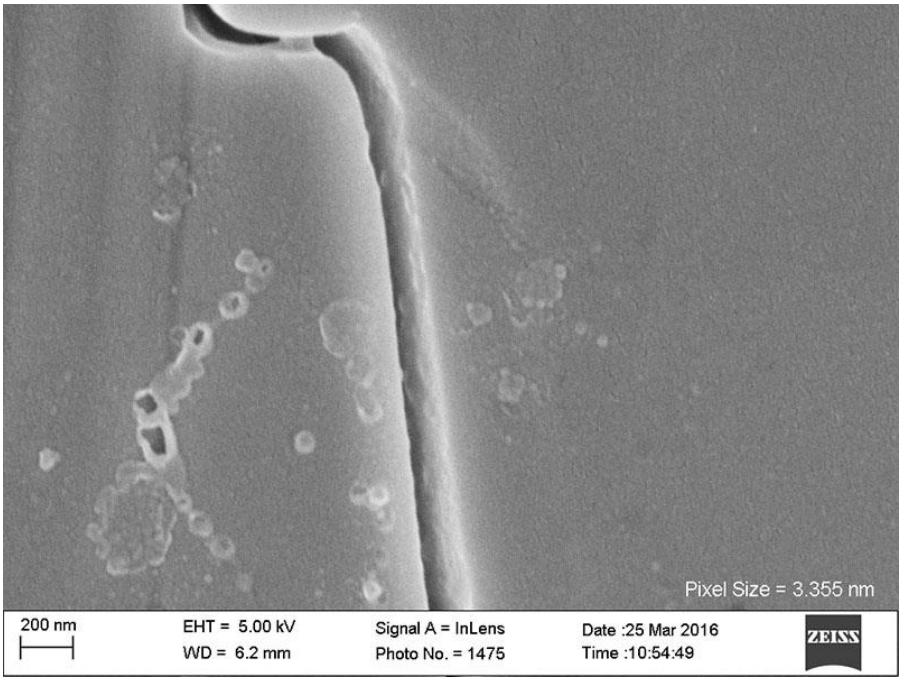

Figure A.182: Inlens SE micrograph from sample M-3658.5B. Grain boundary 7, image A.

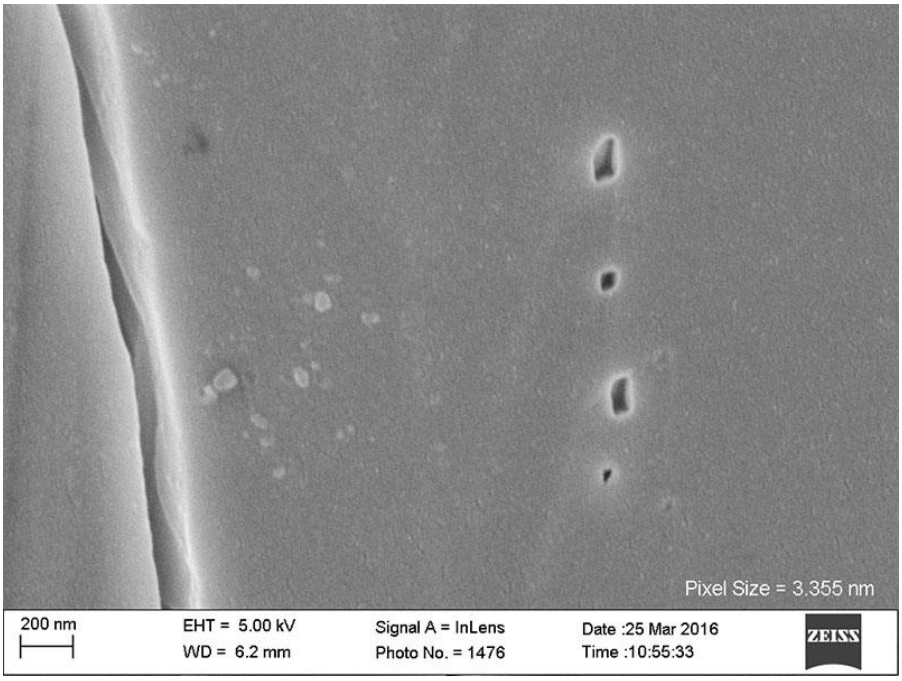

Figure A.183: Inlens SE micrograph from sample M-3658.5B. Grain boundary 7, image B.

Grain Boundary 8 (Calcite-Calcite)

Image	Measurement Number	Length (nm)
A	1	173.88
A	2	151.67
A	3	160.56
A	4	164.50
A	5	148.79
A	6	179.30
A	7	178.97
B	1	43.85
B	2	45.22
B	3	32.53
B	4	45.50
B	5	41.62
B	6	50.21
C	1	171.21
C	2	162.67
C	3	162.45
C	4	173.12
C	5	179.75
D	1	165.24
D	2	165.26
D	3	173.50
D	4	165.26
D	5	170.77
E	1	180.84
E	2	180.20
E	3	142.15
E	4	146.73
	Mean Aperture	139.10

Table A.101: NGBC measurements and mean aperture from grain boundary 8 in sample M-3658.5B.

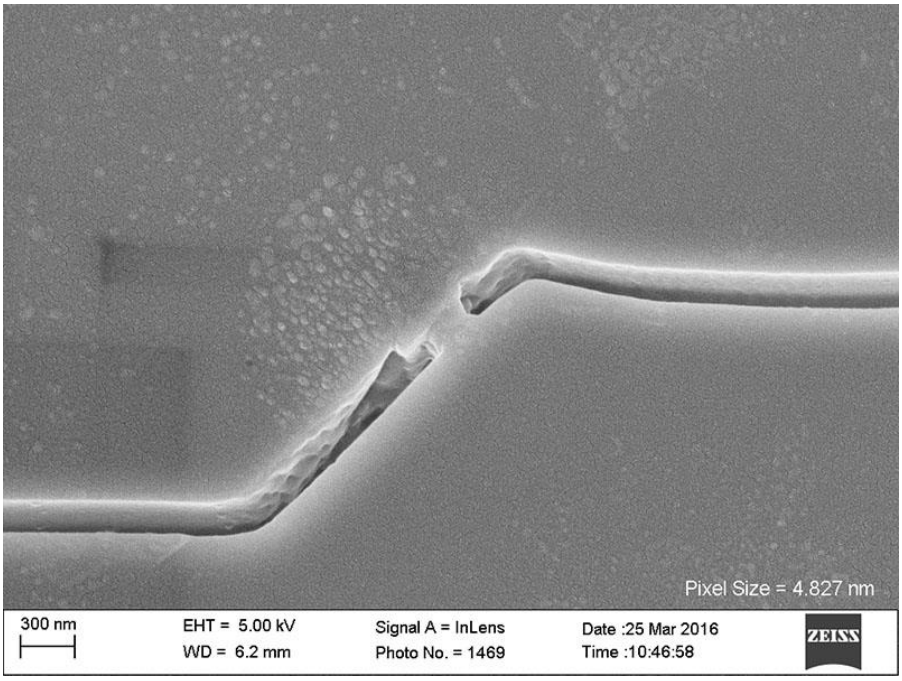

Figure A.184: Inlens SE micrograph from sample M-3658.5B. Grain boundary 8, image A.

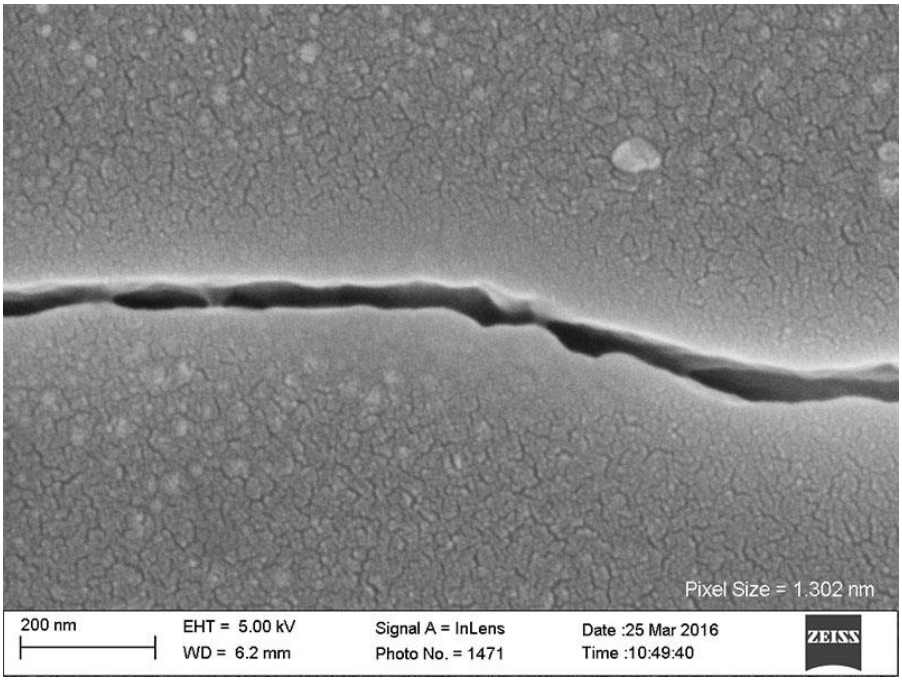

Figure A.185: Inlens SE micrograph from sample M-3658.5B. Grain boundary 8, image B.

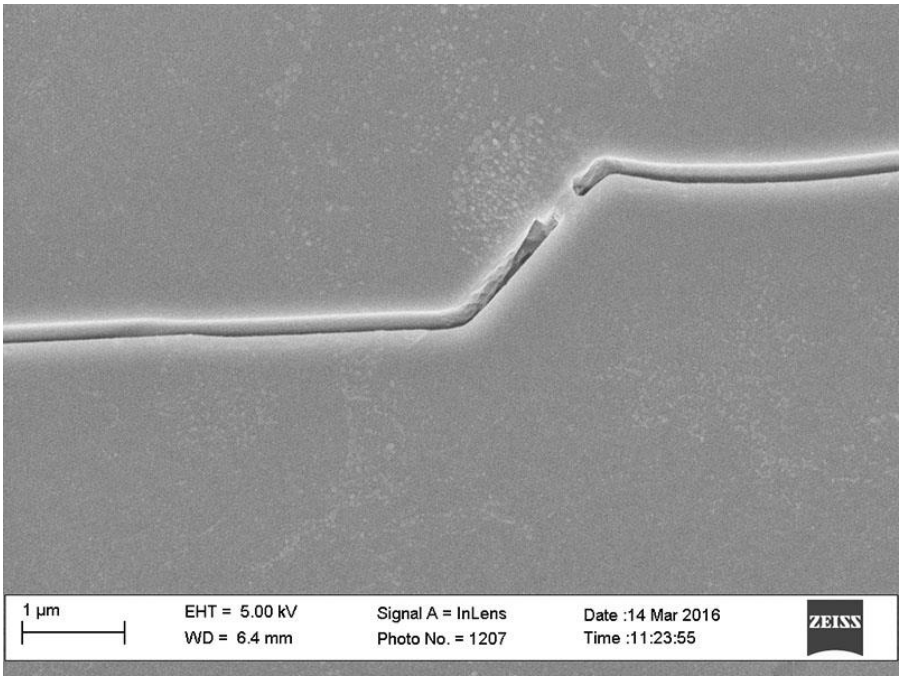

Figure A.186: Inlens SE micrograph from sample M-3658.5B. Grain boundary 8, image C.

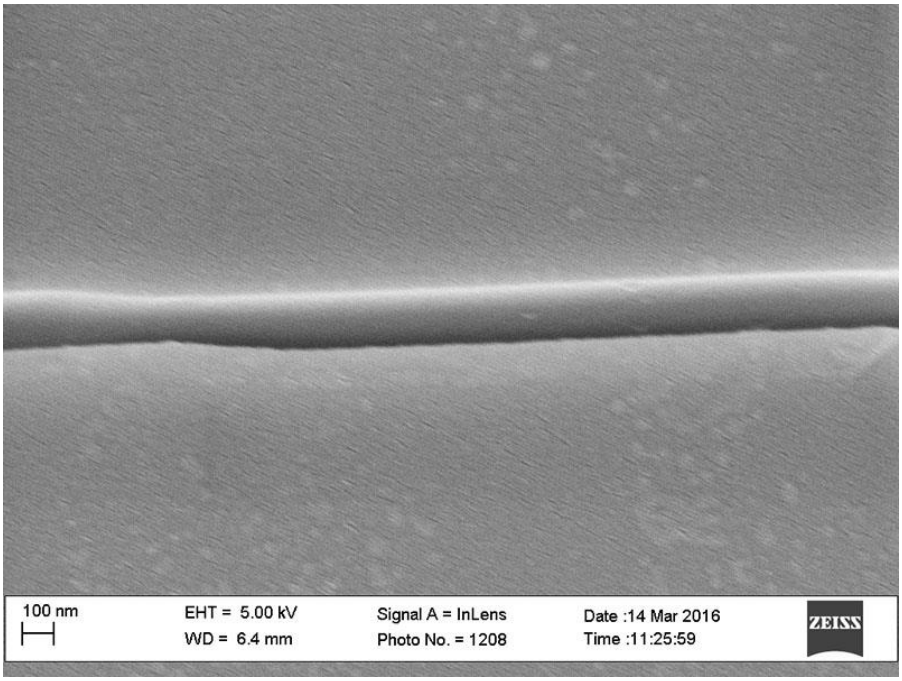

Figure A.187: Inlens SE micrograph from sample M-3658.5B. Grain boundary 8, image D.

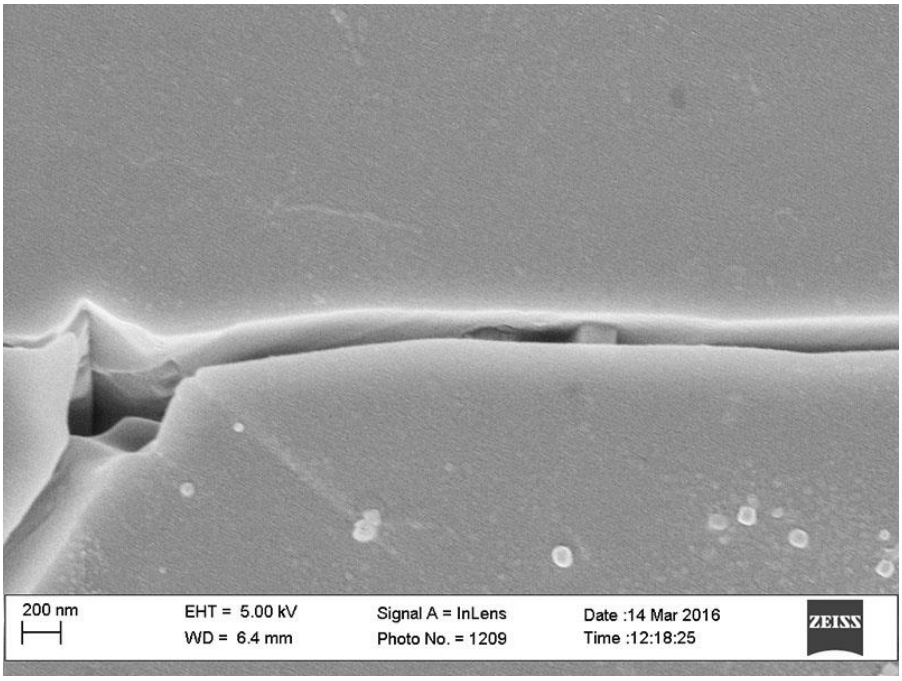

Figure A.188: Inlens SE micrograph from sample M-3658.5B. Grain boundary 8, image E.

Grain Boundary 9(Calcite-Calcite)

Image	Measurement Number	Length (nm)
A	1	178.39
A	2	179.18
A	3	197.55
	Mean Aperture	185.04

Table A.102: NGBC measurements and mean aperture from grain boundary 9 in sample M-3658.5B.

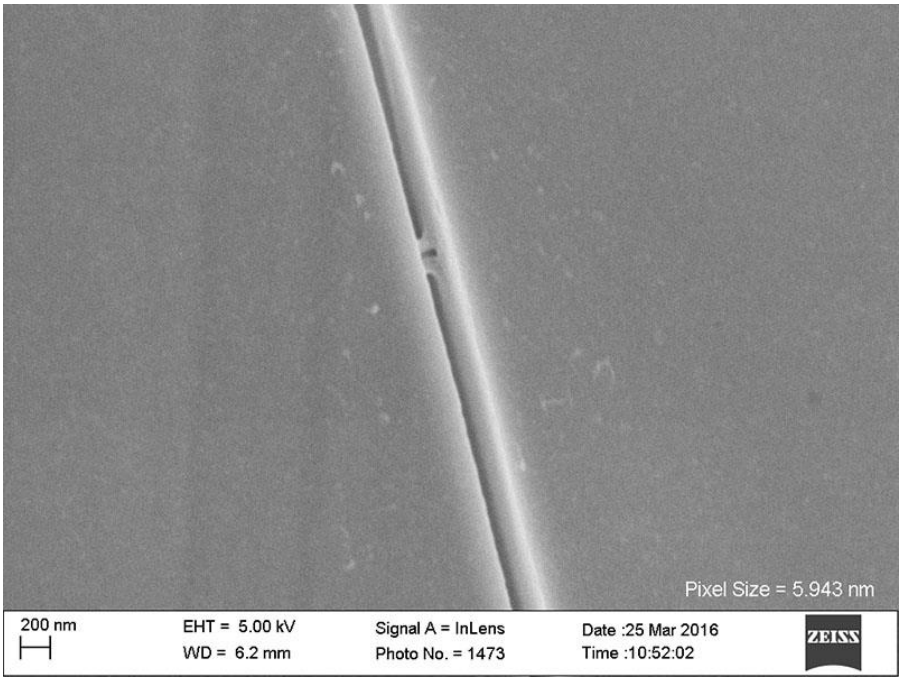

Figure A.189: Inlens SE micrograph from sample M-3658.5B. Grain boundary 9, image A.

Grain Boundary 10(Calcite-Calcite)

Image	Measurement Number	Length (nm)
A	1	115.51
A	2	88.57
A	3	120.20
	Mean Aperture	108.09

Table A.103: NGBC measurements and mean aperture from grain boundary 10 in sample M-3658.5B.

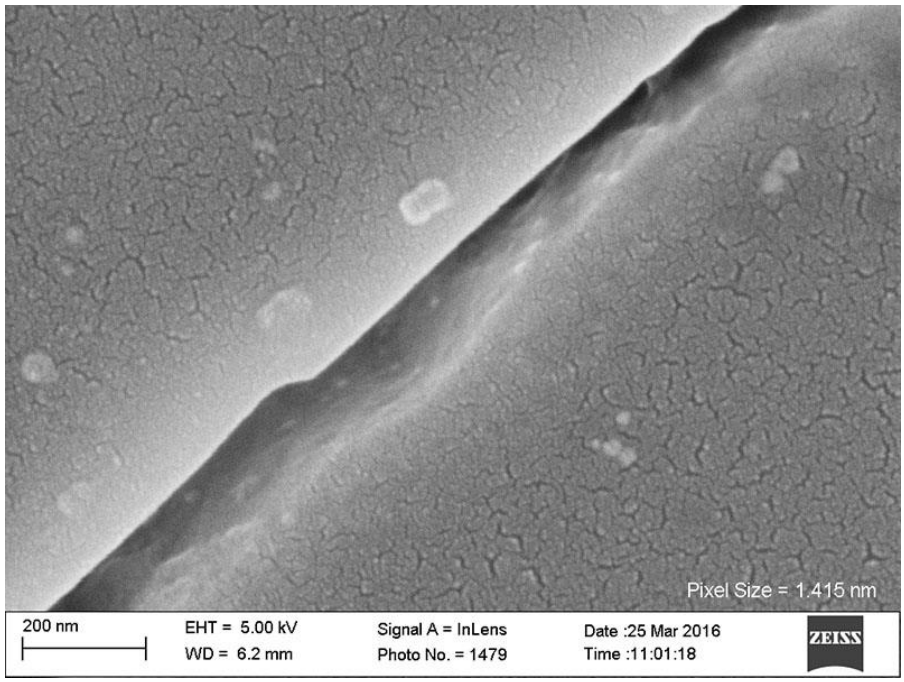

Figure A.190: Inlens SE micrograph from sample M-3658.5B. Grain boundary 10, image A.

Grain Boundary 11(Calcite-Calcite)

Image	Measurement Number	Length (nm)
A	1	101.01
A	2	91.12
A	3	142.85
A	4	116.41
A	5	87.35
A	6	91.64
B	1	134.19
B	2	103.76
B	3	134.11
B	4	111.58
B	5	101.48
B	6	96.14
B	7	144.41
	Mean Aperture	112.00

Table A.104: NGBC measurements and mean aperture from grain boundary 11 in sample M-3658.5B.

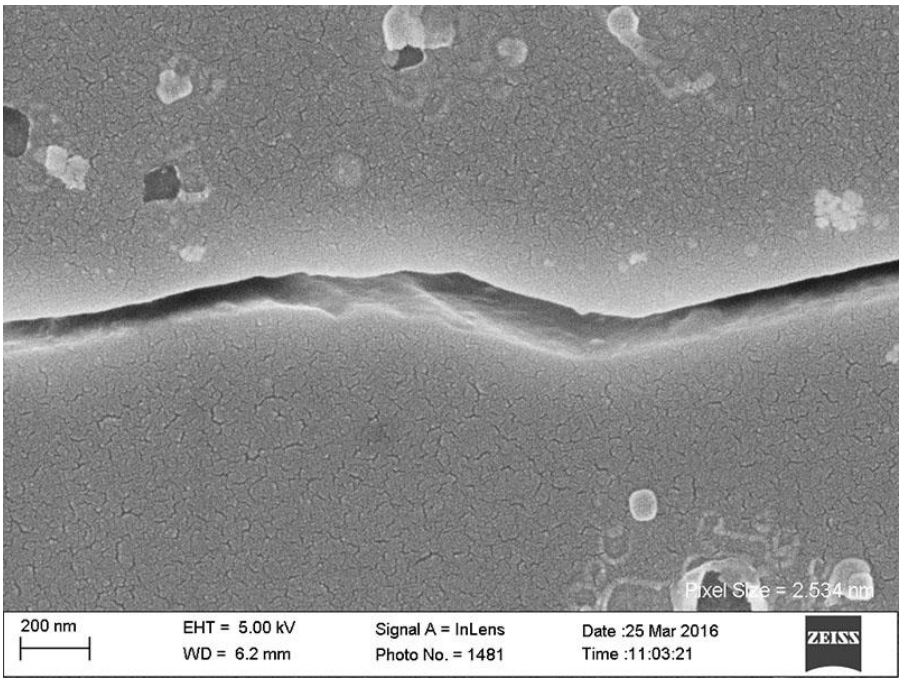

Figure A.191: Inlens SE micrograph from sample M-3658.5B. Grain boundary 11, image A.

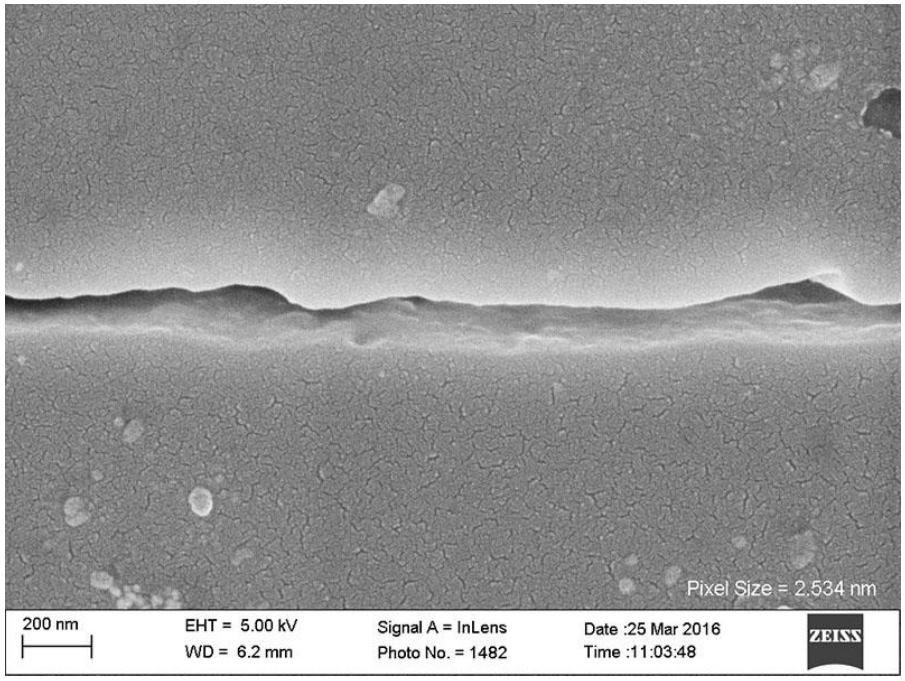

Figure A.192: Inlens SE micrograph from sample M-3658.5B. Grain boundary 11, image B.

Grain Boundary 12(Calcite-Calcite)

Image	Measurement Number	Length (nm)
A	1	157.09
B	1	138.32
B	2	159.83
B	3	131.03
B	4	139.15
B	5	145.50
	Mean Aperture	145.15

Table A.105: NGBC measurements and mean aperture from grain boundary 12 in sample M-3658.5B.

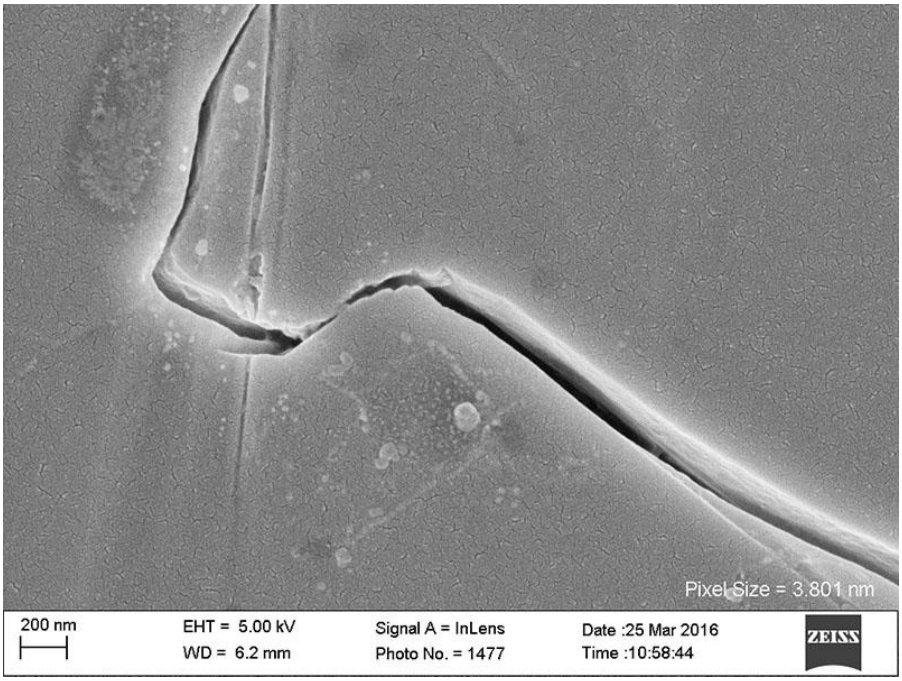

Figure A.193: Inlens SE micrograph from sample M-3658.5B. Grain boundary 12, image A.

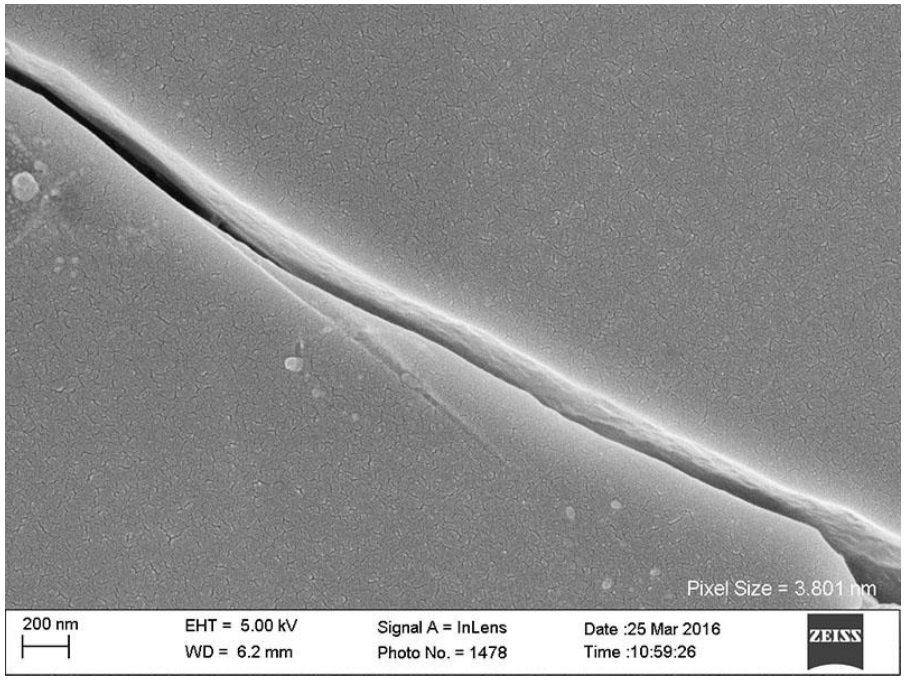

Figure A.194: Inlens SE micrograph from sample M-3658.5B. Grain boundary 12, image B.

SAMPLE HF-18000, HAYNESVILLE FORMATION

Mineral Cement	Rock Type	Sampled Depth (ft)	Sampled Depth (m)	Max burial depth (m)	Exhumed (m)	Max T (°C)	Range (nm)	Sample Mean (nm)
Calcite	Shale	18000	~5000	5486.4	0	150-170	36-150	78.81

Table A.106: Summary of sample HF-18000

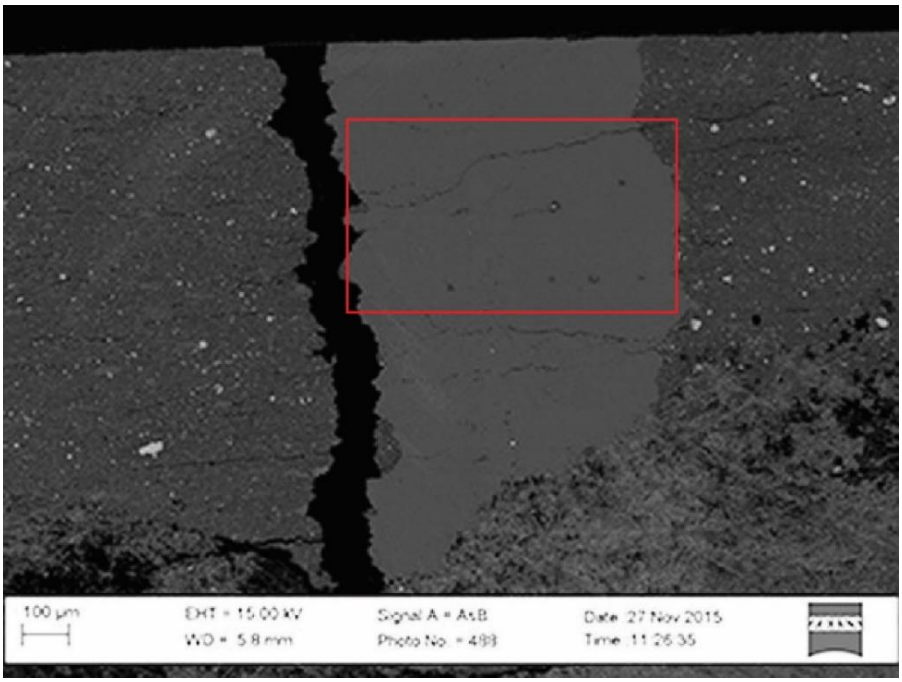

Figure A.195: Inlens SE micrograph of sample HF-18000. Box indicates area imaged for EBSD and NGBC aperture measurements.

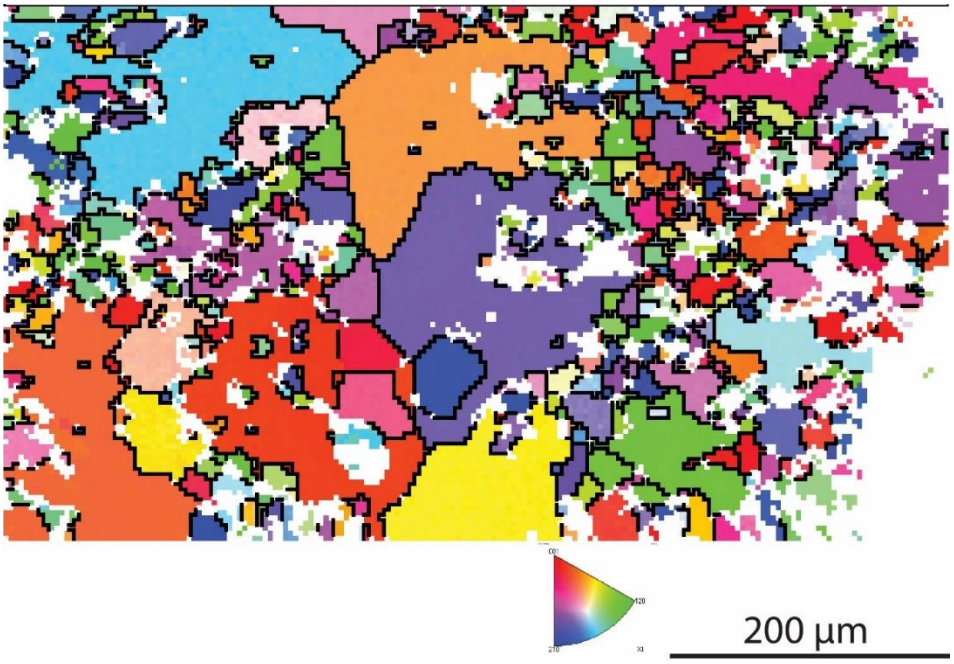

Figure A.196: EBSD inverse pole figure from sample HF-18000.

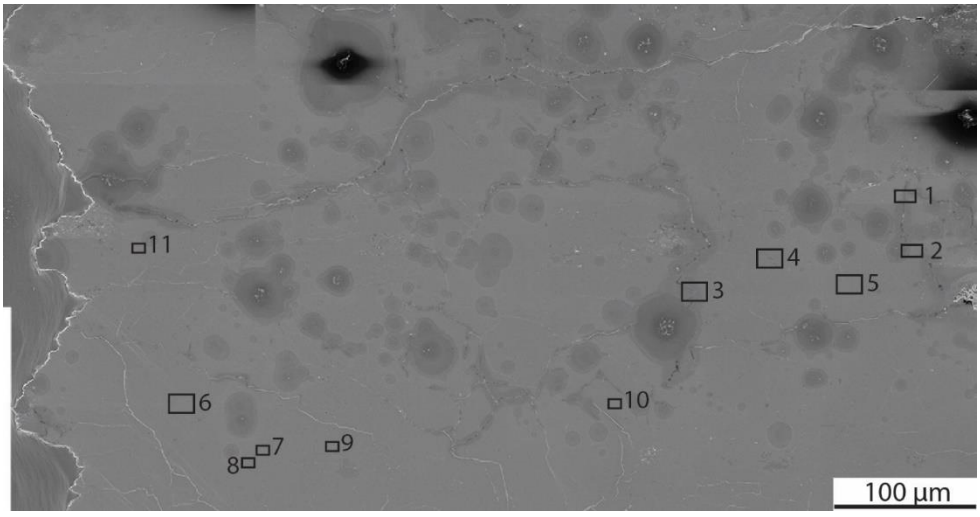

Figure A.197: Inlens SE mosaic of sample HF-18000. Boxes indicate location of grain boundaries used for NGBC aperture measurements.

Grain Boundary	Mean Aperture
1	51.93
2	45.96
3	66.04
4	84.24
5	37.58
6	112.77
7	150.39
8	40.97
9	36.55
10	47.48
11	192.97
Sample Mean	78.81

Table A.107: NGBC mean apertures and sample mean from sample HF-18000.

Grain Boundary 1

Image	Measurement Number	Length (nm)
A	1	52.14
A	2	50.78
A	3	59.28
A	4	45.52
	Mean Aperture	51.93

Table A.108: NGBC measurements and mean aperture from grain boundary 1 in sample HF-18000.

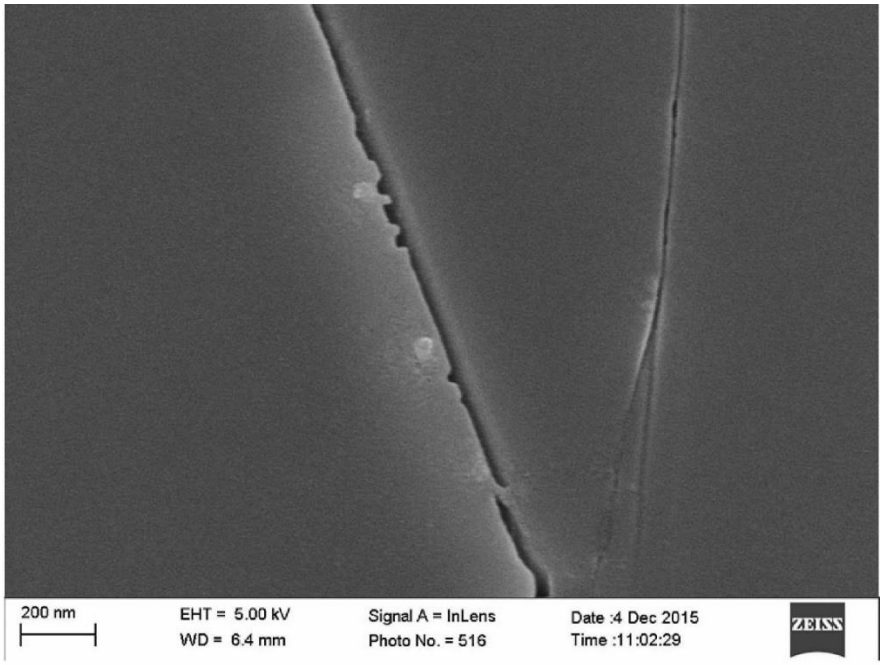

Figure A.198: Inlens SE micrograph from sample HF-18000. Grain boundary 1, image A.

Grain Boundary 2

Image	Measurement Number	Length (nm)
A	1	40.62
A	2	41.98
A	3	46.21
A	4	47.38
B	1	48.23
B	2	46.76
B	3	34.49
B	4	38.57
B	5	30.64
C	1	61.52
C	2	66.37
C	3	48.72
	Mean Aperture	45.96

Table A.109: NGBC measurements and mean aperture from grain boundary 2 in sample HF-18000.

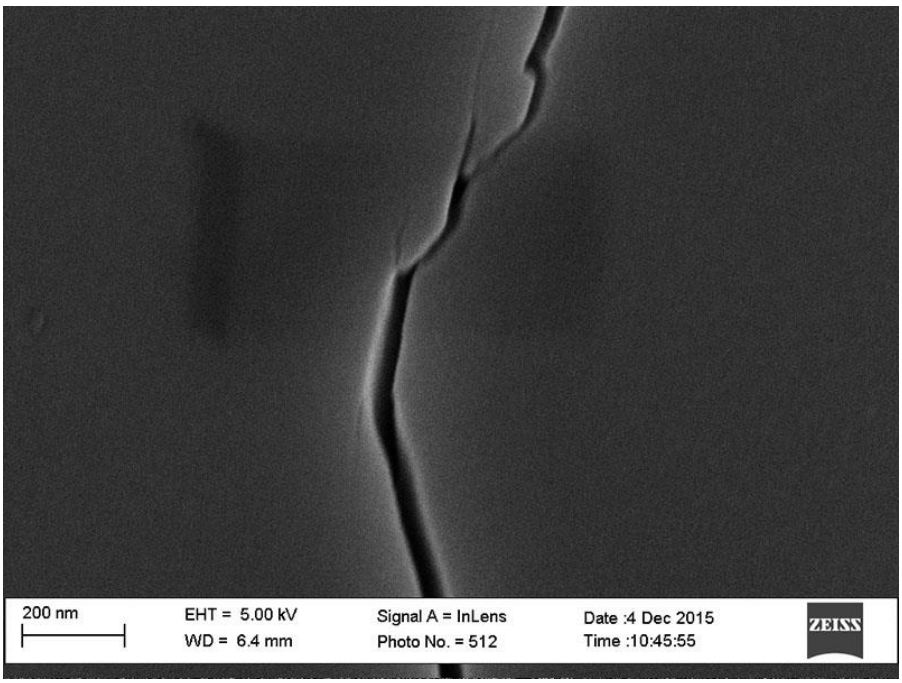

Figure A.199: Inlens SE micrograph from sample HF-18000. Grain boundary 2, image A.

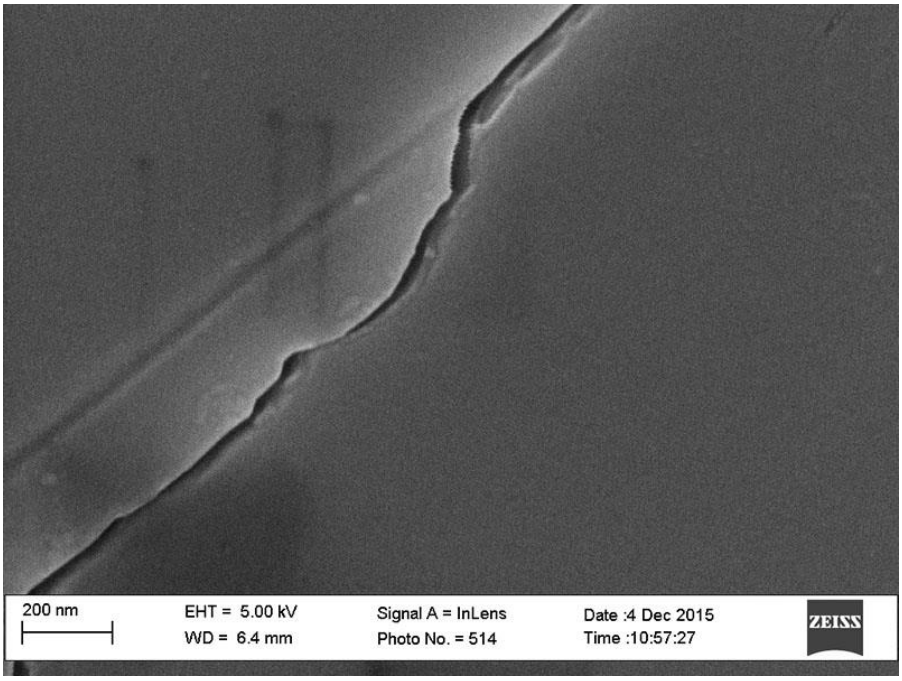

Figure A.200: Inlens SE micrograph from sample HF-18000. Grain boundary 2, image B.

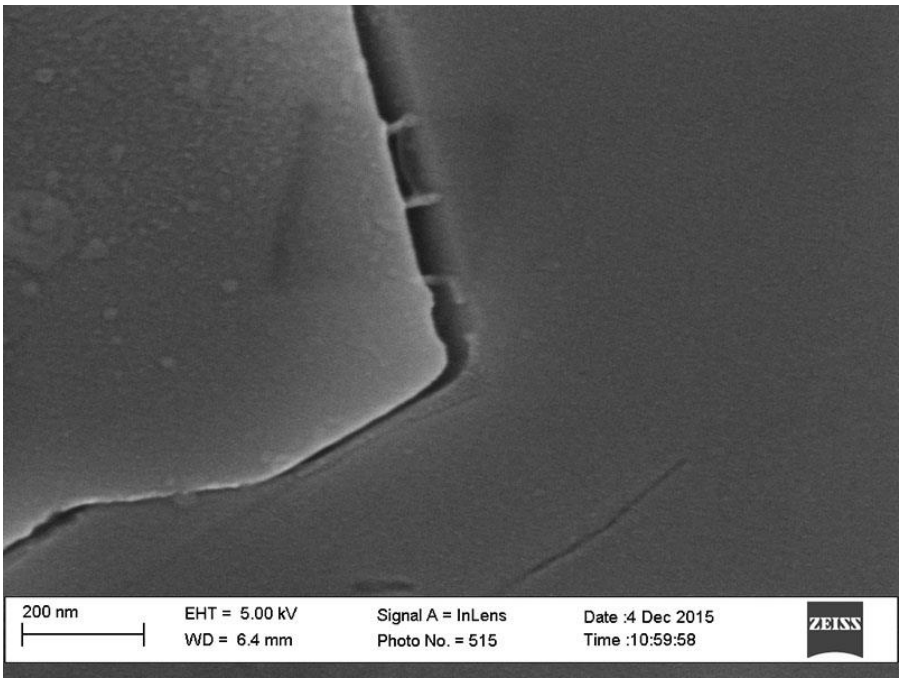

Figure A.201: Inlens SE micrograph from sample HF-18000. Grain boundary 2, image C.

Grain Boundary 3

Image	Measurement Number	Length (nm)
A	1	65.03
A	2	67.05
	Mean Aperture	66.04

Table A.110: NGBC measurements and mean aperture from grain boundary 3 in sample HF-18000.

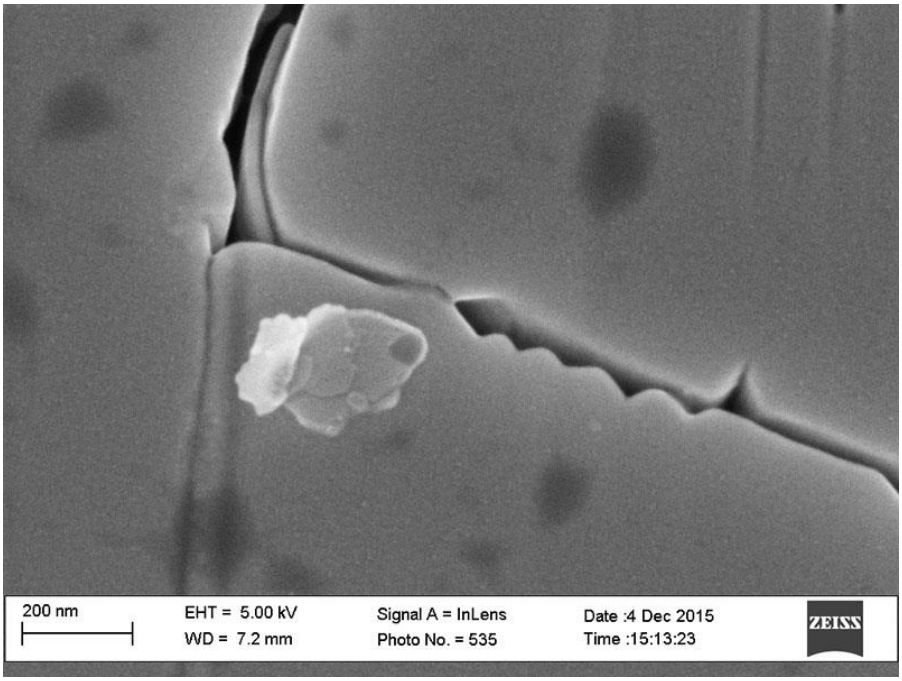

Figure A.202: Inlens SE micrograph from sample HF-18000. Grain boundary 3, image A.

Grain Boundary 4

Image	Measurement Number	Length (nm)
A	1	99.62
A	2	84.02
A	3	83.38
A	4	93.21
A	5	92.74
A	6	73.69
A	7	63.01
	Mean Aperture	84.24

Table A.111: NGBC measurements and mean aperture from grain boundary 4 in sample HF-18000.

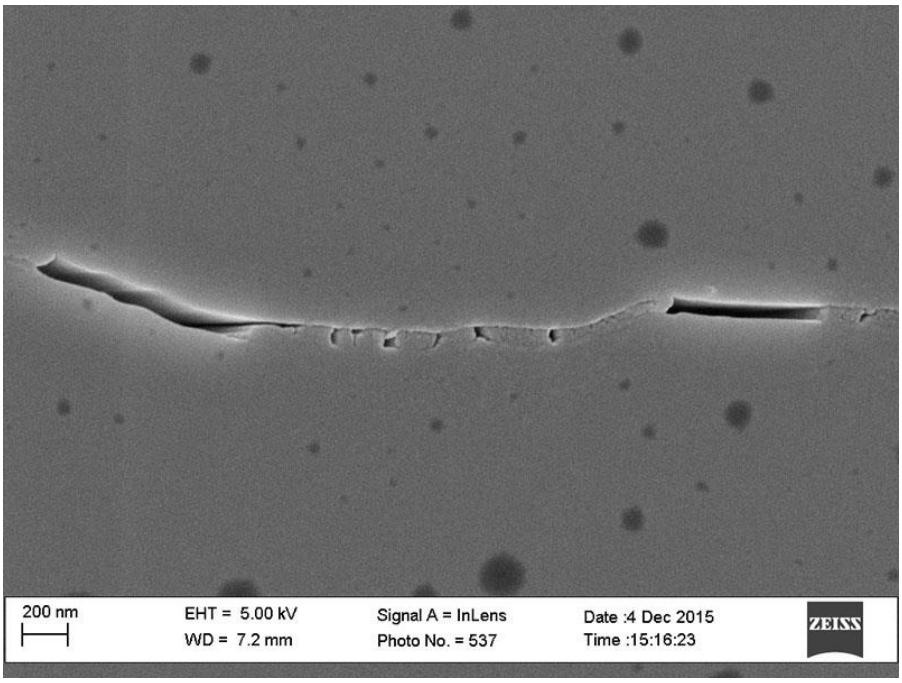

Figure A.203: Inlens SE micrograph from sample HF-18000. Grain boundary 4, image A.

Grain Boundary 5

Image	Measurement Number	Length (nm)
A	1	32.59
A	2	34.90
A	3	38.48
A	4	44.35
	Mean Aperture	37.58

Table A.112: NGBC measurements and mean aperture from grain boundary 5 in sample HF-18000.

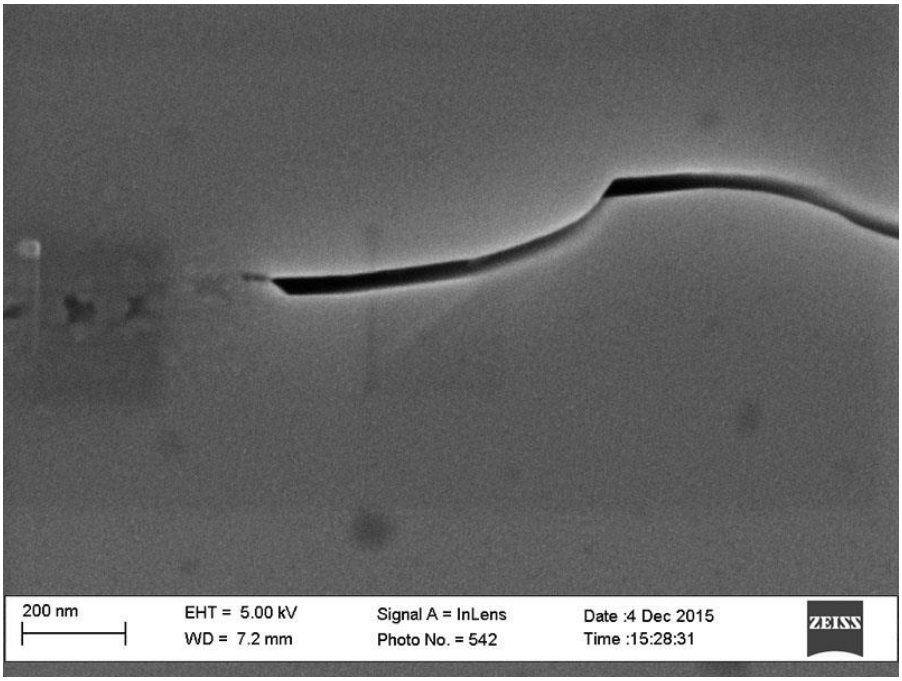

Figure A.204: Inlens SE micrograph from sample HF-18000. Grain boundary 5, image A.

Grain Boundary 6

Image	Measurement Number	Length (nm)
A	1	156.48
A	2	150.71
A	3	112.51
A	4	86.32
A	5	100.55
A	1	81.58
A	2	43.19
A	3	131.26
A	4	134.17
A	5	130.87
	Mean Aperture	112.77

Table A.113: NGBC measurements and mean aperture from grain boundary 6 in sample HF-18000.

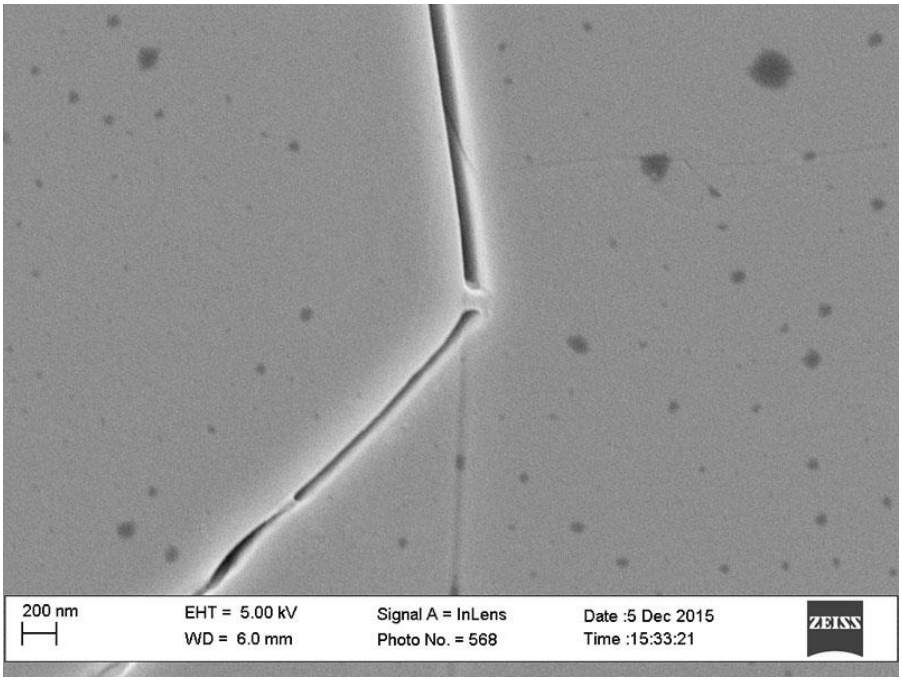

Figure A.205: Inlens SE micrograph from sample HF-18000. Grain boundary 6, image A.

Grain Boundary 7

Image	Measurement Number	Length (nm)
A	1	256.60
A	2	250.90
A	3	47.84
A	4	158.79
A	5	164.27
A	6	66.50
A	7	180.89
A	8	77.30
	Mean Aperture	150.39

Table A.114: NGBC measurements and mean aperture from grain boundary 7 in sample HF-18000.

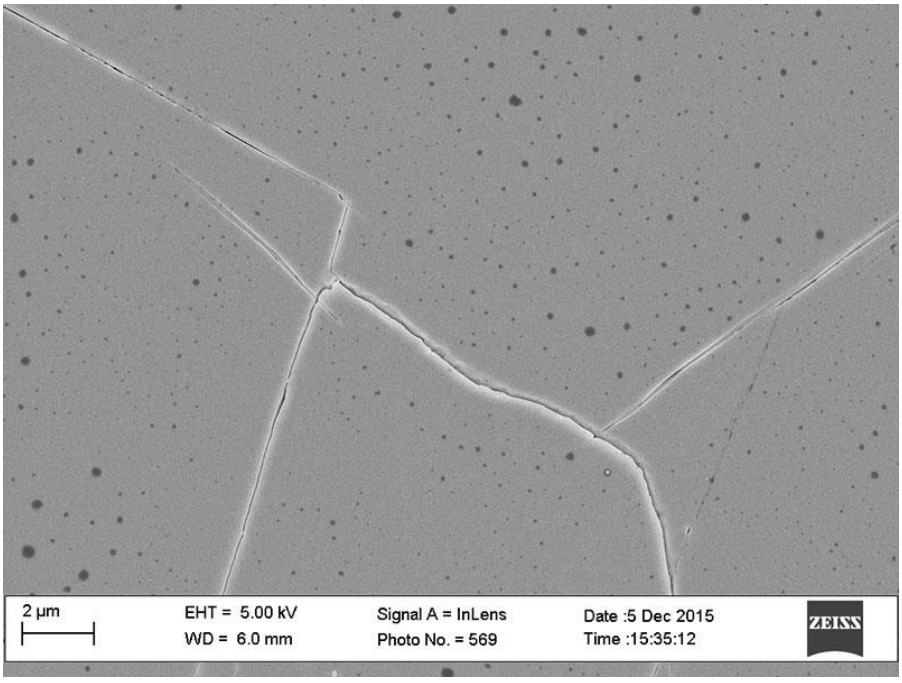

Figure A.206: Inlens SE micrograph from sample HF-18000. Grain boundary 7, image A.

Grain Boundary 8

Image	Measurement Number	Length (nm)
A	1	34.72
A	2	28.79
A	3	46.79
A	4	53.58
	Mean Aperture	40.97

Table A.115: NGBC measurements and mean aperture from grain boundary 8 in sample HF-18000.

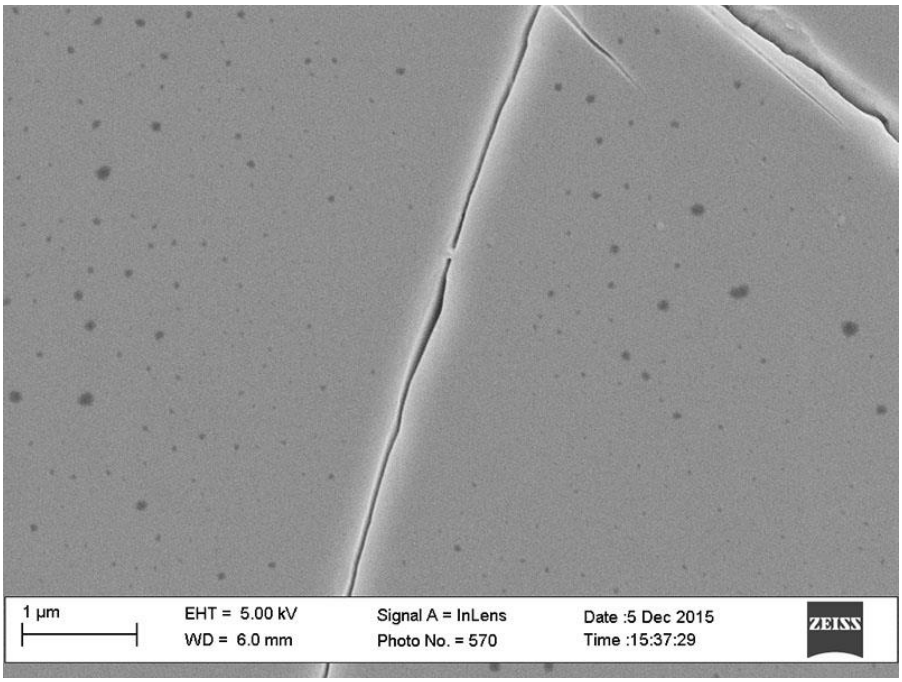

Figure A.207: Inlens SE micrograph from sample HF-18000. Grain boundary 8, image A.

Grain Boundary 9

Image	Measurement Number	Length (nm)
A	1	22.22
A	2	29.27
A	3	23.99
A	4	53.73
B	1	40.53
B	2	36.40
B	3	34.68
B	4	51.59
	Mean Aperture	36.55

Table A.116: NGBC measurements and mean aperture from grain boundary 9 in sample HF-18000.

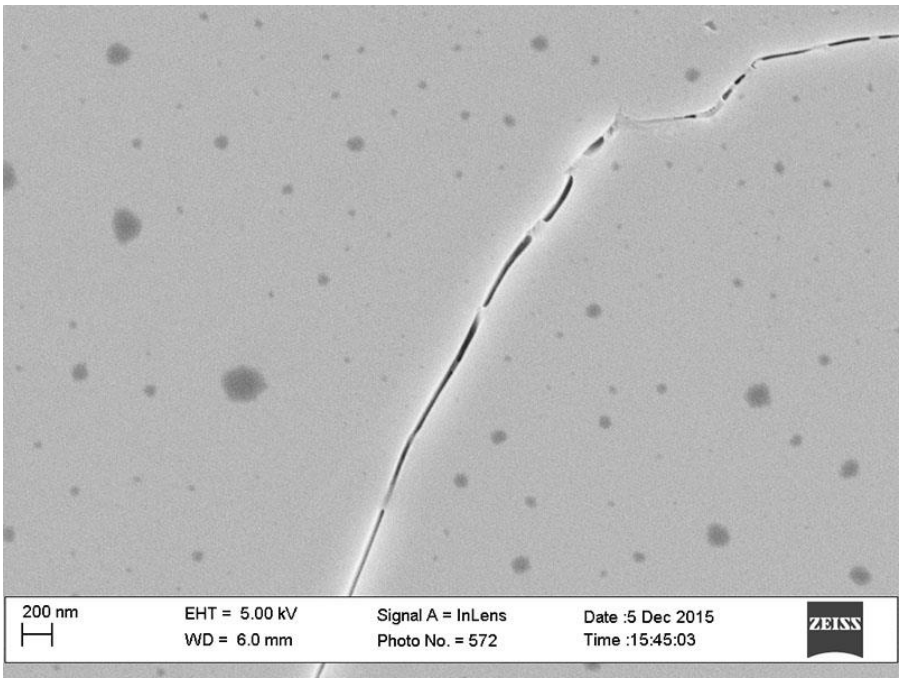

Figure A.208: Inlens SE micrograph from sample HF-18000. Grain boundary 9, image A.

Grain Boundary 10

Image	Measurement Number	Length (nm)
A	1	54.98
A	2	44.44
A	3	43.02
	Mean Aperture	47.48

Table A.117: NGBC measurements and mean aperture from grain boundary 10 in sample HF-18000.

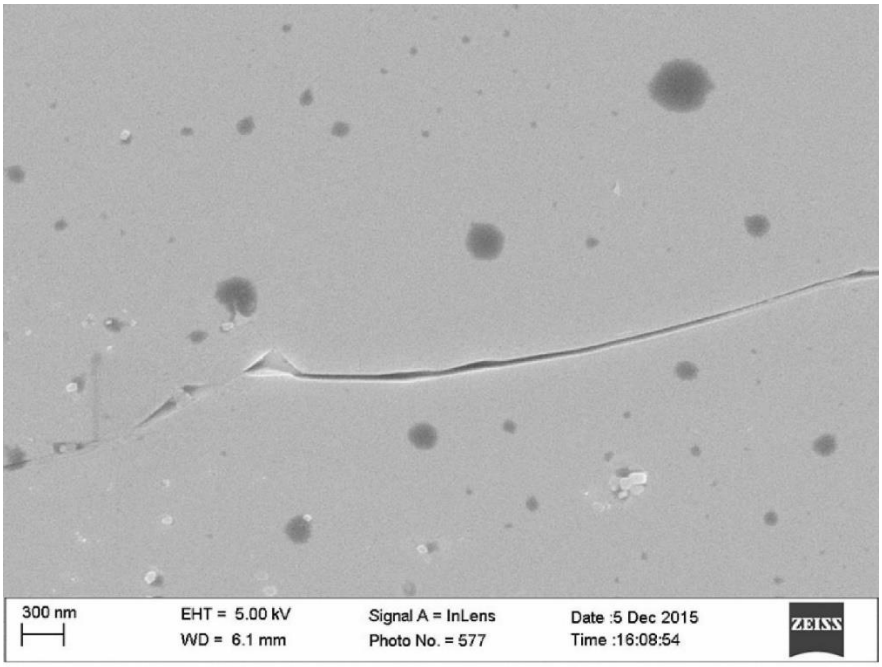

Figure A.209: Inlens SE micrograph from sample HF-18000. Grain boundary 10, image A.

Grain Boundary 11

Image	Measurement Number	Length (nm)
A	1	188.37
A	2	198.08
A	3	171.59
A	4	210.00
A	5	196.80
	Mean Aperture	192.97

Table A.118: NGBC measurements and mean aperture from grain boundary 11 in sample HF-18000.

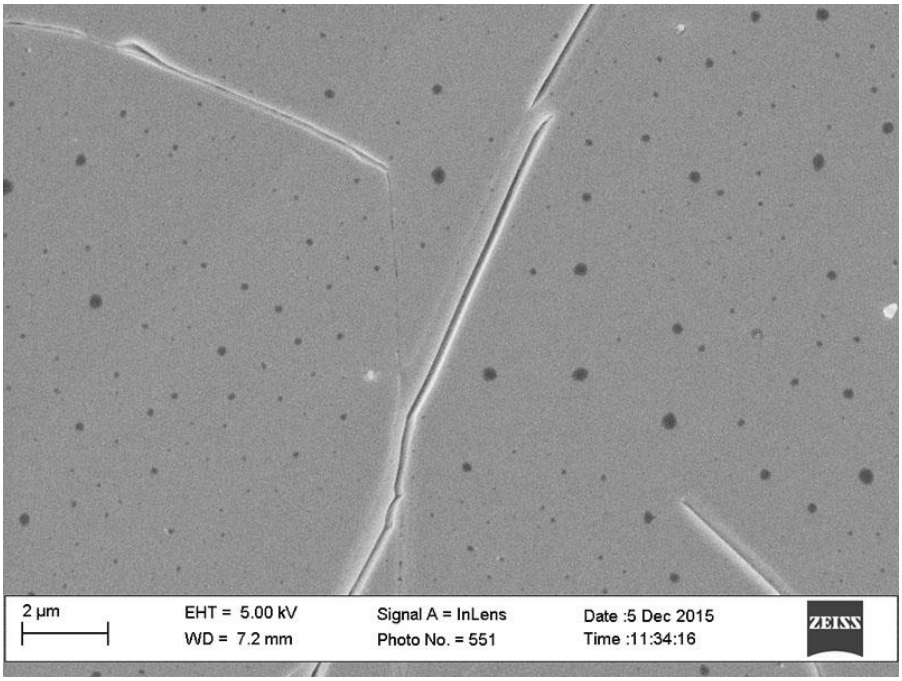

Figure A.210: Inlens SE micrograph from sample HF-18000. Grain boundary11, image A.

SAMPLE 12-GC-12, NIKANASSIN FORMATION

Mineral Cement	Rock Type	Sampled Depth (ft)	Sampled Depth (m)	Max burial depth (m)	Exhumed (m)	Max T (°C)	Range (nm)	Sample Mean (nm)
Calcite - Quartz	Sandstone	Outcrop	Surface	7000	7000	170-200	25-298	166.15
Quartz	Sandstone	Outcrop	Surface	7000	7000	170-200	67-356	232.11

Table A.119: Summary of sample 12-GC-12.

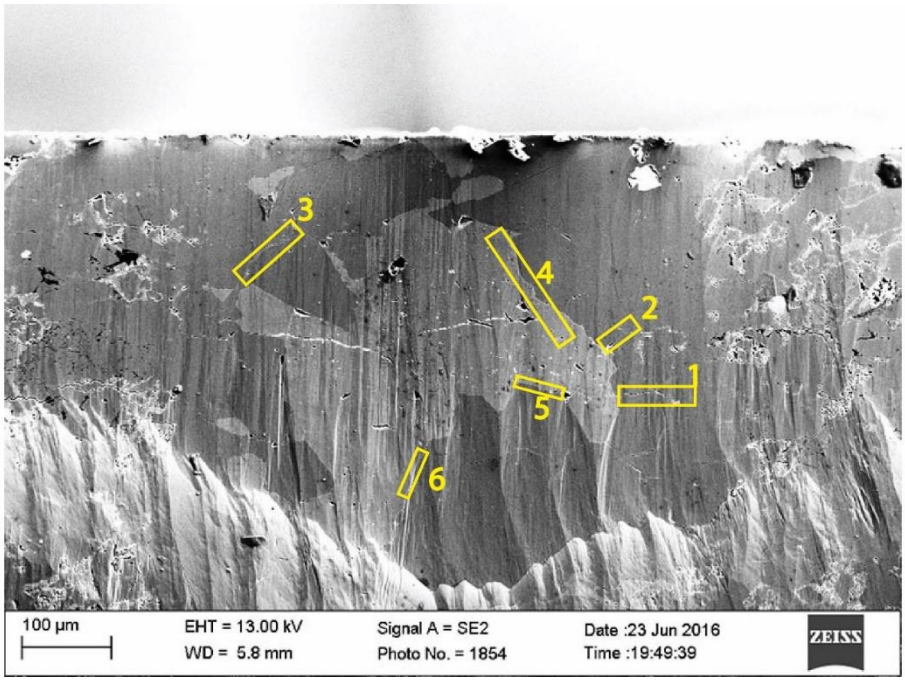

Figure A.211: SE2 micrograph of sample 12-GC-12. Boxes indicate locations of grain boundaries used for NGBC measurements.

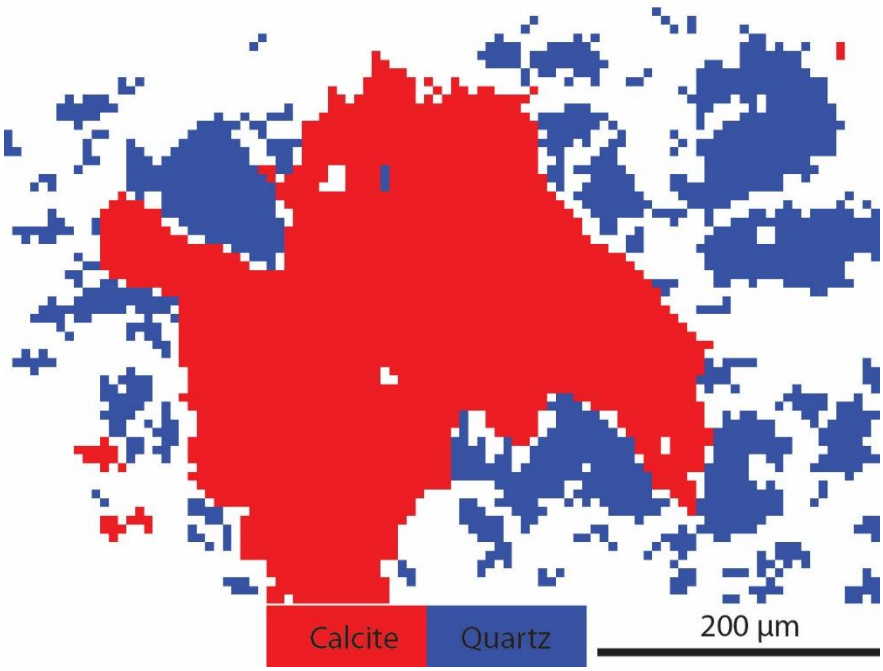

Figure A.212: EBSD phase map from sample 12-GC-12.

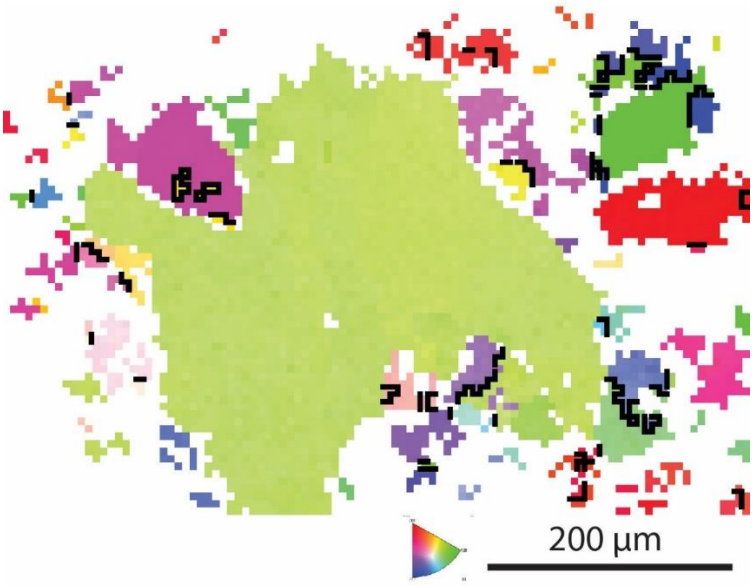

Figure A.213: EBSD inverse pole figure from sample 12-GC-12.

Grain Boundary	Mean Aperture
1.00	273.20
2.00	67.48
3.00	355.65
Sample Mean	232.11

Table A.120: NGBC mean apertures and sample mean within quartz grain boundaries from sample 12-GC-12.

Grain Boundary	Mean Aperture
4	175.40
5	24.99
6	298.06
Sample Mean	166.15

Table A.121: NGBC mean apertures and sample mean within calcite-quartz phase boundaries from sample 12-GC-12.

Grain Boundary 1 (Quartz-Quartz)

Image	Measurement number	Length (nm)
A	1	297.60
A	2	199.52
A	3	338.92
A	4	256.76
	Mean Aperture	273.20

Table A.122: NGBC measurements and mean aperture from grain boundary 1 in sample 12-GC-12.

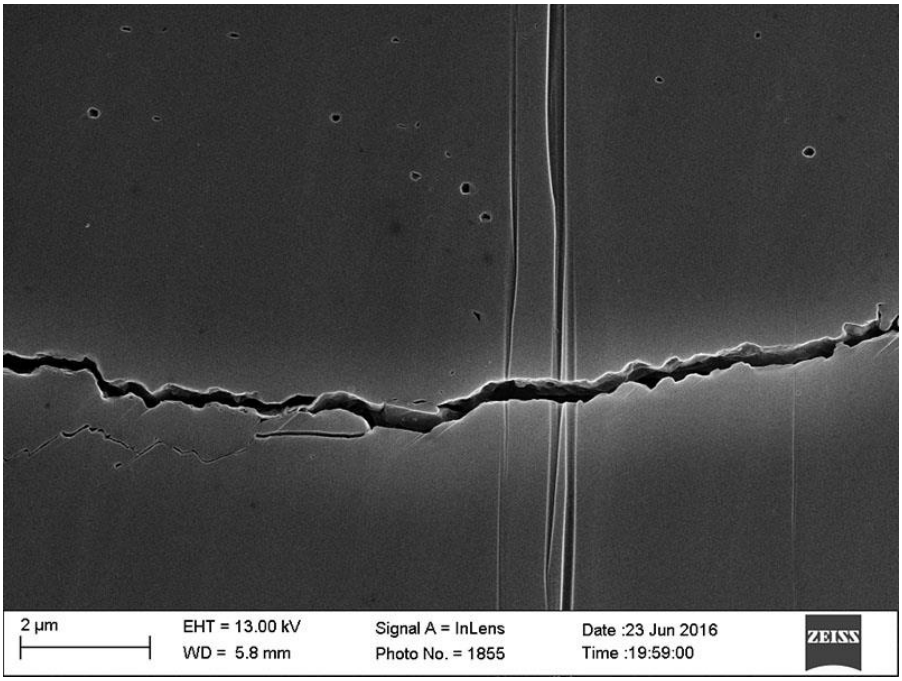

Figure A.214: Inlens SE micrograph from sample 12-GC-12. Grain boundary 1, image A.

Grain Boundary 2 (Quartz-Quartz)

Image	Measurement number	Length (nm)
A	1	66.35
A	2	70.35
A	3	69.33
A	4	59.54
A	5	59.54
A	6	63.60
A	7	76.35
A	8	68.99
A	9	70.35
A	10	70.35
	Mean Aperture	67.48

Table A.123: NGBC measurements and mean aperture from grain boundary 2 in sample 12-GC-12.

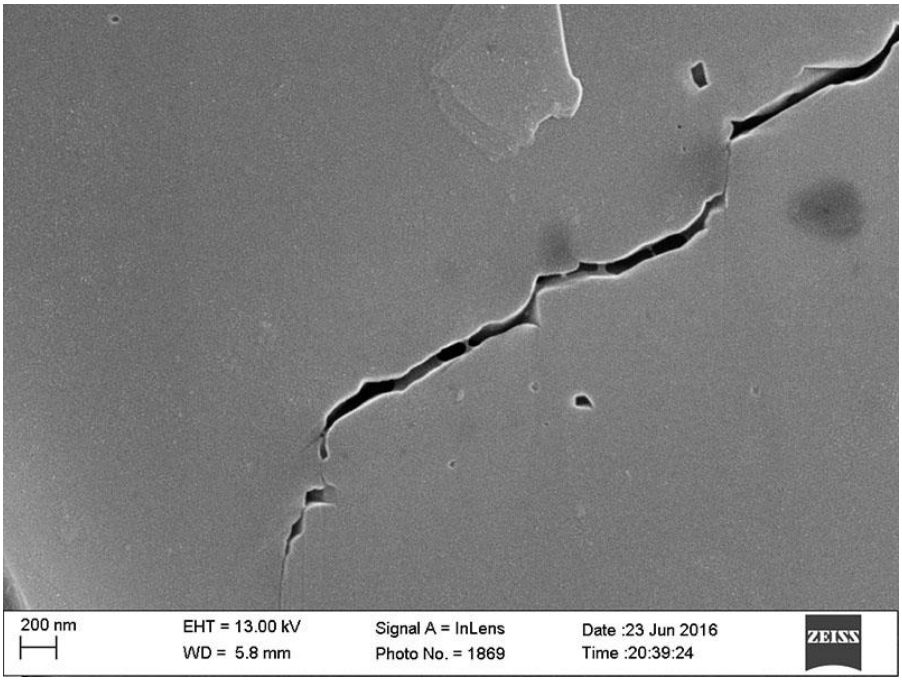

Figure A.215: Inlens SE micrograph from sample 12-GC-12. Grain boundary 2, image A.

Grain Boundary 3 (Quartz-Quartz)

Image	Measurement number	Length (nm)
A	1	397.57
A	2	365.82
A	3	381.36
A	4	382.68
B	1	385.69
B	2	393.71
B	3	411.13
B	4	392.93
B	5	384.50
C	1	271.03
C	2	277.40
C	3	291.07
C	4	317.21
C	5	326.97
	Mean Aperture	355.65

Table A.124: NGBC measurements and mean aperture from grain boundary3 in sample 12-GC-12.

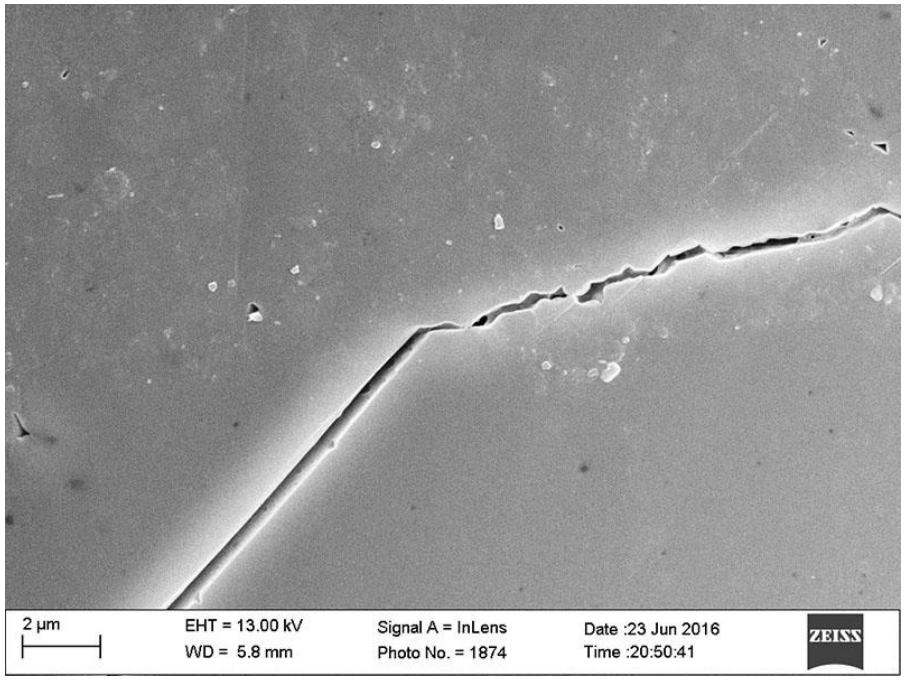

Figure A.216: Inlens SE micrograph from sample 12-GC-12. Grain boundary 3, image A.

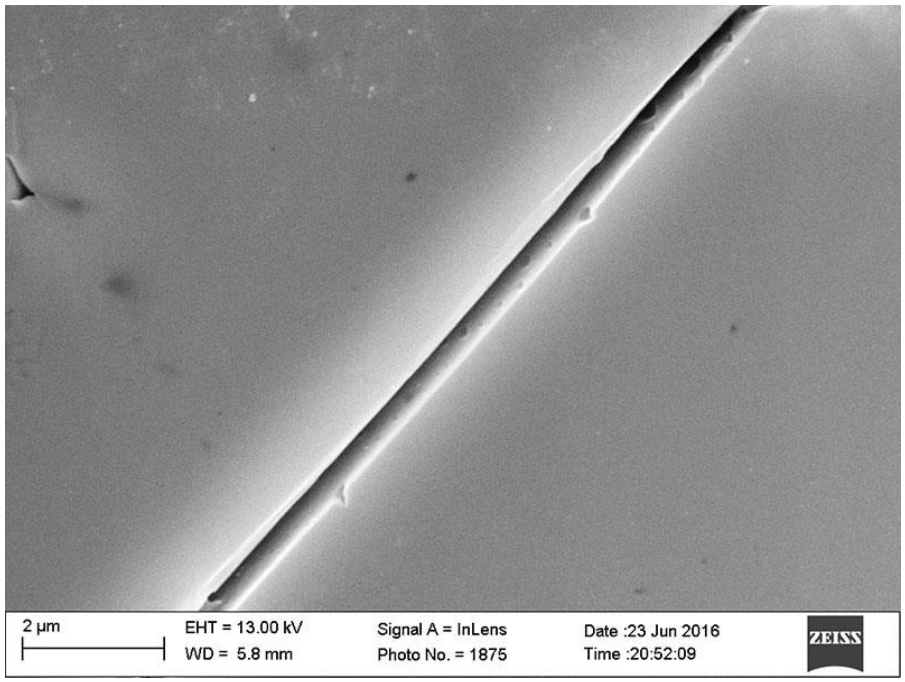

Figure A.217: Inlens SE micrograph from sample 12-GC-12. Grain boundary 3, image B.

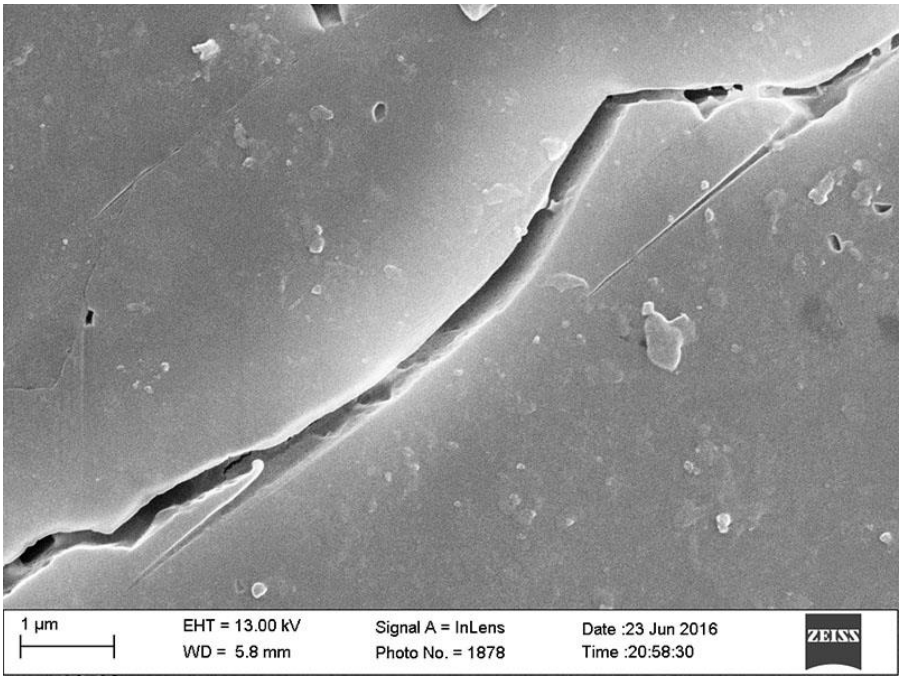

Figure A.218: Inlens SE micrograph from sample 12-GC-12. Grain boundary 3, image C.

Grain Boundary 4 (Calcite-Quartz)

Image	Measurement number	Length (nm)
A	1	239.95
A	2	223.22
A	3	194.03
A	4	189.70
A	5	166.38
A	6	171.30
A	7	171.30
A	8	148.81
A	9	189.70
A	10	194.03
A	11	179.19
B	1	128.56
B	2	116.42
B	3	102.85
B	4	116.42
B	5	102.85
B	6	116.42
B	7	116.42
C	1	289.91
C	2	280.49
C	3	259.70
C	4	297.49
D	5	119.51
D	6	119.51
D	7	140.85
D	8	119.51
D	9	119.51
D	10	119.51
E	1	235.38
E	2	242.62
E	3	134.18
E	4	160.07
E	5	111.65
E	6	168.50
	Mean Aperture	175.40

Table A.125: NGBC measurements and mean aperture from grain boundary 4 in sample 12-GC-12.

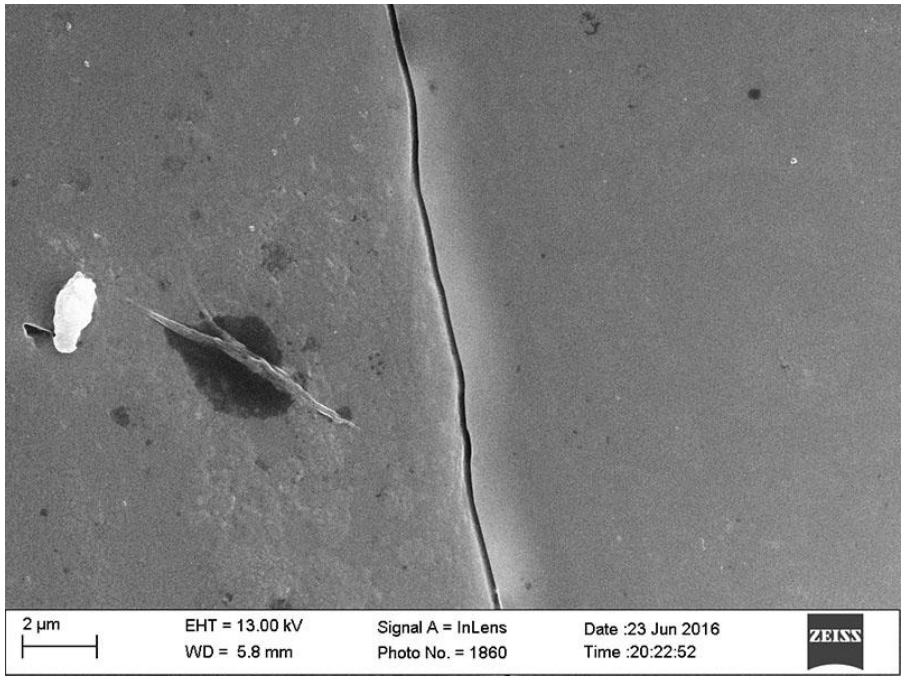

Figure A.219: Inlens SE micrograph from sample 12-GC-12. Grain boundary 4, image A.

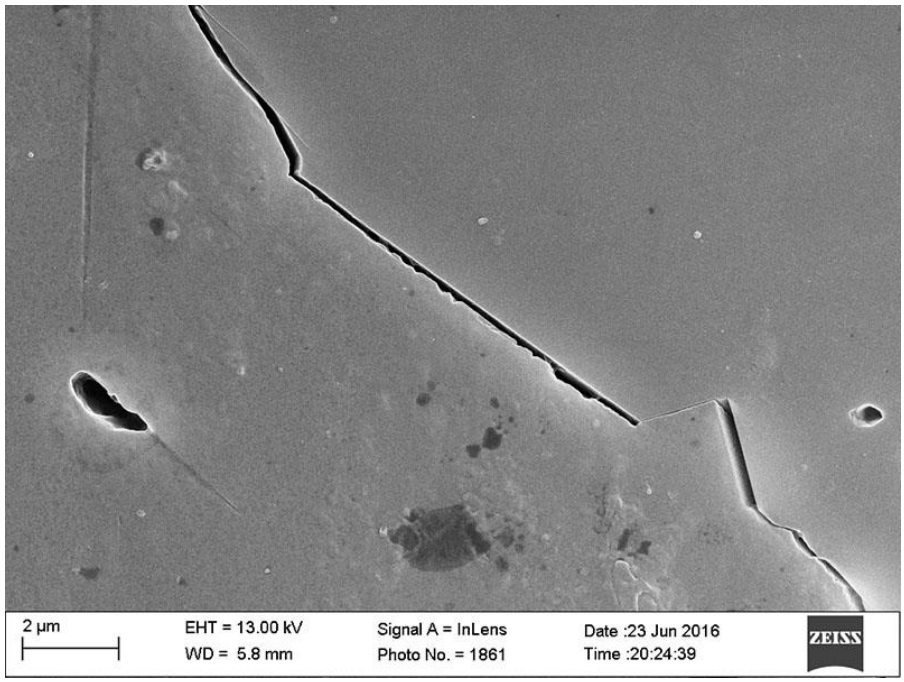

Figure A.220: Inlens SE micrograph from sample 12-GC-12. Grain boundary 4, image B.

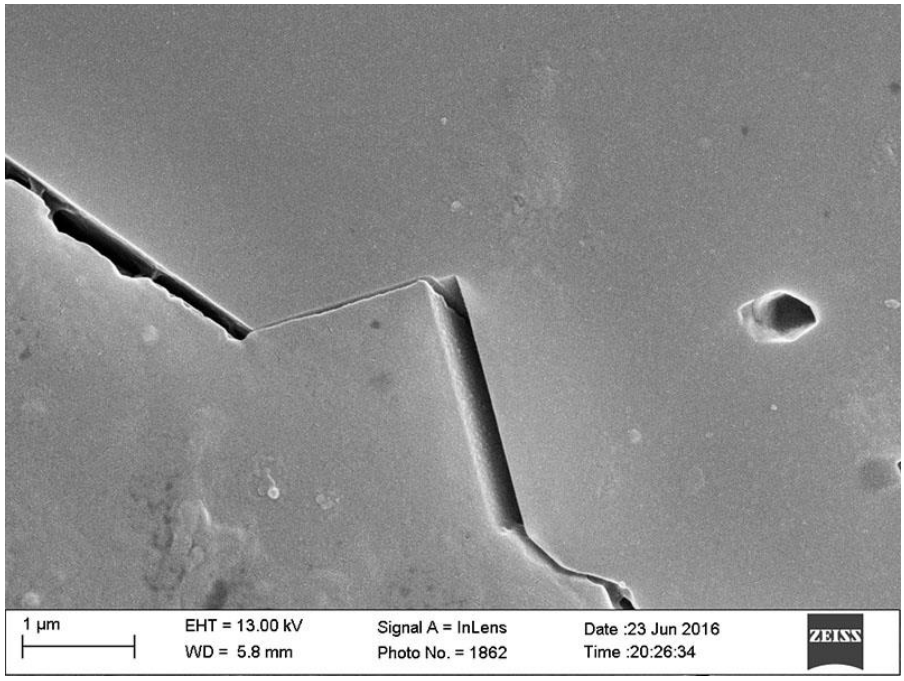

Figure A.221: Inlens SE micrograph from sample 12-GC-12. Grain boundary 4, image C.

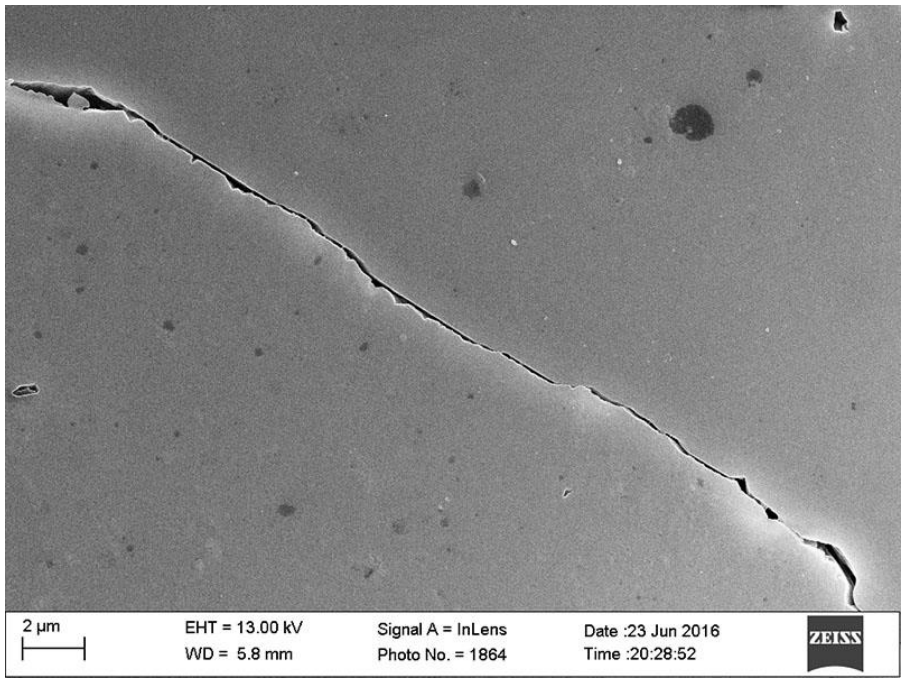

Figure A.222: Inlens SE micrograph from sample 12-GC-12. Grain boundary y 4, image D.

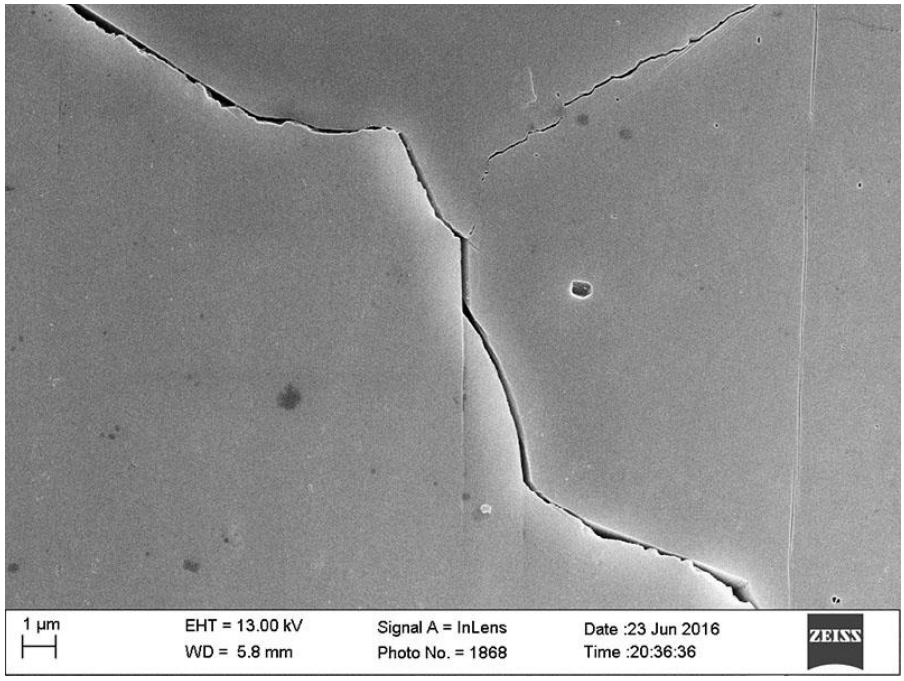

Figure A.223: Inlens SE micrograph from sample 12-GC-12. Grain boundary 4, image E.

Grain Boundary 5 (Calcite-Quartz)

Image	Measurement number	Length (nm)
A	1	23.64
A	2	21.99
A	3	29.33
	Mean Aperture	24.99

Table A.126: NGBC measurements and mean aperture from grain boundary 5 in sample 12-GC-12.

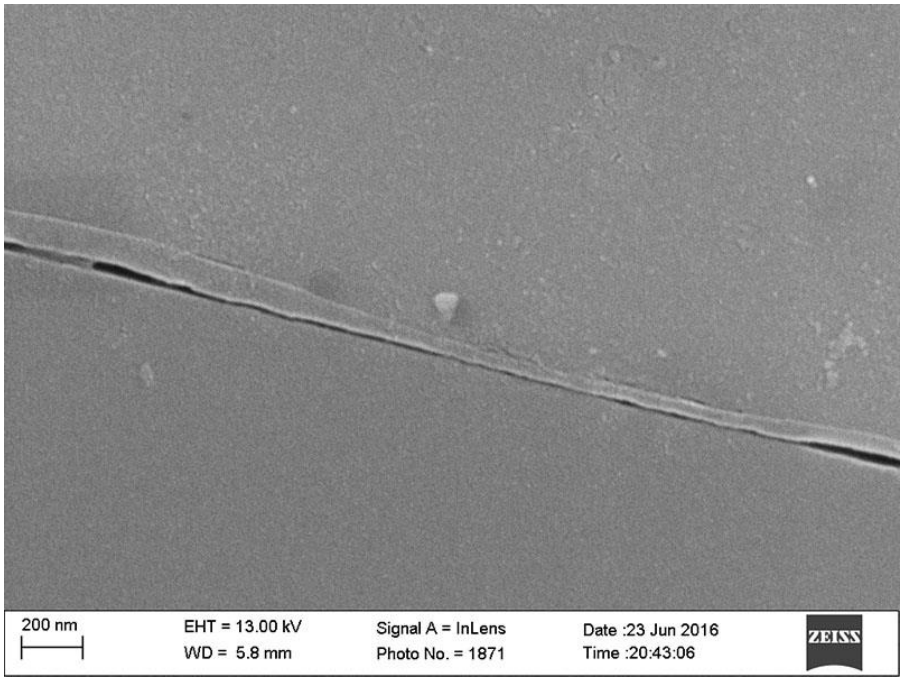

Figure A.224: Inlens SE micrograph from sample 12-GC-12. Grain boundary 5, image A.

Grain Boundary 6 (Calcite-Quartz)

Image	Measurement number	Length (nm)
A	1	322.58
A	2	258.06
A	3	273.72
A	4	288.52
A	5	347.43
	Mean Aperture	298.06

Table A.127: NGBC measurements and mean aperture from grain boundary 6 in sample 12-GC-12.

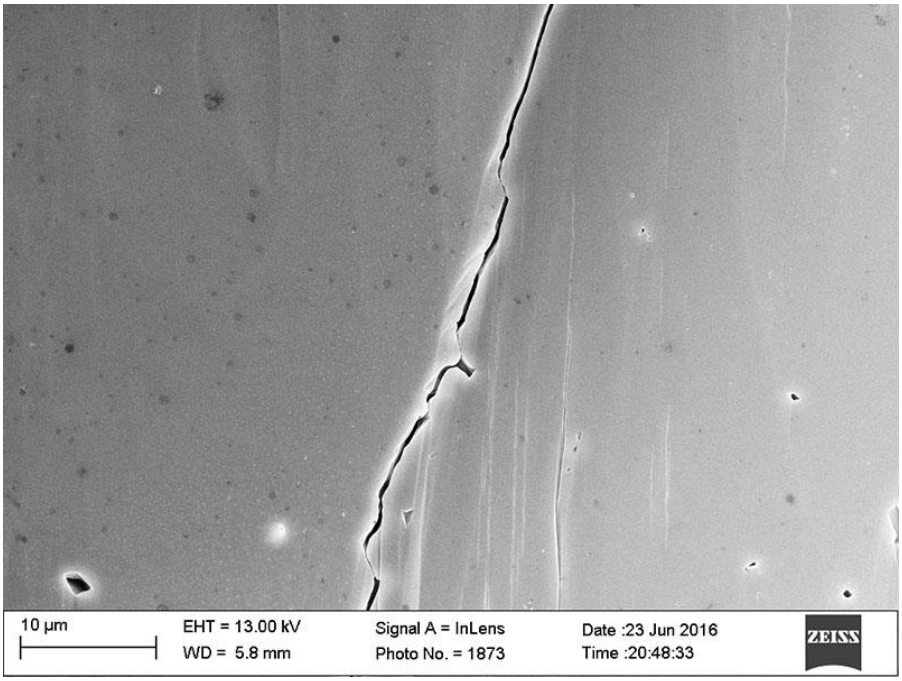

Figure A.225: Inlens SE micrograph from sample 12-GC-12. Grain boundary 6, image A.

SAMPLE 12-GC-9, NIKANASSIN FORMATION

Mineral Cement	Rock Type	Sampled Depth (ft)	Sampled Depth (m)	Max burial depth (m)	Exhumed (m)	Max T (^{o}C)	Range (nm)	Sample Mean (nm)
Calcite	Sand-stone	Outcrop	Surface	7000	7000	170-200	103-345	231.87

Table A.128: Summary of sample 12-GC-9.

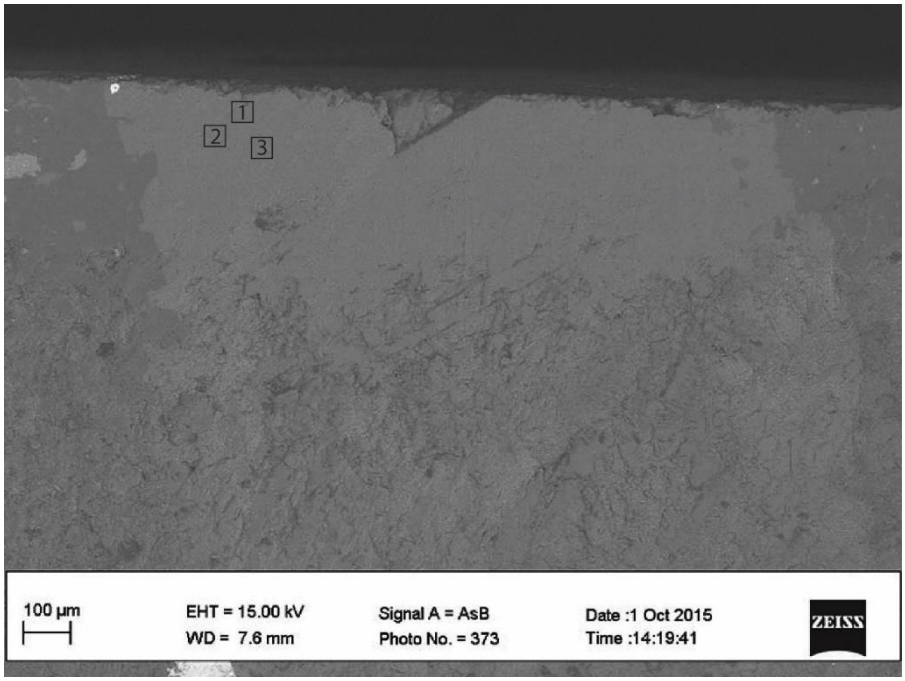

Figure A.226: BSE micrograph of sample 12-GC-9. Boxes indicate areas imaged for NGBC aperture measurements.

Grain Boundary	Mean Aperture
1	345.33
2	247.15
3	103.12
Sample Mean	231.87

Table A.129: NGBC mean apertures and sample mean from sample 12-GC-9

Grain Boundary 1

Image	Measurement	Length (nm)
A	1	348.48
A	1	357.89
A	1	357.89
A	1	332.87
A	1	329.53
	Mean Aperture	345.33

Table A.130: NGBC measurements and mean aperture from grain boundary 1 in sample 12-GC-9.

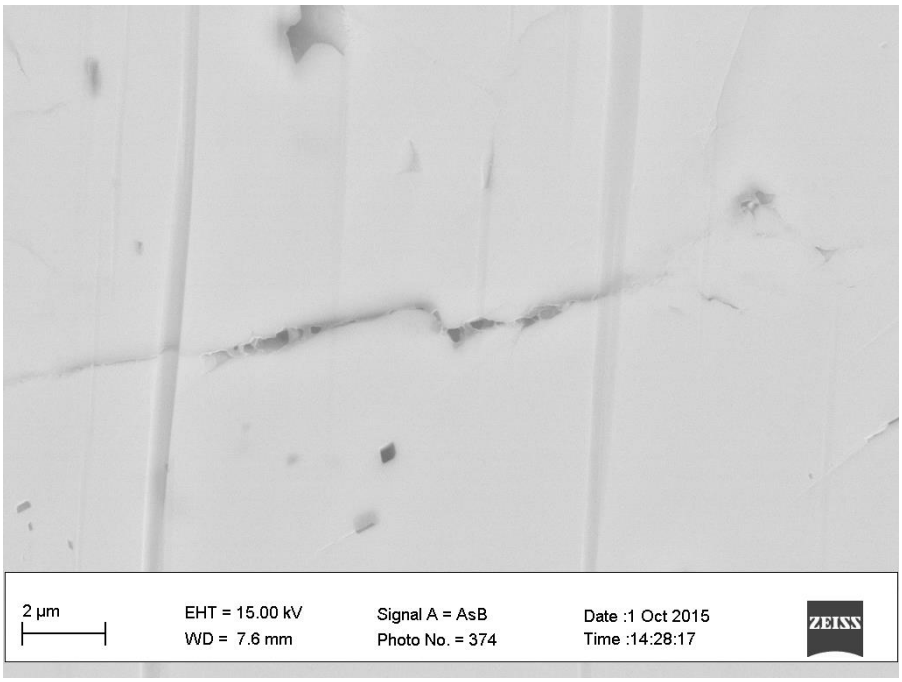

Figure A.227: Inlens SE micrograph from sample 12-GC-9. Grain boundary 1, image A.

Grain Boundary 2

Image	Measurement	Length (nm)
A	2	284.83
A	2	256.87
A	2	199.74
	Mean Aperture	247.15

Table A.131: NGBC measurements and mean aperture from grain boundary 2 in sample 12-GC-9.

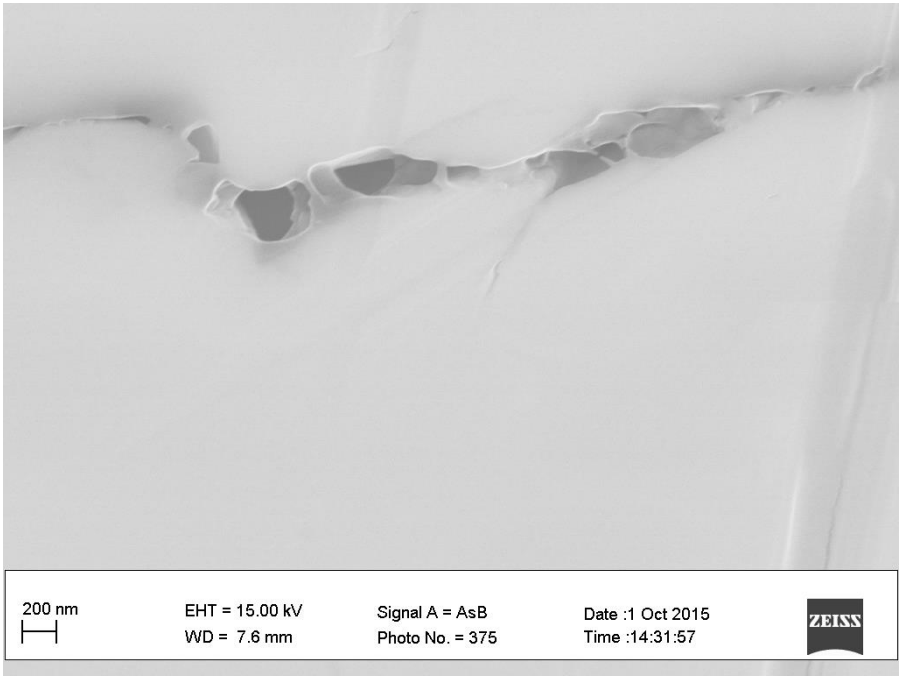

Figure A.228: Inlens SE micrograph from sample 12-GC-9. Grain boundary 2, image A.

Grain Boundary 3

Image	Measurement	Length (nm)
A	3	138.05
A	3	135.84
A	3	137.76
A	3	96.78
A	3	55.13
A	3	55.13
	Mean Aperture	103.12

Table A.132: NGBC measurements and mean aperture from grain boundary 3 in sample 12-GC-9.

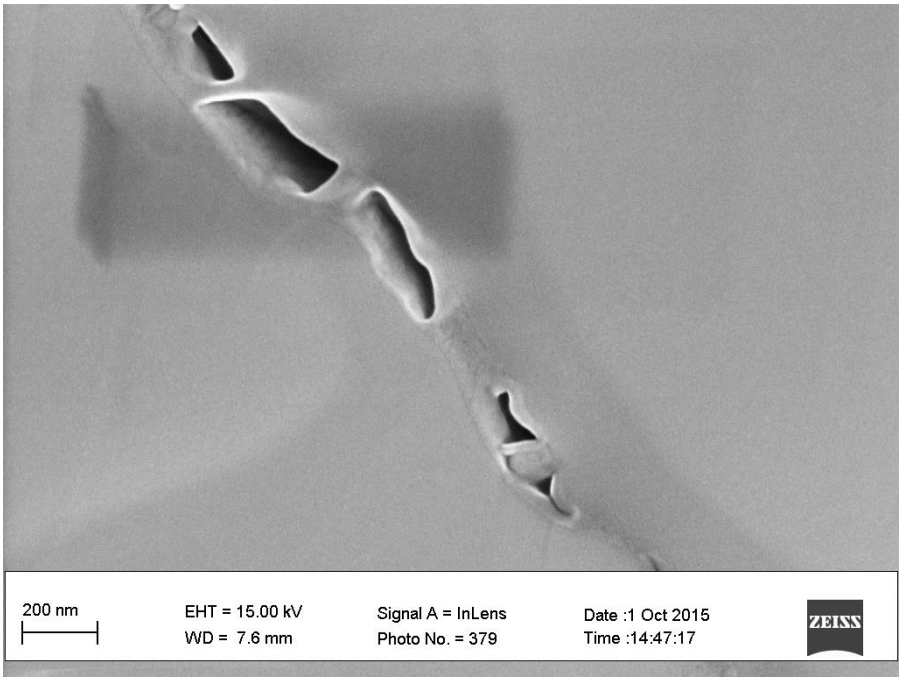

Figure A.229: Inlens SE micrograph from sample 12-GC-9. Grain boundary 3, image A.

SAMPLE 12-RF-2, CARDIUM FORMATION

Mineral Cement	Rock Type	Sampled Depth (ft)	Sampled Depth (m)	Max burial depth (m)	Exhumed (m)	Max T (°C)	Range (nm)	Sample Mean (nm)
Calcite	Sandstone	Outcrop	Surface	5000	5000	100-120	70-280	201.39

Table A.133: Summary of sample 12-RF-2

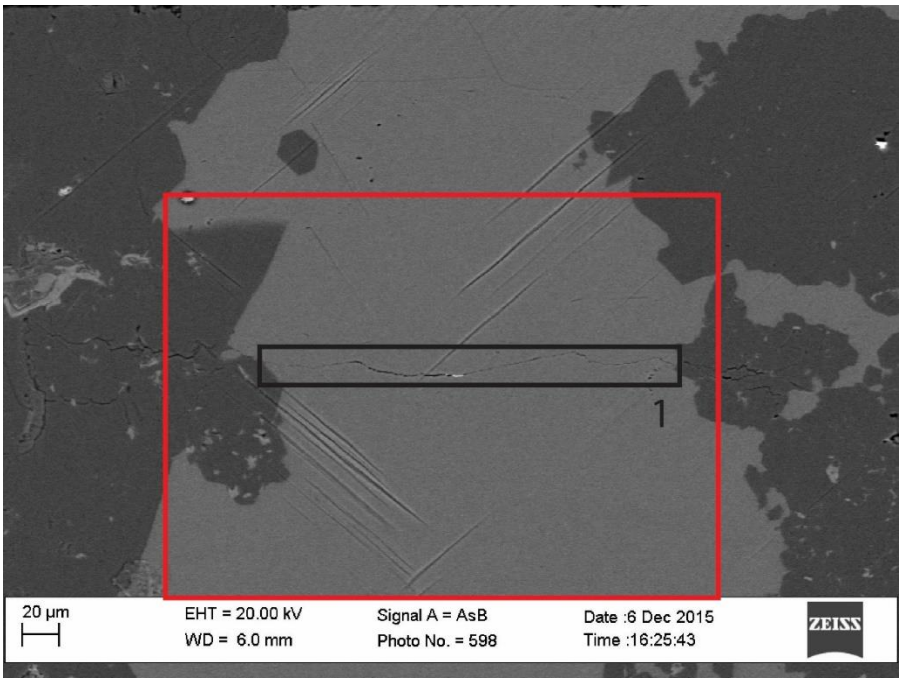

Figure A.230 BSE micrograph of sample 12-RF-2. Red box indicates areas imaged for EBSD. Black box indicates location of grain boundary used for NGBC aperture measurements as mapped by EBSD.

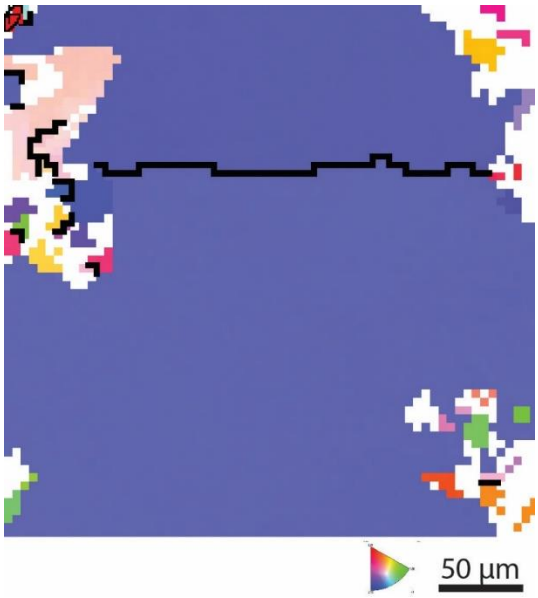

Figure A.231: EBSD inverse pole figure from sample 12-RF-2.

Grain Boundary	Mean Aperture
1	201.39
Sample Mean	201.39

Table A.134: NGBC mean apertures and sample mean from sample 12-RF-2

Grain Boundary 1

Image	Measurement Number	Length (nm)
A	1	268.0727
A	2	277.7945
A	3	254.5334
A	4	268.0727
B	1	102.4044
B	2	70.53669
B	3	168.2904
	Mean Aperture	201.3864

Table A.135: NGBC measurements and mean aperture from grain boundaries 1 in sample 12-RF-2.

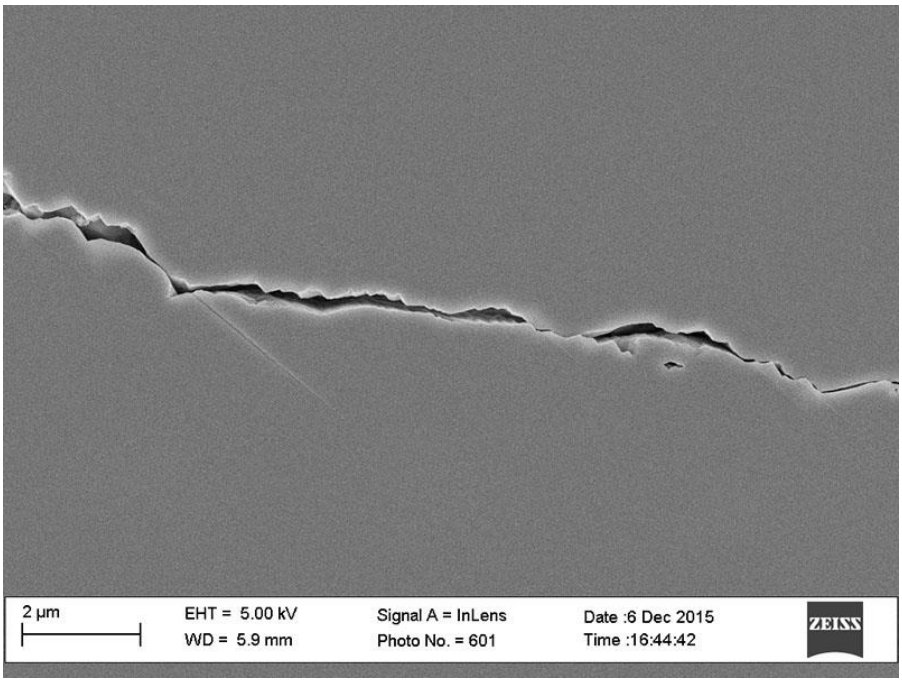

Figure A.232: Inlens SE micrograph from sample 12-RF-2. Grain boundary 1, image A.

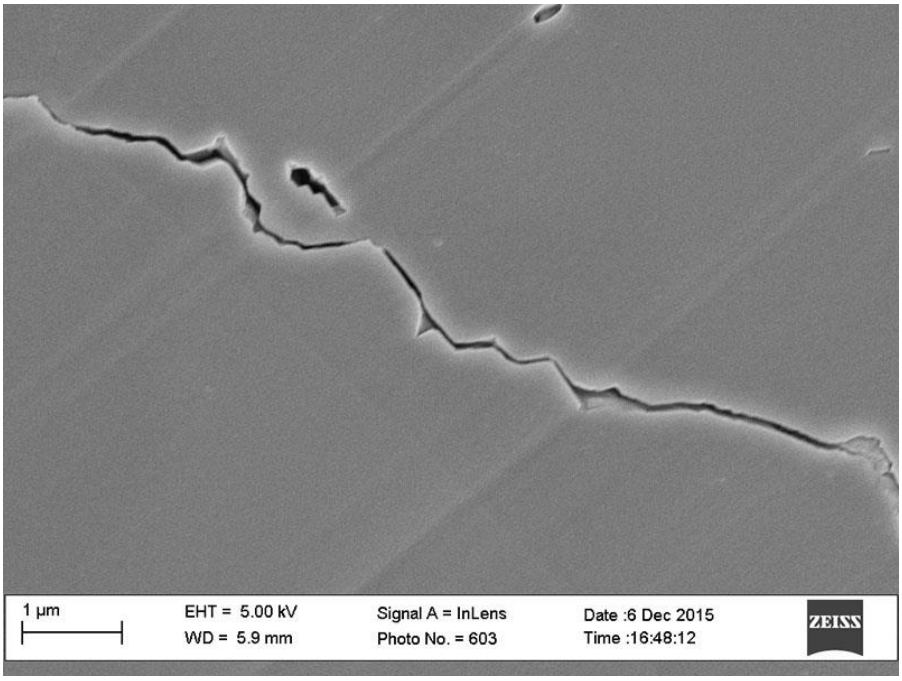

Figure A.233: Inlens SE micrograph from sample 12-RF-2. Grain boundary 1, image B.

SAMPLE: 12-BR-3, CARDIUM FORMATION

Mineral Cement	Rock Type	Sampled Depth (ft)	Sampled Depth (m)	Max burial depth (m)	Exhumed (m)	Max T (°C)	Range (nm)	Sample Mean (nm)
Quartz	Sandstone	Outcrop	Surface	5000	5000	100-120	65-165	101.34

Table A.136: Summary of sample 12-BR-3

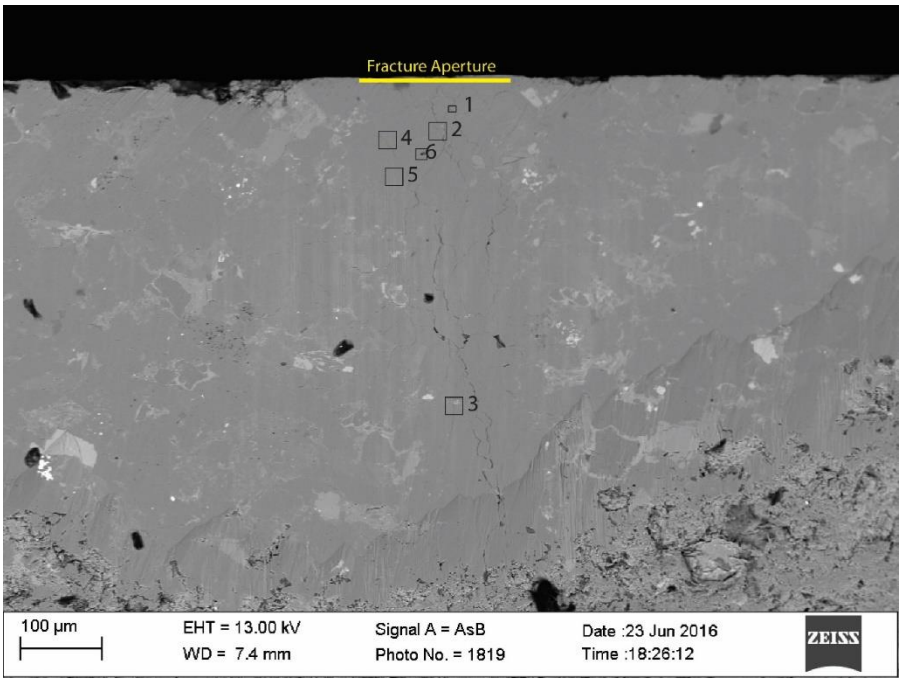

Figure A.234: BSE micrograph of sample 12-BR-3. Boxes indicate areas imaged for NGBC aperture measurements.

Grain Boundary	Mean Aperture (nm)
1	104.56
2	165.08
3	75.88
4	64.87
5	130.05
6	67.60
Sample Mean	101.34

Table A.137: NGBC mean apertures and sample mean from sample 12-BR-3.

Grain Boundary 1

Image	Measurement Number	Length
A	1	106.6976
A	2	110.0548
A	3	99.80636
A	4	109.0794
A	5	97.18059
	Mean Aperture	104.5638

Table A.138: NGBC measurements and mean aperture from grain boundary 1 in sample 12-BR-3.

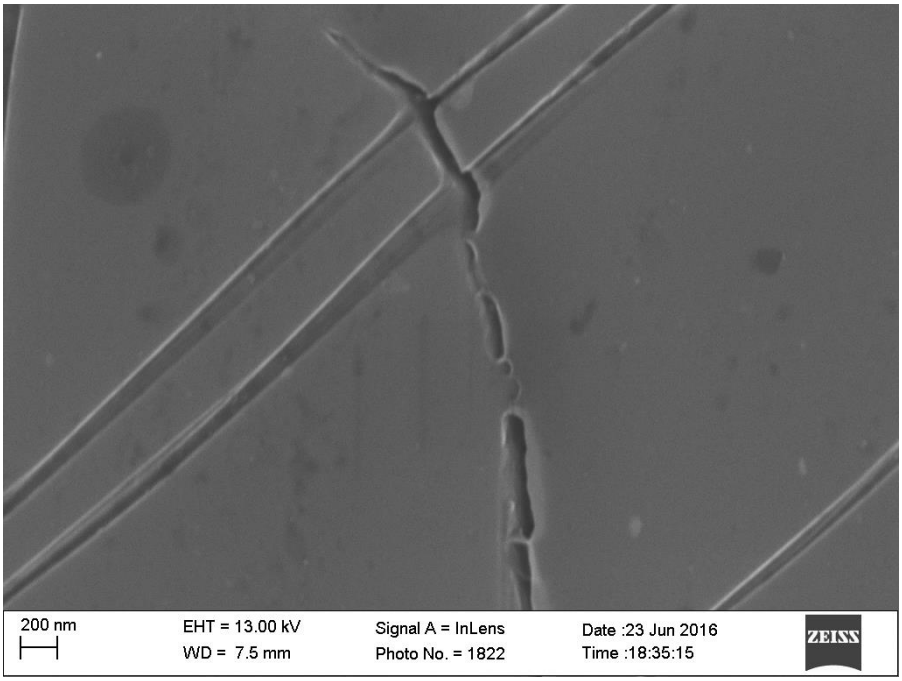

Figure A.235: Inlens SE micrograph from sample 12-BR-3. Grain boundary 1, image A.

Grain Boundary 2

Image	Measurement Number	Length
A	1	155.8137
A	2	164.9825
A	3	177.5785
A	4	152.0776
A	5	174.9349
	Mean Aperture	165.0774

Table A.139: NGBC measurements and mean aperture from grain boundary 2 in sample 12-BR-3.

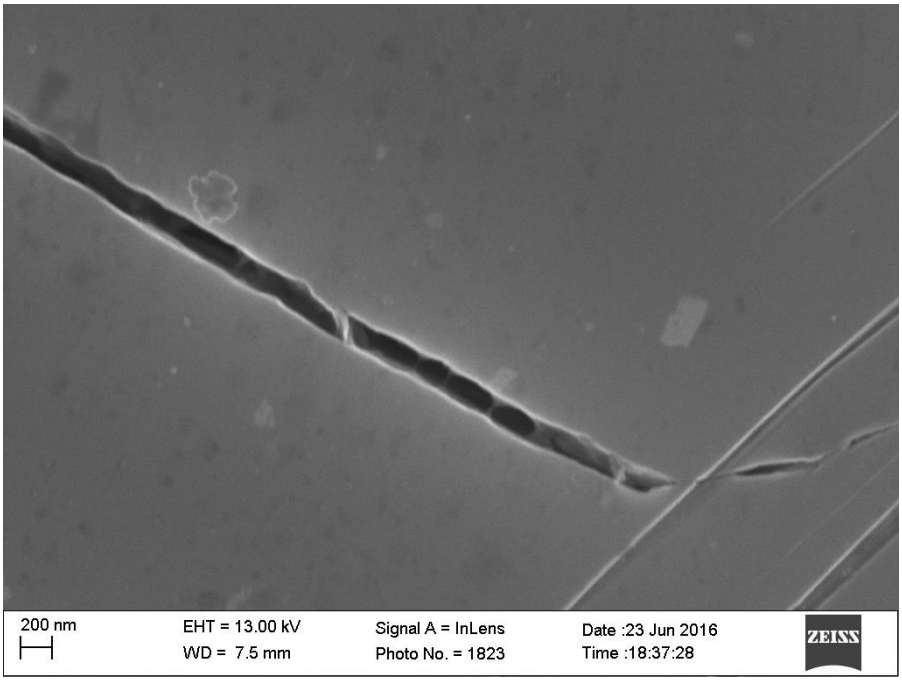

Figure A.236: Inlens SE micrograph from sample 12-BR-3. Grain boundary 2, image A.

Grain Boundary 3

Image	Measurement Number	Length
A	1	78.22813
A	2	80.0394
A	3	81.78375
A	4	68.48067
A	5	83.45354
A	6	94.80536
A	7	104.9624
A	8	72.83624
A	9	84.03665
A	10	49.33489
A	11	72.77938
A	12	58.17888
A	13	66.39249
A	14	67.01853
	Mean Aperture	75.88074

Table A.140: NGBC measurements and mean aperture from grain boundary 7 in sample 12-BR-3.

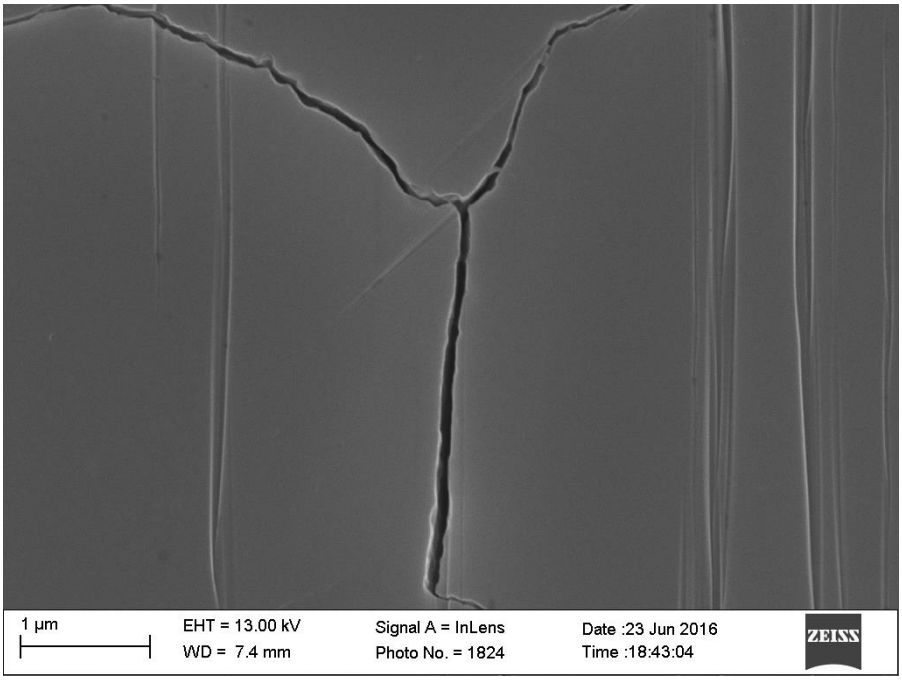

Figure A.237: Inlens SE micrograph from sample 12-BR-3. Grain boundary 3, image A.

Grain Boundary 4

Image	Measurement Number	Length
A	1	75.20942
A	2	91.21805
A	3	68.12708
A	4	57.99696
A	5	55.6372
A	6	52.83556
A	7	53.0548
	Mean Aperture	64.86844

Table A.141: NGBC measurements and mean aperture from grain boundary 4 in sample 12-BR-3.

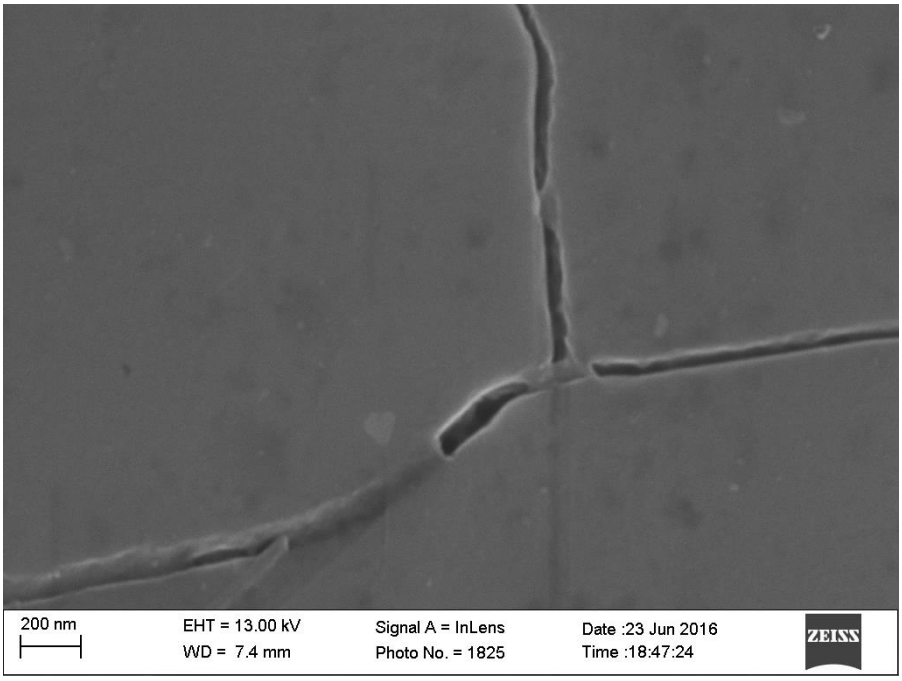

Figure A.238: Inlens SE micrograph from sample 12-BR-3. Grain boundary 4, image A.

Grain Boundary 5

Image	Measurement Number	Length
A	1	91.15936
A	2	139.5768
A	3	146.7617
A	4	147.1125
A	5	125.616
	Mean Aperture	130.0453

Table A.142: NGBC measurements and mean aperture from grain boundary 5 in sample 12-BR-3.

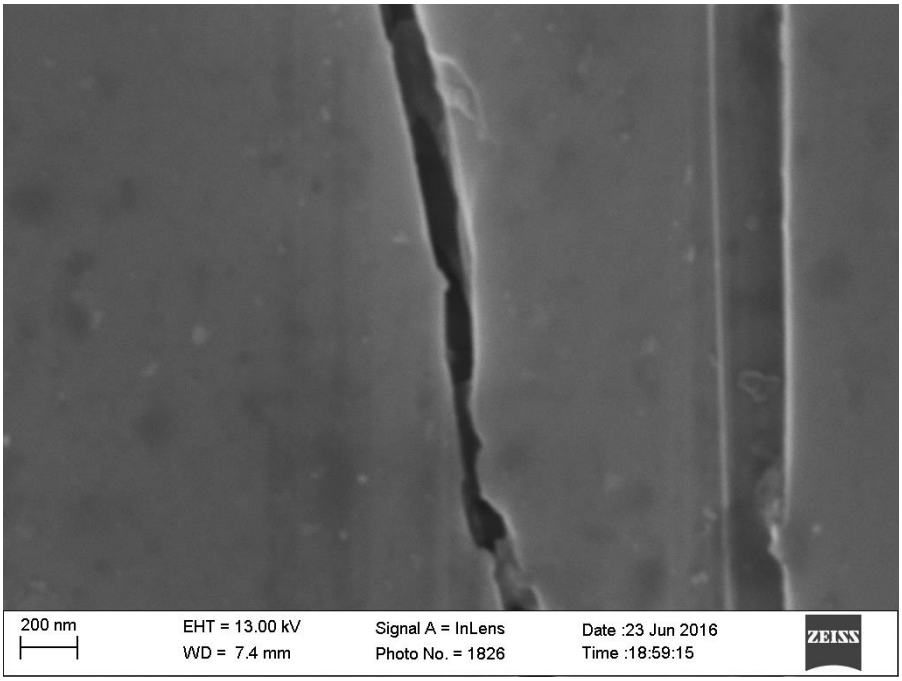

Figure A.239: Inlens SE micrograph from sample 12-BR-3. Grain boundary 5, image A.

Grain Boundary 6

Image	Measurement Number	Length
A	1	64.54289
A	2	54.57686
A	3	74.7403
A	4	59.99162
A	5	71.39235
B	1	67.47032
B	2	74.40564
B	3	74.84234
B	4	66.46419
	Mean Aperture	67.60294

Table A.143: NGBC measurements and mean aperture from grain boundary 6 in sample 12-BR-3.

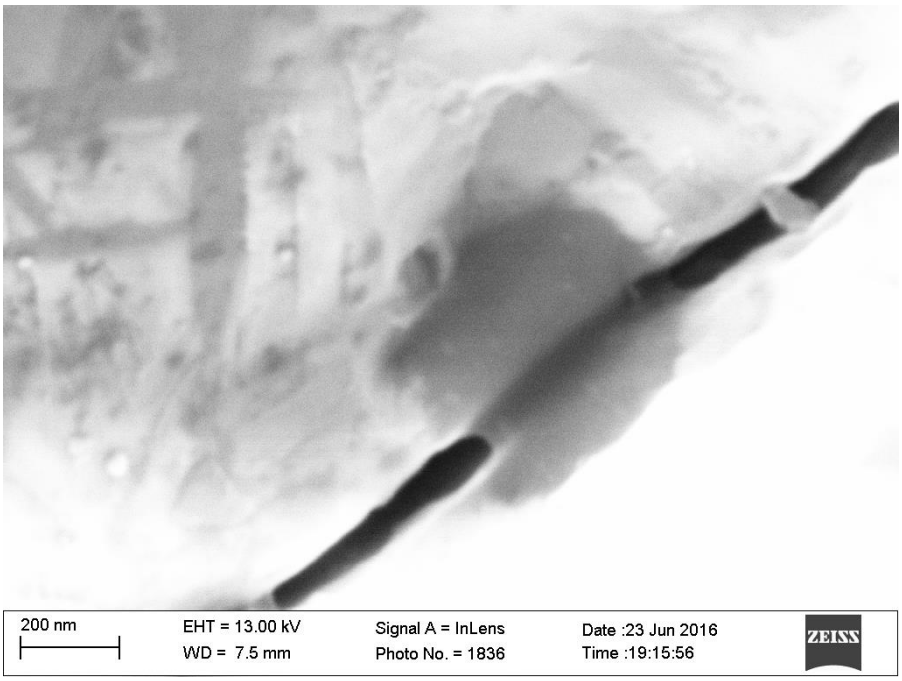

Figure A.240: Inlens SE micrograph from sample 12-BR-3. Grain boundary 6, image A.

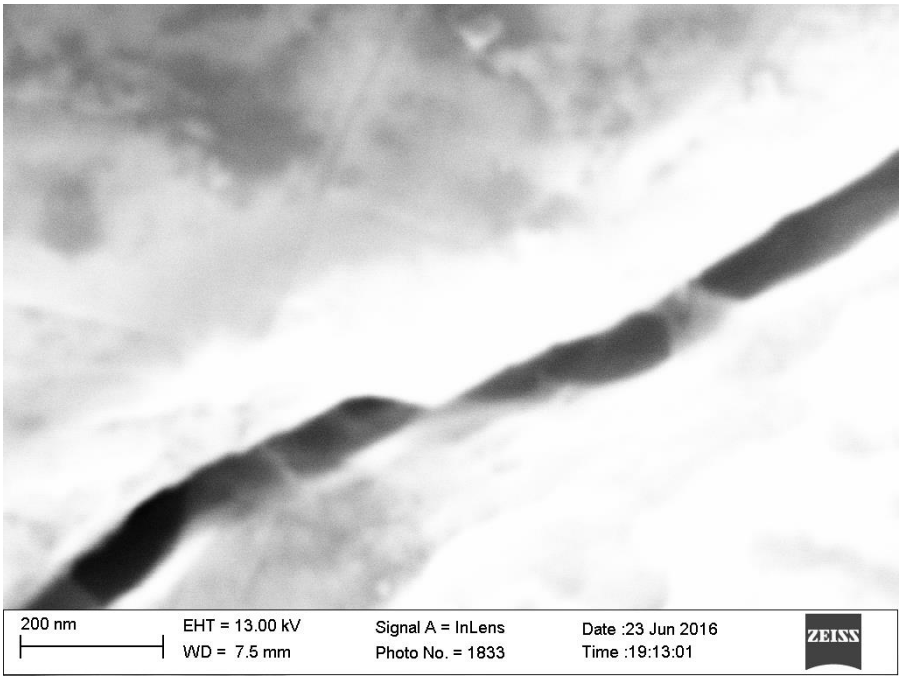

Figure A.241: Inlens SE micrograph from sample 12-BR-3. Grain boundary 6, image A.

BRTC1-12083, BARNETT FORMATION

Mineral Cement	Rock Type	Sampled Depth (ft)	Sampled Depth (m)	Max burial depth (m)	Exhumed (m)	Max T (^{o}C)	Range (nm)
Shale	12083	3682.898	3682.898	0	105-110	45-223	128.67

Table A.144: Summary of sample BRTC1-12083

Figure A.242: Inlens SE micrograph of sample BRTC1-12083. Box indicates area imaged for EBSD analysis and NGBC aperture measurements.

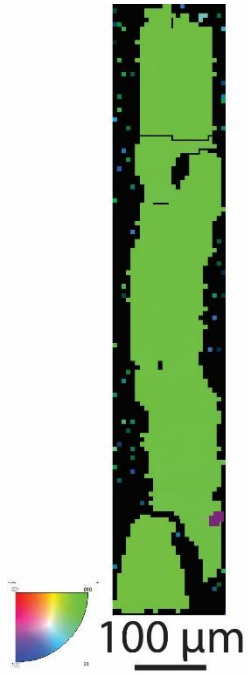

Figure A.243: EBSD inverse pole figure from sample BRTC1-12083.

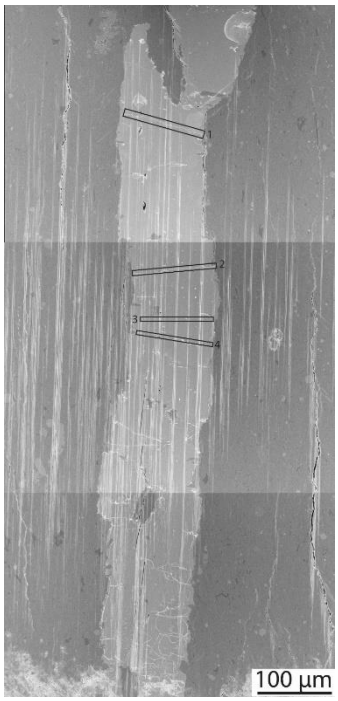

Figure A.244: Inlens SE mosaic of sample BRTC1-12083. Boxes indicate location of grain boundaries used for NGBC aperture measurements.

Grain Boundary	Mean Aperture
1	164.30
2	222.89
3	45.35
4	82.13
Overall Sample Mean	128.67

Table A.145: NGBC mean apertures and sample mean from sample BRTC1-12083.

Grain Boundary 1

Image	Measurement Number	Length (nm)
A	1	173.00
A	2	154.56
A	3	157.97
A	4	171.66
	Mean Aperture	164.30

Table A.146: NGBC measurements and mean aperture from grain boundary 1 in sample BRTC1-12083.

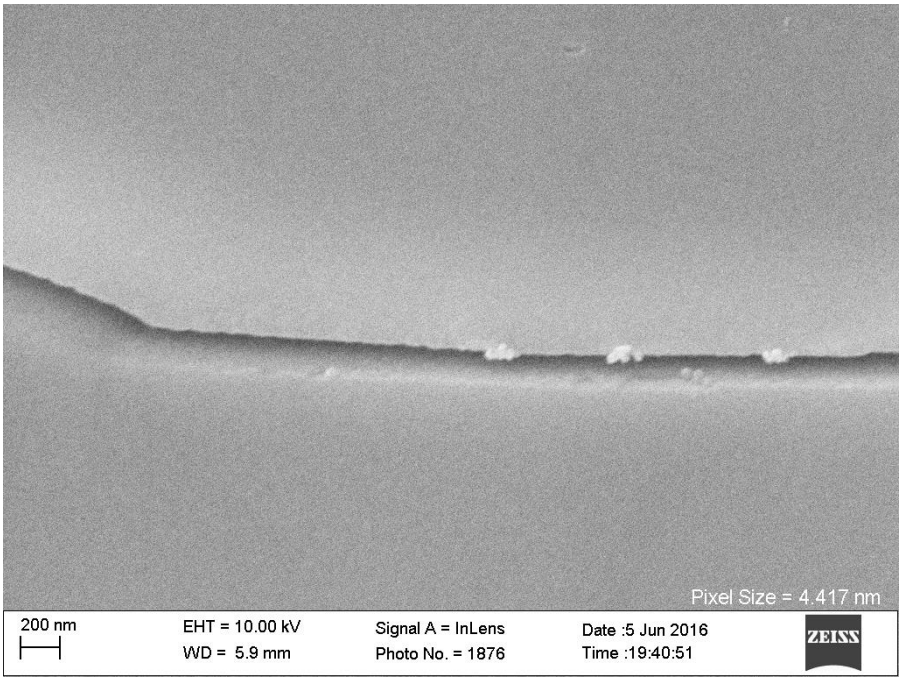

Figure A.245: Inlens SE micrograph from sample BRTC1-12083. Grain boundary 1, image.

Grain Boundary 2

Image	Grain Number	Length (nm)
A	1	240.86
A	2	204.92
	Mean Aperture	222.89

Table A.147: NGBC measurements and mean aperture from grain boundary 2 in sample BRTC1-12083.

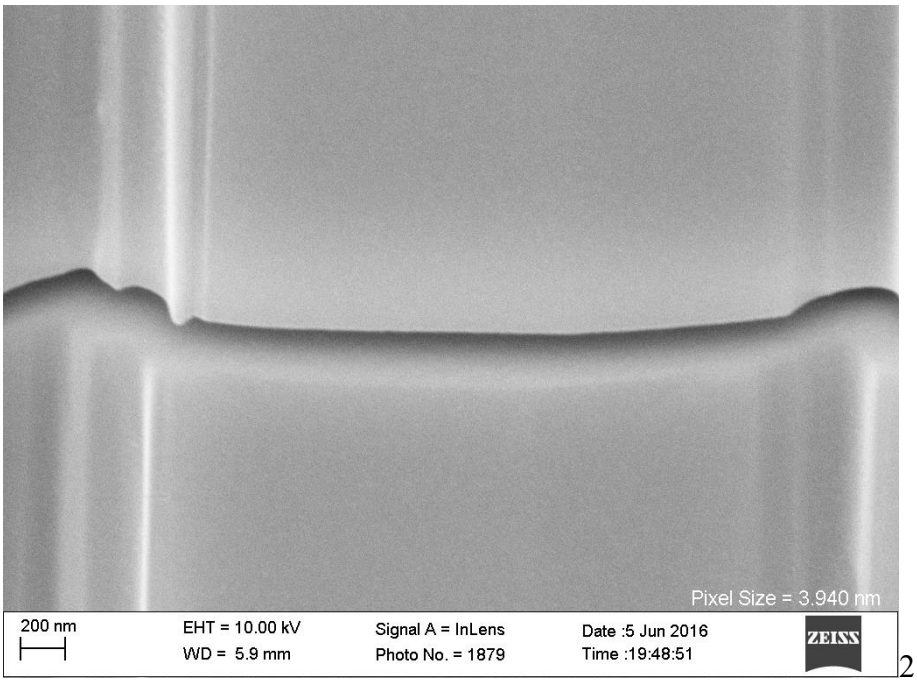

2

Figure A.246: Inlens SE micrograph from sample BRTC1-12083. Grain boundary 2, image A.

Grain Boundary 3

Image	Grain Number	Length (nm)
A	1	45.62
A	2	42.81
A	3	42.16
A	4	48.07
A	5	48.07
	Mean Aperture	45.35

Table A.148: NGBC measurements and mean aperture from grain boundary3 in sample BRTC1-12083.

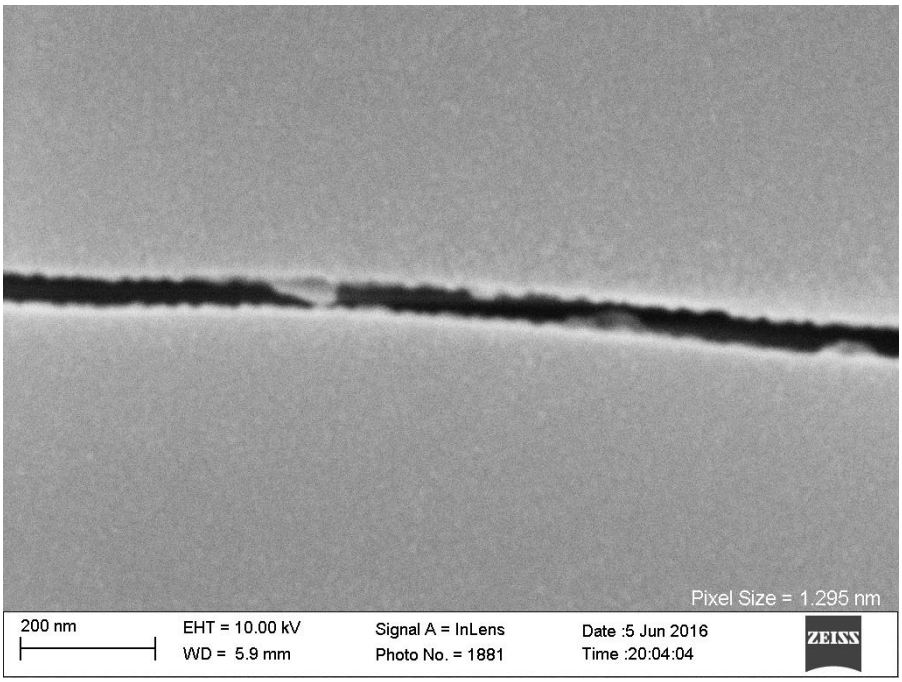

Figure A.247: Inlens SE micrograph from sample BRTC1-12083. Grain boundary 3, image A.

Grain Boundary 4

Image	Grain Number	Length (nm)
A	1	88.87
A	2	71.64
A	3	85.87
	Mean Aperture	82.13

Table A.149: NGBC measurements and mean aperture from grain boundary 4 in sample BRTC1-12083.

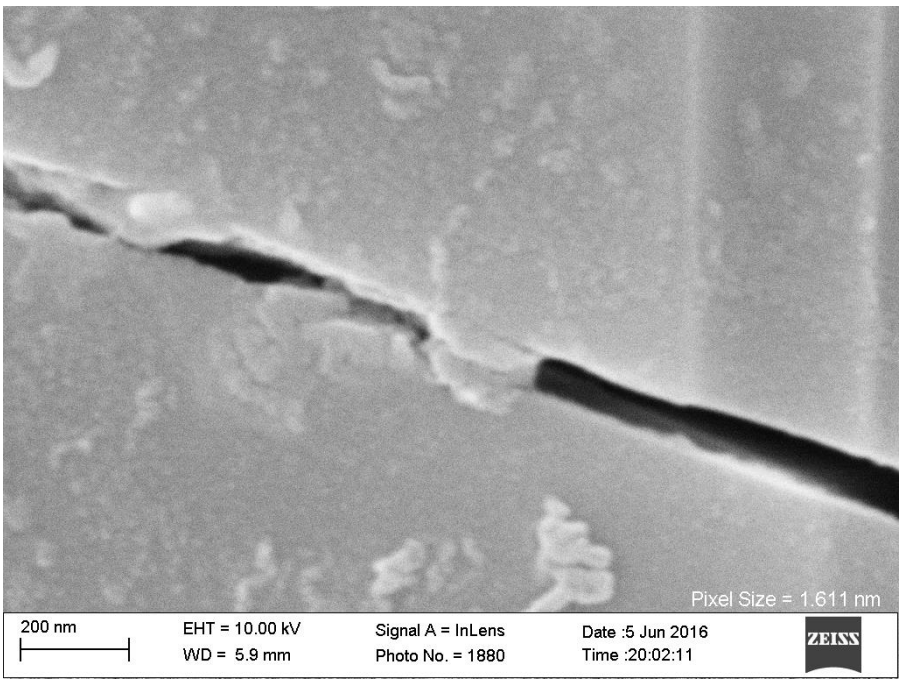

Figure A.248: Inlens SE micrograph from sample BRTC1-12083. Grain boundary 4, image A.

BRTC1-12421, BARNETT FORMATION

Mineral Cement	Rock Type	Sampled Depth (ft)	Sampled Depth (m)	Max burial depth (m)	Exhumed (m)	Max T (°C)	Range (nm)	Sample Mean (nm)
Calcite	Shale	12421	3785	3785	0	105-110	17.6	17.60
Calcite-Barite	Shale	12421	3785	3785	0	105-110	81-400	240.7

Table A.150: Summary of sample BRTC1-12421

Figure A.249: Inlens SE micrograph of sample BRTC1-12421. Red box indicates area imaged for EBSD analysis and NGBC aperture measurements. Black boxes indicate locations of grain boundaries used for NGBC aperture measurements.

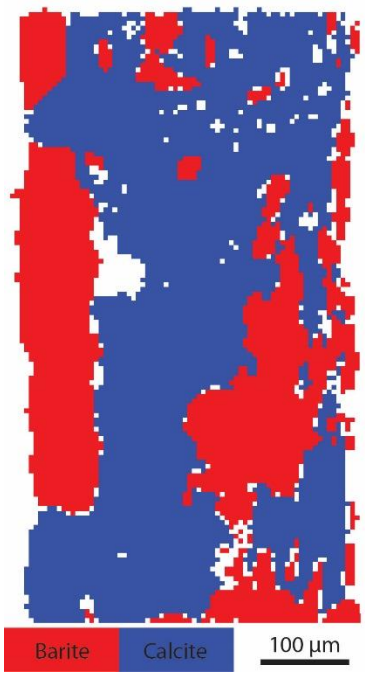

Figure A.250: EBSD phase map from sample BRTC1-12421.

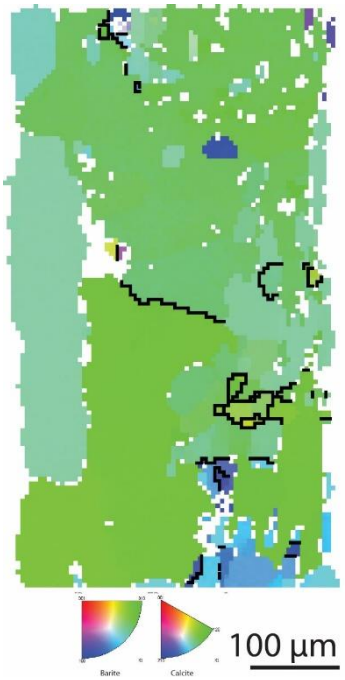

Figure A.251: EBSD inverse pole figure from sample BRTC1-12421.

Grain Boundary	Mean Aperture
1	17.6
Sample Mean	17.6

Table A.151: NGBC mean apertures and sample mean within calcite grain boundaries from sample BRTC1-12421.

Grain Boundary	Mean Aperture
2	400.29
3	81.11
Sample Mean	240.70

Table A.152: NGBC mean apertures and sample mean within calcite-barite phase boundaries from sample BRTC1-12421.

Grain Boundary 1 (Calcite-Calcite)

A	1	22.31
A	2	18.88
A	3	16.61
A	4	23.46
A	5	21.01
B	1	12.60
B	2	13.24
B	3	12.65
	Mean Aperture	17.60

Table A.153: NGBC measurements and mean aperture from grain boundary 1 in sample BRTC1-12083.

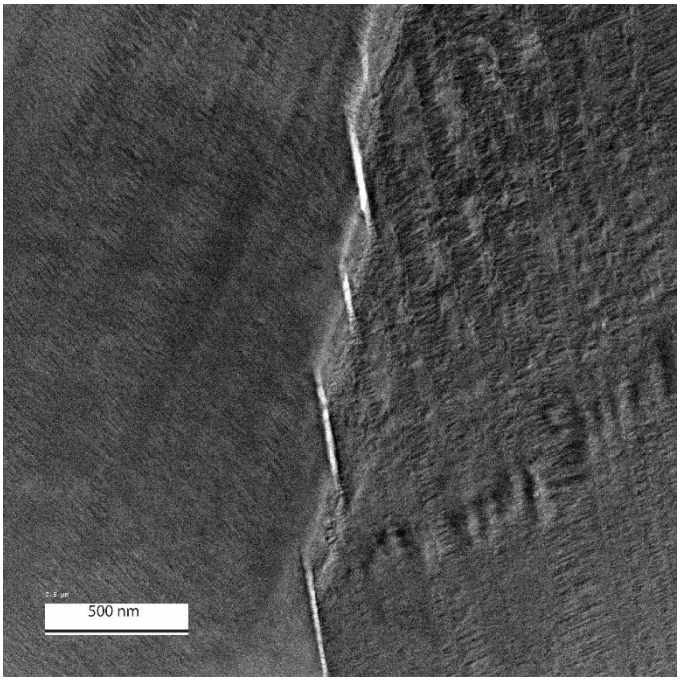

Figure A.252: Bright field TEM micrograph from sample BRTC1-12421. Grain boundary 1, image B.

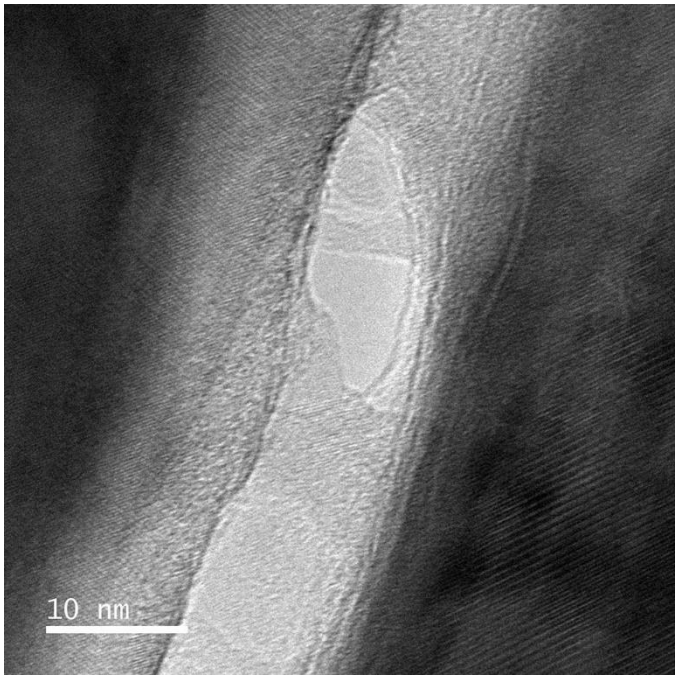

Figure A.253: Bright field TEM micrograph from sample BRTC1-12421. Grain boundary 1, image B.

Grain Boundary 2 (Calcite-Barite)

Image	Measurement Number	Length (nm)
A	1	926.41
A	2	976.28
A	3	1053.74
B	1	96.68
B	2	75.19
B	3	110.60
B	4	96.08
B	5	125.73
B	6	141.90
	Mean Aperture	400.29

Table A.154: NGBC measurements and mean aperture from grain boundary 2 in sample BRTC1-12421.

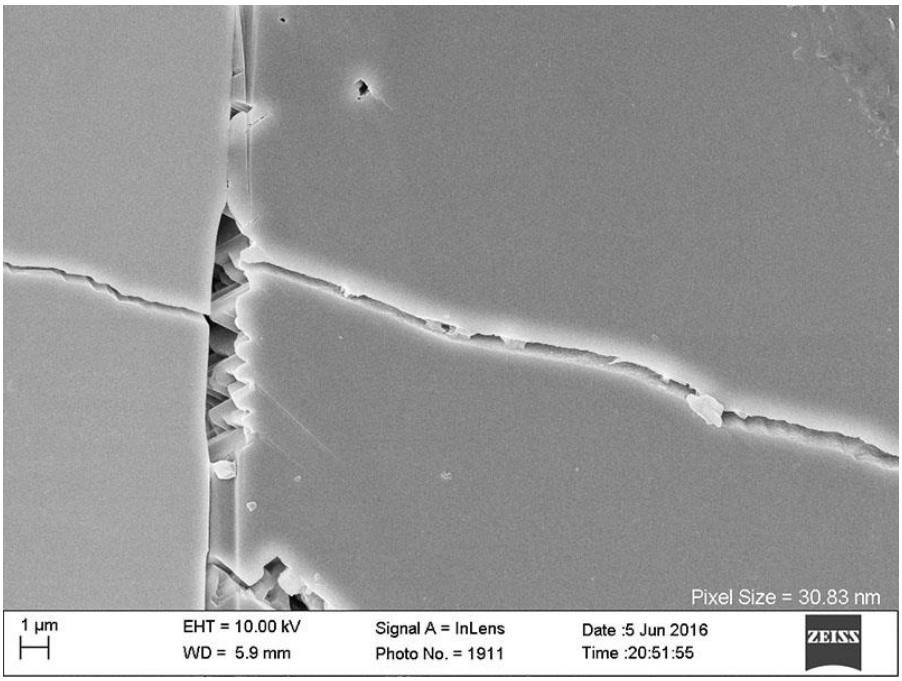

Figure A.254: Inlens SE micrograph from sample BRTC1-12421. Grain boundary 2, image A.

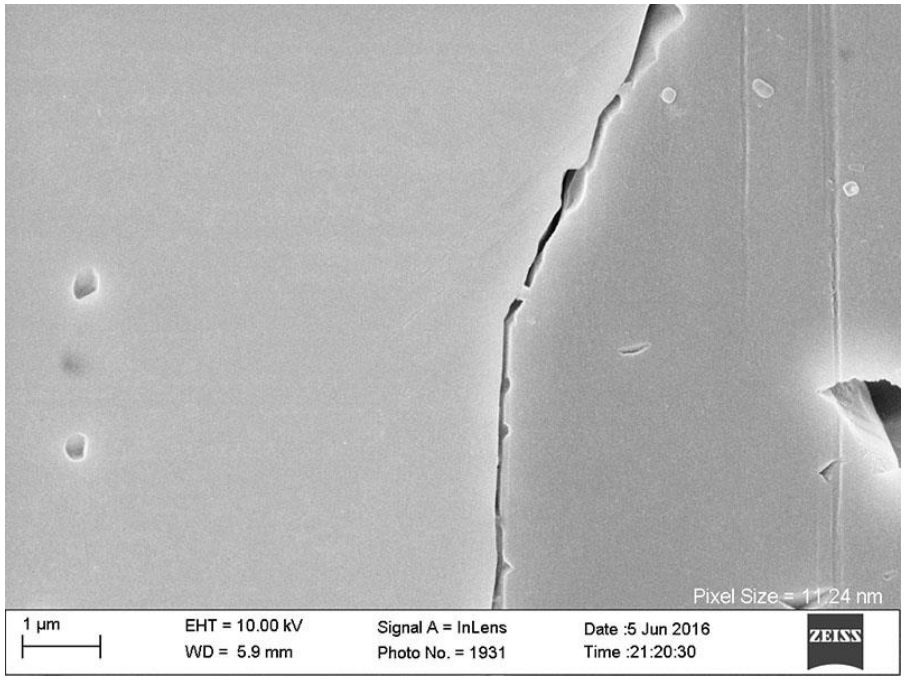

Figure A.255: Inlens SE micrograph from sample BRTC1-12421. Grain boundary 2, image B.

Grain Boundary 3 (Calcite-Barite)

Image	Measurement Number	Length (nm)
A	1	67.74
A	2	58.79
A	3	81.19
A	4	79.45
A	5	108.37
A	6	91.10
	Mean Aperture	81.11

Table A.155: NGBC measurements and mean aperture from grain boundary 3 in sample BRTC1-12421.

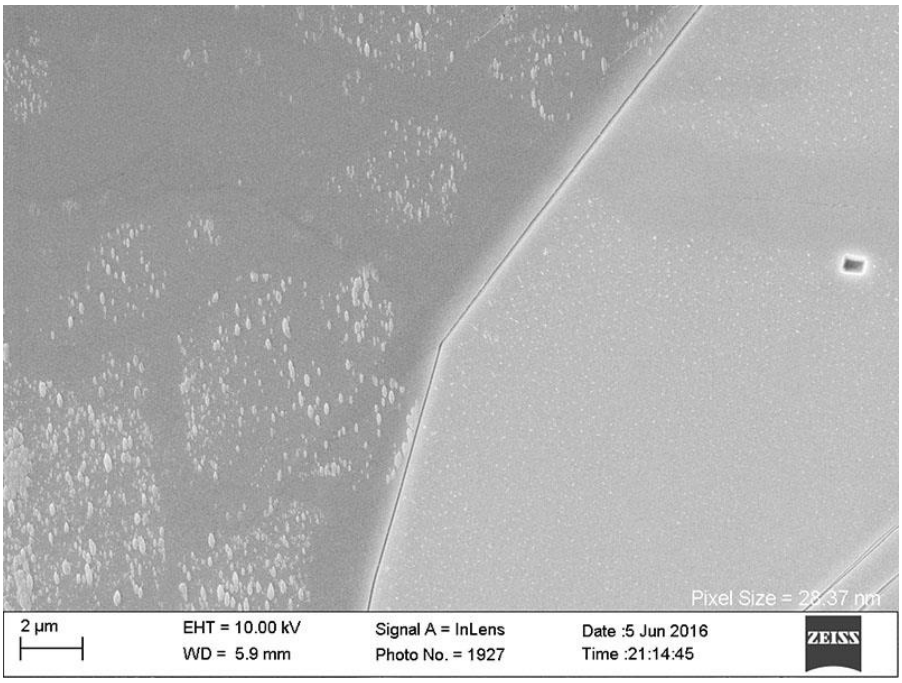

Figure A.256: Inlens SE micrograph from sample BRTC1-12421. Grain boundary 3, image A.

SAMPLE 06212-2, CAMPITO FORMATION

Mineral Cement	Rock Type	Sampled Depth (ft)	Sampled Depth (m)	Max burial depth (m)	Exhumed (m)	Max T (°C)	Range (nm)	Sample Mean (nm)
Quartz	Quartzite	Outcrop	Surface	10000	10000	~250	60-600	226.56
Calcite-Quartz	Quartzite	Outcrop	Surface	10000	10000	~250	60.15	60.15

Table A.156: Summary of sample 06212-2

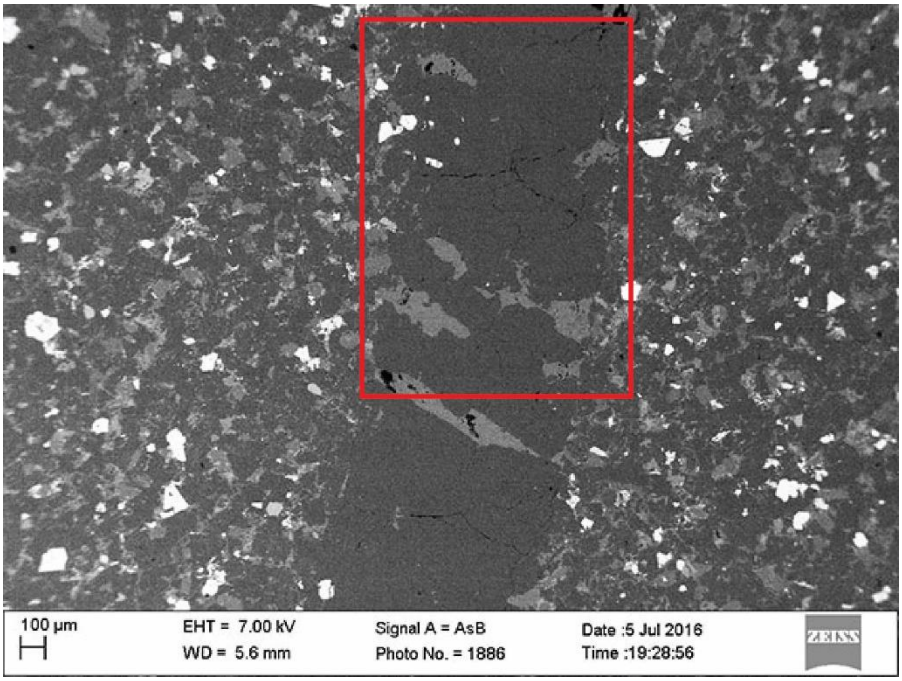

Figure A.257: BSE micrograph of sample 06212-2. Red box indicates area imaged for EBSD analysis and NGBC aperture measurements.

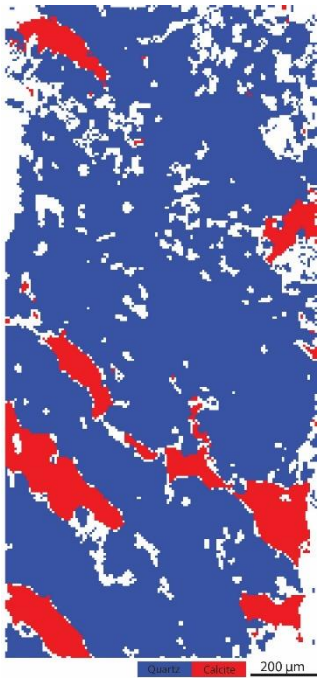

Figure A.258: EBSD phase map from sample 06212-2.

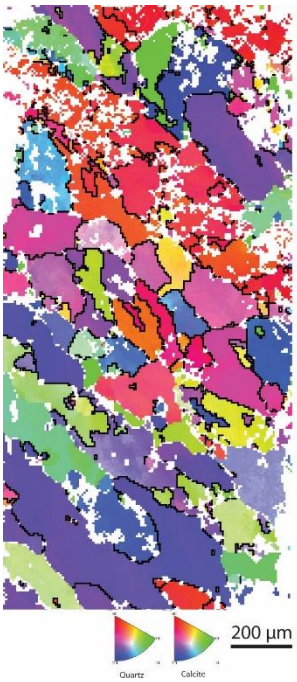

Figure A.259: EBSD inverse pole figure from sample 06212-2.

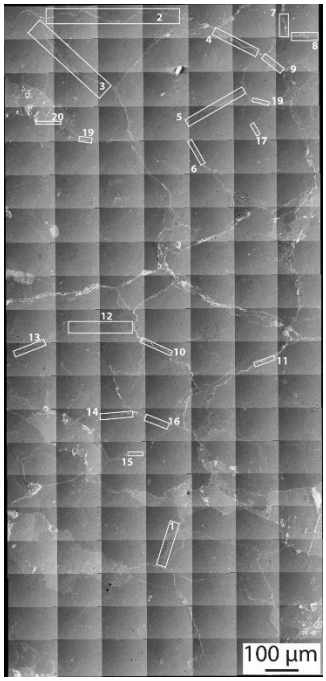

Figure A.260: Inlens SE mosaic of sample 0612-2. Boxes indicate location of grain boundaries used for NGBC aperture measurements.

GB Number	Mean Aperture (nm)
1	334.11
2	327.16
3	235.89
4	600.45
5	182.16
6	154.29
7	347.46
8	175.64
9	166.83
10	370.81
11	416.11
12	105.63
13	71.50
14	134.35
15	72.47
16	98.48
17	148.51
18	285.99
19	76.79
Overall sample mean	226.56

Table A.157: NGBC mean apertures and sample mean within quartz grain boundaries from sample 0612.2.

Grain Boundary	Mean Aperture
20	60.15
Sample Mean	60.15

Table A.158: NGBC mean apertures and sample mean within quartz-calcite phase boundaries from sample 0612.2.

Grain Boundary 1

Image	Measurement Number	Aperture (nm)
A	1	322.98
A	2	345.24
	Mean Aperture	334.11

Table A.159: NGBC measurements and mean aperture from grain boundary 1 in sample 0612-2.

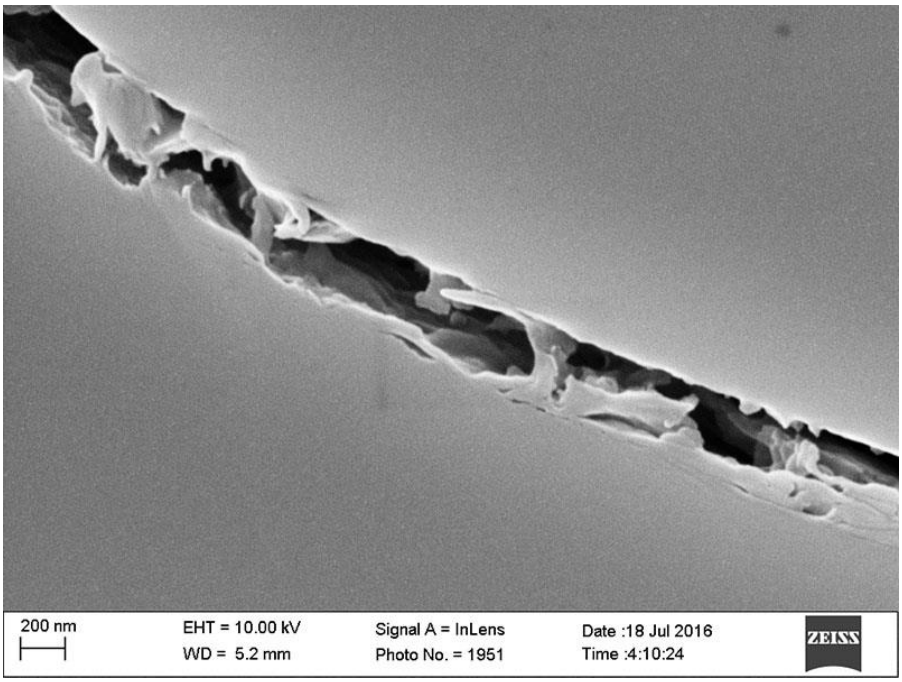

Figure A.261: Inlens SE micrograph from sample 06121-2. Grain boundary 1, image A.

Grain Boundary 2

Image	Measurement Number	Aperture (nm)
A	1	480.13
A	2	465.16
A	3	474.26
A	4	419.16
B	1	237.26
B	2	211.21
B	3	256.28
B	4	234.98
B	5	165.99
	Mean Aperture	327.16

Table A.160: NGBC measurements and mean aperture from grain boundary 2 in sample 0612-2.

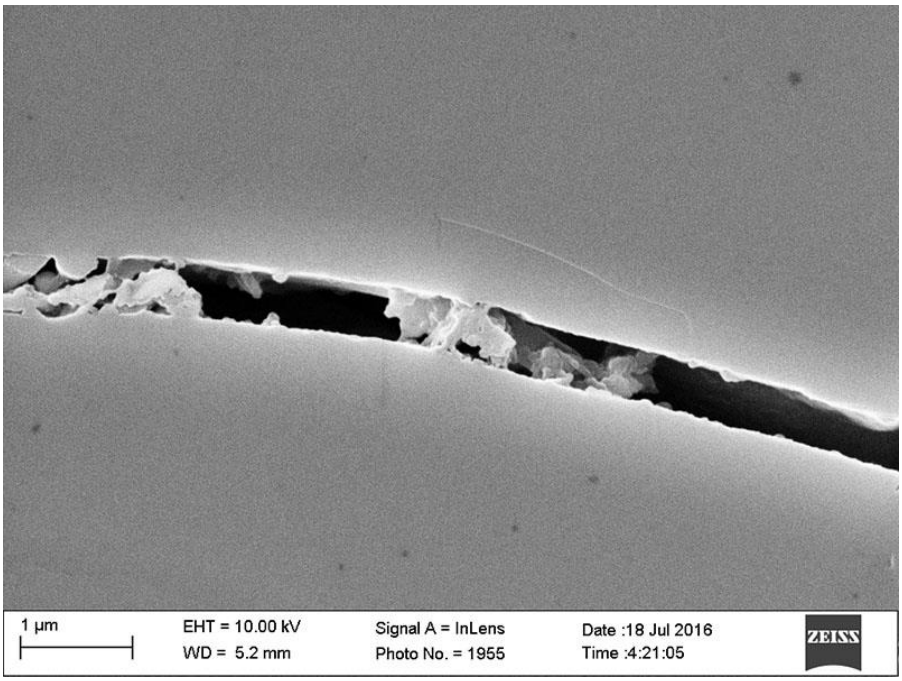

Figure A.262: Inlens SE micrograph from sample 06121-2. Grain boundary 2, image A.

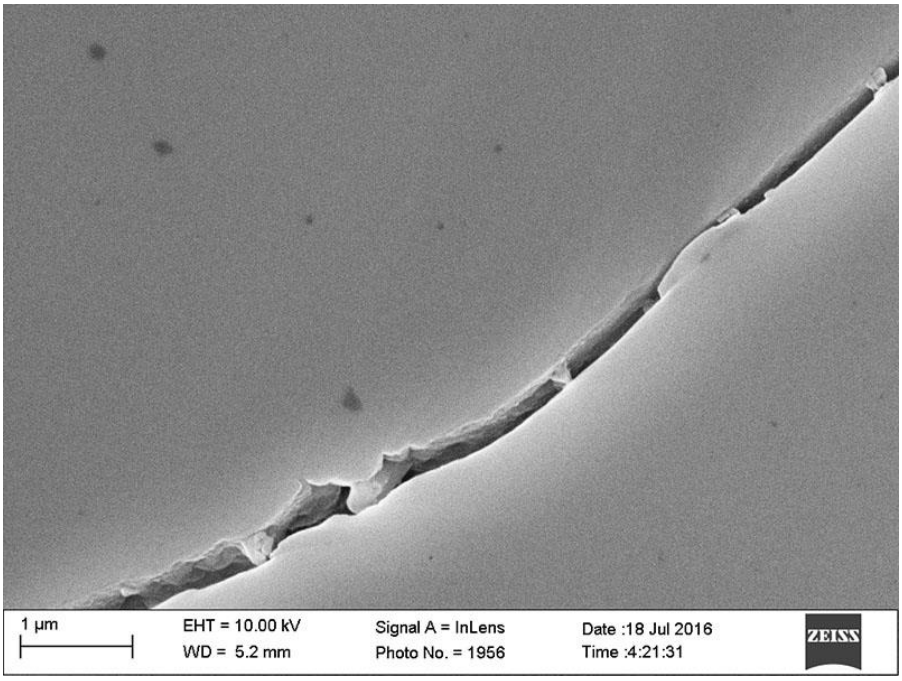

Figure A.263: Inlens SE micrograph from sample 06121-2. Grain boundary 2, image B.

Grain Boundary 3

Image	Measurement Number	Aperture (nm)
A	1	215.83
A	2	219.10
A	3	204.33
A	4	190.07
A	5	175.97
A	6	184.96
A	7	208.47
A	8	314.86
B	1	246.45
B	2	298.52
B	3	258.68
B	4	259.17
B	5	290.10
	Mean Aperture	235.89

Table A.161: NGBC measurements and mean aperture from grain boundary 3 in sample 0612-2.

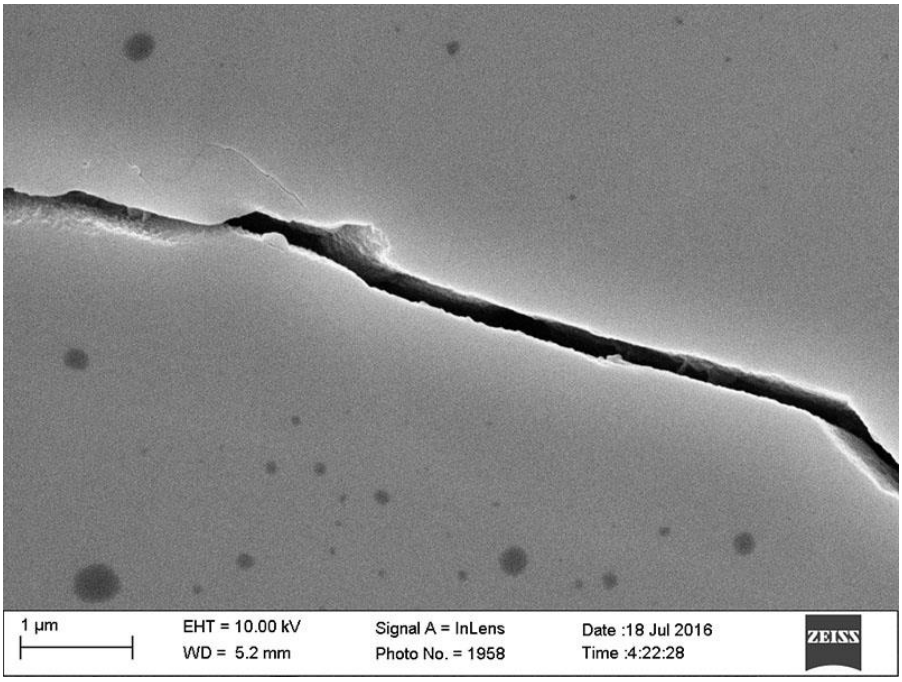

Figure A.264: Inlens SE micrograph from sample 06121-2. Grain boundary 3, image A.

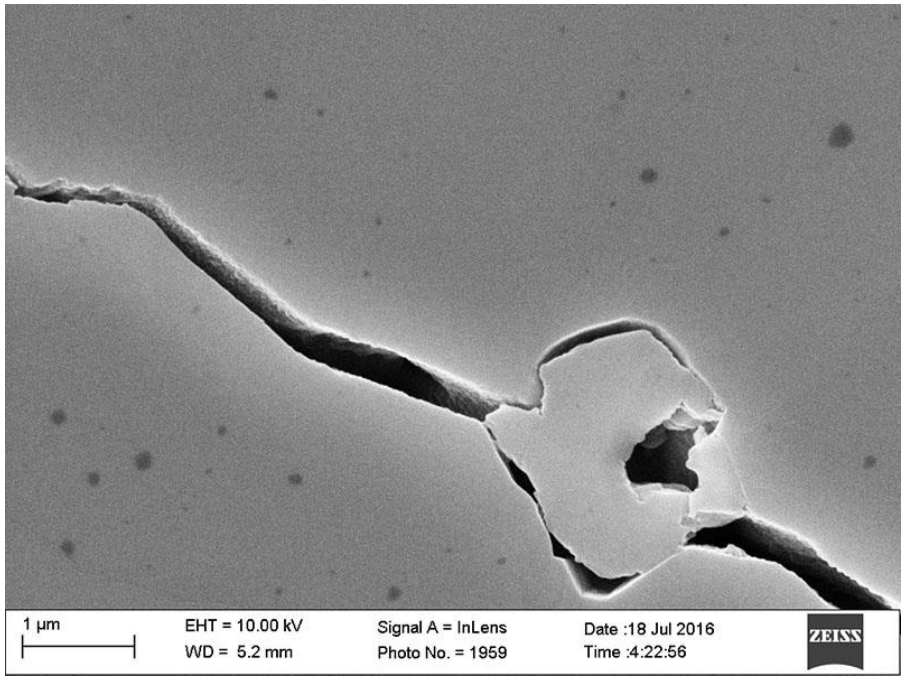

Figure A.265: Inlens SE micrograph from sample 06121-2. Grain boundary 3, image B.

Grain Boundary 4

Image	Measurement Number	Aperture (nm)
A	1	569.91
A	2	576.74
A	3	551.29
A	4	614.12
A	5	625.26
A	6	665.37
	Mean Aperture	600.45

Table A.162: NGBC measurements and mean aperture from grain boundary 4 in sample 0612-2.

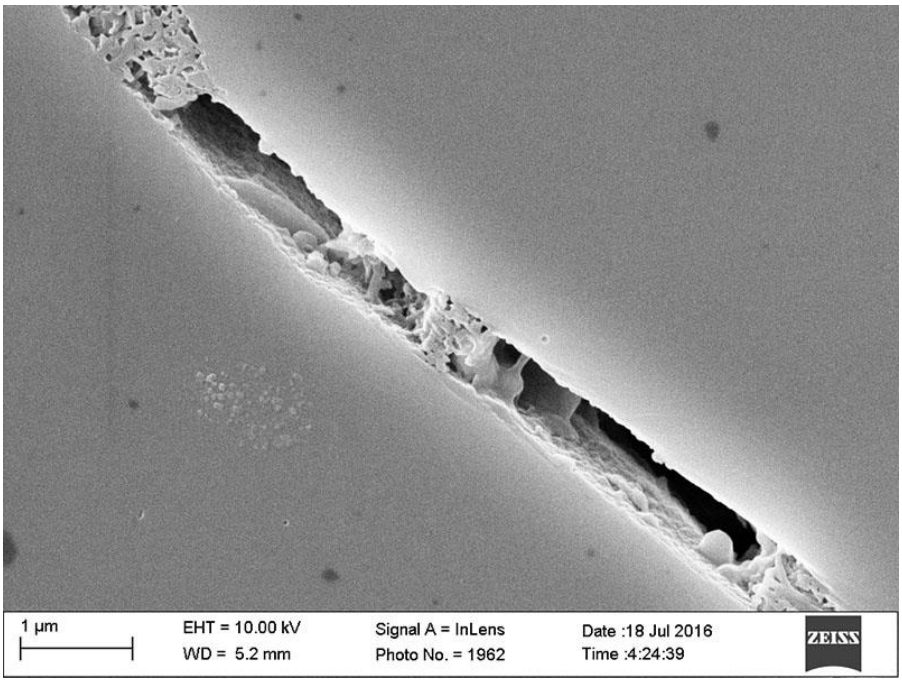

Figure A.266: Inlens SE micrograph from sample 06121-2. Grain boundary 4, image A.

Grain Boundary 5

Image	Measurement Number	Aperture (nm)
A	1	179.62
A	2	183.09
A	3	169.38
A	4	183.95
A	5	221.30
B	1	178.10
B	2	178.10
B	3	169.49
B	4	152.13
B	5	197.41
B	6	191.25
	Mean Aperture	182.16

Table A.163: NGBC measurements and mean aperture from grain boundary 5 in sample 0612-2.

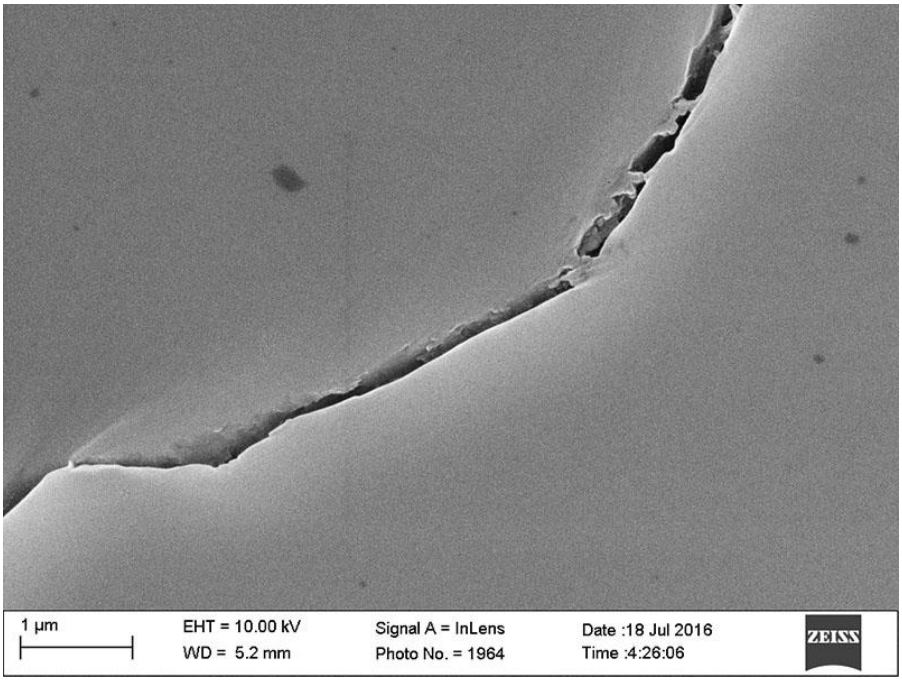

Figure A.267: Inlens SE micrograph from sample 06121-2. Grain boundary 5, image A.

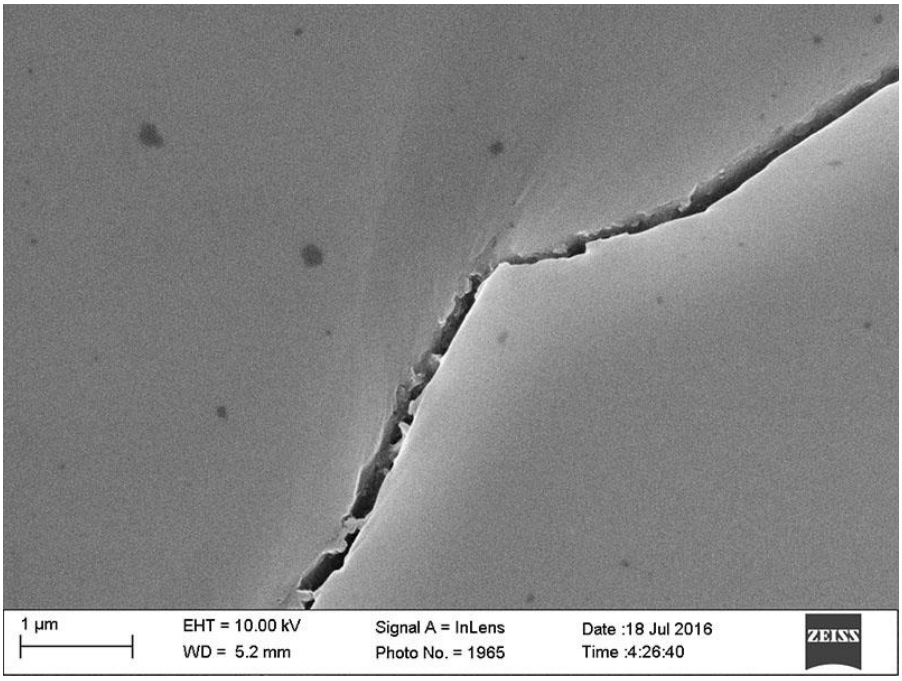

Figure A.268: Inlens SE micrograph from sample 06121-2. Grain boundary 5, image B.

Grain Boundary 6

Image	Measurement Number	Aperture (nm)
A	1	136.06
A	2	148.24
A	3	143.21
A	4	157.14
A	5	167.51
A	1	165.98
A	2	154.20
A	3	147.26
A	4	169.04
A	Mean Aperture	154.29

Table A.164: NGBC measurements and mean aperture from grain boundary 6 in sample 0612-2.

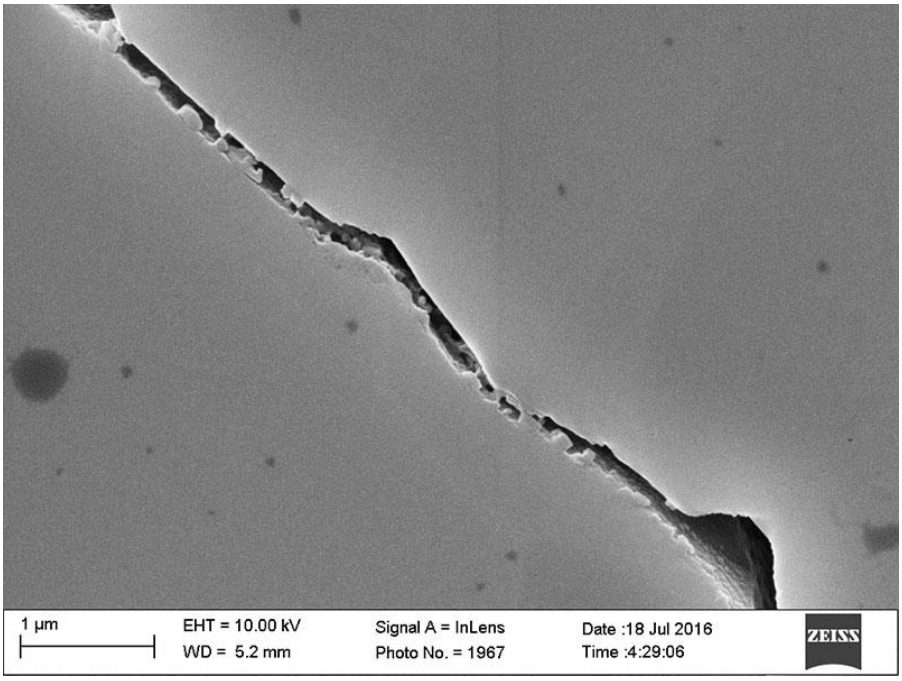

Figure A.269: Inlens SE micrograph from sample 06121-2. Grain boundary 6, image A.

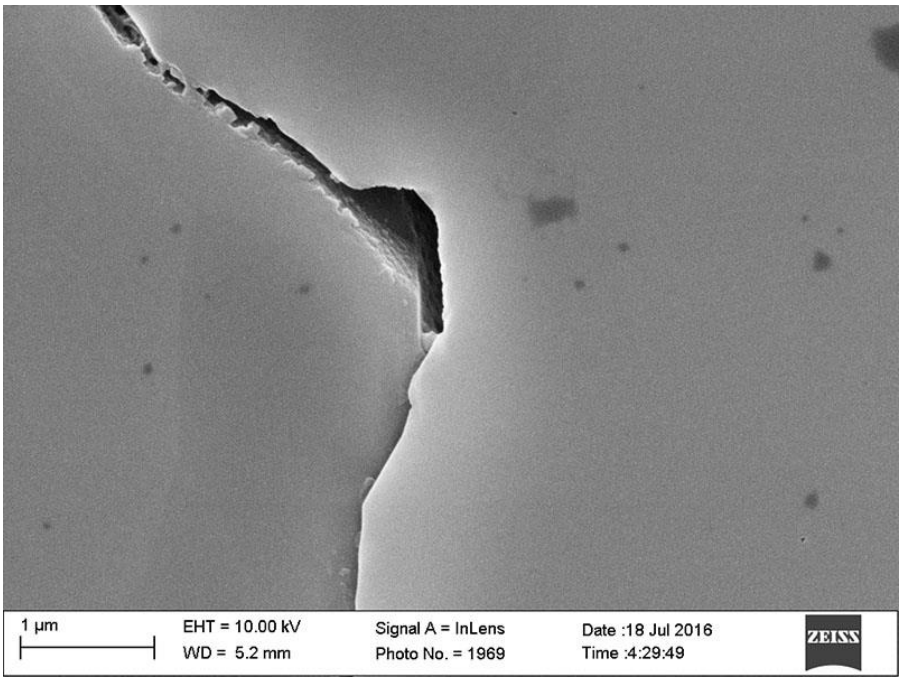

Figure A.270: Inlens SE micrograph from sample 06121-2. Grain boundary 6, image B.

Grain Boundary 7

Image	Measurement Number	Aperture (nm)
A	1	339.41
A	2	337.17
A	3	378.66
A	4	356.37
A	5	335.38
A	6	337.80
	Mean Aperture	347.46

Table A.165: NGBC measurements and mean aperture from grain boundary 7 in sample 0612-2.

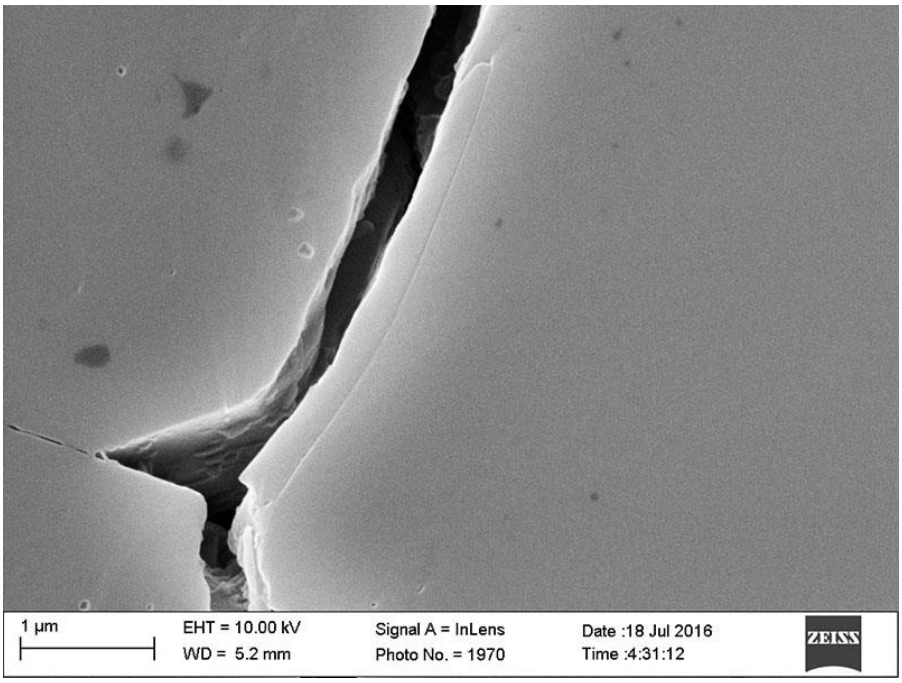

Figure A.271: Inlens SE micrograph from sample 06121-2. Grain boundary 7, image A.

Grain Boundary 8

Image	Measurement Number	Aperture (nm)
A	1	213.88
A	2	156.20
A	3	161.39
A	4	197.10
A	5	160.16
A	6	168.69
A	7	183.55
A	8	150.67
A	9	182.82
A	10	169.15
A	11	188.40
	Mean Aperture	175.64

Table A.166: NGBC measurements and mean aperture from grain boundary 8 in sample 0612-2.

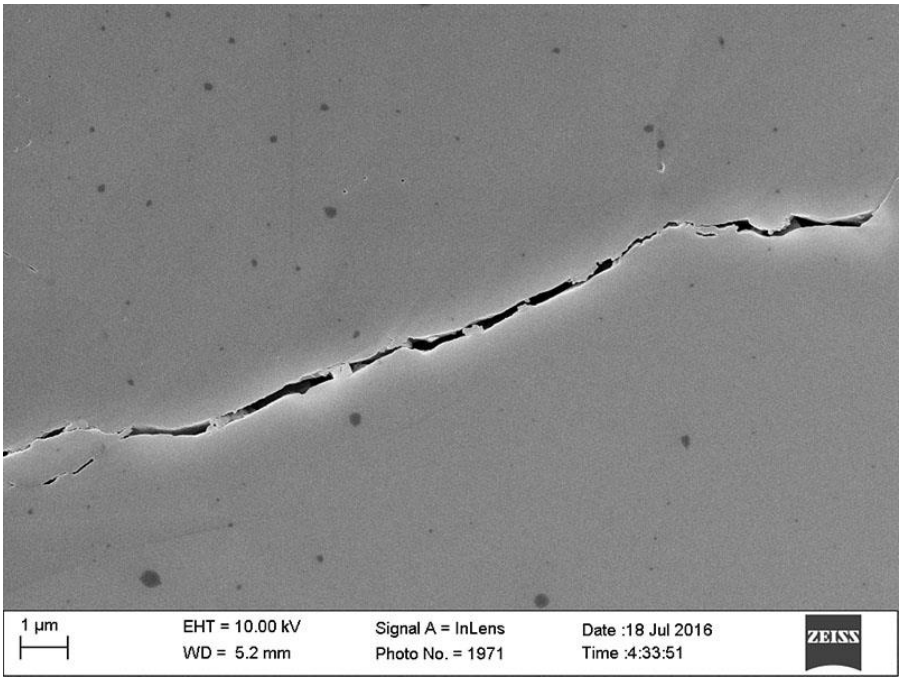

Figure A.272: Inlens SE micrograph from sample 06121-2. Grain boundary 8, image A.

Grain Boundary 9

Image	Measurement Number	Aperture (nm)
A	1	156.27
A	2	160.77
A	3	159.74
A	4	162.84
A	5	174.27
A	6	163.93
A	7	189.96
	Mean Aperture	166.83

Table A.167: NGBC measurements and mean aperture from grain boundary 9 in sample 0612-2.

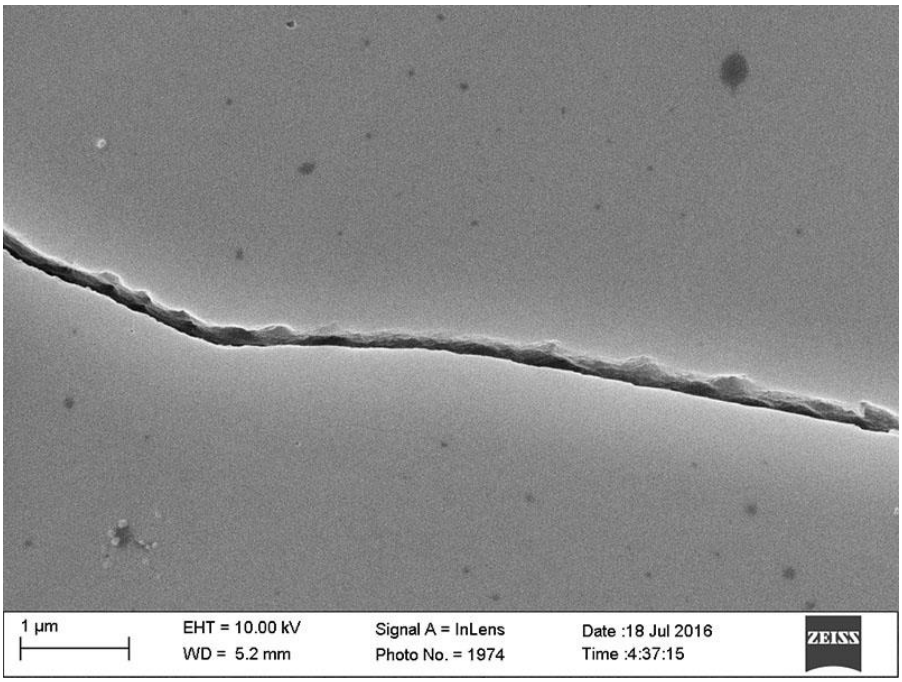

Figure A.273: Inlens SE micrograph from sample 06121-2. Grain boundary 9, image A.

Grain Boundary 10

Image	Measurement Number	Aperture (nm)
A	1	392.17
A	2	387.15
B	1	282.19
B	2	342.56
B	3	415.45
B	4	405.37
	Mean Aperture	370.81

Table A.168: NGBC measurements and mean aperture from grain boundary 10 in sample 0612-2.

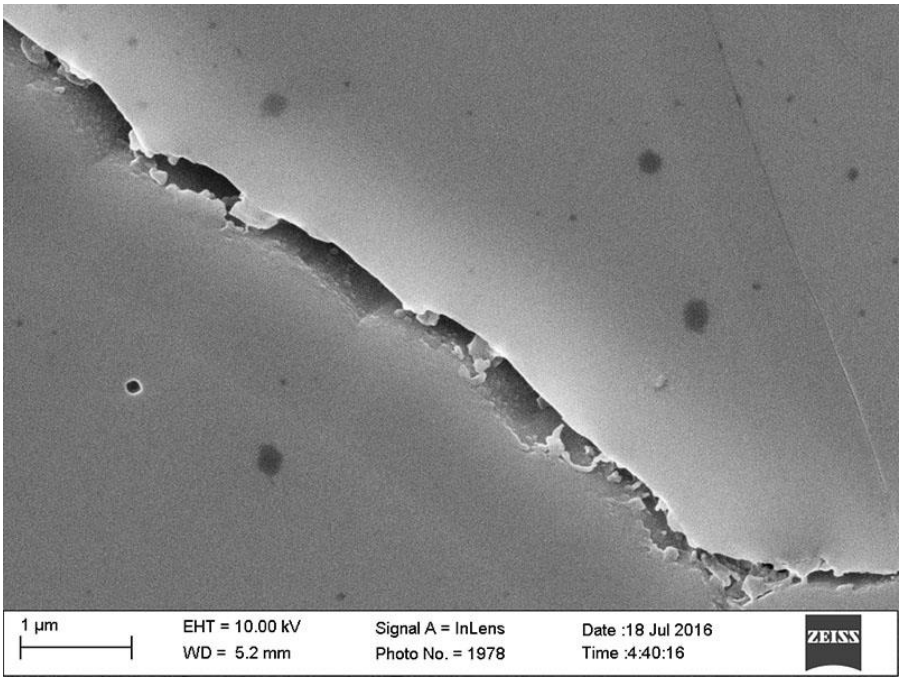

Figure A.274: Inlens SE micrograph from sample 06121-2. Grain boundary 10, image A.

Grain Boundary 11

Image	Measurement Number	Aperture (nm)
A	1	361.21
A	2	426.91
A	3	395.75
A	4	401.26
A	5	362.79
A	6	482.09
A	7	490.95
A	8	407.90
	Mean Aperture	416.11

Table A.169: NGBC measurements and mean aperture from grain boundary 11 in sample 0612-2.

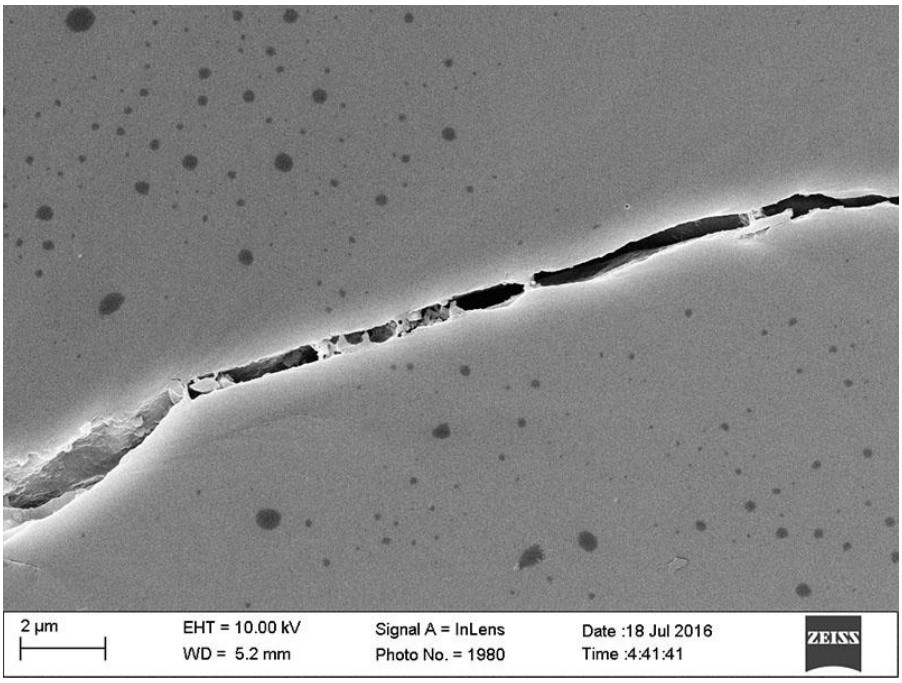

Figure A.275: Inlens SE micrograph from sample 06121-2. Grain boundary 11, image A.

Grain Boundary 12

Image	Measurement Number	Aperture (nm)
A	1	78.43
A	2	106.19
A	3	112.90
A	4	133.99
A	5	115.99
A	6	101.28
A	7	107.86
A	8	137.30
A	9	96.39
A	10	84.94
A	11	86.59
	Mean Aperture	105.63

Table A.170: NGBC measurements and mean aperture from grain boundary 12 in sample 0612-2.

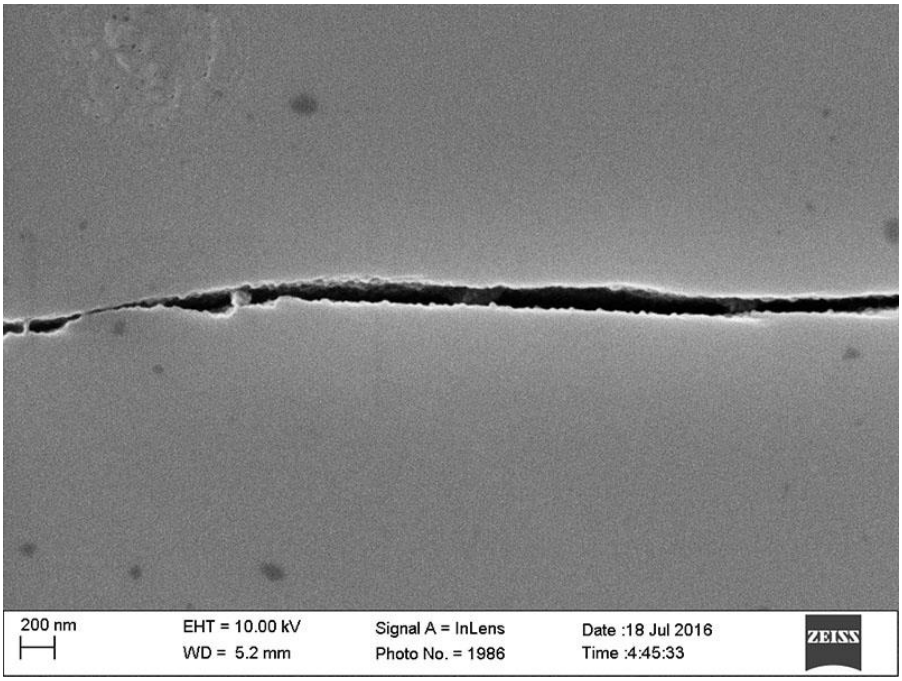

Figure A.276: Inlens SE micrograph from sample 06121-2. Grain boundary 12, image. A

Grain Boundary 13

Image	Measurement Number	Aperture (nm)
A	1	68.61
A	2	92.70
A	3	69.90
A	4	66.58
A	5	67.14
A	6	67.62
A	7	67.95
	Mean Aperture	71.50

Table A.171: NGBC measurements and mean aperture from grain boundary 13 in sample 0612-2.

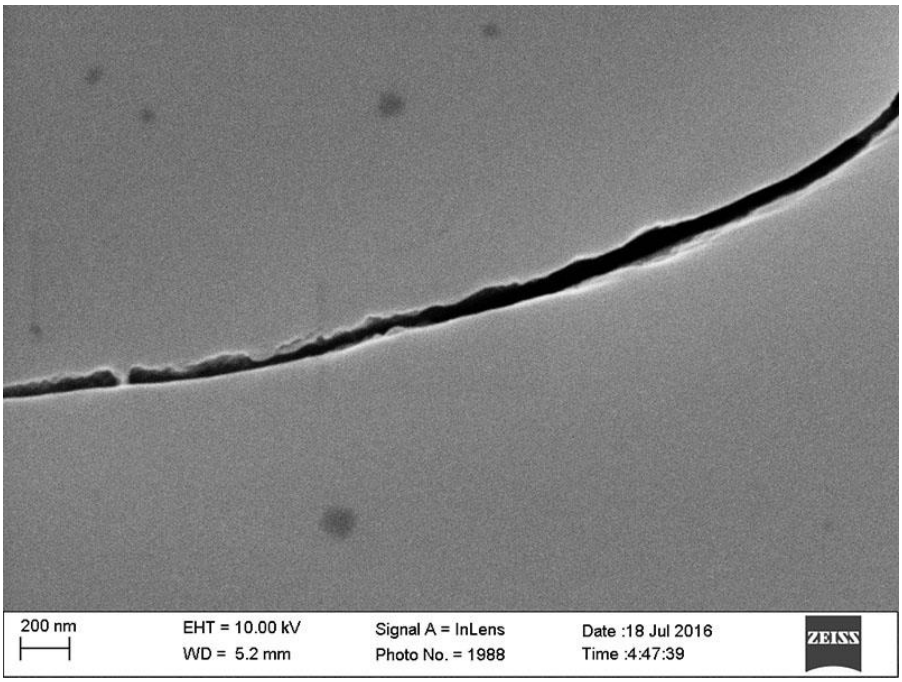

Figure A.277: Inlens SE micrograph from sample 06121-2. Grain boundary 13, image A.

Grain Boundary 14

Image	Measurement Number	Aperture (nm)
A	1	129.86
A	2	129.35
A	3	124.64
A	4	104.58
A	5	205.83
A	6	121.62
A	7	151.01
A	8	167.29
A	9	158.53
A	10	125.53
A	11	137.11
A	12	127.04
A	13	121.26
A	14	137.47
A	15	105.41
A	16	113.80
A	17	102.98
A	18	145.83
A	19	117.04
A	20	141.91
A	21	151.47
A	22	173.18
A	23	140.51
A	24	178.13
A	25	116.63
A	26	93.81
A	27	105.70
	Mean Aperture	134.35

Table A.172: NGBC measurements and mean aperture from grain boundary 14 in sample 0612-2.

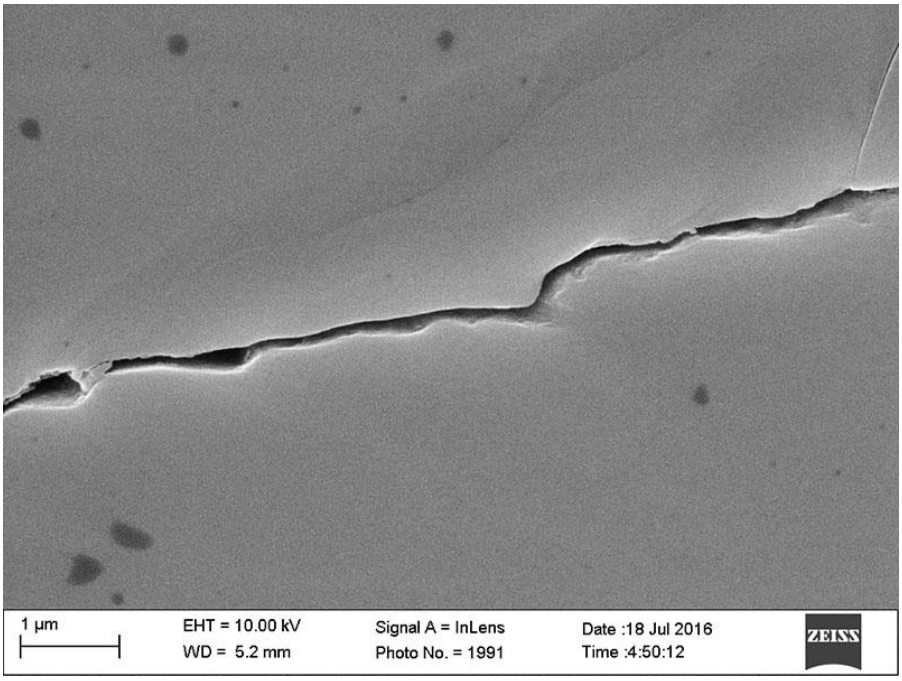

Figure A.278: Inlens SE micrograph from sample 06121-2. Grain boundary 14, image A.

Grain Boundary 15

Image	Measurement Number	Aperture (nm)
A	1	56.96
A	2	105.44
A	3	43.35
A	4	84.12
	Mean Aperture	72.47

Table A.173: NGBC measurements and mean aperture from grain boundary 15 in sample 0612-2.

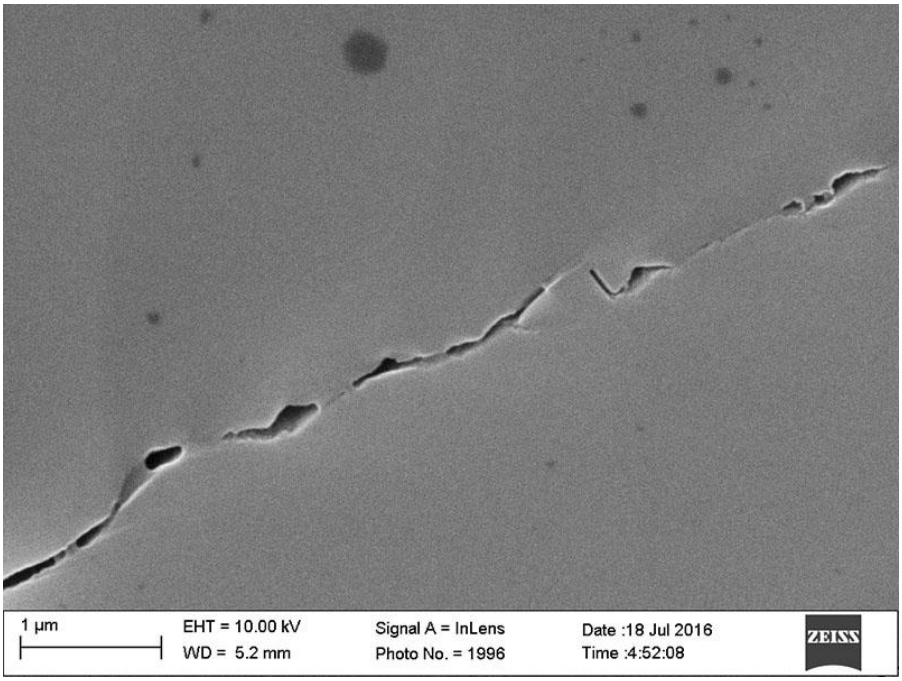

Figure A.279: Inlens SE micrograph from sample 06121-2. Grain boundary 15, image A.

Grain Boundary 16

Image	Measurement Number	Aperture (nm)
A	1	104.27
A	2	133.31
A	3	104.27
A	4	133.52
A	5	131.27
A	6	104.40
A	7	115.54
A	8	93.45
A	9	110.36
A	10	95.37
A	11	89.71
A	12	117.42
A	13	111.79
A	14	99.02
B	1	75.02
B	2	54.10
B	3	67.89
B	4	60.88
B	5	80.82
B	6	87.17
	Mean Aperture	98.48

Table A.174: NGBC measurements and mean aperture from grain boundary 16 in sample 0612-2.

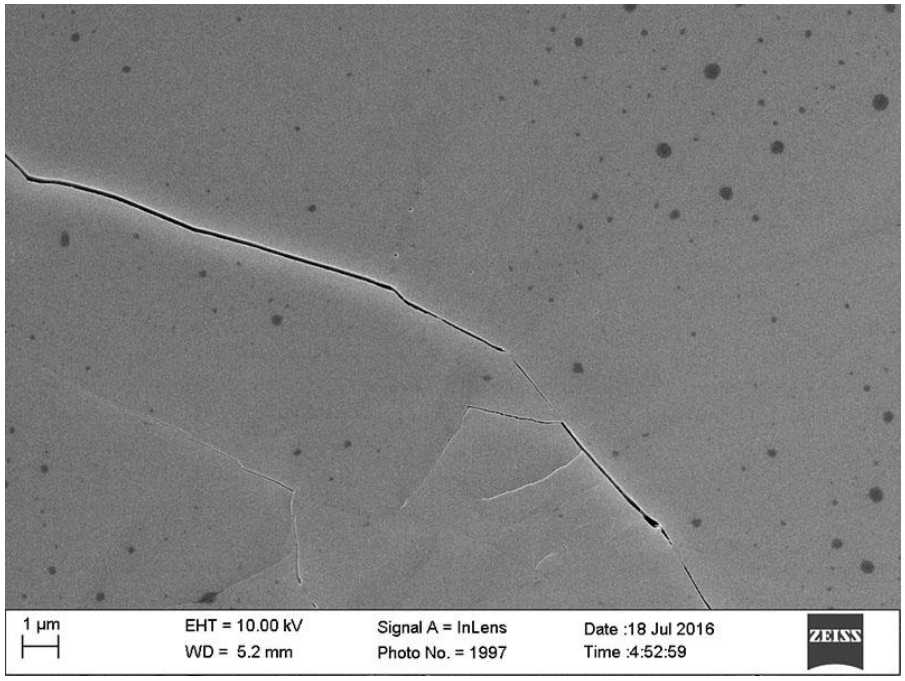

Figure A.280: Inlens SE micrograph from sample 06121-2. Grain boundary 16, image A.

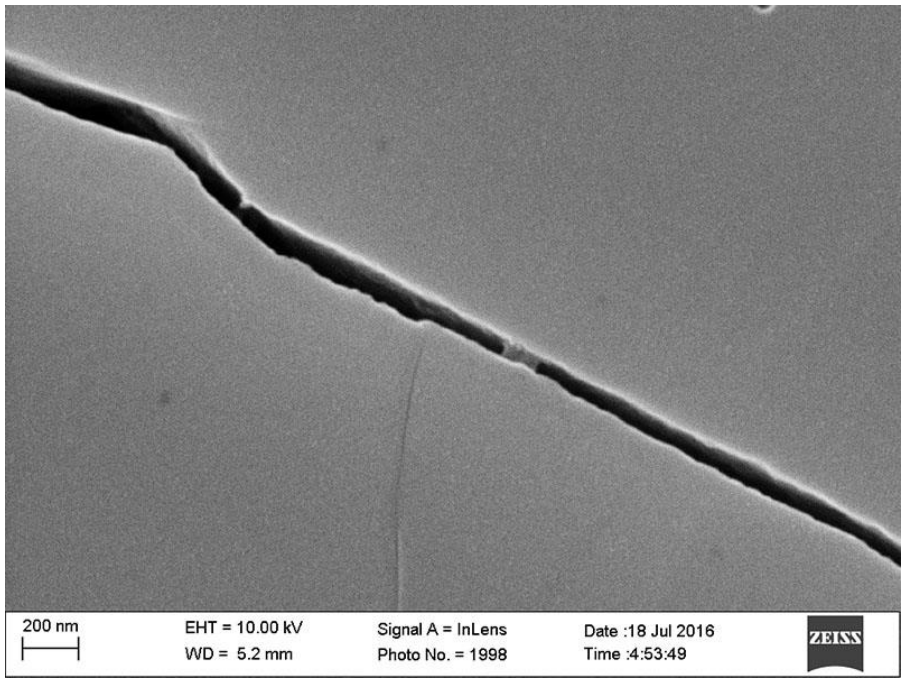

Figure A.281: Inlens SE micrograph from sample 06121-2. Grain boundary 16, image B.

Grain Boundary 17

Image	Measurement Number	Aperture (nm)
A	1	163.57
A	2	169.81
A	3	218.09
A	4	192.76
B	1	180.70
B	2	175.61
B	3	172.48
B	4	181.95
B	5	136.36
C	1	122.64
C	2	131.40
C	3	98.49
C	4	110.42
C	5	89.00
C	6	84.38
	Mean Aperture	148.51

Table A.175: NGBC measurements and mean aperture from grain boundary 17 in sample 0612-2.

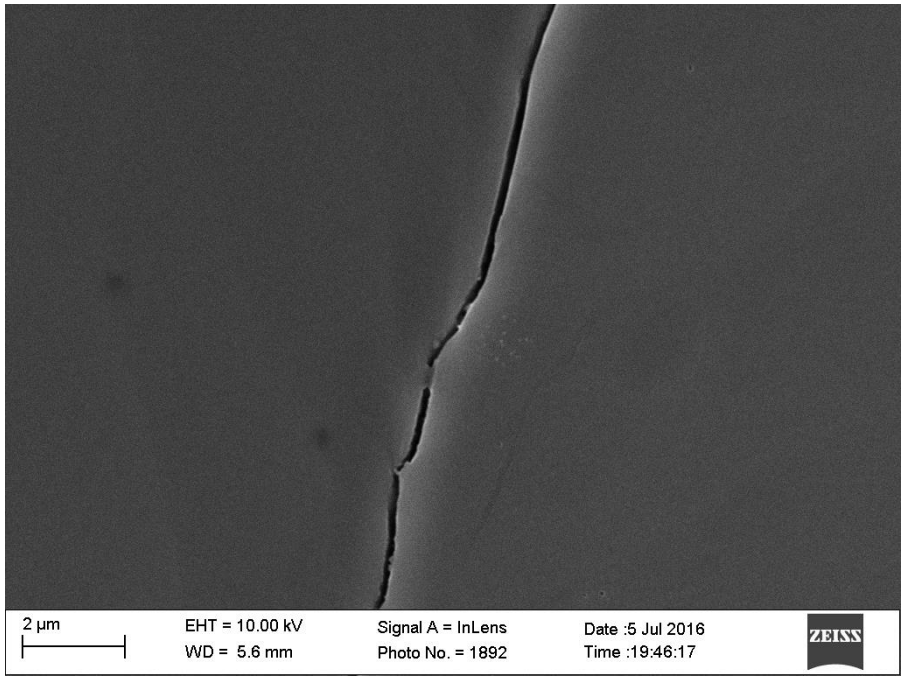

Figure A.282: Inlens SE micrograph from sample 06121-2. Grain boundary 17, image A.

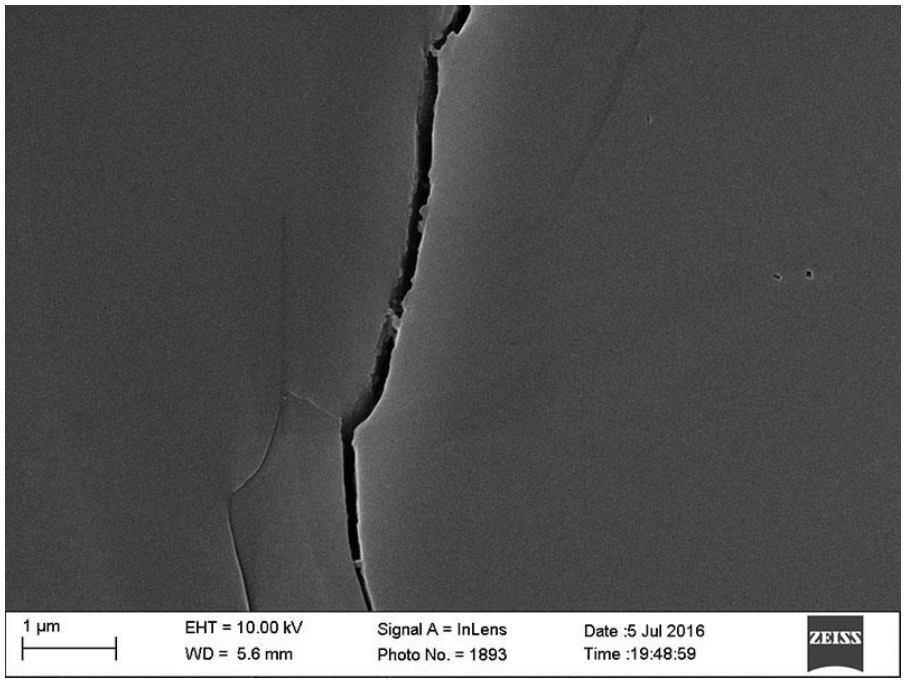

Figure A.283: Inlens SE micrograph from sample 06121-2. Grain boundary 17, image B.

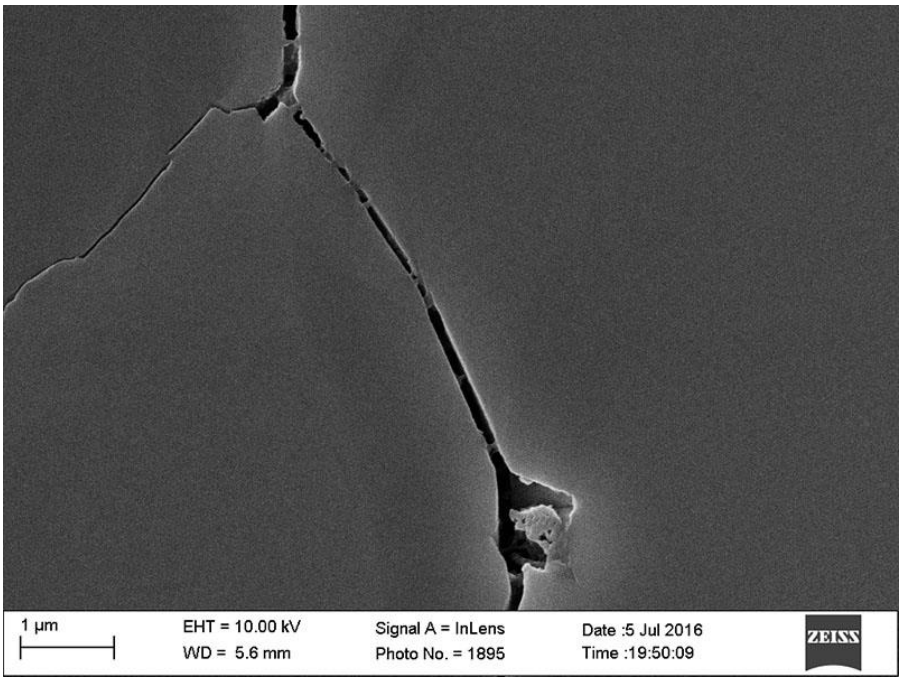

Figure A.284: Inlens SE micrograph from sample 06121-2. Grain boundary 17, image C.

Grain Boundary 18

Image	Measurement Number	Aperture (nm)
A	1	284.30
A	2	270.76
A	3	287.66
A	4	299.23
A	5	301.53
A	6	278.32
A	7	280.14
	Mean Aperture	285.99

Table A.176: NGBC measurements and mean aperture from grain boundary 18 in sample 0612-2.

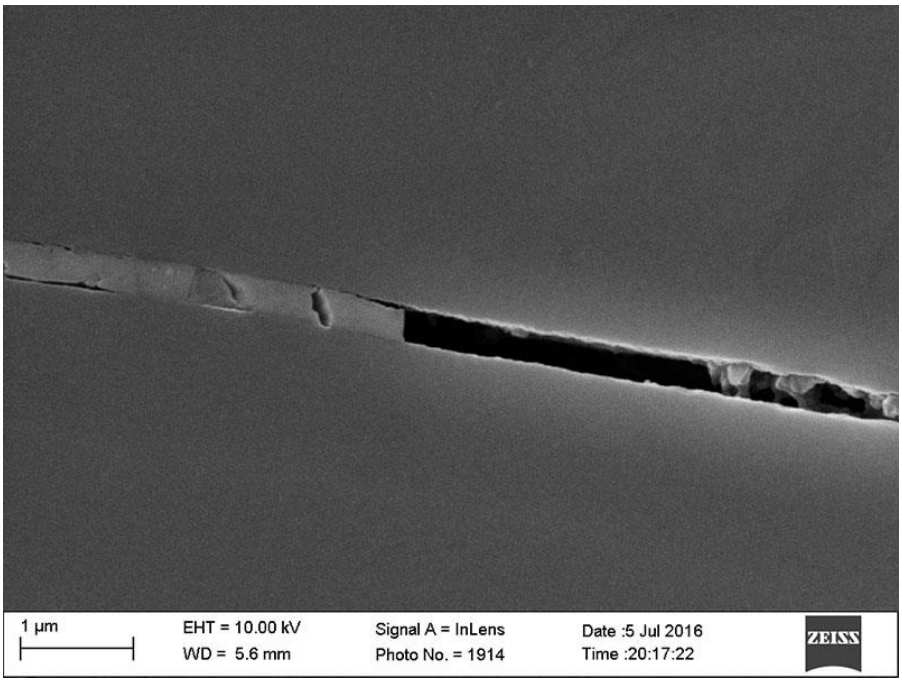

Figure A.285: Inlens SE micrograph from sample 06121-2. Grain boundary 18, image A.

Grain Boundary 19

Image	Measurement Number	Aperture (nm)
A	1	64.60
A	2	87.10
A	3	77.42
A	4	90.32
A	5	64.52
	Mean Aperture	76.79

Table A.177: NGBC measurements and mean aperture from grain boundary 19 in sample 0612-2.

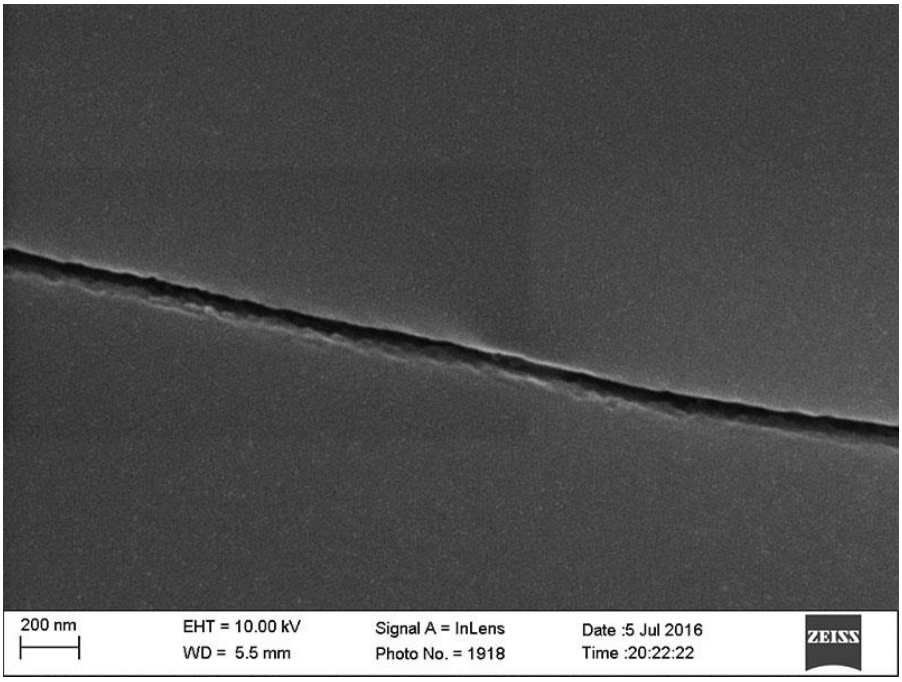

Figure A.286: Inlens SE micrograph from sample 06121-2. Grain boundary 19, image A.

Grain Boundary 20 (Calcite-Quartz)

Image	Measurement Number	Aperture (nm)
A	1	61.75
A	2	60.56
A	3	54.62
A	4	62.73
A	5	69.88
A	6	51.36
	Mean Aperture	60.15

Table A.178: NGBC measurements and mean aperture from grain boundary 20 in sample 0612-2.

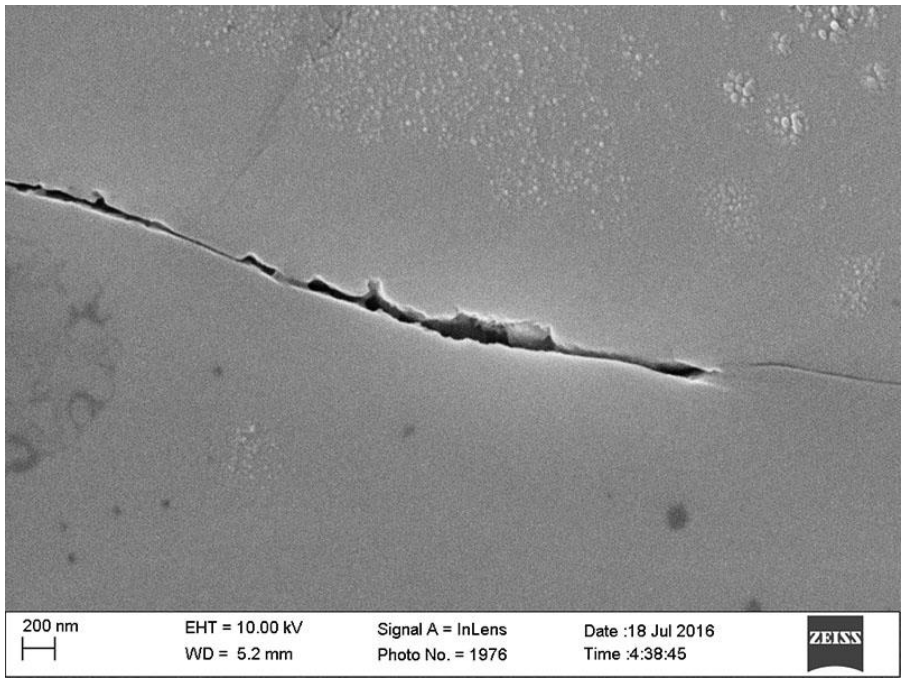

Figure A.287: Inlens SE micrograph from sample 06121-2. Grain boundary 20, image A.

SAMPLE: SFOT-1-10106.8, TRAVIS PEAK FORMATION

Mineral Cement	Rock Type	Sampled Depth (ft)	Sampled Depth (m)	Max burial depth (m)	Exhumed (m)	Max T (°C)	Range (nm)	Sample Mean (nm)
Quartz	Sand-stone	10106.8	3080.553	3480.553	400	140-170	63-145	98.46

Table A.179: Summary of sample SFOT-1-10106.8

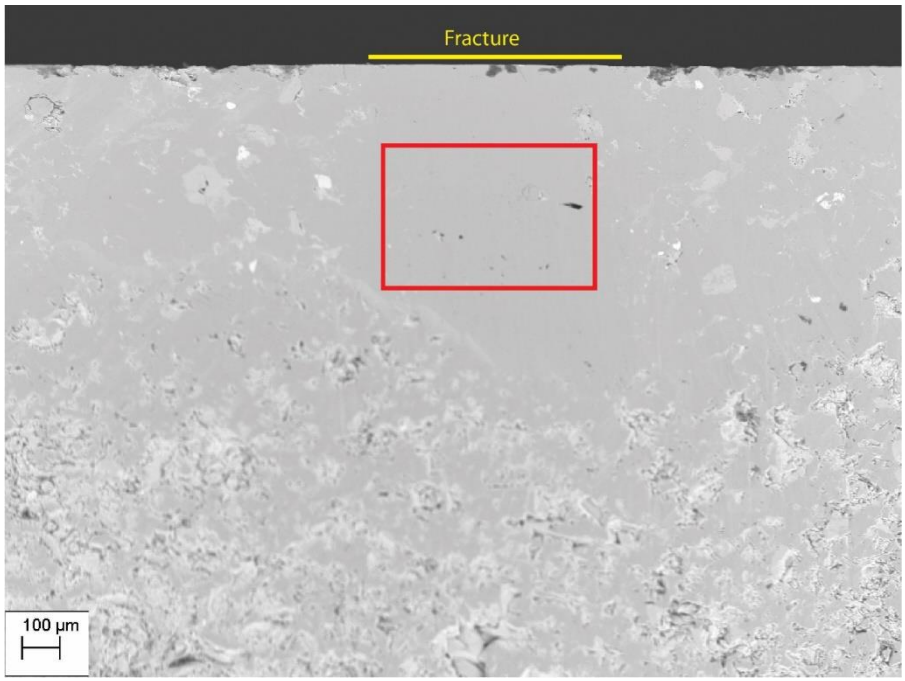

Figure A.288: BSE micrograph of sample SFOT-1-10106.8. Red box indicates area imaged for EBSD analysis and NGBC aperture measurements.

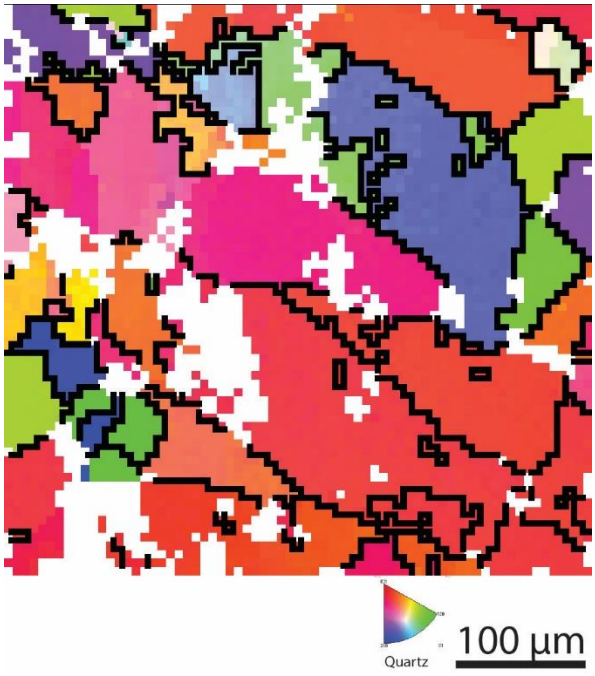

Figure A.289: EBSD inverse pole figure from sample SFOT-1-10106.8.

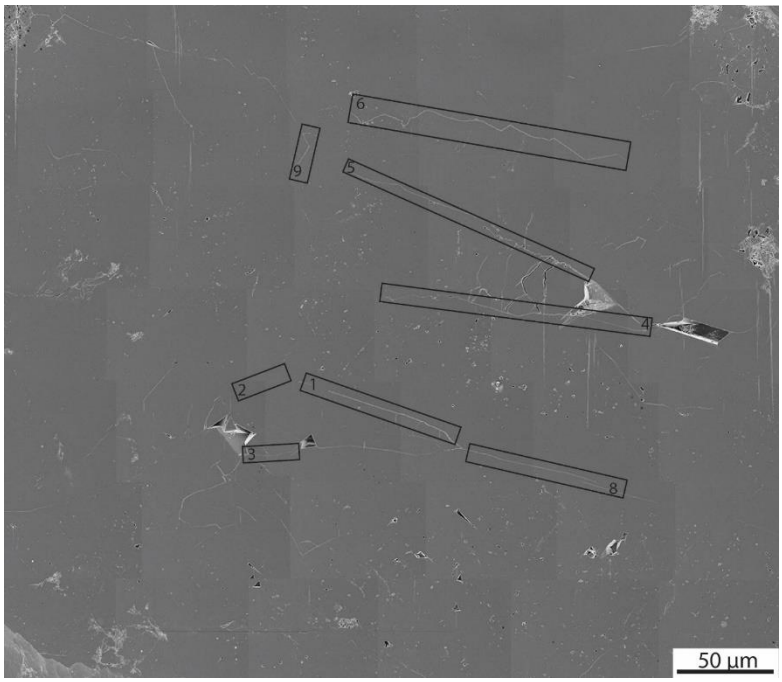

Figure A.290: Inlens SE mosaic of sample SFOT-1-10106.8. Boxes indicate location of grain boundaries used for NGBC aperture measurements.

Grain Boundary	Mean Aperture (nm)
1	144.85
2	134.76
3	63.41
4	85.68
5	67.90
6	118.20
7	110.74
8	70.64
9	89.97
Sample Mean	98.46

Table A.180: NGBC mean aperture and sample mean from grain boundaries in sample SFOT-1-10106.8

Grain Boundary 1

Image	Measurement Number	Length (nm)
A	1	142.66
A	2	147.45
A	3	144.43
	Mean Aperture	144.85

Table A.181: NGBC measurements and mean aperture from grain boundary 1 in sample SFOT-1-10106.8.

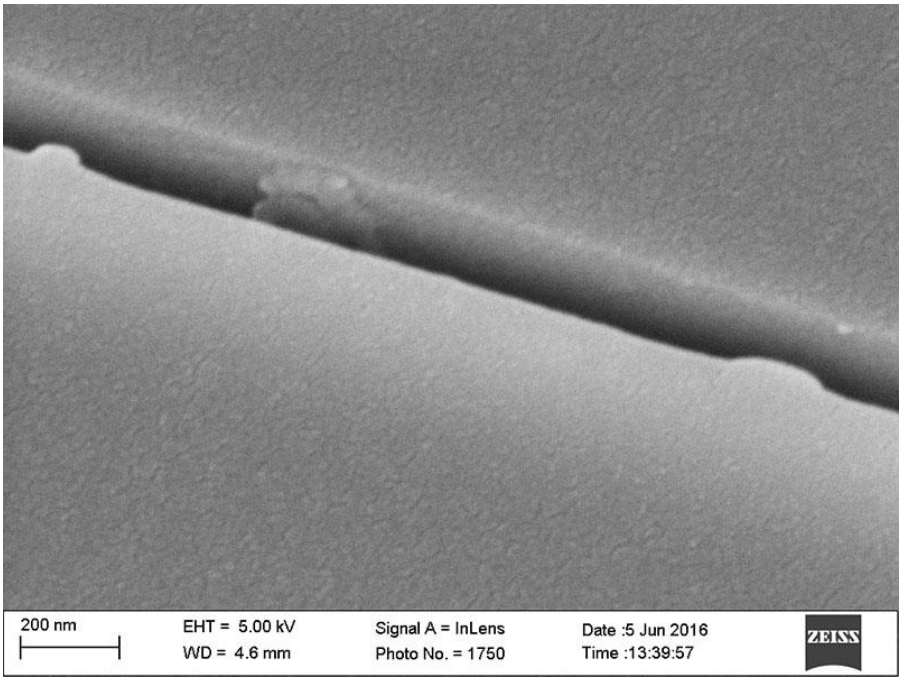

Figure A.291: Inlens SE micrograph from sample SFOT-1-10106.8. Grain boundary 1, image A.

Grain Boundary 2

Image	Measurement Number	**Length (nm)**
A	1	134.68
A	2	131.13
A	3	133.71
A	4	138.24
A	5	136.05
	Mean Aperture	134.76

Table A.182: NGBC measurements and mean aperture from grain boundary 2 in sample SFOT-1-10106.8.

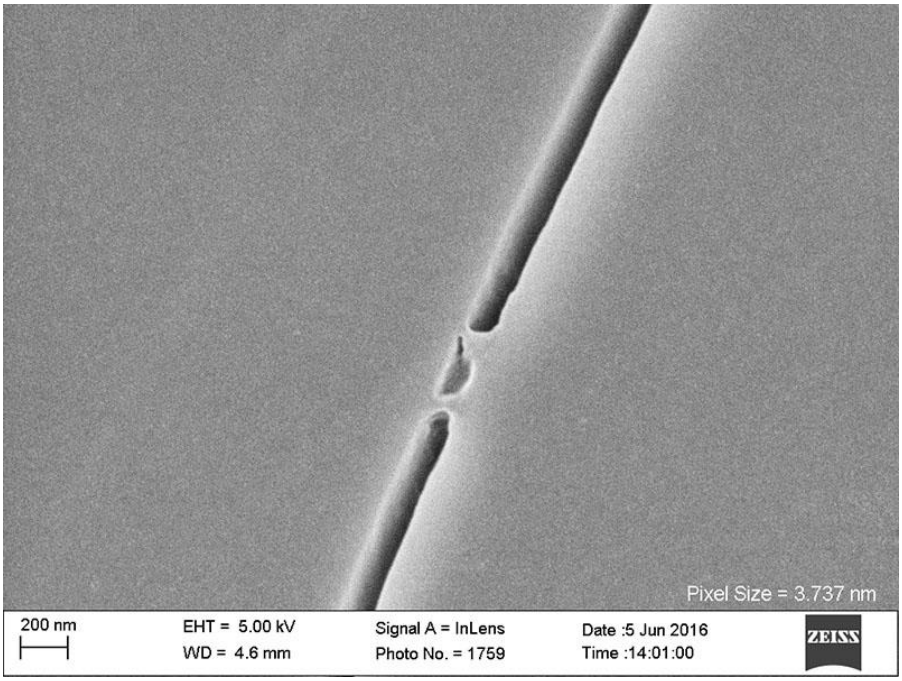

Figure A.292: Inlens SE micrograph from sample SFOT-1-10106.8. Grain boundary2, image A.

Grain Boundary 3

Image	Measurement Number	Length (nm)
A	1	82.65
A	2	85.96
A	3	65.93
A	4	66.53
B	1	49.00
B	2	51.80
B	3	42.02
	Mean Aperture	63.41

Table A.183: NGBC measurements and mean aperture from grain boundary 3 in sample SFOT-1-10106.8.

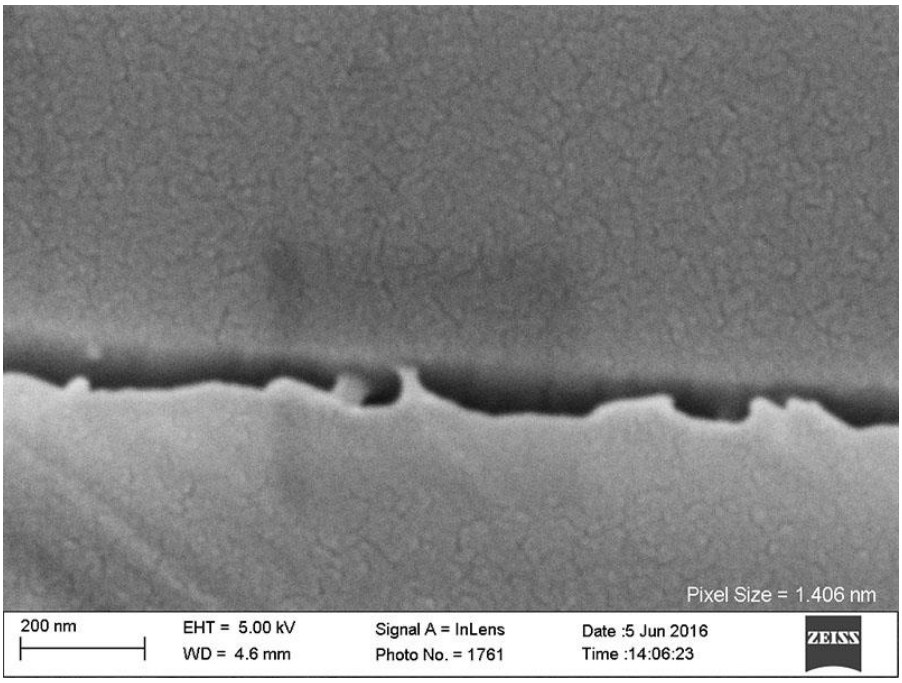

Figure A.293: Inlens SE micrograph from sample SFOT-1-10106.8. Grain boundary 3, image A.

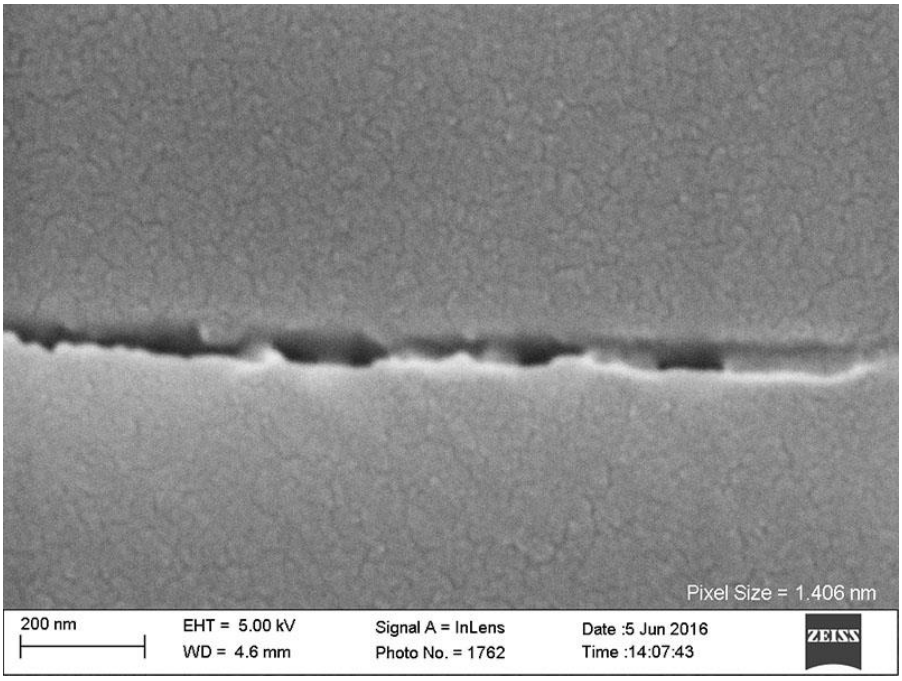

Figure A.294: Inlens SE micrograph from sample SFOT-1-10106.8. Grain boundary3, image B.

Grain Boundary 4

Image	Measurement Number	Length (nm)
A	1	90.09
A	2	103.83
A	3	71.35
A	4	92.97
A	5	70.16
	Mean Aperture	85.68

Table A.184: NGBC measurements and mean aperture from grain boundary 4 in sample SFOT-1-10106.8.

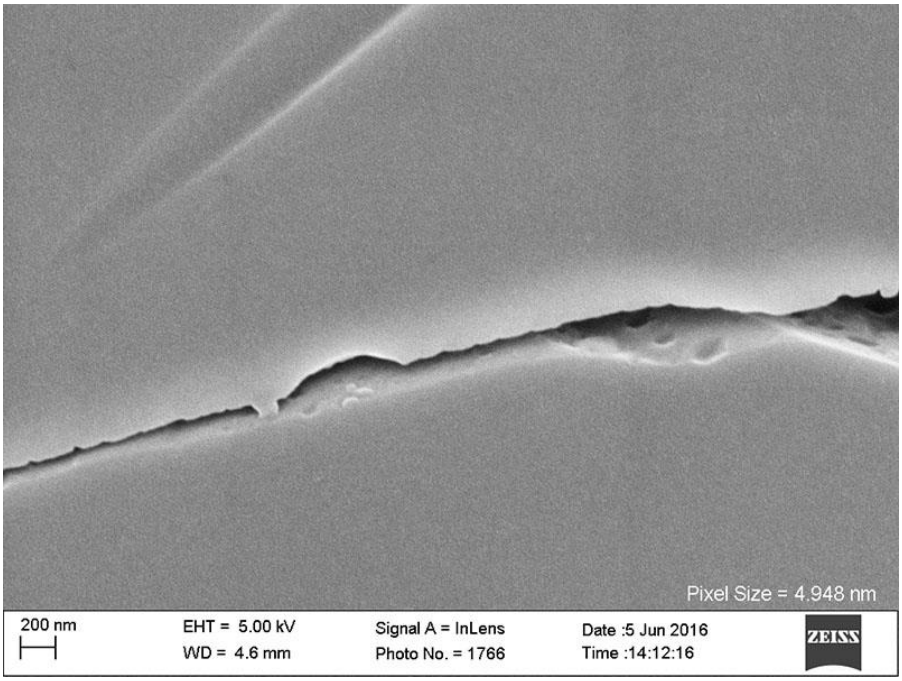

Figure A.295: Inlens SE micrograph from sample SFOT-1-10106.8. Grain boundary4, image A.

Grain Boundary 5

Image	**Measurement Number**	**Length (nm)**
A	1	74.45
A	2	76.78
A	3	90.81
A	4	107.20
A	5	39.60
A	6	116.28
A	7	81.39
A	8	74.45
B	1	45.62
B	2	83.46
B	3	86.03
B	4	83.63
B	5	94.42
B	6	95.94
C	1	109.56
C	2	105.81
C	3	95.75
C	4	106.67
C	5	103.19
D	1	13.45
D	2	22.64
D	3	22.64
D	4	17.18
E	1	38.48
E	2	22.00
E	3	41.51
E	4	39.66
E	5	48.85
E	6	31.73
	Mean Aperture	67.90

Table A.185: NGBC measurements and mean aperture from grain boundary 5 in sample SFOT-1-10106.8.

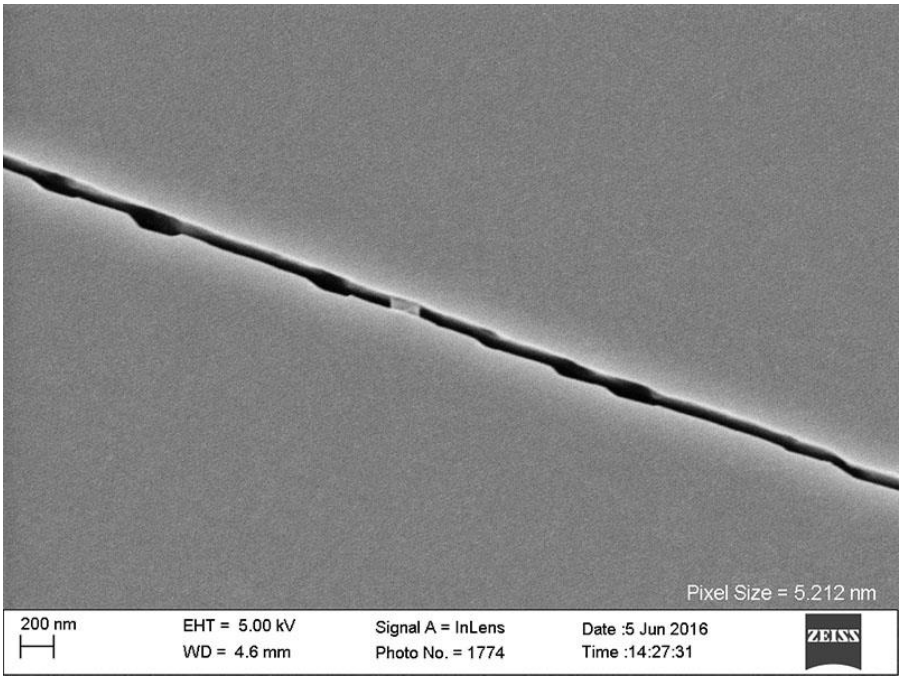

Figure A.296: Inlens SE micrograph from sample SFOT-1-10106.8. Grain boundary 5, image. A

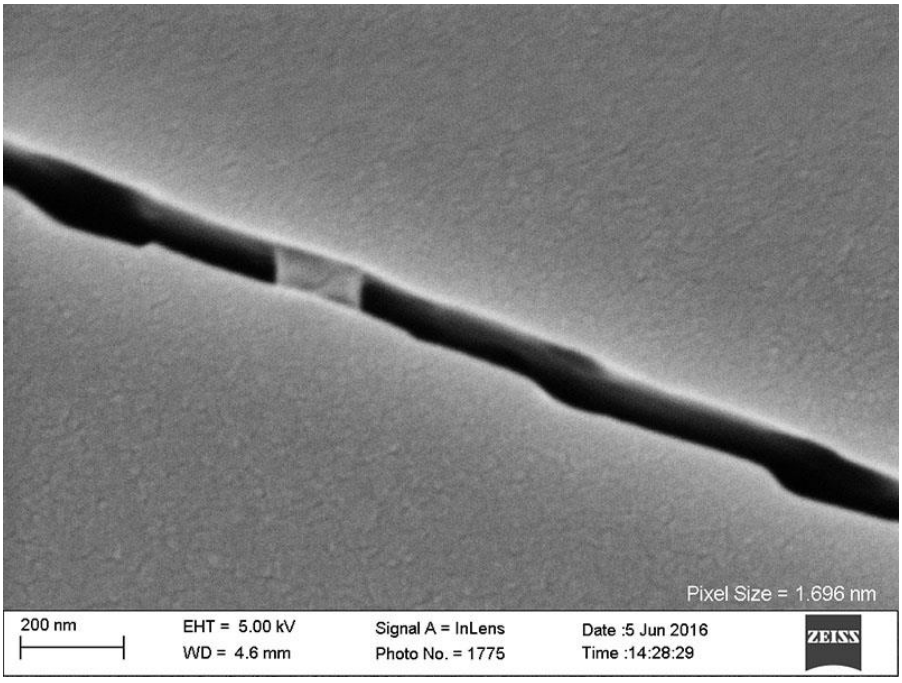

Figure A.297: Inlens SE micrograph from sample SFOT-1-10106.8. Grain boundary5, image B.

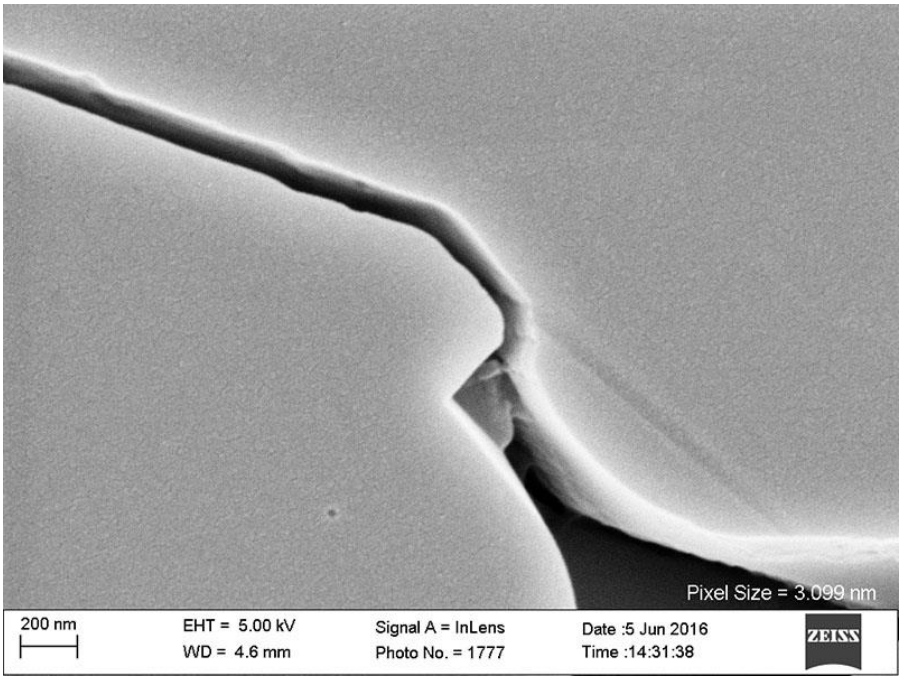

Figure A.298: Inlens SE micrograph from sample SFOT-1-10106.8. Grain boundary 5, image C.

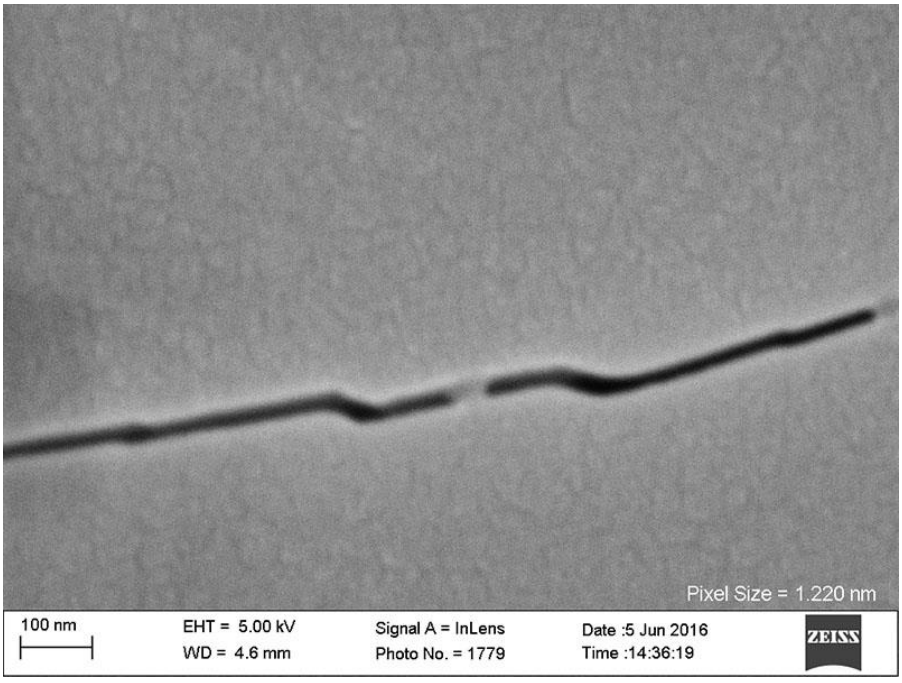

Figure A.299: Inlens SE micrograph from sample SFOT-1-10106.8. Grain boundary 5, image D.

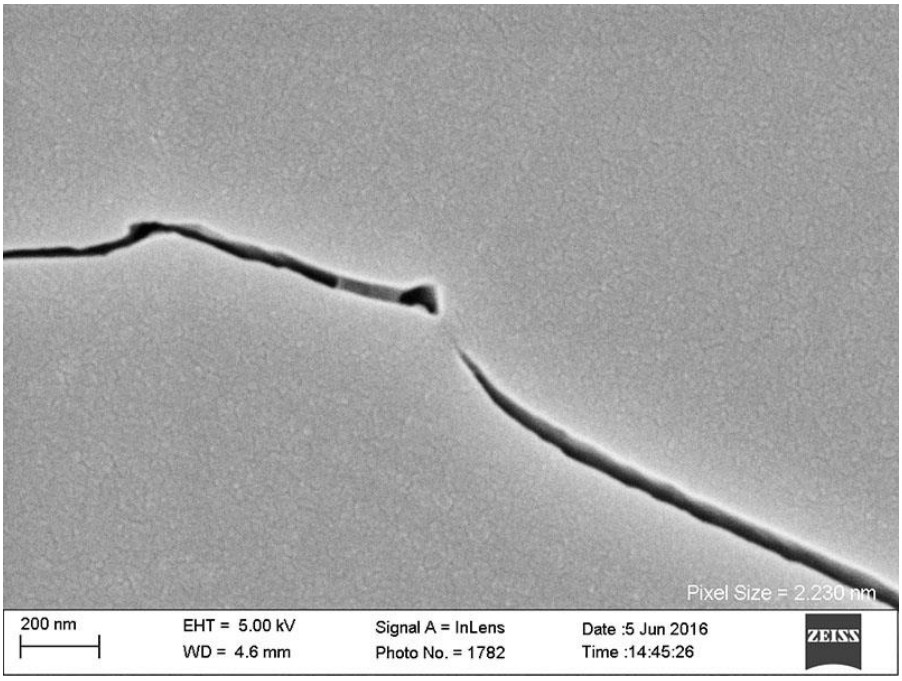

Figure A.300: Inlens SE micrograph from sample SFOT-1-10106.8. Grain boundary 5, image E.

Grain Boundary 6

Image	Measurement Number	**Length (nm)**
A	1	102.62
A	2	101.58
A	3	59.85
A	4	134.97
A	5	122.73
B	1	140.59
B	2	126.00
B	3	157.23
	Mean Aperture	118.20

Table A.186: NGBC measurements and mean aperture from grain boundary 6 in sample SFOT-1-10106.8.

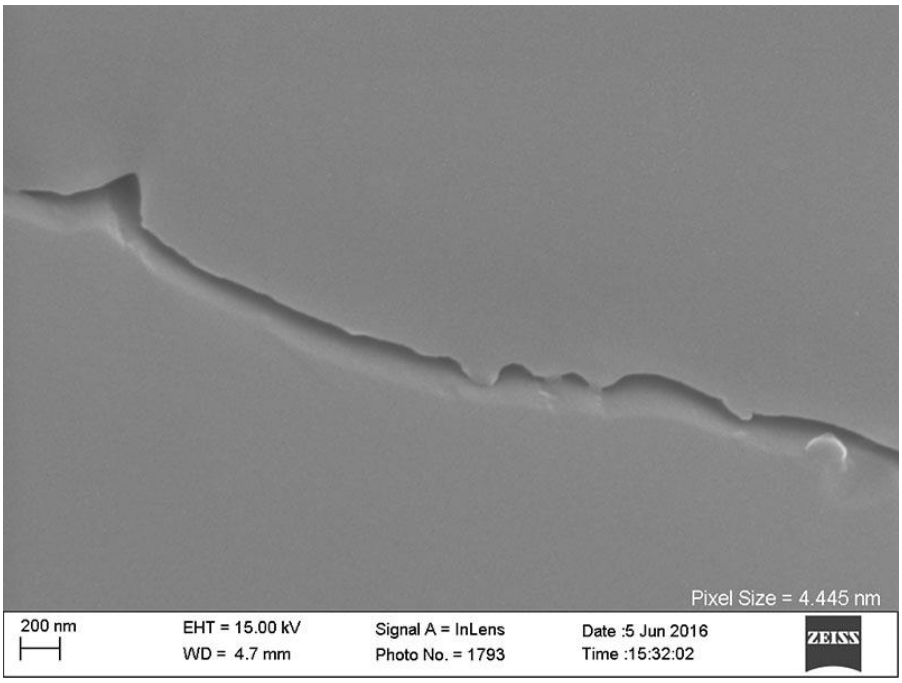

Figure A.301: Inlens SE micrograph from sample SFOT-1-10106.8. Grain boundary 6, image A.

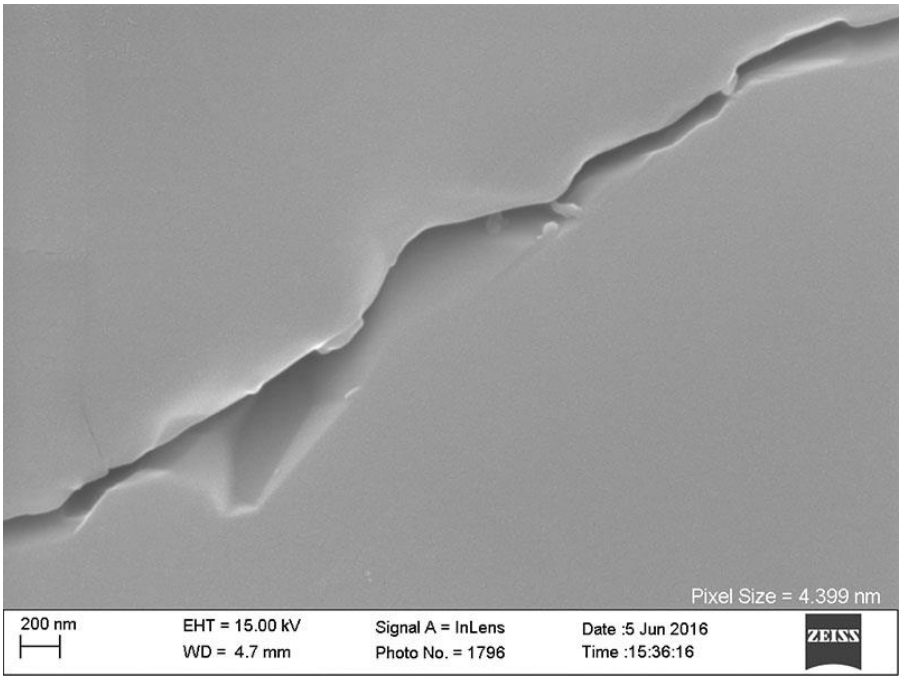

Figure A.302: Inlens SE micrograph from sample SFOT-1-10106.8. Grain boundary 6, image B.

Grain Boundary 7

Image	**Measurement Number**	**Length (nm)**
A	1	101.92
A	2	102.95
A	3	97.80
A	4	101.50
A	5	85.89
B	1	125.28
B	2	125.54
B	3	112.64
B	4	116.48
B	5	115.17
B	6	127.12
B	7	116.62
	Mean Aperture	110.74

Table A.187: NGBC measurements and mean aperture from grain boundary 7 in sample SFOT-1-10106.8.

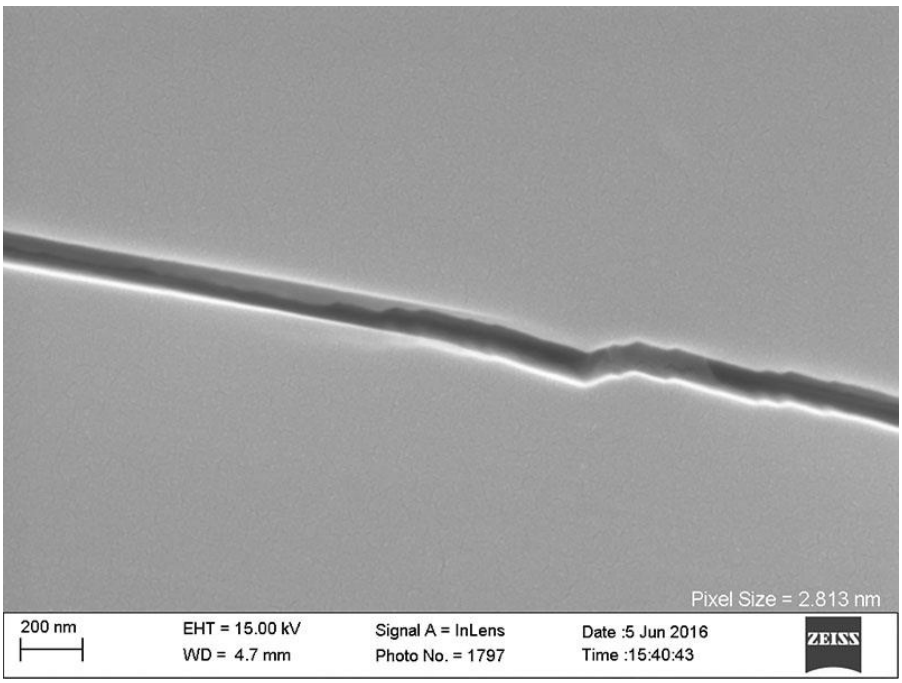

Figure A.303: Inlens SE micrograph from sample SFOT-1-10106.8. Grain boundary7, image A.

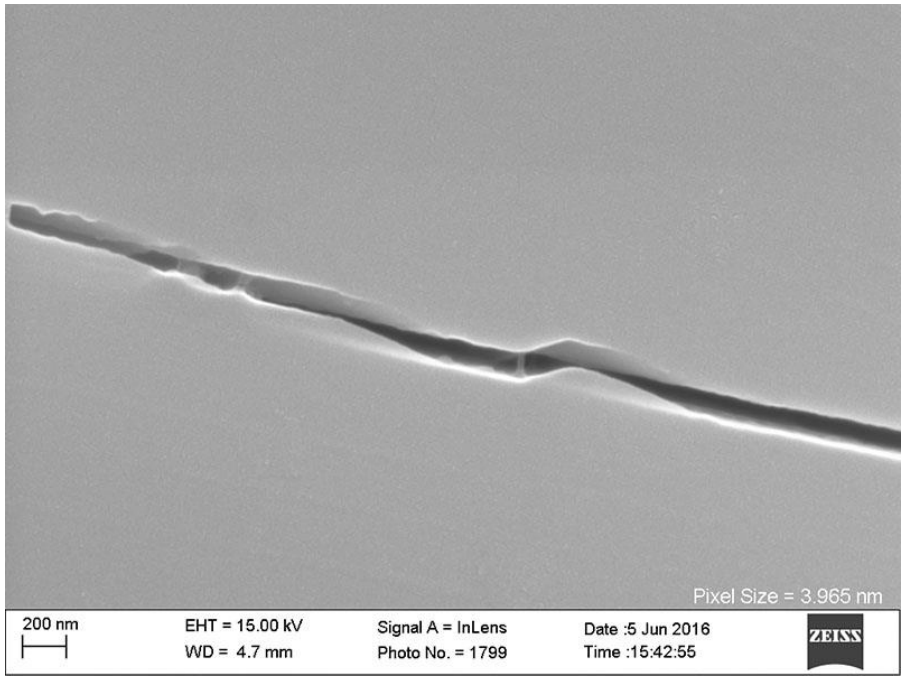

Figure A.304: Inlens SE micrograph from sample SFOT-1-10106.8. Grain boundary7, image B.

Grain Boundary 8

Image	**Measurement Number**	**Length (nm)**
A	1	80.78
A	2	72.50
A	3	75.23
A	4	61.18
A	5	66.26
A	6	67.89
	Mean Aperture	70.64

Table A.188: NGBC measurements and mean aperture from grain boundary 8 in sample SFOT-1-10106.8.

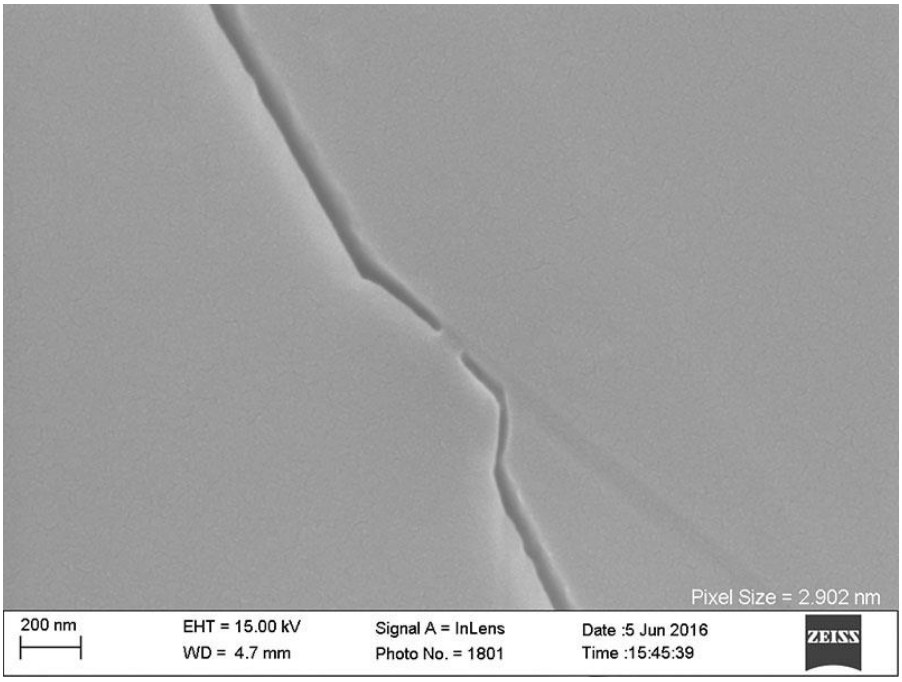

Figure A.305: Inlens SE micrograph from sample SFOT-1-10106.8. Grain boundary 8, image A.

Grain Boundary 9

Image	**Measurement Number**	**Length (nm)**
A	1	106.25
A	2	102.61
A	3	112.06
A	4	93.20
A	5	66.86
A	6	81.60
A	7	67.20
	Mean Aperture	89.97

Table A.189: NGBC measurements and mean aperture from grain boundary 9 in sample SFOT-1-10106.8.

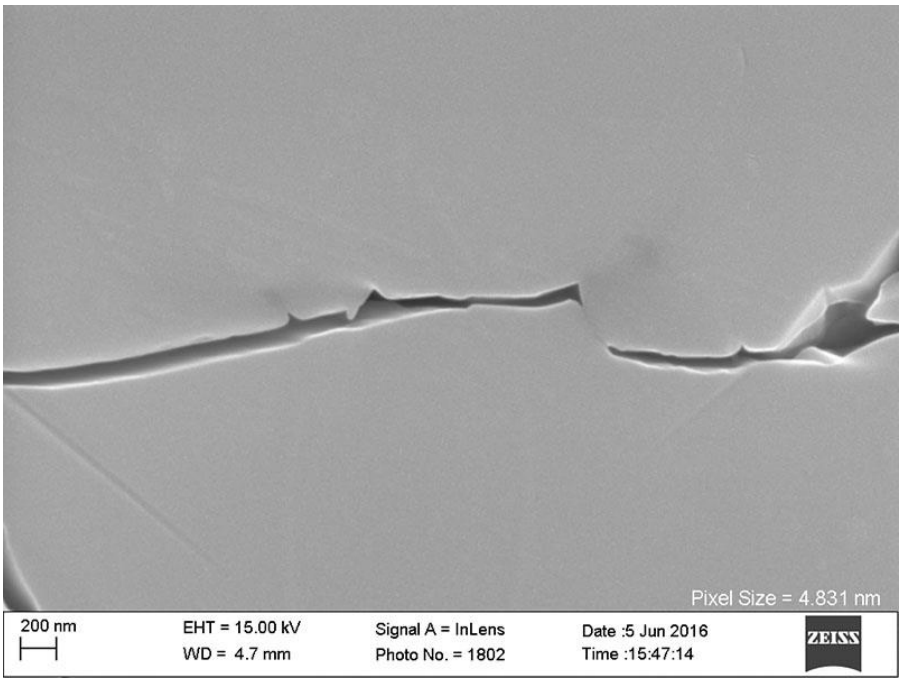

Figure A.306: Inlens SE micrograph from sample SFOT-1-10106.8. Grain boundary 9, image A.

SAMPLE: A1-4982.2, MONTEREY FORMATION

Mineral Cement	Rock Type	Sampled Depth (ft)	Sampled Depth (m)	Max burial depth (m)	Exhumed (m)	Max T (^{o}C)	Range (nm)	Sample Mean (nm)
Dolomite	Dolo-stone	4982.2	1518.575	2319	800.4254	110	215-402	302.36

Table A.190: Summary of sample A1-4982.2

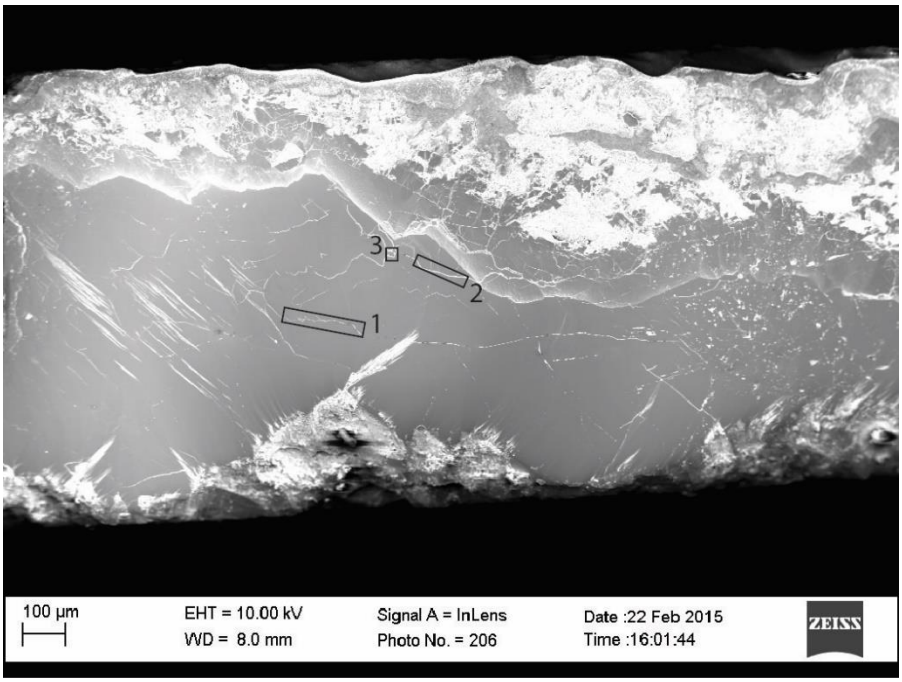

Figure A.307: Inlens SE micrograph of sample A1-4982.2. Boxes indicate locations used for NGBC aperture measurements.

Grain Boundary	Mean Aperture (nm)
1	290.35
2	214.35
3	402.38
Sample Mean	302.36

Table A.191: NGBC mean aperture and sample mean from grain boundaries in sample A1-4982.2.

Grain Boundary 1

Image	Measurement	Length (nm)
A	1	311.77
A	2	213.47
A	3	233.68
A	4	297.33
B	1	341.72
B	2	318.85
B	3	384.57
B	4	275.58
B	5	235.21
B	6	275.58
B	7	306.03
	Mean Aperture	**290.35**

Table A.192: NGBC measurements and mean aperture from grain boundary 1 in sample A1-4982.2.

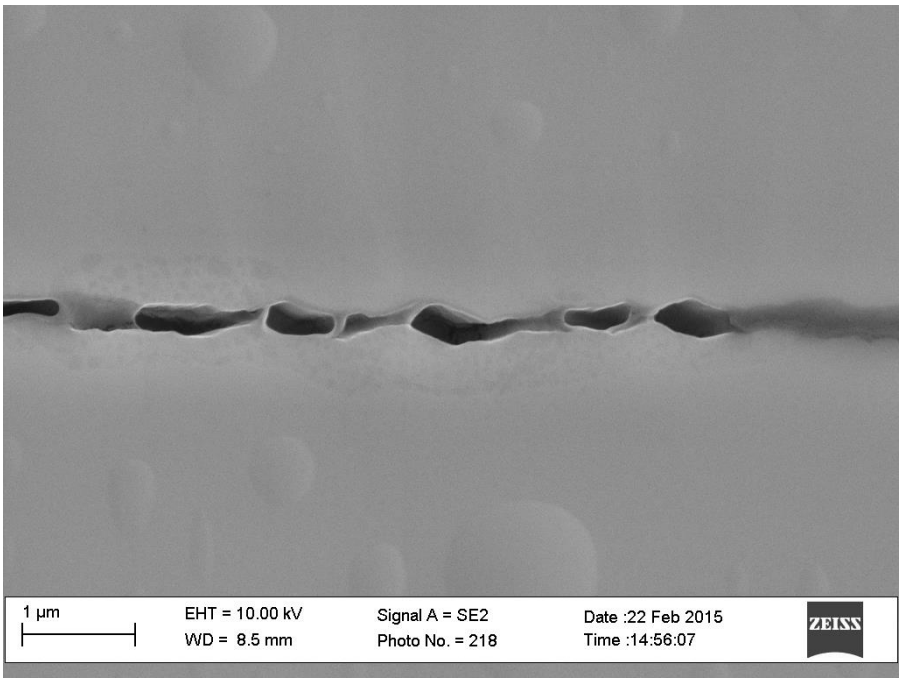

Figure A.308: Inlens SE micrograph from sample A1-4982.2. Grain boundary 1, image A.

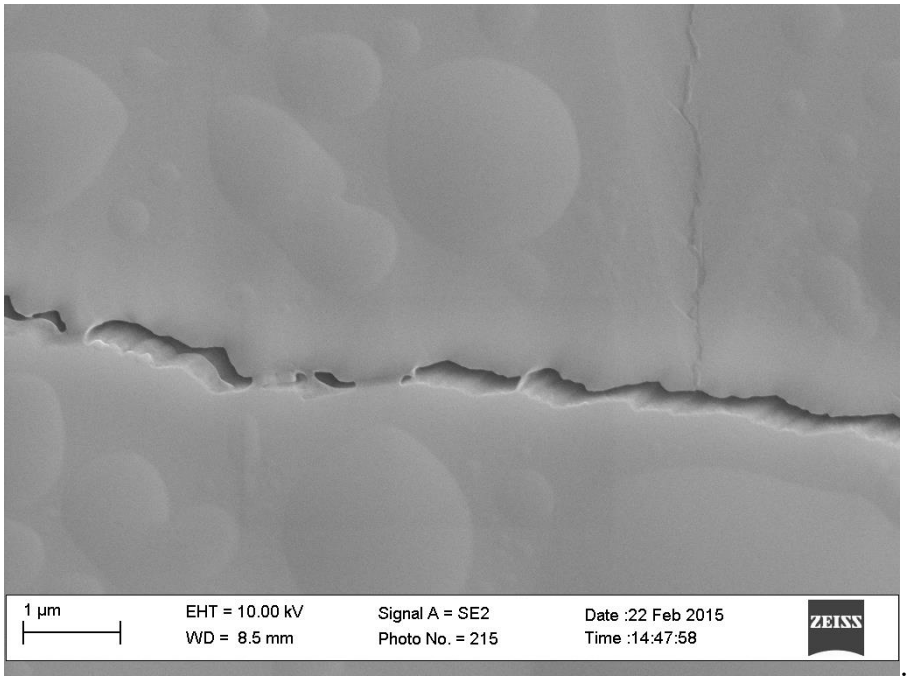

Figure A.309: Inlens SE micrograph from sample A1-4982.2. Grain boundary 1, image B.

Grain Boundary 2

Image	Measurement	Length (nm)
A	1	194.27
A	2	180.89
A	3	263.18
A	4	219.05
	Mean Aperture	214.35

Table A.193: NGBC measurements and mean aperture from grain boundary 2 in sample A1-4982.2.

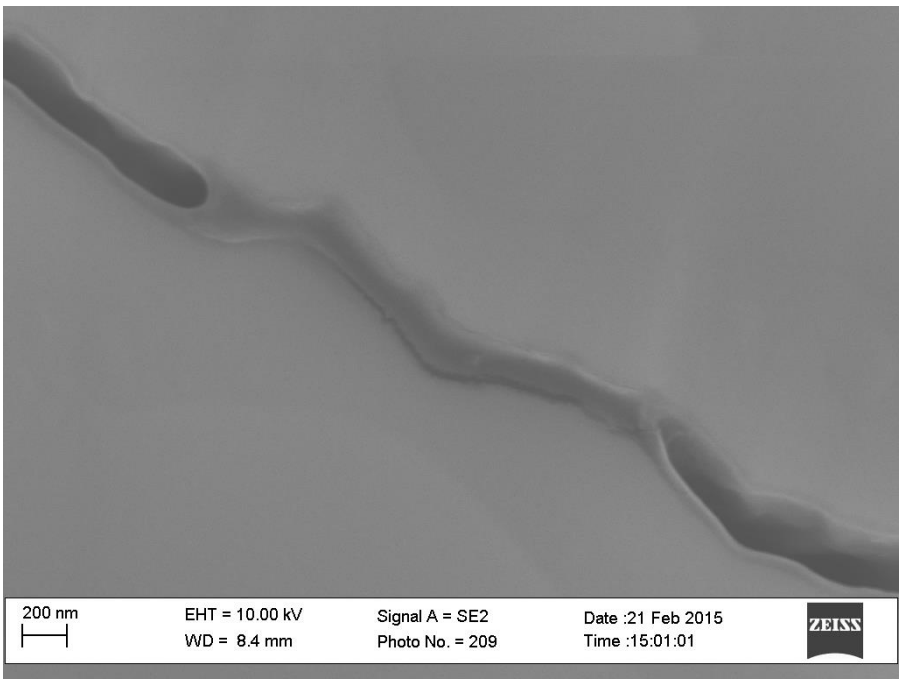

Figure A.310: Inlens SE micrograph from sample A1-4982.2. Grain boundary 2, image A.

Grain Boundary 3

Image	Measurement	Length (nm)
A	1	345.36
A	2	459.41
	Mean Aperture	**402.38**

Table A.194: NGBC measurements and mean aperture from grain boundary 3 in sample A1-4982.2.

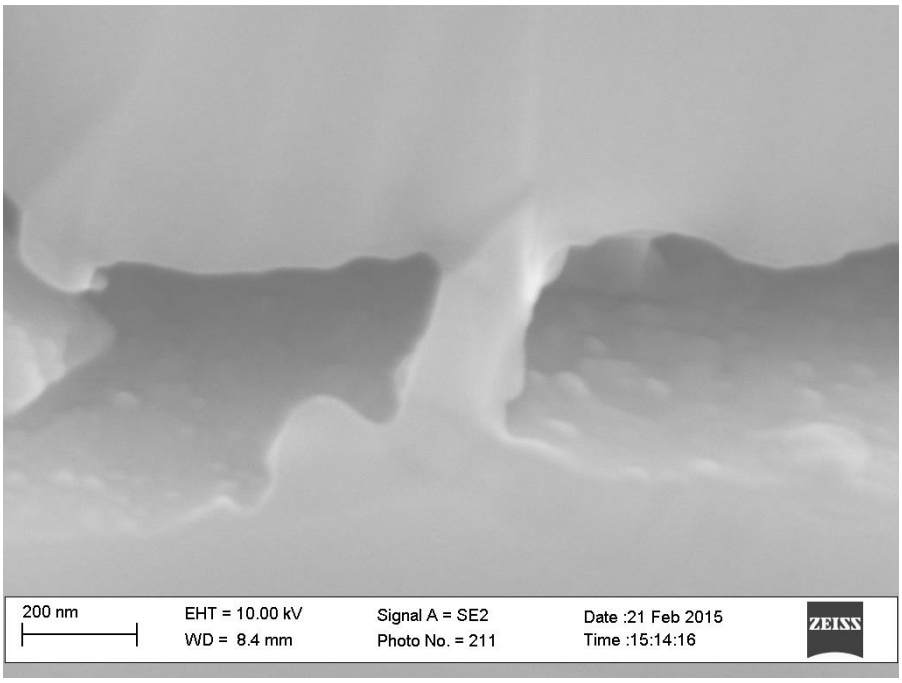

Figure A.311: Inlens SE micrograph from sample A1-4982.2. Grain boundary 3, image A.

SAMPLE: 2/26/95-2, MONTEREY FORMATION

Mineral Cement	Rock Type	Sampled Depth (ft)	Sampled Depth (m)	Max burial depth (m)	Exhumed (m)	Max T (^{o}C)	Range (nm)	Sample Mean (nm)
Dolomite	Dolo-stone	Outcrop	Surface	750	750	80	112-122	117.26

Table A.195: Summary of sample 2/26/95-2

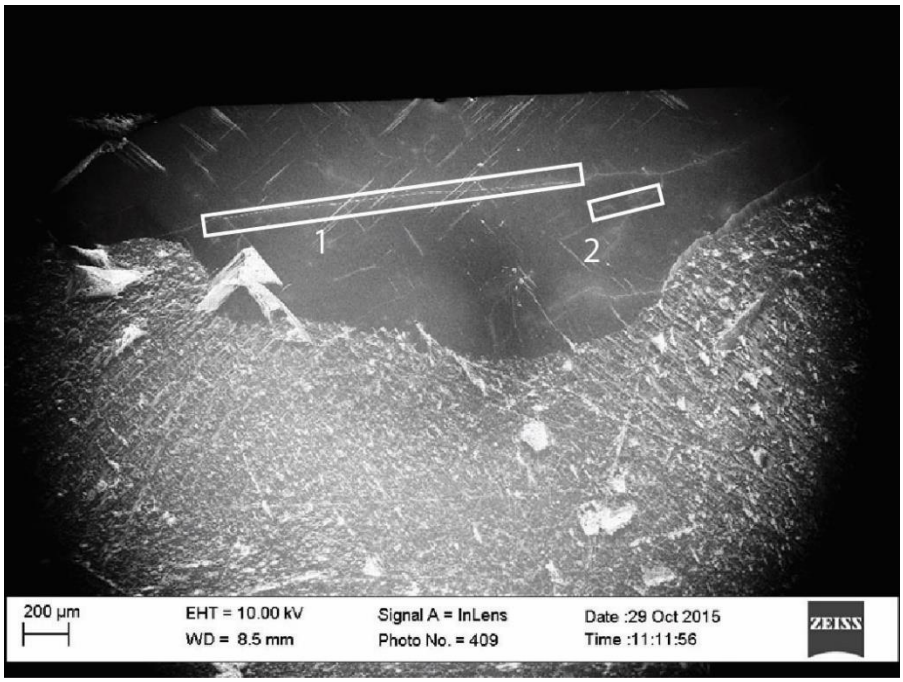

Figure A.312: Inlens SE micrograph of sample 2/26/95-2. Boxes indicate locations used for NGBC aperture measurements.

Grain Boundary	Mean Aperture
1	**122.52**
2	**112.01**
Sample Mean	117.26

Table A.196: NGBC mean aperture and sample mean from grain boundaries in sample 2/26/95-2

Grain Boundary 1

Image	Measurement Number	Length
A	1	272.92
A	2	245.90
A	3	229.74
A	4	207.62
A	5	245.29
B	1	28.13
B	2	24.26
B	3	24.48
B	4	24.05
B	5	23.31
B	6	22.03
Mean Aperture		**122.52**

Table A.197: NGBC measurements and mean aperture from grain boundary 1 in sample 2/26/95-2.

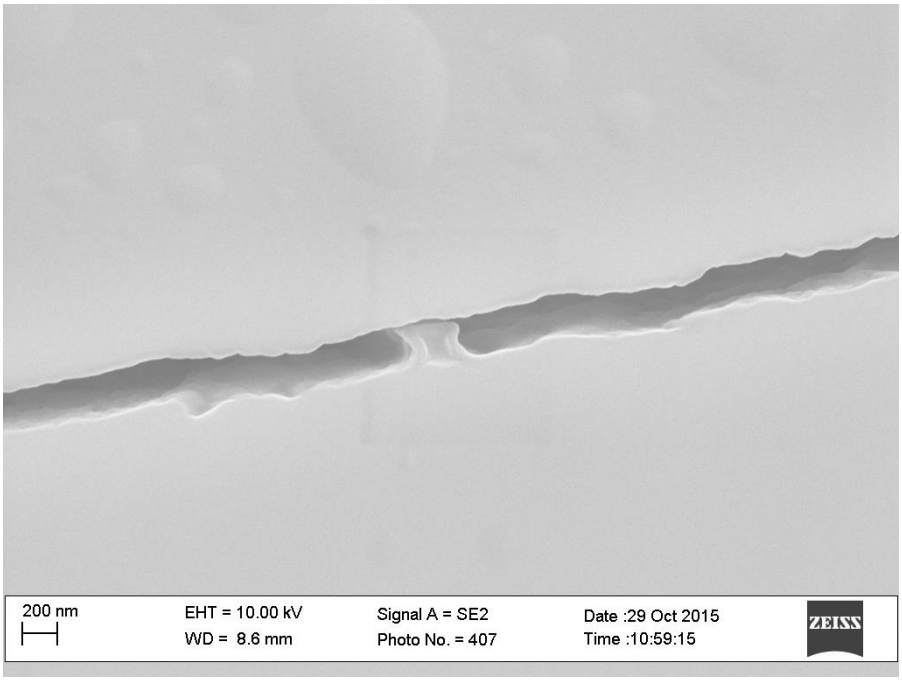

Figure A.313: Inlens SE micrograph from sample 2/26/95-2. Grain boundary1, image B.

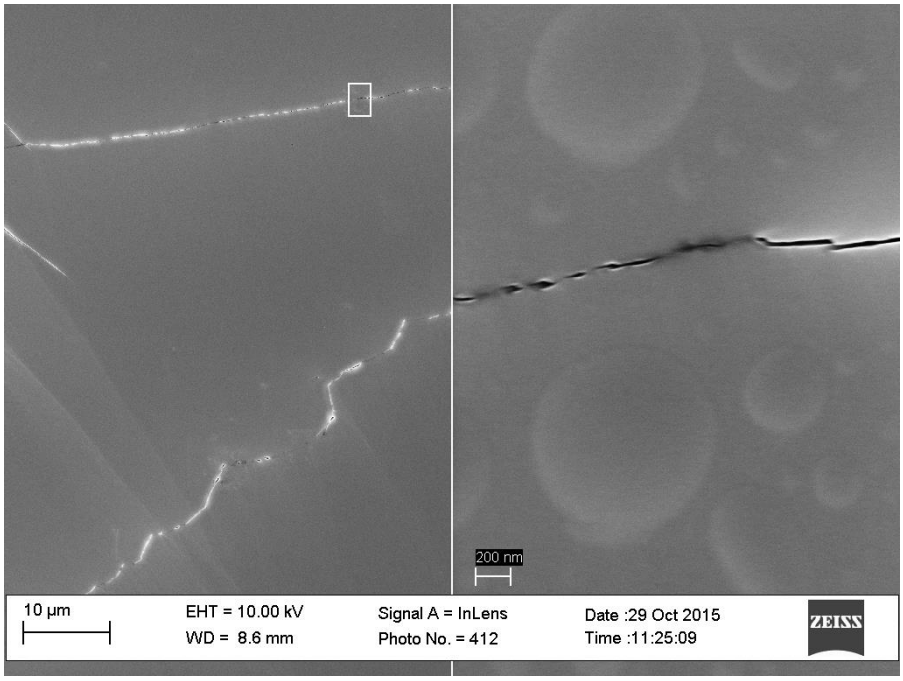

Figure A.314: Dual magnification inlens SE micrograph from sample 2/26/95-2. Grain boundary 1, image B.

Grain Boundary 2

Image	Measurement Number	Length
A	1	97.94
A	2	135.29
A	3	121.87
A	4	92.92
	Mean Aperture	**112.01**

Table A.198: NGBC measurements and mean aperture from grain boundary 2 in sample 2/26/95-2.

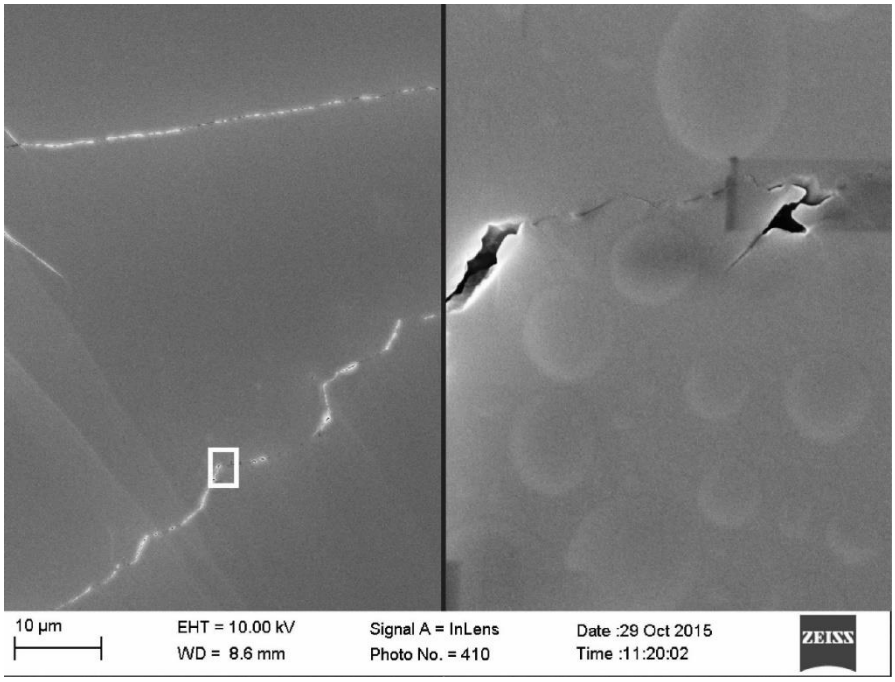

Figure A.315: Dual magnification inlens SE micrograph from sample 2/26/95-2. Grain boundary 2, image A.

Appendix B: NGBC Textural Characterization Images

SAMPLE: NAM-2774.5, NEW ALBANY FORMATION

Flat, Mating Contacts

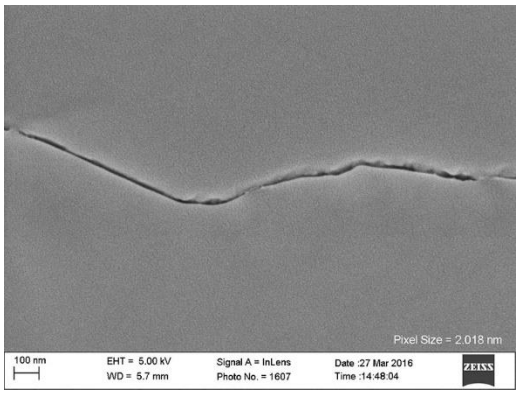

Figure B.1: Inlens SE micrograph from sample NAM-2774.5 showing example of NGBC containing a flat, mating contact.

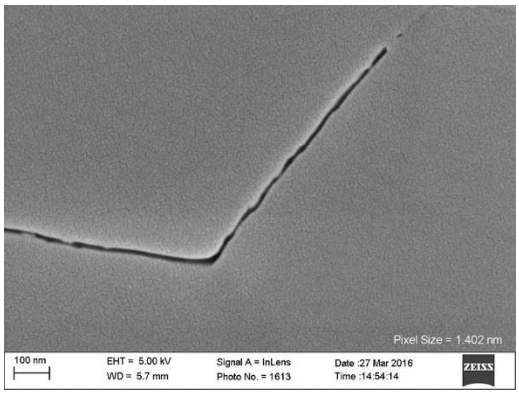

Figure B.2: Inlens SE micrograph from sample NAM-2774.5 showing example of NGBC containing a flat, mating contact.

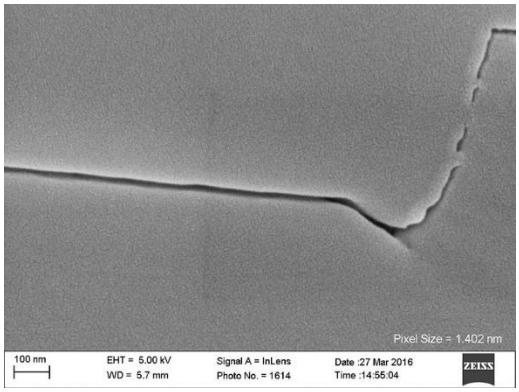

Figure B.3: Inlens SE micrograph from sample NAM-2774.5 showing example of NGBC containing a flat, mating contact.

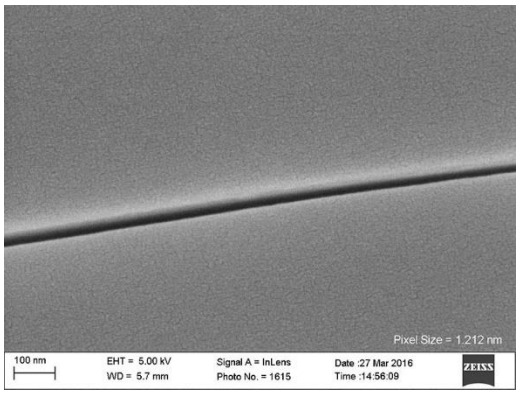

Figure B.4: Inlens SE micrograph from sample NAM-2774.5 showing example of NGBC containing a flat, mating contact.

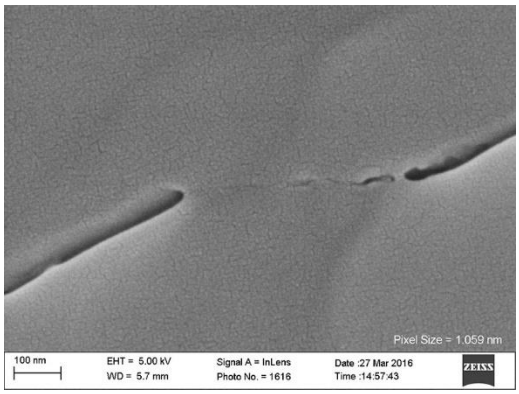

Figure B.5: Inlens SE micrograph from sample NAM-2774.5 showing example of NGBC containing a flat, mating contact.

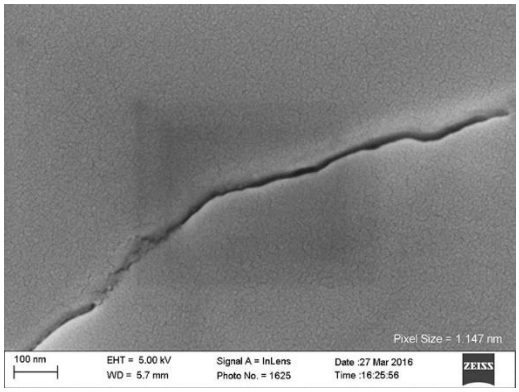

Figure B.6: Inlens SE micrograph from sample NAM-2774.5 showing example of NGBC containing a flat, mating contact.

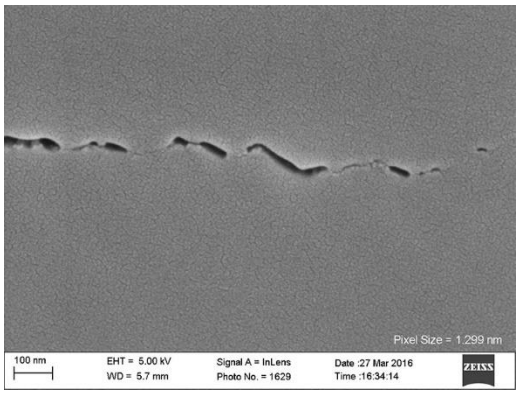

Figure B.7: Inlens SE micrograph from sample NAM-2774.5 showing example of NGBC containing a flat, mating contact.

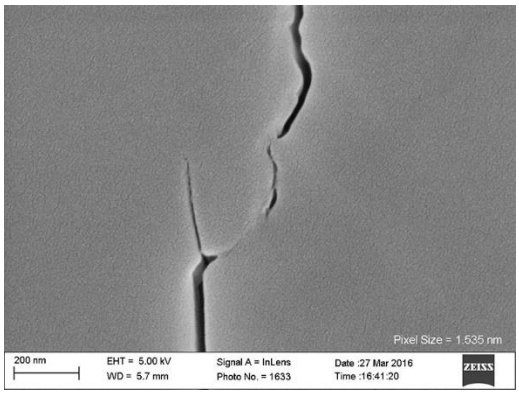

Figure B.8: Inlens SE micrograph from sample NAM-2774.5 showing example of NGBC containing a flat, mating contact.

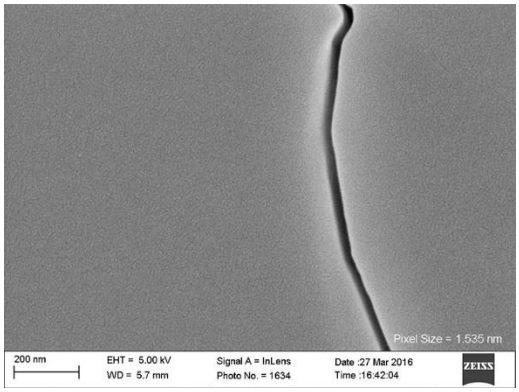

Figure B.9: Inlens SE micrograph from sample NAM-2774.5 showing example of NGBC containing a flat, mating contact.

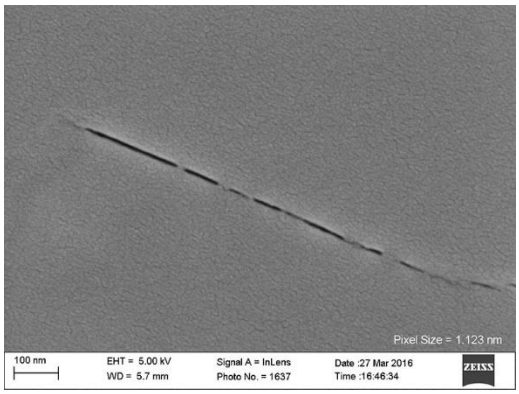

Figure B.10: Inlens SE micrograph from sample NAM-2774.5 showing example of NGBC containing a flat, mating contact.

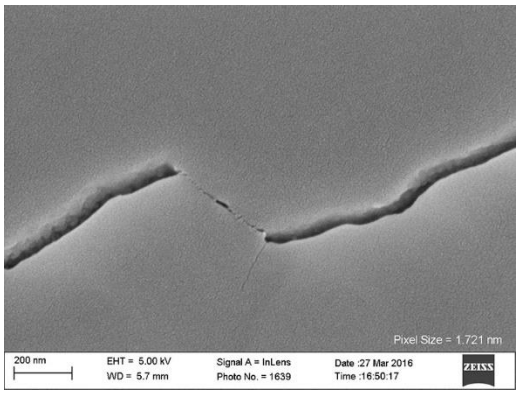

Figure B.11: Inlens SE micrograph from sample NAM-2774.5 showing example of NGBC containing a flat, mating contact.

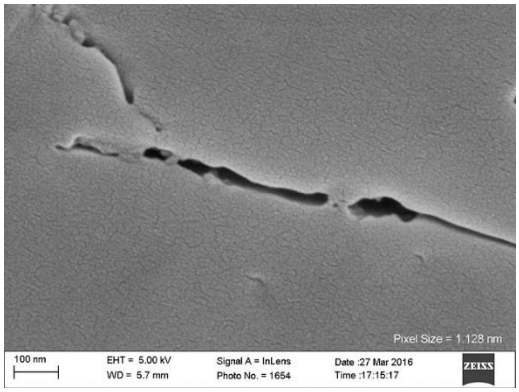

Figure B.12: Inlens SE micrograph from sample NAM-2774.5 showing example of NGBC containing a flat, mating contact.

Cuspate-lobate

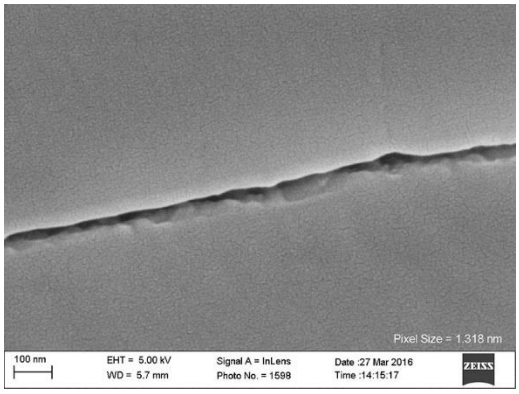

Figure B.13: Inlens SE micrograph from sample NAM-2774.5 showing example of NGBC containing a cuspate-lobate texture.

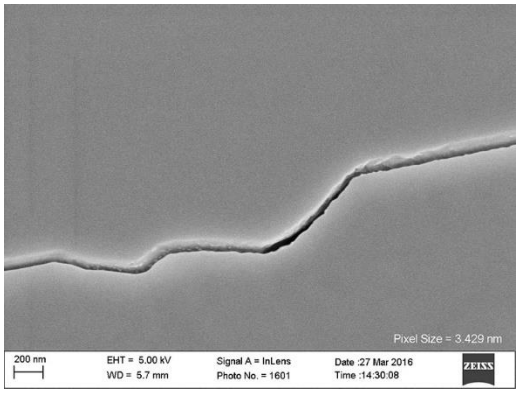

Figure B.14: Inlens SE micrograph from sample NAM-2774.5 showing example of NGBC containing a cuspate-lobate texture.

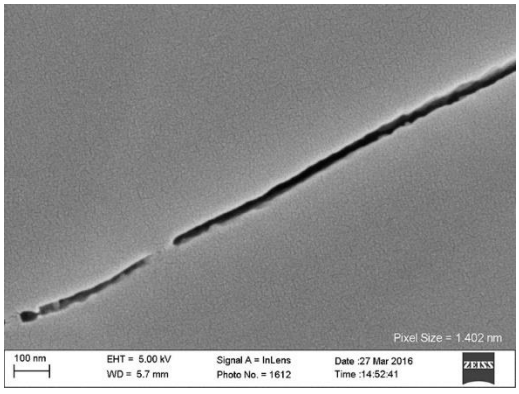

Figure B.15: Inlens SE micrograph from sample NAM-2774.5 showing example of NGBC containing a cuspate-lobate texture.

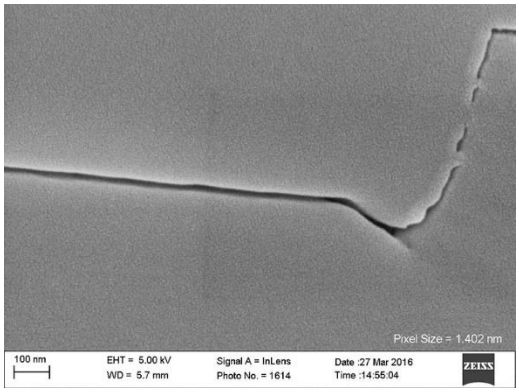

Figure B.16: Inlens SE micrograph from sample NAM-2774.5 showing example of NGBC containing a cuspate-lobate texture.

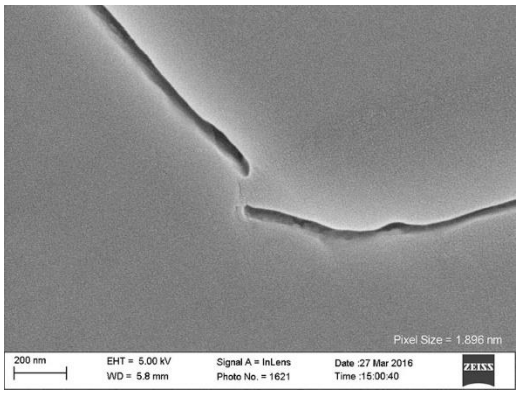

Figure B.17: Inlens SE micrograph from sample NAM-2774.5 showing example of NGBC containing a cuspate-lobate texture.

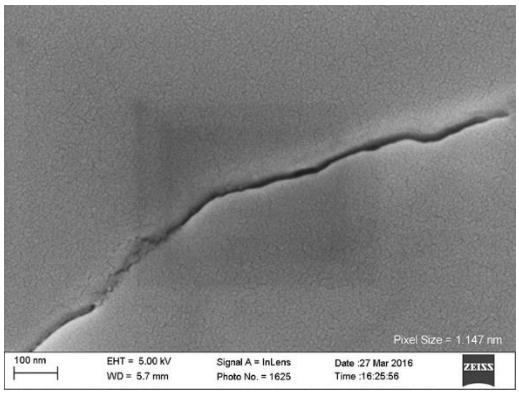

Figure B.18: Inlens SE micrograph from sample NAM-2774.5 showing example of NGBC containing a cuspate-lobate texture.

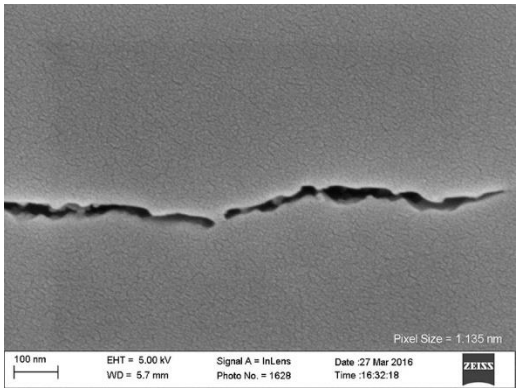

Figure B.19.: Inlens SE micrograph from sample NAM-2774.5 showing example of NGBC containing a cuspate-lobate texture.

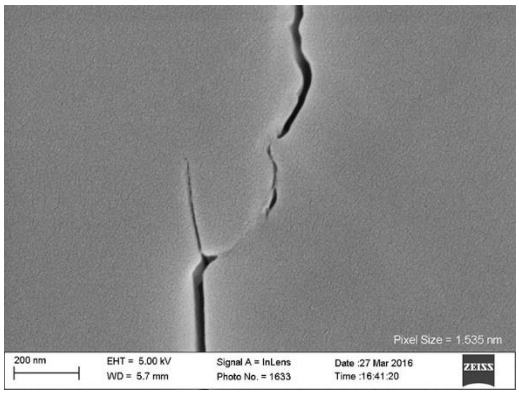

Figure B.20: Inlens SE micrograph from sample NAM-2774.5 showing example of NGBC containing a cuspate-lobate texture.

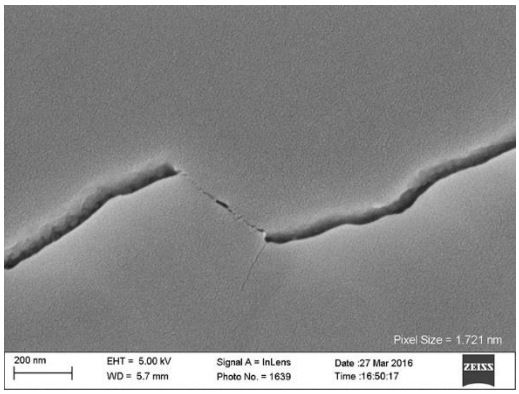

Figure B.21: Inlens SE micrograph from sample NAM-2774.5 showing example of NGBC containing a cuspate-lobate texture.

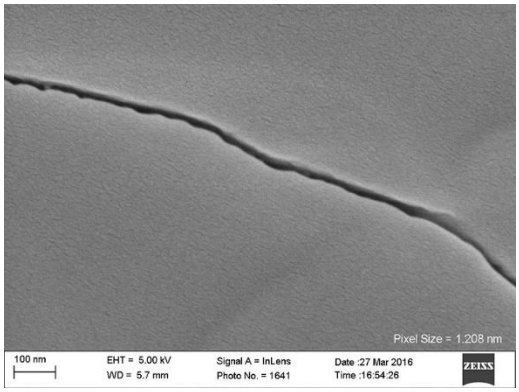

Figure B.22: Inlens SE micrograph from sample NAM-2774.5 showing example of NGBC containing a cuspate-lobate texture.

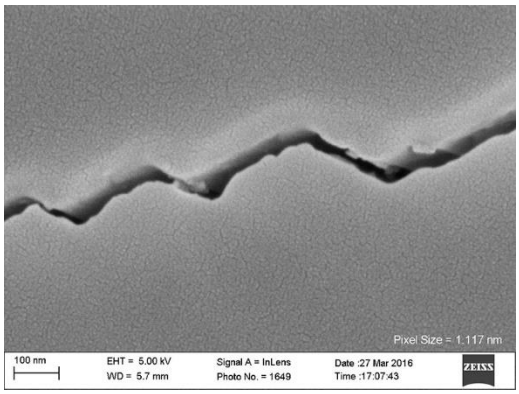

Figure B.23: Inlens SE micrograph from sample NAM-2774.5 showing example of NGBC containing a cuspate-lobate texture.

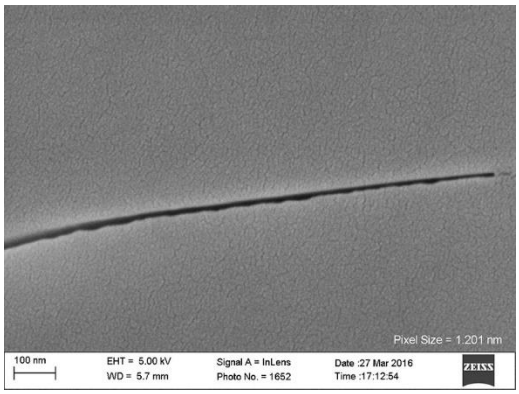

Figure B.24: Inlens SE micrograph from sample NAM-2774.5 showing example of NGBC containing a cuspate-lobate texture.

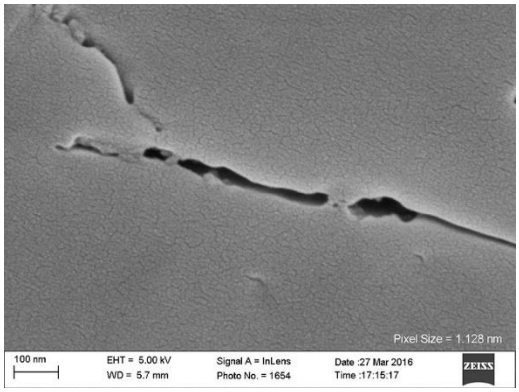

Figure B.25: Inlens SE micrograph from sample NAM-2774.5 showing example of NGBC containing a cuspate-lobate texture.

Negative Crystal

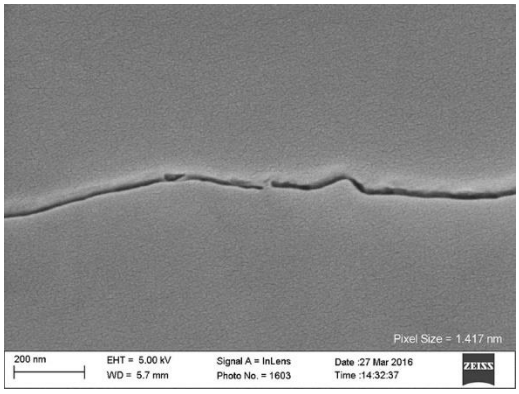

Figure B.26: Inlens SE micrograph from sample NAM-2774.5 showing example of NGBC containing negative crystal structures at the grain boundary.

Meniscus shaped Pore

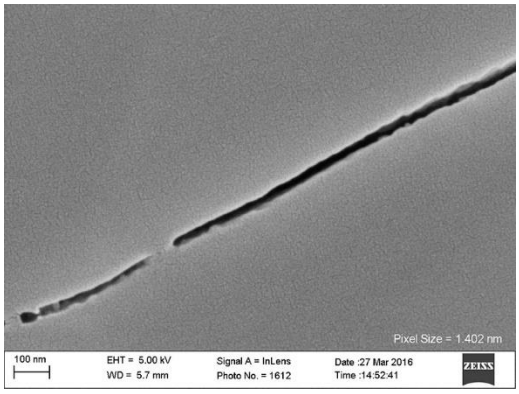

Figure B.27: Inlens SE micrograph from sample NAM-2774.5 showing example of NGBC containing bridging cements that create a meniscus shaped pore.

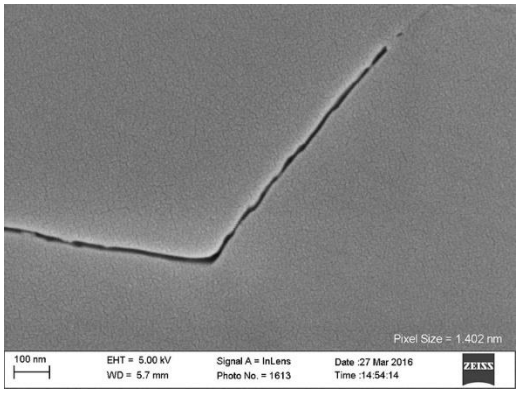

Figure B.28: Inlens SE micrograph from sample NAM-2774.5 showing example of NGBC containing bridging cements that create a meniscus shaped pore.

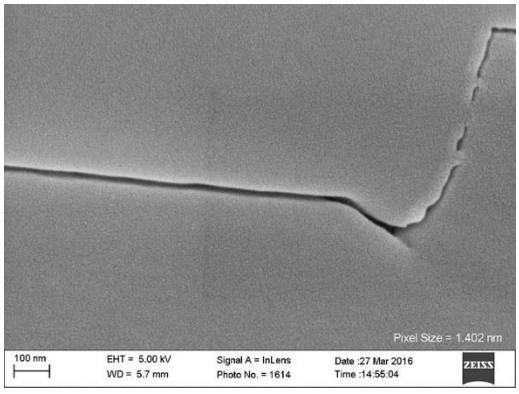

Figure B.29: Inlens SE micrograph from sample NAM-2774.5 showing example of NGBC containing bridging cements that create a meniscus shaped pore.

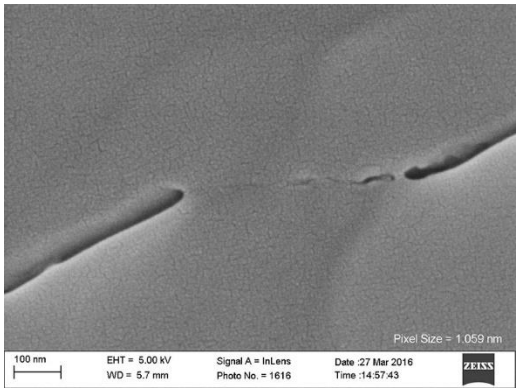

Figure B.30: Inlens SE micrograph from sample NAM-2774.5 showing example of NGBC containing bridging cements that create a meniscus shaped pore.

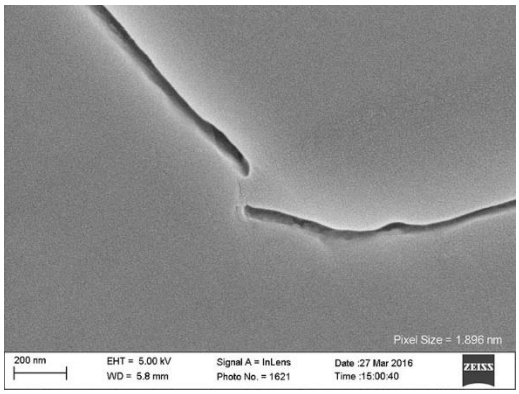

Figure B.31: Inlens SE micrograph from sample NAM-2774.5 showing example of NGBC containing bridging cements that create a meniscus shaped pore.

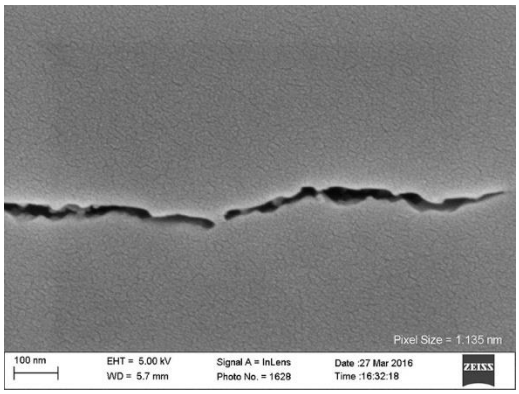

Figure B.32: Inlens SE micrograph from sample NAM-2774.5 showing example of NGBC containing bridging cements that create a meniscus shaped pore.

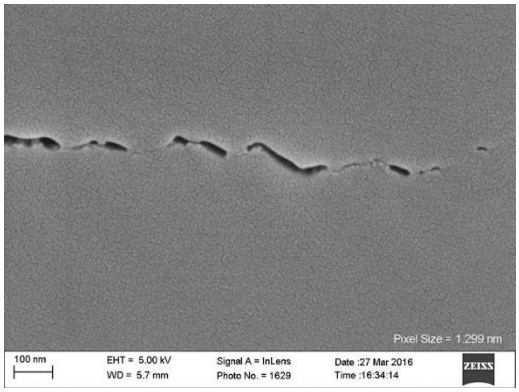

Figure B.33: Inlens SE micrograph from sample NAM-2774.5 showing example of NGBC containing bridging cements that create a meniscus shaped pore.

Rectangular Shaped Pore

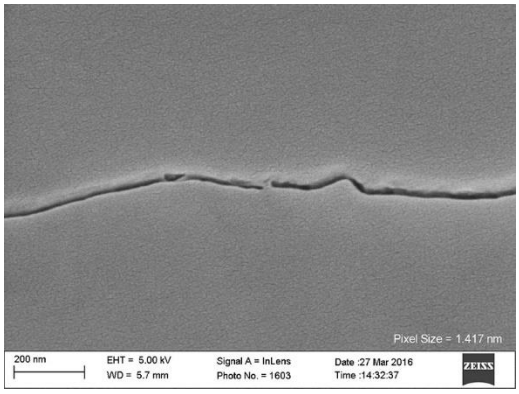

Figure B.34: Inlens SE micrograph from sample NAM-2774.5 showing example of NGBC containing bridging cements that create a rectangular shaped pore.

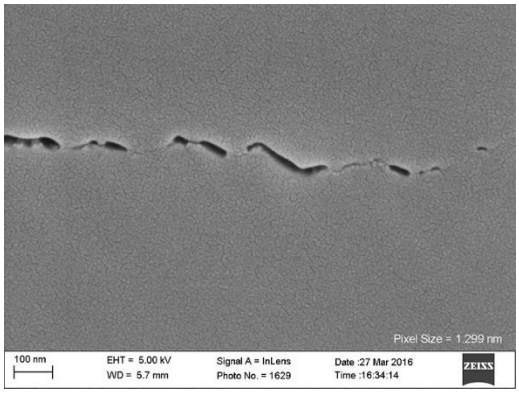

Figure B.35: Inlens SE micrograph from sample NAM-2774.5 showing example of NGBC containing bridging cements that create a rectangular shaped pore.

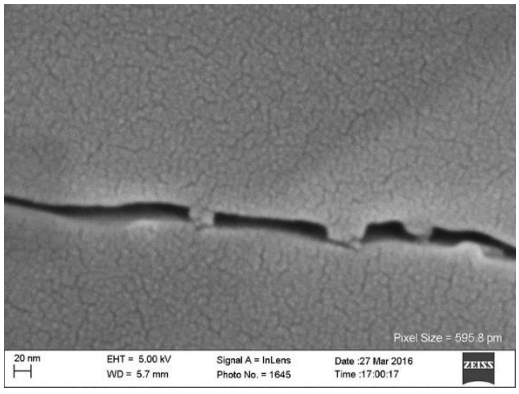

Figure B.36: Inlens SE micrograph from sample NAM-2774.5 showing example of NGBC containing bridging cements that create a rectangular shaped pore.

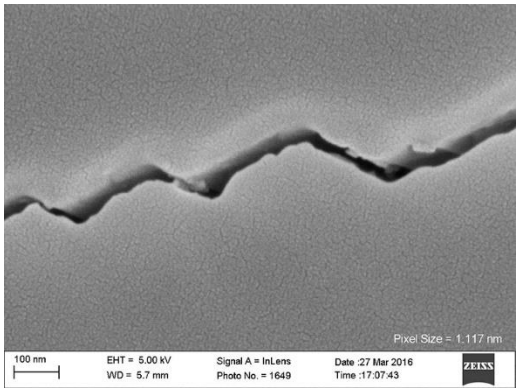

Figure B.37: Inlens SE micrograph from sample NAM-2774.5 showing example of NGBC containing bridging cements that create a rectangular shaped pore.

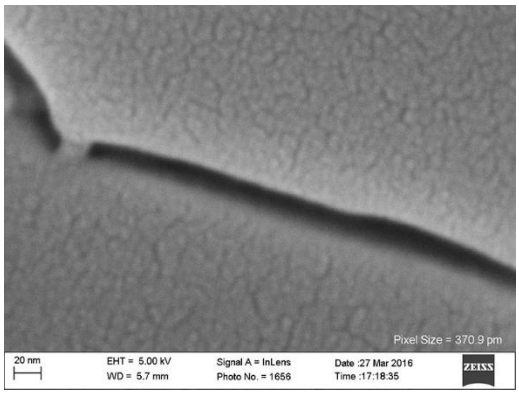

Figure B.38: Inlens SE micrograph from sample NAM-2774.5 showing example of NGBC containing bridging cements that create a rectangular shaped pore.

Partial Bridge

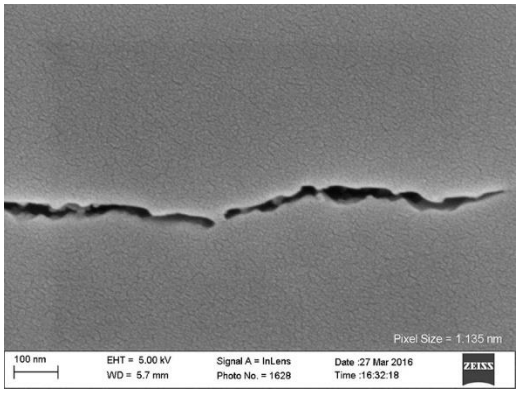

Figure B.39: Inlens SE micrograph from sample NAM-2774.5 showing example of NGBC containing partially bridging cements that do not completely traverse the entire aperture of the NGBC.

SAMPLE: NAM-2784, NEW ALBANY FORMATION

Flat, Mating Contacts

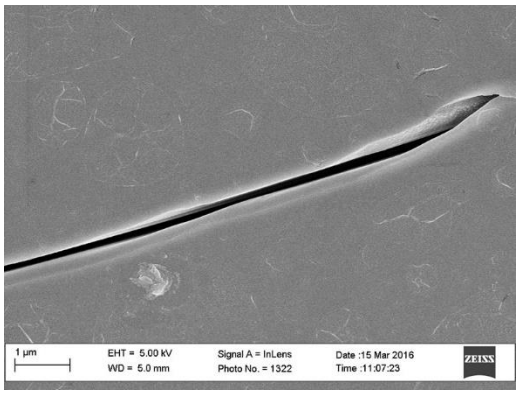

Figure B.40: Inlens SE micrograph from sample NAM-2784 showing example of NGBC containing a flat, mating contact.

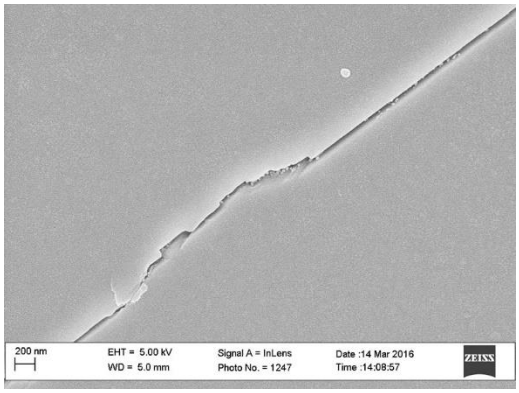

Figure B.41: Inlens SE micrograph from sample NAM-2784 showing example of NGBC containing a flat, mating contact.

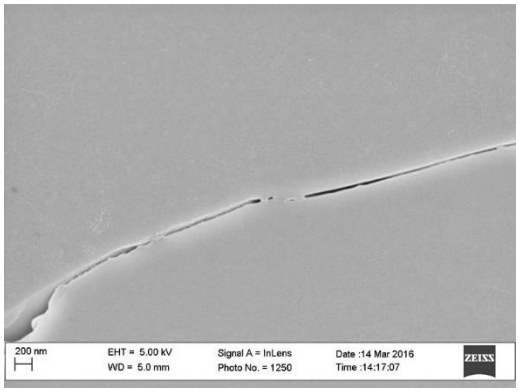

Figure B.42: Inlens SE micrograph from sample NAM-2784 showing example of NGBC containing a flat, mating contact.

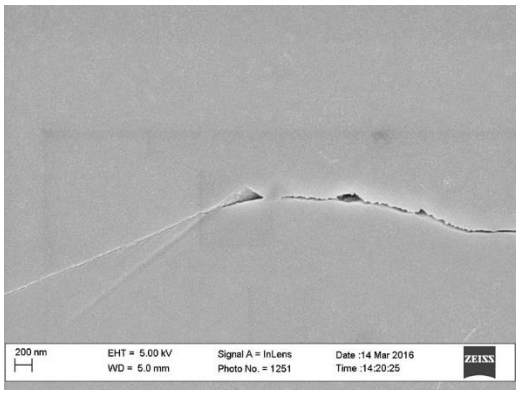

Figure B.43: Inlens SE micrograph from sample NAM-2784 showing example of NGBC containing a flat, mating contact.

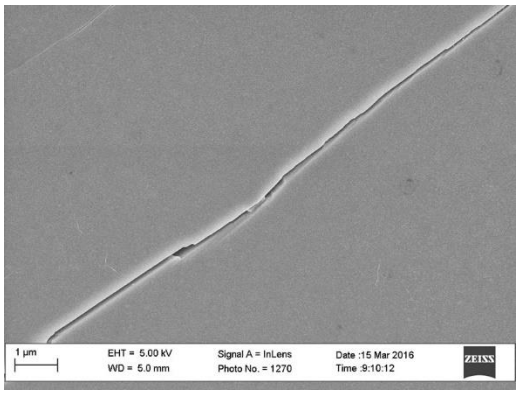

Figure B.44: Inlens SE micrograph from sample NAM-2784 showing example of NGBC containing a flat, mating contact.

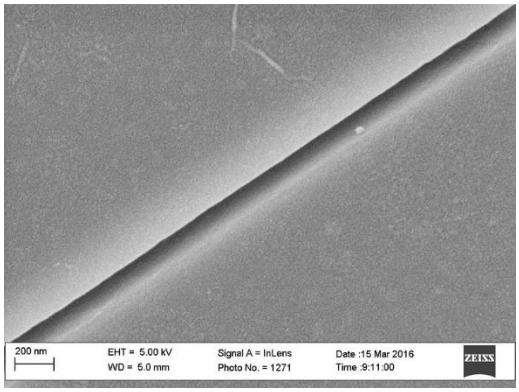

Figure B.45: Inlens SE micrograph from sample NAM-2784 showing example of NGBC containing a flat, mating contact.

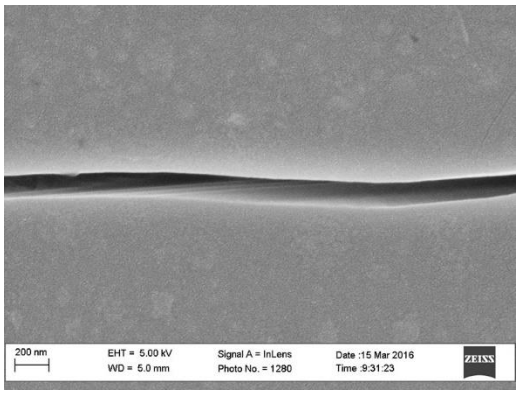

Figure B.46: Inlens SE micrograph from sample NAM-2784 showing example of NGBC containing a flat, mating contact.

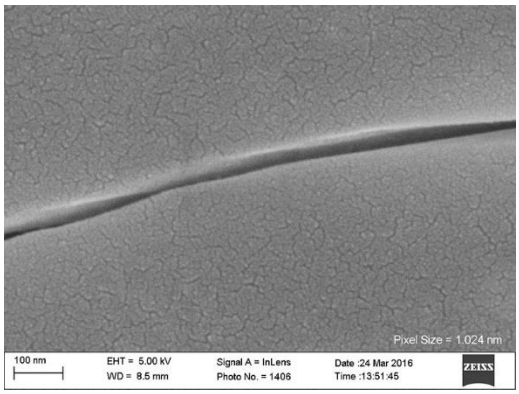

Figure B.47: Inlens SE micrograph from sample NAM-2784 showing example of NGBC containing a flat, mating contact.

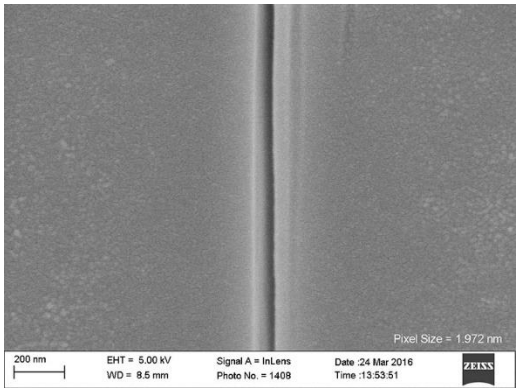

Figure B.48: Inlens SE micrograph from sample NAM-2784 showing example of NGBC containing a flat, mating contact.

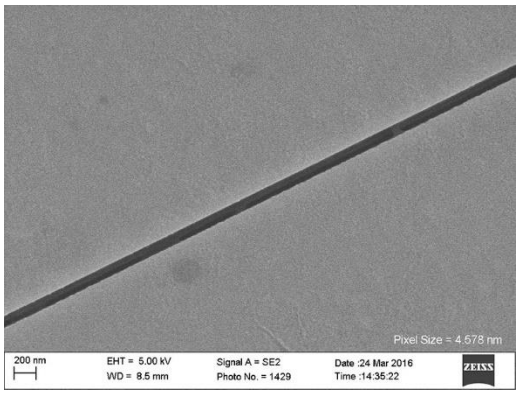

Figure B.49: Inlens SE micrograph from sample NAM-2784 showing example of NGBC containing a flat, mating contact.

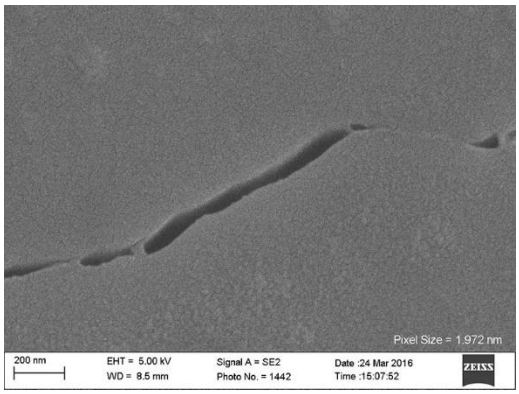

Figure B.50: Inlens SE micrograph from sample NAM-2784 showing example of NGBC containing a flat, mating contact.

Cuspate-lobate

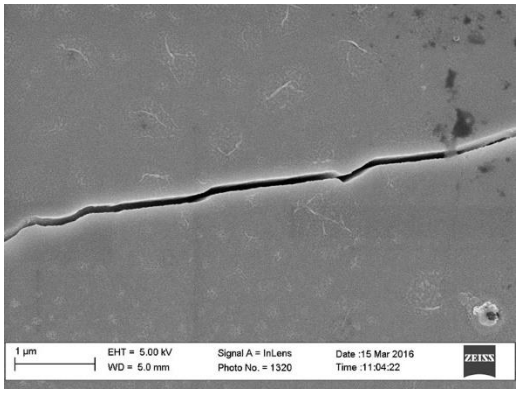

Figure B.51: Inlens SE micrograph from sample NAM-2784 showing example of NGBC containing a cuspate-lobate texture.

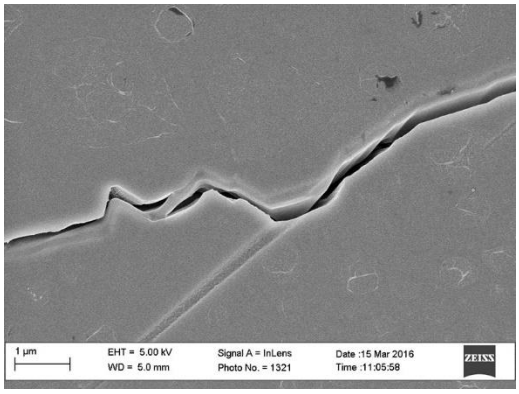

Figure B.52: Inlens SE micrograph from sample NAM-2784 showing example of NGBC containing a cuspate-lobate texture.

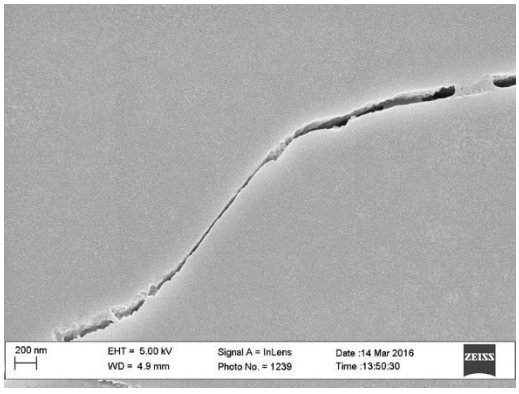

Figure B.53: Inlens SE micrograph from sample NAM-2784 showing example of NGBC containing a cuspate-lobate texture.

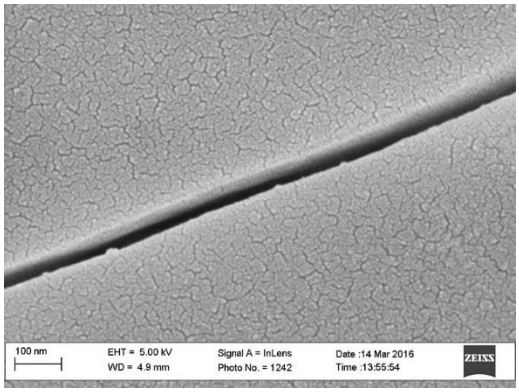

Figure B.54: Inlens SE micrograph from sample NAM-2784 showing example of NGBC containing a cuspate-lobate texture.

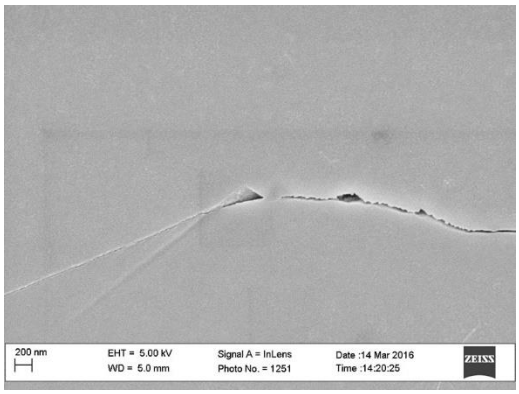

Figure B.55: Inlens SE micrograph from sample NAM-2784 showing example of NGBC containing a cuspate-lobate texture.

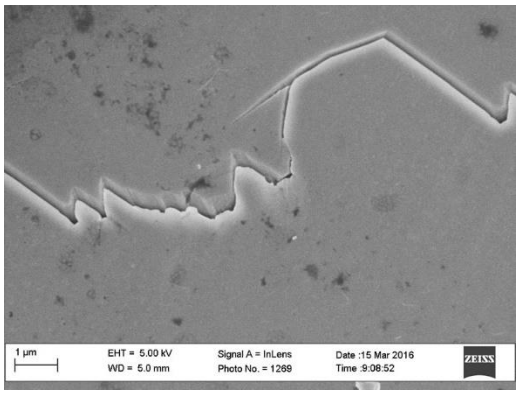

Figure B.56: Inlens SE micrograph from sample NAM-2784 showing example of NGBC containing a cuspate-lobate texture.

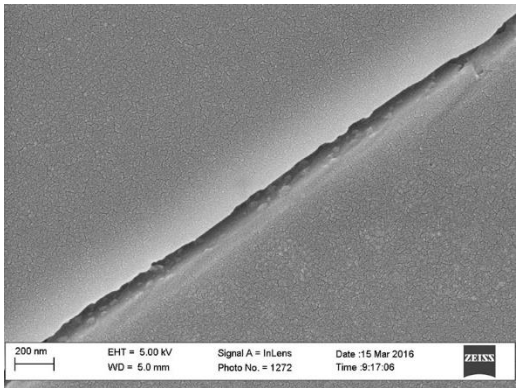

Figure B.57: Inlens SE micrograph from sample NAM-2784 showing example of NGBC containing a cuspate-lobate texture.

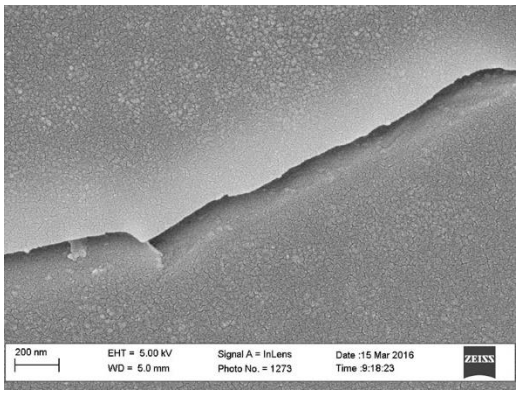

Figure B.58: Inlens SE micrograph from sample NAM-2784 showing example of NGBC containing a cuspate-lobate texture.

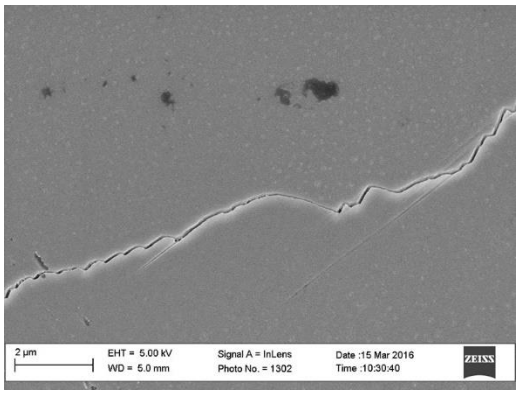

Figure B.59: Inlens SE micrograph from sample NAM-2784 showing example of NGBC containing a cuspate-lobate texture.

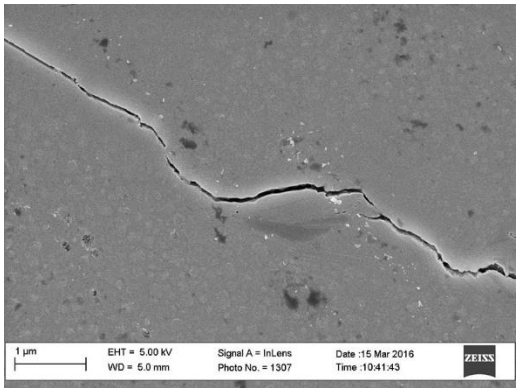

Figure B.60: Inlens SE micrograph from sample NAM-2784 showing example of NGBC containing a cuspate-lobate texture.

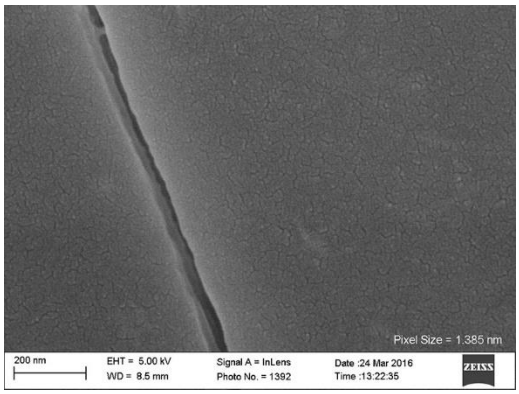

Figure B.61: Inlens SE micrograph from sample NAM-2784 showing example of NGBC containing a cuspate-lobate texture.

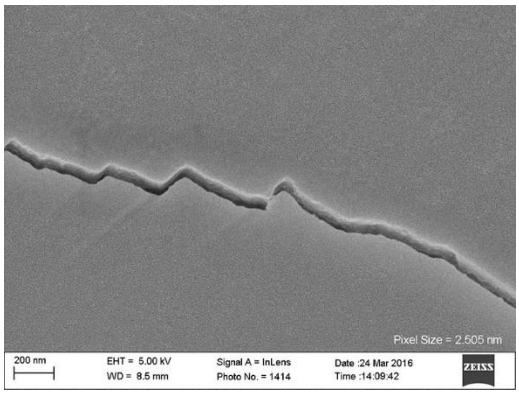

Figure B.62: Inlens SE micrograph from sample NAM-2784 showing example of NGBC containing a cuspate-lobate texture.

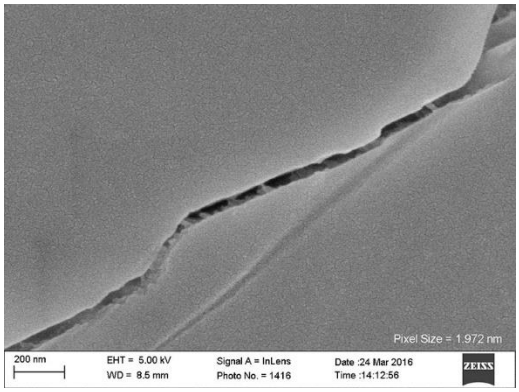

Figure B.63: Inlens SE micrograph from sample NAM-2784 showing example of NGBC containing a cuspate-lobate texture.

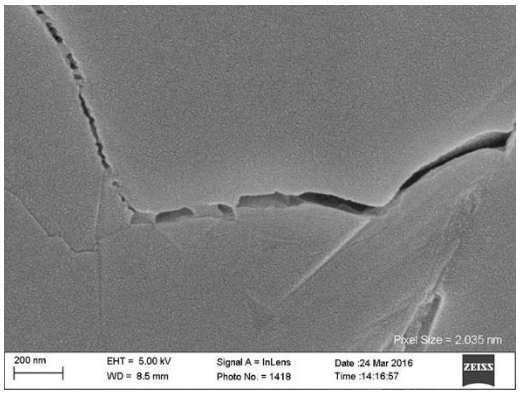

Figure B.64: Inlens SE micrograph from sample NAM-2784 showing example of NGBC containing a cuspate-lobate texture.

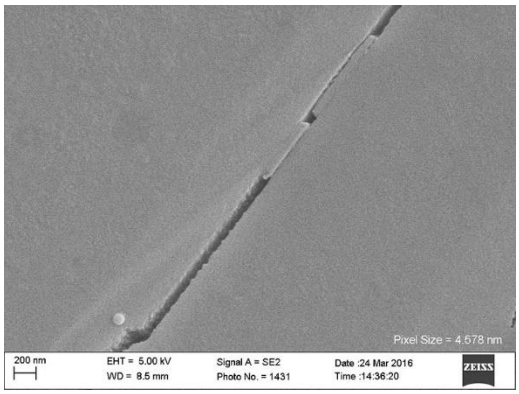

Figure B.65: Inlens SE micrograph from sample NAM-2784 showing example of NGBC containing a cuspate-lobate texture.

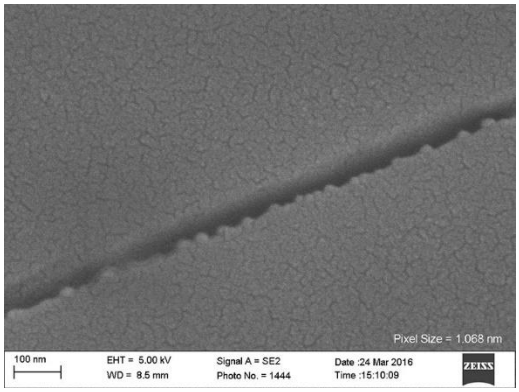

Figure B.66: Inlens SE micrograph from sample NAM-2784 showing example of NGBC containing a cuspate-lobate texture.

Negative Crystal

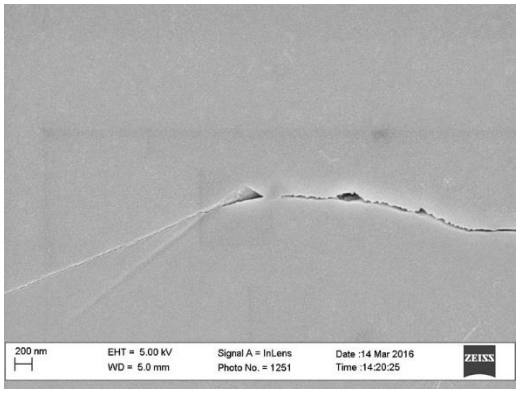

Figure B.67: Inlens SE micrograph from sample NAM-2784 showing example of NGBC containing negative crystal structures at the grain boundary.

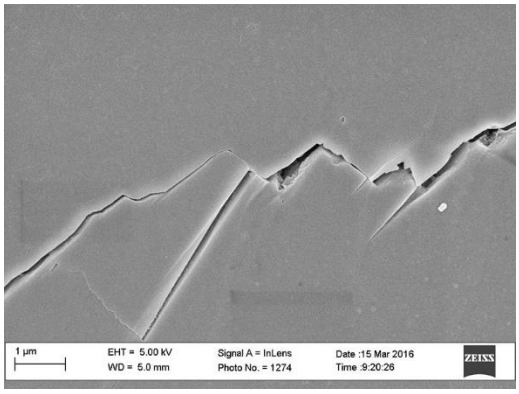

Figure B.68: Inlens SE micrograph from sample NAM-2784 showing example of NGBC containing negative crystal structures at the grain boundary.

Meniscus shaped Pore

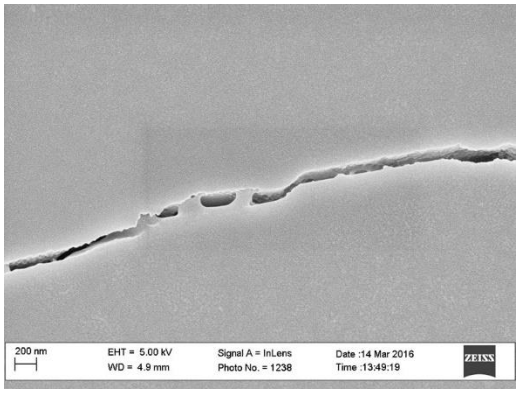

Figure B.69: Inlens SE micrograph from sample NAM-2784 showing example of NGBC containing bridging cements that create a meniscus shaped pore.

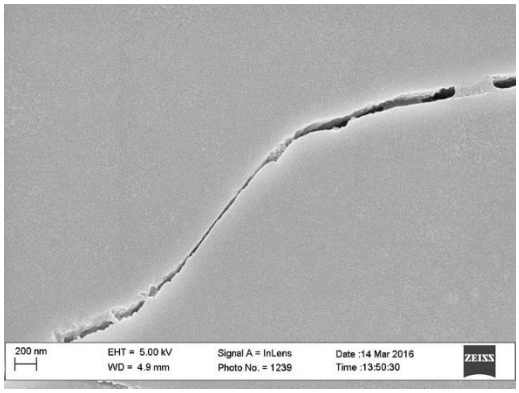

Figure B.70: Inlens SE micrograph from sample NAM-2784 showing example of NGBC containing bridging cements that create a meniscus shaped pore.

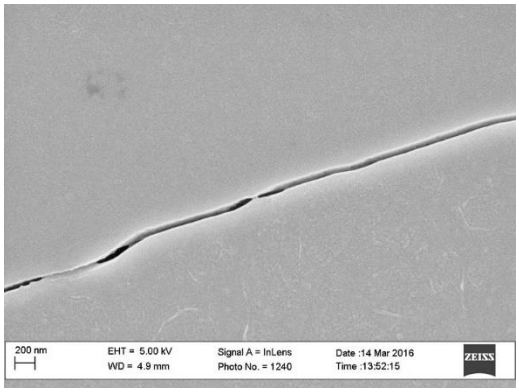

Figure B.71: Inlens SE micrograph from sample NAM-2784 showing example of NGBC containing bridging cements that create a meniscus shaped pore.

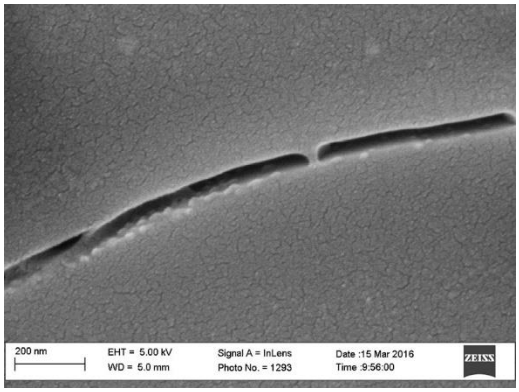

Figure B.72: Inlens SE micrograph from sample NAM-2784 showing example of NGBC containing bridging cements that create a meniscus shaped pore.

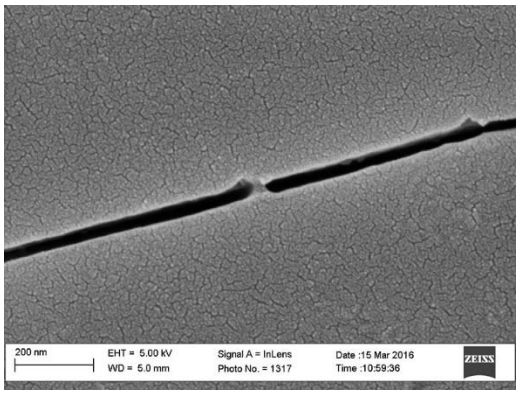

Figure B.73: Inlens SE micrograph from sample NAM-2784 showing example of NGBC containing bridging cements that create a meniscus shaped pore.

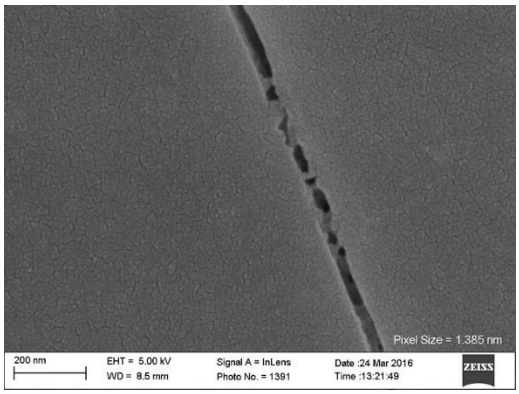

Figure B.74: Inlens SE micrograph from sample NAM-2784 showing example of NGBC containing bridging cements that create a meniscus shaped pore.

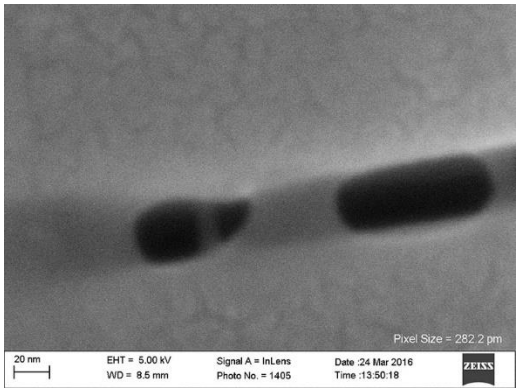

Figure B.75: Inlens SE micrograph from sample NAM-2784 showing example of NGBC containing bridging cements that create a meniscus shaped pore.

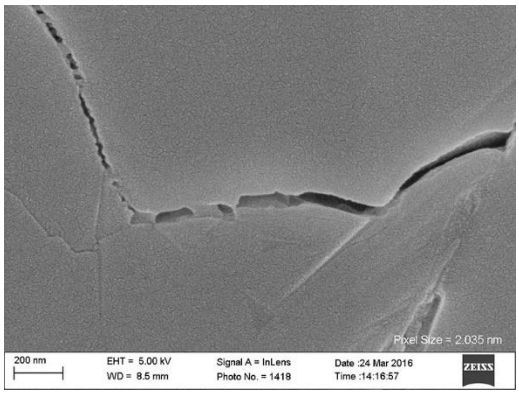

Figure B.76: Inlens SE micrograph from sample NAM-2784 showing example of NGBC containing bridging cements that create a meniscus shaped pore.

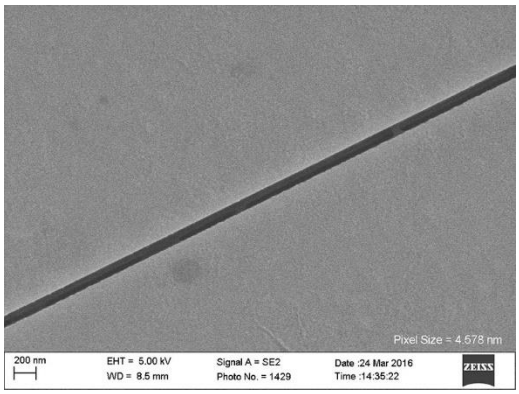

Figure B.77: Inlens SE micrograph from sample NAM-2784 showing example of NGBC containing bridging cements that create a meniscus shaped pore.

Rectangular Shaped Pore

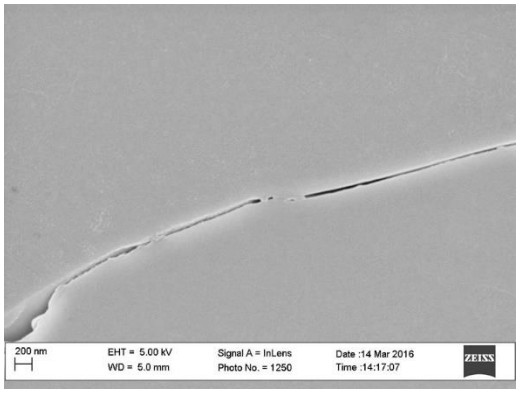

Figure B.78: Inlens SE micrograph from sample NAM-2784.showing example of NGBC containing bridging cements that create a rectangular shaped pore.

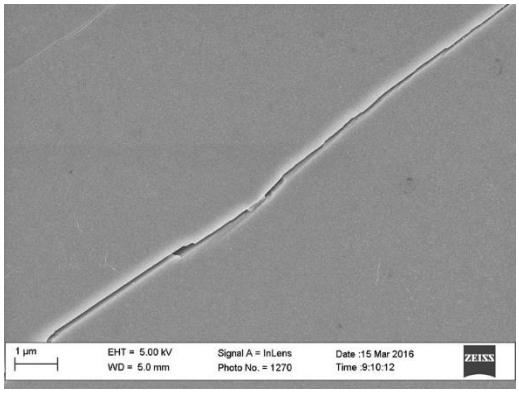

Figure B.79: Inlens SE micrograph from sample NAM-2784.showing example of NGBC containing bridging cements that create a rectangular shaped pore.

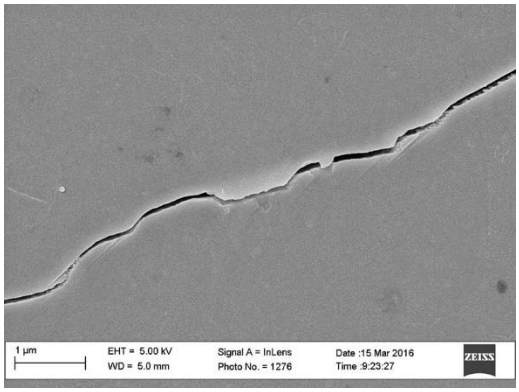

Figure B.80: Inlens SE micrograph from sample NAM-2784.showing example of NGBC containing bridging cements that create a rectangular shaped pore.

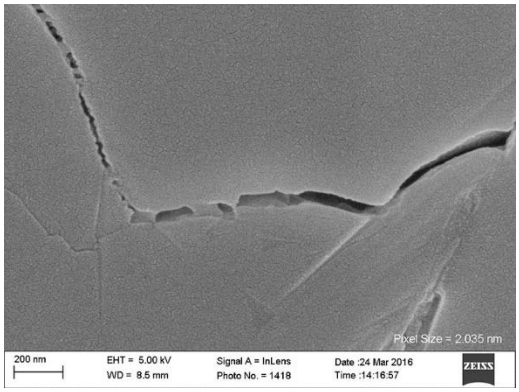

Figure B.81: Inlens SE micrograph from sample NAM-2784.showing example of NGBC containing bridging cements that create a rectangular shaped pore.

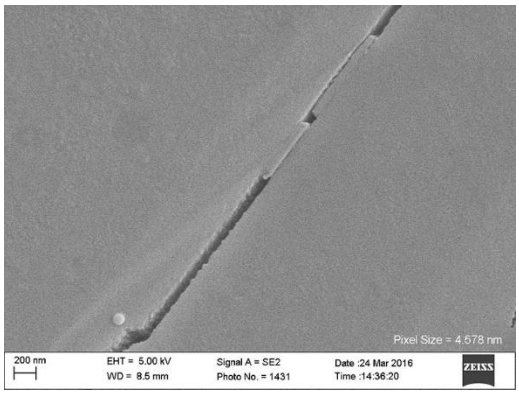

Figure B.82: Inlens SE micrograph from sample NAM-2784.showing example of NGBC containing bridging cements that create a rectangular shaped pore.

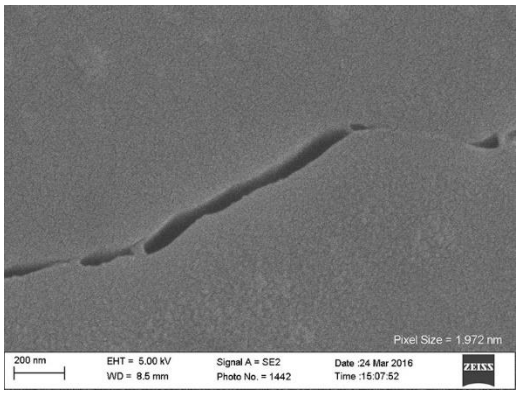

Figure B.83: Inlens SE micrograph from sample NAM-2784.showing example of NGBC containing bridging cements that create a rectangular shaped pore.

Partial Bridge

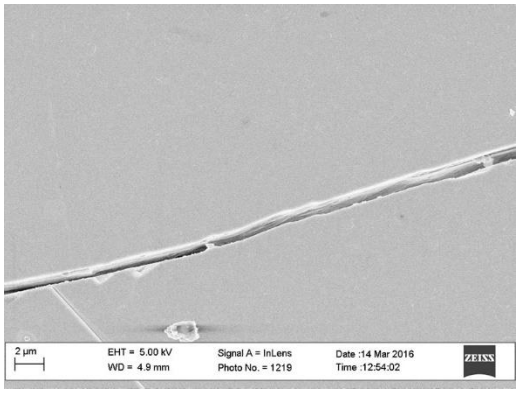

Figure B.84: Inlens SE micrograph from sample NAM-2784 showing example of NGBC containing partially bridging cements that do not completely traverse the entire aperture of the NGBC.

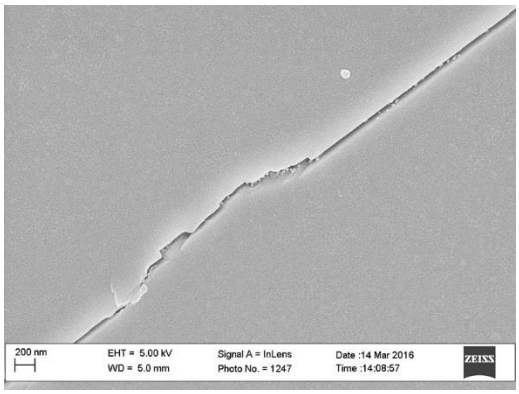

Figure B.85: Inlens SE micrograph from sample NAM-2784 showing example of NGBC containing partially bridging cements that do not completely traverse the entire aperture of the NGBC.

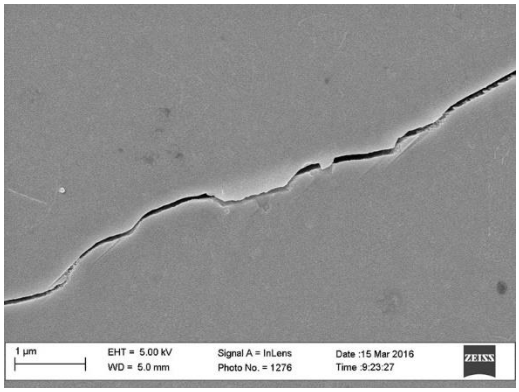

Figure B.86: Inlens SE micrograph from sample NAM-2784 showing example of NGBC containing partially bridging cements that do not completely traverse the entire aperture of the NGBC.

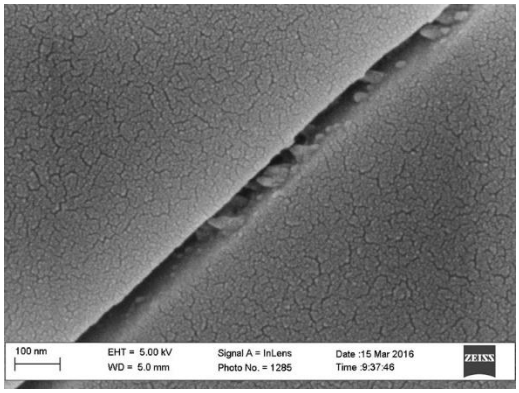

Figure B.87: Inlens SE micrograph from sample NAM-2784 showing example of NGBC containing partially bridging cements that do not completely traverse the entire aperture of the NGBC.

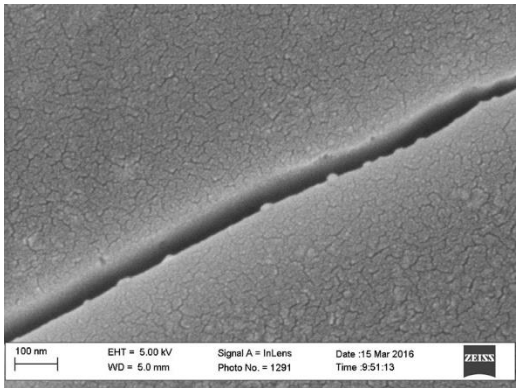

Figure B.88: Inlens SE micrograph from sample NAM-2784 showing example of NGBC containing partially bridging cements that do not completely traverse the entire aperture of the NGBC.

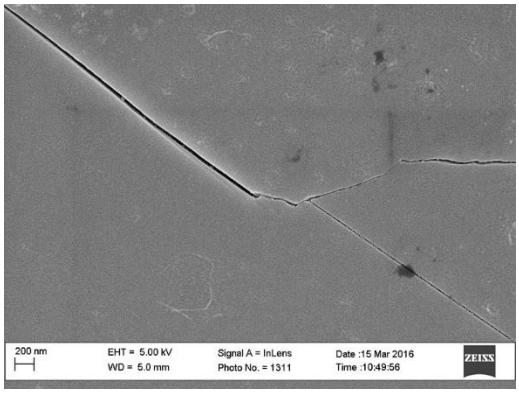

Figure B.89: Inlens SE micrograph from sample NAM-2784 showing example of NGBC containing partially bridging cements that do not completely traverse the entire aperture of the NGBC.

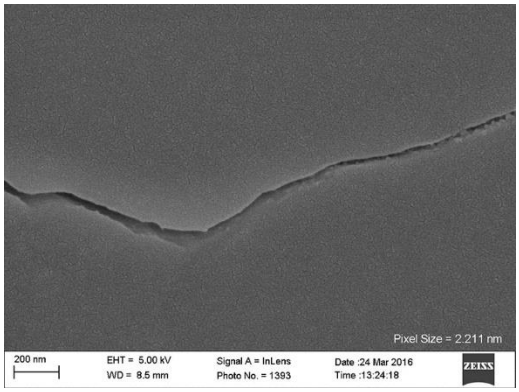

Figure B.90: Inlens SE micrograph from sample NAM-2784 showing example of NGBC containing partially bridging cements that do not completely traverse the entire aperture of the NGBC.

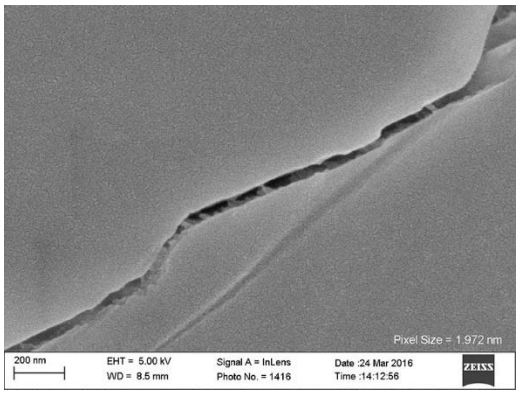

Figure B.91: Inlens SE micrograph from sample NAM-2784 showing example of NGBC containing partially bridging cements that do not completely traverse the entire aperture of the NGBC.

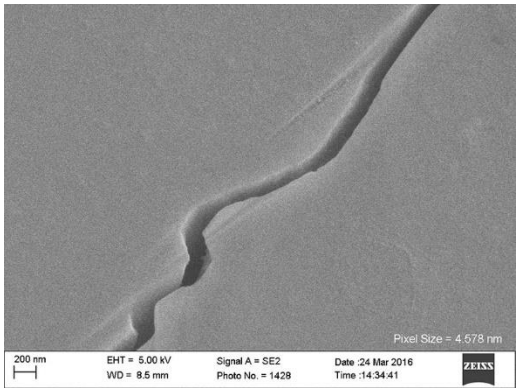

Figure B.92: Inlens SE micrograph from sample NAM-2784 showing example of NGBC containing partially bridging cements that do not completely traverse the entire aperture of the NGBC.

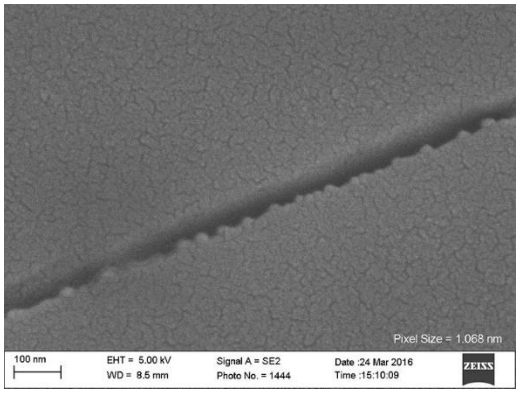

Figure B.93: Inlens SE micrograph from sample NAM-2784 showing example of NGBC containing partially bridging cements that do not completely traverse the entire aperture of the NGBC.

SAMPLE NAC-3590-1, NEW ALBANY FORMATION

Flat, Mating Contacts

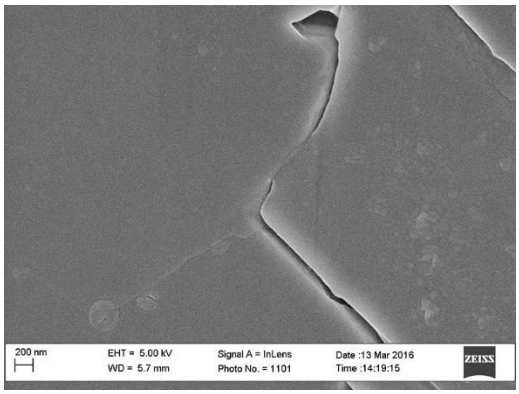

Figure B.94: Inlens SE micrograph from sample NAC-3590-1 showing example of NGBC containing a flat, mating contact.

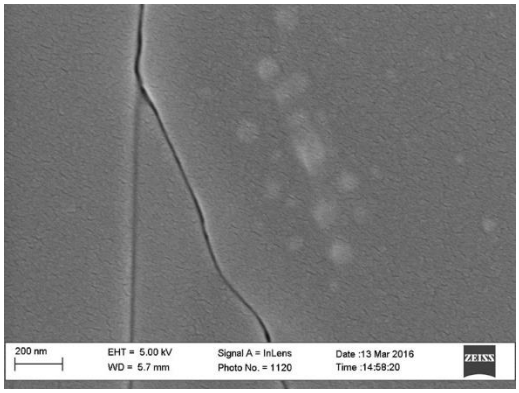

Figure B.95: Inlens SE micrograph from sample NAC-3590-1 showing example of NGBC containing a flat, mating contact.

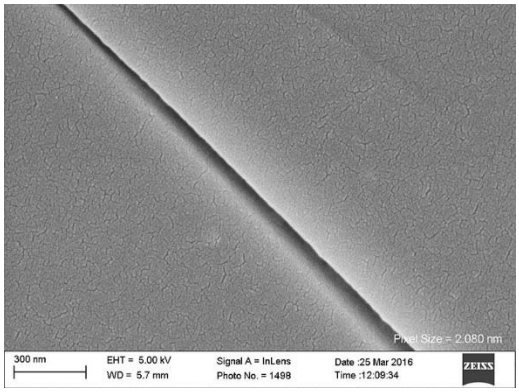

Figure B.96: Inlens SE micrograph from sample NAC-3590-1 showing example of NGBC containing a flat, mating contact.

Cuspate-lobate

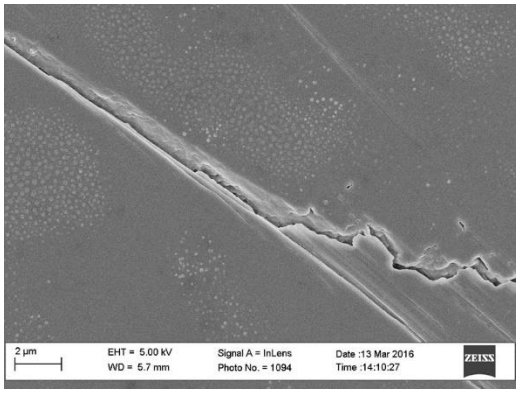

Figure B.97: Inlens SE micrograph from sample NAC-3590-1 showing example of NGBC containing a cuspate-lobate texture.

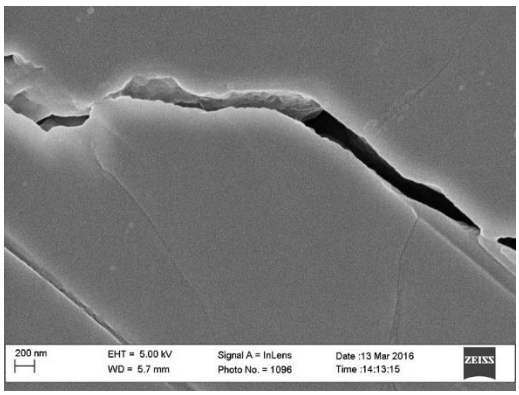

Figure B.98: Inlens SE micrograph from sample NAC-3590-1 showing example of NGBC containing a cuspate-lobate texture.

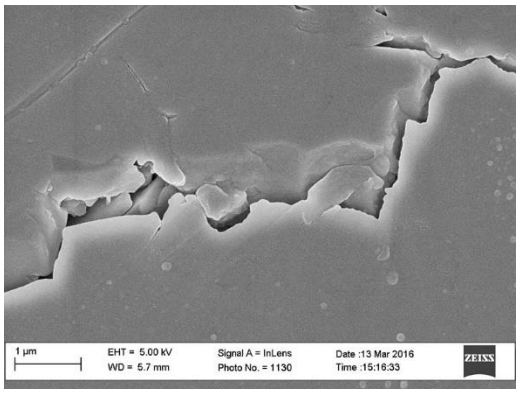

Figure B.99: Inlens SE micrograph from sample NAC-3590-1 showing example of NGBC containing a cuspate-lobate texture.

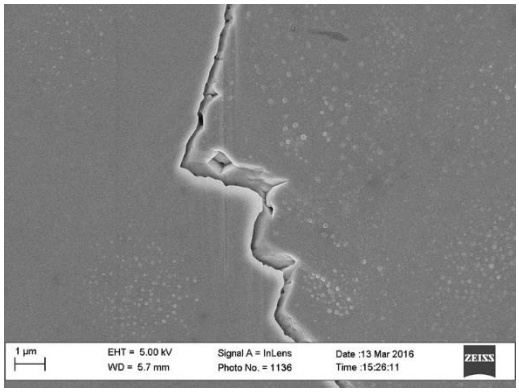

Figure B.100: Inlens SE micrograph from sample NAC-3590-1 showing example of NGBC containing a cuspate-lobate texture.

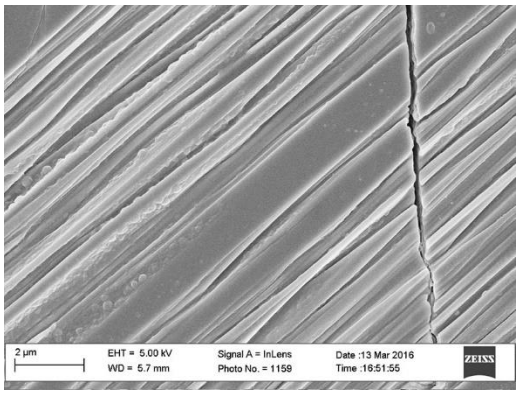

Figure B.101: Inlens SE micrograph from sample NAC-3590-1 showing example of NGBC containing a cuspate-lobate texture.

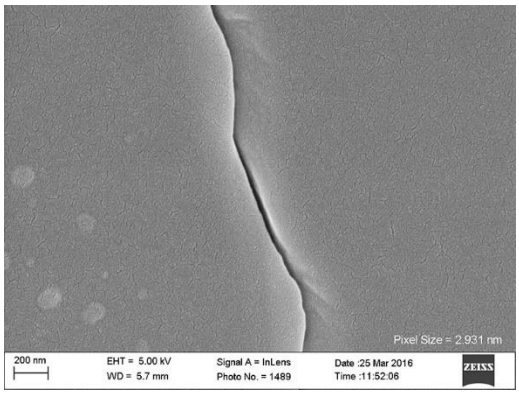

Figure B.102: Inlens SE micrograph from sample NAC-3590-1 showing example of NGBC containing a cuspate-lobate texture.

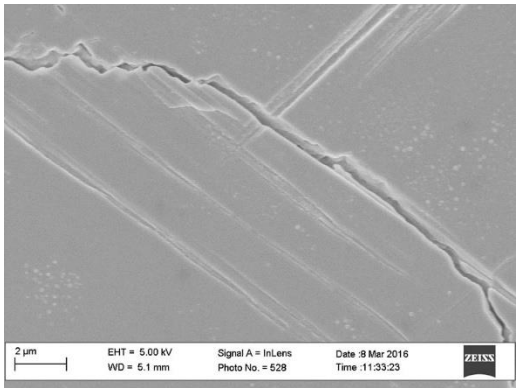

Figure B.103: Inlens SE micrograph from sample NAC-3590-1 showing example of NGBC containing a cuspate-lobate texture.

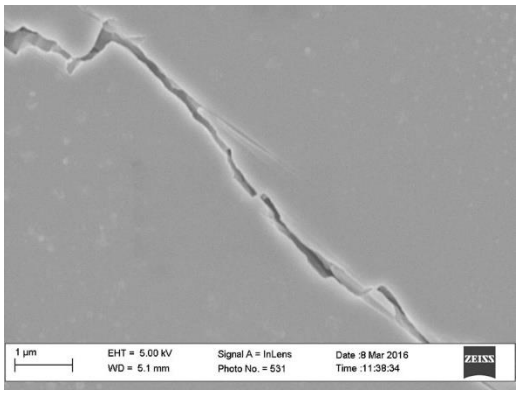

Figure B.104: Inlens SE micrograph from sample NAC-3590-1 showing example of NGBC containing a cuspate-lobate texture.

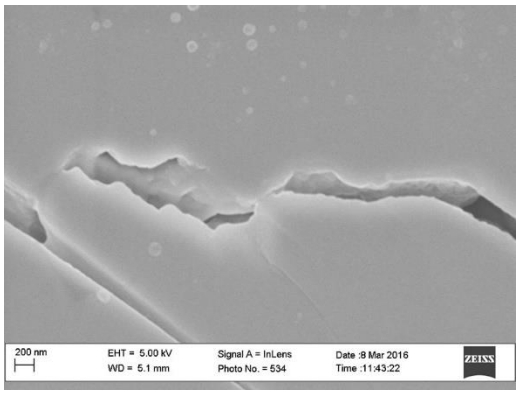

Figure B.105: Inlens SE micrograph from sample NAC-3590-1 showing example of NGBC containing a cuspate-lobate texture.

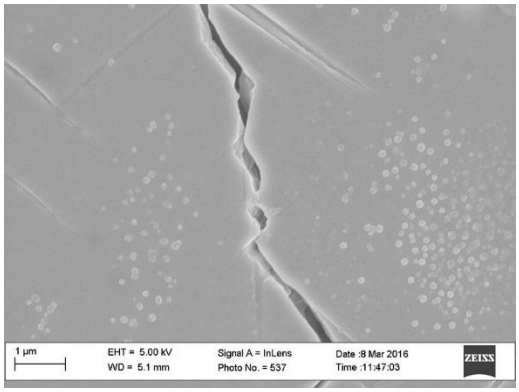

Figure B.106: Inlens SE micrograph from sample NAC-3590-1 showing example of NGBC containing a cuspate-lobate texture.

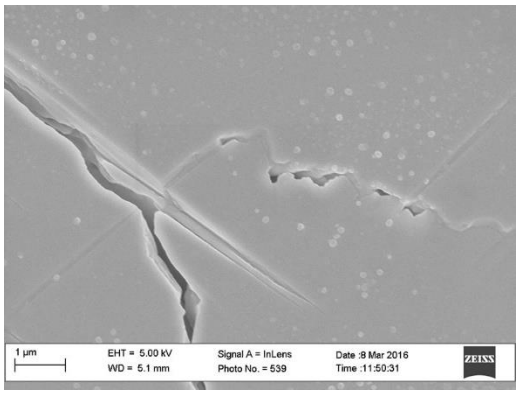

Figure B.107: Inlens SE micrograph from sample NAC-3590-1 showing example of NGBC containing a cuspate-lobate texture.

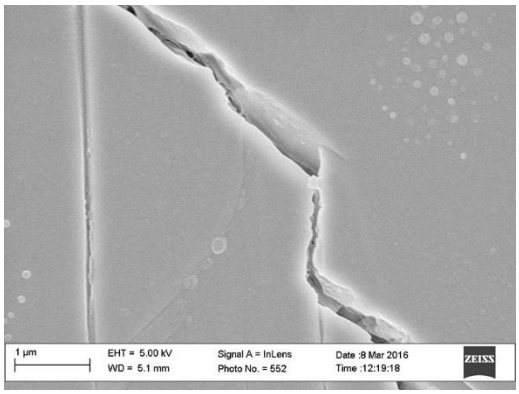

Figure B.108: Inlens SE micrograph from sample NAC-3590-1 showing example of NGBC containing a cuspate-lobate texture.

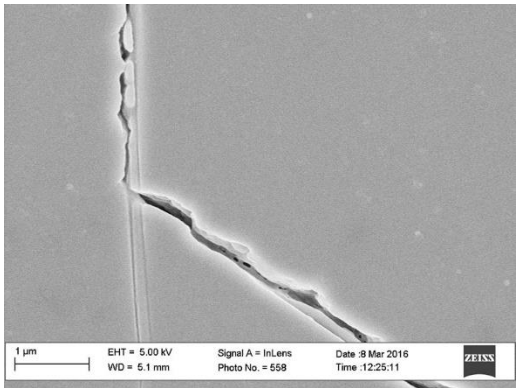

Figure B.109: Inlens SE micrograph from sample NAC-3590-1 showing example of NGBC containing a cuspate-lobate texture.

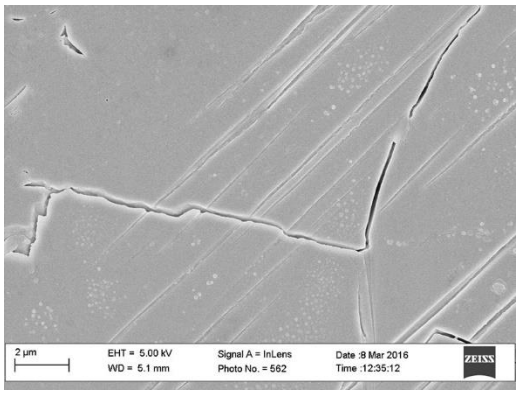

Figure B.110: Inlens SE micrograph from sample NAC-3590-1 showing example of NGBC containing a cuspate-lobate texture.

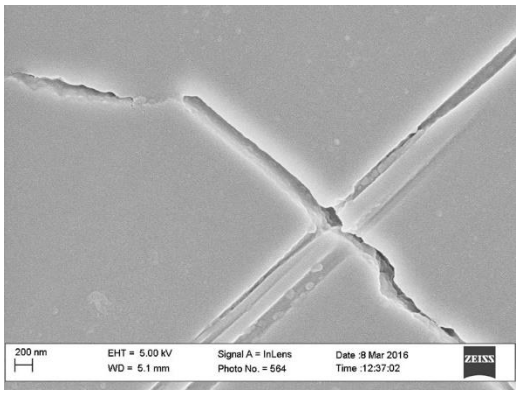

Figure B.111: Inlens SE micrograph from sample NAC-3590-1 showing example of NGBC containing a cuspate-lobate texture.

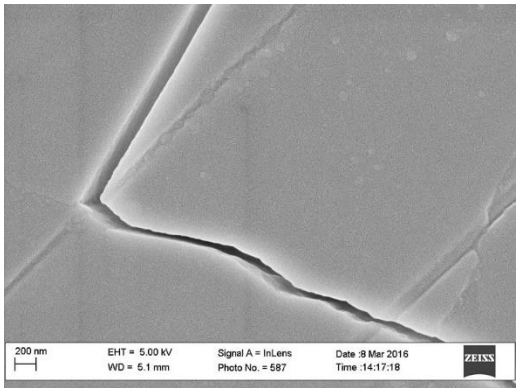

Figure B.112: Inlens SE micrograph from sample NAC-3590-1 showing example of NGBC containing a cuspate-lobate texture.

Negative Crystal

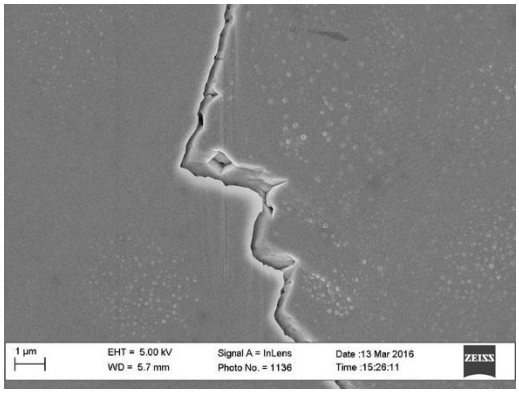

Figure B.113: Inlens SE micrograph from sample NAC-3590-1 showing example of NGBC containing negative crystal structures at the grain boundary.

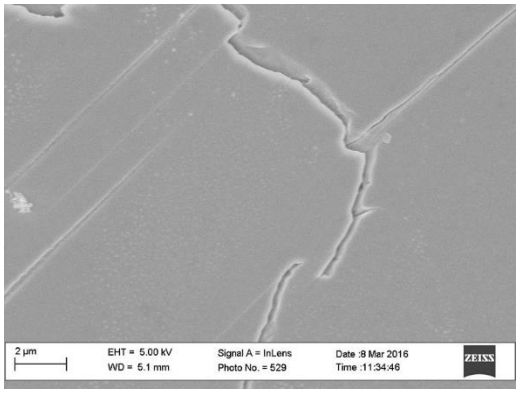

Figure B.114: Inlens SE micrograph from sample NAC-3590-1 showing example of NGBC containing negative crystal structures at the grain boundary.

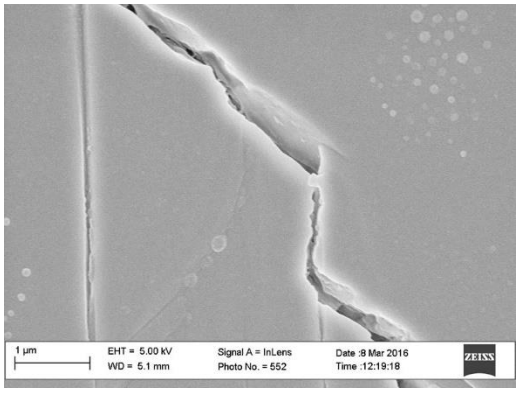

Figure B.115: Inlens SE micrograph from sample NAC-3590-1 showing example of NGBC containing negative crystal structures at the grain boundary.

Meniscus shaped Pore

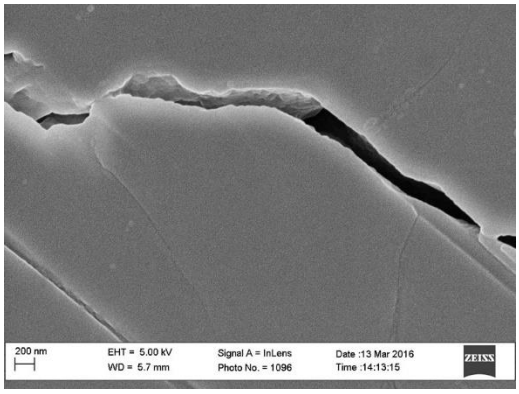

Figure B.116: Inlens SE micrograph from sample NAC-3590-1 showing example of NGBC containing bridging cements that create a meniscus shaped pore.

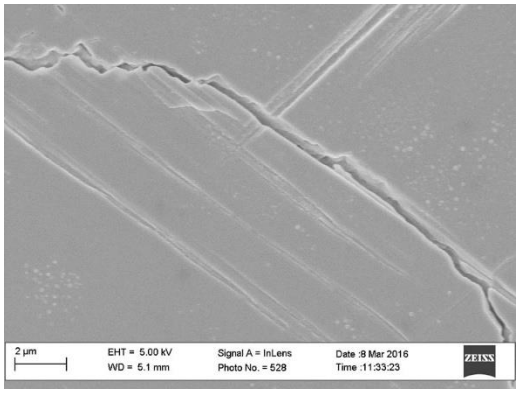

Figure B.117: Inlens SE micrograph from sample NAC-3590-1 showing example of NGBC containing bridging cements that create a meniscus shaped pore.

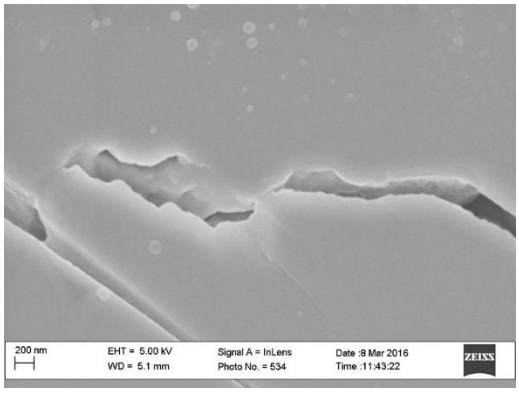

Figure B.118: Inlens SE micrograph from sample NAC-3590-1 showing example of NGBC containing bridging cements that create a meniscus shaped pore.

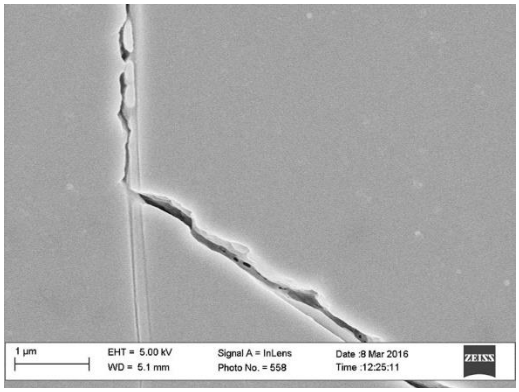

Figure B.119: Inlens SE micrograph from sample NAC-3590-1 showing example of NGBC containing bridging cements that create a meniscus shaped pore.

Rectangular Shaped Pore

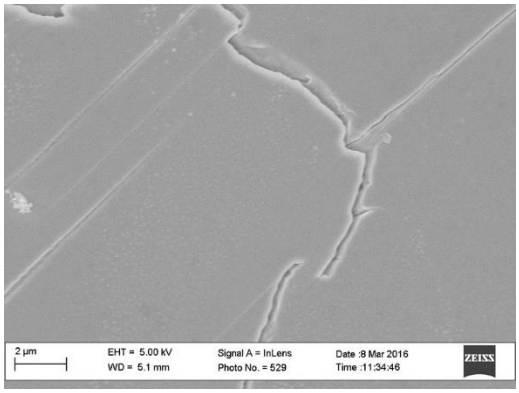

Figure B.120: Inlens SE micrograph from sample NAC-3590-1 showing example of NGBC containing bridging cements that create a rectangular shaped pore.

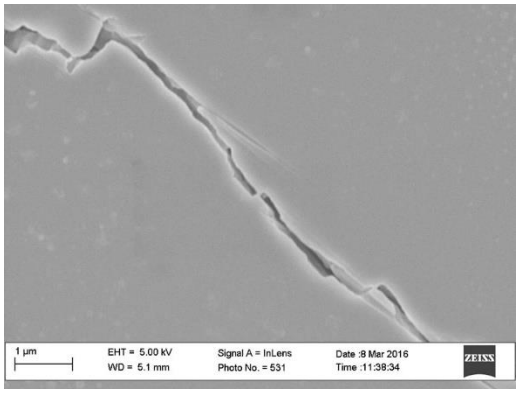

Figure B.121: Inlens SE micrograph from sample NAC-3590-1 showing example of NGBC containing bridging cements that create a rectangular shaped pore.

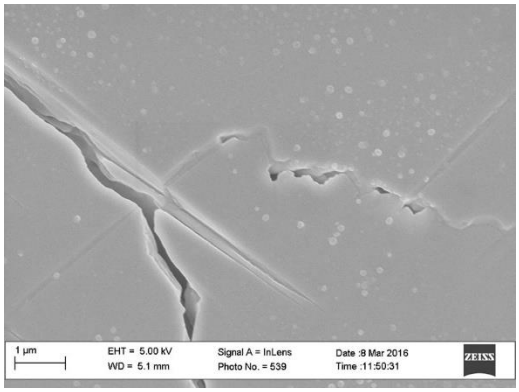

Figure B.122: Inlens SE micrograph from sample NAC-3590-1 showing example of NGBC containing bridging cements that create a rectangular shaped pore.

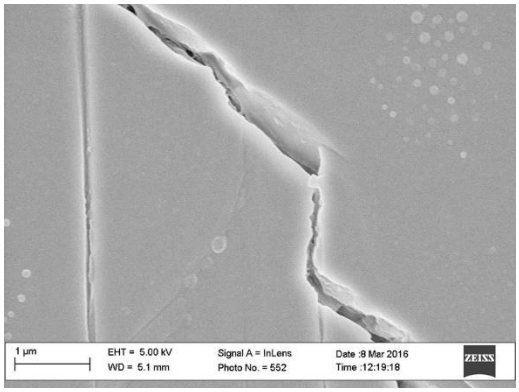

Figure B.123: Inlens SE micrograph from sample NAC-3590-1 showing example of NGBC containing bridging cements that create a rectangular shaped pore.

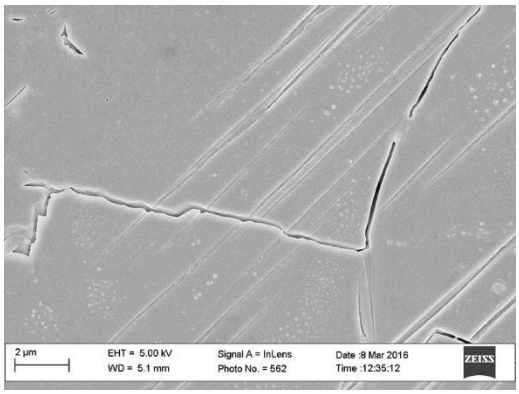

Figure B.124: Inlens SE micrograph from sample NAC-3590-1 showing example of NGBC containing bridging cements that create a rectangular shaped pore.

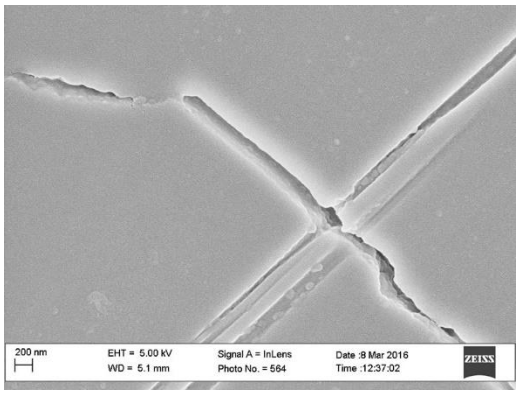

Figure B.125: Inlens SE micrograph from sample NAC-3590-1 showing example of NGBC containing bridging cements that create a rectangular shaped pore.

SAMPLE: NAC-3590-2, NEW ALBANY FORMATION

Flat, Mating Contacts

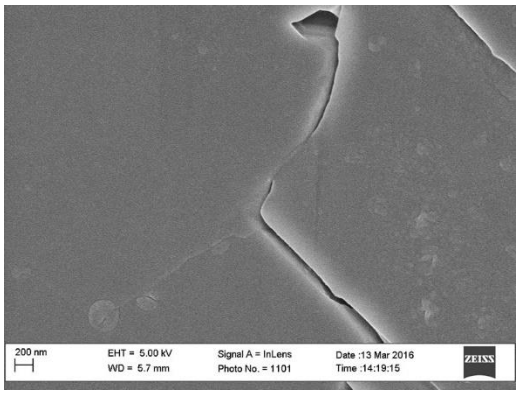

Figure B.126: Inlens SE micrograph from sample NAC-3590-2 showing example of NGBC containing a flat, mating contact.

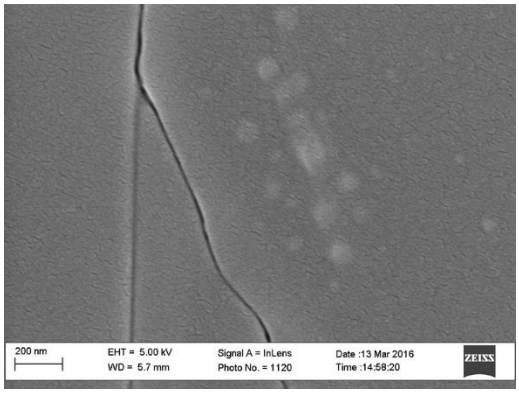

Figure B.127: Inlens SE micrograph from sample NAC-3590-2 showing example of NGBC containing a flat, mating contact.

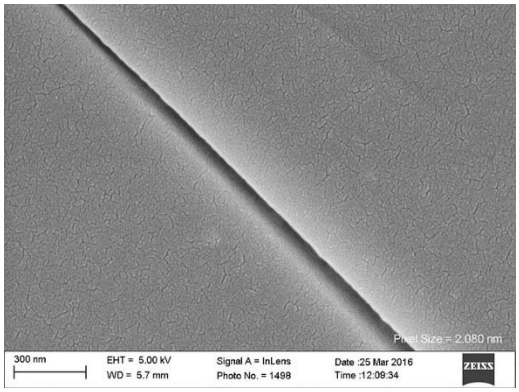

Figure B.128: Inlens SE micrograph from sample NAC-3590-2 showing example of NGBC containing a flat, mating contact.

Cuspate-lobate

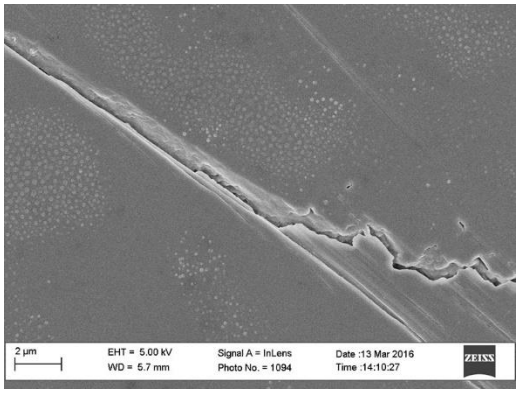

Figure B.129: Inlens SE micrograph from sample NAC-3590-2 showing example of NGBC containing a cuspate-lobate texture.

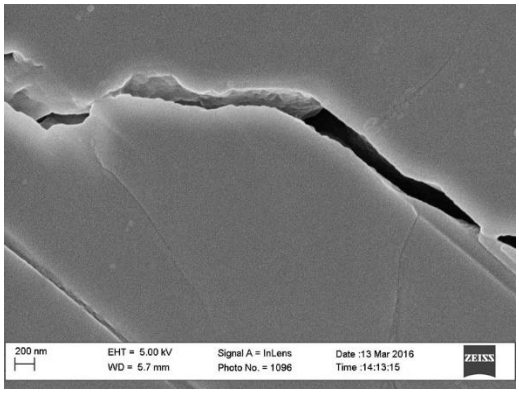

Figure B.130: Inlens SE micrograph from sample NAC-3590-2 showing example of NGBC containing a cuspate-lobate texture.

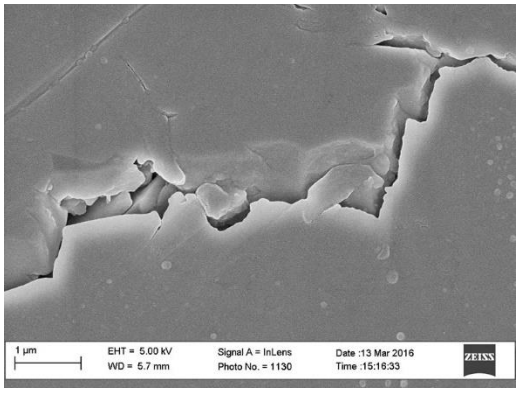

Figure B.131: Inlens SE micrograph from sample NAC-3590-2 showing example of NGBC containing a cuspate-lobate texture.

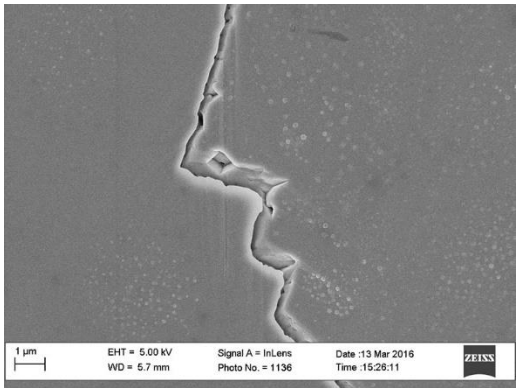

Figure B.132: Inlens SE micrograph from sample NAC-3590-2 showing example of NGBC containing a cuspate-lobate texture.

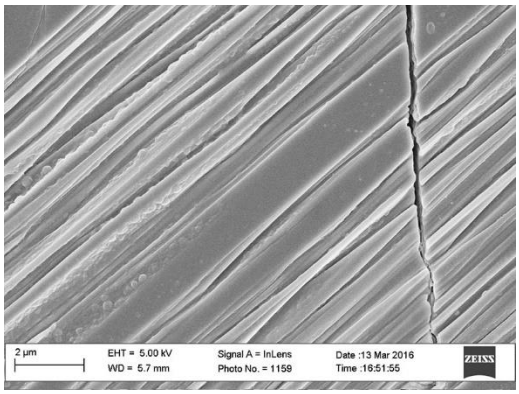

Figure B.133: Inlens SE micrograph from sample NAC-3590-2 showing example of NGBC containing a cuspate-lobate texture.

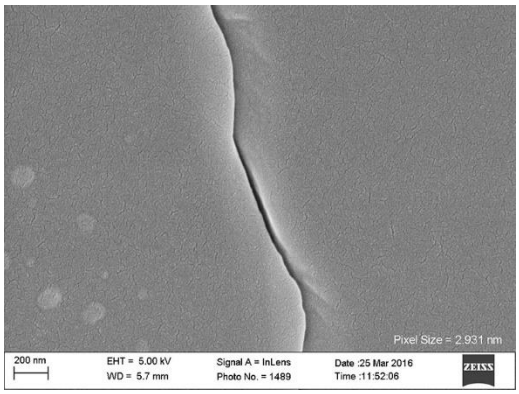

Figure B.134: Inlens SE micrograph from sample NAC-3590-2 showing example of NGBC containing a cuspate-lobate texture.

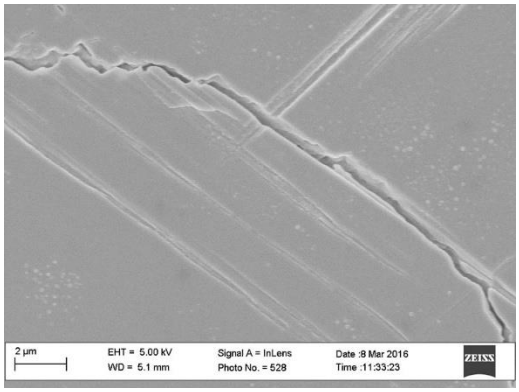

Figure B.135: Inlens SE micrograph from sample NAC-3590-2 showing example of NGBC containing a cuspate-lobate texture.

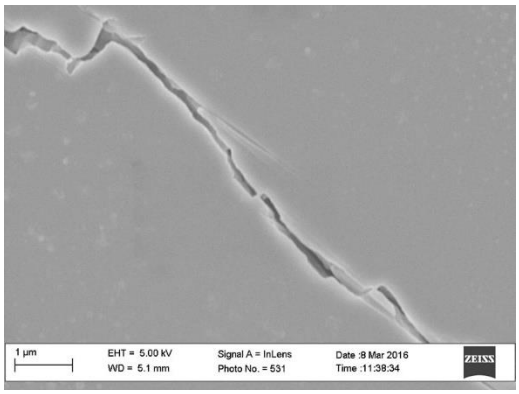

Figure B.136: Inlens SE micrograph from sample NAC-3590-2 showing example of NGBC containing a cuspate-lobate texture.

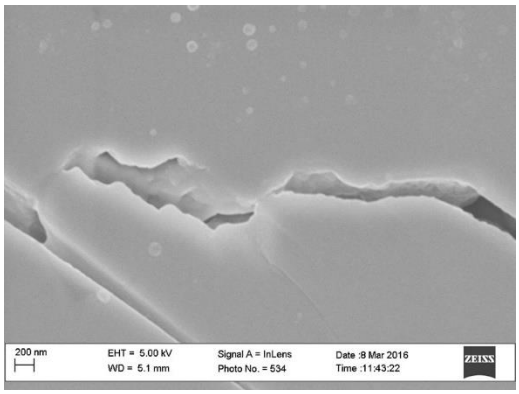

Figure B.137: Inlens SE micrograph from sample NAC-3590-2 showing example of NGBC containing a cuspate-lobate texture.

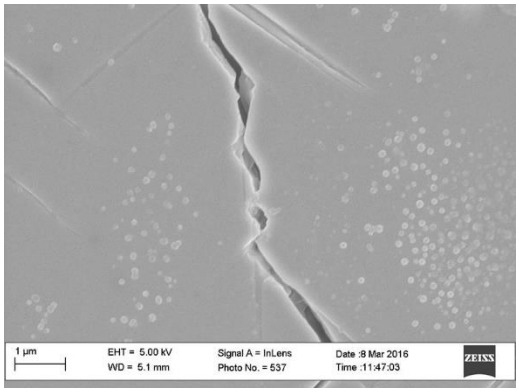

Figure B.138: Inlens SE micrograph from sample NAC-3590-2 showing example of NGBC containing a cuspate-lobate texture.

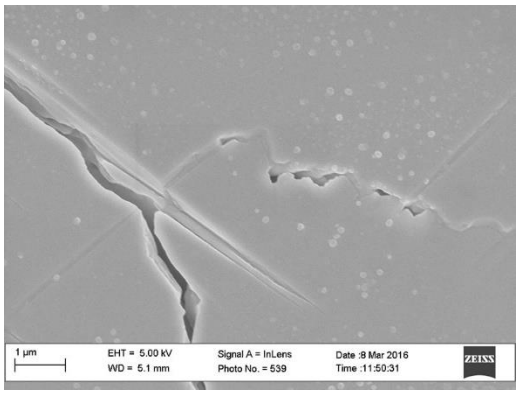

Figure B.139: Inlens SE micrograph from sample NAC-3590-2 showing example of NGBC containing a cuspate-lobate texture.

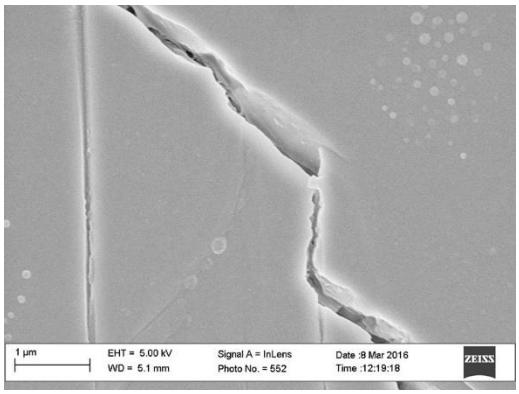

Figure B.140: Inlens SE micrograph from sample NAC-3590-2 showing example of NGBC containing a cuspate-lobate texture.

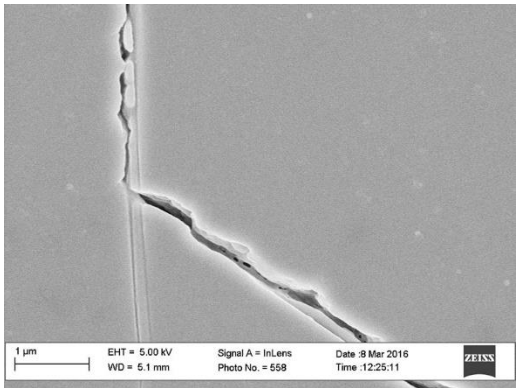

Figure B.141: Inlens SE micrograph from sample NAC-3590-2 showing example of NGBC containing a cuspate-lobate texture.

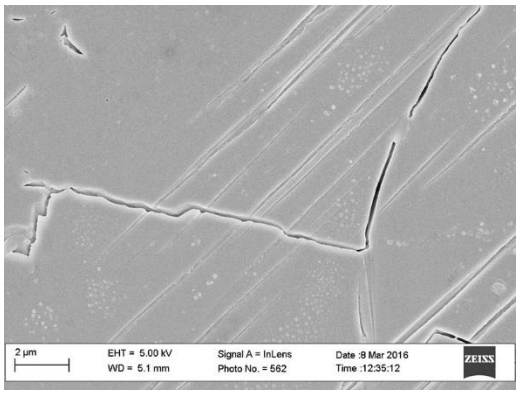

Figure B.142: Inlens SE micrograph from sample NAC-3590-2 showing example of NGBC containing a cuspate-lobate texture.

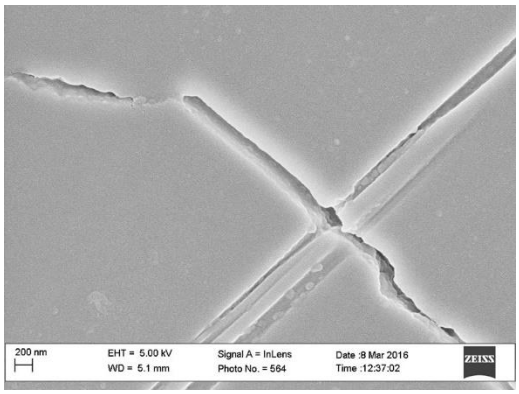

Figure B.143: Inlens SE micrograph from sample NAC-3590-2 showing example of NGBC containing a cuspate-lobate texture.

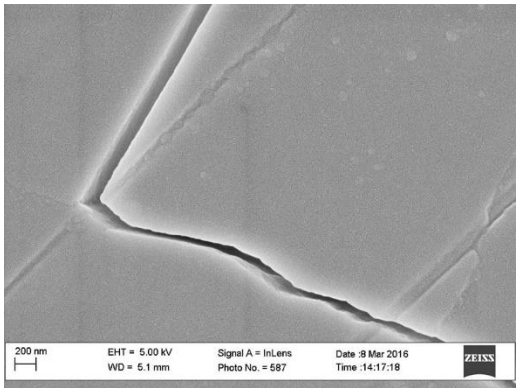

Figure B.144: Inlens SE micrograph from sample NAC-3590-2 showing example of NGBC containing a cuspate-lobate texture.

Negative Crystal

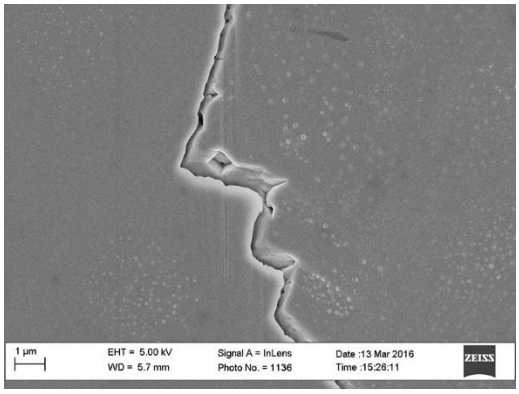

Figure B.145: Inlens SE micrograph from sample NAC-3590-2 showing example of NGBC containing negative crystal structures at the grain boundary.

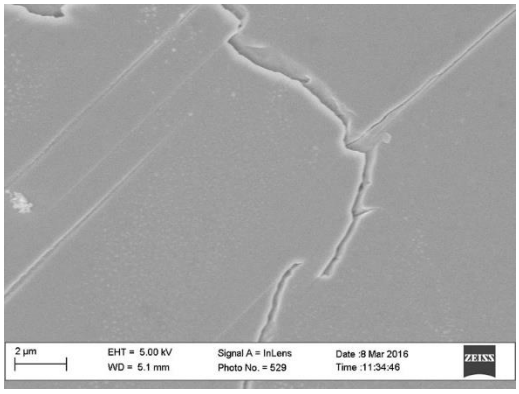

Figure B.146: Inlens SE micrograph from sample NAC-3590-2 showing example of NGBC containing negative crystal structures at the grain boundary.

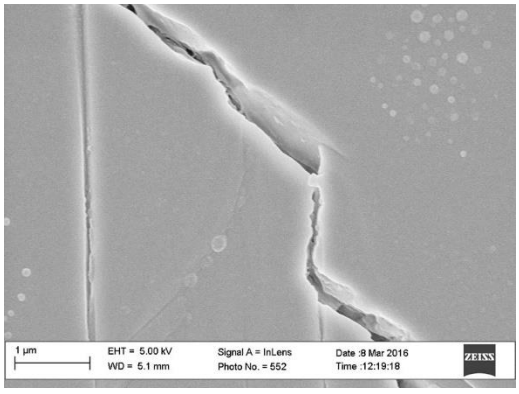

Figure B.147: Inlens SE micrograph from sample NAC-3590-2 showing example of NGBC containing negative crystal structures at the grain boundary.

Meniscus shaped Pore

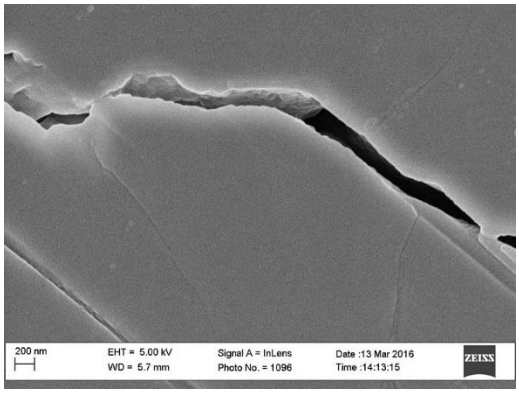

Figure B.148: Inlens SE micrograph from sample NAC-3590-2 showing example of NGBC containing bridging cements that create a meniscus shaped pore.

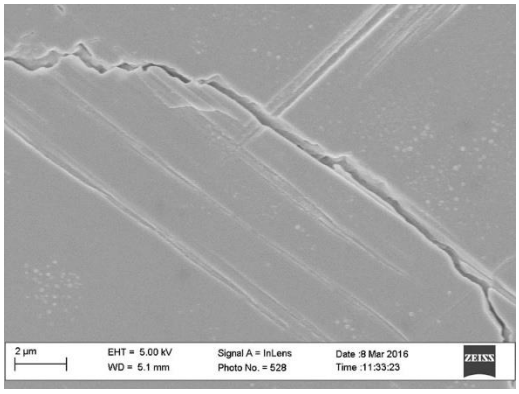

Figure B.149: Inlens SE micrograph from sample NAC-3590-2 showing example of NGBC containing bridging cements that create a meniscus shaped pore.

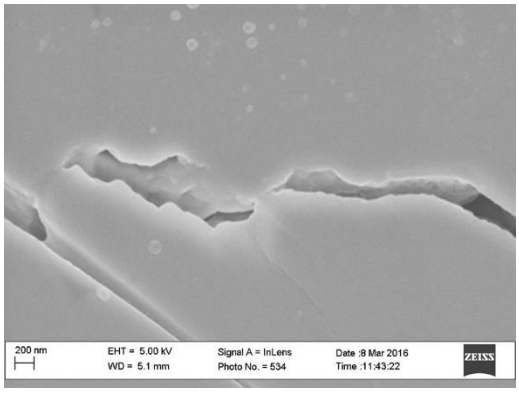

Figure B.150: Inlens SE micrograph from sample NAC-3590-2 showing example of NGBC containing bridging cements that create a meniscus shaped pore.

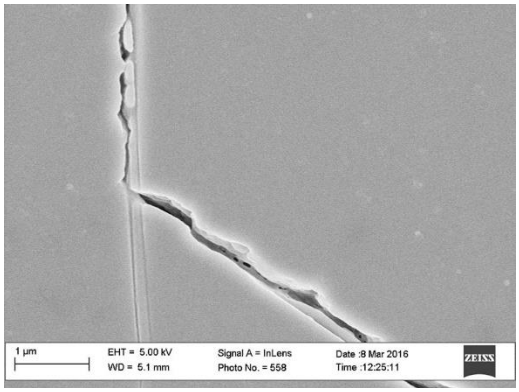

Figure B.151: Inlens SE micrograph from sample NAC-3590-2 showing example of NGBC containing bridging cements that create a meniscus shaped pore.

Rectangular Shaped Pore

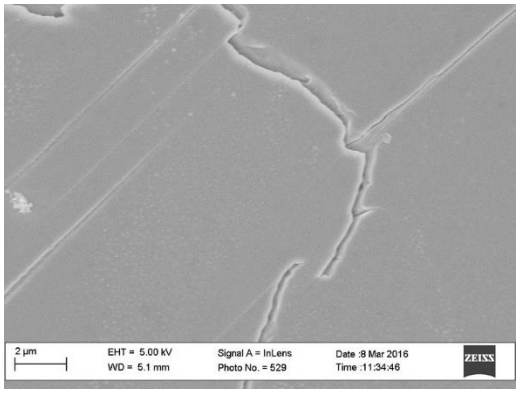

Figure B.152: Inlens SE micrograph from sample NAC-3590-2 showing example of NGBC containing bridging cements that create a rectangular shaped pore.

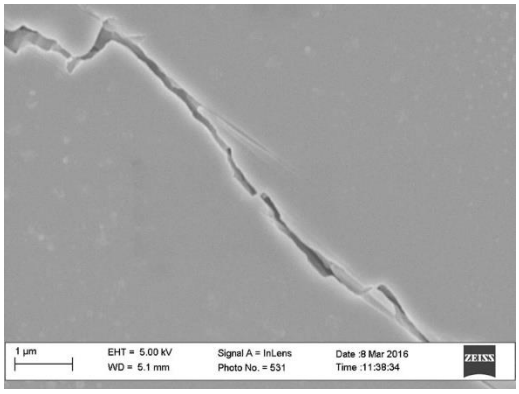

Figure B.153: Inlens SE micrograph from sample NAC-3590-2 showing example of NGBC containing bridging cements that create a rectangular shaped pore.

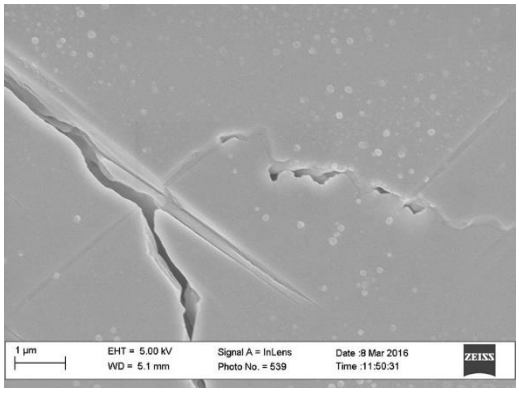

Figure B.154: Inlens SE micrograph from sample NAC-3590-2 showing example of NGBC containing bridging cements that create a rectangular shaped pore.

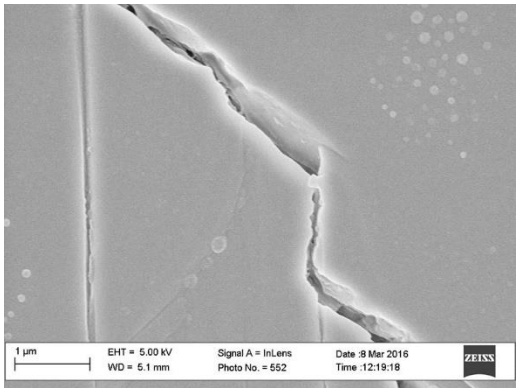

Figure B.155: Inlens SE micrograph from sample NAC-3590-2 showing example of NGBC containing bridging cements that create a rectangular shaped pore.

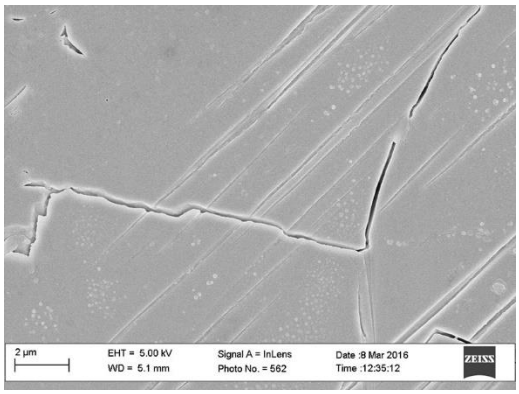

Figure B.156: Inlens SE micrograph from sample NAC-3590-2 showing example of NGBC containing bridging cements that create a rectangular shaped pore.

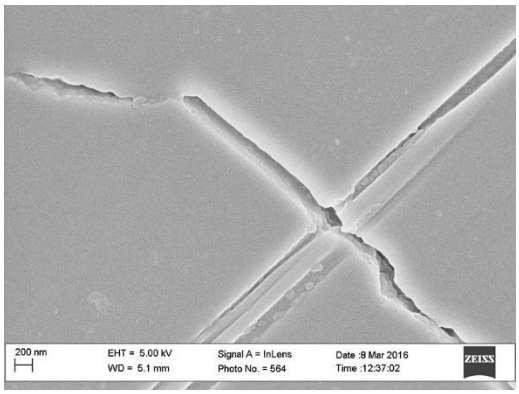

Figure B.157: Inlens SE micrograph from sample NAC-3590-2 showing example of NGBC containing bridging cements that create a rectangular shaped pore.

SAMPLE M-3658.5B, MARCELLUS FORMATION

Flat, Mating Contacts

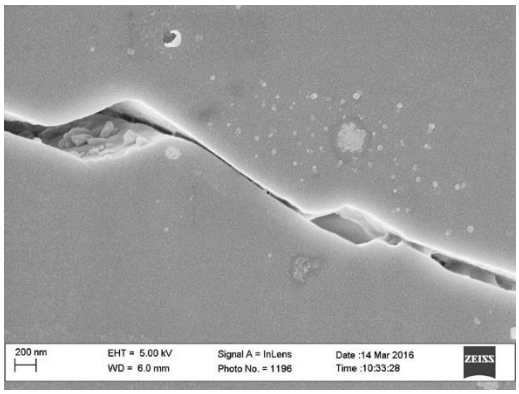

Figure B.158: Inlens SE micrograph from sample M-3658.5B showing example of NGBC containing a flat, mating contact.

Cuspate-lobate

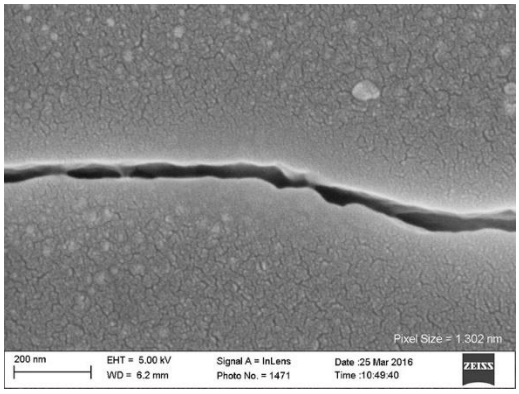

Figure B.159: Inlens SE micrograph from sample M-3658.5B showing example of NGBC containing a cuspate-lobate texture.

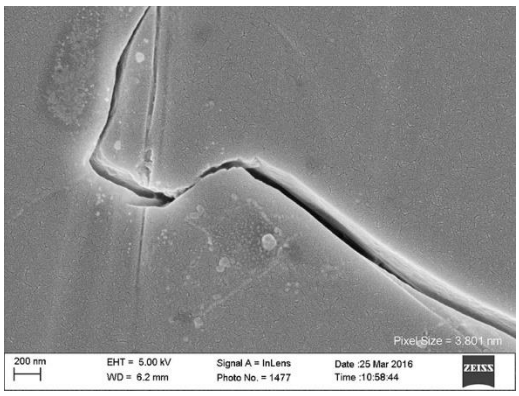

Figure B.160: Inlens SE micrograph from sample M-3658.5B showing example of NGBC containing a cuspate-lobate texture.

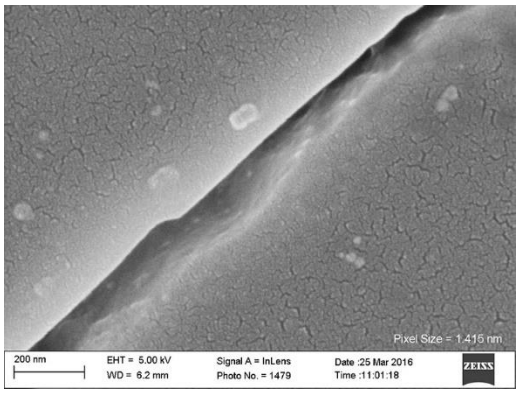

Figure B.161: Inlens SE micrograph from sample M-3658.5B showing example of NGBC containing a cuspate-lobate texture.

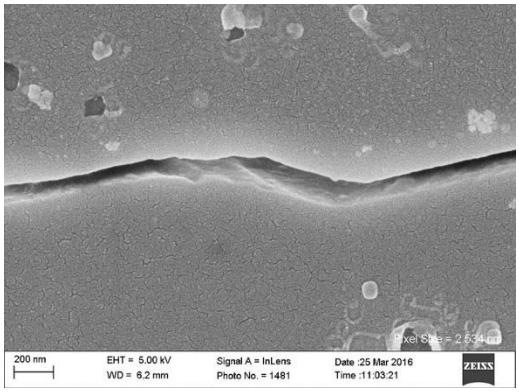

Figure B.162: Inlens SE micrograph from sample M-3658.5B showing example of NGBC containing a cuspate-lobate texture.

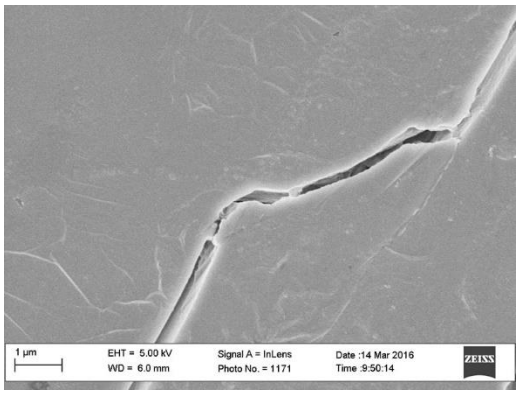

Figure B.163: Inlens SE micrograph from sample M-3658.5B showing example of NGBC containing a cuspate-lobate texture.

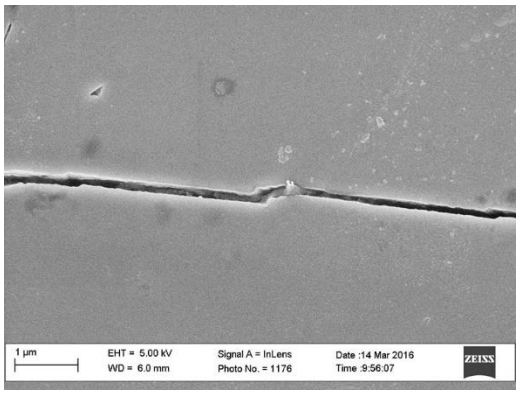

Figure B.164: Inlens SE micrograph from sample M-3658.5B showing example of NGBC containing a cuspate-lobate texture.

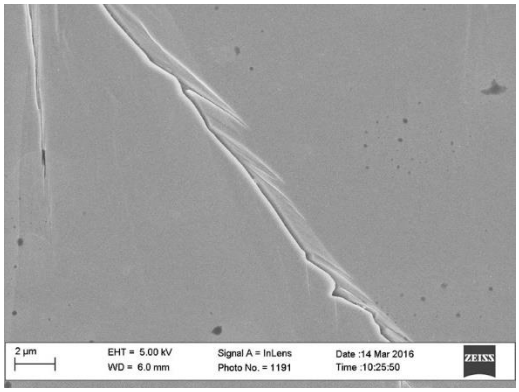

Figure B.165: Inlens SE micrograph from sample M-3658.5B showing example of NGBC containing a cuspate-lobate texture.

Negative Crystal

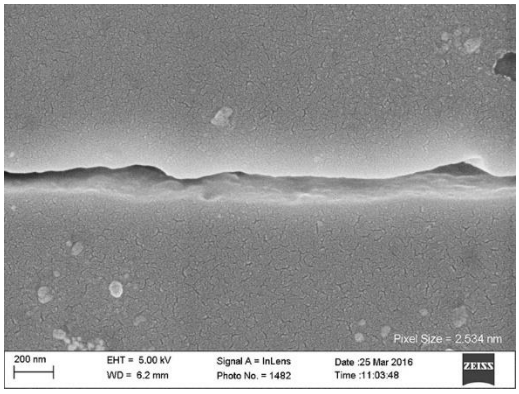

Figure B.166: Inlens SE micrograph from sample M-3658.5B showing example of NGBC containing negative crystal structures at the grain boundary.

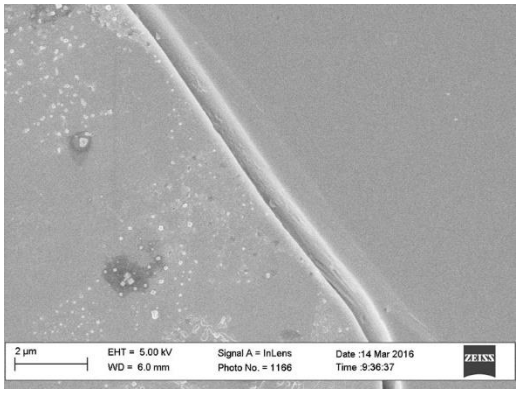

Figure B.167: Inlens SE micrograph from sample M-3658.5B showing example of NGBC containing negative crystal structures at the grain boundary.

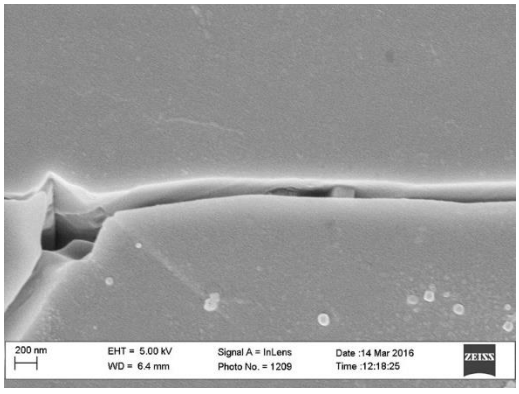

Figure B.168: Inlens SE micrograph from sample M-3658.5B showing example of NGBC containing negative crystal structures at the grain boundary.

Meniscus shaped Pore

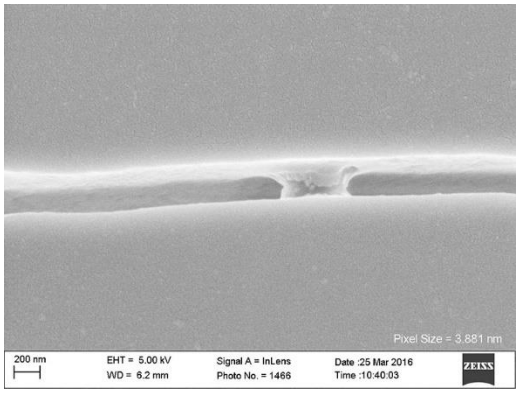

Figure B.169: Inlens SE micrograph from sample M-3658.5B showing example of NGBC containing bridging cements that create a meniscus shaped pore.

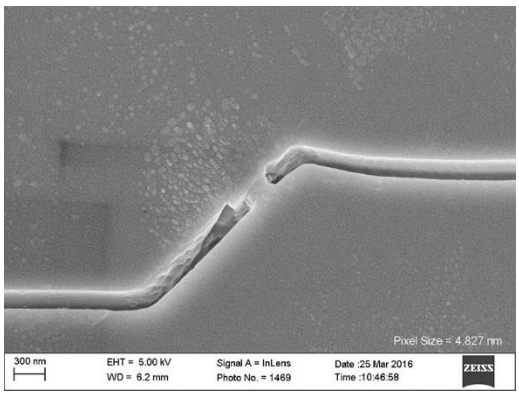

Figure B.170: Inlens SE micrograph from sample M-3658.5B showing example of NGBC containing bridging cements that create a meniscus shaped pore.

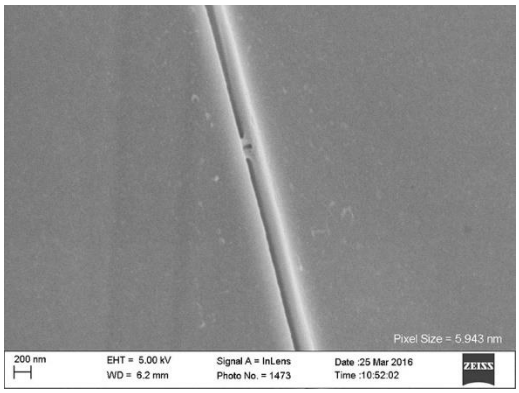

Figure B.171: Inlens SE micrograph from sample M-3658.5B showing example of NGBC containing bridging cements that create a meniscus shaped pore.

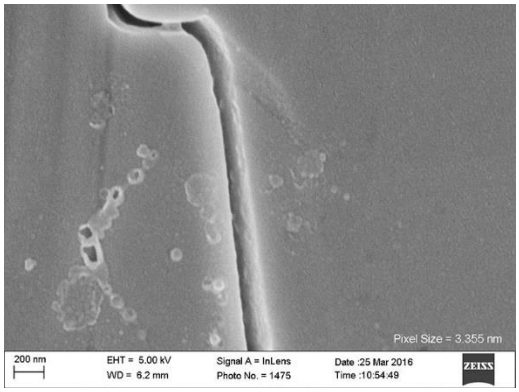

Figure B.172: Inlens SE micrograph from sample M-3658.5B showing example of NGBC containing bridging cements that create a meniscus shaped pore.

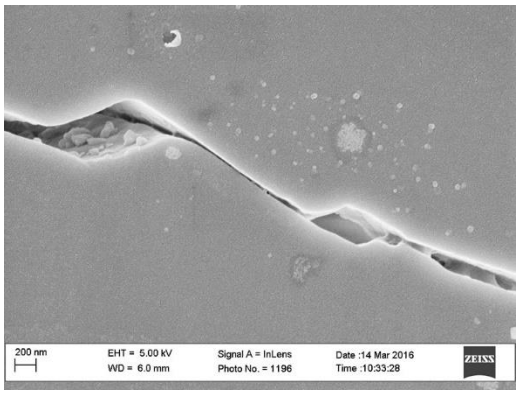

Figure B.173: Inlens SE micrograph from sample M-3658.5B showing example of NGBC containing bridging cements that create a meniscus shaped pore.

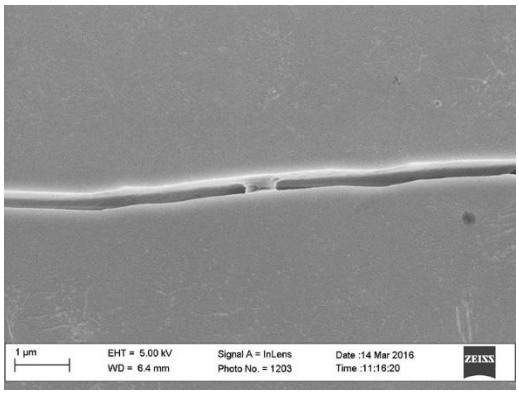

Figure B.174: Inlens SE micrograph from sample M-3658.5B showing example of NGBC containing bridging cements that create a meniscus shaped pore.

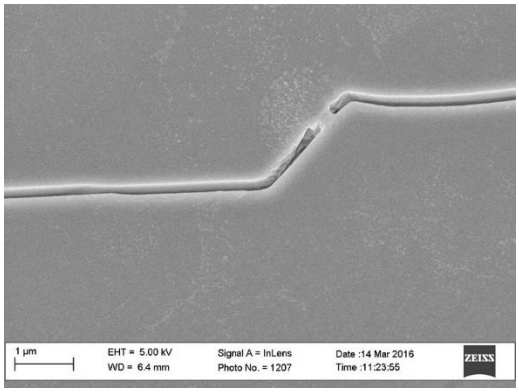

Figure B.175: Inlens SE micrograph from sample M-3658.5B showing example of NGBC containing bridging cements that create a meniscus shaped pore.

SAMPLE HF-18000, HAYNESVILLE FORMATION

Flat, Mating Contacts

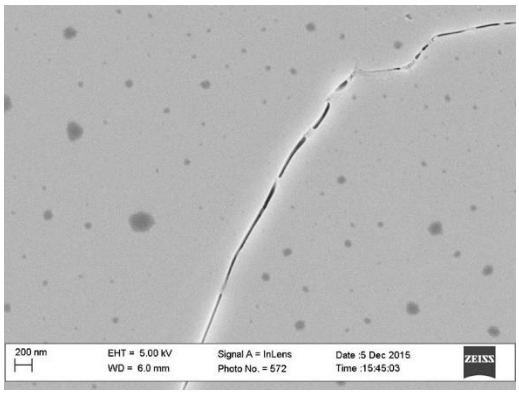

Figure B.176: Inlens SE micrograph from sample HF-18000 showing example of NGBC containing a flat, mating contact.

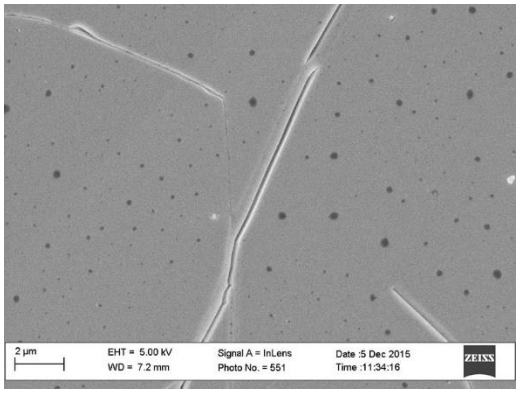

Figure B.177: Inlens SE micrograph from sample HF-18000 showing example of NGBC containing a flat, mating contact.

Cuspate-lobate

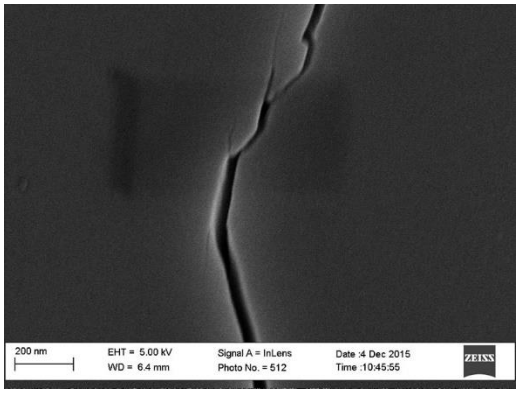

Figure B.178: Inlens SE micrograph from sample HF-18000 showing example of NGBC containing a cuspate-lobate texture.

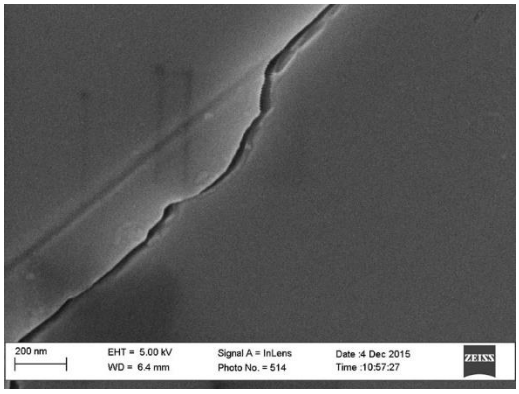

Figure B.179: Inlens SE micrograph from sample HF-18000 showing example of NGBC containing a cuspate-lobate texture.

Meniscus shaped Pore

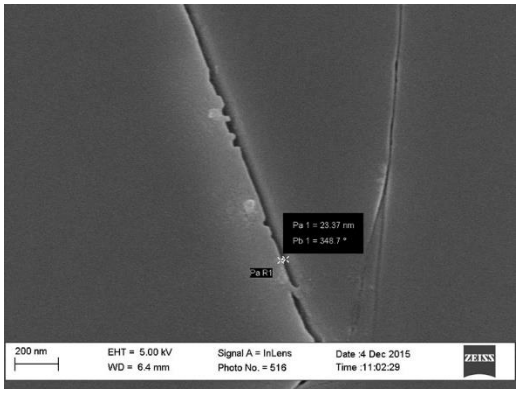

Figure B.180: Inlens SE micrograph from sample HF-18000 showing example of NGBC containing bridging cements that create a meniscus shaped pore.

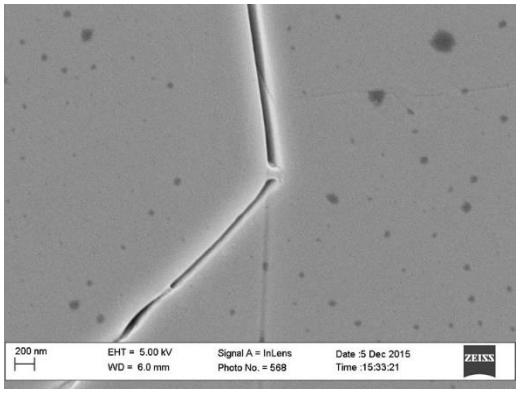

Figure B.181: Inlens SE micrograph from sample HF-18000 showing example of NGBC containing bridging cements that create a meniscus shaped pore.

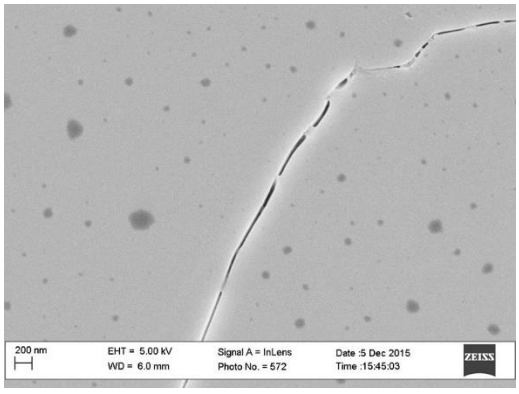

Figure B.182: Inlens SE micrograph from sample HF-18000 showing example of NGBC containing bridging cements that create a meniscus shaped pore.

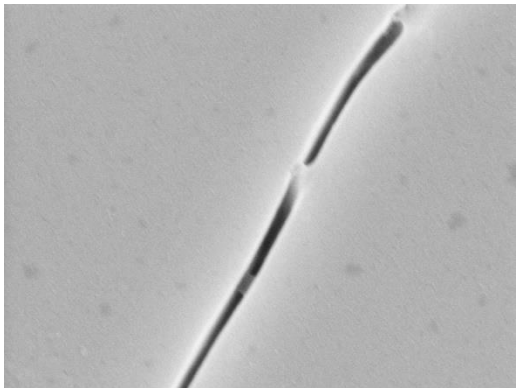

Figure B.183: Inlens SE micrograph from sample HF-18000 showing example of NGBC containing bridging cements that create a meniscus shaped pore.

Rectangular Shaped Pore

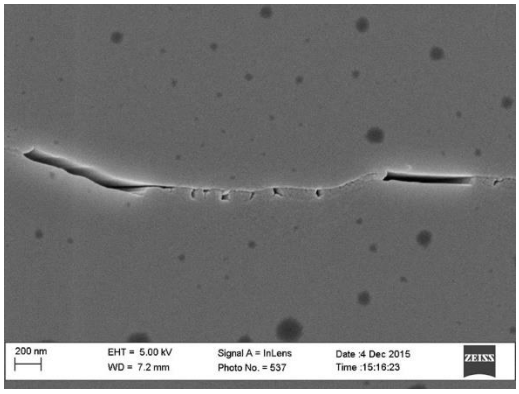

Figure B.184: Inlens SE micrograph from sample HF-18000 showing example of NGBC containing bridging cements that create a rectangular shaped pore.

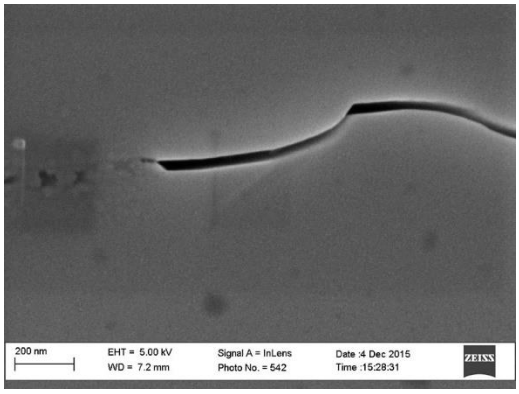

Figure B.185: Inlens SE micrograph from sample HF-18000 showing example of NGBC containing bridging cements that create a rectangular shaped pore.

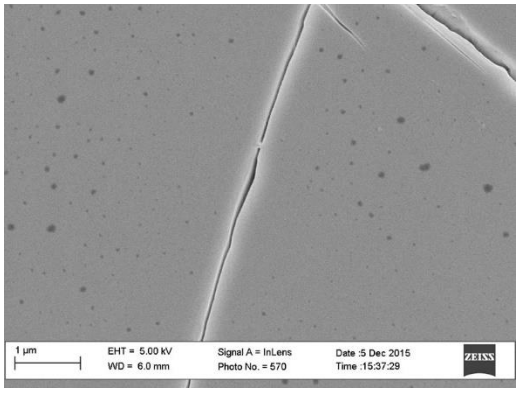

Figure B.186: Inlens SE micrograph from sample HF-18000 showing example of NGBC containing bridging cements that create a rectangular shaped pore.

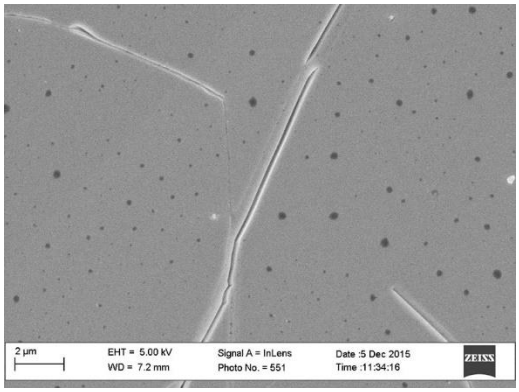

Figure B.187: Inlens SE micrograph from sample HF-18000 showing example of NGBC containing bridging cements that create a rectangular shaped pore.

Partial Bridge

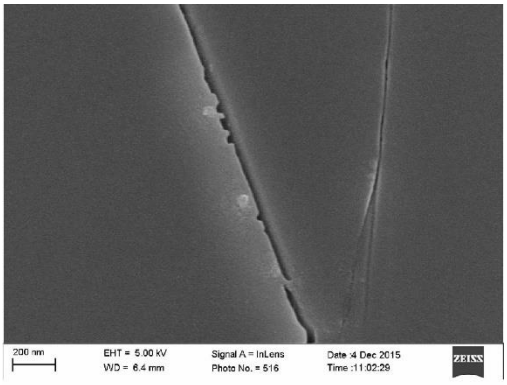

Figure B.188: Inlens SE micrograph from sample HF-18000 showing example of NGBC containing partially bridging cements that do not completely traverse the entire aperture of the NGBC.

SAMPLE 12-GC-12, NIKANASSIN FORMATION

Flat, Mating Contacts

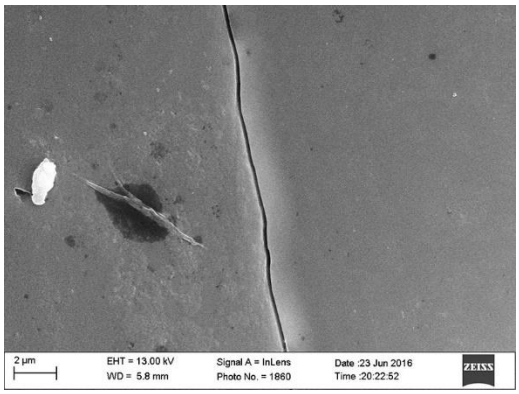

Figure B.189: Inlens SE micrograph from sample 12-GC-12 showing example of NGBC containing a flat, mating contact.

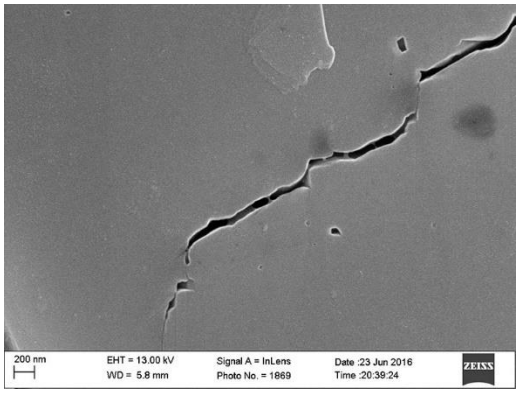

Figure B.190: Inlens SE micrograph from sample 12-GC-12 showing example of NGBC containing a flat, mating contact.

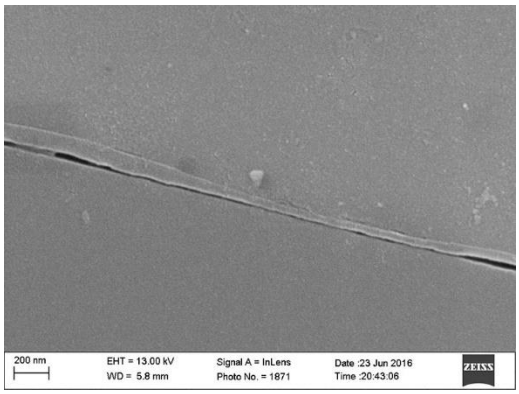

Figure B.191: Inlens SE micrograph from sample 12-GC-12 showing example of NGBC containing a flat, mating contact.

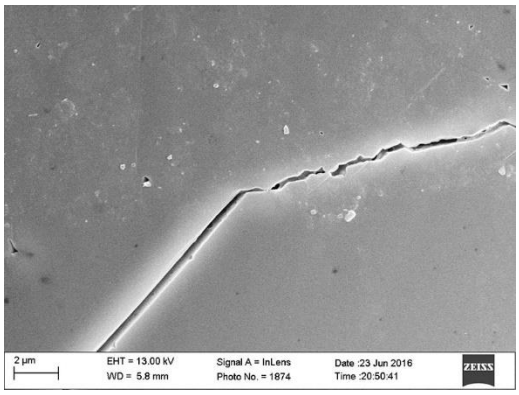

Figure B.192: Inlens SE micrograph from sample 12-GC-12 showing example of NGBC containing a flat, mating contact.

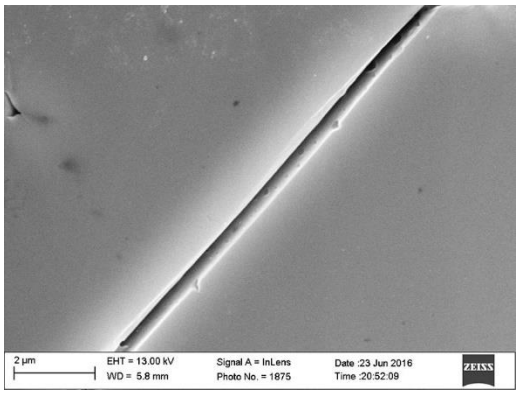

Figure B.193: Inlens SE micrograph from sample 12-GC-12 showing example of NGBC containing a flat, mating contact.

Cuspate-lobate

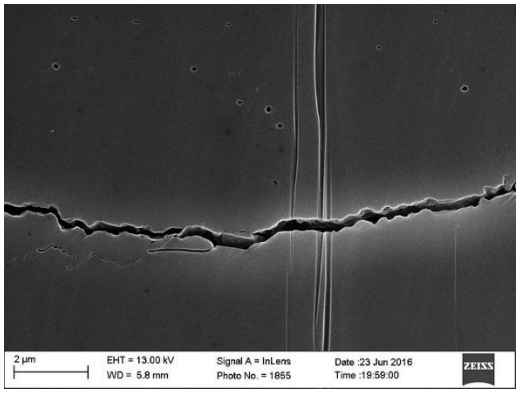

Figure B.194: Inlens SE micrograph from sample 12-GC-12 showing example of NGBC containing a cuspate-lobate texture.

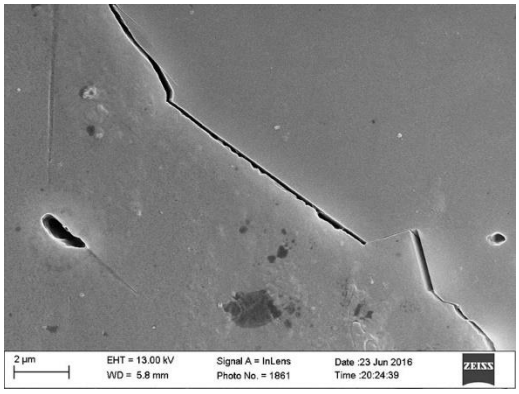

Figure B.195: Inlens SE micrograph from sample 12-GC-12 showing example of NGBC containing a cuspate-lobate texture.

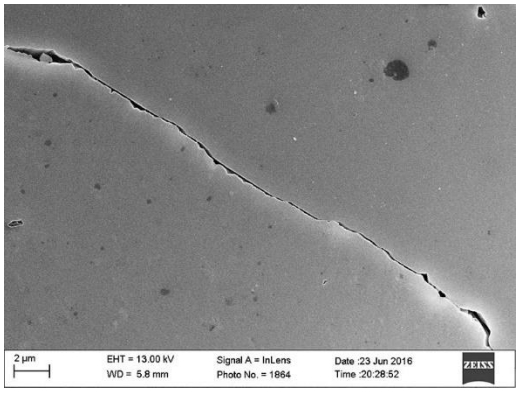

Figure B.196: Inlens SE micrograph from sample 12-GC-12 showing example of NGBC containing a cuspate-lobate texture.

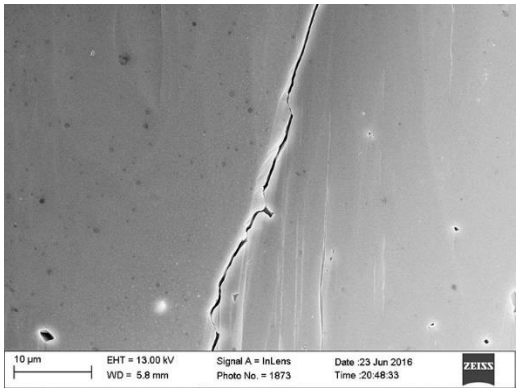

Figure B.197: Inlens SE micrograph from sample 12-GC-12 showing example of NGBC containing a cuspate-lobate texture.

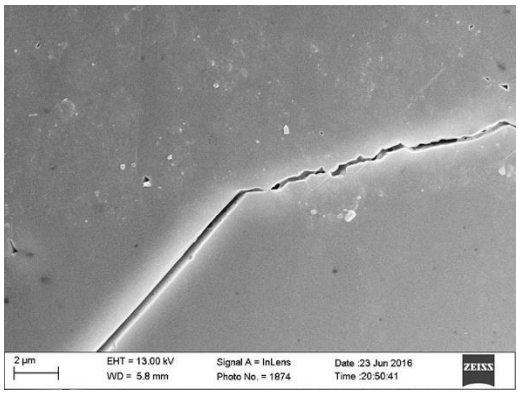

Figure B.198: Inlens SE micrograph from sample 12-GC-12 showing example of NGBC containing a cuspate-lobate texture.

Negative Crystal

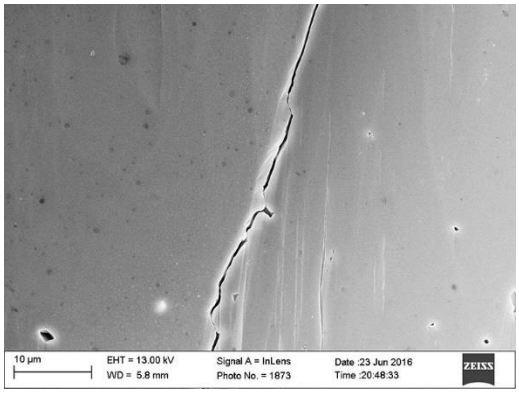

Figure B.199: Inlens SE micrograph from sample 12-GC-12 showing example of NGBC containing negative crystal structures at the grain boundary.

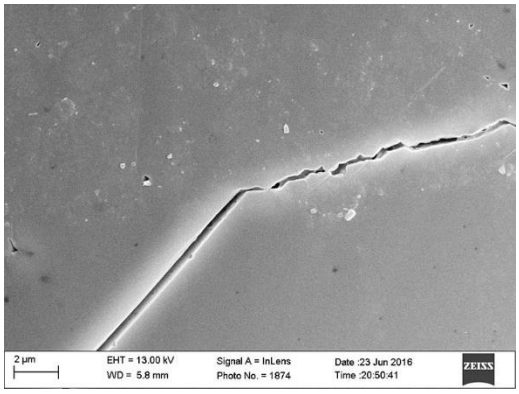

Figure B.200: Inlens SE micrograph from sample 12-GC-12 showing example of NGBC containing negative crystal structures at the grain boundary.

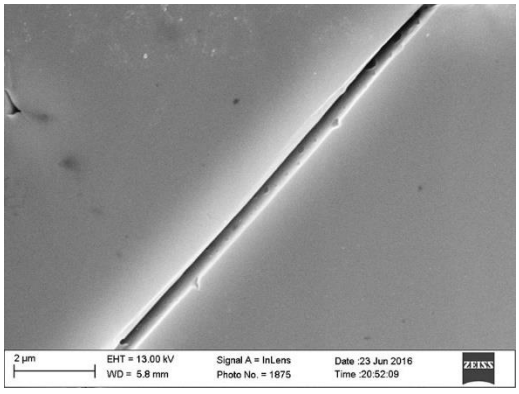

Figure B.201: Inlens SE micrograph from sample 12-GC-12 showing example of NGBC containing negative crystal structures at the grain boundary.

Meniscus shaped Pore

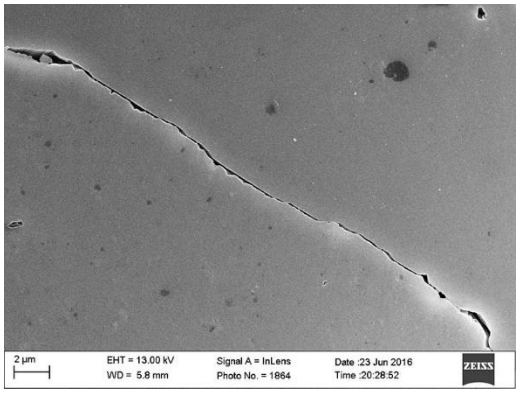

Figure B.202: Inlens SE micrograph from sample 12-GC-12 showing example of NGBC containing bridging cements that create a meniscus shaped pore.

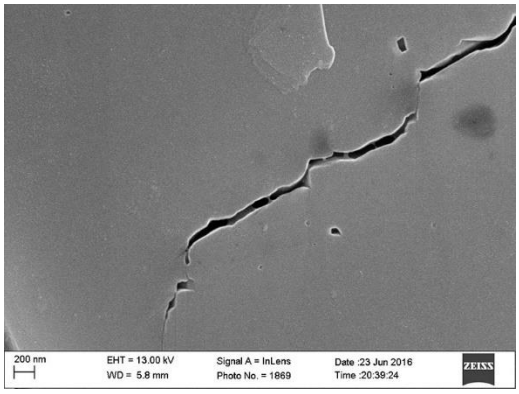

Figure B.203: Inlens SE micrograph from sample 12-GC-12 showing example of NGBC containing bridging cements that create a meniscus shaped pore.

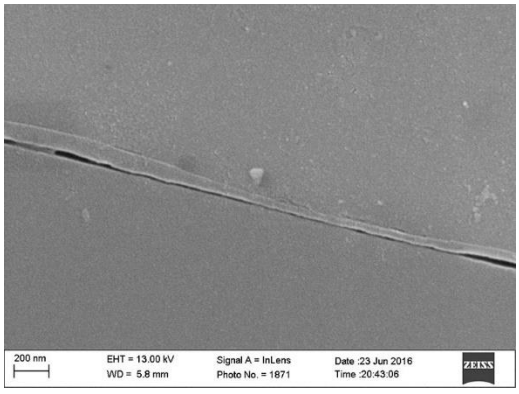

Figure B.204: Inlens SE micrograph from sample 12-GC-12 showing example of NGBC containing bridging cements that create a meniscus shaped pore.

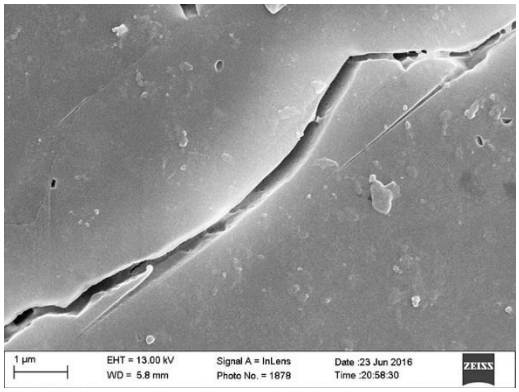

Figure B.205: Inlens SE micrograph from sample 12-GC-12 showing example of NGBC containing bridging cements that create a meniscus shaped pore.

SAMPLE 12-GC-9, NIKANASSIN FORMATION

Flat, Mating Contacts

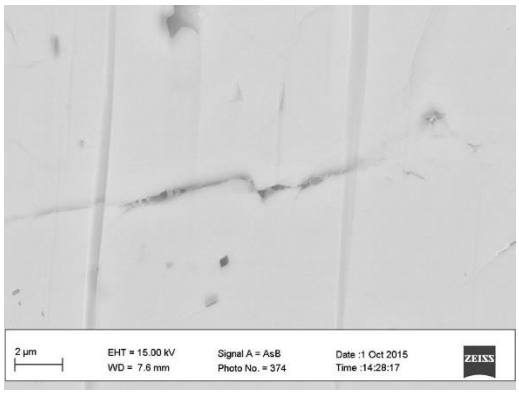

Figure B.206: BSE micrograph from sample 12-GC-9 showing example of NGBC containing a flat, mating contact.

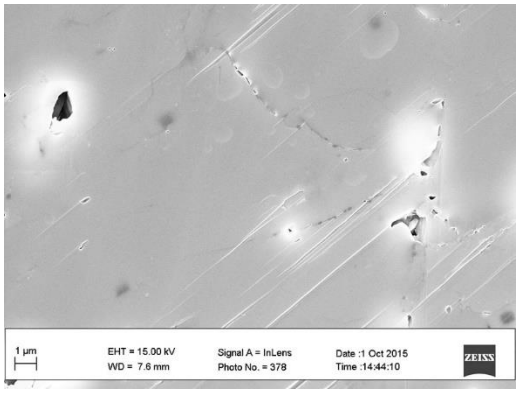

Figure B.207: Inlens SE micrograph from sample 12-GC-9 showing example of NGBC containing a flat, mating contact.

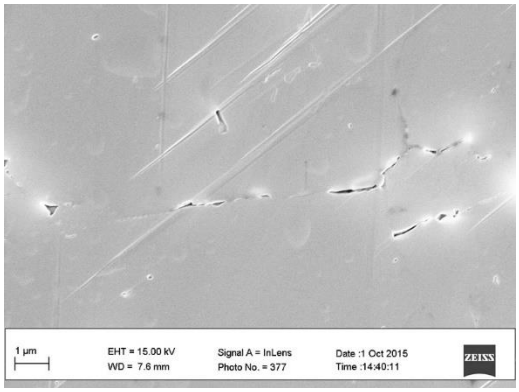

Figure B.208: Inlens SE micrograph from sample 12-GC-9 showing example of NGBC containing a flat, mating contact.

Meniscus shaped Pore

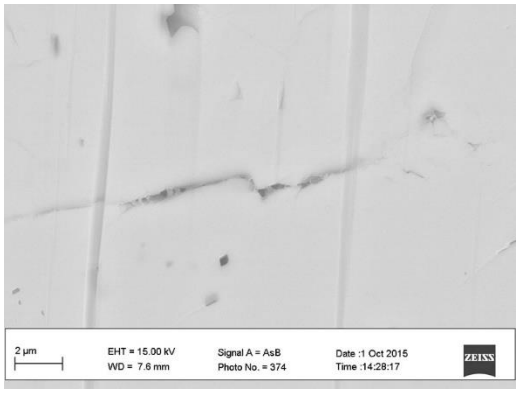

Figure B.209: Inlens SE micrograph from sample 12-GC-9 showing example of NGBC containing bridging cements that create a meniscus shaped pore.

Figure B.210: Inlens SE micrograph from sample 12-GC-9 showing example of NGBC containing bridging cements that create a meniscus shaped pore.

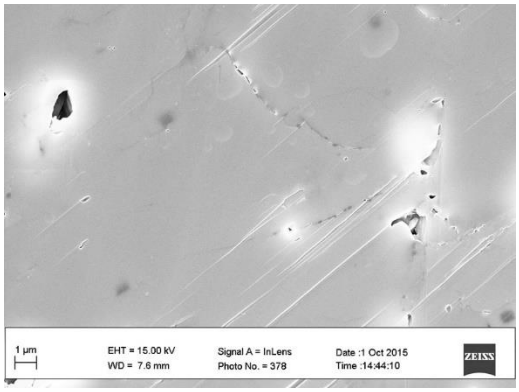

Figure B.211: Inlens SE micrograph from sample 12-GC-9 showing example of NGBC containing bridging cements that create a meniscus shaped pore.

Rectangular Shaped Pore

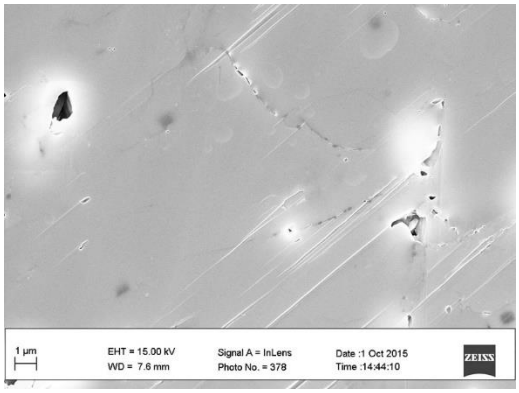

Figure B.212: Inlens SE micrograph from sample 12-GC-9 showing example of NGBC containing bridging cements that create a rectangular shaped pore.

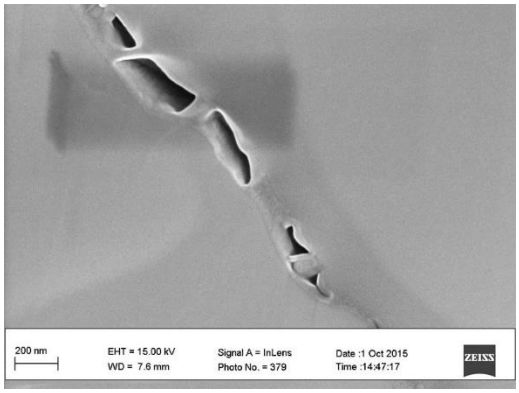

Figure B.213: Inlens SE micrograph from sample 12-GC-9 showing example of NGBC containing bridging cements that create a rectangular shaped pore.

SAMPLE 12-RF-2, CARDIUM FORMATION

Flat, Mating Contacts

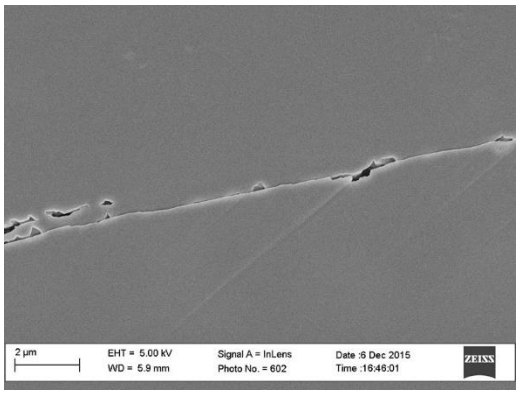

Figure B.214: Inlens SE micrograph from sample 12-RF-2 showing example of NGBC containing a flat, mating contact.

Cuspate-lobate

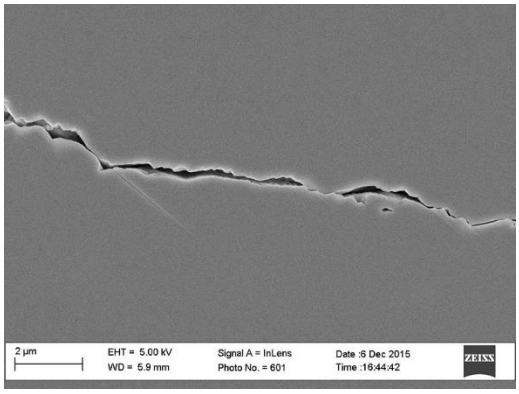

Figure B.215: Inlens SE micrograph from sample 12-RF-2 showing example of NGBC containing a cuspate-lobate texture.

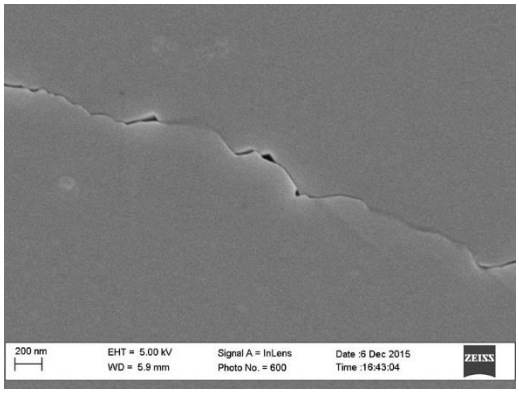

Figure B.216: Inlens SE micrograph from sample 12-RF-2 showing example of NGBC containing a cuspate-lobate texture.

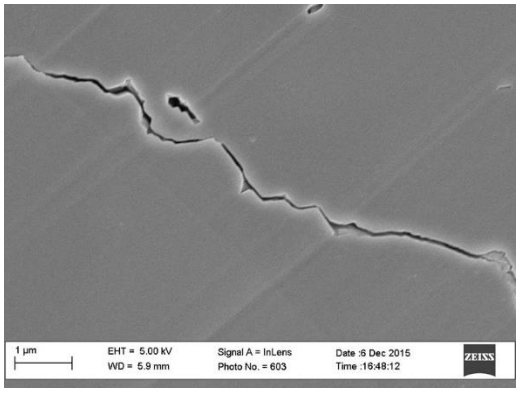

Figure B.217: Inlens SE micrograph from sample 12-RF-2 showing example of NGBC containing a cuspate-lobate texture.

SAMPLE: 12-BR-3, CARDIUM FORMATION

Flat, Mating Contacts

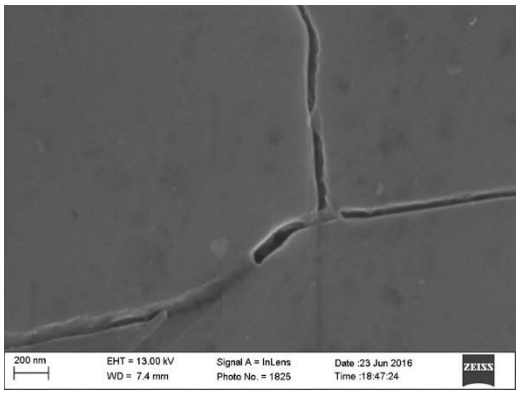

Figure B.218: Inlens SE micrograph from sample 12-BR-3 showing example of NGBC containing a flat, mating contact.

Cuspate-lobate

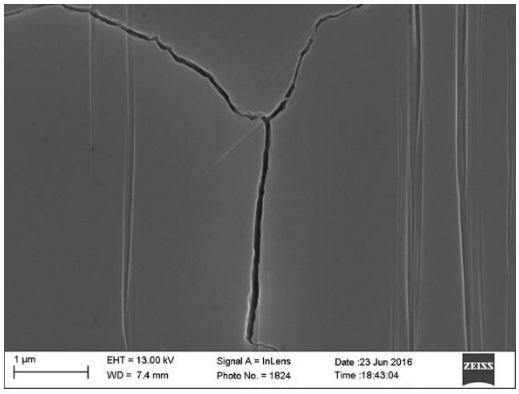

Figure B.219: Inlens SE micrograph from sample 12-BR-3 showing example of NGBC containing a cuspate-lobate texture.

Meniscus shaped Pore

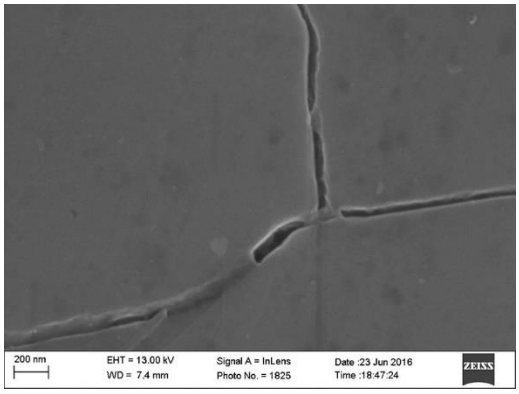

Figure B.220: Inlens SE micrograph from sample 12-BR-3 showing example of NGBC containing bridging cements that create a meniscus shaped pore.

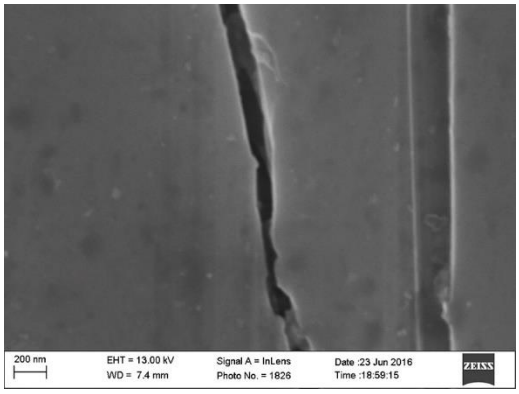

Figure B.221: Inlens SE micrograph from sample 12-BR-3 showing example of NGBC containing bridging cements that create a meniscus shaped pore.

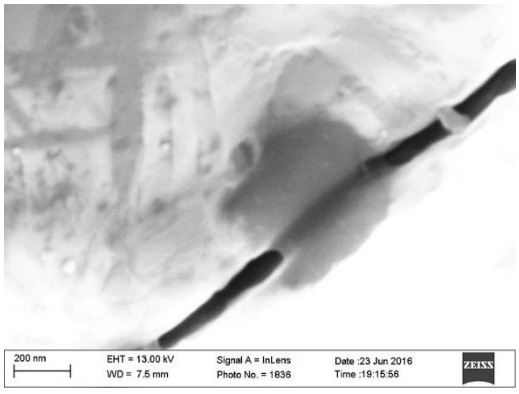

Figure B.222: Inlens SE micrograph from sample 12-BR-3 showing example of NGBC containing bridging cements that create a meniscus shaped pore.

Rectangular Shaped Pore

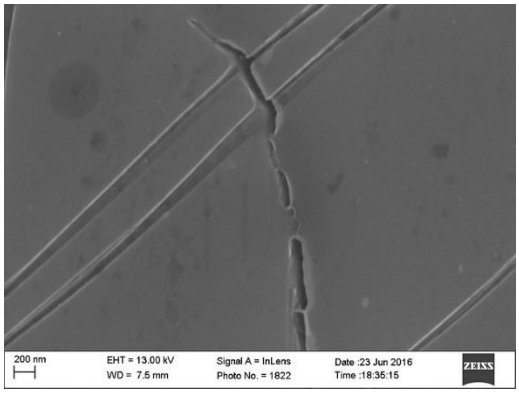

Figure B.223: Inlens SE micrograph from sample 12-BR-3 showing example of NGBC containing bridging cements that create a rectangular shaped pore.

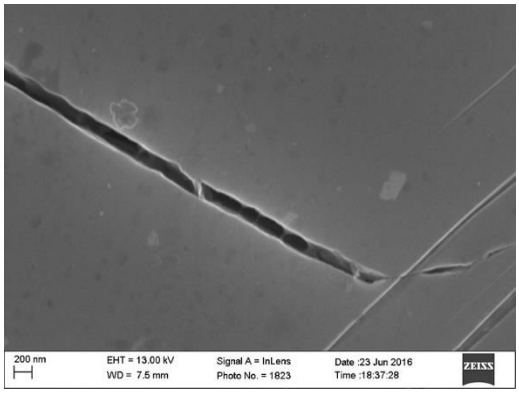

Figure B.224: Inlens SE micrograph from sample 12-BR-3 showing example of NGBC containing bridging cements that create a rectangular shaped pore.

BRTC1-12083, BARNETT FORMATION

Cuspate-lobate

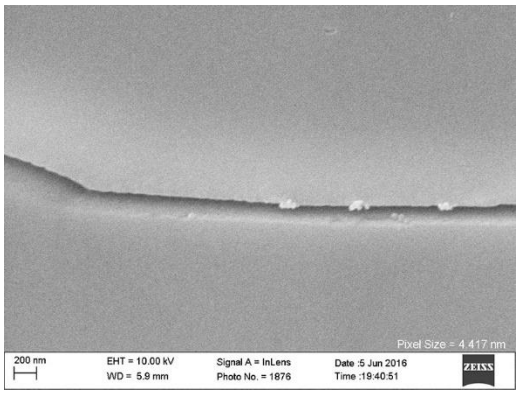

Figure B.225: Inlens SE micrograph from sample BRTC1-12083 showing example of NGBC containing a cuspate-lobate texture.

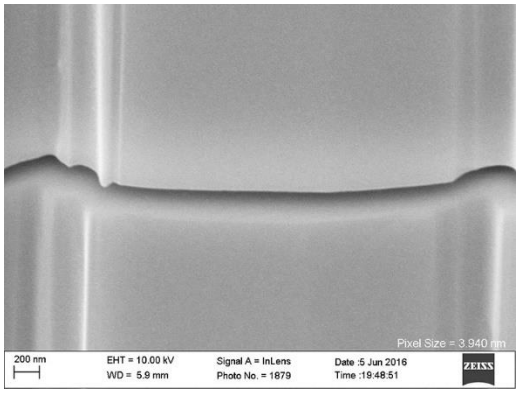

Figure B.226: Inlens SE micrograph from sample BRTC1-12083 showing example of NGBC containing a cuspate-lobate texture.

BRTC1-12421, BARNETT FORMATION

Flat, Mating Contacts

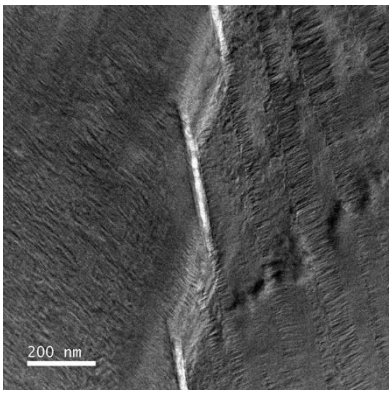

Figure B.227: Bright field TEM micrograph from sample BRTC1-12421 showing example of NGBC containing a flat, mating contact.

SAMPLE 06212-2, CAMPITO FORMATION

Cuspate-lobate

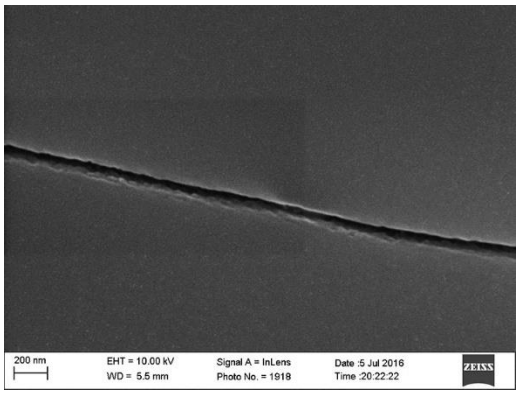

Figure B.228: Inlens SE micrograph from sample 06212-2 showing example of NGBC containing a cuspate-lobate texture.

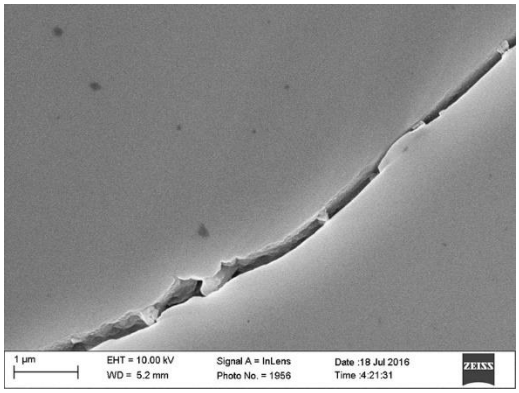

Figure B.229: Inlens SE micrograph from sample 06212-2 showing example of NGBC containing a cuspate-lobate texture.

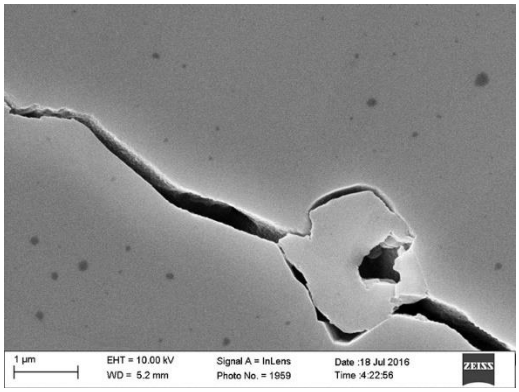

Figure B.230: Inlens SE micrograph from sample 06212-2 showing example of NGBC containing a cuspate-lobate texture.

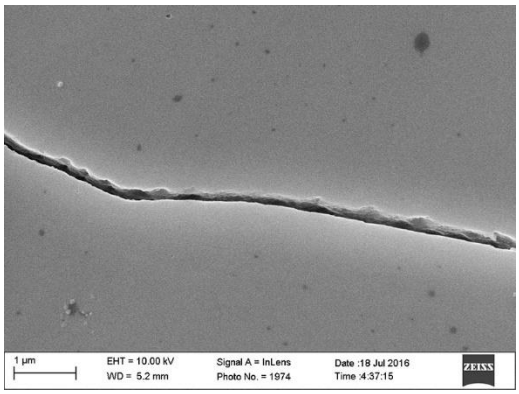

Figure B.231: Inlens SE micrograph from sample 06212-2 showing example of NGBC containing a cuspate-lobate texture.

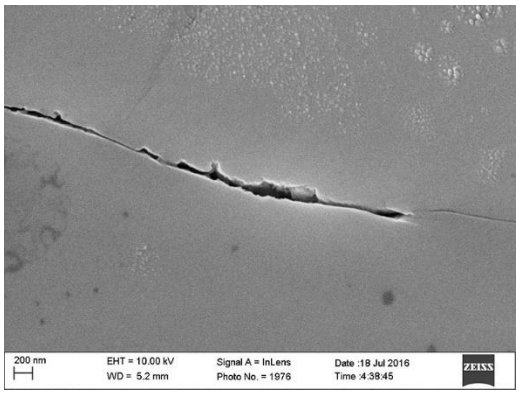

Figure B.232: Inlens SE micrograph from sample 06212-2 showing example of NGBC containing a cuspate-lobate texture.

Negative Crystal

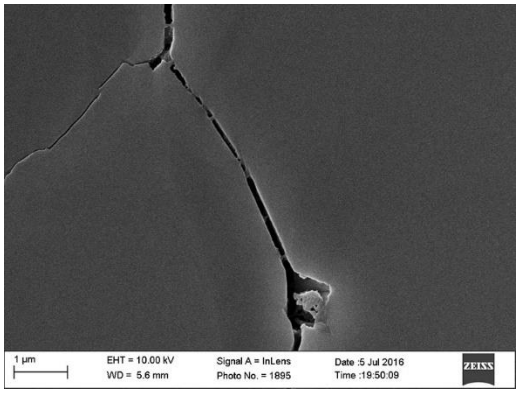

Figure B.233: Inlens SE micrograph from sample 06212-2 showing example of NGBC containing negative crystal structures at the grain boundary.

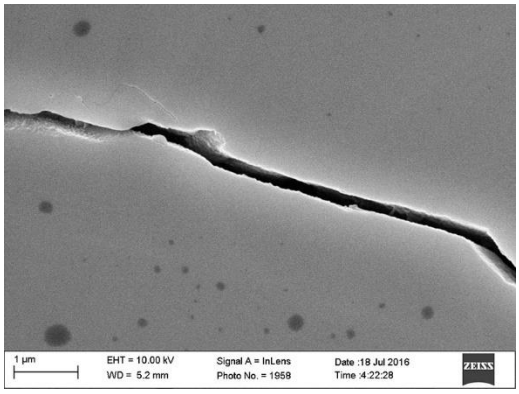

Figure B.234: Inlens SE micrograph from sample 06212-2 showing example of NGBC containing negative crystal structures at the grain boundary.

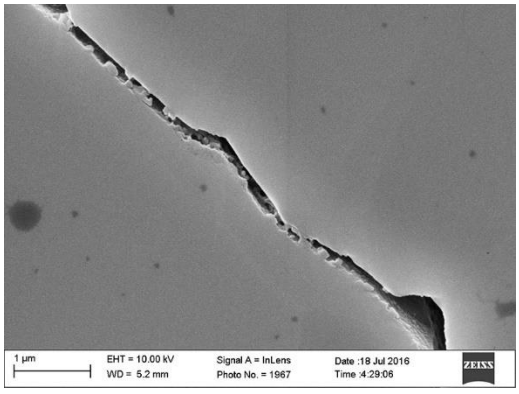

Figure B.235: Inlens SE micrograph from sample 06212-2 showing example of NGBC containing negative crystal structures at the grain boundary.

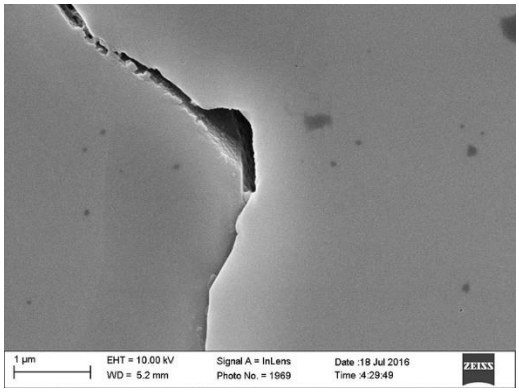

Figure B.236: Inlens SE micrograph from sample 06212-2 showing example of NGBC containing negative crystal structures at the grain boundary.

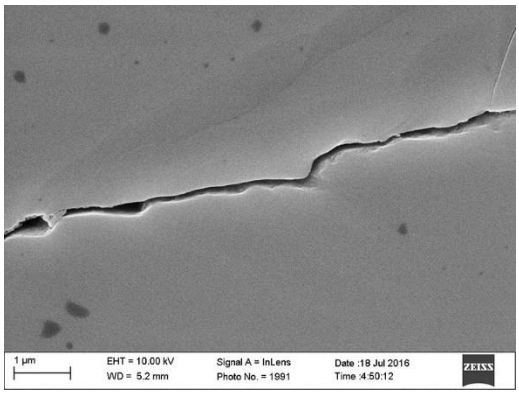

Figure B.237: Inlens SE micrograph from sample 06212-2 showing example of NGBC containing negative crystal structures at the grain boundary.

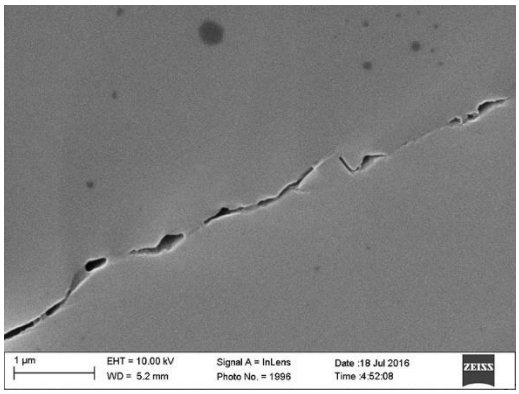

Figure B.238: Inlens SE micrograph from sample 06212-2 showing example of NGBC containing negative crystal structures at the grain boundary.

Meniscus shaped Pore

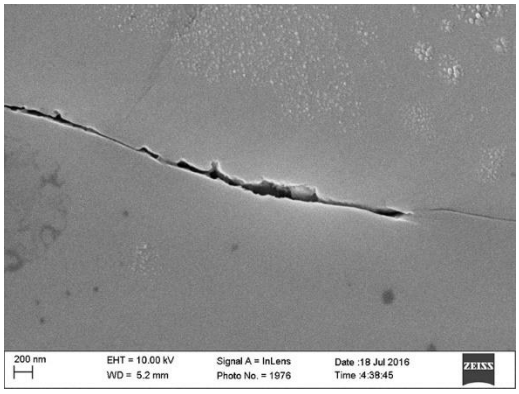

Figure B.239: Inlens SE micrograph from sample 06212-2 showing example of NGBC containing bridging cements that create a meniscus shaped pore.

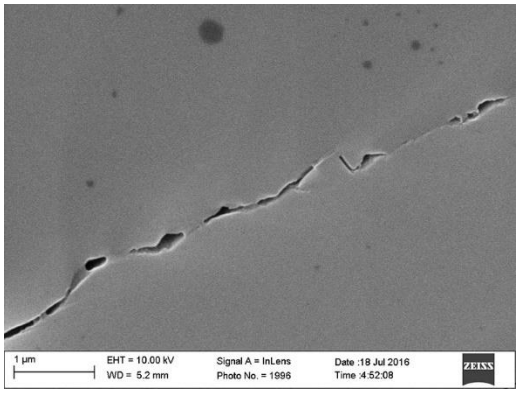

Figure B.240: Inlens SE micrograph from sample 06212-2 showing example of NGBC containing bridging cements that create a meniscus shaped pore.

Rectangular Shaped Pore

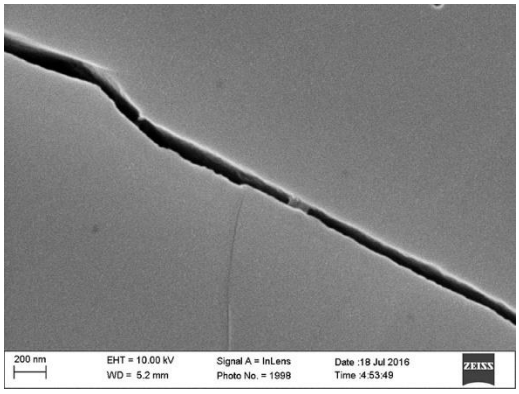

Figure B.241: Inlens SE micrograph from sample 06212-2 showing example of NGBC containing bridging cements that create a rectangular shaped pore.

Partial Bridge

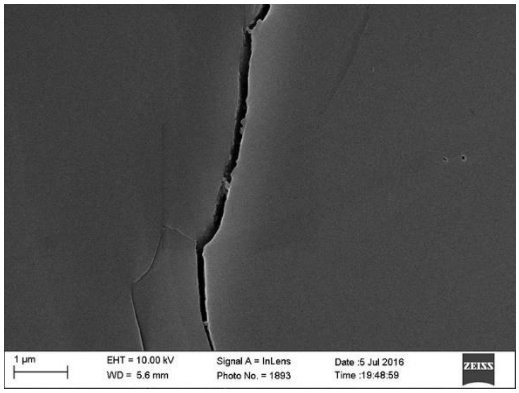

Figure B.242: Inlens SE micrograph from sample 06212-2 showing example of NGBC containing partially bridging cements that do not completely traverse the entire aperture of the NGBC.

SAMPLE: SFOT-1-10106.8, TRAVIS PEAK FORMATION

Flat, Mating Contacts

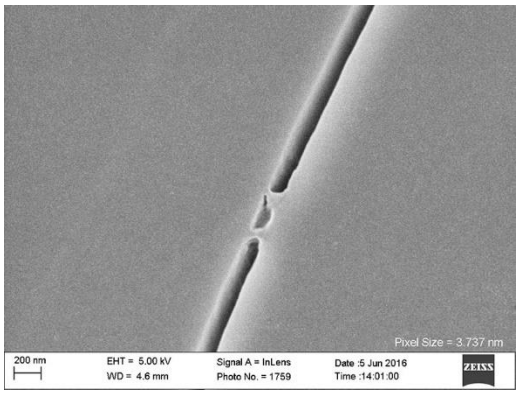

Figure B.243: Inlens SE micrograph from sample SFOT-1-10106.8 showing example of NGBC containing a flat, mating contact.

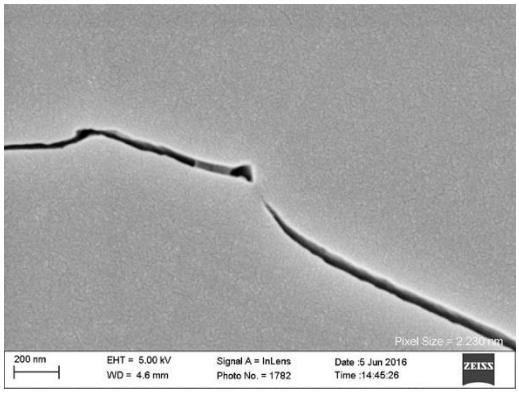

Figure B.244: Inlens SE micrograph from sample SFOT-1-10106.8 showing example of NGBC containing a flat, mating contact.

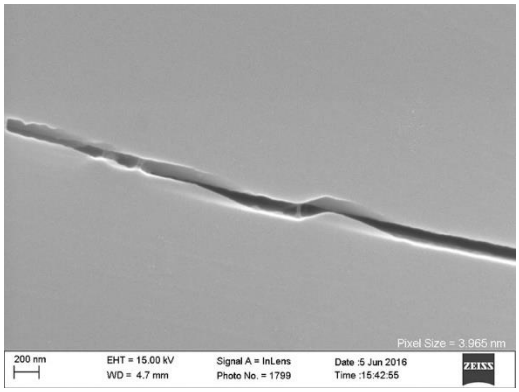

Figure B.245: Inlens SE micrograph from sample SFOT-1-10106.8 showing example of NGBC containing a flat, mating contact.

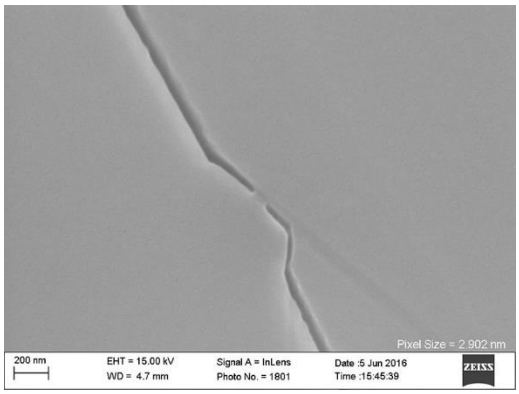

Figure B.246: Inlens SE micrograph from sample SFOT-1-10106.8 showing example of NGBC containing a flat, mating contact.

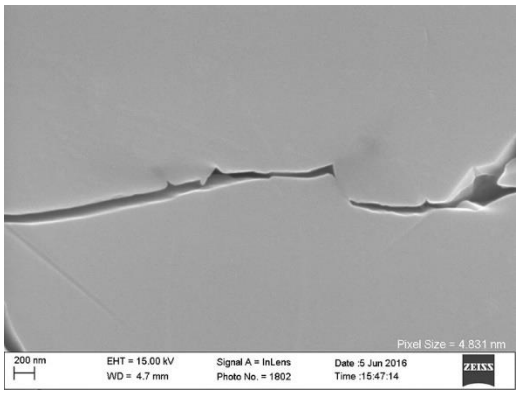

Figure B.247: Inlens SE micrograph from sample SFOT-1-10106.8 showing example of NGBC containing a flat, mating contact.

Cuspate-lobate

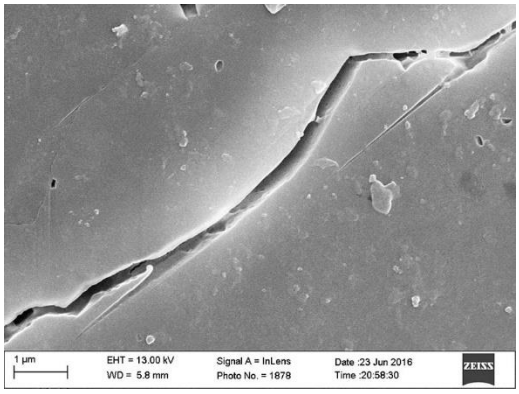

Figure B.248: Inlens SE micrograph from sample SFOT-1-10106.8 showing example of NGBC containing a cuspate-lobate texture.

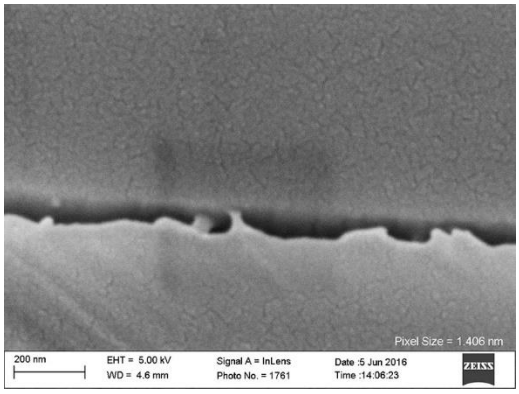

Figure B.249: Inlens SE micrograph from sample SFOT-1-10106.8 showing example of NGBC containing a cuspate-lobate texture.

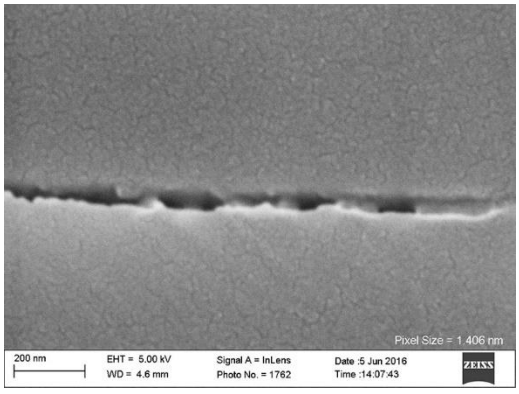

Figure B.250: Inlens SE micrograph from sample SFOT-1-10106.8 showing example of NGBC containing a cuspate-lobate texture.

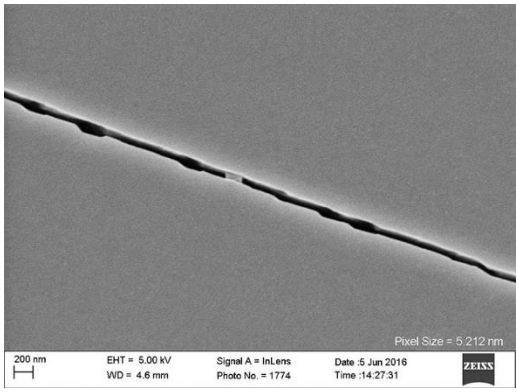

Figure B.251: Inlens SE micrograph from sample SFOT-1-10106.8 showing example of NGBC containing a cuspate-lobate texture.

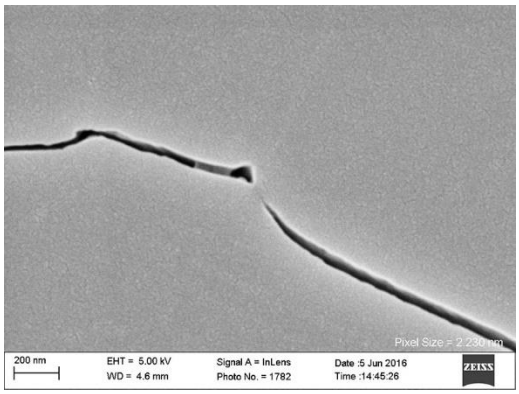

Figure B.252: Inlens SE micrograph from sample SFOT-1-10106.8 showing example of NGBC containing a cuspate-lobate texture.

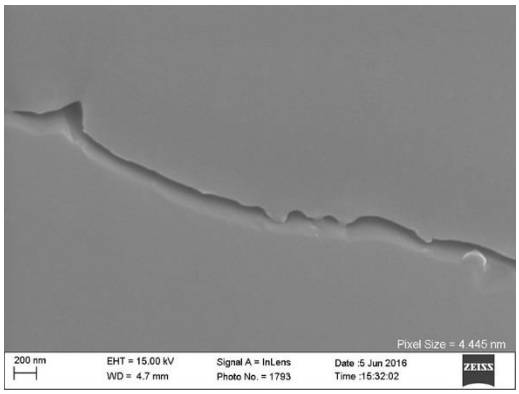

Figure B.253: Inlens SE micrograph from sample SFOT-1-10106.8 showing example of NGBC containing a cuspate-lobate texture.

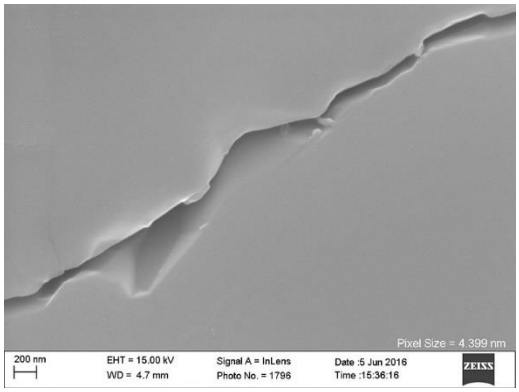

Figure B.254: Inlens SE micrograph from sample SFOT-1-10106.8 showing example of NGBC containing a cuspate-lobate texture.

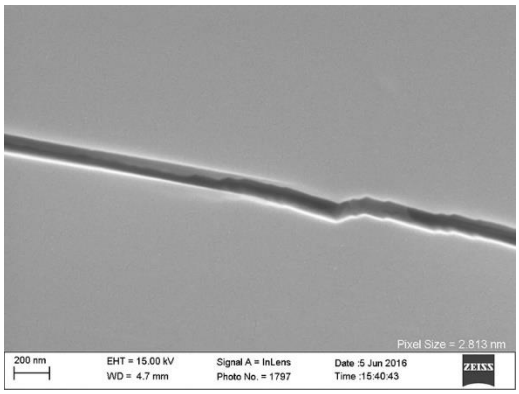

Figure B.255: Inlens SE micrograph from sample SFOT-1-10106.8 showing example of NGBC containing a cuspate-lobate texture.

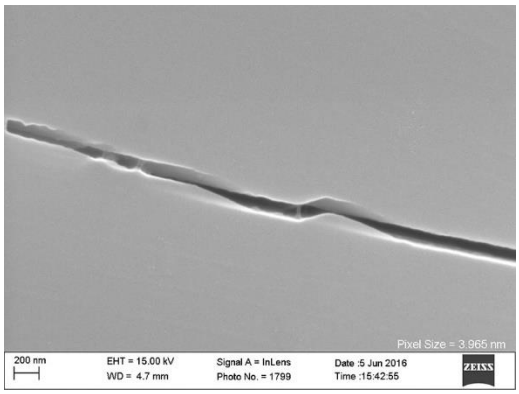

Figure B.256: Inlens SE micrograph from sample SFOT-1-10106.8 showing example of NGBC containing a cuspate-lobate texture.

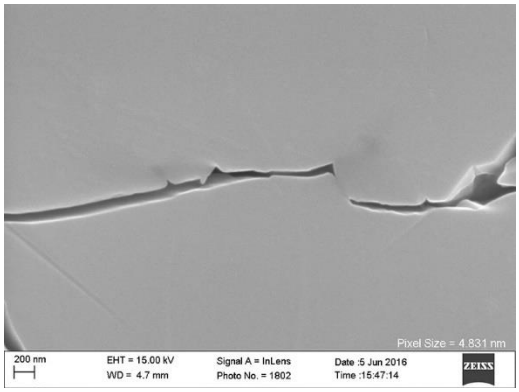

Figure B.257: Inlens SE micrograph from sample SFOT-1-10106.8 showing example of NGBC containing a cuspate-lobate texture.

Negative Crystal

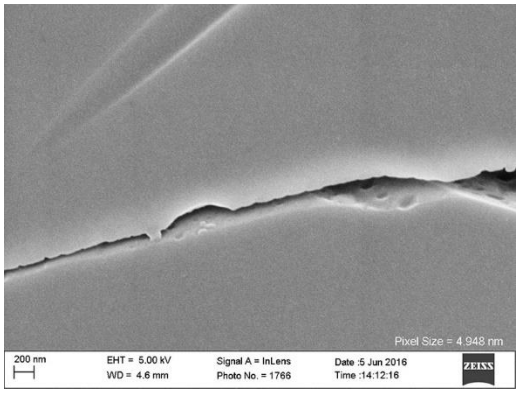

Figure B.258: Inlens SE micrograph from sample SFOT-1-10106.8 showing example of NGBC containing negative crystal structures at the grain boundary

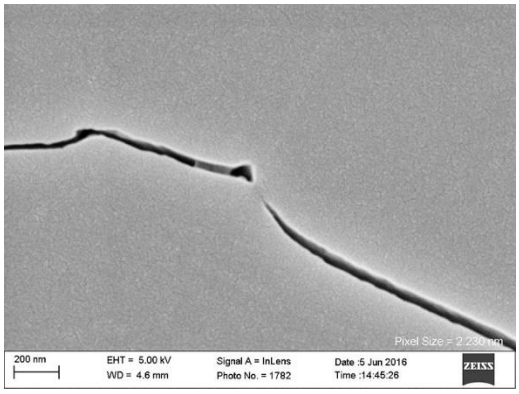

Figure B.259: Inlens SE micrograph from sample SFOT-1-10106.8 showing example of NGBC containing negative crystal structures at the grain boundary

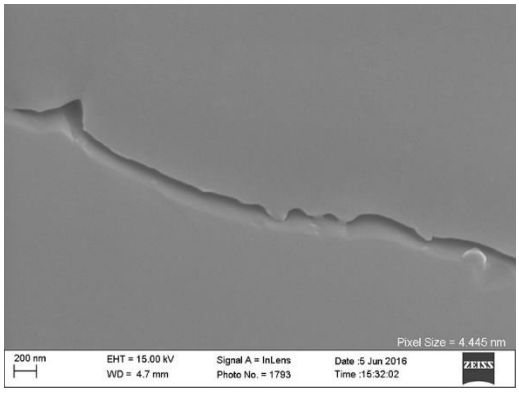

Figure B.260: Inlens SE micrograph from sample SFOT-1-10106.8 showing example of NGBC containing negative crystal structures at the grain boundary

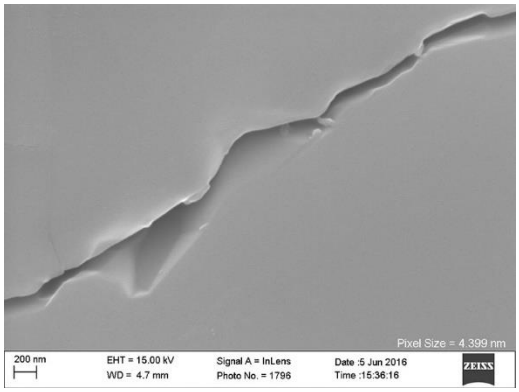

Figure B.261: Inlens SE micrograph from sample SFOT-1-10106.8 showing example of NGBC containing negative crystal structures at the grain boundary

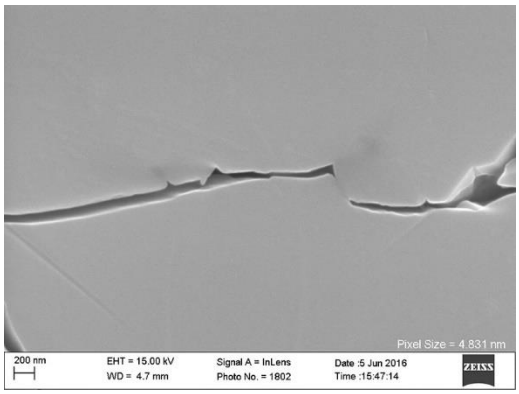

Figure B.262: Inlens SE micrograph from sample SFOT-1-10106.8 showing example of NGBC containing negative crystal structures at the grain boundary

Meniscus shaped Pore

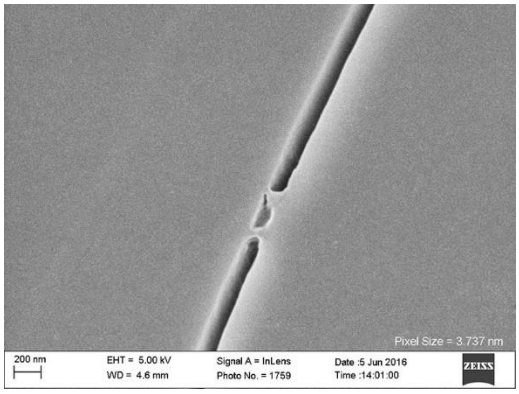

Figure B.263: Inlens SE micrograph from sample SFOT-1-10106.8 showing example of NGBC containing bridging cements that create a meniscus shaped pore.

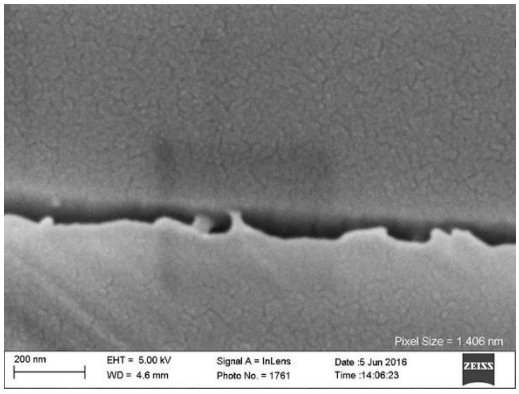

Figure B.264: Inlens SE micrograph from sample SFOT-1-10106.8 showing example of NGBC containing bridging cements that create a meniscus shaped pore.

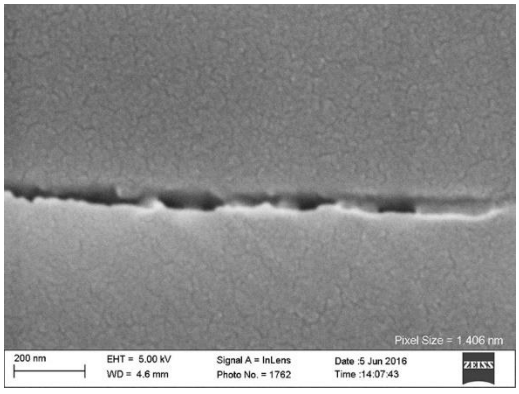

Figure B.265: Inlens SE micrograph from sample SFOT-1-10106.8 showing example of NGBC containing bridging cements that create a meniscus shaped pore.

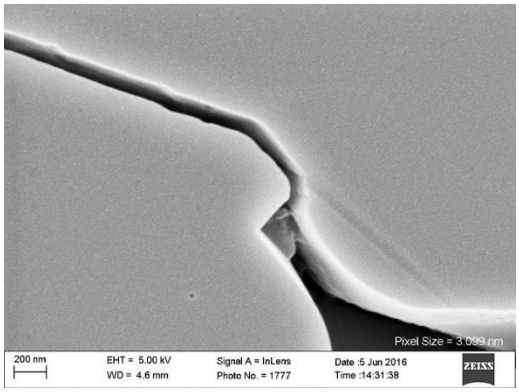

Figure B.266: Inlens SE micrograph from sample SFOT-1-10106.8 showing example of NGBC containing bridging cements that create a meniscus shaped pore.

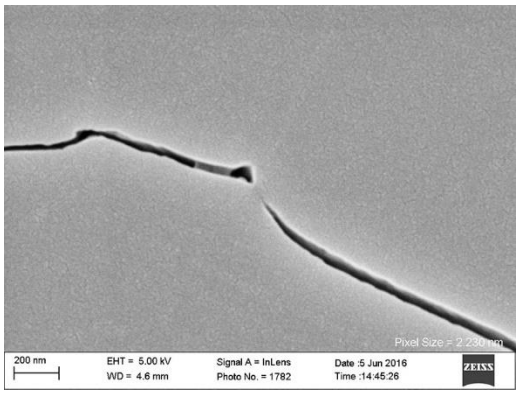

Figure B.267: Inlens SE micrograph from sample SFOT-1-10106.8 showing example of NGBC containing bridging cements that create a meniscus shaped pore.

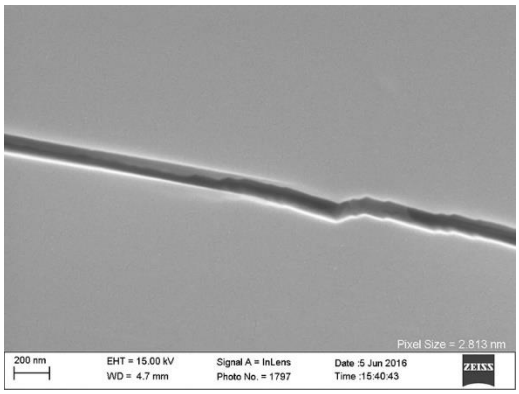

Figure B.268: Inlens SE micrograph from sample SFOT-1-10106.8 showing example of NGBC containing bridging cements that create a meniscus shaped pore.

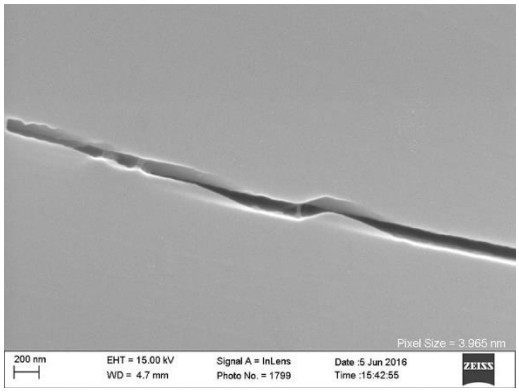

Figure B.269: Inlens SE micrograph from sample SFOT-1-10106.8 showing example of NGBC containing bridging cements that create a meniscus shaped pore.

Rectangular Shaped Pore

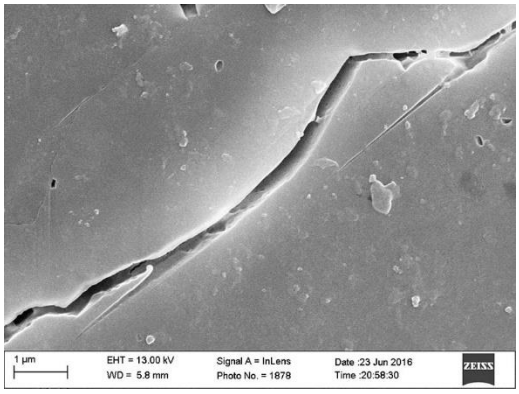

Figure B.270: Inlens SE micrograph from sample SFOT-1-10106.8 showing example of NGBC containing bridging cements that create a rectangular shaped pore.

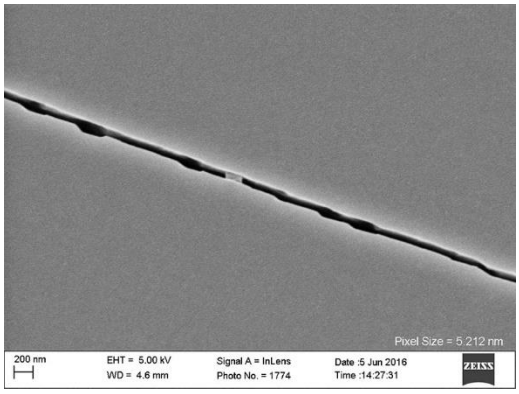

Figure B.271: Inlens SE micrograph from sample SFOT-1-10106.8 showing example of NGBC containing bridging cements that create a rectangular shaped pore.

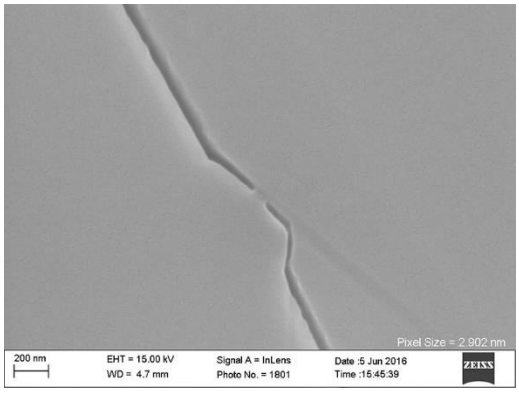

Figure B.272: Inlens SE micrograph from sample SFOT-1-10106.8 showing example of NGBC containing bridging cements that create a rectangular shaped pore.

Partial Bridge

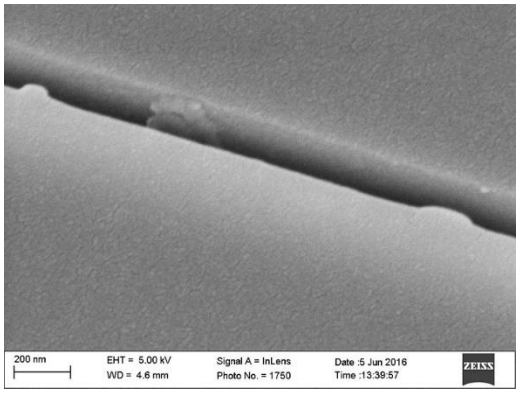

Figure B.273: Inlens SE micrograph from sample SFOT-1-10106.8 showing example of NGBC containing partially bridging cements that do not completely traverse the entire aperture of the NGBC.

SAMPLE: A1-4982.2, MONTEREY FORMATION

Cuspate-lobate

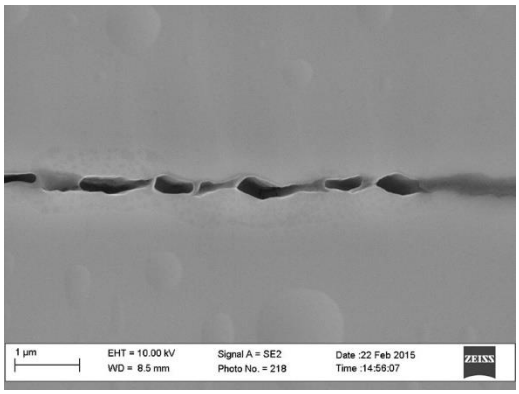

Figure B.274: Inlens SE micrograph from sample A1-4982.2 showing example of NGBC containing a cuspate-lobate texture.

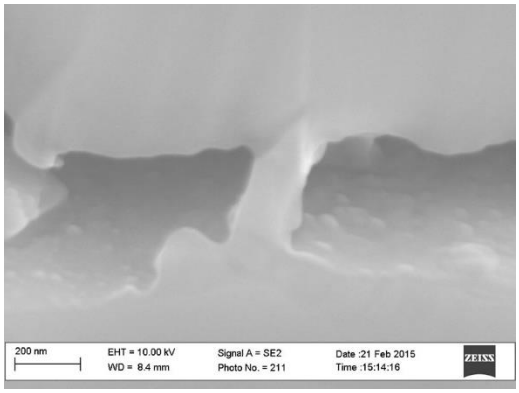

Figure B.275: Inlens SE micrograph from sample A1-4982.2 showing example of NGBC containing a cuspate-lobate texture.

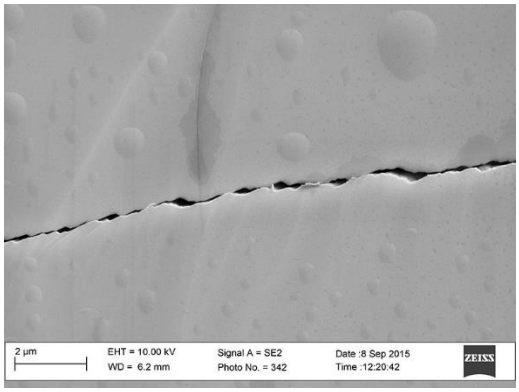

Figure B.276: Inlens SE micrograph from sample A1-4982.2 showing example of NGBC containing a cuspate-lobate texture.

Meniscus shaped Pore

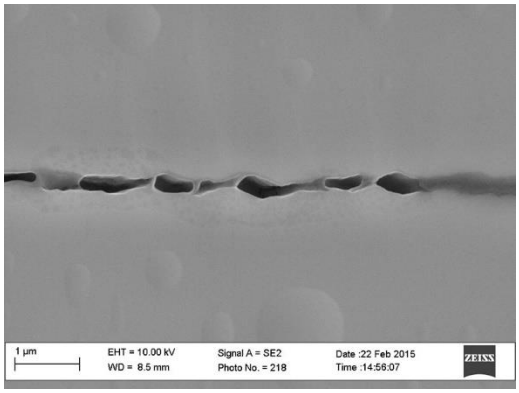

Figure B.277: Inlens SE micrograph from sample A1-4982.2 showing example of NGBC containing bridging cements that create a meniscus shaped pore.

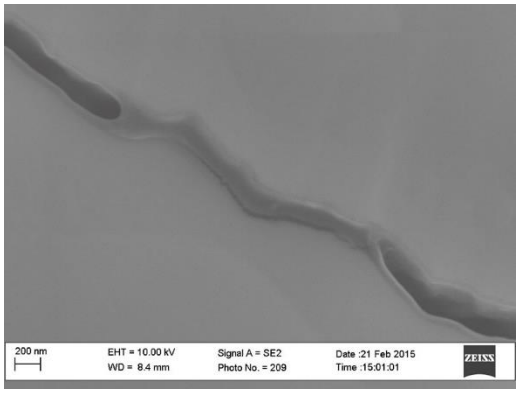

Figure B.278: Inlens SE micrograph from sample A1-4982.2 showing example of NGBC containing bridging cements that create a meniscus shaped pore.

Rectangular Shaped Pore

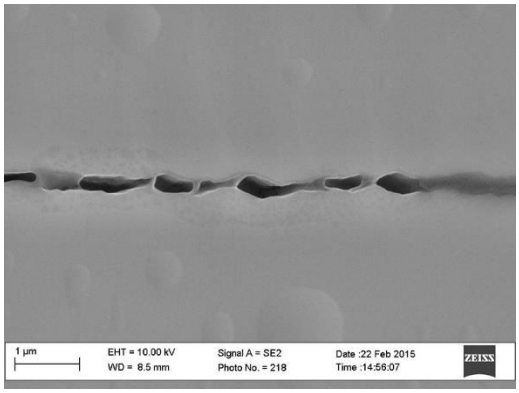

Figure B.279: Inlens SE micrograph from sample A1-4982.2 showing example of NGBC containing bridging cements that create a rectangular shaped pore.

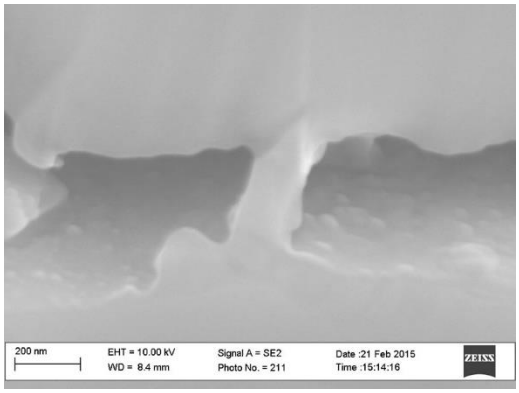

Figure B.280: Inlens SE micrograph from sample A1-4982.2 showing example of NGBC containing bridging cements that create a rectangular shaped pore.

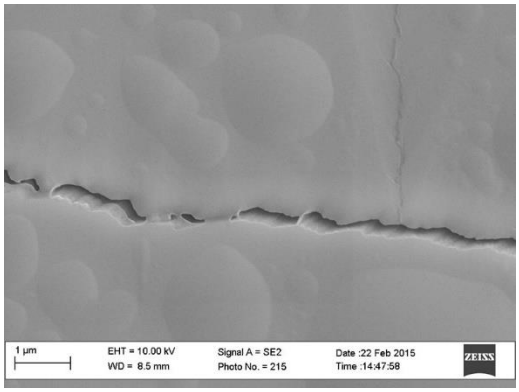

Figure B.281: Inlens SE micrograph from sample A1-4982.2 showing example of NGBC containing bridging cements that create a rectangular shaped pore.

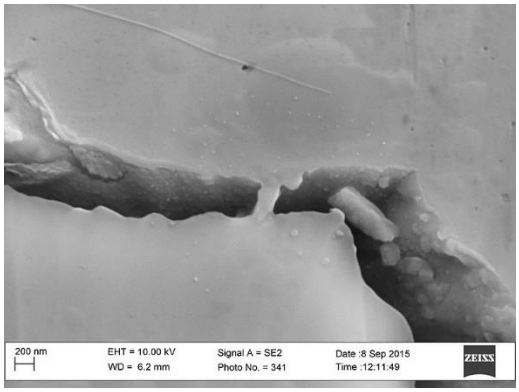

Figure B.282: Inlens SE micrograph from sample A1-4982.2 showing example of NGBC containing bridging cements that create a rectangular shaped pore.

SAMPLE: 2/26/95-2, MONTEREY FORMATION

Flat, Mating Contacts

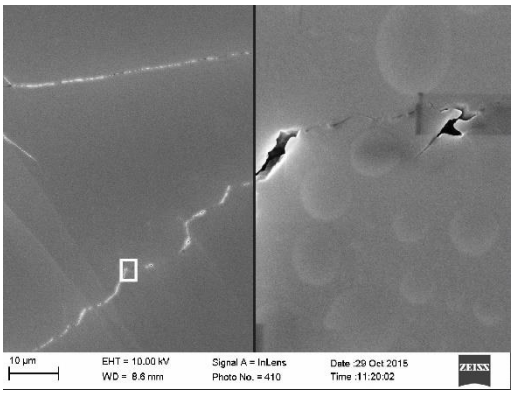

Figure B.283: Inlens SE micrograph from sample 2/26/95-2 showing example of NGBC containing a flat, mating contact.

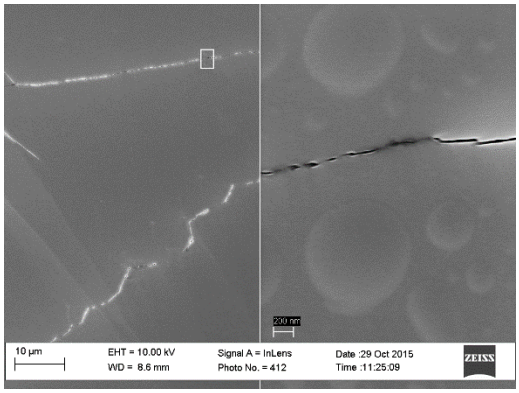

Figure B.284: Inlens SE micrograph from sample 2/26/95-2 showing example of NGBC containing a flat, mating contact.

Cuspate-lobate

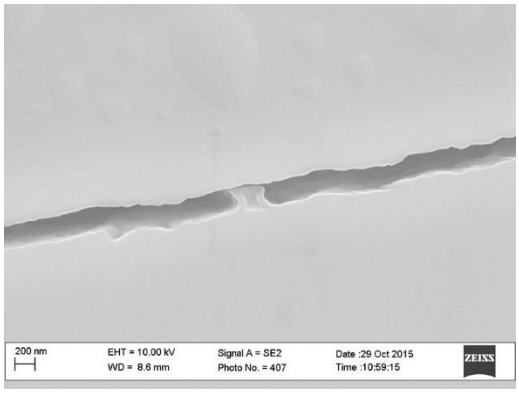

Figure B.285: Inlens SE micrograph from sample 2/26/95-2 showing example of NGBC containing a cuspate-lobate texture.

Meniscus shaped Pore

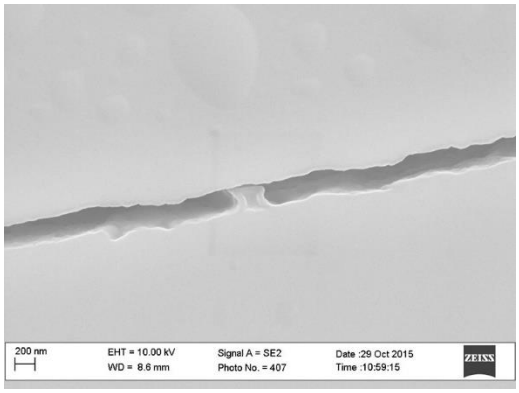

Figure B.286: Inlens SE micrograph from sample 2/26/95-2 showing example of NGBC containing bridging cements that create a meniscus shaped pore.

Appendix C: NGBC Misorientation Plots

I investigated whether there is a relationship between the grain boundary aperture and the misorientation between 2 grain. To do this, misorientation values were obtained from Oxford's Channel 5 software using the misorientation profile feature. Prior to noise reduction, I obtained misorientation values relative to the first point of a line segment traversing the grain boundary. The first misorientation value at the neighboring grain was taken as the misorientation of the grain boundary between the two grain. The plots that follow are mean apertures of grain boundaries as a function of misorientation angle. I found no correlation between mean aperture and misorientation.

SAMPLE: NAM-2774.5, NEW ALBANY FORMATION

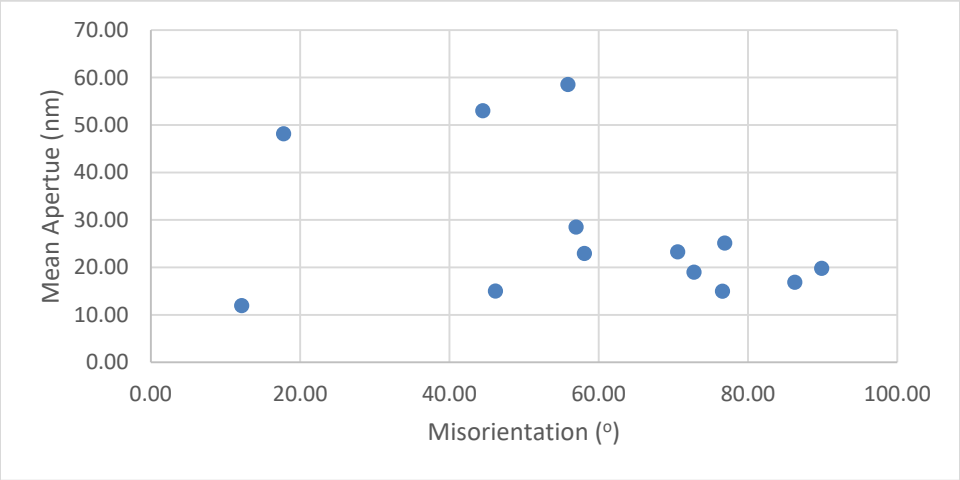

Figure C.1 : Mean aperture plotted as a function of misorientation angle for sample NAM-2774.5.

SAMPLE: NAM-2784, NEW ALBANY FORMATION

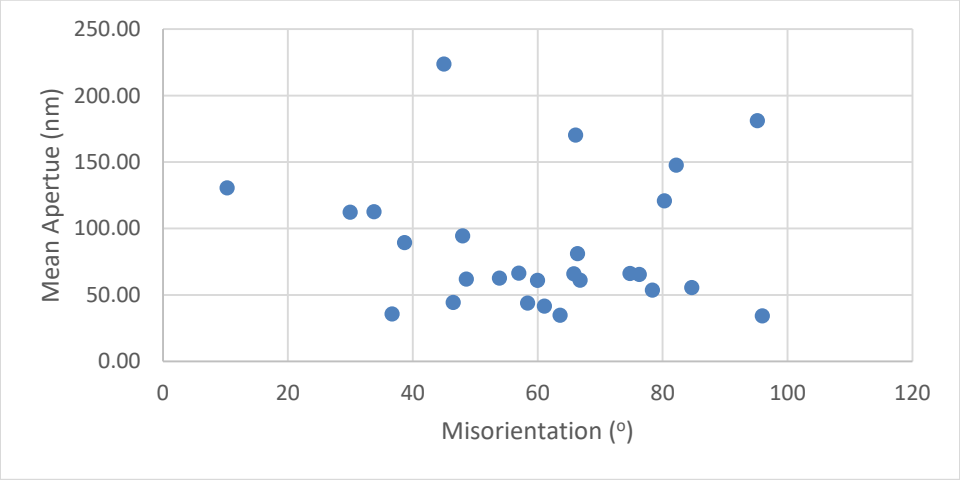

Figure C.2 : Mean aperture plotted as a function of misorientation angle for sample NAM-2784.

SAMPLE NAC-3590-1, NEW ALBANY FORMATION

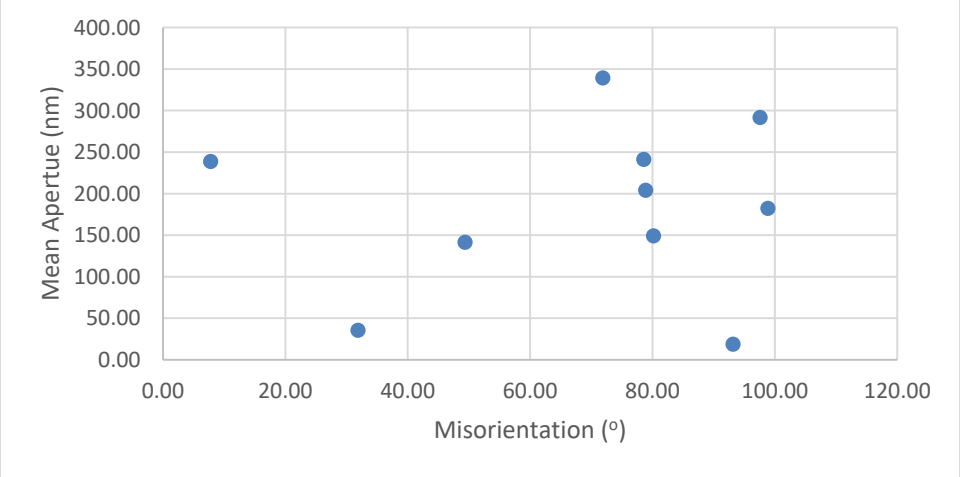

Figure C.3 : Mean aperture plotted as a function of misorientation angle for sample NAC-3590-1.

SAMPLE: NAC-3590-2, NEW ALBANY FORMATION

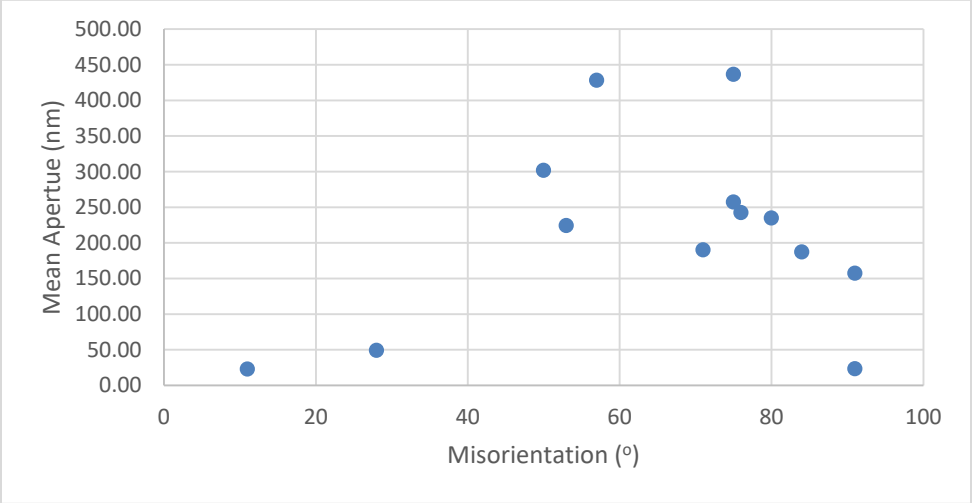

Figure C.4 : Mean aperture plotted as a function of misorientation angle for sample NAC-3590-2.

SAMPLE M-3658.5B, MARCELLUS FORMATION

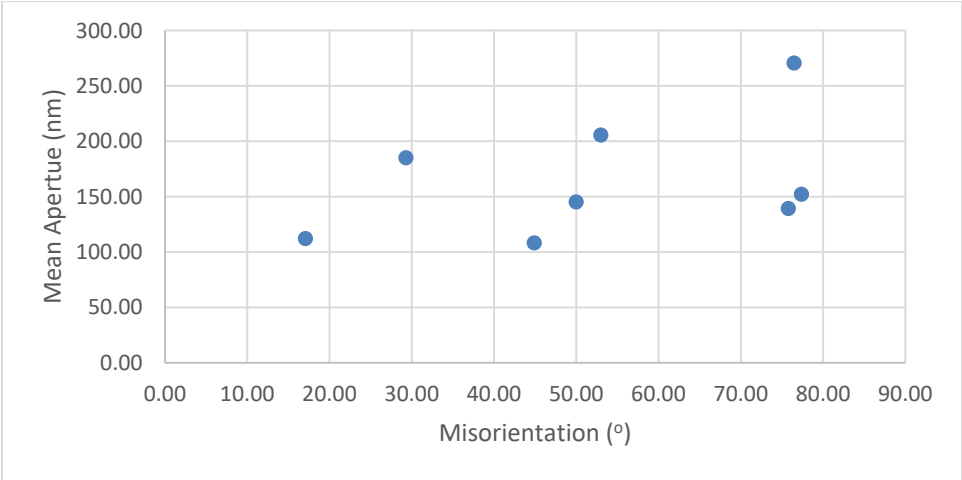

Figure C.5 : Mean aperture plotted as a function of misorientation angle for sample M-3658.5.

SAMPLE 06212-2, CAMPITO FORMATION

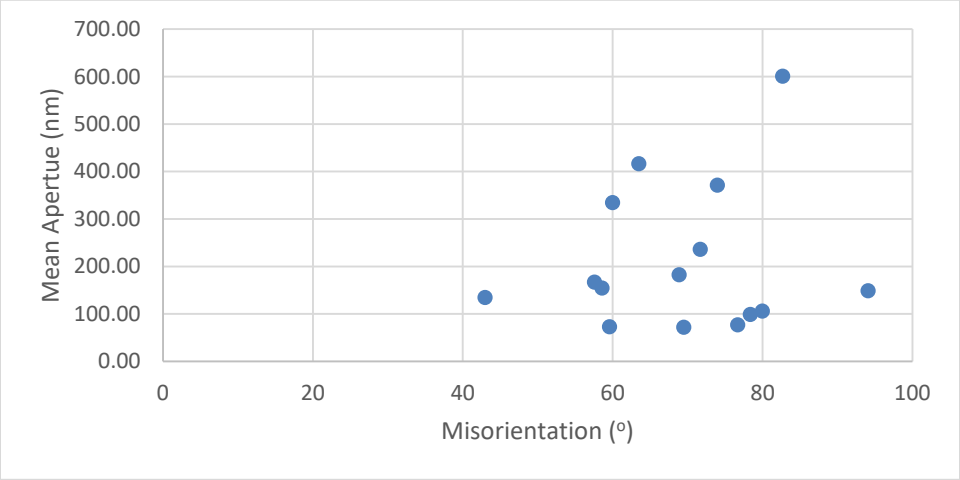

Figure C.6 : Mean aperture plotted as a function of misorientation angle for sample 06212-2.

SAMPLE: SFOT-1-10106.8, TRAVIS PEAK FORMATION

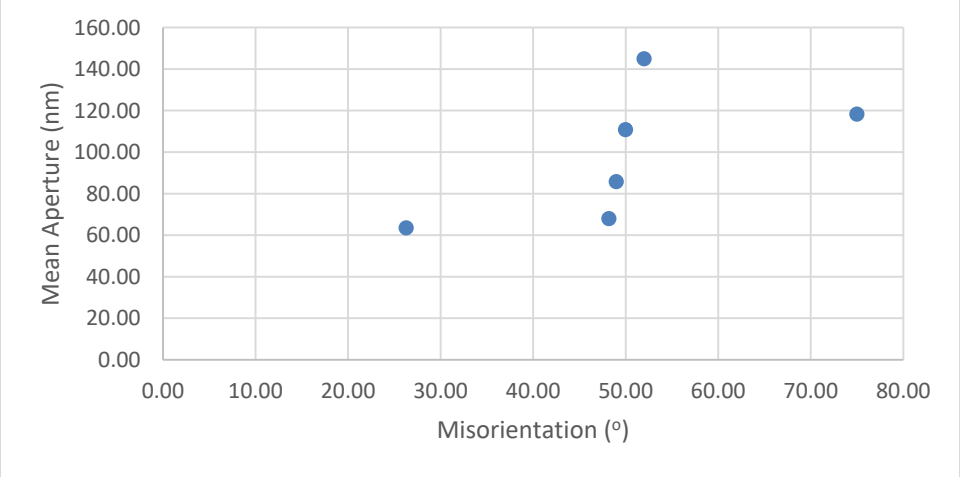

Figure C.7 : Mean aperture plotted as a function of misorientation angle for sample SFOT-1-10106.8.

Appendix D: TEM Imaging

SAMPLE: NAM-2774.5, NEW ALBANY FORMATION

Sample Preparation

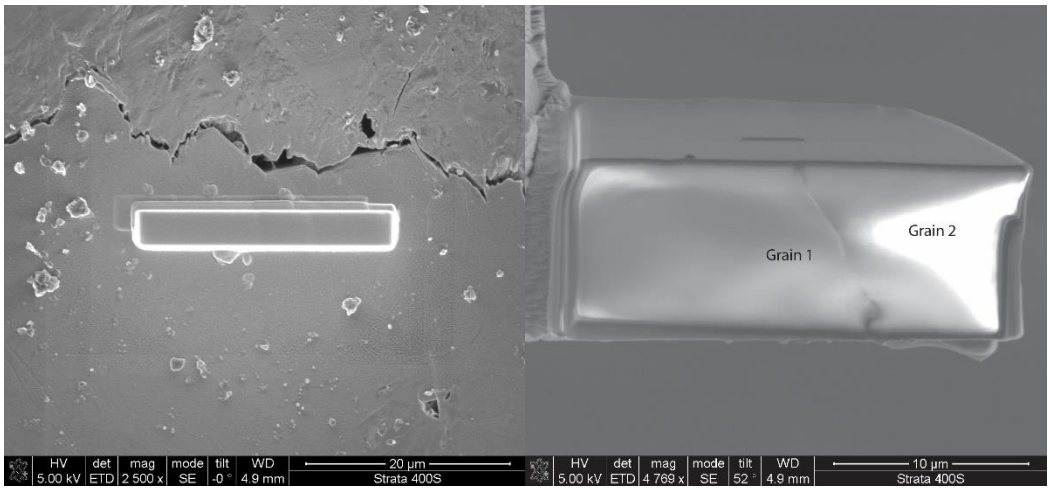

Figure D.1: Sample NAM-2744.5 with platinum coat prior to FIB cutting and lift out (left) and after liftout (right).

Bright Field TEM

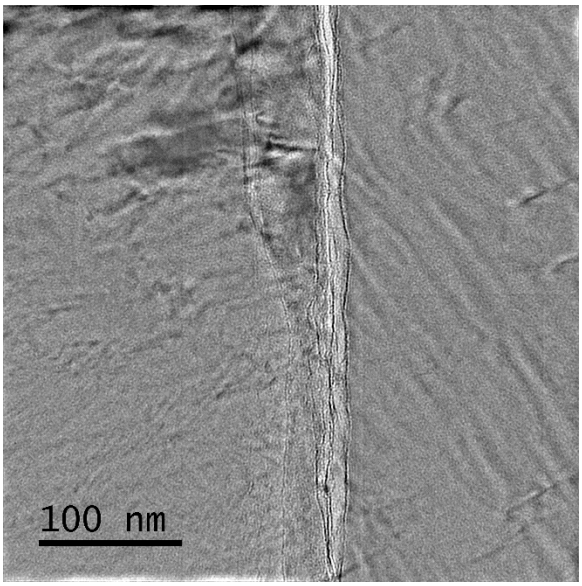

Figure D.2: Bright field TEM image of grain boundary 9 from sample NAM-7844.5.

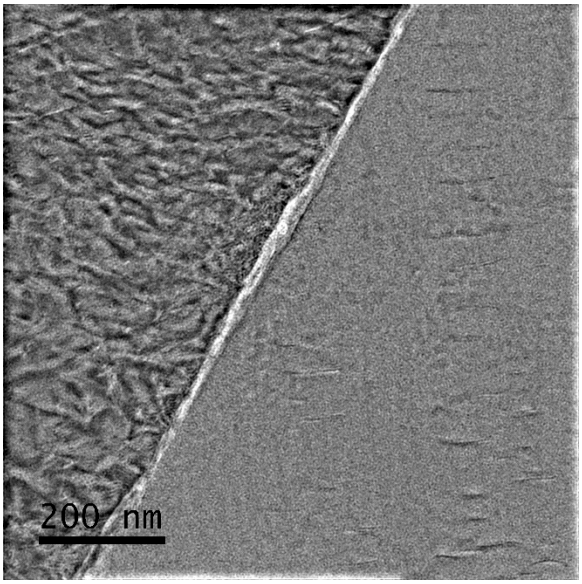

Figure D.3: Bright field TEM image of grain boundary 9 from sample NAM-2744.5.

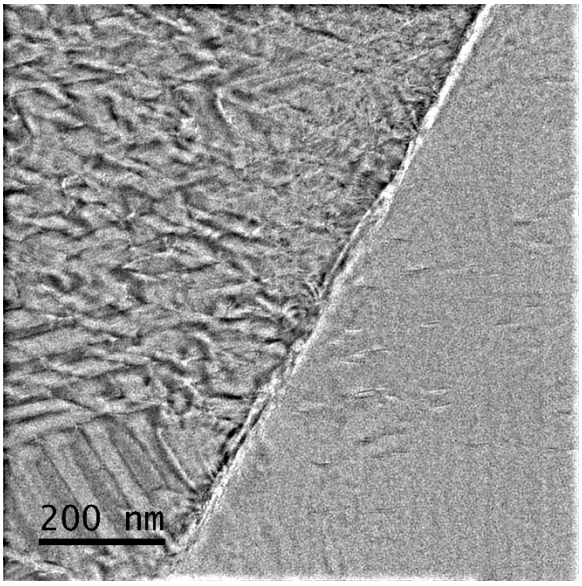

Figure D.4: Bright field TEM image of grain boundary 9 from sample NAM-2744.5.

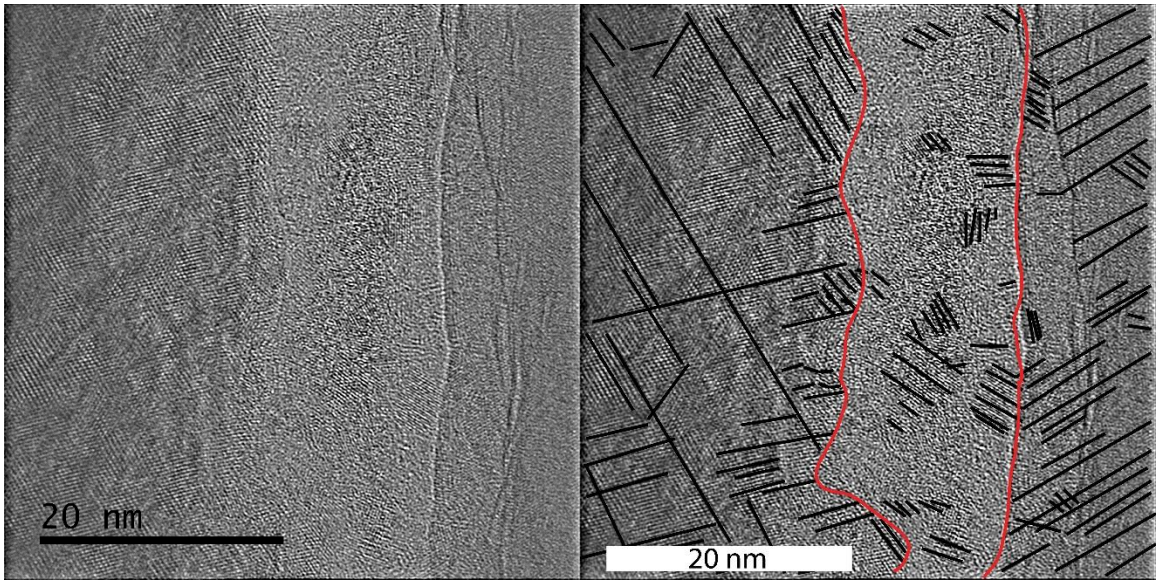

Figure D.5: Filtered HRTEM micrograph from grain boundary 9 in sample NAM-2774.5 (left) with lattice orientations highlighted with black lines and domains of lattice orientations outlined in red (left).

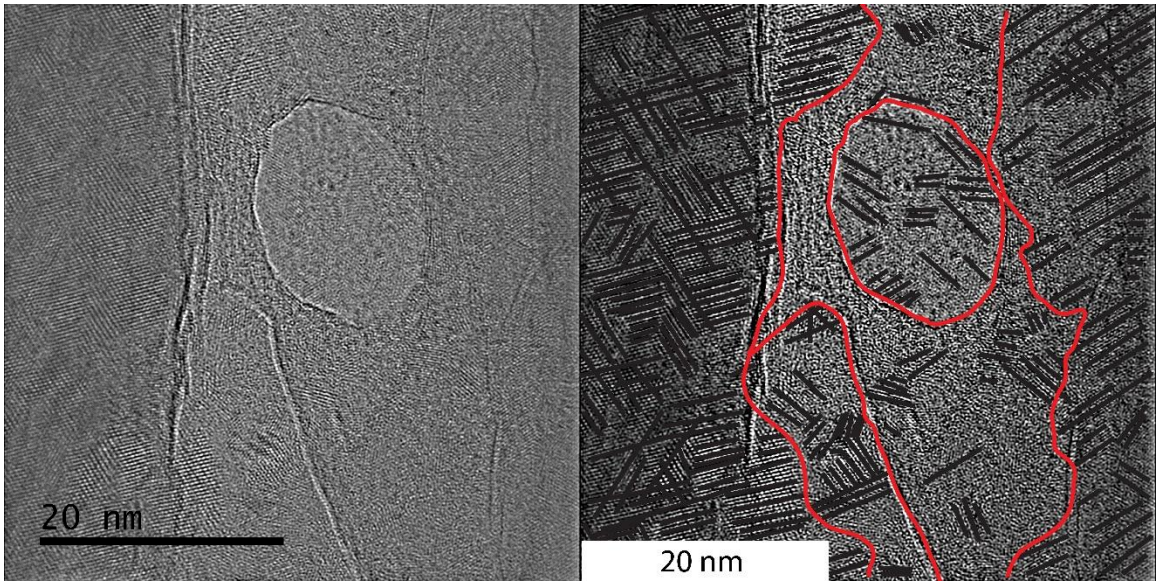

Figure D.6: Filtered HRTEM micrograph from grain boundary 9 in sample NAM-2774.5 (left) with lattice orientations highlighted with black lines and domains of lattice orientations outlined in red (left).

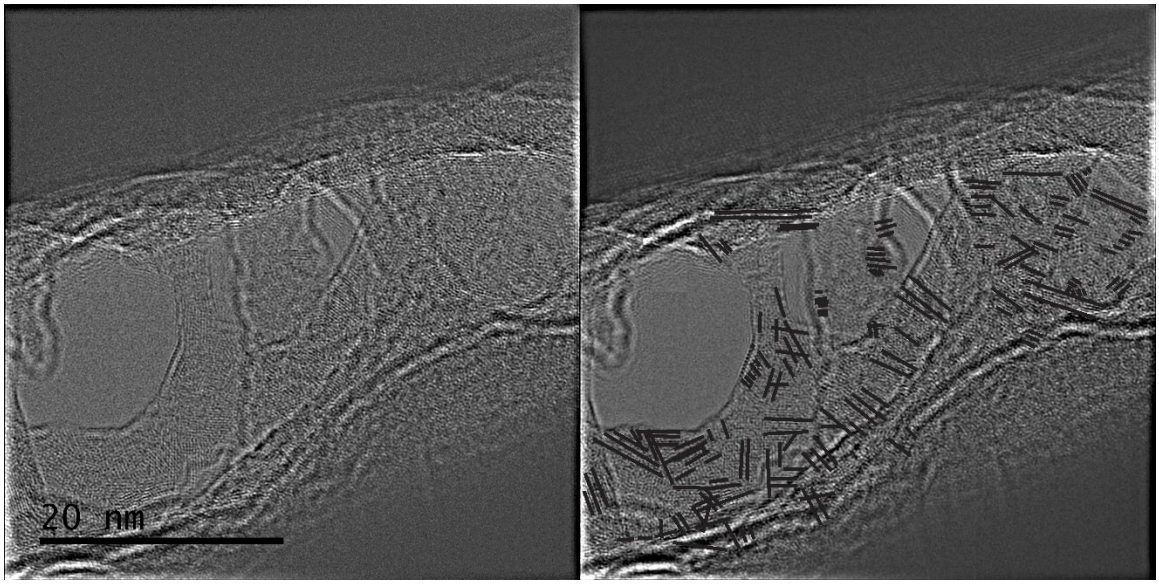

Figure D.7: Filtered HRTEM micrograph from grain boundary 9 in sample NAM-2774.5 (left) with lattice orientations highlighted with black lines and domains of lattice orientations outlined in red (left).

STEM Chemical Analysis

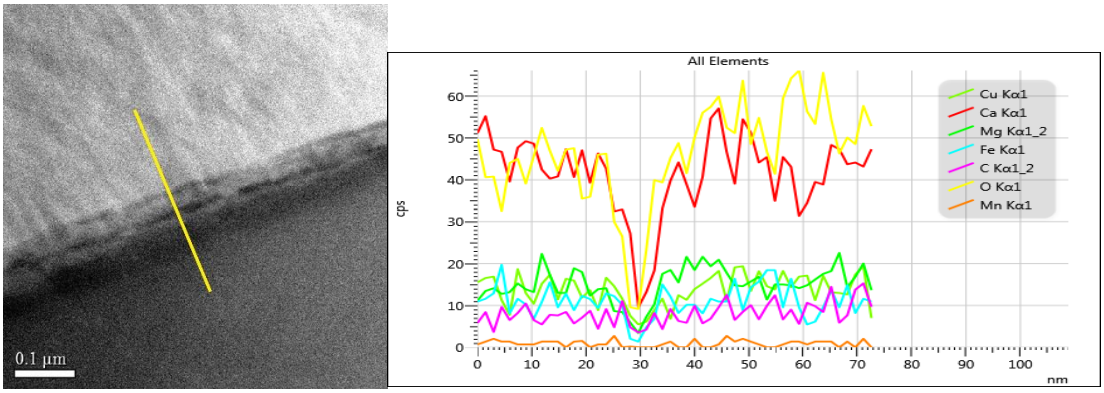

Figure D.8: Dark field TEM image with location of STEM linescan in yellow (left). Results of EDXS analysis along yellow line to left (right) from sample NAM-2744.5.

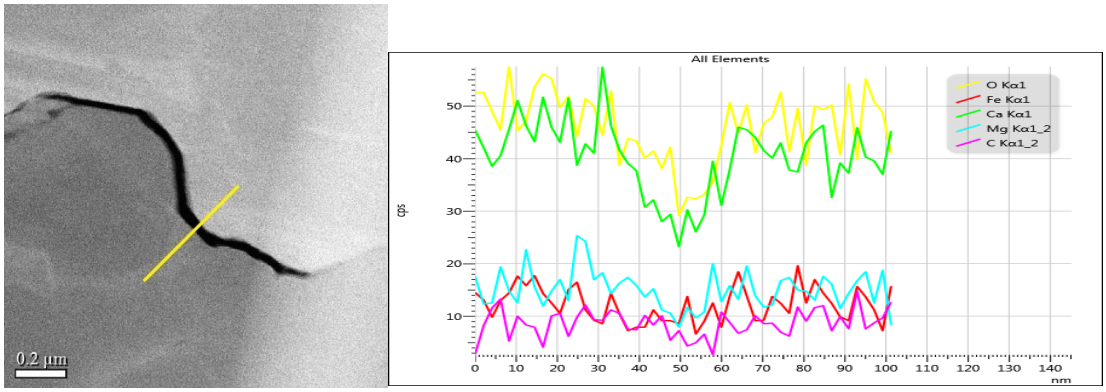

Figure D.9: Dark field TEM image with location of STEM linescan in yellow (left). Results of EDXS analysis along yellow line to left (right) from sample NAM-2744.5.

BRTC1-12421, BARNETT FORMATION

Sample Preparation

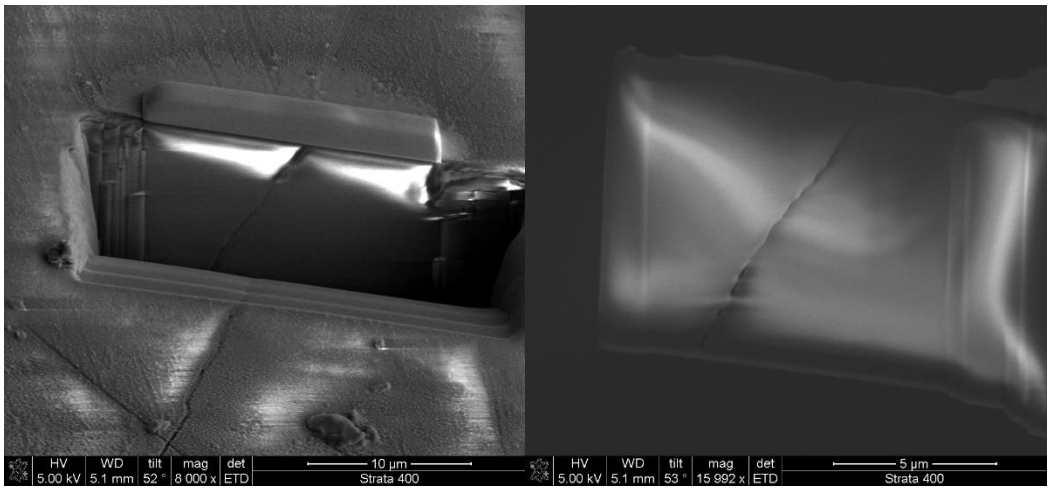

Figure D.10: Sample BRTC1-12421 with platinum coat after fib cutting and prior to lift out (left) and after liftout (right).

Bright Field TEM

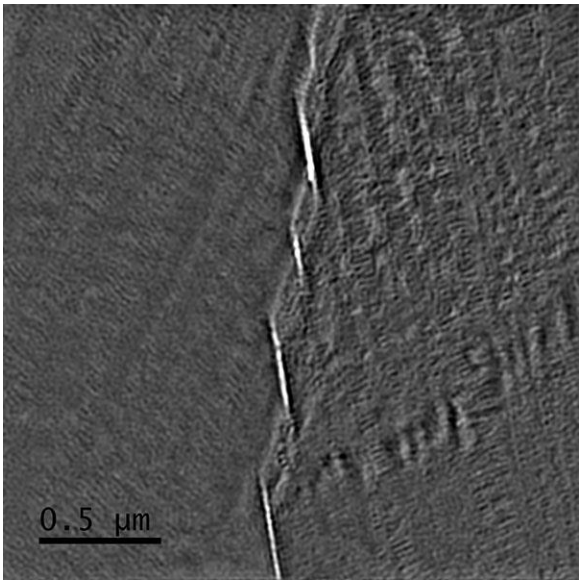

Figure D.11: Bright field TEM image of grain boundary 1 from sample BRTC1-12421.

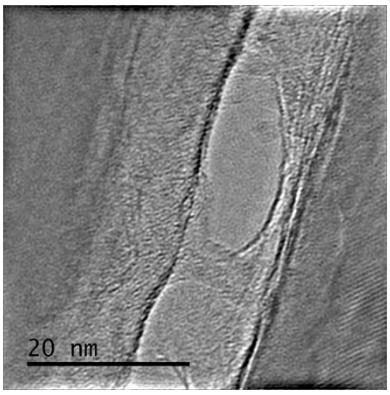

Figure D.12: Bright field TEM image of grain boundary 1 from sample BRTC1-12421.

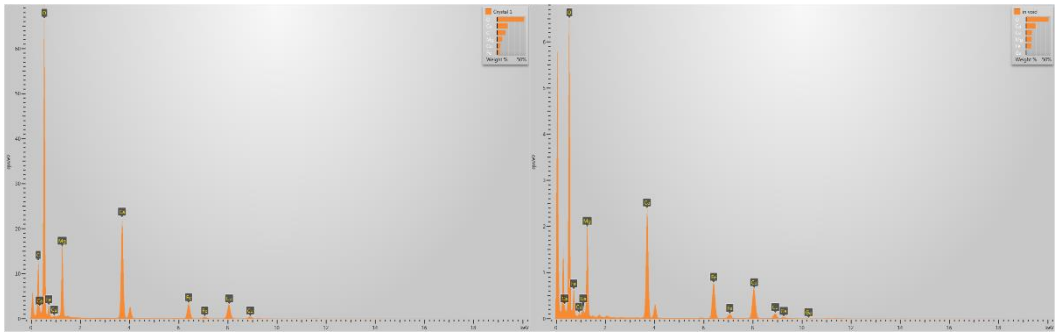

Figure D.13: Results of spot analysis from a calcite grain (left) and within a grain boundary void withing grain boundary 1 of sample BRTC1-12421.

References

Alcantar, N., Israelachvili, J., and Boles, J., 2003, Forces and ionic transport between mica surfaces: implications for pressure solution: Geochimica et Cosmochimica Acta, v. 67, no. 7, p. 1289–1304, doi: 10.1016/S0016-7037(02)01270-X.

Alcantar, N., Israelachvili, J., and Boles, J., 2003, Forces and ionic transport between mica surfaces: implications for pressure solution: Geochimica et Cosmochimica Acta, v. 67, no. 7, p. 1289–1304, doi: 10.1016/S0016-7037(02)01270-X.

Anders, M.H., Laubach, S.E., and Scholz, C.H., 2014, Microfractures: A review: Journal of Structural Geology, v. 69, p. 377–394, doi: 10.1016/j.jsg.2014.05.011.

Anders, M.H., Laubach, S.E., and Scholz, C.H., 2014, Microfractures: A review: Journal of Structural Geology, v. 69, p. 377–394, doi: 10.1016/j.jsg.2014.05.011.

Angheluta, L., Jettestuen, E., and Mathiesen, J., 2009, Thermodynamics and roughening of solid-solid interfaces: Physical Review E, v. 79, no. 3, doi: 10.1103/PhysRevE.79.031601.

Angheluta, L., Jettestuen, E., and Mathiesen, J., 2009, Thermodynamics and roughening of solid-solid interfaces: Physical Review E, v. 79, no. 3, doi: 10.1103/PhysRevE.79.031601.

Anzalone, A., Boles, J., Greene, G., Young, K., Israelachvili, J., and Alcantar, N., 2006, Confined fluids and their role in pressure solution: Chemical Geology, v. 230, no. 3, p. 220–231.

Banfield, J.F., 2000, Aggregation-Based Crystal Growth and Microstructure Development in Natural Iron Oxyhydroxide Biomineralization Products: Science, v. 289, no. 5480, p. 751–754, doi: 10.1126/science.289.5480.751.

Banfield, J.F., 2000, Aggregation-Based Crystal Growth and Microstructure Development in Natural Iron Oxyhydroxide Biomineralization Products: Science, v. 289, no. 5480, p. 751–754, doi: 10.1126/science.289.5480.751.

Batzle, M.L., and Simmons, G., 1977, Geothermal systems: Rocks, fluids, fractures: The Earth's Crust, p. 233–242.

Becker, A., 1995, Quartz pressure solution: influence of crystallographic orientation: Journal of Structural Geology, v. 17, no. 10, p. 1395–1405.

Bernard, S., Horsfield, B., Schulz, H.-M., Wirth, R., Schreiber, A., and Sherwood, N., 2012, Geochemical evolution of organic-rich shales with increasing maturity: A STXM and TEM study of the Posidonia Shale (Lower Toarcian, northern Germany): Marine and Petroleum Geology, v. 31, no. 1, p. 70–89.

Bisschop, J., and Dysthe, D.K., 2006, Instabilities and Coarsening of Stressed Crystal Surfaces in Aqueous Solution: Physical Review Letters, v. 96, no. 14, doi: 10.1103/PhysRevLett.96.146103.

Brown, S.R., 1995, Simple mathematical model of a rough fracture: Journal of Geophysical Research: Solid Earth, v. 100, no. B4, p. 5941–5952.

Bukovská, Z., Wirth, R., and Morales, L.F.G., 2015, Pressure solution in rocks: focused ion beam/transmission electron microscopy study on orthogneiss from South Armorican Shear Zone, France: Contributions to Mineralogy and Petrology, v. 170, no. 3, doi: 10.1007/s00410-015-1186-8.

Cacas, M.C., Ledoux, E., de Marsily, G., Barbreau, A., Calmels, P., Gaillard, B., and Margritta, R., 1990, Modeling fracture flow with a stochastic discrete fracture network: Calibration and validation: 2. The transport model: Water Resources Research, v. 26, no. 3, p. 491–500, doi: 10.1029/WR026i003p00491.

Cahn, J.W., and Hilliard, J.E., 1958, Free Energy of a Nonuniform System. I. Interfacial Free Energy: The Journal of Chemical Physics, v. 28, no. 2, p. 258–267, doi: 10.1063/1.1744102.

Cantwell, P.R., Tang, M., Dillon, S.J., Luo, J., Rohrer, G.S., and Harmer, M.P., 2014, Grain boundary complexions: Acta Materialia, v. 62, p. 1–48, doi: 10.1016/j.actamat.2013.07.037.

Cobbold, P.R., Zanella, A., Rodrigues, N., and Løseth, H., 2013, Bedding-parallel fibrous veins (beef and cone-in-cone): Worldwide occurrence and possible significance in terms of fluid overpressure, hydrocarbon generation and mineralization: Marine and Petroleum Geology, v. 43, p. 1–20, doi: 10.1016/j.marpetgeo.2013.01.010.

Cocks, A.C.F., and Ashby, M.F., 1982, On creep fracture by void growth: Progress in Materials Science, v. 27, no. 3–4, p. 189–244.

Croizé, D., Renard, F., Bjørlykke, K., and Dysthe, D.K., 2010, Experimental calcite dissolution under stress: Evolution of grain contact microstructure during pressure solution creep: Journal of Geophysical Research, v. 115, no. B9, doi: 10.1029/2010JB000869.

Curtis, M.E., Ambrose, R.J., and Sondergeld, C.H., 2010, Structural Characterization of Gas Shales on the Micro- and Nano-Scales, in SPE-137693-MS, Society of Petroleum Engineers, SPE.

Curtis, M.E., Cardott, B.J., Sondergeld, C.H., and Rai, C.S., 2012, Development of organic porosity in the Woodford Shale with increasing thermal maturity: Shale Gas and Shale Oil Petrology and Petrophysics, v. 103, p. 26–31, doi: 10.1016/j.coal.2012.08.004.

De Boer, R.B., Nagtegaal, P.J.C., and Duyvis, E.M., 1977, Pressure solution experiments on quartz sand: Geochimica et Cosmochimica Acta, v. 41, no. 2, p. 257IN1261-260IN4264.

de Meer, S., Spiers, C.J., and Nakashima, S., 2005, Structure and diffusive properties of fluid-filled grain boundaries: An in-situ study using infrared (micro) spectroscopy:

Earth and Planetary Science Letters, v. 232, no. 3–4, p. 403–414, doi: 10.1016/j.epsl.2004.12.030.

de Meer, S., Spiers, C.J., Peach, C.J., and Watanabe, T., 2002, Diffusive properties of fluid-filled grain boundaries measured electrically during active pressure solution: Earth and Planetary Science Letters, v. 200, no. 1, p. 147–157.

De Yoreo, J.J., Gilbert, P.U.P.A., Sommerdijk, N.A.J.M., Penn, R.L., Whitelam, S., Joester, D., Zhang, H., Rimer, J.D., Navrotsky, A., Banfield, J.F., Wallace, A.F., Michel, F.M., Meldrum, F.C., Colfen, H., et al., 2015, Crystallization by particle attachment in synthetic, biogenic, and geologic environments: Science, v. 349, no. 6247, p. aaa6760-aaa6760, doi: 10.1126/science.aaa6760.

den Brok, S.B., 1998, Effect of microcracking on pressure-solution strain rate: The Gratz grain-boundary model: Geology, v. 26, no. 10, p. 915–918.

Den Brok, S.W.J., and Morel, J., 2001, The effect of elastic strain on the microstructure of free surfaces of stressed minerals in contact with an aqueous solution: Geophysical Research Letters, v. 28, no. 4, p. 603–606.

Desbois, G., Urai, J.L., and de Bresser, J.H.P., 2012, Fluid distribution in grain boundaries of natural fine-grained rock salt deformed at low differential stress (Qom Kuh salt fountain, central Iran): Implications for rheology and transport properties: Journal of Structural Geology, v. 43, p. 128–143, doi: 10.1016/j.jsg.2012.07.002.

Desbois, G., Urai, J.L., Kukla, P.A., Konstanty, J., and Baerle, C., 2011, High-resolution 3D fabric and porosity model in a tight gas sandstone reservoir: a new approach to investigate microstructures from mm-to nm-scale combining argon beam cross-sectioning and SEM imaging: Journal of Petroleum Science and Engineering, v. 78, no. 2, p. 243–257.

Dewers, T., and Ortoleva, P., 1990, Force of crystallization during the growth of siliceous concretions: Geology, v. 18, no. 3, p. 204–207.

Doungkaew, N., 2016, Fracture Aperture Profiles as Indicators of Fracture Growth Enviornments: An Integrated Study of Fracture Aperture Growth in the Campito Formation of Eastern California [Thesis]: The University of Texas at Austin, 173 p.

Dutton, S.P., and Diggs, T.N., 1990, History of quartz cementation in the lower cretaceous Travis peak formation, East Texas: Journal of Sedimentary Research, v. 60, no. 2.

Dysthe, D.K., 2002, Fluid in mineral interfaces—molecular simulations of structure and diffusion: Geophysical Research Letters, v. 29, no. 7, doi: 10.1029/2001GL013208.

Dysthe, D.K., Podladchikov, Y., Renard, F., Feder, J., and Jamtveit, B., 2002, Universal scaling in transient creep: Physical Review Letters, v. 89, no. 24, p. 246102.

Dysthe, D.K., Renard, F., Feder, J., Jamtveit, B., Meakin, P., and Jøssang, T., 2003, High-resolution measurements of pressure solution creep: Physical Review E, v. 68, no. 1, doi: 10.1103/PhysRevE.68.011603.

Eichhubl, P., and Boles, J.R., 1998, Vein formation in relation to burial diagenesis in the Miocene Monterey Formation, Arroyo Burro Beach, Santa Barbara, California:

Eker, E., and Akin, S., 2006, Lattice Boltzmann simulation of fluid flow in synthetic fractures: Transport in porous media, v. 65, no. 3, p. 363–384.

Elliott, D., 1973, Diffusion flow laws in metamorphic rocks: Geological Society of America Bulletin, v. 84, no. 8, p. 2645–2664.

Engelder, T., Lash, G.G., and Uzcátegui, R.S., 2009, Joint sets that enhance production from Middle and Upper Devonian gas shales of the Appalachian Basin: AAPG bulletin, v. 93, no. 7, p. 857–889.

Evans, M.A., 1995, Fluid inclusions in veins from the Middle Devonian shales: A record of deformation conditions and fluid evolution in the Appalachian Plateau: Geological Society of America Bulletin, v. 107, no. 3, p. 327–339.

Fletcher, R.C., and Merino, E., 2001, Mineral growth in rocks: kinetic-rheological models of replacement, vein formation, and syntectonic crystallization: Geochimica et Cosmochimica Acta, v. 65, no. 21, p. 3733–3748.

Gale, J.F., Lander, R.H., Reed, R.M., and Laubach, S.E., 2010, Modeling fracture porosity evolution in dolostone: Journal of Structural Geology, v. 32, no. 9, p. 1201–1211.

Gale, J.F.W., and Holder, J., 2010, Natural fractures in some US shales and their importance for gas production, in Petroleum Geology: From Mature Basins to New Frontiers—Proceedings of the 7th Petroleum Geology Conference, Geological Society of London, p. 1131–1140.

Gale, J.F.W., Laubach, S.E., Olson, J.E., Eichhuble, P., and Fall, A., 2014, Natural Fractures in shale: A review and new observations: AAPG Bulletin, v. 98, no. 11, p. 2165–2216, doi: 10.1306/08121413151.

Gale, J.F.W., Reed, R.M., and Holder, J., 2007, Natural fractures in the Barnett Shale and their importance for hydraulic fracture treatments: AAPG Bulletin, v. 91, no. 4, p. 603–622, doi: 10.1306/11010606061.

Gasparrini, M., Sassi, W., and Gale, J.F.W., 2014, Natural sealed fractures in mudrocks: A case study tied to burial history from the Barnett Shale, Fort Worth Basin, Texas, USA: Marine and Petroleum Geology, v. 55, p. 122–141, doi: 10.1016/j.marpetgeo.2013.12.006.

Ghoussoub, J., and Leroy, Y.M., 2001, Solid–fluid phase transformation within grain boundaries during compaction by pressure solution: Journal of the Mechanics and Physics of Solids, v. 49, no. 10, p. 2385–2430.

Gibbs, J.W., 1878, On the equilibrium of heterogeneous substances: American Journal of Science, , no. 96, p. 441–458.

Gottstein, G., and Shvindlerman, L.S., 2010, Grain boundary migration in metals: thermodynamics, kinetics, applications: Taylor & Francis, Boca Raton.

Gratier, J.-P., 1993, Experimental pressure solution of halite by an indenter technique: Geophysical Research Letters, v. 20, no. 15, p. 1647–1650.

Gratier, J.-P., Dysthe, D.K., and Renard, F., 2013, The Role of Pressure Solution Creep in the Ductility of the Earth's Upper Crust, in Advances in Geophysics, Elsevier, p. 47–179.

Gratier, J.-P., Frery, E., Deschamps, P., Royne, A., Renard, F., Dysthe, D., Ellouz-Zimmerman, N., and Hamelin, B., 2012, How travertine veins grow from top to bottom and lift the rocks above them: The effect of crystallization force: Geology, v. 40, no. 11, p. 1015–1018, doi: 10.1130/G33286.1.

Gratier, J.-P., Guiguet, R., Renard, F., Jenatton, L., and Bernard, D., 2009, A pressure solution creep law for quartz from indentation experiments: Journal of Geophysical Research, v. 114, no. B3, doi: 10.1029/2008JB005652.

Gratier, J.-P., Renard, F., and Labaume, P., 1999, How pressure solution creep and fracturing processes interact in the upper crust to make it behave in both a brittle and viscous manner: Journal of Structural Geology, v. 21, no. 8, p. 1189–1197.

Greene, G.W., Kristiansen, K., Meyer, E.E., Boles, J.R., and Israelachvili, J.N., 2009, Role of electrochemical reactions in pressure solution: Geochimica et Cosmochimica Acta, v. 73, no. 10, p. 2862–2874, doi: 10.1016/j.gca.2009.02.012.

Hardebol, N.J., Callot, J.P., Bertotti, G., and Faure, J.L., 2009, Burial and temperature evolution in thrust belt systems: Sedimentary and thrust sheet loading in the SE Canadian Cordillera: Burial History Appraisal Of SE Canadian Cordillera: Tectonics, v. 28, no. 3, p. n/a-n/a, doi: 10.1029/2008TC002335.

Hay, R.S., and Evans, B., 1988, Intergranular distribution of pore fluid and the nature of high-angle grain boundaries in limestone and marble: Journal of Geophysical Research: Solid Earth, v. 93, no. B8, p. 8959–8974.

Heidug, W.K., 1995, Intergranular solid-fluid phase transformations under stress: The effect of surface forces: Journal of Geophysical Research: Solid Earth, v. 100, no. B4, p. 5931–5940.

Hickman, S.H., and Evans, B., 1991, Experimental pressure solution in halite: the effect of grain/interphase boundary structure: Journal of the Geological Society, v. 148, no. 3, p. 549–560.

Hickman, S.H., and Evans, B., 1995, Kinetics of pressure solution at halite-silica interfaces and intergranular clay films: Journal of Geophysical Research: Solid Earth, v. 100, no. B7, p. 13113–13132.

Hood, S.D., Nelson, C.S., and Kamp, P.J., 2003, Modification of fracture porosity by multiphase vein mineralization in an Oligocene nontropical carbonate reservoir, Taranaki Basin, New Zealand: AAPG bulletin, v. 87, no. 10, p. 1575–1597.

Hull, D., and Rimmer, D.E., 1959, The growth of grain-boundary voids under stress: Philosophical Magazine, v. 4, no. 42, p. 673–687.

Israelachvili, J.N., Kristiansen, K., Gebbie, M.A., Lee, D.W., Donaldson, S.H., Das, S., Rapp, M.V., Banquy, X., Valtiner, M., and Yu, J., 2013, The Intersection of Interfacial Forces and Electrochemical Reactions: The Journal of Physical Chemistry B, v. 117, no. 51, p. 16369–16387, doi: 10.1021/jp408144g.

Jettestuen, E., Bisschop, J., and Dysthe, D.K., 2009, Dissolution–precipitation recrystallization of miscut crystal surfaces under stress: Journal of Crystal Growth, v. 311, no. 6, p. 1576–1583.

Kalkreuth, W., and McMechan, M., 1996, Coal rank and burial history of Cretaceous-Tertiary strata in the Grande Cache and Hinton areas, Alberta, Canada: implications for fossil fuel exploration: Canadian Journal of Earth Sciences, v. 33, no. 6, p. 938–957.

Kang, S.-J.L., 2004, Sintering: densification, grain growth and microstructure: Butterworth-Heinemann.

Karcz, Z., Aharonov, E., Ertas, D., Polizzotti, R., and Scholz, C.H., 2008, Deformation by dissolution and plastic flow of a single crystal sodium chloride indenter: An experimental study under the confocal microscope: Journal of Geophysical Research: Solid Earth, v. 113, no. B4.

Keller, M.A., and Isaacs, C.M., 1985, An evaluation of temperature scales for silica diagenesis in diatomaceous sequences including a new approach based on the Miocene Monterey Formation, California: Geo-Marine Letters, v. 5, no. 1, p. 31–35.

Koehn, D., Malthe-Sørenssen, A., and Passchier, C.W., 2006, The structure of reactive grain-boundaries under stress containing confined fluids: Chemical Geology, v. 230, no. 3–4, p. 207–219, doi: 10.1016/j.chemgeo.2006.02.026.

Kristiansen, K., Valtiner, M., Greene, G.W., Boles, J.R., and Israelachvili, J.N., 2011, Pressure solution–The importance of the electrochemical surface potentials: Geochimica et Cosmochimica Acta, v. 75, no. 22, p. 6882–6892.

Kruhl, J.H., 2001, Crystallographic control on the development of foam textures in quartz, plagioclase and analogue material: International Journal of Earth Sciences, v. 90, no. 1, p. 104–117.

Kruhl, J.H., and Peternell, M., 2002, The equilibration of high-angle grain boundaries in dynamically recrystallized quartz: the effect of crystallography and temperature: Micro structural Processes: A Special Issue in Honor of the Career Contributions

of R.H. Vernon, v. 24, no. 6–7, p. 1125–1137, doi: 10.1016/S0191-8141(01)00096-7.

Kruhl, J.H., Wirth, R., and Morales, L.F.G., 2013, Quartz grain boundaries as fluid pathways in metamorphic rocks: QUARTZ GRAIN BOUNDARIES: Journal of Geophysical Research: Solid Earth, v. 118, no. 5, p. 1957–1967, doi: 10.1002/jgrb.50099.

Lander, R.H., and Laubach, S.E., 2015, Insights into rates of fracture growth and sealing from a model for quartz cementation in fractured sandstones: Geological Society of America Bulletin, v. 127, no. 3–4, p. 516–538.

Lander, R.H., Larese, R.E., and Bonnell, L.M., 2008, Toward more accurate quartz cement models: The importance of euhedral versus noneuhedral growth rates: AAPG Bulletin, v. 92, no. 11, p. 1537–1563, doi: 10.1306/07160808037.

Landry, C.J., Eichhubl, P., Prodanović, M., and Wilkins, S., 2016, Nanoscale grain boundary channels in fracture cement enhance flow in mudrocks: Nanoscale Grain Boundary Channels in Fracture Cement: Journal of Geophysical Research: Solid Earth, v. 121, no. 5, p. 3366–3376, doi: 10.1002/2016JB012810.

Larala, V.J., Johnson, W.C., and Voorhees, P.W., 1989, The kinetics of ostwald ripening in stressed solids: The low volume fraction limit: Scripta metallurgica, v. 23, no. 10, p. 1749–1754.

Laubach, S.E., 2003, Practical approaches to identifying sealed and open fractures: AAPG bulletin, v. 87, no. 4, p. 561–579.

Laubach, S.E., and Ward, M.E., 2006, Diagenesis in porosity evolution of opening-mode fractures, Middle Triassic to Lower Jurassic La Boca Formation, NE Mexico: Tectonophysics, v. 419, no. 1–4, p. 75–97, doi: 10.1016/j.tecto.2006.03.020.

Lehner, F.K., 1995, A model for intergranular pressure solution in open systems: Tectonophysics, v. 245, no. 3–4, p. 153–170, doi: 10.1016/0040-1951(94)00232-X.

Lehner, F.K., and Bataille, J., 1984, Nonequilibrium thermodynamics of pressure solution: Pure and Applied Geophysics, v. 122, no. 1, p. 53–85.

Liteanu, E., Niemeijer, A., Spiers, C.J., Peach, C.J., and Bresser, J.H.P., 2012, The effect of CO2 on creep of wet calcite aggregates: Journal of Geophysical Research: Solid Earth, v. 117, no. B3.

Loucks, R.G., Reed, R.M., Ruppel, S.C., and Hammes, U., 2012, Spectrum of pore types and networks in mudrocks and a descriptive classification for matrix-related mudrock pores: AAPG bulletin, v. 96, no. 6, p. 1071–1098.

Loucks, R.G., Reed, R.M., Ruppel, S.C., and Jarvie, D.M., 2009, Morphology, Genesis, and Distribution of Nanometer-Scale Pores in Siliceous Mudstones of the

Mississippian Barnett Shale: Journal of Sedimentary Research, v. 79, no. 12, p. 848–861, doi: 10.2110/jsr.2009.092.

Luo, M., Baker, M.R., and LeMone, D.V., 1994, Distribution and generation of the overpressure system, eastern Delaware basin, western Texas and southern New Mexico: AAPG bulletin, v. 78, no. 9, p. 1386–1405.

Mancktelow, N.S., and Pennacchioni, G., 2004, The influence of grain boundary fluids on the microstructure of quartz-feldspar mylonites: Journal of Structural Geology, v. 26, no. 1, p. 47–69.

Mancktelow, N.S., Grujic, D., and Johnson, E.L., 1998, An SEM study of porosity and grain boundary microstructure in quartz mylonites, Simplon Fault Zone, Central Alps: Contributions to Mineralogy and Petrology, v. 131, no. 1, p. 71–85.

McCrory, P.A., 1995, Neogene geohistory analysis of Santa Maria Basin, California, and its relationship to transfer of central California to the Pacific plate: Geological Survey.

Milodowski, A.E., Gillespie, M.R., Naden, J., Fortey, N.J., Shepherd, T.J., Pearce, J.M., and Metcalfe, R., 1998, The petrology and paragenesis of fracture mineralization in the Sellafield area, west Cumbria: Proceedings of the Yorkshire Geological Society, v. 52, no. 2, p. 215–241.

Mullins, W.W., 1956, Two-Dimensional Motion of Idealized Grain Boundaries: Journal of Applied Physics, v. 27, no. 8, p. 900–904.

Nudelman, F., Sonmezler, E., Bomans, P.H.H., de With, G., and Sommerdijk, N.A.J.M., 2010, Stabilization of amorphous calcium carbonate by controlling its particle size: Nanoscale, v. 2, no. 11, p. 2436, doi: 10.1039/c0nr00432d.

Nunn, J.A., 2012, Burial and thermal history of the Haynesville shale: Implications for overpressure, gas generation, and natural hydrofracture:

Olanipekun, B.J., and Azmy, K., 2016, Genesis and morphology of intracrystalline nanopores and mineral micro inclusions hosted in burial dolomite crystals: Application of Broad Ion Beam-Scanning Electron Microscope (BIB-SEM): Marine and Petroleum Geology, v. 74, p. 1–11, doi: 10.1016/j.marpetgeo.2016.03.029.

Olgaard, D.L., and Fitz Gerald, J.D., 1993, Evolution of pore microstructures during healing of grain boundaries in synthetic calcite rocks: Contributions to Mineralogy and Petrology, v. 115, no. 2, p. 138–154.

Olson, J.E., Laubach, S.E., and Lander, R.H., 2009, Natural fracture characterization in tight gas sandstones: Integrating mechanics and diagenesis: AAPG bulletin, v. 93, no. 11, p. 1535–1549.

Oron, A.P., and Berkowitz, B., 1998, Flow in rock fractures: The local cubic law assumption reexamined: Water Resources Research, v. 34, no. 11, p. 2811–2825.

Paterson, M.S., 1973, Nonhydrostatic thermodynamics and its geologic applications: Reviews of Geophysics, v. 11, no. 2, p. 355–389.

Philip, Z.G., Jennings Jr, J.W., Olson, J.E., and Holder, J., 2002, Modeling coupled fracture-matrix fluid flow in geomechanically simulated fracture networks, in SPE Annual Technical Conference and Exhibition, Society of Petroleum Engineers.

Pollard, D.D., and Aydin, A., 1988, Progress in understanding jointing over the past century: Geological Society of America Bulletin, v. 100, no. 8, p. 1181–1204.

Priester, L., 2013, Grain Boundaries: Springer Netherlands, Dordrecht.

Putnis, A., 2002, Mineral replacement reactions: from macroscopic observations to microscopic mechanisms: Mineralogical Magazine, v. 66, no. 5, p. 689–708.

Putnis, A., and John, T., 2010, Replacement processes in the Earth's crust: Elements, v. 6, no. 3, p. 159–164.

Putnis, A., and Putnis, C.V., 2007, The mechanism of reequilibration of solids in the presence of a fluid phase: Journal of Solid State Chemistry, v. 180, no. 5, p. 1783–1786, doi: 10.1016/j.jssc.2007.03.023.

Raj, R., 1982, Creep in polycrystalline aggregates by matter transport through a liquid phase: Journal of Geophysical Research: Solid Earth, v. 87, no. B6, p. 4731–4739.

Raj, R., and Chyung, C.K., 1981, Solution-precipitation creep in glass ceramics: Acta Metallurgica, v. 29, no. 1, p. 159–166.

Read, W.T., and Shockley, W., 1950, Dislocation models of crystal grain boundaries: Physical Review, v. 78, no. 3, p. 275.

Renard, F., and Ortoleva, P., 1997, Water films at grain-grain contacts: Debye-Hückel, osmotic model of stress, salinity, and mineralogy dependence: Geochimica et Cosmochimica Acta, v. 61, no. 10, p. 1963–1970.

Renard, F., Ortoleva, P., and Gratier, J.P., 1997, Pressure solution in sandstones: influence of clays and dependence on temperature and stress: Tectonophysics, v. 280, no. 3, p. 257–266.

Renard, F., Park, A., Ortoleva, P., and Gratier, J.-P., 1999, An integrated model for transitional pressure solution in sandstones: Tectonophysics, v. 312, no. 2, p. 97–115.

Revil, A., 2001, Pervasive pressure solution transfer in a quartz sand: Journal of Geophysical Research: Solid Earth, v. 106, no. B5, p. 8665–8686, doi: 10.1029/2000JB900465.

Revil, A., Leroy, P., Ghorbani, A., Florsch, N., and Niemeijer, A.R., 2006, Compaction of quartz sands by pressure solution using a cole-cole distribution of relaxation times: Journal of Geophysical Research: Solid Earth, v. 111, no. B9.

Riedel, H., 1987, Fracture at high temperatures: Springer-Verlag, Berlin; New York.

Robin, P.-Y.F., 1978, Pressure solution at grain-to-grain contacts: Geochimica et Cosmochimica Acta, v. 42, no. 9, p. 1383–1389.

Rohrer, G.S., 2011, Grain boundary energy anisotropy: a review: Journal of Materials Science, v. 46, no. 18, p. 5881–5895, doi: 10.1007/s10853-011-5677-3.

Rollett, A., Humphreys, F.J., Rohrer, G.S., and Hatherly, M., 2004, Recrystallization and related annealing phenomena: Elsevier.

Røyne, A., and Dysthe, D.K., 2012, Rim formation on crystal faces growing in confinement: Journal of Crystal Growth, v. 346, no. 1, p. 89–100, doi: 10.1016/j.jcrysgro.2012.03.019.

Røyne, A., Meakin, P., Malthe-Sørenssen, A., Jamtveit, B., and Dysthe, D.K., 2011, Crack propagation driven by crystal growth: EPL (Europhysics Letters), v. 96, no. 2, p. 24003, doi: 10.1209/0295-5075/96/24003.

Rutter, E.H., and Elliott, D., 1976, The kinetics of rock deformation by pressure solution [and discussion]: Philosophical Transactions of the Royal Society of London A: Mathematical, Physical and Engineering Sciences, v. 283, no. 1312, p. 203–219.

Schenk, O., and Urai, J.L., 2004, Microstructural evolution and grain boundary structure during static recrystallization in synthetic polycrystals of Sodium Chloride containing saturated brine: Contributions to Mineralogy and Petrology, v. 146, no. 6, p. 671–682.

Schmid, S.M., Panozzo, R., and Bauer, S., 1987, Simple shear experiments on calcite rocks: rheology and microfabric: Journal of structural Geology, v. 9, no. 5–6, p. 747–778.

Secor, D.T., 1965, Role of fluid pressure in jointing: American Journal of Science, v. 263, no. 8, p. 633–646, doi: 10.2475/ajs.263.8.633.

Shukla, R., Ranjith, P., Haque, A., and Choi, X., 2010, A review of studies on CO 2 sequestration and caprock integrity: Fuel, v. 89, no. 10, p. 2651–2664.

Sorby, H.C., 1864, On the direct correlation of mechanical and chemical forces: Journal of the Franklin Institute, v. 77, no. 2, p. 97–106.

Spiers, C., and Schutjens, P., 1999, Intergranular Pressure Solution in NaCl: Grain-to-Grain Contact Experiments under the Optical Microscope: Revue de l'Institut Français du Pétrole, v. 54, no. 6, p. 729–750.

Spiers, C.J., and Schutjens, P.M., 1990, Densification of crystalline aggregates by fluid-phase diffusional creep, in Deformation processes in minerals, ceramics and rocks, Springer, p. 334–353.

Spiers, C.J., S. De Meer, A. R. Niemeijer, and X. Zhang, 2003, Kinetics of rock deformation by pressure solution and the role of thin aqueous films: Frontiers Science Series, p. 129–158.

Steiger, M., 2005, Crystal growth in porous materials—II: Influence of crystal size on the crystallization pressure: Journal of crystal growth, v. 282, no. 3, p. 470–481.

Stephens, C.J., Ladden, S.F., Meldrum, F.C., and Christenson, H.K., 2010, Amorphous Calcium Carbonate is Stabilized in Confinement: Advanced Functional Materials, v. 20, no. 13, p. 2108–2115, doi: 10.1002/adfm.201000248.

Strąpoć, D., Mastalerz, M., Schimmelmann, A., Drobniak, A., and Hasenmueller, N.R., 2010, Geochemical constraints on the origin and volume of gas in the New Albany Shale (Devonian–Mississippian), eastern Illinois Basin: AAPG Bulletin, v. 94, no. 11, p. 1713–1740, doi: 10.1306/06301009197.

Stünitz, H., and Gerald, J.F., 1993, Deformation of granitoids at low metamorphic grade. II: Granular flow in albite-rich mylonites: Tectonophysics, v. 221, no. 3–4, p. 299–324.

Sutton, A.P., and Balluffi, R.W., 1995, Interfaces in crystalline materials:

Tada, R., and Siever, R., 1986, Experimental knife-edge pressure solution of halite: Geochimica et Cosmochimica Acta, v. 50, no. 1, p. 29–36.

Tokan-Lawal, A., Prodanovic, M., Landry, C.J., and Eichhubl, P., 2017, Influence of Numerical Cementation on Multiphase Displacement in Rough Fractures: Transport in Porous Media, v. 116, no. 1, p. 275–293, doi: 10.1007/s11242-016-0773-0.

Twiss, R.J., and Moores, E.M., 1992, Structural geology: Macmillan.

Urai, J.L., 1983, Water assisted dynamic recrystallization and weakening in polycrystalline bischofite: Tectonophysics, v. 96, no. 1–2, p. 125–157.

Urai, J.L., Means, W.D., and Lister, G.S., 1986, Dynamic recrystallization of minerals: Mineral and rock deformation: laboratory studies: The Paterson volume, p. 161–199.

van Noort, R., Spiers, C.J., and Peach, C.J., 2007, Effects of orientation on the diffusive properties of fluid-filled grain boundaries during pressure solution: Physics and Chemistry of Minerals, v. 34, no. 2, p. 95–112, doi: 10.1007/s00269-006-0131-9.

Van Noort, R., Spiers, C.J., and Peach, C.J., 2011, Structure and properties of loaded silica contacts during pressure solution: impedance spectroscopy measurements under hydrothermal conditions: Physics and Chemistry of minerals, v. 38, no. 7, p. 501.

van Noort, R., Visser, H.J.M., and Spiers, C.J., 2008, Influence of grain boundary structure on dissolution controlled pressure solution and retarding effects of grain boundary healing: Journal of Geophysical Research, v. 113, no. B3, doi: 10.1029/2007JB005223.

Vernon, R.H., 2004, A practical guide to rock microstructure: Cambridge university press.

Vollbrecht, A., Rust, S., and Weber, K., 1991, Development of microcracks in granites during cooling and uplift: examples from the Variscan basement in NE Bavaria, Germany: Journal of Structural Geology, v. 13, no. 7, p. 787–799.

Voorhees, P.W., 1985, The theory of Ostwald ripening: Journal of Statistical Physics, v. 38, no. 1, p. 231–252.

Walderhaug, O., 1996, Kinetic modeling of quartz cementation and porosity loss in deeply buried sandstone reservoirs: AAPG bulletin, v. 80, no. 5, p. 731–745.

Walderhaug, O., 2000, Modeling quartz cementation and porosity in Middle Jurassic Brent Group sandstones of the Kvitebjørn field, northern North Sea: AAPG bulletin, v. 84, no. 9, p. 1325–1339.

Walderhaug, O., Lander, R.H., Bjørkum, P.A., Oelkers, E.H., Bjørlykke, K., and Nadeau, P.H., 2009, Modelling quartz cementation and porosity in reservoir sandstones: examples from the Norwegian continental shelf: Quartz cementation in sandstones, p. 39–49.

Walton, I., and McLennan, J., 2013, The role of natural fractures in shale gas production, in ISRM International Conference for Effective and Sustainable Hydraulic Fracturing, International Society for Rock Mechanics.

Wang, F.P., and Reed, R.M., 2009, Pore Networks and Fluid Flow in Gas Shales, in SPE-124253-MS, Society of Petroleum Engineers, SPE.

Wassmann, S., and Stöckhert, B., 2013, Rheology of the plate interface—dissolution precipitation creep in high pressure metamorphic rocks: Tectonophysics, v. 608, p. 1–29.

Weyl, P.K., 1959, Pressure solution and the force of crystallization: a phenomenological theory: Journal of Geophysical Research, v. 64, no. 11, p. 2001–2025, doi: 10.1029/JZ064i011p02001.

Wiltschko, D.V., and Morse, J.W., 2001, Crystallization pressure versus “crack seal” as the mechanism for banded veins: Geology, v. 29, no. 1, p. 79–82.

Wirth, R., 2009, Focused Ion Beam (FIB) combined with SEM and TEM: Advanced analytical tools for studies of chemical composition, microstructure and crystal structure in geomaterials on a nanometre scale: Chemical Geology, v. 261, no. 3–4, p. 217–229, doi: 10.1016/j.chemgeo.2008.05.019.

Wolf, D., 1990, Structure-energy correlation for grain boundaries in fcc metals—IV. Asymmetrical twist (general) boundaries: Acta Metallurgica et Materialia, v. 38, no. 5, p. 791–798.

Wolf, D., and Merkle, K.L., 1992, Correlation between the structure and energy of grain boundaries in metals: Chapman & Hall(UK), 1992, p. 87–150.

Yan, M.F., Cannon, R.M., and Bowen, H.K., 1976, Grain boundary migration in ceramics: Massachusetts Institute of Technology, Materials Processing Center.

Zimmerman, R.W., and Bodvarsson, G.S., 1996, Hydraulic conductivity of rock fractures: Transport in porous media, v. 23, no. 1, p. 1–30.

Zoback, M.D., 2007, Reservoir geomechanics: Cambridge University Press, Cambridge.

Zubtsov, S., Renard, F., Gratier, J.-P., Guiguet, R., Dysthe, D.K., and Traskine, V., 2004, Experimental pressure solution compaction of synthetic halite/calcite aggregates: Tectonophysics, v. 385, no. 1–4, p. 45–57, doi: 10.1016/j.tecto.2004.04.016.